Green Energy and Technology

Jahangir Hossain
Apel Mahmud *Editors*

Large Scale Renewable Power Generation

Advances in Technologies for Generation, Transmission and Storage

Springer

Green Energy and Technology

For further volumes:
http://www.springer.com/series/8059

Jahangir Hossain · Apel Mahmud
Editors

Large Scale Renewable Power Generation

Advances in Technologies for Generation, Transmission and Storage

Springer

Editors
Jahangir Hossain
Griffith School of Engineering
Griffith University
Gold Coast, QLD
Australia

Apel Mahmud
Electrical and Electronics Engineering
Swinburne University of Technology
Hawthorn, VIC
Australia

ISSN 1865-3529 ISSN 1865-3537 (electronic)
ISBN 978-981-4585-29-3 ISBN 978-981-4585-30-9 (eBook)
DOI 10.1007/978-981-4585-30-9
Springer Singapore Heidelberg New York Dordrecht London

Library of Congress Control Number: 2014930184

Printed on acid-free paper

Springer is part of Springer Science+Business Media (www.springer.com)

Editorial Advisory Board

Reviewers

Preface

The electrical grid in the twenty-first century is experiencing major changes all over the world in order to become smarter, cleaner, more efficient, and reliable. Among different sources of renewable energy, wind and solar energy are gaining popularity in most countries. Due to the variable nature of renewable energy sources, in terms of power including real and reactive power, output voltage, and frequency, it is a major challenging issue for the current power industry to integrate large-scale wind and solar photovoltaic (PV) energy into the grid. There are over 69.68 GW of PV and 250 GW of wind power generation installed worldwide. More than 200 PV power plants have already been installed in the world, each of them generating an output of more than 10 MW. In these plants, 34 are located in Spain and 26 in Germany. The number of PV power plants will continue to rise. More than 250 PV power plants will be installed for the next few years. The output power of today's wind generators has exceeded 7 MW. For example, since 2011 ENERCON has been producing wind turbine E-126/7500 with a power capacity of 7.5 MW. Currently, Sway Turbine and Windtec Solutions are developing 10 MW wind turbine generators, which are expected to be commercially available by 2015.

This book is intended to cover the technical and regulatory issues related to the large-scale renewable power generation, transmission and distribution, storage, and protection to form a smart grid with sustainable environment. A main objective of the book is to show the relevance of large-scale renewable power generation and the role that this emerging field of technology can play for the transition toward a sustainable world. The latest developments and advances in technology, materials, systems, and processes in energy generation, transmission and distribution, energy storage, and protection are highlighted in this book.

The book is focused on different issues, such as generation, transmission and distribution, storage, and protection. It presents the critical issues related to large-scale renewable power generation, such as uncertainty modeling techniques, statistical characteristics of renewable sources, energy conversion efficiency, and compact and lightweight generation systems. It also contains the development of medium voltage converters for step-up-transformer-less direct grid integration of renewable generation units, grid codes, and resiliency analysis for large-scale renewable power generation, active power and frequency control, and HVDC transmission. The emerging SMES technology for controlling and integrating large-scale renewable power systems is also discussed. As the protection issues

with large-scale distributed renewable power systems will be different compared to the existing protection system for one-way power flow, this book will provide new protection technique for renewable generators.

"Taxonomy of Uncertainty Modeling Techniques in Renewable Energy System Studies" of this book discusses different uncertainty modeling tools used for renewable energy system studies and then the appropriate ones for renewable energies are identified. The probabilistic modeling and statistical characteristics of aggregated wind power in large electrical systems are discussed in "Probabilistic Modeling and Statistical Characteristics of Aggregate Wind Power" and the conversion efficiency improvement methodology for GaAs solar cells are presented in "Conversion Efficiency Improvement in GaAs Solar Cells." "Emerging SMES Technology into Energy Storage Systems and Smart Grid Applications" presents the application of superconducting magnetic energy storage (SMES) in the energy storage systems and the future smart grids. Different multilevel converter topologies with switching and control issues analyzed for their medium voltage applications are provided in "Multilevel Converters for Step-Up-Transformer-Less Direct Integration of Renewable Generation Units with Medium Voltage Smart Microgrids." "A Review of Interconnection Rules for Large-Scale Renewable Power Generation" presents a comprehensive study of the grid interconnection rules set by various transmission system operators and regulators for large renewable-based power plants. A complex network framework-based network resiliency (percolation) analysis, for the future grid with large-scale renewable energy, is presented in "Resiliency Analysis of Large-Scale Renewable Enriched Power Grid: A Network Percolation-Based Approach." The aims of "Frequency Control and Inertial Response Schemes for the Future Power Networks" and "Active Power and Frequency Control Considering Large-Scale RES" are to present the fundamental aspects about system frequency and active power control for the power networks with low inertia renewable.

One of the important aspects of renewable energy integration is to analyze its impact on power system reliability which is discussed in "Impact of Large Penetration of Correlated Wind Generation on Power System Reliability" and "HVDC Transmission for Offshore Wind Farm" present an overview of different topologies for grid integration of offshore wind farms. The protection schemes, technical challenges, and difficulties for different wind generators are given in "Wind Farm Protection" and its impact on distance relay is discussed in "Wind Power Plants and FACTS Devices Influence in the Performance of Distance Relays." Next the protection scheme of high voltage direct current (HVDC) transmission systems for large-scale offshore wind farms is presented in "Protection Schemes for Meshed VSC-HVDC Transmission Systems for Large-Scale Offshore Wind Farms."

As brushless doubly-fed reluctance generator (BDFRG) for large-scale grid-connected wind turbines is a promising technology, its operation and control strategy are addressed in "Control of Emerging Brushless Doubly-Fed Reluctance Wind Turbine Generators" and an optimal energy management in energy hub for intermittent wind power is presented in "Energy Hub Management with

Intermittent Wind Power." Finally, "Adopting the IEC Common Information Model to Enable Smart Grid Interoperability and Knowledge Representation Processes" discusses the philosophy and processes underpinning smart grid information interoperability to enable power utilities to build and control the emerging smart grid and it elaborates upon how the common information model fits within a standardized power system interoperability framework.

Contents

Taxonomy of Uncertainty Modeling Techniques in Renewable Energy System Studies 1
Alireza Soroudi

Probabilistic Modeling and Statistical Characteristics of Aggregate Wind Power 19
H. Louie and J. M. Sloughter

Conversion Efficiency Improvement in GaAs Solar Cells 53
Narottam K. Das and Syed M. Islam

Emerging SMES Technology into Energy Storage Systems and Smart Grid Applications 77
Jian Xun Jin

Multilevel Converters for Step-Up-Transformer-Less Direct Integration of Renewable Generation Units with Medium Voltage Smart Microgrids 127
Md. Rabiul Islam, Youguang Guo and Jianguo Zhu

A Review of Interconnection Rules for Large-Scale Renewable Power Generation 151
Tareq Aziz, Tapan K. Saha and Nadarajah Mithulananthan

Resiliency Analysis of Large-Scale Renewable Enriched Power Grid: A Network Percolation-Based Approach 173
A. B. M. Nasiruzzaman and H. R. Pota

Frequency Control and Inertial Response Schemes for the Future Power Networks 193
F. Gonzalez-Longatt

Active Power and Frequency Control Considering Large-Scale RES 233
Elyas Rakhshani and Pedro Rodriguez

Impact of Large Penetration of Correlated Wind Generation on Power System Reliability 273
Carmen L. T. Borges and Julio A. S. Dias

HVDC Transmission for Offshore Wind Farms 289
Raymundo Enrique Torres Olguin, Alejandro Garces and Gilbert Bergna

Wind Farm Protection 311
Waqar A. Qureshi and Nirmal-Kumar C. Nair

Wind Power Plants and FACTS Devices' Influence on the Performance of Distance Relays 331
L. A. Trujillo Guajardo and A. Conde Enríquez

Protection Schemes for Meshed VSC-HVDC Transmission Systems for Large-Scale Offshore Wind Farms 369
J. Yang and J. E. Fletcher

Control of Emerging Brushless Doubly-Fed Reluctance Wind Turbine Generators 395
Sul Ademi and Milutin Jovanovic

Energy Hub Management with Intermittent Wind Power 413
Alireza Soroudi, Behnam Mohammadi-Ivatloo and Abbas Rabiee

Adopting the IEC Common Information Model to Enable Smart Grid Interoperability and Knowledge Representation Processes 439
N. B. Hargreaves, S. M. Pantea and G. A. Taylor

Taxonomy of Uncertainty Modeling Techniques in Renewable Energy System Studies

Alireza Soroudi

Abstract With the introduction of new concepts in operation and planning of power systems, decision making is becoming more critical than ever before. These concepts include restructuring, smart grids, and the importance of environmental concerns. The art of decision making is defined as choosing the best action among available choices considering the constraints and input data of the problem. Decision making is usually a complex task which becomes more sophisticated when the input data of the problem are subject to uncertainty. This chapter presents a critical review of the state-of-the-art uncertainty in handling tools for renewable energy studies. Different uncertainty modeling tools are first introduced and then the appropriate ones for renewable energies are identified. Then, each method is implemented on a simple two-bus case study.

1 Introduction

Power system studies include a wide range of issues from short term (e.g. real-time, hourly, daily, and weekly operating decisions) to long-term horizons (e.g., planning or policy making). The decision making process involves dealing with uncertain input data especially in engineering systems. Due to the increasing penetration level of renewable energy resources, like wind and solar power, the uncertainty is increased in operation and investment decisions of various involved entities. Different techniques have been developed to deal with uncertainties in decision making. It is of interest to know the differences and similarities as well as the application areas. In this chapter, a new standard classification of uncertainty modeling techniques for renewable energy resource impact assessment under

A. Soroudi (✉)
Faculty of New Sciences and Technologies, University of Tehran, Tehran, Iran
e-mail: soroudi@ut.ac.ir; Alireza.soroudi@gmail.com

J. Hossain and A. Mahmud (eds.), *Large Scale Renewable Power Generation*, Green Energy and Technology, DOI: 10.1007/978-981-4585-30-9_1,

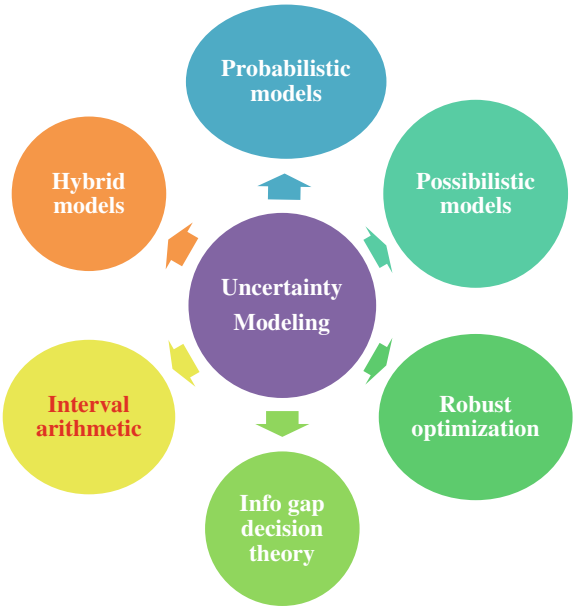

Fig. 1 Different uncertainty handling tools

uncertainty is proposed. These methods are introduced and implemented and their strengths and weaknesses demonstrated. The existing uncertainty modeling techniques cover a wide range such as probabilistic approach [1, 2], possibilistic approach [3], hybrid possibilistic-probabilistic approaches [4], information gap decision theory [5], and robust optimization [6, 7] as shown in Fig. 1.

Among these methods, the probabilistic techniques are more appropriate for impact assessment of renewable energies. The main reason for this fact is that the output of renewable energy resources basically depends on the characteristics of their primary energy resources such as solar radiation, wind speed, environmental temperature, etc. The historic data of these parameters is usually available and they can be modeled using a probability density function (PDF).

2 Probabilistic Approach

In this approach, a multivariate function, namely y, $y = f(X)$ is available. X is a vector containing the uncertain parameters of the form $X = \{x_1, x_2, \ldots, x_n\}$. It is assumed that the PDF of X is known. The question is how to determine the PDF of y? Three probabilistic uncertainty modeling techniques are described here as follows:

2.1 Monte Carlo Simulation

The Monte Carlo simulation (MCS) is an iterative method which is carried out as the following steps [8]:

Step 1. Set MSC counter $c = 1$.
Step 2. Generate a sample for the vector X using the PDF of each component x_i.
Step 3. Calculate y_c assuming that $X = X_c$ as $y_c = f(X_c)$.
Step 4. Calculate the expected value of y, $\Xi(\mathrm{y})$ as $\Xi(\mathrm{y}) = \frac{\sum_{c'} \mathrm{y}_{c'}}{\mathrm{c}}$.
Step 5. Calculate the variance of y, $\sigma(y)$ as $\sigma(y) = \Xi\left(\mathrm{Y}^2\right) - \Xi^2(\mathrm{Y})$.
Step 6. Stopping criteria is met? End, Else set counter $c = c + 1$ and go to Step 2.
Step 7. End.

The stopping criteria can be defined in various ways such as maximum number of MCS iterations, convergence of the expected value of y, etc.

- The strength of MCS method can be listed as follows:

– It is not needed to exactly know the f for calculating the y. The problem can be solved as a black box which receives samples and gives an output for each.
– It also works well in non-differentiable and non-convex problems (complex systems) as well as behavior problems.
– It supports all PDF types.
– It is intuitive and relatively easy to implement [9].

- The shortcomings of MCS method can be listed as follows:

– It is only applicable in problems that are described using a PDF.
– The computation burden is usually high since it is iterative and needs several evaluations of function f.
– This technique is approximate [9].

There are some methods for reducing the computational burden of MCS like Latin Hypercube Sampling (LHS) [10]. It is also applied in practical applications such as power systems reliability analysis with renewable energy sources [11, 12], probabilistic load flow [13, 14], evaluation of available load supply capability for distribution system [15], and assessment of capacity factor of distributed wind generation in microgrids [16].

2.2 Monte Carlo Simulation

The Point Estimate Method (PEM) is a strong technique which approximately calculates the expected value and variance of y based on the PDF of x_i. If there are n uncertain parameters in vector X then this method performs 2n calculations to

obtain the $\Xi(y)$ and $\Xi(y^2)$. The PEM is implemented through the following steps [17, 18]:

Step 1. Set $\Xi(y) = \Xi(y^2) = 0$. and $\zeta = 1$

Step 2. Determine the locations and probabilities of concentrations $\gamma_{\zeta,i}$ and $\pi_{\zeta,i}$, respectively as follows:

$$\gamma_{\zeta,\mathrm{i}} = \frac{1}{2}\frac{M_3(x_\zeta)}{\sigma^3_{x_\zeta}} + (-1)^{i+1}\sqrt{n + \frac{1}{2}\left(\frac{M_3(x_\zeta)}{\sigma^3_{x_\zeta}}\right)^2} \tag{1}$$

$$\pi_{\zeta,\mathrm{i}} = (-1)^i \frac{\gamma_{\zeta,3-\mathrm{i}}}{2n\sqrt{n + \frac{1}{2}\left(\frac{M_3(x_\zeta)}{\sigma^3_{x_\zeta}}\right)^2}} \tag{2}$$

where $M_3(x_\zeta)$ is the third moment of parameter x_ζ.

Step 3. Determine the concentration points $x_{\zeta,i}$, as given below.

$$x_{\zeta,\mathrm{i}} = \mu_{x_i} + \gamma_{\zeta,\mathrm{i}} \times \sigma_{x_i}, \quad i = 1,\ 2 \tag{3}$$

where, μ_{x_i} and σ_{x_i} are mean and standard deviation of x_ζ, respectively.

$$X = [x_1, x_2, \ldots, x_{\zeta,i}, \ldots, x_n], i = 1, 2 \tag{4}$$

Step 4. Calculate $\Xi(Y^2), \Xi^2(Y)$ using:

$$\Xi(y) = \Xi(y) + \sum_{i=1}^{2} \pi_{\zeta,i} f(x_1, x_2, \ldots, x_{\zeta,i}, \ldots, x_n) \tag{5}$$

$$\Xi(y^2) = \Xi(y^2) + \sum_{i=1}^{2} \pi_{\zeta,i} f^2(x_1, x_2, \ldots, x_{\zeta,i}, \ldots, x_n) \tag{6}$$

Step 5. $\zeta = \zeta + 1$ if $\zeta < n$ then go to Step 2; else continue

Step 6. Calculate the mean and the standard deviation as follows:

$$\mu_y = \Xi(y) \tag{7}$$

$$\sigma_y = \sqrt{\Xi(y^2) - \Xi^2(y)} \tag{8}$$

- The strength of PEM method can be listed as follows:

– It is a non-iterative, computationally efficient technique.
– It is simple and easy to implement.
– There is no convergence problem.
– It is applicable to problems with spatial correlation among multiple uncertain input parameters [19].

- The shortcomings of PEM method can be listed as follows:

– It only gives the mean and standard deviation of the uncertain output [20].
– No information about the shape of the PDF of the output is provided [19].
– It gives more reliable answers for non-skewed PDFs [20].
– It is only applicable in problems which are described using a PDF.

This method is applied in various applications such as: Probabilistic power flow [21, 22], probabilistic optimal power flow in electricity markets [23], and transfer capability assessment [24].

2.3 Scenario-Based Decision Making

Usually the uncertain parameters have infinite uncountable realizations. However, it is impossible to consider all these realizations. Instead, the realization space is divided into countable finite sections (scenarios) with a specific weight (probability). To do this, a list of scenarios is generated using the PDF of each uncertain parameter, X. The expected value of output variable, y, $\Xi(y)$ is calculated as follows:

$$\Xi(y) = \pi_s \times f(X_s) \tag{9}$$

where $\sum_s \pi_s = 1$and $\pi_s$is the probability of scenario s.

- The strength of scenario-based decision making method can be listed as follows:

– It is computationally efficient and simple to implement.
– It converts the contentious space of uncertain environment into discrete finite scenarios with a given probability.

- The shortcomings of scenario-based decision making method can be listed as follows:

– It only gives the expected values of the uncertain output.
– The method is approximate.
– The model size tends to increase drastically with the number of considered scenarios.
– It requires probabilistic inputs and does not support uncertain parameters which are not described probabilistically.

This method is applied in various applications such as: Probabilistic determination of pilot points for zonal voltage control [25], stochastic scheduling for simulation of wind-integrated power systems [26], and wind power impact assessment [4].

3 Uncertainty Modeling of Wind Turbine Power Generation and Load

In this section the common ways of modeling wind power and load uncertainty are discussed.

3.1 Wind Turbine Power Generation Modeling

Suppose that the probability density function (PDF) of wind speed (v) is known in the region under study and it is described as follows [4]:

$$\mathrm{PDF}(v) = \frac{2v}{c^2}\exp\left(-\left(\frac{v}{c}\right)^2\right) \tag{10}$$

The theoretical power obtained from wind at wind speed v depends on the air density (ρ), radius of the rotor determining its swept area (R), power coefficient (Cp), blade-pitch angle (β), and the tip-speed ratio (λ) [27]. It is described as follows:

$$P^w(v) = \frac{1}{2}\rho\pi R^2 C_p(\lambda,\beta)v^3 \tag{11}$$

where $P^w(v)$ is the power captured by the rotor of a wind turbine.

The producible power of wind turbine in wind speed v can be approximated by a linear relation as described in (12).

$$P^w(v) = \begin{cases} 0 & v \le v^c_{\text{in}} \; or \; v \ge v^c_{\text{out}} \\ \frac{v - v^c_{\text{in}}}{v_{\text{rated}} - v^c_{\text{in}}} P^w_r & v^c_{\text{in}} \le v \le v_{\text{rated}} \\ P^w_r & v_{\text{rated}} \le v \le v^c_{\text{out}} \end{cases} \tag{12}$$

The approximate linear power curve of a wind turbine is depicted in Fig. 2. This method of wind power generation uncertainty modeling is used for various applications like DG impact assessment [4] and optimal multi-area generation schedule considering renewable resources [28].

The formulation of power curve provided in (12) is the theoretical power curve. In practice, the actual power curve (which relates the wind speed with the wind turbine power generations) deviates from its theoretical value due to the following reasons [29]:

- Wind speed measurement errors.
- Variations in air density which affects the output power.
- Yaw and pitch misalignments.
- Shading effects and wind obstacles caused by neighboring turbines.

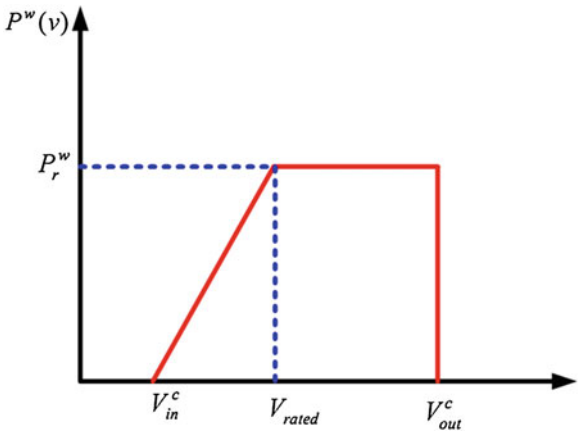

Fig. 2 Power curve of a wind turbine

3.2 Probabilistic Modeling of Load

In this case, it is assumed that the historic data of load is in hand and it can be modeled using probabilistic approach. The normal distribution is an appropriate choice for modeling the load as shown in Fig. 3. The only necessary data for this uncertainty modeling is the mean and variance of historic data. This method of load uncertainty modeling is used for DG planning [30, 31], optimization of power system operation [32].

3.3 Possibilistic Modeling of Load

The possibilistic modeling of uncertainty or fuzzy arithmetic refers to a model developed by Zadeh in 1965 [33]. In this approach, a membership function is assigned to each uncertain parameter $\tilde{X}$ which describes the behavior and the known data about it. The membership function defines the degree that the component x belongs to fuzzy set$\tilde{X}$. Recall the function $\tilde{y} = f(\tilde{X})$; if the membership function of X, $\mu(x)$ is known then what is the membership function of y, $\mu(y)$? One of the common fuzzy membership functions is fuzzy trapezoidal number (FTN) with a notation $\tilde{X} = (x_{\min}, x_{\min}^{l}, x_{\max}^{l}, x_{\max})$ as shown in Fig. 4. The membership function of $\tilde{y}$ is determined using the α-cut method as follows [34]. The α-cut of parameter X is a set which contains all components x which belong to $\tilde{X}$ with the degree more than α as calculated in (13).

$$X^{\alpha} = \left\{ x \in \tilde{X} | \mu(x) \geq \alpha \right\} \tag{13}$$

The α-cut of each uncertain parameter, x_i^{α}, is determined using (13), then the α-cut of y, y^{α}, is calculated as follows:

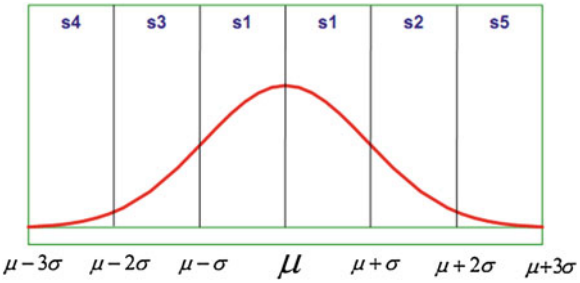

Fig. 3 Stochastic model of load

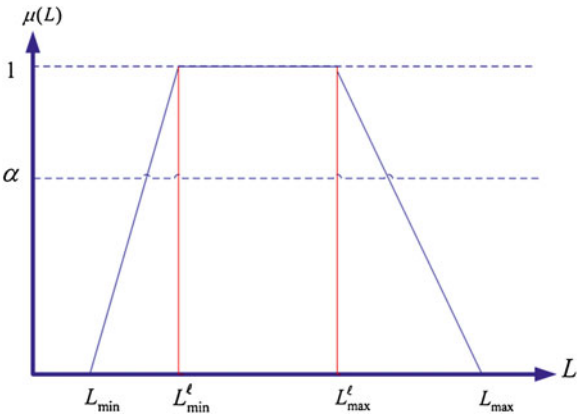

Fig. 4 Fuzzy model of load

$$y^{\alpha} = (\underline{y}^{\alpha}, \bar{y}^{\alpha}) \tag{14}$$

$$\underline{y}^{\alpha} = \min f(X^{\alpha}) \tag{15}$$

$$\bar{y}^{\alpha} = \max f(X^{\alpha}) \tag{16}$$

In other words, for each α-cut, the upper/lower bounds of y^{α} are calculated. After determination of membership function for y, it is sometimes necessary to convert it into a real number. This procedure is called deffuzzification [35]. Different deffuzzification techniques exist such as centroid method [36], weighted average deffuzzification technique, etc. The deffuzzified value of a given fuzzy quantity, i.e. $\tilde{Y}$, is calculated as follows:

$$Y^{*} = \frac{\int \mu_Y(y).ydy}{\int ydy} \tag{17}$$

This method of load uncertainty modeling is used for power flow [37], DG impact assessment [3].

4 Simulation Results

The introduced approaches are implemented in GAMS [38] environment solved by CONOPT solver running on an Intel® CoreTM2 Duo Processor T5300 (1.73 GHz) PC with 1 GB RAM. In order to illustrate the concept of each introduced uncertainty modeling method, a simple two-bus network is used as shown in Fig. 5. A load is fed by a wind turbine (WT) and through a feeder with the impedance of $Z = R + jX(\Omega)$. The apparent power of load is $L = S \prec \theta = S(\cos(\theta) + j\cos(\theta))$. It is assumed that the magnitude of load (S) is uncertain. Another uncertain parameter is the power generation of WT. The rated capacity of wind turbine is 0.1 pu.

The impedance of the line is $Z < \theta = 0.2667 < 1.0717$ pu. The sending end voltage is kept constant as $E = 1.05$ pu. The mean value of load is $S = 0.2$ pu with $\cos(\varphi) = 0.9$ lag.

$$y = f(S, P^w(v)) \tag{18}$$

subject to:
(19)–(21)

$$P = -P^w(v) + \frac{VE}{Z}\cos(\theta + \delta) - \frac{V^2}{Z}\cos(\theta) \tag{19}$$

$$Q = \frac{VE}{Z}\sin(\theta + \delta) - \frac{V^2}{Z}\sin(\theta) \tag{20}$$

$$S = P + jQ \tag{21}$$

$$P = S\cos(\theta) \tag{22}$$

$$Q = S\sin(\theta) \tag{23}$$

$$P_{\text{loss}} = P_{\text{grid}} - P \tag{24}$$

The function f can be defined based on the requirement of the decision maker. It can be active losses, voltage magnitude at load bus, etc.

In case there is no uncertainty about the load value and assuming zero power injection by WT, the problem is solved and the values of unknown variables are found to be as follows: $V = 1.006$ pu, $\delta = -0.029$ Rad, $P_{\text{loss}} = 0.005$ pu, $P_{\text{grid}} = 0.185$ pu. The scale parameter of Rayleigh PDF for wind speed is 8, respectively. The $v_{in}^c, v_{rated}, v_{out}^c$ are 4, 14, 25 (m/s), respectively.

4.1 Monte Carlo Simulation

In this section, it is assumed that the wind generation is dependent on wind speed as described in Sect. 3.1. The uncertainty of load is modeled probabilistically

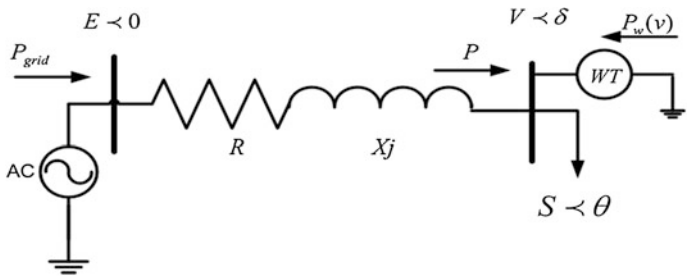

Fig. 5 Simple two-bus illustrative network

using a normal PDF as shown in Fig. 3. The mean value of load is $S = 0.2$ pu with $\cos(\varphi) = 0.9$ lag. The variance of load is 1 % of its mean value. In this case, the results are as follows:

$$\Xi(P_{\text{loss}}) = 0.0038 \text{ pu},\ \sigma(P_{\text{loss}}) = 1.9202 \times 10^{-6} \text{ pu},\ \Xi(V) = 1.0108 \text{ pu}, \sigma(V) = 3.5841 \times 10^{-5} \text{ pu}.$$

The stopping criteria is defined as the maximum number of iterations that should not exceed 2000. This number chosen is arbitrary, however, it is a typical choice for the maximum number of MCS iterations. It can be observed in Figs. 6 and 7 that the expected values of uncertain parameters are converged in iteration 1000.

4.2 Point Estimate Method

Using the PEM gives the $\Xi(P_{\text{loss}}) = 0.0037$ pu $\sigma(P_{\text{loss}}) = 1.1319 \times 10^{-3}$ pu, $\Xi(V) = 1.0111$ pu $\sigma(V) = 4.5865 \times 10^{-3}$ pu.

4.3 Scenario Based

The probability that wind speed is in scenario s ($v_{1,s} \leq v \leq v_{2,s}$) is calculated as follows:

$$\pi_s = \int_{v_{1,s}}^{v_{2,s}} \frac{2v}{c^2} \exp\left(-\left(\frac{v}{c}\right)^2\right) dv \tag{25}$$

$$v_s = \frac{v_{1,s} + v_{2,s}}{2} \tag{26}$$

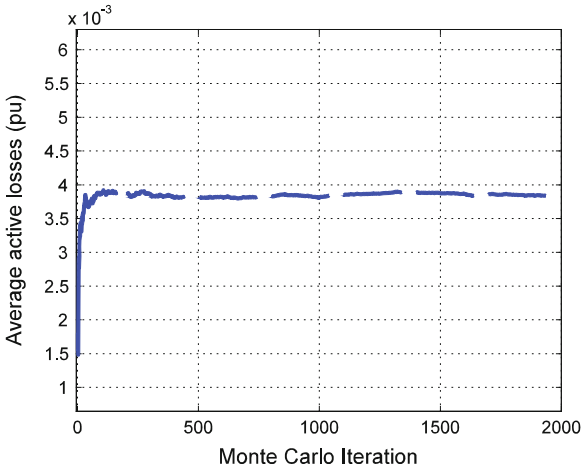

Fig. 6 Convergence of active losses in MCS

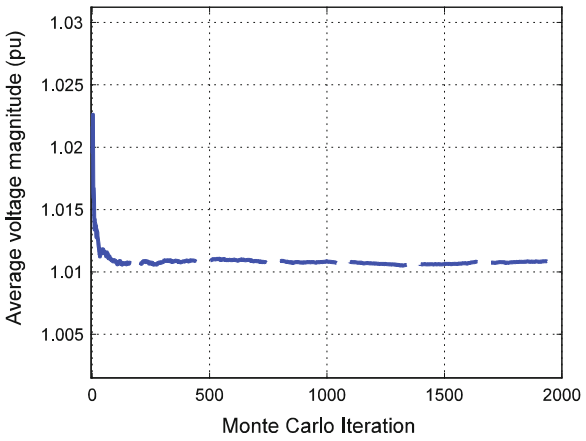

Fig. 7 Convergence of voltage magnitude at receiving end in MCS

where $v_{1,s}, v_{2,s}$ are the limits of wind speed's interval in states. The generated power of wind turbine in states is calculated using the obtained v_s and (12). The percentages of producible wind power in each scenario are given in Table 1.

In order to cover the whole wind speed variation range, 12 different scenarios are considered in this study. The scenario s1 refers to the case where the wind speed is more than v_{out}^c or less than v_{in}^c. The scenario s12 refers to the case where the wind speed is between v_{rated} and v_{out}^c. The probabilities of these scenarios occurring are calculated using (25). The scenarios s2–s11 are those considered for the wind speed between v_{in}^c and v_{rated}. This interval is divided into ten scenarios. The scenarios describing the load values and the associated probabilities are given in Table 2.

Table 1 Wind turbine available percentages of rated power in different scenarios

Scenario	$P^w(\%)$	π_s
S1	0	0.2059
S2	5	0.0661
S3	15	0.1123
S4	20	0.1037
S5	35	0.1122
S6	45	0.0912
S7	55	0.0773
S8	65	0.0501
S9	75	0.0451
S10	85	0.0326
S11	95	0.0250
S12	100	0.0784

Table 2 Normal PDF states for electric load

Scenario	Mean value	π_s
S4	$\mu - 2.5\sigma$	2.5
S3	$\mu - 1.5\sigma$	13.8
S1	μ	68.0
S2	$\mu + 1.5\sigma$	13.8
S5	$\mu + 2.5\sigma$	2.5

The combined set of scenarios as well as the corresponding loss and voltage are given in Table 3. The expected values of active losses and voltage magnitude are 0.0041 and 1.0110 pu, respectively.

4.4 Hybrid Case

In this case, it is assumed that the PDF of wind speed is available, however, no historic data is at hand for load values. This situation can be handled using the fuzzy arithmetic and expert opinion regarding the membership function of load. The expert gives the following trapezoidal fuzzy number for describing the nature of uncertainty. $S = (0.16, 0.18, 0.22, 0.25)$. Using the introduced technique in Sects. 2.3 and 3.3, the problem described in (14) is solved for each scenario and the components of output's TFN are calculated. The FTN values of active loss and voltage magnitude in different scenarios are given in Table 4. The expected fuzzy membership function of active losses and voltage magnitude are shown in Figs. 8 and 9, respectively.

The crisp values of active loss and voltage magnitude are 0.0042 and 1.0105 pu, respectively. In order to have a better understanding of the obtained results, the expected values of active loss and voltage magnitude given by different methods

Table 3 Values of load and wind power generation in different scenarios

S#	P_{loss}	V	P^w	S	π_s	S#	P_{loss}	V	P^w	S	π_s
s1	0.0048	1.0076	0	0.1950	0.0051	s31	0.0027	1.0151	0.0550	0.1950	0.0019
s2	0.0049	1.0071	0	0.1970	0.0278	s32	0.0028	1.0147	0.0550	0.1970	0.0104
s3	0.0050	1.0064	0	0.2000	0.1400	s33	0.0029	1.0140	0.0550	0.2000	0.0526
s4	0.0052	1.0057	0	0.2030	0.0278	s34	0.0030	1.0133	0.0550	0.2030	0.0104
s5	0.0053	1.0053	0	0.2050	0.0051	s35	0.0031	1.0129	0.0550	0.2050	0.0019
s6	0.0046	1.0083	0.0050	0.1950	0.0017	s36	0.0024	1.0164	0.0650	0.1950	0.0013
s7	0.0047	1.0078	0.0050	0.1970	0.0089	s37	0.0025	1.0160	0.0650	0.1970	0.0068
s8	0.0048	1.0071	0.0050	0.2000	0.0449	s38	0.0026	1.0153	0.0650	0.2000	0.0341
s9	0.0050	1.0064	0.0050	0.2030	0.0089	s39	0.0027	1.0146	0.0650	0.2030	0.0068
s10	0.0051	1.0060	0.0050	0.2050	0.0017	s40	0.0028	1.0142	0.0650	0.2050	0.0013
s11	0.0041	1.0097	0.0150	0.1950	0.0028	s41	0.0021	1.0178	0.0750	0.1950	0.0011
s12	0.0042	1.0092	0.0150	0.1970	0.0152	s42	0.0022	1.0173	0.0750	0.1970	0.0061
s13	0.0044	1.0085	0.0150	0.2000	0.0764	s43	0.0023	1.0167	0.0750	0.2000	0.0307
s14	0.0045	1.0078	0.0150	0.2030	0.0152	s44	0.0024	1.0160	0.0750	0.2030	0.0061
s15	0.0046	1.0074	0.0150	0.2050	0.0028	s45	0.0025	1.0155	0.0750	0.2050	0.0011
s16	0.0039	1.0103	0.0200	0.1950	0.0026	s46	0.0019	1.0191	0.0850	0.1950	0.0008
s17	0.0040	1.0099	0.0200	0.1970	0.0140	s47	0.0020	1.0186	0.0850	0.1970	0.0044
s18	0.0042	1.0092	0.0200	0.2000	0.0705	s48	0.0020	1.0180	0.0850	0.2000	0.0222
s19	0.0043	1.0085	0.0200	0.2030	0.0140	s49	0.0021	1.0173	0.0850	0.2030	0.0044
s20	0.0044	1.0081	0.0200	0.2050	0.0026	s50	0.0022	1.0169	0.0850	0.2050	0.0008
s21	0.0034	1.0124	0.0350	0.1950	0.0028	s51	0.0017	1.0204	0.0950	0.1950	0.0006
s22	0.0034	1.0119	0.0350	0.1970	0.0151	s52	0.0017	1.0200	0.0950	0.1970	0.0034
s23	0.0036	1.0113	0.0350	0.2000	0.0763	s53	0.0018	1.0193	0.0950	0.2000	0.0171
s24	0.0037	1.0106	0.0350	0.2030	0.0151	s54	0.0019	1.0186	0.0950	0.2030	0.0034
s25	0.0038	1.0101	0.0350	0.2050	0.0028	s55	0.0020	1.0182	0.0950	0.2050	0.0006
s26	0.0030	1.0138	0.0450	0.1950	0.0023	s56	0.0016	1.0210	0.1000	0.1950	0.0020
s27	0.0031	1.0133	0.0450	0.1970	0.0123	s57	0.0016	1.0206	0.1000	0.1970	0.0106
s28	0.0032	1.0126	0.0450	0.2000	0.0620	s58	0.0017	1.0199	0.1000	0.2000	0.0533
s29	0.0033	1.0120	0.0450	0.2030	0.0123	s59	0.0018	1.0193	0.1000	0.2030	0.0106
s30	0.0034	1.0115	0.0450	0.2050	0.0023	s60	0.0019	1.0188	0.1000	0.2050	0.0020

Table 4 FTN values of active loss and voltage magnitude in different scenaarios

S#	V				P_{loss}			
s1	0.9948	1.0018	1.0110	1.0155	0.0032	0.0040	0.0062	0.0081
s2	0.9955	1.0025	1.0117	1.0162	0.0030	0.0038	0.0059	0.0078
s3	0.9969	1.0039	1.0131	1.0176	0.0027	0.0035	0.0054	0.0072
s4	0.9976	1.0046	1.0137	1.0182	0.0025	0.0033	0.0052	0.0069
s5	0.9998	1.0067	1.0158	1.0202	0.0021	0.0028	0.0045	0.0061
s6	1.0012	1.0081	1.0171	1.0215	0.0018	0.0024	0.0041	0.0056
s7	1.0026	1.0095	1.0184	1.0229	0.0016	0.0022	0.0037	0.0052
s8	1.0040	1.0108	1.0198	1.0242	0.0014	0.0019	0.0034	0.0047
s9	1.0054	1.0122	1.0211	1.0255	0.0012	0.0017	0.0030	0.0043
s10	1.0067	1.0135	1.0224	1.0267	0.0010	0.0015	0.0027	0.0040
s11	1.0081	1.0149	1.0237	1.0280	0.0009	0.0013	0.0025	0.0036
s12	1.0088	1.0155	1.0243	1.0287	0.0008	0.0012	0.0023	0.0034

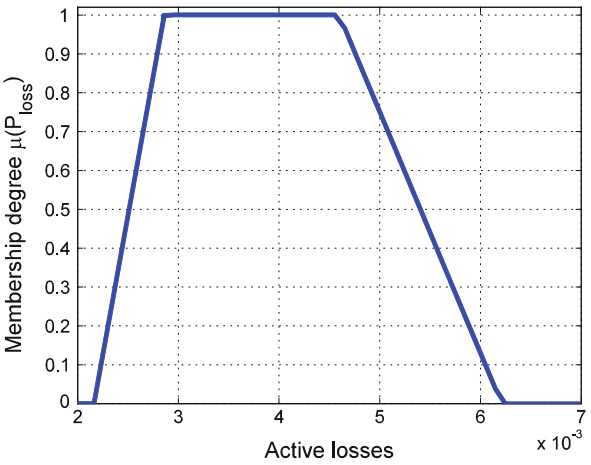

Fig. 8 Expected fuzzy membership function of active losses

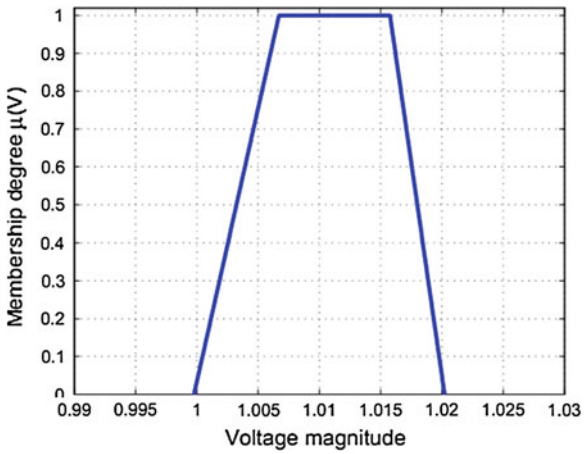

Fig. 9 Expected fuzzy membership function of voltage magnitude

are described in Table 5, although the case analyzed in hybrid method is inherently different from the first three ones. In the first three stochastic cases, the value of load was described using a probabilistic method. It did not hold for the hybrid case. In this case, the load was described using a fuzzy membership function. Obviously the computational burden of hybrid case is higher than scenario based approach since it needs to run two optimizations in each α level. In this simulation, just two α levels are considered ($\alpha = 0, 1$) so four optimizations are needed to obtain the final solution.

Table 5 The expected values of active loss and voltage magnitude obtained by different methods

Method	Voltage	P_{loss}
MCS	1.0108	0.0038
PEM	1.0111	0.0037
Scenario based	1.0110	0.0041
Hybrid	1.0105	0.0042

5 Future Research

The following is a list of possible future studies that tangent this chapter:

- The possibility of uncertainty handling in hybrid modes (when different types of uncertainties exist in problem) should be investigated.
- With the deregulation of the power system industry, the uncertainties of renewable energies are not limited to their power generation output. The decisions of the private sector regarding the investment are also subject to uncertainty.
- The introduced stochastic uncertainty handling tools provide the possibility of tradeoff for the decision maker between the accuracy and the high computational performance.
- With the development of smart grid concepts, methods that will provide accuracy with low computational burden have to be developed. This would make the decision maker enable to use them in real-time applications.

6 Conclusion

The taxonomy of uncertainty modeling of renewable energies is introduced in this chapter. Three main stochastic methods including Monte Carlo simulation, point estimate method, and scenario-based modeling are analyzed and implemented. The simulation results showed that although Monte Carlo simulation is inherently an iterative approximate model for handling the stochastic uncertainties, it is more accurate than others. On the other hand, the computational burden of this method is higher than the rest of them. This chapter also deals with situations where both stochastic and possibilistic uncertainties exist in the problem. The applicability of each model is demonstrated by applying it on a simple two-bus network.

Acknowledgments To my lovely, beautiful, and faithful wife, Soudeh Ziapour Razlighi. She always comforts and consoles, never complains or interferes, asks nothing, and endures all.

References

1. Soroudi A, Aien M, Ehsan M (2012) A probabilistic modelling of photo voltaic modules and wind power generation impact on distribution networks. IEEE Syst J 6(2):254–259
2. Rabiee A, Soroudi A (2013) Stochastic multi-period OPF model of power systems with HVDC-connected intermittent wind power generation. IEEE Trans Power Deliv 99:1–1
3. Soroudi A, Ehsan M, Caire R, Hadjsaid N (2011) Possibilistic evaluation of distributed generations impacts on distribution networks. IEEE Trans Power Syst 26(4):2293–2301
4. Soroudi A (2012) Possibilistic-scenario model for dg impact assessment on distribution networks in an uncertain environment. IEEE Trans Power Syst 27(3):1283–1293
5. Soroudi A, Ehsan M (2013) IGDT based robust decision making tool for DNOs in load procurement under severe uncertainty. IEEE Trans Smart Grid 4(2):886–895
6. Soroudi A (2013) Smart self-scheduling of Gencos with thermal and energy storage units under price uncertainty. Int Trans Electr Energy Syst 1–11. Available via http://dx.doi.org/10.1002/etep.1780
7. Soroudi A (2013) Robust optimization based self scheduling of hydro-thermal Genco in smart grids. Energy 61(1):262–271
8. Mooney CZ (1997) Monte Carlo simulation, vol 116. Sage, Newbury Park
9. Smid J, Verloo D, Barker G, Havelaar A (2010) Strengths and weaknesses of Monte Carlo simulation models and bayesian belief networks in microbial risk assessment. Int J Food Microbiol 139(Supplement no 0):S57–S63
10. Iman RL (2008) Latin hypercube sampling. Wiley Online Library, New York
11. Shu Z, Jirutitijaroen P (2011) Latin hypercube sampling techniques for power systems reliability analysis with renewable energy sources. IEEE Trans Power Syst 26(4):2066–2073
12. Jirutitijaroen P, Singh C (2008) Comparison of simulation methods for power system reliability indexes and their distributions. IEEE Trans Power Syst 23(2):486–493
13. Yu H, Chung C, Wong KP, Lee H, Zhang J (2009) Probabilistic load flow evaluation with hybrid latin hypercube sampling and cholesky decomposition. IEEE Trans Power Syst 24(2):661–667
14. Hajian M, Rosehart W, Zareipour H (2013) Probabilistic power flow by montecarlo simulation with latinsupercube sampling. IEEE Trans Power Syst 28(2):1550–1559
15. Zhang S, Cheng H, Zhang L, Bazargan M, Yao L (2013) Probabilistic evaluation of available load supply capability for distribution system. IEEE Trans Power Syst 28(3):3215–3225
16. Diaz G, Abd-el Motaleb A, Mier V (2013) On the capacity factor of distributed wind generation in droop-regulated microgrids. IEEE Trans Power Syst 28(2):1738–1746
17. Soroudi A, Afrasiab M (2012) Binary pso-based dynamic multi-objective model for distributed generation planning under uncertainty. Renew Power Gener IET 6(2):67–78
18. Hong H (1998) An efficient point estimate method for probabilistic analysis. Reliab Eng Syst Safety 59(3):261–267
19. Russelli C (2008) Probabilistic methods applied to the bearing capacity problem. Inst. fur Geotechnik
20. He J, Sllfors G (1994) An optimal point estimate method for uncertainty studies. Appl Math Model 18(9):494–499
21. Morales J, Perez-Ruiz J (2007) Point estimate schemes to solve the probabilistic power flow. IEEE Trans Power Syst 22(4):1594–1601
22. Su C-L (2005) Probabilistic load-flow computation using point estimate method. IEEE Trans Power Syst 20(4):1843–1851
23. Verbic G, Canizares C (2006) Probabilistic optimal power flow in electricity markets based on a two-point estimate method. IEEE Trans Power Syst 21(4):1883–1893
24. Su C-L, Lu C-N (2005) Two-point estimate method for quantifying transfer capability uncertainty. IEEE Trans Power Syst 20(2):573–579
25. Amraee T, Soroudi A, Ranjbar A (2012) Probabilistic determination of pilot points for zonal voltage control. Gener Transm Distrib IET 6(1):1–10

26. Sturt A, Strbac G (2012) Efficient stochastic scheduling for simulation of wind-integrated power systems. IEEE Trans Power Syst 27(1):323–334
27. Lydia M, Selvakumar AI, Kumar SS, Kumar GEP (2013) Advanced algorithms for wind turbine power curve modelling. IEEE Trans Sustain Energy 4(3):827–835
28. Soroudi A, Rabiee A (2013) Optimal multi-area generation schedule considering renewable resources mix: a real-time approach. Gener Transm Distrib IET 7(9):1011–1026
29. Schlechtingen M, Santos IF, Achiche S (2013) Using data-mining approaches for wind turbine power curve monitoring: A comparative study. IEEE Trans Sustain Energy 4(3):671–679
30. Soroudi A, Ehsan M (2010) "Multi-objective planning model for integration of distributed generations in deregulated power systems. Iran J Sci Technol Trans B Eng 34(3):307–324
31. Soroudi A, Caire R, Hadjsaid N, Ehsan M (2011) Probabilistic dynamic multi-objective model for renewable and non-renewable distributed generation planning. Gener Transm Distrib IET 5(11):1173–1182
32. Zhu J (2009) Optimization of power system operation, vol 49. Wiley.com, New York
33. Zadeh LA (1965) Fuzzy sets. Inf Control 8(3):338–353
34. Buckley JJ, Eslami E, Feuring T (2002) Fuzzy mathematics in economics and engineering. Physica-Verlag, Heidelberg
35. Fortemps P, Roubens M (1996) Ranking and deffuzzification methods based on area compensation. Fuzzy Sets Syst 82(3):319–330
36. Starczewski JT (2013) Defuzzification of uncertain fuzzy sets. In: Advanced concepts in fuzzy logic and systems with membership uncertainty. Springer, Berlin, pp 77–135
37. Matos MA, Gouveia EM (2008) The fuzzy power flow revisited. IEEE Trans Power Syst 23(1):213–218
38. Brooke AMA, Kendrick D, Roman R (1998) GAMS: a user's guide. GAMS Development Corporation, Washington

Probabilistic Modeling and Statistical Characteristics of Aggregate Wind Power

H. Louie and J. M. Sloughter

Abstract The stochasticity of the electrical power output by wind turbines poses special challenges to power system operation and planning. Increasing penetration levels of wind and other weather-driven renewable resources exacerbate the uncertainty and variability that must be managed. This chapter focuses on the probabilistic modeling and statistical characteristics of aggregated wind power in large electrical systems. The mathematical framework for probabilistic models—accounting for geographic diversity and the smoothing effect—is developed, and the selection and application of parametric models is discussed. Statistical characteristics from several real systems with high levels of wind power penetration are provided and analyzed.

Keywords Copulas · Correlation · Geographic diversity · Smoothing effect · Wind generators · Wind power modeling

1 Introduction

Wind turbines are classified as weather-driven renewable resources due to the dependency of their power output on local meteorological conditions [1]. These conditions are inherently transient and often erratic. Consequently, the power output by wind turbines—hereafter also simply referred to as "wind power"—is appropriately characterized as being *variable* and *uncertain*. Variability refers to

H. Louie (✉)
Department of Electrical and Computer Engineering, Seattle University, 901 12th Ave, Seattle WA 98122, USA
e-mail: louieh@seattleu.edu

J. M. Sloughter
Department of Mathematics, Seattle University, 901 12th Ave, Seattle WA 98122, USA
e-mail: sloughtj@seattleu.edu

J. Hossain and A. Mahmud (eds.), *Large Scale Renewable Power Generation*, Green Energy and Technology, DOI: 10.1007/978-981-4585-30-9_2,

the unintentional tendency for wind power to change—perhaps rapidly—from one moment to the next, whereas uncertainty refers to the wide range of unknown future values of wind power.

The stochasticity of wind power is a concern for system operators, as the legacy electric grid was designed to be operated with primarily deterministic sources [2, 3]. Although stochastic, wind power often exhibits identifiable patterns and quantifiable statistical distributions, which can be modeled and exploited to better manage the system. These models, whether mathematically formalized or tacitly understood, have applications in several areas, including wind power forecast systems, stochastic unit-commitment programs, risk analysis, and Monte Carlo-based simulations for resource planning and research [4–6].

This chapter focuses on the *aggregate* system-wide wind power, rather than the wind power from individual wind plants or turbines. We are motivated to take this macro-level view because for many system operators it is the aggregate—not individual—wind power that is of utmost concern. Our goal is to identify and develop probabilistic models of aggregate wind power and analyze its statistical characteristics. More specifically, we use parametric distributions—probability density functions (pdf) and cumulative distribution functions (cdf)—to model the instantaneous and moment-to-moment variations of aggregate wind power.

The remainder of this chapter is organized as follows. Section 2 describes the general characteristics of aggregate wind power. Section 3 formulates an idealized probabilistic model of wind power output from an individual wind plant. Aspects of geographic diversity including correlation, dependency structures, and practical considerations are discussed in Sect. 4, leading to probabilistic models for instantaneous and moment-to-moment wind power variation in Sect. 5. Aggregate wind power data from four large systems are analyzed and discussed in Sect. 6. The concluding remarks are given in Sect. 7.

2 General Characteristics of Aggregate Wind Power

Aggregate wind power is defined as the sum of the real power delivered by all wind plants in a system as measured at their point of interconnection with the grid. We are concerned with both the instantaneous and moment-to-moment variations of aggregate wind power. The statistical characteristics of instantaneous aggregate wind power provide information about the uncertainty, whereas the statistical characteristics of moment-to-moment variation of aggregate wind power provide information about the variability. Rather than formulating models in the power domain, it is more useful to do so in the normalized power domain. This facilitates easier comparison and allows the models to be scaled to the desired capacity level, increasing their applicability. The units in the normalized power domain are per-unit (p.u.), where the normalization is done with respect to the total capacity of the wind plants in the system.

The characteristics of aggregate wind power are derived from—but different than—the characteristics of wind power from individual wind plants. Aggregate wind power is strongly influenced by the *geographic diversity* of the wind plants in the system. Geographic diversity is a term describing the tendency for wind plants in different wind regimes and separated by large distances to exhibit low correlation in their instantaneous wind power and moment-to-moment variations.

Many aspects of geographic diversity have been widely explored in the literature [7–21]. All other things being equal, a system with high geographic diversity has lower variability and uncertainty than one with low geographic diversity. The reduction of variability caused by geographic diversity is also known as the *smoothing effect*. The benefits of high geographic diversity include less frequent occurrences of extremely high and low power output; less frequent ramp events; and improved accuracy of wind power forecasts. The results are greater economy and reliability, decreased reserve requirements, and more efficient commitment and dispatch of generators [22].

2.1 Uncertainty of Aggregate Wind Power

We first consider the uncertainty characteristics of aggregate wind power. The definition of uncertainty can be subjective, with several appropriate interpretations possible, depending on the application or situation. For example, a system operator may be concerned about the probability of extremely high or low aggregate wind power. In this case uncertainty is best measured using quantiles. Another operator may be interested in the general spread of potential values of aggregate wind power, in which case the standard deviation is an appropriate measure. Rather than strictly defining uncertainty, our approach is to recognize that the uncertainty information of aggregate wind power is contained in its probability density function, from which the quantiles, standard deviation, and other metrics of uncertainty can be measured or computed.

The shape of the probability density function can be approximated by constructing an empirical histogram of instantaneous aggregate wind power. Figure 1a shows a typical histogram of wind power from an individual wind plant and is provided for comparison purposes. Figure 1b–d shows aggregate wind power from three large systems. We will discuss the specific details of these systems and others in greater detail in Sect. 6. For now it suffices to know that each system has over 4 GW of installed wind capacity—a considerable amount. The computed standard deviation is provided with each plot. From inspection of Fig. 1, we make two important observations: (1) the modality of the wind power from an individual wind plant is different from that of wind power aggregated across a large system, and (2) different systems exhibit different uncertainty characteristics.

By most measures, the system corresponding to Fig. 1b has higher uncertainty than other systems. The standard deviation is greater than in other systems, and there are more frequent occurrences of zero and near rated (1.0 p.u.) power

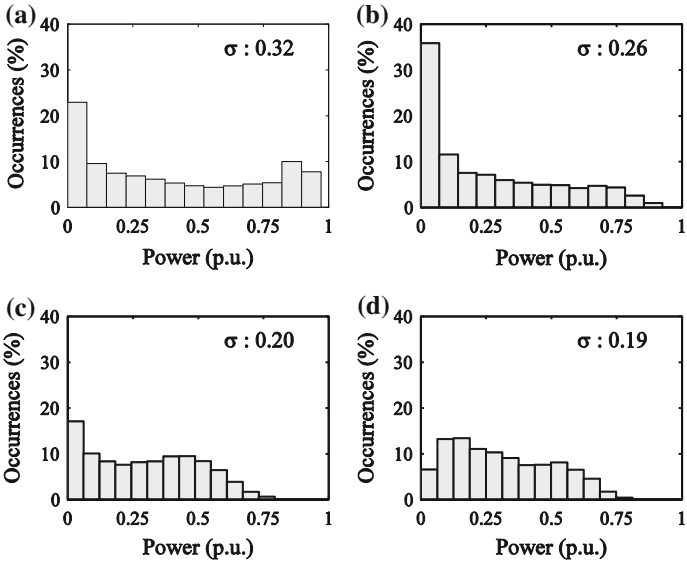

Fig. 1 Histograms of normalized wind power from an individual wind plant (**a**), and from large systems (**b–d**) with standard deviation displayed. **a** Single wind plant, **b** Lower diversity, **c** Medium diversity and **d** Higher diversity

production. These characteristics are similar to those of the individual wind plant, and as such the system can be described as having low geographic diversity. The wind plants in systems with low geographic diversity are often in close proximity—perhaps separated by 200 km or less—and are in the same or similar wind regime. The Bonneville Power Administration (BPA) is an example of a system with low geographic diversity.

The system corresponding to Fig. 1c exhibits less uncertainty than Fig. 1b. The standard deviation and occurrences of low output are reduced, and the maximum power output rarely exceeds 0.75 p.u. Figure 1d exhibits the lowest uncertainty of the systems, which is characteristic of a system with appreciable geographic diversity. Episodes of extremely low and high production are rare, and the standard deviation is lower than the others. Systems with this level of geographic diversity tend to have wind plants spread over very large territories. The Midwest ISO (MISO) and PJM systems are examples of systems with higher geographic diversity.

It is evident that there is no proto-typical histogram or probability density function of instantaneous aggregate wind power, and so the uncertainty will vary depending on system specifics—mainly the level of geographic diversity. Our approach, therefore, is to seek a flexible multi-parametric model capable of representing the commonly exhibited probability density function shapes by systems with various levels of geographic diversity.

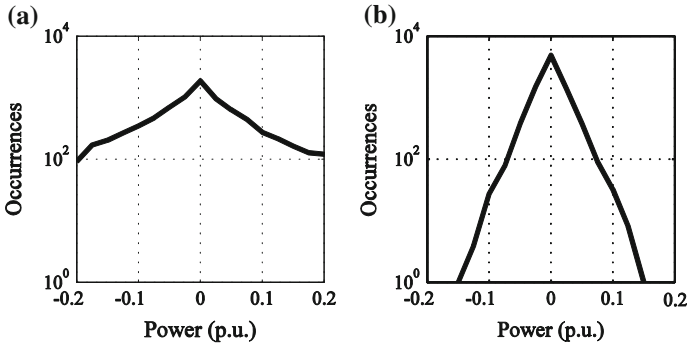

Fig. 2 Normalized hourly variability in wind power from an individual wind plant (**a**) and a large system (**b**) over the course of 1 year

2.2 Variability of Aggregate Wind Power

Instantaneous wind power values provide us with information on uncertainty, but we are also interested in wind power variability. The variability of wind power is examined through the statistical characteristics of wind power variation. Wind power variation is defined as the difference in instantaneous wind power at two points in time, usually 1 h: $\Delta P[t] = P[t] - P[t-q]$ where ΔP is the variation of wind power, t is the time, and q is the variation period. Similar to our approach with uncertainty, the variability of aggregate wind power is assessed by considering the probability density function of ΔP, as well as its statistical characteristics such as standard deviation and quantiles. We will see that variability in aggregate wind power is strongly influenced by geographic diversity.

Figure 2 shows typical normalized hour-to-hour wind power variation in an individual wind plant (a) and system (b) over a period of 1 year. Note that for clarity the ordinate is logarithmically scaled. The trace for the individual wind plant is much broader than for the system aggregate, indicating more frequent extreme variability. Aggregation, therefore, tends to smooth wind power variability. In Fig. 2a, b, the nearly linear decrease in occurrences on the logarithmically scaled ordinate suggests that an appropriate parametric model will have an exponential form. The slope of the decrease is influenced by the geographic diversity of the system, as well as the variation period, with shorter periods having steeper slopes.

In the above we have briefly described typical uncertainty and variability characteristics of aggregate wind power. These characteristics depend on the geographic diversity in a system, as well as the characteristics of the constituent individual wind plants. Therefore in order to thoughtfully propose aggregate wind power models, we must begin by modeling individual wind plants and then establishing the mathematical framework for geographic diversity's effect on uncertainty and variability.

3 Individual Wind Plant Model

The characteristics of aggregate wind power—especially at low levels of geographic diversity—depend on the characteristics of the system's constituent wind plants. We first derive an analytic model of wind plant power output under idealized conditions: that the wind speed follows a parametric probability density function and the energy conversion process is deterministic, among other assumptions. We conclude the section by considering non-idealities in wind plant power production.

The power delivered by a wind plant P_i is the sum of the real power produced by its constituent wind turbines, less collector system losses:

$$P_i = \sum_{j=1}^{M} P_{\mathrm{WT},j} - P_{L,i} \tag{1}$$

where M is the number of wind turbines in the wind plant, $P_{\mathrm{WT},j}$ is the real power generated by the jth wind turbine and $P_{\mathrm{L},i}$ is the ith wind plant's collector system losses at the current operating state.

Although (1) appears straightforward, wind turbines are nonlinear energy conversion devices whose power output is primarily dependent on wind speed, which is a random variable. This implies that P_i will be stochastic, and that a probabilistic model of P_i can be derived by transforming the probability density function of the wind speed.

3.1 Probabilistic Wind Speed Model

Let $\tilde{v}$ be a random variable representing the wind speed at a certain wind turbine with corresponding probability density function $f_v(\tilde{v})$. The presence of the tilde indicates that the variable is random. We can approximate $f_v(\tilde{v})$ by the repeated independent sampling of $\tilde{v}$. These samples can be binned into a histogram and scaled to approximate $f_v(\tilde{v})$. Two typical, yet specific, scaled histograms of wind speed are shown in Fig. 3.

Although histograms are helpful visual approximations of probability density functions, it is often desirable to represent them using a parametric function. Let $\hat{f}_v(\tilde{v}, \boldsymbol{\theta})$ be the model of $f_v(\tilde{v})$ with parameters arranged in the vector $\boldsymbol{\Theta}$. For the sake of brevity, we will suppress $\boldsymbol{\Theta}$ in all distributions hereafter, so that, for example, $\hat{f}_v(\tilde{v})$ represents the parametric model of $f_v(\tilde{v})$.

Returning to Fig. 3, we see that each histogram is asymmetric with a distinctly positive skewness, indicating that high wind speeds are less frequent than low wind speeds. These characteristics can be modeled using the three-parameter Generalized Gamma distribution [23]. However, estimating the parameters of this distribution can be difficult. Instead, the two-parameter Weibull distribution, which

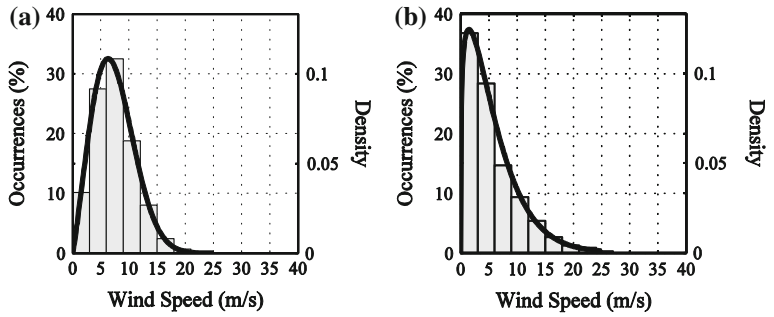

Fig. 3 Histograms of wind speed from two locations with fit Weibull probability density functions. **a** wind speed distribution for location 1, **b** wind speed distribution for location 2

is a special case of the Generalized Gamma distribution, is commonly used. The Weibull probability density function [24] is

$$\hat{f}_{\tilde{v}}(\tilde{v}) = \begin{cases} 0 & \tilde{v} < 0 \\ \frac{k}{\lambda}\left(\frac{\tilde{v}}{\lambda}\right)^{k-1} e^{-(\tilde{v}/\lambda)^k} & \tilde{v} \geq 0 \end{cases} \tag{2}$$

where k and λ are the shape and scale parameters, respectively. The parameters can be estimated from sampled data using the maximum likelihood estimation (MLE) method or the method of moments, though for the Weibull distribution these methods can be mathematically cumbersome [25, 26]. Examples of Weibull distributions with parameters estimated using MLE are shown as the solid traces in Fig. 3. In each case, the parametric function is a reasonable approximation to the data.

The two-parameter Weibull model can often be simplified to a single parameter model without appreciably sacrificing accuracy. For locations with wind regimes suitable for wind plant development, the estimated shape parameter of the Weibull distribution is often near 2.0. Therefore, the Weibull distribution can be reduced to the Rayleigh distribution [24]. A useful feature of the Rayleigh distribution is that its parameter can be estimated with the method of moments using only the mean of the wind speed, which is sometimes the only quantity available.

3.2 Idealized Wind Turbine Power Curve

We next examine the effect of the wind turbine in shaping the wind power probability density function. Wind turbines convert a portion of the kinetic energy into a mass of moving air to electrical energy by way of electric generator. The electrical power output by a wind turbine is computed from:

$$\tilde{P}_{\mathrm{WT}} = \frac{1}{2} C_{\mathrm{p}} A \rho \tilde{v}^3 \tag{3}$$

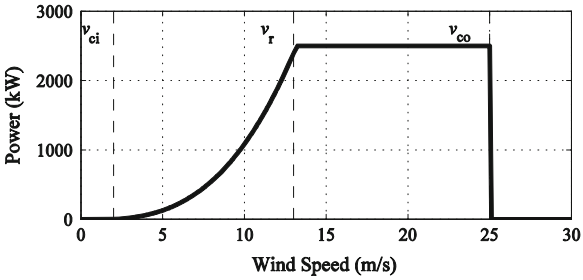

Fig. 4 Idealized *power curve* of a 2.5 MW wind turbine with cut-in speed of 2.5 m/s, rated wind speed of 3 m/s, and cut-out wind speed of 25 m/s

where C_p is the dimensionless power coefficient, A is the area swept by the rotor blades in m^2, and ρ and $\tilde{v}$ are the density and velocity of the air mass incident to the wind turbine, in kg/m^3 and m/s, respectively [27]. The power coefficient represents the overall efficiency of the energy conversion process, which depends on turbine design and operating state. If a constant C_p can be maintained, then the wind speed and wind power are cubically related. Under low or high wind speed conditions the wind turbine is operated such that C_p is zero, for reasons discussed later. Although (3) is useful, a more common and illustrative way to show the relationship between wind speed and wind turbine power output is with the power curve.

A power curve deterministically maps each wind speed to the corresponding power output of a wind turbine. An example of an idealized power curve is shown in Fig. 4. In general, there are four regions of operation.

3.2.1 Below Cut-in Wind Speed $(v < v_{ci})$

At low wind speeds no electrical power is produced and C_p is zero. The power in the wind is not enough to either overcome the friction of the drivetrain, or to result in positive net power production. The threshold wind speed at which power generation begins is known as the cut-in wind speed (v_{ci}).

3.2.2 Between Cut-in and Rated Wind Speed $(v_{ci} \leq v < v_r)$

When the wind speed is between the cut-in and rated wind speed (v_r), the wind turbine generates power. In this region, the turbine is designed or controlled to maximize C_p, and a nearly cubic wind speed-turbine power relationship is observed. This relationship can be approximated as

$$P_{WT} = av^3 - bP_r \tag{4}$$

where a and b are coefficients and P_r is the rated power of the wind turbine [27].

The coefficients can be determined by enforcing $P_r = av_r^3 - bP_r$ and $0 = av_{ci}^3 - bP_r$ and then numerically solving the resulting set of equations.

3.2.3 Between Rated and Cut-out Wind Speed $(v_r \leq v < v_{co})$

At wind speeds above rated and below cut-out (v_{co}), the wind turbine is controlled to maintain constant power production. As the wind speed increases over this region constant power is maintained by reducing C_p through active pitch control or passive stall design.

3.2.4 At and Above Cut-out Wind Speed $(v_{co} \leq v)$

At excessively high wind speeds, the wind turbine is in danger of mechanical failure. The turbine is aerodynamically slowed and stopped, and then mechanically locked into place to prevent rotation. C_p is zero over this region.

The effect of the varying power coefficient can be implicitly accounted for by expressing (3) as the piecewise function $P_{WT} = g(v)$, where $g(v)$:

$$P_{WT} = g(v) = \begin{cases} 0 & v < v_{ci} \\ av^3 - bP_r & v_{ci} \leq v < v_r \\ P_r & v_r \leq v < v_{co} \\ 0 & v_{co} \leq v \end{cases} \tag{5}$$

As previously mentioned, the power curve in Fig. 4 and expressed as (5) are idealized. Most utility-scale wind turbine manufacturers develop the power curve for a particular wind turbine model under carefully controlled conditions according to accepted standards [28]. Field performance of wind turbines can be inconsistent and appreciably differ from the manufacturer-supplied power curve. These non-idealities are discussed in detail in Sect. 3.4.

3.3 Idealized Wind Plant Model

A basic model of power from a wind plant is

$$\tilde{P}_i = M\tilde{P}_{WT} = Mg(\tilde{v}) \tag{6}$$

where $\tilde{P}_i$ is the total real power from the M wind turbines of wind plant i. This model makes several assumptions, such as all wind turbines experience the same wind speed and have the same power curve. We will discuss the reasonableness of these assumptions in Sect. 3.4. However, for the following, we will assume that (6) holds. Since $\tilde{P}_i$ is a random variable, we can characterize it with a probability density function or cumulative distribution function (cdf).

Let the cdf of the wind speed be $F_v(\tilde{v})$ and let the cdf of the wind power from the wind plant be $F_P(\tilde{P}_i)$. The cdf of the power from the wind plant is the piecewise function:

$$F_P(\tilde{P}_i) = \begin{cases} F_v(v_{\text{ci}}) + 1 - F_v(v_{\text{co}}) & \tilde{P}_i = 0 \\ F_v\left(g^{-1}\left(\tilde{P}_i/M\right)\right) + 1 - F_v(v_{\text{co}}) & 0 < \tilde{P}_i < MP_r \\ 1 & \tilde{P}_i = MP_r \end{cases} \tag{7}$$

where $g^{-1}(P_{\text{WT}})$ is the inverse power curve.

We can see that this gives us the following probabilities:

$$\begin{aligned} \Pr\{\tilde{P}_{\text{i}} = 0\} &= F_v(v_{\text{ci}}) + 1 - F_v(v_{\text{co}}) \\ \Pr\{0 < \tilde{P}_{\text{i}} < MP_{\text{r}}\} &= F_v(v_{\text{r}}) - F_v(v_{\text{ci}}) \\ \Pr\{\tilde{P}_{\text{i}} = MP_{\text{r}}\} &= F_v(v_{\text{co}}) - F_v(v_{\text{r}}) \end{aligned} \tag{8}$$

As there is a measurable probability of wind power being exactly equal to either 0 or MP_r, we do not have a purely continuous distribution function. We instead have a mixed discrete/continuous distribution function.

Our pdf for wind power, then, will need to use the Dirac delta function $\delta(\cdot)$ to address the probabilities of wind power being exactly equal to either 0 or MP_r. For all other values of wind power, we can calculate the pdf using the traditional change-of-variables method. Using (5), the inverse power curve for the region between 0 and MP_{r} is

$$v = g^{-1}(P_{\text{WT}}) = \left(\frac{P_{\text{WT}} + bP_r}{a}\right)^{1/3} \tag{9}$$

The corresponding probability density function of wind power for this region is found by taking the derivative of (7) with respect to $\tilde{P}_i$ so that:

$$\begin{aligned} f_P(\tilde{P}_i) &= \frac{\mathrm{d}F_P(\tilde{P}_i)}{\mathrm{d}\tilde{P}_i} = \frac{\mathrm{d}F_v\left(g^{-1}\left(\tilde{P}_i/M\right)\right)}{\mathrm{d}\tilde{P}_i} = \frac{\mathrm{d}F_v\left(g^{-1}\left(\tilde{P}_i/M\right)\right)}{\mathrm{d}g^{-1}\left(\tilde{P}_i/M\right)} \cdot \frac{\mathrm{d}g^{-1}\left(\tilde{P}_i/M\right)}{\mathrm{d}\tilde{P}_i} \\ &= \frac{\mathrm{d}F_v(\tilde{v})}{\mathrm{d}\tilde{v}} \cdot \frac{\mathrm{d}g^{-1}\left(\tilde{P}_i/M\right)}{\mathrm{d}\tilde{P}_i} \end{aligned} \tag{10}$$

We note that $\frac{\mathrm{d}F_v(\tilde{v})}{\mathrm{d}\tilde{v}}$ is just the pdf of the wind speed $\hat{f}_v(\tilde{v})$ evaluated at $\tilde{v} = g^{-1}\left(\tilde{P}_i/M\right)$ and that

$$\frac{\mathrm{d}g^{-1}\left(\tilde{P}_i/M\right)}{\mathrm{d}\tilde{P}_i} = \frac{\left(\frac{\tilde{P}_i/M + bPr}{a}\right)^{-2/3}}{3aM} \tag{11}$$

For the specific case of a Weibull wind speed distribution (10) becomes:

$$f_p(\tilde{P}_i) = \left(\frac{k}{\lambda} \left(\frac{g^{-1}\left(\tilde{P}_i/M\right)}{\lambda} \right)^{k-1} e^{-\left(\frac{g^{-1}\left(\tilde{P}_i/M\right)}{\lambda} \right)^{k}} \right) \frac{\left(\frac{\tilde{P}_i/M + bPr}{a} \right)^{-2/3}}{3aM}. \quad (12)$$

We now have closed-form algebraic expressions for the probability density function of wind power when $0 < \tilde{P}_i < MP_r$.

Applying (6), the idealized individual wind plant model for a Weibull distribution of wind speed is therefore:

$$f_p(\tilde{P}_i) = \left(\frac{k}{\lambda} \left(\frac{g^{-1}\left(\tilde{P}_i/M\right)}{\lambda} \right)^{k-1} e^{-\left(\frac{g^{-1}\left(\tilde{P}_i/M\right)}{\lambda} \right)^{k}} \right) \frac{\left(\frac{\tilde{P}_i/M + bPr}{a} \right)^{-2/3}}{3aM} + (F_v(v_{ci}) + 1 - F_v(v_{co}))\delta(\tilde{P}_i) + (F_v(v_{co}) - F_v(v_r))\delta(\tilde{P}_i - MP_r) \quad (13)$$

For $0 \le \tilde{P}_i \le MP_r$, and 0 everywhere else. For a Rayleigh distribution of wind speed:

$$f_p(\tilde{P}_i) = \left(\left(\frac{g^{-1}\left(\tilde{P}_i/M\right)}{\lambda^2} \right) e^{-\left(\frac{g^{-1}\left(\tilde{P}_i/M\right)^2}{2\lambda^2} \right)} \right) \frac{\left(\frac{\tilde{P}_i/M + bPr}{a} \right)^{-2/3}}{3aM} + (F_v(v_{ci}) + 1 - F_v(v_{co}))\delta(\tilde{P}_i) + (F_v(v_{co}) - F_v(v_r))\delta(\tilde{P}_i - MP_r) \quad (14)$$

again for $0 \le \tilde{P}_i \le MP_r$, and 0 everywhere else.

The models of individual wind plant power output in (13) and (14) were analytically derived and are dependent only on a small number of wind speed and power curve parameters. Figure 5 shows an example of the pdf and cdf of a wind plant. We note that the pdf shown is similar in appearance to that of Fig. 1a, which is reassuring. However, there are differences, particularly near rated power. Our analytic model overestimates the probability of rated power production from the wind plant. This discrepancy is an artifact of the idealized assumptions implied by (6). Despite the differences the derived model has utility—it serves as a reasonable starting point in the absence of additional data, and it allows for further analytic manipulation, as we will see later.

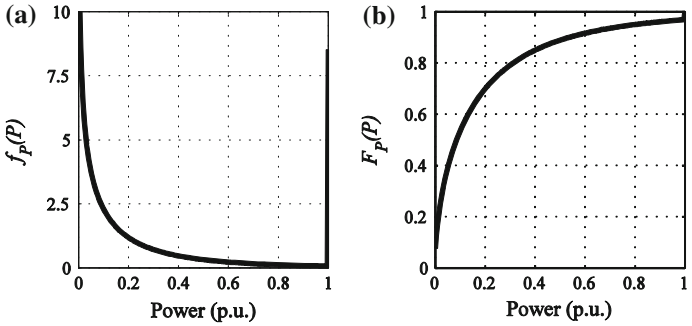

Fig. 5 Analytic pdf (**a**) and cdf (**b**) of wind power from an individual wind plant with *power curve* in Fig. 4 and a Rayleigh distribution of wind speed with scale parameter $\lambda = 5$

3.4 Non-idealized Wind Plant Modeling

The derived probability density functions in (14) and (15) are idealized models of wind power under several assumptions implied by (6), including:

1. the collector system is lossless;
2. all wind turbines are in service;
3. the power curves are deterministic for each wind turbine;
4. the wind speed and air density are the same at each wind turbine.

The first and second assumptions allow the wind plant to reach 100 % rated output. However, collector system losses are nonzero—usually between 1 and 5 % [29]—and wind turbines are routinely taken out of service due to scheduled maintenance or malfunction. A typical wind turbine requires regularly scheduled maintenance at 6 month intervals, although online condition monitoring may yield more optimal schedules [30]. Maintenance and malfunction-related outages can last several hours or longer, with offshore wind turbines generally requiring longer outages. For these reasons, a large wind plant may have one or more wind turbines out of service at any given time. Although rated power is not achieved, occurrences of near rated power may be common, as shown in Fig. 1a.

The third assumption, while greatly simplifying the model, is not substantiated by empirical data. Even after correcting for air density, power production strays from the manufacturer-supplied power curve for several reasons, including: dependency of power output on wind direction; forced curtailment; wind shear and turbulence; manufacturing and installation defects; efficiency degradation over time; and internal power consumption for control systems, lighting, pumps, and other functions. These effects are illustrated by an empirical power curve. An empirical power curve is constructed by plotting repeated in situ simultaneous measurements of wind speed and wind power, as shown in Fig. 6. It is clear from this figure that the idealized power curve model in (5) does not capture the true in situ relationship between wind speed and wind power.

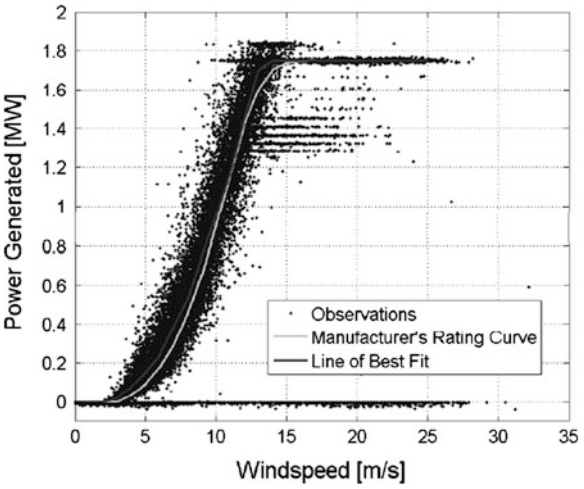

Fig. 6 Empirical *power curve* of a wind turbine showing effects of non-idealities © 2007 IEEE. Reprinted, with permission, from [31]

The fourth assumption implied by (6) is naïve, though often used. In reality, wind turbines can be separated by several kilometres and installed in varying terrain. The wind turbines almost never simultaneously experience the same wind speed. In other words, there is geographic diversity within each wind plant that must be accounted for. Over the years, several approaches to more realistically account for non-idealities in power curves have been proposed [32–34]. Some involve creating sub-groups of wind turbines, where each sub-group has its own wind speed. Other methods involve creating data-driven wind plant power curves using statistical methods. Provided they are well-defined, wind plant power curves can be used in place of (5) to analytically derive a probabilistic model of wind power using the same steps detailed in Sect. 3.3.

To summarize our progress, we started by identifying suitable parametric probabilistic models of wind speed: Rayleigh or Weibull. We then developed pdfs and cdfs for individual wind plant power output by transforming the wind speed models using an idealized power curve, as in (13) and (14). This method can be used to account for non-idealities using a wind plant power curve if desired. We are now poised to consider the aggregate power production from a fleet of wind plants in a common system. To do this, we must model the correlation and dependency of wind power among the wind plants. In other words, we must model the geographic diversity.

4 Geographic Diversity

The most important influencer of the uncertainty and variability of aggregate wind power is the geographic diversity of the system. A system's geographic diversity is a reference to the general level of dependence between the wind power from its

constituent wind plants. Dependence is often quantified using a correlation coefficient, with lower correlation generally resulting in decreased uncertainty and variability. The goal of this section is to formulate the mathematic basis for this phenomenon, discuss factors influencing correlation and dependency, as well as to comment on practical considerations.

4.1 Theoretical Basis

Aggregate wind power can mathematically be represented as

$$\tilde{P}_{\text{agg}} = \frac{1}{N}\sum_{i=1}^{N}\frac{\tilde{P}_i}{C_i} \tag{15}$$

where $\tilde{P}_{\text{agg}}$ is the normalized aggregate wind power, N is the number of wind plants considered, and C_i and P_{i} are the capacity and real power delivered by the ith wind plant.

Hereafter, subscripts are used to associate a variable with a specific wind plant, so that x_{n} pertains to the nth wind plant. We start with the idealized assumption that the wind speed at each wind plant $\tilde{v}_1, \ldots, \tilde{v}_N$ are independent random variables. Consequently, $\tilde{P}_1, \ldots, \tilde{P}_N$ will also be independent random variables, and are therefore uncorrelated.

As a result of the assumption of independence, the probability distribution of the aggregate power output is found through convolution and change-of-variables:

$$f_{P_{\text{agg}}}\left(\tilde{P}_{\text{agg}}\right) = \left(N\sum_{i=1}^{N} C_i\right) f_{P_1}\left(\tilde{P}_1\right) * \cdots * f_{P_N}\left(\tilde{P}_N\right) \tag{16}$$

where * is the convolution operator.

By the Central Limit Theorem, as N increases $f_{P_{\text{agg}}}\left(\tilde{P}_{\text{agg}}\right)$ will approach the Gaussian distribution so that:

$$f_{P_{\text{agg}}}\left(\tilde{P}_{\text{agg}}\right) = \frac{1}{\sigma_{\text{agg}}\sqrt{2\pi}} e^{-\frac{\left(\tilde{P}_{\text{agg}}-\mu_{\text{agg}}\right)^2}{2\sigma_{\text{agg}}^2}} N \to \inf \tag{17}$$

where μ_{agg} and σ_{agg} are the mean and standard deviation of $f_{P_{\text{agg}}}\left(\tilde{P}_{\text{agg}}\right)$. The transformation of the probability density function to a Gaussian distribution according to the Central Limit Theorem has important implications to the uncertainty of aggregate wind power.

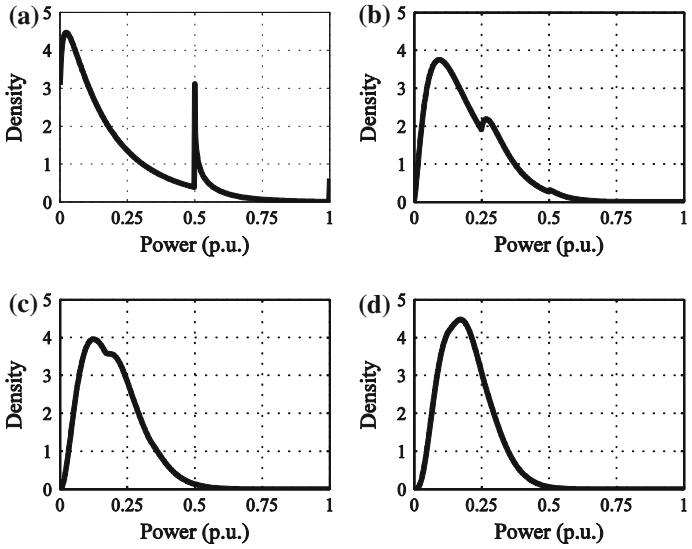

Fig. 7 Probability density functions of normalized aggregate wind power for systems with 2 (**a**), 4 (**b**), 6 (**c**) and 8 (**d**) wind plants under assumption of independence

4.2 Uncertainty and Variability Reduction

The normalized aggregate wind power's statistical variance will decrease as more wind plants are added to the system according to

$$\sigma_{\text{agg}}^2 = \frac{1}{N^2}\sum_{i=1}^{N}\sigma_i^2 \tag{18}$$

where σ_i^2 is the variance of the normalized power output of the *i*th wind plant. The decrease in variance causes the Gaussian distribution to contract, which can be interpreted as a decrease in the uncertainty of the wind power.

The evolution of $f_{P_{\text{agg}}}\left(\tilde{P}_{\text{agg}}\right)$ to a Gaussian distribution can be noticeable even for small values of *N*. This is illustrated in Fig. 7 where $f_{P_{agg}}\left(\tilde{P}_{\text{agg}}\right)$ for $N = 2, 4, 6,$ and 8 are plotted using numerical convolution based on the pdf in Fig. 5a and assuming independence in power output. Note how the distribution contracts as more wind plants are aggregated, resulting in decreased standard deviation and decreased probability of extremely high or low power output. In other words, the uncertainty decreases.

The effects of geographic diversity also apply to the moment-to-moment variation in aggregate wind power: under the assumption of independence, as more wind plants are aggregated the moment-to-moment variation approaches a Gaussian distribution with decreasing variance.

The preceding derivation showed the mathematical mechanism by which geographic diversity reduces uncertainty and variability in aggregate wind power. Its foundation is the assumption that the wind speed (and power) at all N wind plants are independent, and hence not correlated, but how realistic and restrictive is this assumption? It is intuitive that a pair of wind plants in close proximity will experience similar wind conditions. However, if they are separated by several hundred kilometres, the same claim becomes unreasonable. In other words, wind power tends to exhibit high spatial dependency of its correlation. It is these features that ultimately determine the geographic diversity of a system.

4.3 Correlation of Instantaneous Wind Power

The dependency of two random variables can be quantified by correlation coefficients. The correlation coefficient does not fully capture the underlying dependency structure between the variables as the joint distribution would, but nonetheless it is useful in quantifying the dependency. Among the most used correlation coefficients are Pearson's ρ and Kendall's τ. Pearson's ρ measures linear correlation, whereas Kendall's τ measures rank correlation [35]. There is no compelling reason to believe that wind power would be linearly correlated, and it has been argued that Kendall's τ is a more suitable metric for wind speed or power [36]. Nonetheless, many studies to date have focused strictly on Pearson's ρ. Whichever metric is used, it is widely recognized that there exists a strong relationship between separation distance and correlation coefficient [10–16].

Empirical studies have shown that the relationship between separation distance and correlation coefficient can be modeled as

$$\tau = e^{-rd^s} \tag{19}$$

where r is the so-called decay constant, s is the stretching coefficient, and d is the distance between wind plants in kilometers [7, 16]. Figure 8 shows the computed Kendall's τ for various randomly sampled wind plant pairings obtained from the NREL Eastern Wind Integration Data Set [37]. Similar traces have been reported for Pearson's ρ [7, 14]. The solid trace is for hourly averaged data; the dashed trace is for daily-averaged data. The decay and stretching coefficients for the hourly averaged data are 0.0037 and 0.92, respectively; and 0.0096 and 0.81 for the daily averaged data, respectively. In general, longer averaging periods result in larger correlation coefficients. Zero correlation in wind power among wind plant pairs does occur but is rare, and when it does occur it is usually at separation distances greater than 1,000 km.

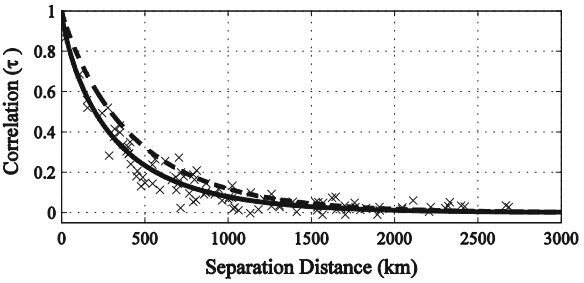

Fig. 8 Kendall's τ computed for 100 samples with hourly averaging (*solid*) and daily averaging (*dashed*). Only the data points for hourly averaging are shown for the sake of clarity

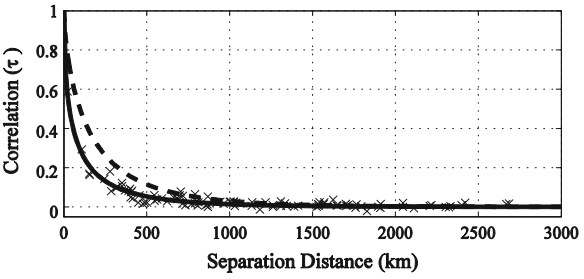

Fig. 9 Kendall's τ computed for 100 samples of aggregate wind power variation with hourly variation periods (*solid*) and 6-hourly variation periods (*dashed*). Only the data points for hourly variation periods are shown for the sake of clarity

4.4 Correlation of Wind Power Variation

Geographic diversity tends to have more pronounced effect on the moment-to-moment variation of wind power than on instantaneous wind power. Figure 9 shows the rank correlation coefficient for variation periods of 1 h (solid) and 6 h (dashed) for the same 100 wind plant pairs that were considered in the previous section. As before, an equation of the form of (19) suitably fits the data. The decay and stretching coefficients are 0.108 and 0.532 for the hourly variation, and 0.029 and 0.692 for the 6-hourly variation, respectively. From Fig. 9, and in general, longer variation periods tend to have higher correlation than short ones.

When compared to instantaneous power, the correlation coefficients of wind power variations are smaller and decay faster with distance. Near-zero correlation is exhibited at closer distances, around 750 km. The reduction of variation (smoothing effect), therefore, is noticeable in many systems.

4.5 Other Factors Influencing Correlation

Correlation of wind power is not solely dependent on separation distance. Other variables influencing correlation of wind power are:

- Terrain. Wind plants located close to each other but in different terrain may experience different wind regimes, which may decrease correlation.

- Averaging and variation period. Shorter periods tend to exhibit less correlation. Compare, for example, the solid and dashed lines in Figs. 8 and 9.
- Direction of the separation. For example, many North America wind plants with East–West separation have greater correlation than those with North–South separation [38].
- Number of wind turbines. Correlation between aggregate wind power in systems tends to be higher than the correlation between wind plants of individual wind turbines [16]. High frequency fluctuations tend to be uncorrelated and are filtered by dispersed wind turbines.

It is also notable that the correlation coefficient itself may exhibit erratic variation. Wind plant pairs may exhibit high correlation one day, and low correlation the next [15, 18].

4.6 Wind Power Dependency Structures

The correlation coefficient, while useful in quantifying dependence, does not provide sufficient information to construct the pdf of aggregate wind power from a pair of wind plants. Rather, information on the dependency structure of the wind power contained in the pair's joint distribution is needed.

The dependency structure of wind power is best explained visually and by considering the bi-variate case. Figure 10 shows typical, yet specific, contour plots of joint probability density functions for four different wind plant pairs, each with different rank correlation coefficients. The darker shading indicates greater density. The marginal histograms are shown on the top and right side of each plot.

Inspecting Fig. 10 shows how rank correlation tends to influence the joint distribution of wind power. At the lowest levels of correlation (Fig. 10a), mutually high power output is rare. Mutually low power output does occur, but that is an artifact of the marginal distributions having increased density at low power output.

At correlation levels in Fig. 10b—around 0.25—a concentration of higher density appears in the area of mutually high power output, but the density at mutually lower power remains. As correlation increases (Fig. 10c, d), the density begins to align along the diagonal, with areas of increased density at the extremes.

The normalized power output from each wind plant pair can be summed to examine the aggregate wind power in each of the four cases. The resulting histograms of aggregate power are shown in Fig. 11. Note that the power has been re-normalized by dividing the aggregate power by two, using a simplifying assumption that the capacities of each wind plant are identical.

As can be expected from its near-zero correlation, Fig. 11a resembles a system with higher geographic diversity. The standard deviation is lower than the others, and there is decreased probability of extreme power output. As correlation increases in Fig. 11b–d, so does the standard deviation and propensity for extreme power output. In Fig. 11d, the histogram appears similar to that of an individual wind plant, which is a signature of low geographic diversity.

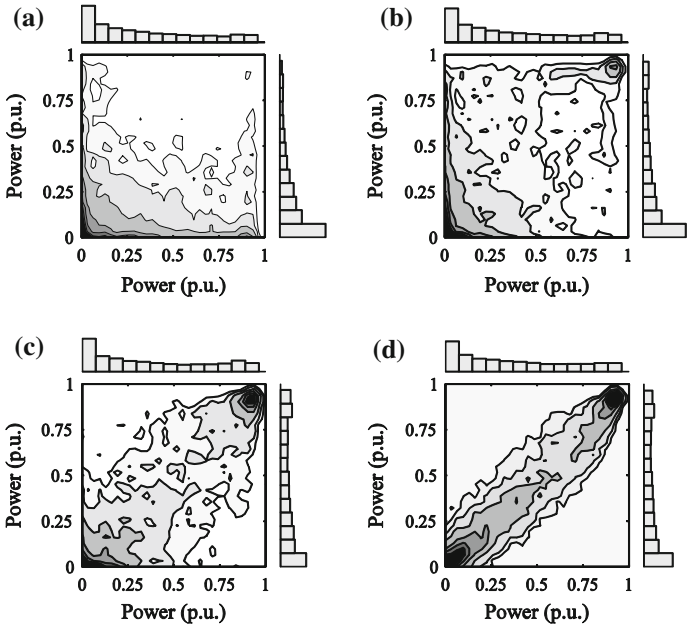

Fig. 10 Joint probability density function contours for wind plant pairs with increasing rank correlation. *Darker shading* indicates greater density. **a** $\tau = 0.01$, **b** $\tau = 0.25$, **c** $\tau = 0.52$ and **d** $\tau = 0.76$

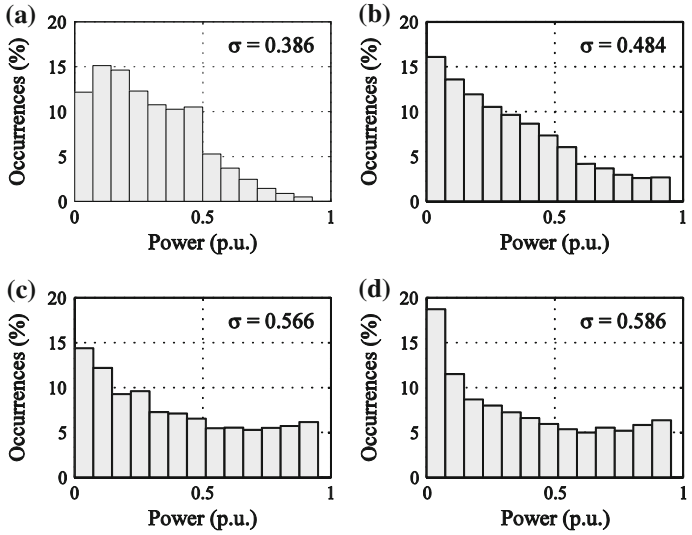

Fig. 11 Histograms of aggregate wind power for increasing rank correlation coefficients. **a** $\tau = 0.01$, **b** $\tau = 0.25$, **c** $\tau = 0.52$ and **d** $\tau = 0.76$

Figure 11 also illustrates that the wind plants in a system do not need be uncorrelated to realize the benefits of geographic diversity. Rather, uncertainty and variability are decreased even if the wind plants exhibit higher correlation—although not as noticeably as if the wind plants are uncorrelated.

4.7 Multivariate Models and Simulation

In the special case that aggregate and individual wind power need to be modeled or simulated, a multivariate model is required. For example, a Monte Carlo simulation can be performed by sampling from the joint distribution of the power from the wind plants. However, a proper joint distribution model must be identified.

Returning to Fig. 10, we see that the joint distributions do not obviously conform to any common parametric functions, and are certainly not Gaussian. One reason for this is that the marginal distributions add complexity to the overall structure. It is possible to decouple the influence of the marginal distributions from the joint by transforming the data from the wind power domain to the rank/uniform domain by way of the cdf of the individual wind plants. The result is uniform marginal distributions, with a joint distribution that is more amenable to parametric modeling. The resulting dependency structure can be modeled using copulas [39]. Though beyond the scope of this chapter, other works have shown that Gumbel and Gaussian copulas are appropriate for multi-variate wind power dependency modeling [40, 41]. The selection of a specific copula depends on the number of wind plants and the desired rank correlation.

One method of Monte Carlo simulation of wind power using copulas is: (1) identify the separation distances of the wind plants to be modeled; (2) using (19), compute the corresponding rank correlation matrix; (3) select an appropriate multivariate copula to model the dependency structure, using the correlation coefficient to determine the copula's parameters; (4) randomly draw the desired number of samples from the copula in the rank/uniform domain; (5) transform the samples to the wind power domain using the inverse cdf of (7). See [40, 41] for additional implementation details.

4.8 Practical Considerations

Geographic diversity can theoretically reduce uncertainty and variability of aggregate wind power. However, in many systems, the perceived benefits of geographic diversity have failed to materialize. There are four main reasons for this [16]:

1. In many electricity markets, the system-wide benefits of reduced uncertainty and variability do not directly translate into gains for individual wind plants—they do not have compelling economic reasons to seek geographic diversity.

2. Wind plants tend to have greater capacities, resulting in high concentrations of wind turbines.
3. There is limited access to suitable transmission limits the number of geographically diverse regions that can be interconnected.
4. There is only so much geographic diversity that can be had. In a given region, as wind plants are added, the benefits of geographic diversity saturate. Additionally, large-scale forces such as insolation similarly influence very wide areas (e.g., the continental United States).

In this section we have shown that geographic diversity, particularly in the separation distance between wind plants, reduces dependency and correlation. This in turn leads to a transformation of the probability density function of instantaneous and moment-to-moment variations in aggregate wind power toward a Gaussian distribution, with decreased standard deviation, and hence less uncertainty and variability. However, geographic diversity can and should not be viewed as a panacea for eliminating variability and uncertainty. Wind plants exhibit statistically significant correlation at large separation distances, and there are several practical reasons for geographic diversity not to occur. The prospects for variability reduction, however, are better as the correlation of wind power variability rapidly decreases with separation distance.

5 Aggregate Wind Power Models

In many cases, especially in the absence of transmission congestion, we are less concerned about the power from individual wind plants, and more concerned about the aggregate wind power. In these cases, we need not model the individual wind plants, and instead focus only on the aggregate wind power.

In this section we identify appropriate parametric models of the probability density functions of aggregate instantaneous wind power and wind power variation. Parametric approximation has several advantages including: fewer data points are needed to "fill out" the distribution; analytic calculations are more tractable; and the model can be expressed with fewer pieces of information—hopefully just one or two parameters.

5.1 Instantaneous Aggregate Wind Power Model

The shape of the histograms of aggregate wind power in Fig. 1 suggests that we seek a model with two parameters—one controlling the shape at low wind power, the other at high wind power.

One promising candidate is the Beta probability density function:

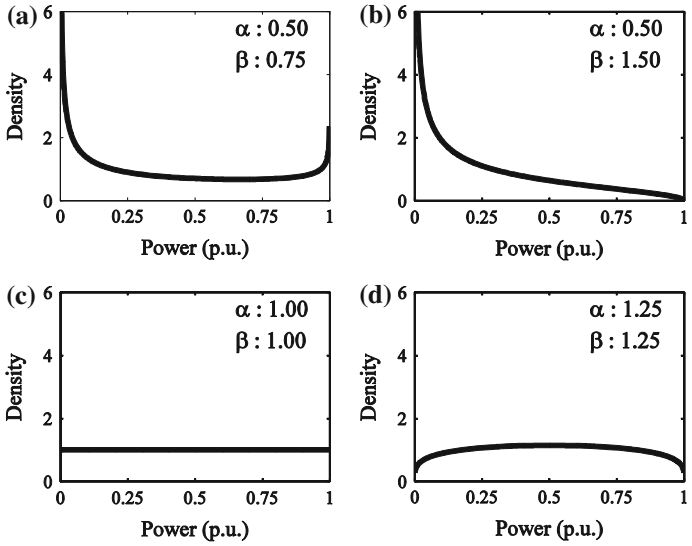

Fig. 12 Examples of Beta probability density functions with various α and β parameters

$$\hat{f}_P\left(\tilde{P}_{\text{agg}}\right) = \frac{\tilde{P}_{\text{agg}}^{\alpha-1} \times \left(1 - \tilde{P}_{\text{agg}}\right)^{\beta-1}}{B(\alpha, \beta)} \tag{20}$$

where $B(\alpha, \beta)$ is the Beta function:

$$B(\alpha, \beta) = \int_0^1 u^{\alpha-1} \times (1-u)^{\beta-1} \mathrm{d}u \tag{21}$$

and α and β are shape parameters and u is the variable of integration. The domain of the Beta pdf is [0, 1], thereby necessitating the use of normalized aggregate wind power values. A wide range of shapes are possible by careful selection of α and β, as shown in Fig. 12.

5.2 Beta Distribution Parameter Selection

An important advantage of using the Beta pdf to model aggregate wind power is that its parameters lend themselves to meaningful interpretation [42]. Values of α that are less than 1 indicate an increasing probability density of 0 or near-zero power output; whereas α values greater than 1 indicate decreasing probability density over this range. The β values have a similar interpretation. If β is greater

than 1, then the probability density decreases toward full power output; whereas if it is less than 1, there is increasing probability density.

In the absence of specific information, heuristic guides can be followed for modeling aggregate wind power. For low diversity, α and β are both greater than 1; for medium diversity $\alpha > 1$ and $\beta < 1$; and for higher diversity $\alpha < 1$, $\beta < 1$ or a Gaussian distribution can be used. Specific values for the parameters can be selected from estimations of the mean and variance.

The shape parameters are related to the mean as

$$\mu = \frac{\alpha}{\alpha + \beta} \tag{22}$$

The mean wind power considered over a length of time is also known as the capacity factor, which ranges between 20 and 40 % for most systems. Therefore the ratio of α to β from 1:1.5 to 1:4 is reasonable. The parameters are related to the variance as

$$\sigma^2 = \frac{\alpha\beta}{(\alpha + \beta)^2(\alpha + \beta + 1)} \tag{23}$$

Typical variance values range from about 0.02 to 0.10.

The parameters of the Beta pdf can be estimated using the method of moments according to

$$\hat{\alpha} = \hat{\mu}\left(\frac{\hat{\mu}(1 - \hat{\mu})}{\hat{\sigma}^2} - 1\right) \tag{24}$$

$$\hat{\beta} = (1 - \hat{\mu})\left(\frac{\hat{\mu}(1 - \hat{\mu})}{\hat{\sigma}^2} - 1\right) \tag{25}$$

where $\hat{\mu}$ and $\hat{\sigma}^2$ are the sampled mean and variance of the wind power data. There is no closed-form MLE of $\hat{\alpha}$ and $\hat{\beta}$, but numerical methods can be used to compute them [43].

Traces of the Beta pdf with parameters fit using MLE to aggregate wind power data from four large systems in different years are found in Figs. 13 and 14. In each case the Beta pdf is able to reasonably approximate the data. A rigorous evaluation of the fit of Beta distributions to aggregate wind power is found in [42].

5.3 Aggregate Wind Power Variation Model

Wind speed and wind power tend to exhibit large autocorrelation coefficients at short time lags. As such $\Delta\tilde{P}$ tends to be near-zero, with only rare occurrences of extreme deviations. The trend is that of symmetric and exponential decay.

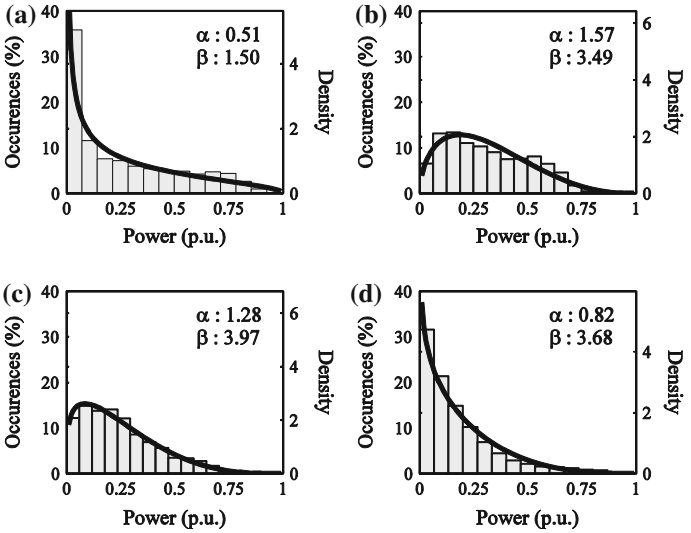

Fig. 13 Normalized aggregate wind power histograms in 2012 with fit Beta probability density functions. **a** BPA, **b** MISO, **c** PJM and **d** 50 Hz

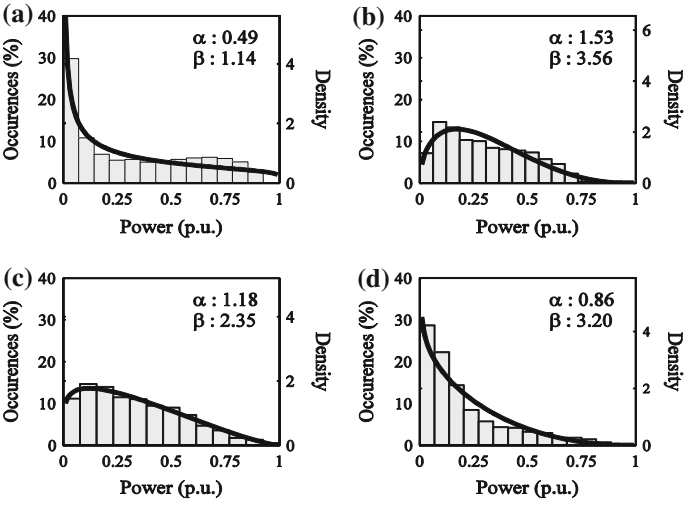

Fig. 14 Normalized aggregate wind power histograms in 2008 with fit Beta probability density functions. **a** BPA, **b** MISO, **c** PJM and **d** 50 Hz

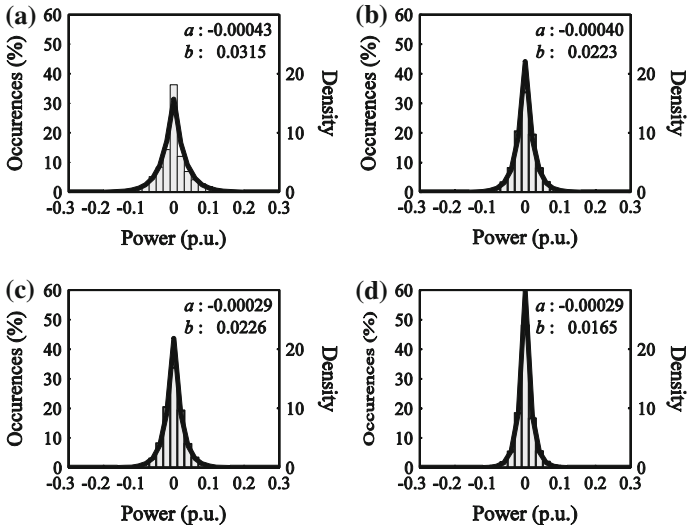

Fig. 15 Normalized aggregate wind power hourly variations in 2012 and fit Laplace probability density functions. **a** BPA, **b** MISO, **c** PJM and **d** 50 Hz

An appropriate distribution for these features is the Laplace distribution, also known as the double exponential distribution. The Laplace pdf is

$$\hat{f}_{\Delta\tilde{P}_{\text{agg}}}\left(\Delta\tilde{P}_{\text{agg}}\right) = \frac{1}{2b} e^{-\left|\Delta\tilde{P}_{\text{agg}} - a/b\right|} \tag{26}$$

where $\Delta\tilde{P}_{\text{agg}}$ is normalized aggregation power output variation and a and b are the location and scale parameters, respectively. The scale parameter is an indicator of the variability, where a larger scale parameter indicates greater variability.

5.4 Laplace Distribution Parameter Selection

The parameters of the Laplace distribution can be fit using MLE method where $\hat{a}$ is equal to the sample median, which is usually zero, and $\hat{b}$ is computed from

$$\hat{b} = \frac{1}{N}\sum_{i=1}^{N}\left|\Delta\tilde{P}_{agg,i} - \hat{a}\right| \tag{27}$$

The scale parameter is generally between 0.015 and 0.04 for 1 h variation periods. The scale parameter tends to increase with longer variation periods. Traces of the Laplace pdf with parameters fit using MLE to hourly aggregate wind power variation data are found in Figs. 15 and 16. In each case the Laplace pdf is

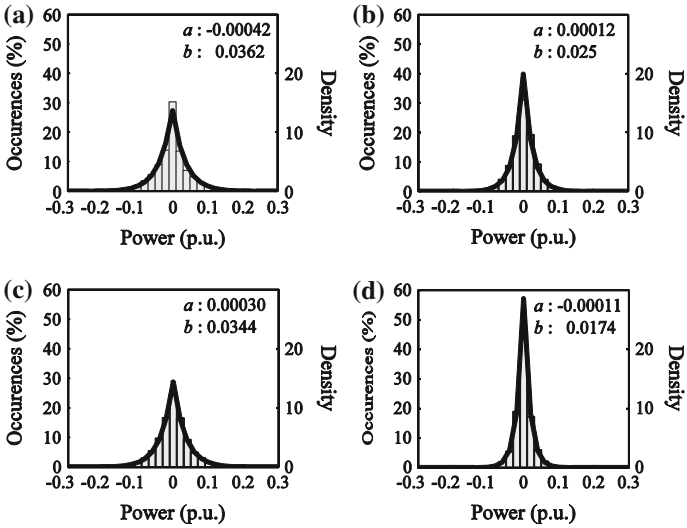

Fig. 16 Normalized aggregate wind power hourly variations in 2008 and fit Laplace probability density functions. **a** BPA, **b** MISO, **c** PJM and **d** 50 Hz

able to reasonably approximate the data. A rigorous evaluation of the fit of Laplace distributions to aggregate wind power is found in [44].

5.5 Influence of Variation Period

An important factor influencing the pdf of wind power variation is the variation period. As discussed in Sect. 4.4, the variation in wind power from wind plants exhibits greater correlation as the variation period increases. Additionally, there is also more time for the wind power to change, so there is greater potential for extreme variation. Figure 17 shows histograms and fit Laplace pdfs for hourly and 4-hourly variation periods. It is clear that a longer variation period results in a broader distribution, and hence, more variability that must be managed. The Laplace distribution is able to reasonably fit the data at both variation periods mainly by adjusting its scale parameter.

6 Statistical Characteristics of Aggregate Wind Power

It has only been within the last several years that aggregate wind power data sets have been made widely available to the research community. In this section we analyze several data sets with the goal of documenting and discussing statistical

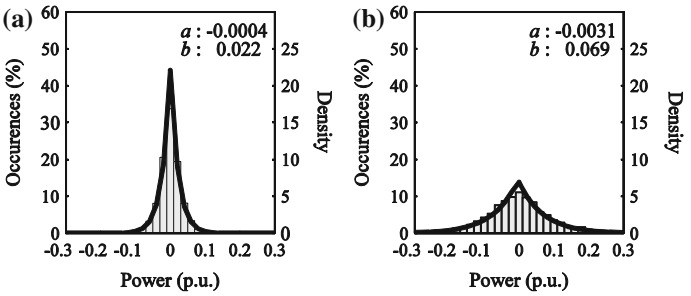

Fig. 17 Normalized aggregate wind power variation histograms and fit Laplace distributions for 1-h (**a**) and 4-h variation periods (**b**)

Table 1 Data set descriptions

System	2008 start capacity (MW)	2008 end capacity (MW)	2012 start capacity (MW)	2012 end capacity (MW)
BPA	1,301	1,671	4,131	4,711
MISO	2,462	4,327	10,514	12,270
PJM	1,150	1,277	5,318	6,457
50 Hz	9,091	9,493	11,570	12,420

characteristics of aggregate wind power, as well as seeking additional insight into geographic diversity.

6.1 Data Set Descriptions

Four data sets of aggregate wind power are considered: Bonneville Power Administration (BPA), Midwest ISO (MISO), PJM Interconnection (PJM), and 50 Hz [45–48]. BPA's territory is located in the Pacific Northwest of the United States, primarily in Washington State and Oregon. MISO has territory in 12 states in the midwest of the United States and in the Canadian province of Manitoba. PJM's territory covers all or parts of 13 states in the eastern portion of the U.S. 50 Hz's territory is in the northern and eastern portion of Germany. Each system has a large amount of wind plant capacity.

The data correspond to hourly averages for the years 2008 and 2012. The data have been normalized to reported system-wide wind capacity. However, these reports are infrequently issued. To overcome this, linear interpolation between reporting dates was used. This inherently introduces some error in the analysis, and so the reported statistics must be interpreted with this in mind. The capacities at the start and end of 2008 and 2012 are provided in Table 1.

Table 2 Instantaneous aggregate wind power statistical information for 2012

System	Mean (p.u.)	Standard deviation (p.u.)	Q(1) (p.u.)	Q(10) (p.u.)	Q(20) (p.u.)	Q(50) (p.u.)	Q(80) (p.u.)	Q(90) (p.u.)	Q(99) (p.u.)
BPA	0.26	0.26	0.00	0.01	0.02	0.16	0.52	0.68	0.85
MISO	0.31	0.19	0.02	0.08	0.13	0.28	0.51	0.58	0.72
PJM	0.25	0.17	0.01	0.05	0.09	0.21	0.39	0.50	0.68
50 Hz	0.18	0.17	0.00	0.02	0.04	0.12	0.28	0.41	0.78

Table 3 Instantaneous aggregate wind power statistical information for 2008

System	Mean (p.u.)	Standard deviation (p.u.)	Q(1) (p.u.)	Q(10) (p.u.)	Q(20) (p.u.)	Q(50) (p.u.)	Q(80) (p.u.)	Q(90) (p.u.)	Q(99) (p.u.)
BPA	0.32	0.29	0.00	0.01	0.03	0.25	0.64	0.76	0.88
MISO	0.30	0.19	0.02	0.08	0.12	0.27	0.49	0.58	0.71
PJM	0.33	0.22	0.01	0.07	0.12	0.30	0.53	0.64	0.89
50 Hz	0.20	0.20	0.01	0.03	0.05	0.13	0.35	0.52	0.80

6.2 Statistical Analysis of Uncertainty

Several statistical quantities of instantaneous aggregate wind power for each system for 2012 and 2008 are provided in Tables 2 and 3, respectively. In addition to the mean and standard deviation, several quantiles were computed, where, for example, Q(50) refers to the median.

The mean values range between 0.18 and 0.33 p.u., and the standard deviation ranges from 0.17 to 0.29 p.u. These typical ranges of mean and standard deviation can be used to construct models of aggregate wind power, as discussed in Sect. 5.2. The Q(99) quantiles indicates the magnitude of rare wind power events. For example, for BPA in 2012, in 99 % of the hours the aggregate wind power was less than or equal to 85 % of the rated capacity. This means that 1 % of year—approximately 88 h—the power was greater than 0.85 p.u. For all systems, the values corresponding to the 99 % quantile ranged between 0.68 and 0.88 p.u. Extremely low values were common: the 10 % quantile is 0.08 p.u. or less in all cases. In other words, in each system the power output is less than 8 % of rated capacity for nearly 876 h each year. The relatively high frequency of low power output has system-wide generation capacity implications. In general, the systems have very different levels of uncertainty that must be managed by their operators. By several measures, MISO, PJM, and 50 Hz have less uncertainty than BPA.

6.3 Statistical Analysis of Variability

The statistics for hour-to-hour variation for each system in 2012 and 2008 are provided in Tables 4 and 5, respectively. The variations of aggregate wind power

Table 4 Aggregate wind power hourly variation for 2012

System	Standard deviation (p.u.)	Kurtosis	Q(1) (p.u.)	Q(10) (p.u.)	Q(20) (p.u.)	Q(50) (p.u.)	Q(80) (p.u.)	Q(90) (p.u.)	Q(99) (p.u.)
BPA	0.048	7.0	−0.130	−0.053	−0.029	0.00	0.026	0.057	0.144
MISO	0.030	4.4	−0.79	−0.036	−0.022	0.00	0.021	0.036	0.083
PJM	0.032	28.2	−0.84	−0.035	−0.022	0.00	0.021	0.037	0.083
50 Hz	0.024	6.5	−0.66	−0.027	−0.015	0.00	0.014	0.027	0.072

Table 5 Instantaneous aggregate wind power hourly variation for 2008

System	Standard deviation (p.u.)	Kurtosis	Q(1) (p.u.)	Q(10) (p.u.)	Q(20) (p.u.)	Q(50) (p.u.)	Q(80) (p.u.)	Q(90) (p.u.)	Q(99) (p.u.)
BPA	0.054	8.2	−0.138	−0.061	−0.034	0.00	0.030	0.061	0.167
MISO	0.034	5.0	−0.093	−0.041	−0.024	0.00	0.024	0.040	0.089
PJM	0.049	7.3	−0.128	−0.055	−0.032	0.00	0.031	0.055	0.131
50 Hz	0.026	7.0	−0.075	−0.027	−0.015	0.00	0.015	0.029	0.073

in large systems tend to be symmetric, with near-zero mean and median. In most system, the variations are less than 0.06 p.u. in magnitude for over 80 % of the hours. Extreme outliers corresponding to changes of ± 0.08 to 0.17 p.u. do occur, but are rare. The standard deviations range from 0.024 to 0.054 p.u. In each system, the variations are leptokurtic, indicating a higher occurrence of "tail event" variations. In general, MISO, PJM, and 50 Hz have less variability than BPA.

6.4 Effect of Capacity on Uncertainty and Variability

The effect of capacity and capacity increases on aggregate wind power uncertainty and variability are often of interest as system operators anticipate and plan for increased amounts of wind plants in their system. The specifics of how the uncertainty and variability associated with aggregate wind power are related to capacity depend on the build-out of the wind plants in the system, and are difficult to analytically derive. However, based on the available data and past experience, there are several general observations that can be made:

1. Systems with larger installed capacities do not necessarily exhibit less uncertainty and variability in aggregate wind power than systems with smaller capacities.
2. Additions of wind plant capacity to a system tend reduce uncertainty and variability.
3. Within a given system, the benefits of geographic diversity can become saturated and insensitive to increases in capacity.

As an example of the first observation, we compare the statistics of instantaneous power in PJM and BPA. At the end of 2012, there was 4.7 GW of installed wind capacity in BPA. At the end of 2008 in PJM there was 1.3 GW of installed wind capacity. It would seem that BPA should have less uncertainty given its much higher installed capacity and therefore greater opportunity for geographic diversity. However, the standard deviation of PJM (0.22 p.u.) was less than that of BPA (26 p.u.). BPA also generally exhibited more occurrences of extremely low and high power production, as shown by the quantiles in Tables 2 and 3. A similar example for variability can be made by comparing 2008 MISO data with 2008 BPA data. These cases should not be misinterpreted as evidence that systems with higher capacities of wind plants have greater uncertainty and variability than those with lower capacities. Rather, they are simply examples that the contrary is not always the case. The important concept is that different systems experience different build-outs of wind plants—some lead to appreciable geographic diversity, others do not.

The second observation—that additions of wind plant capacity to a system tend reduce uncertainty and variability—is observed by comparing the statistics of each system in 2008–2012. In each system, the standard deviation of the instantaneous power and power variation decreased from 2008 to 2012. The exception is MISO, whose standard deviation of instantaneous power remained the same. Regardless, the data support the general notion that wind plant capacity additions decrease uncertainty and variability.

The final observation—that the benefits of uncertainty and variability reduction can become saturated—is supported by examining the sensitivity of uncertainty and variability to capacity addition. For BPA, PJM and 50 Hz, for every 1 GW of new wind plant installations, the standard deviation of instantaneous wind power decreased by just one percentage point, based upon year-end capacity values. For MISO, the standard deviation did not change, despite an increase in 8 GW of wind power. The quantiles in many systems also showed modest changes despite large capacity additions. The modest effects of capacity additions on uncertainty can be seen by inspecting Figs. 13 and 14. The histograms and approximated probability density functions of the system do not appear appreciably different in 2012 than they did in 2008, despite several thousand megawatts of wind plant installations in each system. The histograms and probability density functions of variations in Figs. 15 and 16, however, have more noticeable differences.

The sensitivity of variability to changes in capacity are mixed. The standard deviation of wind power variability in BPA and PJM decreased by approximately 0.25 % point for each 1 GW of new capacity. A change in percentage point of this magnitude is appreciable since the standard deviations of variation are all less than 6 %. However, both MISO and 50 Hz exhibited small changes to their standard deviation between 2008 and 2012.

7 Conclusions

Many power systems around the world now have total installed wind plant capacities in excess of several gigawatts. System operators must manage the inherent uncertainty and variability of the aggregate wind power in their systems in order to maintain reliability and economic efficiency. The characteristics of aggregate wind power can be quite different from individual wind plants, depending on the level of geographic diversity in the system. Tools such as wind power forecast systems, stochastic unit commitment, and resource planning require reasonable and practical probabilistic models of aggregate wind power and wind power variation as inputs.

This chapter demonstrated that the uncertainty and variability exhibited by aggregate wind power can be reasonably represented using parsimonious parametric models. More specifically, the two-parameter Beta distribution is well suited for modeling instantaneous aggregate wind power and the two-parameter Laplace distribution is well suited for modeling moment-to-moment variation.

Several aspects of geographic diversity were explored. Among the main conclusions are that geographic diversity should not be viewed as a panacea for the challenges of wind integration. Reduction in variability—the smoothing effect—is noticeable, but reduction in uncertainty requires exceedingly large geographic areas. Appreciable correlation of instantaneous power amongst wind plants can exist at distances approaching 1,000 km. Clustering and other practical considerations also limit the amount of geographic diversity that occurs in many systems. Analysis of several systems showed that the effects of geographic diversity, particularly on uncertainty, saturate when installations of wind plants reach several gigawatts in total.

References

1. Burton T, Sharpe D, Jenkins N, Bossanyi E (2001) Wind energy handbook. Wiley, West Sussex
2. Smith JC, Milligan M, DeMeo EA, Parsons B (2007) Utility wind integration and operating impact state of the art. IEEE Trans Power Syst 22:900–908. doi:10.1109/TPWRS.2007.901598
3. Smith JC, Thresher R, Zavadil R, DeMeo EA, Piwko R, Ernst B, Ackerman T (2009) A mighty wind. IEEE Power Energy Mag 7:41–51. doi:10.1109/MPE.2008.931492
4. Tuohy A, Meibom P, Denny E, O'Malley M (2009) Unit commitment for systems with significant wind penetration. IEEE Trans Power Syst 24:592–601. doi:10.1109/TPWRS.2009.2016470
5. Ruiz P, Philbrick CR, Zak E, Cheung K, Sauer P (2008) Applying stochastic programming to the unit commitment problem. In: Probabilistic methods applied to power systems; 2008
6. Pinson P, Kariniotakis G (2010) Conditional prediction intervals of wind power generation. IEEE Trans Power Syst 25:1845–1856
7. Hasche B (2010) General statistics of geographically dispersed wind power. Wind Energy 13:773–784. doi:10.1002/we.397

8. EnerNex Corporation (2011) Eastern wind integration and transmission study. Technical report NREL/SR-5500-47078, NREL, Golden, CO, USA
9. GE Energy (2010) Western wind and solar integration study. Technical report NREL/SR-550-47434, NREL, Golden, CO, USA 2010
10. McNerney G, Richardson R (1992) The statistical smoothing of power delivered to utilities by multiple wind turbines. IEEE Trans Energy Convers 7(4):644–647. doi:10.1109/60.182646
11. Archer C, Jacobson M (2003) Spatial and temporal distributions of U.S. winds and wind power at 80 m derived from measurements. J Geophys Res 108(D9):10–1–10–20
12. Wan Y (2004) Wind power plant behaviors: analyses of long-term wind power data. Technical report NREL/TP-500-36551
13. Holttinen H (2005) Hourly wind power variations in the Nordic countries. Wind Energy 8:173–195
14. Ernst B, Wan Y, Kirby B (1999) Short-term power fluctuation of wind turbines: analyzing data from the German 250-MW measurement program from the ancillary services viewpoint. Technical report NREL/CP-500-26722
15. Wan Y, Milligan M, Parsons B (2003) Output power correlation between adjacent wind power plants. J Sol Energy Eng 125:551–555
16. Louie H (2013) Correlation and statistical characteristics of aggregate wind power in large transcontinental systems. Wind Energy. doi:10.1002/we.1597
17. Tastu J, Pinson P, Kotwa E, Madsen H, Nielsen H (2011) Spatio-temporal analysis and modeling of short-term wind power forecast errors. Wind Energy 14:43–60. doi:10.1002/we.401
18. Nanahara T, Asari M, Maejima T, Sato T, Yamaguchi K, Shibata M (2004) Smoothing effects of distributed wind turbines. Part 2. Coherence among power output of distant wind turbines. Wind Energy 7:75–85. doi:10.1002/we.108
19. Krich A, Milligan M (2005) The impact of wind energy on hourly load following requirements: an hourly and seasonal analysis. Technical report NREL/CP-500-38061
20. Wan Y (2011) Analysis of wind power ramping behavior in ERCOT. Technical report NREL/TP-5500-49218 2011
21. Gibescu M, Brand A, Kling W (2008) Estimation of variability and predictability of large-scale wind energy in the Netherlands. Wind Energy 12:241–260. doi:10.1002/we.291
22. Milligan M (2000) Modelling utility-scale wind power plants. Part 2: Capacity credit. Wind Energy 3:167–206. doi:10.1002/we.36
23. Sloughter JM, Gneiting T, Raftery AE (2010) Probabilistic wind speed forecasting using ensembles and Bayesian model averaging. J Am Stat Assoc 105:25–35. doi:10.1198/jasa.2009.ap08615
24. Papoulis A, Pillai SU (2002) Probability, random variables and stochastic processes, 4th edn. McGraw-Hill, New York
25. Justus CG, Hargraves WR, Mikhail A, Graber D (1978) Methods for estimating wind speed frequency distributions. J Appl Meteorol 17:350–353
26. Tuzuner A, Yu Z (2008) A theoretical analysis on parameter estimation for the weibull wind speed distribution. IEEE PES General Meeting 2008
27. Twidell J, Weir T (2006) Renew Energy Res, 2nd edn. Taylor & Francis, London
28. International Electrotechnical Commission (2005), Power performance measurements of electricity producing wind turbines. Standard 61400-12-1
29. Camm EH, Behnke MR, Bolado O et al (2009) Wind power plant substation and collector system redundancy, reliability and economics. IEEE PES general meeting 2009
30. Fischer K, Besnard F, Bertling L (2012) Reliability-centered maintenance for wind turbines based on statistical analysis and practical experience. IEEE Trans Energy Convers 27(184):195. doi:10.1109/TEC.2011.2176129
31. Potter CW, Gil H, McCaa J (2007) Wind power data for grid integration studies. IEEE PES general meeting

32. Hayes B, Ilie I, Porpodas A, Djokic S, Chicco G. Equivalent power curve model of a wind farm based on field measurement data. In: IEEE PowerTech; 2011
33. Jin T, Tian Z (2010) Uncertainty analysis for wind energy production with dynamic power curves. In: Probabilistic methods applied to power systems; 2010
34. Collins J, Parkes J, Tindal A (2009) Forecasting for utility-scale wind farms—the power model challenge. In: CIGRE/IEEE joint symposium on integration of wide-scale renewable resources into the power delivery system 2009
35. Kendall M (1938) A new measure of rank correlation. Biometrika 30:81–89
36. Louie H (2012) Evaluating Archimedean copula models of wind speed for wind power modeling. Power Africa 2012:1–5. doi:10.1109/PowerAfrica.6498610
37. Wind integration datasets (2011) National Renewable Energy Laboratory. http://www.nrel.gov/wind/integrationdatasets. Accessed 1 July 2013
38. Osborn D, Hendersen M, Nickell B, Lasher W, Liebold C, Adams J, Caspary J (2011) Driving forces behind wind. Power Energy Mag 9:60–74
39. Nelsen R (2006) An introduction to copulas, 2nd edn. Springer, New York
40. Louie H (2012) Evaluation of bivariate Archimedean and elliptical copulas to model wind power dependency structures. Wind Energy. doi:10.1002/we.1571
41. Díaz G (2013) A note on the multivariate Archimedean dependence structure in small wind generation sites. Wind Energy. doi:10.1002/we.1633
42. Louie H (2010) Characterizing and modelling aggregate wind plant power output in large systems. IEEE PES general meeting; 2010, pp 1–8
43. Beckman RJ, Tietjen GL. Maximum likelihood estimation for the beta distribution. J Stat Comput Simul 7:253–258
44. Louie H (2010) Evaluation of probabilistic models of wind plant power output characteristics. In: Probabilistic methods applied to power systems; 2010, pp 442–447, doi: 10.1109/PMAPS.2010.5528963
45. McManus B (2013) Wind generation & total load in the BPA balancing authority. Bonneville Power Administration. http://www.transmission.bpa.gov/Business/Operations/Wind/default.aspx. Accessed 1 July 2013
46. Market reports (2013). MISO. https://www.midwestiso.org/Library/MarketReports/. Accessed 1 July 2013
47. Operational analysis (2013). PJM interconnection www.pjm.com/markets-and-operations/ops-analysis.aspx. Accessed 1 July 2013
48. Archive wind power (2013). 50 Hertz. http://www.50hertz.com/en/1983.htm. Accessed 1 July 2013

Conversion Efficiency Improvement in GaAs Solar Cells

Narottam K. Das and Syed M. Islam

Abstract The finite-difference time domain (FDTD) tool is used to simulate the reflection losses of subwavelength grating (SWG) structure in GaAs solar cells. The SWG structures act as an excellent alternative antireflective (AR) coating due to its capacity to reduce the reflection losses in GaAs solar cells. The SWG structures allow the gradual change in refractive index that confirms an excellent AR coating and light trapping properties, when compared with the planar thin film structures. The nanorod (nano-grating) structure acts as a single layer AR coating, whereas the triangular (conical or perfect cone) and parabolic (i.e., trapezoidal or truncated cone) shaped nano-grating structures act as a multilayer AR coating. The simulation results show that the reflection loss of triangular (conical or perfect cone) shaped nano-grating structure having a 300 nm grating height and an 830 nm period is ~ 2 %, which is about 28 % less than that of flat type substrates. The simulated results show that the light reflection of a rectangular shaped grating structure is ~ 30 %, however, the light reflection becomes ~ 2 % for a triangular (conical or perfect cone) shaped nano-grating structure, because the refractive index changes gradually in several steps and reduces the reflection losses. It is also noticed that the intermediate structures (trapezoidal and parabolic shaped), the light reflection loss is lower than the rectangular shaped nano-grating structure but higher than the triangular shaped nano-grating structure. The simulated results confirm that the reduction of light reflection losses in GaAs solar cell will increase the conversion efficiency. Therefore, this analysis confirmed that the triangular (i.e., perfect cone or conical) shaped nano-grating structures are an excellent alternative AR coating for the improvement of conversion efficiency in GaAs solar cells.

N. K. Das (✉) · S. M. Islam
Centre for Smart Grid and Sustainable Power Systems, Department of Electrical and Computer Engineering, Curtin University, Perth, WA 6845, Australia
e-mail: narottam.das@curtin.edu.au

S. M. Islam
e-mail: s.islam@curtin.edu.au

J. Hossain and A. Mahmud (eds.), *Large Scale Renewable Power Generation*, Green Energy and Technology, DOI: 10.1007/978-981-4585-30-9_3,

Keywords FDTD simulation · Nanostructures · Reflection loss · Solar cells · Subwavelength grating (SWG) · Triangular or conical shaped grating

1 Introduction

1.1 Background of Solar Energy

The World Bank statistics displayed a number for the global population which reaches almost 7 billion human lives by the end of 2011 [1]. This huge number of the human race strongly influences energy consumption on a daily basis. The International Energy Agency (IEA) recorded consumer energy usage on 2010 as 535 ExaJoule (1 eJ = 10^{18} J) and this number will keep increasing as time goes by [2]. However, more than 80 % of that energy has already been extracted from limited sources, such as coal, natural oil, and natural gas. If this continues, extinction and even disappearance of some resources may be faced in the short term. To avoid this critical condition, renewable energy sources such as solar cells (i.e., solar energy) need to be developed and to assist in providing energy for the demand of the world community.

The creation of the universe is such that all the planets revolve around the sun which is at the center. Rotation of each planet makes it possible for the sun's coverage in almost all regions daily every year. The Earth, the planet where human beings live, receives 89 petaWatts (PW) of solar radiation through its atmosphere. In total, up to 3,850,000 eJ sun heat absorbed by clouds, oceans, and lands per year. This irradiation is extremely big compared to the global energy consumption [3, 4]. Thus, the sun is one of the best sources of new energy (i.e., solar cells or energy) source because of its availability and unlimited source.

Therefore, in this modern technology era, people should maximize the availability of renewable energy in order to fulfill their demand for electricity which keeps increasing. Photovoltaic (PV) system is a device that can convert sunlight as renewable energy into DC voltage. This system is then connected with an inverter, so the generated DC electricity is transformed into AC source and is applicable for household usage. With the aid of solar cells, there is high possibility of decrement in the demand on fossil fuels as energy sources.

Nevertheless, the performance of solar cell these days is still far from satisfactory. Despite its high initial cost, electrical energy generation depends highly on the surrounding situation. The most common condition is during cloudy days, the cell will produce less power compared to when the sun is shining bright. The installation place of the PV module is also a consideration as there are four seasons in a country and therefore is tendency for temperature variation. It can be lower than 0 °C during the winter and may be more than 35 °C during the summer. Compared to a tropical country with an average temperature of 30 °C throughout

the year, these varying seasons may decrease the cell performance, because it cannot reach its maximum power point.

There are several problems also with the PV cell itself. Because semiconductor is used as the main element of a solar cell, it can be chosen from many different materials. Nowadays, silicon is one of the most popular semiconductors because of its wide availability, making it cheaper to construct and produce. However, efficiency of the silicon solar cell is considerably low compared to Gallium Arsenide (GaAs) and others. The assembly process of the module itself can affect the performance of the device. Any manufacturer defect may create losses of energy through cells junction and dropped to earth connection.

Because of that, solar cell efficiency is required to be improved in terms of its conversion efficiency to make use of plentiful solar energy. This chapter is focused on how to optimize the cell performance, so that it can convert more sunlight into useable energy. The improvement focuses on the design of each cell and devices that might help instruct better final results. In this way, new methods on manufacturing solar cell is available to produce ample solar energy in the future for the next generation.

In history, solar energy has been defined as the radiant light and heat emitted by the sun. The PV effect was discovered approximately 173 years ago since the understanding of the PV effect by Becquerel. Hence, solar energy can be converted into electrical energy by the use of such PV panels.

The global population is increasing significantly every year, and in proportion of this situation, the request for electrical energy has increased greatly. The data from World Bank shows that the global electricity consumption has increased by around 40 % per capita over the past 40 years [1]. In order to satisfy the global high demand, natural resources such as oil, gas, coal, and others are used by the chemical power industry leaving most of the existing world assets in a critical condition. Therefore, renewable energy is crucial to take part in terms of covering the electrical energy consumption. The sun has the greatest contribution as it is very popular and almost everyone can see it daily. Fifteen thousand ExaJoule ($1\ \text{Exa} = 10^{18}$) of solar energy passes through our atmosphere every year. So, it is such a waste if the solar energy is not used maximally, where human consumption is still less than 2 ExaJoule [5].

The PV cell is a device that can convert sunlight into electricity using the photoelectric effect introduced by Edmond Becquerel [6]. This solar-electric-energy demand has grown consistently by 20 to 25 % annually over the past 20 years [7]. It is popular among other energy conversion devices, because it does not make any noise and is carbon-emission free during the conversion process. The PV system is also a space-saver for residential and public place purposes. It can be installed on top of the roof, where not much else can be put. The price of the converter has also been decreased compared to the initial cost, when it was introduced the first time by the government. However, the existing PV cell has the lack of conversion efficiency.

Due to wide industrialization as well as urbanization, the world is facing the danger of depletion of its existing energy resources. The alternative solution is to

implement clean renewable energy for the green future. The renewable energy such as solar, wind, thermal, tidal, etc., are all taken into consideration. However, among the different types of renewable energy, solar energy research itself is the best candidate selected for the next generation source of clean energy.

Furthermore, according to the IEA, solar energy has portrayed itself as the most promising, affordable, inexhaustible, sustainable clean energy. Solar energy plays an important role in Australia and the world affecting the nations in different aspects; environmentally friendly, indigenously, socially, and economically.

The only drawback of solar energy is the low absorption rate by the PV panels. Hence, researchers have been trying to come out with different techniques to improve the conversion efficiency of solar panels. The most popular technique of all is the thin film technique. Thin film technique is the implementation of an efficient antireflection (AR) coating for solar cell applications. The AR coating reduces the reflection losses of the cells, hence, increasing the conversion efficiency of the solar cell. The initial idea of the AR coating is based on the nanostructure of a moth's eyes. These nanostructures can reduce the light reflection losses by creating a medium where refractive index increases from one medium to another.

2 Basic Structure Thin Film Solar Cell

Figure 1 shows a three-dimensional (3D) view of a thin film solar cell. The AR coating lies below the cover glasses. The contact grid holds the gallium arsenide (GaAs) substrate and the AR coating together, the bottom layer is the metal backing.

Figure 2 shows the view of a 3D model of the AR coating. The AR coating is made of nano-grating structures.

Figure 3 shows different types of nano–grating structures that are used for the modeling. These are mainly (i) triangular shaped nano-grating, (ii) trapezoidal shaped nano-gratings with different aspect ratios, and (iii) rectangular shaped nano-gratings. By varying the aspect ratios, it is possible to make a triangular shaped nano-grating structure (when the aspect ratio is '0'); trapezoidal shaped nano-grating structure (when the aspect ratios are >0 and <1; however typically, it is '0.1−0.9'); and rectangular shaped nano-grating structure (when the aspect ratio is '1').

The aspect ratio is defined as the ratio between the top length over the base length of a trapezoid, triangle, or a rectangle. For a triangular shaped nano-grating structure: the aspect ratio is 'a/b' = '0'. For the trapezoidal shaped nano-grating structure: the aspect ratio is 'a/b' >'0' and <'1'; typically, it is from '0.1' to '0.9'. For a rectangular shaped nano-grating structure: the aspect ratio is 'a/b' = '1', because 'a' is equal to 'b'.

Subwavelength grating (SWG) structures have been identified as promising candidates for realising high conversion efficiency in solar (photovoltaics) cells

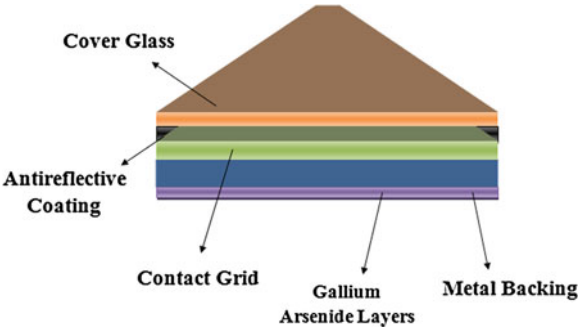

Fig. 1 A 3D model view/ structure of a thin film solar cell

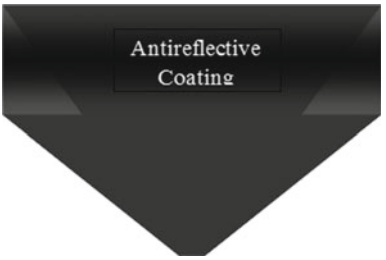

Fig. 2 The view of a 3D model of the AR coating. It is made of nano-grating

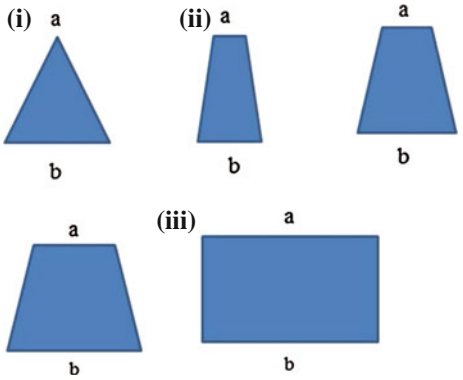

Fig. 3 Schematic diagram of different types of nano-grating structures. These are (*i*) triangular, (*ii*) trapezoidal (with different aspect ratios), and (*iii*) rectangular shaped

due to their low reflection losses. If the pitch (or period) of a single grating structure is less than the wavelength of the incident light, it behaves like a homogeneous medium with an effective refractive index [8]. Therefore, the SWG structures provide gradual changes in refractive index that ensure an excellent AR and light trapping properties compared to a planar or flat type thin film [8, 9]. This type of nanorod (or nano-grating) structure acts as a single layer AR coating, whereas the triangular (such as conical or perfect cone) and parabolic shaped nano-grating structures act as a multilayer broadband AR coating [10, 11].

As reserves of fossil fuels are used up, the need to find an alternative source of energy arises. The solar, hydroelectric, wind, and biomass are considered as renewable energy sources that can be used in a wide range of applications from heating water and generating electricity to supply for telecommunications and transportations, etc. Renewable energy is a clean energy being environmentally friendly. Therefore, the solar cell is a very important area of research for the generation of renewable or green energy in the sustainable future. The solar cell was discovered in the nineteenth century and since then scientists and researchers have been trying to improve its conversion efficiency which is currently 20.3 % for the best reported silicon solar cells [12].

There are various types of losses in solar cells that always reduces the conversion efficiency of solar cells. Among them, reflection loss is one of the most important factors that reduces the conversion efficiency significantly in solar cells. The thin-film AR coating can minimize the reflection losses only for certain wavelengths and the formation of coating film can be a complex process as well having some other drawbacks, such as adhesion and thermal mismatch, etc., and instability under thermal cycling [9, 11]. Therefore, the SWG structure (especially triangular or conical shaped) causes a gradual change in refractive index that lead to a lower reflection losses over a wide range of wavelengths and angles of incidence [9, 11, 13–16].

Finite-difference time domain (FDTD) method is used to simulate the reflection losses for different types of nano-grating structures. The nano-grating profiles are rectangular and triangular (i.e., conical or perfect cone) shaped. From simulation results, an optimum nano-grating height and pitch (or period) for the SWG structures were obtained. If the nano-grating structure has a shorter pitch (or period) than the wavelength of the incident light, it acts as a homogeneous medium with an effective refractive index. The reflection loss for a rectangular shaped SWG structure is >30 %, however, for a triangular (conical or perfect cone) shaped SWG structure, the refractive index changes gradually in several steps and finally the reflection loss becomes $\sim$2 %. However, the intermediate structures (such as, trapezoidal or truncated cone and parabolic shaped), the reflection loss is lower than the rectangular shaped SWG structure but higher than the triangular (i.e., conical or perfect cone) shaped SWG structure. This reduction of reflection losses in solar cell confirms the improvement of the efficiency in solar cells. The optimized SWG structures confirm that the reflection loss is $\sim$2 %, which is $\sim$28 % less than that of a flat type substrate or a rectangular shaped grating structure.

3 Background of AR Coating and SWG Structure

This section discusses the basic background of the AR coating and the SWG structure for the reduction of reflection losses in GaAs solar cells and the improvement in conversion efficiency of solar cells for future sustainable power systems.

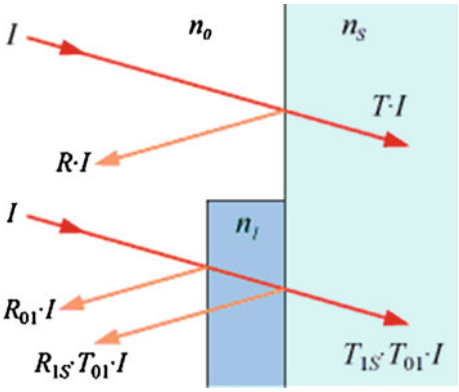

Fig. 4 Light reflection of a glass substrate (*upper portion*) is reduced by using a thin film on the glass substrate (*lower portion*)

3.1 Antireflection Coating

The efficiency of a solar cell can be increased by using an anti-reflection coating that reduces the light reflection losses only for certain wavelengths (such as, Infra-Red, Visible Ultra-Violet gives good performance). Minimum reflectance can be achieved when the refractive index equates to the square root of the refractive indices of two media [9]. The strength of the light reflection depends on the refractive indices of both media and the angle of the surface to the beam of light.

Figure 4 shows the reflection and transmission of a glass substrate with a thin film coating. Here, the light is travelling from air into a common glass substrate (upper portion). The intensity of the incident light is *I*, reflected light is *R.I*, and transmitted light is *T.I*. But when a thin film coating is applied on the glass substrate, it reduces the reflection of light. In this case, *I* is the incident light on the coating, R_{01} is the reflected light at the interface of air and thin film coating, and transmittance light is $T_{01}I$. The incident light at the coating and glass interface is $T_{01}I$, transmittance light is $T_{1s}T_{01}I$ and reflectance light is $R_{1s}T_{01}I$ (as shown in Fig. 4).

The percentage of light reflection can be calculated by using Fresnel equations

$$R = \left(\frac{n_0 - n_s}{n_0 + n_s}\right)^2 \tag{1}$$

where, *R* is the reflection co-efficient or reflectance, n_0 is the refractive index of the first media (air), and n_s is refractive index of the second media (glass substrate).

For such a case, if visible light is travelling from the first media (i.e., air, $n_0 = 1.0$) into the second media (i.e., a common glass substrate, $n_s = 1.5$), the value of *R* (i.e., light reflection) is 4 %. However, when a thin film is added on the glass, it reduces the reflection loss. Then, the new optimum refractive index, $n_1 = \sqrt{(n_0 n_s)} = \sqrt{(1.0*1.5)} = 1.225$. The reflection loss of each interface is 1 %. i.e., the total reflection is 2 %. It was calculated that an intermediate coating between the air and the glass can reduce the reflection losses by half (about 50 %).

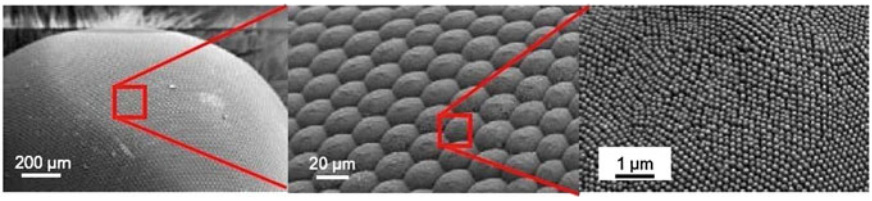

Fig. 5 Moth's-eye is covered by the nano-structured film

However, the formation of a coating film can be a complex process and there are some drawbacks such as adhesion, thermal mismatch, and instability under thermal cycling [9, 11].

3.2 Moth's-Eye Principle

The surface of a moth's eyes is covered with nano-structured film that absorbs the light instead of reflecting it back (as shown in Fig. 5). The nano-structured film consists of a hexagonal pattern bump $\sim$200 nm high, which acts as an antireflective coating; this is because the bumps are smaller than the wavelength of visible light. The refractive index between the air and the surface changes gradually and this gradual change in refractive index decreases the light reflection. This model is suitable for solar cells to reduce the reflection losses and increase the conversion efficiency [13].

3.2.1 SWG Structure

The subwavelength features cause a gradual change in refractive index which acts as a multilayer antireflective coating leading to low reflection over broadband ranges of wavelength and angle of incidence. Figure 6 shows the gradual change of the SWG structure as well as refractive index leading to the low reflection. The nanorod structure acts as a single layer AR coating, whereas the triangular (or conical) shaped SWG structure acts as a multilayer AR coating [11].

AR coating is an optical coating that is applied to the surface of lenses or other optical devices to reduce the reflection. The coating increases the efficiency of optical devices or lenses. Optimum reflection can be obtained when the refractive index equates to the square root of the refractive indices of two media [9]. Multilayer AR coatings can increase the efficiency of solar cells. However, formation of coating film can be a complex process and there are some drawbacks such as adhesion and thermal mismatch, etc., and instability under thermal cycling [8, 9].

The idea of SWG structures has been adopted from moths' eyes. The surface of a moths' eye is covered with nano-structured film that absorbs most of the incident

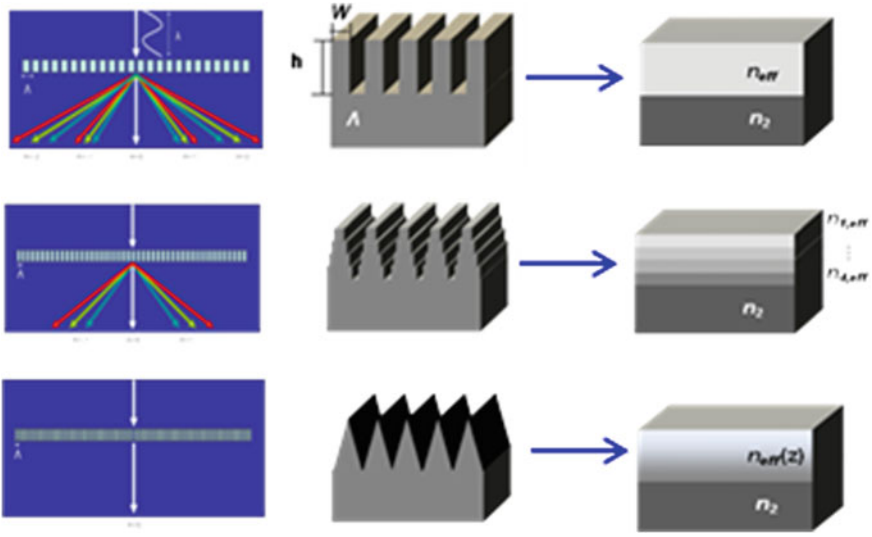

Fig. 6 Light reflection of different nano-grating shapes such as (*i*) a rectangular (*top*), (*ii*) trapezoidal (*middle*), and (*iii*) triangular or conical (*bottom*) shaped SWG structures

light instead of reflecting. The nano-structured film consists of a hexagonal pattern bump which is about 200 nm high. This acts as an AR coating, because the bumps are smaller than the wavelength of the visible light. The refractive index between the air and the surface changes gradually and that decreases the reflection of light. This model is being applied in solar cells to increase or improve the cell conversion efficiency [9].

Figure 7 shows the nano-grating geometry of rectangular and triangular shaped profile and the plot of SWG height versus the effective refractive index (n) for silicon (Si) substrate [16]. It shows that for a rectangular shaped SWG structure, the refractive index changes very sharply from air ($n = 1.0$) to the grating zone or structure (approximately 2.5 at TM mode) [8]. The reflection loss of an SWG structure can be calculated easily using Freshnell's equation (which is very similar to Eq. (1)),

$$R = \left(\frac{n_2 - n_1}{n_2 + n_1}\right)^2 \tag{2}$$

where, n_1 is the refractive index of first medium and n_2 is the refractive index of second medium.

From Fig. 7, the total reflection of the grating structure can be calculated using the following equation:

$$R_{\text{total}} = R_1 + R_2 \tag{3}$$

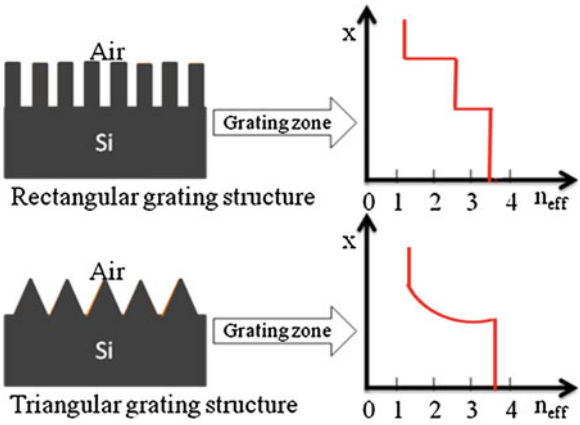

Fig. 7 Nano-structured grating geometry of *rectangular* (or flat type) and *triangular* (or conical) shaped profile and the plot of SWG height versus the effective refractive index (n) for a silicon (Si) substrate

where, R_1 is the reflection at the interface of the air and the grating structure and R_2 is the reflection at the interface of the grating structure and the substrate.

If the grating structure has a shorter pitch (or period) than the wavelength of the incident light, it acts as a homogeneous medium with an effective refractive index [8]. According to Fig. 7, the calculated reflection loss is more than 20.2 % for a rectangular shaped grating structure [8]. In the triangular (or conical) shaped SWG structure, the refractive index changes gradually in several steps, and the reflection becomes less than 8 % [8]. In the parabolic structure, the reflection is lower than the rectangular shaped grating structure but higher than the triangular shaped grating structure (∼5 %) [15].

3.2.2 Geometric Shape of Nano-Gratings

This section discussed briefly the geometric shape of nano-gratings on the substrate of device. The SWGs are namely (i) rectangular shaped SWG structure, (ii) trapezoidal shaped SWG with different aspect ratios (i.e., 0.1, 0.2, 0.5, 0.8 and 0.9), and (iii) triangular shaped SWG structure. These shapes are shown in Fig. 8.

The aspect ratio is defined as the ratio between the top length over the base length of a trapezoid, triangle, or a rectangle. It is clear from Fig. 8 that the aspect ratio is "***a/b***", where, "***a***" is the top length and "***b***" is the base length of the geometric shapes (such as, triangle, trapezoid, and rectangle). For rectangular shaped nano-grating profile, the aspect ratio is '**1**' (i.e., the top and base length of the trapezoid or rectangle is the same or equal) and for the triangular shaped nano-grating profile, the aspect ratio is '**0**' (i.e., the top length of the trapezoid or rectangle is '**0**' compared to the base length of the trapezoid or rectangle). However, for a trapezoidal shaped nano-grating the aspect ratio is ***0 < (a/b) < 1***, i.e., it lies between '0' and '1' (such as, '0.1'−'0.9'). These nano-grating shapes play an important role for light trapping inside the substrate that affect the conversion efficiency of solar cells.

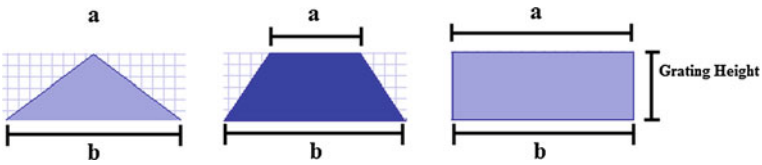

Fig. 8 Geometric shape nano-grating structures used for the simulation

4 Design of Nano-Grating Structures

This section discusses the shape design and modeling of nano-structured gratings (i.e., SWG structures). The modeled nano-structured gratings are (i) rectangular shaped nano-grating profile (as shown in Fig. 9a), (ii) trapezoidal shaped nano-grating profile (as shown in Fig. 9b) with different aspect ratios (i.e., 0.1−0.9), and (iii) triangular shaped nano-grating profile (as shown in Fig. 9c). We discussed all the nano-gratings shape as shown in Fig. 9a, b, and c. For trapezoidal shaped nano-grating profile, the aspect ratio is defined as the ratios between the trapezoid-top and base lengths [10, 14]. For the rectangular shaped nano-grating profile, the aspect ratio is '1' (i.e., the top and base length of the trapezoid is same or equal) and for the triangular shaped nano-grating profile, the aspect ratio is '0' (i.e., the top length of the trapezoid is zero compared to the base length of the trapezoid). These shapes are used for the simulation and the results analyzed for light reflection, transmission, and absorption for the SWG structures [10, 14, 17].

5 FDTD Software for the Simulation of Nanostructures

5.1 The Basics of the FDTD Simulation Method

Optiwave FDTD (OptiFDTD) is a powerful simulation tool, highly integrated, software that allows computer aided design and simulation of advanced passive photonic components. The OptiFDTD software package is based on the FDTD method. The FDTD method has been established as a powerful engineering tool for integrated and diffractive optics device simulations. This is due to its unique combination of features, such as the ability to model light propagation, scattering and diffraction, and reflection and polarization effects. The method allows for the effective and powerful simulation and analysis of sub-micron (nano-scale) devices with very fine structural details. A sub-micron or nanoscale implies a high degree of light confinement and correspondingly, the large refractive index difference of the materials (mostly semiconductors) to be used in a typical device design [18–20].

The OptiFDTD software package was developed by Optiwave Inc. This software is established to aid the user in the design and simulation of advanced passive

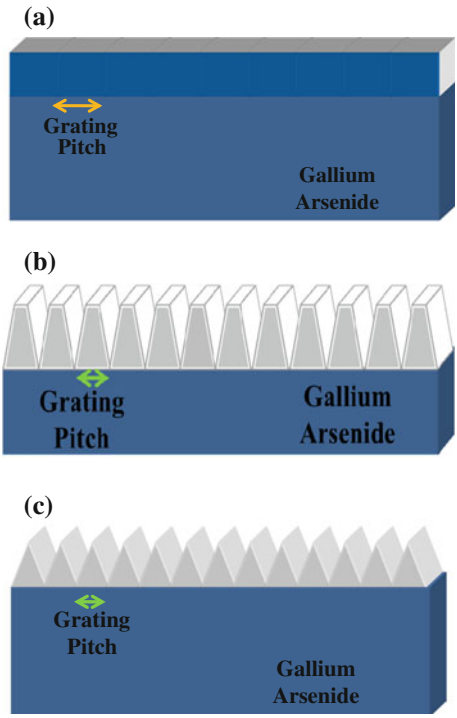

Fig. 9 Nanograting profile for the simulation of light reflection, transmission, and absorption of solar cells, **a** *Rectangular* shaped nano-grating profile, **b** *Trapezoidal* shaped nano-grating profile, where the aspect ratio is varied from 0.1 to 0.9, and **c** *Triangular* (or conical) shaped nano-grating profile. Here, the substrate is Gallium Arsenide (GaAs)

photonic components based on the FDTD method. The FDTD method is used for integrated and diffractive optics simulations due to its ability to model the light propagation, scattering, and diffraction and at the same time monitor light reflection and polarization effects. It can also model material anisotropy and dispersion without any preassumption of field behavior, such as the slowly varying amplitude approximation.

The FDTD method is a simple and intuitive way to solve numerically the partial differential equations. The FDTD method utilizes the central difference approximation to discretize the two Maxwell's curl equations, namely Faraday's and Ampere's laws, both in time and spatial domains, and then it solves the resulting equations numerically to derive the electric and magnetic field distributions at each time step using an explicit leapfrog scheme. The FDTD solution, thus derived, is second-order accurate, and is stable if the time step satisfies the Courant condition. One of the most important attributes of the FDTD algorithm is that it is absurdly parallel in nature because it only requires exchange of information at the interfaces of the sub-domains in the parallel processing scheme.

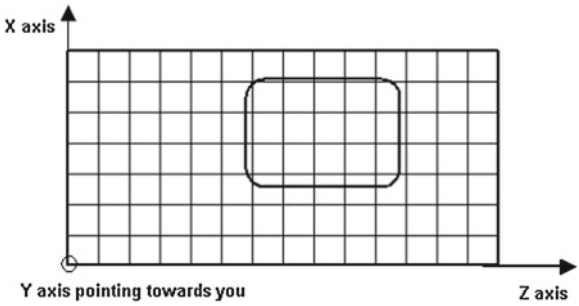

Fig. 10 Numerical representation of a 2D computational domain [20]

5.2 The Equations of 2D FDTD Method

The FDTD approach is based on a direct numerical solution of the time-dependent Maxwell's curl equations. Such as, the photonic device is laid out in the X–Z plane. The propagation is along the Z-direction. The Y-direction is assumed to be infinite in 2D simulation. This assumption removes all the derivatives from Maxwell's equations and splits them into two (TE: Transverse Electric and TM: Transverse Magnetic) independent sets of equations. The 2D computational domain is shown in Fig. 10. The space steps are Δx in the X-direction and Δz in the Z-direction of the X-Z plane. Each mesh point is associated with a specific type of material and contains information about its properties, such as refractive index and dispersion parameters [20].

5.2.1 TE Waves for FDTD Simulation

In the 2D TE wave case (Hx, Ey, Hz—nonzero components, propagation along with Z, transverse field variations along with X) in lossless media, Maxwell's equations can be written in the following form [20]:

$$\frac{\partial E_y}{\partial t} = \frac{1}{\varepsilon}\left(\frac{\partial H_x}{\partial z} - \frac{\partial H_z}{\partial x}\right), \qquad \frac{\partial H_x}{\partial t} = \frac{1}{\mu_0}\frac{\partial E_y}{\partial z}, \qquad \frac{\partial H_z}{\partial t} = -\frac{1}{\mu_0}\frac{\partial E_y}{\partial x} \tag{4}$$

where, $\varepsilon = \varepsilon_0\varepsilon_r$ is the dielectric permittivity and μ_0 is the magnetic permeability of the vacuum. The refractive index is represented by $n = \sqrt{(\varepsilon_r)}$.

Each field is represented by a 2D array—Ey (i,k), Hx (i,k) and Hz (i,k)—corresponding to the 2D mesh grid as given in Fig. 10. The indices i and k account for the number of space steps in the X- and Z- direction, respectively. For the case of TE waves, the location of the fields in the mesh (computational domain) is shown in Fig. 11.

The TE fields stencil can be explained as follows. The Ey field locations coincide with the mesh nodes given in Fig. 10. In Fig. 11, the solid lines represent the mesh given in Fig. 10. The Ey field is considered to be the center of the FDTD

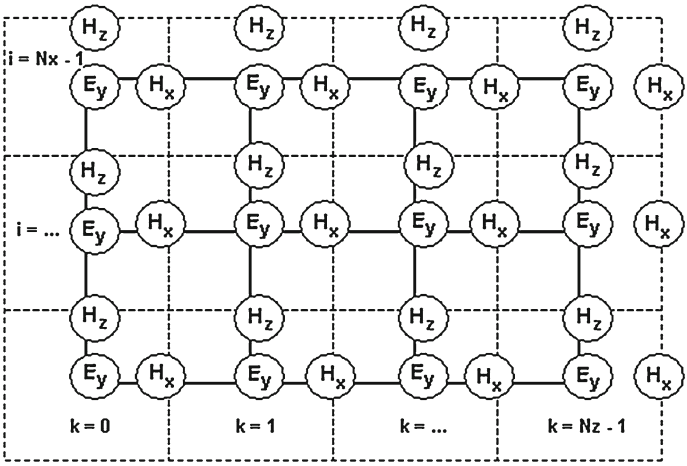

Fig. 11 Location of the TE fields in the computational domain [20]

space cell. The dashed lines form the FDTD cells. The magnetic fields Hx and Hz are associated with cell edges. The locations of the electric fields are associated with integer values of the indices i and k. The Hx field is associated with integer i and $(k + 0.5)$ indices. The Hz field is associated with $(i + 0.5)$ and integer k indices. The numerical analogy in Eq. 4 can be derived from the following relationship [20]:

$$\frac{\partial E_y}{\partial t} = \frac{1}{\varepsilon}\left(\frac{\partial H_x}{\partial z} - \frac{\partial H_z}{\partial x}\right). \tag{5}$$

5.2.2 TM Waves for FDTD Simulation

In the 2D TM wave case (Ex, Hy, Ez—nonzero components, propagation along with Z, transverse field variations along with X) in lossless media, Maxwell's equations take the following form [20]:

$$\frac{\partial H_y}{\partial t} = -\frac{1}{\mu_0}\left(\frac{\partial E_x}{\partial z} - \frac{\partial E_z}{\partial x}\right), \qquad \frac{\partial E_x}{\partial t} = \frac{1}{\mu_0}\frac{\partial H_y}{\partial z}, \qquad \frac{\partial E_z}{\partial t} = \frac{1}{\varepsilon}\frac{\partial H_y}{\partial x}. \tag{6}$$

The location of the TM fields in the computational domain (mesh) follows the same philosophy as shown in Fig. 12.

Now, the electric field components Ex and Ez are associated with the cell edges, while the magnetic field Hy is located at the cell center.

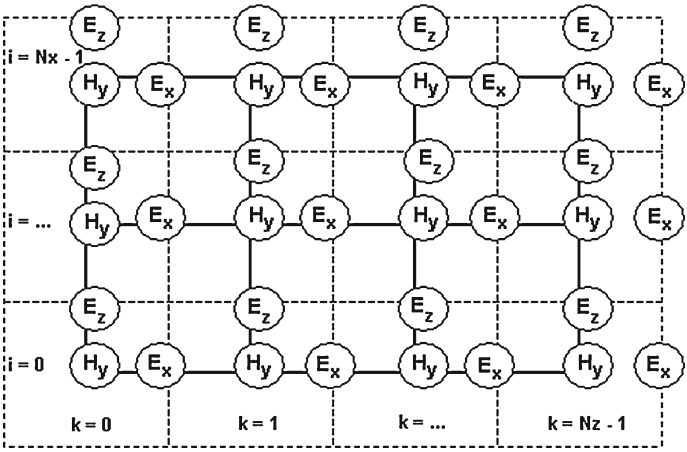

Fig. 12 Location of the TM fields in the computational domain [20]

5.3 Lorentz-Drude Model

5.3.1 Lorentz-Drude Model in Frequency Domain

It has been shown in Ref. [21] that a complex dielectric function for some metals can be expressed in the following form [20]:

$$\varepsilon_r(\omega) = \varepsilon_r^f(\omega) + \varepsilon_r^b(\omega). \tag{7}$$

This form separates explicitly the intraband effects (usually referred to as free electron effects) from interband effect (usually referred to as bound-electron effects). The intraband part of the dielectric function is described by the well-known free-electron or Drude model in Ref. [22–23].

$$\varepsilon_r^f(\omega) = 1 + \frac{\Omega_p^2}{j\omega\Gamma_0 - \omega^2}. \tag{8}$$

The interband part of the dielectric function is described by the simple semi-quantun model resembling the Lorentz results for insulators as

$$\varepsilon_r^b(\omega) = \left(\sum \frac{\Omega_p^2}{\omega_m^2 - \omega^2 + j\omega\Gamma_m} \right) \tag{9}$$

where, ω_p is the plasma frequency, m is the number of oscillators with frequency ω_m and lifetime $1/\Gamma_m$, where $\Omega_p = \sqrt{(G_m)}\omega_m$ is the plasma frequency as associated with intraband transitions with oscillator strength G_0, G_m is related to the oscillator strengths, and damping constant is Γ_0.

The above Lorentz-Drude Model can be expressed as the more general equation

$$\varepsilon_r(\omega) = \varepsilon_{r,\infty} + \sum_{m=0}^{M} \frac{G_m \Omega_p^2}{\omega_m^2 - \omega^2 + j\omega\Gamma_m} \tag{10}$$

where, $\varepsilon_{r,\infty}$ is the relative permittivity in the infinity frequency. Ω_m is the plasma frequency, ω_m is the resonant frequency, and Γ_m is the damping factor or collision frequency.

In this general equation, if only the term $m = 0$ exists, and $\omega_0 = 0$, then the general equation describes the Drude model as in (8). If only the m = 1,….., M term exists, and $\Omega_1 = \Omega_2 = \Omega_3 = \ldots\ldots\ldots = \Omega_M$; then the general model becomes the Lorentz model as in (9). This model can also work as the separate Drude and Lorentz models.

Reference [21] also provided Lorentz-Drude (LD) parameters for 11 noble metals; their unit is in electron volts. Lorentz-Drude parameters for selected materials contain parameters compiled by Optiwave that describe noble metals.

5.3.2 Lorentz-Drude Model in Time Domain

The Lorentz-Drude model shown in (10) is in the frequency domain form. However, the FDTD is a time domain method and therefore it would be suitable for broadband simulations. Therefore, the need to transform (10) to the time domain form so that the FDTD can handle the fullwave-analysis for the Lorentz-Drude material. This transformation to time domain is accomplished using the Polarization philosophy within Maxwell's equation as given below. The Lorentz-Drude model in time domain can be expressed as follows [20]:

$$\mu_0 \frac{\partial \vec{H}}{\partial t} = \nabla \times \vec{E}. \tag{11}$$

$$\varepsilon_{r,\infty}\varepsilon_0 \frac{\partial \vec{E}}{\partial t} + \sum_{m=0}^{M} \frac{\partial \vec{P}_m}{\partial t} = -\nabla \times \vec{H}. \tag{12}$$

$$\frac{\partial^2 \vec{P}_m}{\partial t^2} + \Gamma_m \frac{\partial \vec{P}_m}{\partial t} + \omega_m^2 \vec{P}_m = \varepsilon_0 G_m \Omega_m^2 \vec{E}. \tag{13}$$

The FDTD algorithm is derived based on the above equation.

However, the FDTD simulation results have demonstrated significant enhancement of light absorption for the design of nano-structured devices [10, 16, 17]. The FDTD algorithm was originally proposed by K. S. Yee in 1966 [18] who introduced a modeling technique to solve the Maxwell equations applying finite difference approach (or mathematics). The FDTD algorithm can directly calculate the value of E (Electric field intensity) and H (magnetic field intensity) at different points in the computational domain (i, j, k) [24]. Since then, it has been used for

several applications and many extensions of the basic algorithm have been developed [18–20]. Now, the FDTD method is very much efficient, accurate, and widely used for electromagnetism computations, such as fields and resonant modes.

6 Simulation Results and Discussion

In this section, simulation results of SWG structures and reflection losses are discussed. The simulation results are carried out using the OptiFDTD software package, which is based on the FDTD method developed by Optiwave Inc. [20]. This method is a powerful engineering tool for integrated and diffractive optics device simulations. Light propagation, scattering and diffraction, reflection and polarization effects can be simulated by this method. This software gives numerical solutions by using Maxwell's equation.

Figure 13 shows a simple schematic diagram for the simulation of triangular (or conical) shaped SWG structure of Galium Arsanide (GaAs). The incident light directly hits on top of the SWG structure (or nanostructure). A major portion of light is absorbed by the grating zone (here, these are triangular shaped nano-gratings) due to the gradual change in refractive index in the grating zone, some portion of the light is reflected and the remaining portion of the light is transmitted through the GaAs substrate.

The FDTD method is used to simulate the reflection losses on the SWG structures for high efficiency GaAs solar cells. The nano-grating pitch (or period) and height of the SWG structures were varied to achieve the minimum reflection losses in GaAs solar cells. Figure 14 shows the light reflection losses spectra for several nano-grating heights (such as the heights are from 100 to 400 nm) with different pitches (or periods). The pitches or periods are: (a) 200 nm, (b) 300 nm, (c) 350 nm, (d) 400 nm, and (e) 830 nm. For this simulation, the incident light wavelength is kept constant at 830 nm. The simulated results show that with the increase in nano-grating heights the light reflection reduces and reached to the saturation of light reflection at 300 nm. The simulated results show that when the nano-grating height is $\sim$300 nm the reflection loss is minimum. It is also observed that the light reflection for 300 and 350 nm grating height is very close. This nano-grating height for light reflection is minimum and it is saturated, which is the similar tendency as reported in [10]. When the nano-grating height increases further, such as 400 nm, the light reflection is increases.

Figure 15 shows the simulated light reflection versus the nano-grating height characteristics for a triangular (conical or perfect cone) shaped nano-grating structure of GaAs, having a constant period at 830 nm. The minimum reflection loss ($\sim$2 %) was observed at 300 nm nano-grating height. However, when the nano-grating height is increased to 350 and 400 nm, then the reflection loss increases further to higher order direction. So, it indicates that the nano-grating height about 300 nm has the minimum reflection loss for the GaAs substrate.

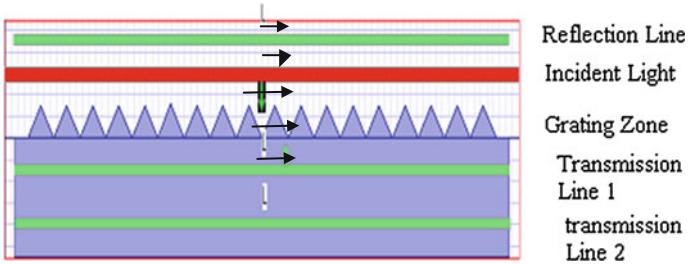

Fig. 13 A simple schematic diagram of triangular (or conical) shaped nano-grating (such as, SWG) structure. The *top red line* represents an incident light source (i.e., incident light that directly hits on the grating zone), *upper green line* represents the reflection line that can detect the reflected light and both the *lower green lines* (inside the substrates) represents the transmission lines (i.e., transmission line 1 and transmission line 2)

It confirms that the nano-grating height ~ 300 nm is the optimum nano-grating height for the minimum reflection loss of GaAs solar cells.

The Poynting theorem implemented to yield the reflection, transmission, and deflection and law of energy conservation implies

$$A + R + T + D = 1 \tag{14a}$$

$$D = \sum_{n \neq 0} R_n + \sum_{n \neq 0} T_n \tag{14b}$$

where, A is the absorption, R is the zeroth-order reflection, T is the zeroth-order transmission, and D is deflection, which includes higher order reflection and transmission. When the dimensions of the structure become comparable to or less than the wavelength of light, the number of diffraction orders is reduced. It is possible to create a structure that allows only the zero-th order to propagate. All the higher orders become evanescent.

Then, the deflection component becomes negligible (i.e., it can assume that $D = 0$). For this reason many researchers just use the equation as follows [25]:

$$\begin{aligned} A + R + T &= 1 \\ A &= 1 - (R + T) \end{aligned} \tag{15}$$

From the FDTD simulation analyzer, the light transmission and reflection can be calculated directly [20]. Then, Eq. (15) is used to calculate the light absorption [20].

7 Minimum Light Reflection for Different Nano-gratings

This section considered different aspect ratios for the nano-grating period or pitches of 830 nm to obtain the minimum light reflection for GaAs solar cells structure.

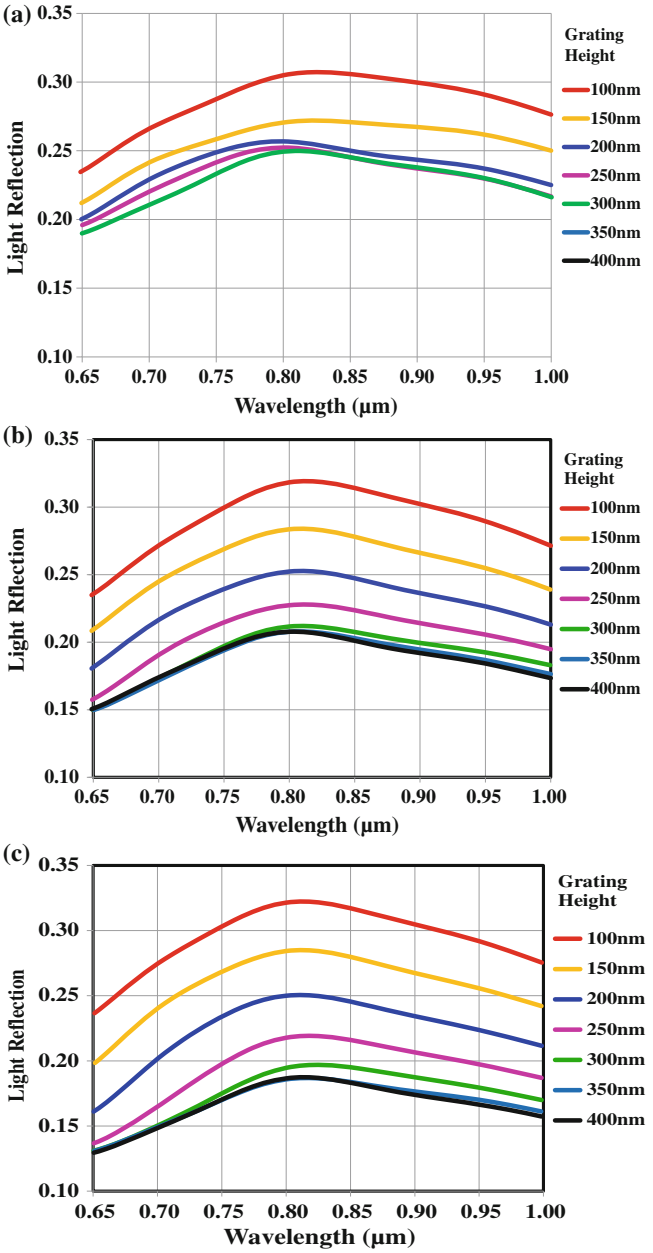

Fig. 14 Light reflection spectra for several nano-grating heights with different pitch (or period). The periods are: **a** 200 nm, **b** 300 nm, **c** 350 nm, **d** 400 nm, and **e** 830 nm. The incident light wavelength is kept constant at 830 nm. **a** *Triangular* (or conical) shaped nano-grating with pitch 200 nm. **b** *Triangular* (or conical) shaped nano-grating with pitch 300 nm. **c** *Triangular* (or conical) shaped nano-grating with pitch 350 nm. **d** *Triangular* (or conical) shaped nano-grating with pitch 400 nm. **e** *Triangular* (or conical) shaped nano-grating with pitch 830 nm

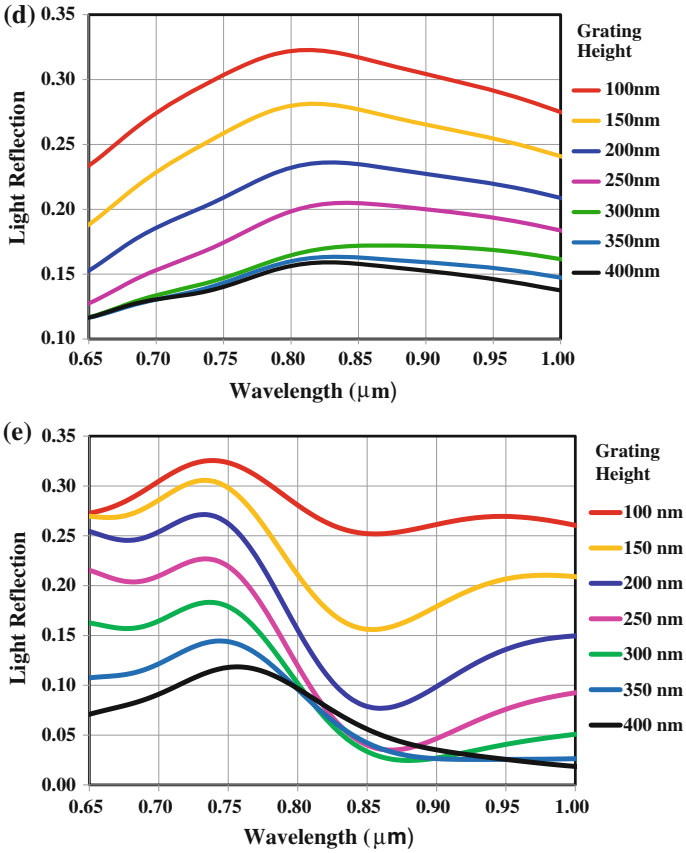

Fig. 14 continued

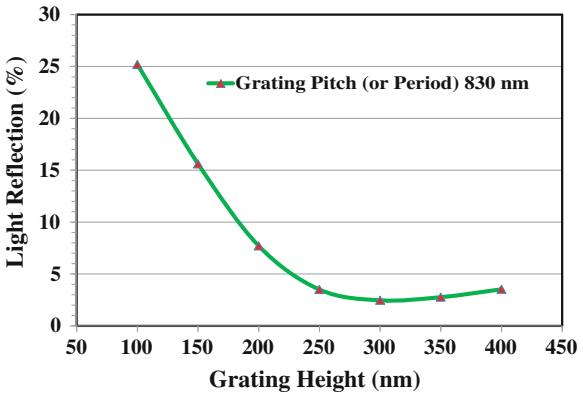

Fig. 15 Light reflection versus grating height characteristics when the grating pitch or period is kept constant at 830 nm

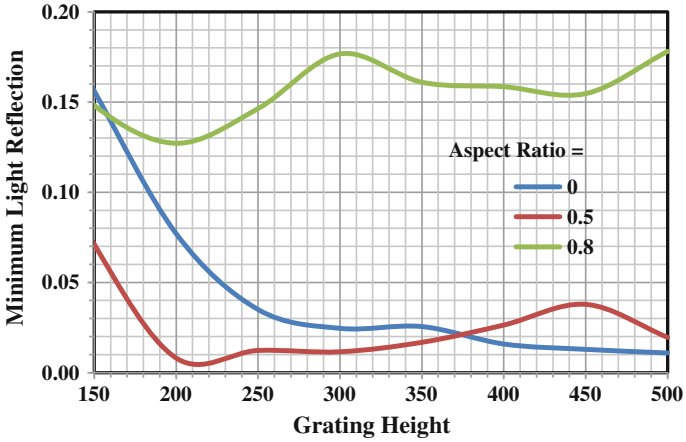

Fig. 16 Minimum light reflection versus grating height characteristics with the grating period or pitch of 830 nm

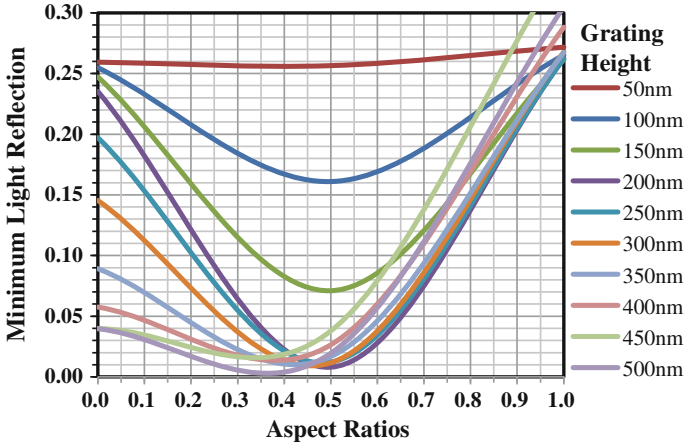

Fig. 17 Minimum light reflection versus the aspect ratio characteristics for different grating heights (50 to 500 nm) when the grating period or pitch is 830 nm

Figure 16 shows the minimum light reflection for the grating pitch (period) of 830 nm. For this case, the minimum light reflection is 1−2 % with the nano-grating height of 300−400 nm, when the aspect ratio is '**0**'. However, the light reflection is increased to 1−4 % (with the aspect ratio 0.5) and grating height of 250−450 nm; and reaches to 13−17 % with the aspect ratio 0.8 and the nano-grating height of 200−450 nm.

Figure 17 shows the minimum light reflection versus the aspect ratio characteristics for different nano-grating heights. For this case, the nano-grating height is

varied from 50 to 500 nm. Here, the grating period is kept constant at 830 nm. Here, the aspect ratio is varied from 0 to 1. As discussed earlier, when the aspect ratio is '0' then the shape of the nano-grating is triangular, when the aspect ratio is >0 but $1<$ then the shape of the nano-grating is trapezoidal, and when the aspect ratio is '1' then the shape of the nano-grating is rectangular. The results show light reflection for 50 nm grating height is >26 %, which is like a flat type ($\sim$30 % light reflection) substrates. From the plot, it shows clearly that when the grating height increasing from 50 to 250–350 nm, then the light reflection is decreasing sharply and drops to $1-2$ % (with the aspect ratio of $0.4-0.6$). However, further increasing the nano-grating height then the reflection loss is increasing rapidly and reached toward 50 nm grating height.

8 Conclusions

This analysis presented the light reflection loss about 2 % with the optimum nano-gratings having height of $\sim$300 nm and period of $\sim$830 nm, which is $\sim$28 % lower than that of flat type substrates. The light reflection was calculated using the FDTD method. The simulated results show that the light reflection of a rectangular shaped grating structure is $\sim$30 %, however, the light reflection becomes $\sim$2 % for a triangular (conical or perfect cone) shaped nano-grating structure, because the refractive index changes gradually in several steps and reduces the light reflection. It is also noticed that for the intermediate structures (such as, trapezoidal and parabolic shaped nano-gratings), the light reflection is lower than the rectangular shaped nano-grating structure but higher than the triangular shaped nano-grating structure. The simulated results confirm that the reduction of light reflection in solar cell will increase the conversion efficiency of GaAs solar cells. Therefore, it is confirmed that the triangular (or conical) shaped nano-grating structure is an excellent alternative AR coating for the high efficiency GaAs solar cells.

Acknowledgments This research is supported by the Centre for Smart Grid and Sustainable Power Systems, the undergraduate and postgraduate research students who worked with us in this research project, and the Faculty of Science and Engineering, Curtin University, Perth, Australia.

Reference

1. Bank W (2012) World Development Indicators and Global Development Finance, http://www.google.com.au/publicdata/. Accessed 9 May 2013
2. World Energy Outlook (2010) International Energy Agency. Paris, France
3. Johns M, Le H-P, Seeman M (2009) Grid-connected solar electronics: contemporary energy issues, University of Californai at Barkley, EE-290 N-3:USA
4. Annual World Solar PV Industry (2009) Report from MarketBuzz

5. King RR et al (2007) 40% efficient metamorphic GaInP/GaInAs/Ge multijunction solar cells. Appl Phy Lett 90
6. Williams R (1960) Becquerel photovoltaic effect in binary compounds. J Chem Phys 32(5):1505–1514
7. Jeyraj Selvaraj NAR (2009) Multilevel inverter For grid-connected PV system employing digital PI controller. IEEE Trans Ind Electron 56(1):149−158
8. Song YM, Lee YT (2009) Simulation of antireflective subwavelength grating structure for optical device applications. In: Proceedings of the 9th international conference on numerical simulations of optoelectronic devices 2009 (NUSOD'09), Gwangju Institute of Science and Technology, Republic of Korea, Sept. 14−17, 2009, pp 103−104
9. Schmid JH, Cheben P, Janz S, Lapointe J, Post E, Delage A, Densmore A, Lamontagne B, Waldron P, Xu D-X (2007) Subwavelength grating structures in planar waveguide facets for modified reflectivity. In: Proceedings of SPIE, vol 6796, 67963E1-10
10. Das N, Karar A, Vasiliev M, Tan CL, Alameh K, Lee YT (2011) Analysis of nano-grating assisted light absorption enhancement in metal-semiconductor-metal photodetectors patterned using focused ion beam lithography. Opt Commun 284:1694–1700
11. Lee YT (2009) High-efficiency GaInP/LCM-GaInP/GaAs triple-junction solar cells with antireflective subwavelength structures. In: Proceedings of the pioneering symposium (PC-02), Gwangu Institute of Science and Technology, Republic of Korea
12. Researchers break solar cell efficiency record (2010) News for efficiency of a solar cell
13. Thelen A (1989) Design of optical interference coatings. McGraw-Hill (McGraw-Hill optical and electro-optical engineering series), New York
14. Sahoo KC, Li Y, Chang EY (2010) Shape effect of silicon nitride subwavelength structure on reflectance for silicon solar cells. IEEE Trans Electron Devoce 57(10):2427−2433
15. Song YM, Jang SJ, Yu JS, Lee YT (2010) Bioinspired parabola subwavelength structures for improved broadband antireflection. Small 6:984–987
16. Moushumy N, Das NK, Alameh K, Lee YT (2011) Design and development of silver nanoparticles to reduce the reflection loss of solar cell. In: Proceedings of the 8th international symposium on "high capacity optical networks and enabling technologies" HONET'11, Riyadh, Kingdom of Saudi Arabia. Paper HS1-6, Dec. 19−21, pp 38−41
17. Das NK, Islam SM (2012) Optimization of nano-grating structure to reduce the reflection losses in GaAs solar cells. In: Proceedings of the Australasian Universities power engineering conference 2012 (AUPEC 2012), Denpasar-Bali, Indonesia, Sept. 26−29
18. Ko HD (2009) Surface plasmon coupled sensor and nanolens. Ph.D. dissertation, The department of electrical engineering, Texas A&M University, Texas, USA
19. Bondeson A, Rylander T, Ingelstrom P (2005) Computational electromagnetics. 1st edn. Springer, New York
20. Finite Difference Time Domain Photonics Simulation Software. OptiFDTD Technical background and tutorials. Version 8. http://www.optiwave.com/products/fdtd_overview.html
21. Rakić AD, Djurišić AB, Elazar JM, Majewski ML (1998) Optical properties of metallic films for vertical- cavity optoelectronic devices. Appl Opt 37:5271–5283
22. Markovic MI, Rakic AD (1990) Determination of reflection coefficients of laser light of wavelength from the surface of aluminum using the Lorentz-Drude model. Appl Opt 29:3479–3483
23. Markovic MI, Rakic AD (1990) Determination of optical properties of aluminum including electron reradiation in the Lorentz-Drude Model. Opt Laser Technol 22:394–398
24. Dhakal D (2009) Analysis of the sub-wavelength grating in OptiFDTD simulator Ch. 1, M.Sc. Thesis, School of engineering and science, Jacobs University, Bremen
25. Ferry VE, Sweatlock LA, Pacifici D, Atwater HA (2008) Plasmonic nanostructure design for efficient light coupling into solar cells. Nano Lett 8(12):4391–4397

Emerging SMES Technology into Energy Storage Systems and Smart Grid Applications

Jian Xun Jin

Abstract With the rapid development of clean and renewable energy technology, energy storage devices are more eagerly required. The applicable high temperature superconducting (HTS) materials achieved arouse the superconducting magnetic energy storage (SMES) devices having unique properties to play a substantial role. Superior characteristics have made the SMES technology attractive and a perspective option to practical applications broadly, especially for smart grids (SGs). SMES technology is described and verified including principle, circuit topology, control strategy, and device performance to form a comprehensive understanding of the emerging energy storage technology using the advanced HTS material and associated technology. SMES application is then introduced with the emphasis to develop relevant concepts to suit smart grids (SGs).

Keywords SMES · HTS · HTS inductor · Smart grid · Energy storage · Energy management · Power inductor charge · Power electronic device · Digital control · Power conditioning system · Bridge-type chopper

1 Introduction

With the rapid development of modern and new technology industries, the ratio of load sensitivity to power quality is continually rising in proportion, which simply means that the modern society has the urgent need for a higher quality of power supply. On the contrary, the problems of electric power supply caused by the rush of reactive power, power system faults, and operating errors, etc., are becoming

J. X. Jin (✉)
Center of Applied Superconductivity and Electrical Engineering, University of Electronic Science and Technology of China, 2006 Xiyuan Road, Gaoxin Western District 611731 Chengdu, Sichuan, China
e-mail: jxjin@uestc.edu.cn

J. Hossain and A. Mahmud (eds.), *Large Scale Renewable Power Generation*, Green Energy and Technology, DOI: 10.1007/978-981-4585-30-9_4,

more and more serious to modern grids. Adequate action is necessary, such as to compensate reactive power and absorb active power using energy storage systems (ESSs). Energy storage devices and application techniques also play an important role to cooperate with modern green, clean, and renewable energy technology in various fields, which devices have different types and principles, from mechanical to chemical and simple structure to novel material.

High temperature superconducting (HTS) materials and technology have reached the stage for practical applications [1–11] and enabled a potential to realize a practical energy storage device, i.e., HTS superconducting magnetic energy storage—HTS SMES. SMES is in general able to offer fast reaction, high power density, high energy density, light weight, low loss, long life, and environment-friendly operation. Superior characteristics made the SMES attractive and a possible option to practical applications in various fields.

SMESs are introduced with the comparison to various energy storage techniques to identify the emerging technology. Principle, circuit topology, control strategy, device performance, and applications are included to form a comprehensive description and understanding of this emerging technology. The contents consequently include the following sections: (i) Comparisons of various energy storage techniques; (ii) Principal SMES circuits and control techniques; (iii) Experimental prototype and application characteristics; (iv) Development status of worldwide SMES devices; (v) SMES application topologies and performance evaluations in power grids; (vi) Prospective SMES applications in cooperation with electric power smart grids (SGs).

2 Energy Storage Techniques

According to the specific principles, there are three main types of energy storage systems (ESSs): (i) Physical energy storage including pumped hydro storage (PHS), compressed air energy storage (CAES), and flywheel energy storage (FES); (ii) Electromagnetic energy storage including superconducting magnetic energy storage (SMES), super-capacitor energy storage (SCES); (iii) Electrochemical energy storage including lead-acid, lithium-ion, sodium sulfur, and fluid flow battery energy storage, etc. Various types of energy storage devices are summarized in Table 1 as a guideline of technical specifications.

Physical energy storage is a kind of relatively mature and practical energy storage technology, which is limited by topographical and geological conditions to implement. The technology of electrochemical energy storage is evolving fastest so far, of which sodium sulfur battery, fluid flow battery, and lithium-ion battery technologies have made great breakthroughs in energy conversion efficiency, safety, and economy with increasingly industrialized applications. The energy conversion efficiency of sodium sulfur battery can reach 80 % with three times energy density as lead-acid battery with a much longer life cycle.

Table 1 Common application characteristics of various ESSs

Type		Nominal power	Compensation time	Advantages	Disadvantages	Applications
I	PHS	100–2000 MW	4–10 h	Large capacity, low cost	Large space, special geological conditions	Peak load shifting, frequency control, backup source
	CAES	100–300 MW	6–20 h	Large capacity, low cost	Large space, special geological conditions	Peak load shifting, frequency control, backup source
	FES	5 kW–1.5 MW	15 s–15 min	High power density	Low energy density	Frequency control, UPS, power quality regulation, power system stability
II	SMES	10 kW–1 MW	5 s–5 min	High power density	Low energy density, high cost	UPS, power quality regulation, power system stability
	SCES	1–10 kW	1 s–1 min	Long service life	Low energy density	Power quality regulation
III	Lead-acid battery	1 kW–50 MW	1 min–4 h	Low cost	Heavy weight, large size, cycle-life limitations	Power quality regulation, backup source, black start, UPS
	Sodium sulfur battery	1 kW–50 MW	1 min–6 h	Large capacity	Low energy density	Peak load shifting, frequency control, backup source
	Fluid flow battery	10 kW–10 MW	1–20 h	High power and energy density, high efficiency	High cost	Distributed generation stability, backup source
	Lithium-ion battery	1 kW–10 MW	1 min–4 h	Small size, low weight, high energy density, high efficiency	High cost	Distributed generation stability, power quality regulation

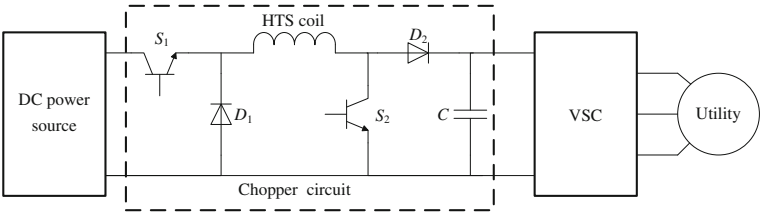

Fig. 1 Circuit topology of a typical power conditioning system

SMES devices can store the electric energy as electromagnetic energy in the superconducting inductor and release the stored energy if required. Comparing with other energy storage devices, SMES devices have fast response time, high power density, high energy storage efficiency, and long lifetime with little environmental pollution. The current focus on the applied superconducting technology for SMES has been moving to the industrial applications from the laboratory research stage, and the technology has been well verified for practical applications from small to large-scale units.

SMES applications are most commonly associated with the electrical power systems, such as considered for use in SGs recently, meanwhile other applications can also readily be found such as in electric vehicles (EVs), uninterruptible power supplies (UPSs), and power devices with special functions.

3 SMES Circuit and Control Techniques

3.1 Principle and Operation Theory

In general, the SMES-based power apparatuses have the dynamic electric energy exchange between a superconducting coil and an external interface for a power system. With regard to the SMES control, a conventional chopper having two power switches and two power diodes is mostly applied to link the HTS coil to the DC bus and to achieve the bidirectional power exchange for managing the generated power of distributed generators (DGs) or maintaining the uninterruptible power of critical electric equipment. As shown in Fig. 1, a typical power conditioning system (PCS) with voltage source converter (VSC), it has three main operation states, i.e., energy charge state, energy storage state, and energy discharge state. The HTS coil is charged by a DC power source through the power switches S_1, S_2, then stores its magnetic energy through the power switch S_2 and the power diode D_1, and finally discharges its stored energy to the external load through the power diodes D_1 and D_2, respectively. Figure 2 shows the operation principles of the conventional chopper.

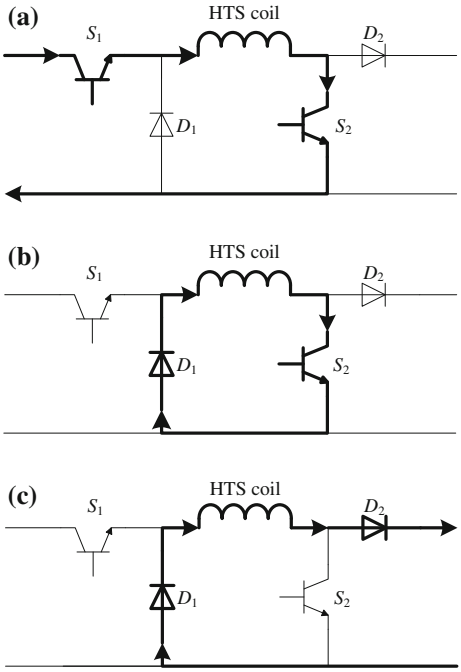

Fig. 2 Operation principles of the conventional chopper. **a** Energy charge state; **b** Energy storage state; **c** Energy discharge state

According to the state-of-the-art power electronic technologies [12], the applicable voltage rating of the insulated gate bipolar translators (IGBTs) is between 0.5 and 6.5 kV. Since the most SMES devices currently are developed for low voltage power distribution applications [13], having operation voltages across the HTS coils at kV level, IGBTs are normally applied to form a conventional chopper. Even when the operation voltage across the HTS coils drops to 750 V in the ongoing 2.4 GJ SMES project [14], IGBTs still have the advantages over MOSFETs. However, if the applicable voltage ratings are below 500 V, the metal oxide semiconductor field effect transistors (MOSFETs) are more suitable to achieve high-efficiency and high power energy conversions for various end-users' applications such as EVs [15] and UPSs [16]. Meanwhile, the turn-on resistances in the commercial low-voltage MOSFETs have already been reduced to Milliohm level or below, which results in much lower consumed power than that in the power diodes.

Recently, new focuses of low-voltage SMES applications have been formed for various power end-users. The rapid developments of hydrogen-powered fuel cell vehicles (FCVs) make it available to cool the HTS or MgB_2 coils by fully making use of the onboard liquid hydrogen (LH_2). The SMES technology has been technically verified [17, 18] to improve the fast repeated charge–discharge performance for regenerative braking. Meanwhile, some low-voltage direct-current (LVDC) power transmission systems have been proposed and studied to connect with various DC output type distributed generators (DGs) [19] such as photovoltaic (PV) cells and fuel cells (FCs), and to supply the electric loads in the commercial and

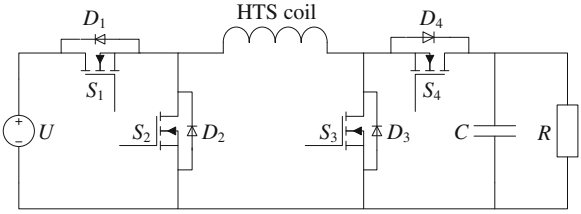

Fig. 3 Topology of the bridge-type chopper

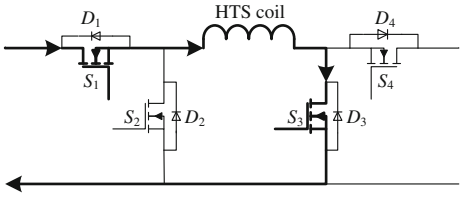

Fig. 4 Energy charge state of the bridge-type chopper

residential buildings [20]. The superconducting DC cable with nearly zero energy loss has been applied to achieve high power and long-distance power transmission, with an additional SMES device introduced to enhance the whole power transfer capacity and stability [21, 22]. In the above low-voltage applications, several considerable benefits from the SMES technology can be derived to improve the power quality for the end-user, to achieve high-efficiency operation for energy saving, and to lower the capital cost of the SMES device. Therefore, beside the current large-scale SMES applications for power transmission and distribution, small-scale SMES devices also have very promising application prospects for use in the power end-user systems.

Consequently, a new bridge-type chopper using MOSFETs is proposed [23] and analyzed to reduce the energy loss for low-voltage applications. The circuit topology of the bridge-type chopper is shown in Fig. 3. It mainly consists of four low-loss power electronic switches, i.e., MOSFETs S_1–S_4 paralleled with their reverse diodes D_1–D_4, and a DC-link capacitor C paralleled to the load R. Like the conventional chopper, it also has the same three main operation states. In addition, owning to the inevitable turn-on and turn-off delayed time of a practical power switch, two transient operation states are necessary to avoid potential short circuits of the DC power supply and DC-link capacitor.

When the bridge-type chopper operates at energy charge state, the HTS coil L is charged by a DC power supply U through S_1 and S_3, as shown in Fig. 4. The circuit voltage equation can be expressed by

$$U - L\frac{\mathrm{d}I_L(t)}{\mathrm{d}t} - I_L(t)(R_L + 2R_s) = 0 \tag{1}$$

where $I_L(t)$, transient current through the HTS coil; R_L, lossy resistance from the connection junctions and current leads in the HTS coil; R_s, turn-on resistance of the MOSFET unit.

When $I_L(t)$ reaches its reference value, the bridge-type chopper comes into the energy storage state. As shown in Fig. 5, the HTS coil L will form a transient

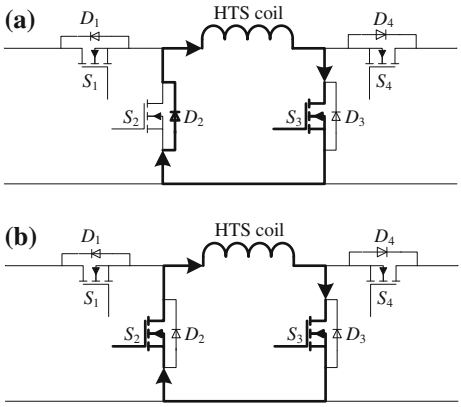

Fig. 5 Energy storage state of the bridge-type chopper. **a** Transient storage state; **b** Steady storage state

energy storage circuit through D_2 and S_3 during the first transient storage time period 0–T_i, and then form a steady energy storage circuit through S_2 and S_3 after T_i. T_i is the time duration of a transient operation state, which is larger than both the turn-on and turn-off time durations of a MOSFET. The circuit voltage equations in the above two energy storage states can be expressed by

$$L\frac{\mathrm{d}I_L(t)}{\mathrm{d}t} + I_L(t)(R_L + R_s + R_d) + U_d = 0 \tag{2}$$

$$L\frac{\mathrm{d}I_L(t)}{\mathrm{d}t} + I_L(t)(R_L + 2R_s) = 0 \tag{3}$$

Where U_d, stationary voltage drop across the diode unit; R_d, turn-on resistance of the diode unit.

The circuit current equation in the load side can be expressed by

$$C\frac{\mathrm{d}U_R(t)}{\mathrm{d}t} + \frac{U_R(t)}{R} = 0 \tag{4}$$

where $U_R(t)$, transient voltage across the load R; C, snubber capacitance of the DC-link capacitor.

When $U_R(t)$ is below its reference value, the bridge-type chopper comes into the energy discharge state. As shown in Fig. 6, the HTS coil L will exist as part of a transient energy discharge circuit through S_2 and D_4 during the first transient discharge time period 0–T_i, and then exists as part of a steady energy discharge circuit through S_2 and S_4 after T_i. The circuit voltage equations in the above two energy discharge states can be expressed by

$$L\frac{\mathrm{d}I_L(t)}{\mathrm{d}t} + I(t)(R_L + R_s + R_d) + U_d + U_R(t) = 0 \tag{5}$$

$$L\frac{\mathrm{d}I_L(t)}{\mathrm{d}t} + I(t)(R_L + 2R_s) + U_R(t) = 0. \tag{6}$$

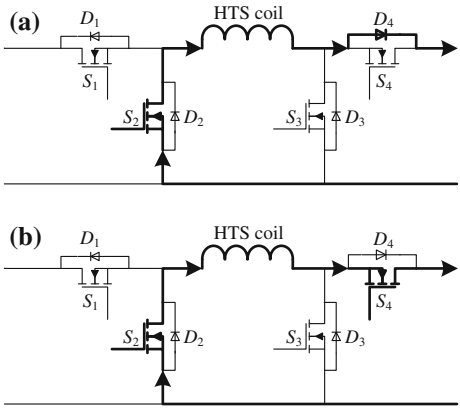

Fig. 6 Energy discharge state of the bridge-type chopper. **a** Transient discharge state; **b** Steady discharge state

Table 2 Digitized operation states of the two choppers

"$S_1S_2S_3S_4$"	System operation states	
	Bridge-type chopper	Conventional chopper
"1010"	Charge state	Charge state
"0010"	Transient storage state	Storage state
"0110"	Steady storage state	N/A
"0100"	Transient discharge state	N/A
"0101"	Steady discharge state	N/A
"0000"	N/A	Discharge state

The circuit current equation in the load side can be expressed by

$$I_L(t) - C\frac{\mathrm{d}U_R(t)}{\mathrm{d}t} - \frac{U_R(t)}{R} = 0 \tag{7}$$

3.2 Principle of Control and Protection

Defining the turn-on or turn-off status of a power switch as "1" or "0", the system operation states of the bridge-type and conventional choppers can be digitalized, as shown in Table 2. Besides the three steady operation states of charge state, storage state, and discharge state in the conventional chopper, the bridge-type one has two more transient operation states to avoid the short circuits of the power source and DC-link capacitor, as shown in Fig. 7. In practice, the HTS coil is normally controlled to carry out the bidirectional energy exchanges with the external system. A digital control method is consequently introduced to achieve the controlled energy charge, storage, and discharge processes. In normal operation, when the load resistor is operated at a power swell state, the real-time operation state of the

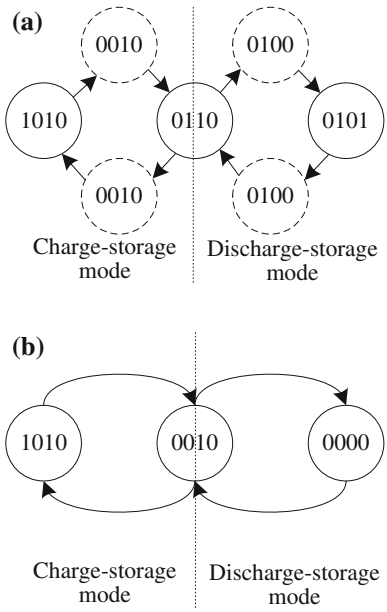

Fig. 7 Digital state diagram of the two choppers. **a** Bridge-type chopper; **b** Conventional chopper

two choppers will be converted between charge state and storage state alternately to absorb the surplus power. Similarly, when the load resistor is operated at a power sag state, the real-time operation state will be converted between discharge state and storage state alternately to compensate the shortfall power. The above two dynamic processes can be defined as "charge-storage mode" and "discharge-storage mode".

A concept of maximum permissible relative voltage error $\lambda_m(t)$ is introduced to divide the three main operation states, and can be expressed by

$$\lambda_m(t) = \left| \frac{U_{\max}(t) - U_r(t)}{U_r(t)} \right| \tag{8}$$

where $U_{\max}(t)$ and $U_r(t)$ are the maximum overshoot voltage and rated voltage across the DC-link capacitor and resistive load; U_r is reference voltage.

Thus the three main operation states are described as follows: (i) When the instantaneous relative voltage error $\lambda(t)$ meets the condition of $-\lambda_m(t) \leq \lambda(t) \leq \lambda_m(t)$, the chopper is operated at energy storage state; (ii) When $\lambda(t)$ meets the condition of $\lambda(t) < -\lambda_m(t)$, the chopper is operated at energy discharge state; (iii) When $\lambda(t)$ meets the condition of $\lambda(t) > \lambda_m(t)$, the chopper is operated at energy charge state. During the dynamic energy exchange processes, the chopper will be operated at a charge-storage mode or a discharge-storage mode when $I_L(t)$ is larger than the shortfall current $I_{\text{sh}}(t)$ or surplus current $I_{\text{su}}(t)$. I_{Lr} is the rated current through the HTS coil. The whole operation flow diagram of the digital control method developed is shown in Fig. 8.

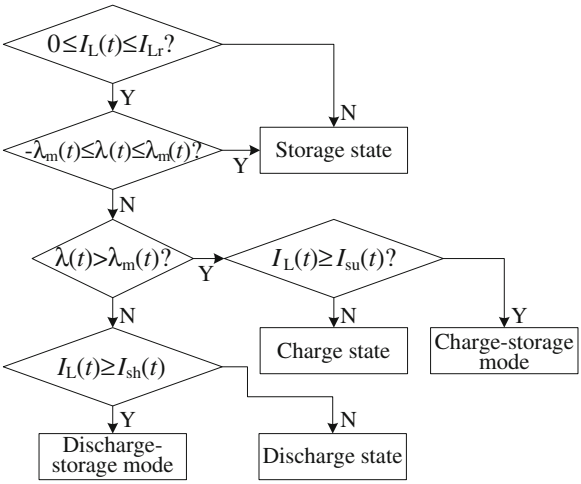

Fig. 8 Operation flow diagram of the digital control method

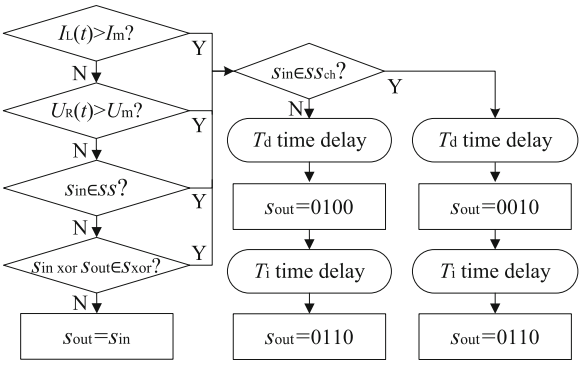

Fig. 9 Operation flow diagram of fault detection and protection

In addition, a fault detection and protection module is particularly required to avoid the potential risks like short circuit, overcurrent, and overvoltage. Four main fault operations are described as follows: (i) $I_L(t)$ exceeds its maximum allowable value I_m; (ii) $U_R(t)$ exceeds its maximum allowable value U_m; (iii) The current input signals s_{in} of the module do not belong to the sequences ss of all the digital control signals in Fig. 7; (iv) The value of s_{in} xor s_{out} does not belong to the sequences s_{xor} of "0001", "0010", "0100", and "1000". If a fault operation is detected, the current operation state should be converted into storage state immediately, as shown in Fig. 9. s_{out} is the last output signals of the module. ss_{ch} is the sequences of the digital control signals in the charge-storage mode. T_d is an inevitable time delay in a practical digital control system.

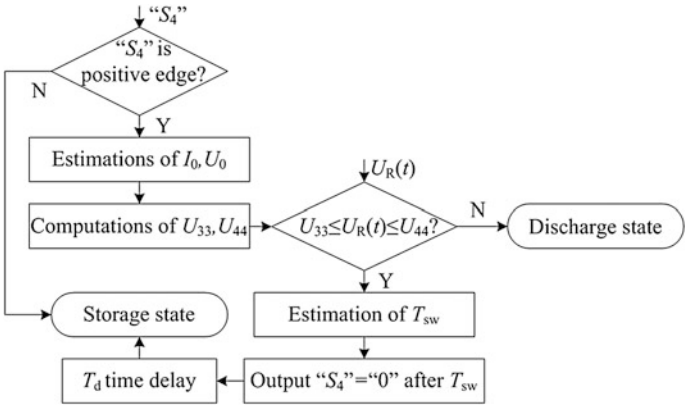

Fig. 10 The whole prediction control process of the proposed method

3.3 Principle and Implementation of a Novel Digital Prediction Control Method

To achieve high-performance applications and avoid operation risks caused by various real-time statuses such as critical current, AC loss, and electromagnetic force, superconducting magnets generally need to operate precisely during the charge, storage, and discharge processes. However, owning to the existence of an inevitable time delay consisting of the sampling time of the controlled variables, computing time of the digital control chip, and implementing time of the controlled objects [24, 25], the digital control signals from a practical digital system usually lag behind the changes of the controlled variables, which results in some undesired overshoots.

A new digital prediction control method is proposed to limit the controlled variables into their desired reference ripple ranges. The principle is to predict the instantaneous time t_r when the practical controlled variable, e.g., $U_R(t)$, reaches its reference value and to output the corresponding digital control signals at $t_r - T_d$ in advance. The whole prediction control process during the discharge-storage mode is shown in Fig. 10 and particularly presented as follows.

3.3.1 The Estimations of the Initial Current and Voltage Values by Linear Extrapolation Method

Assume that the digital control chip outputs the state-switching signals at a certain time t_1, and the time interval from the nearest sampling time to t_1 is T_2, thus the bridge-type chopper will change its operation state at $t_1 + T_d$. However, $I_L(t)$ and $U_R(t)$ at $t_1 + T_d$ are very difficult to be sampled precisely because the practical sampling time period T_s cannot be infinitely small. The number of the sampled

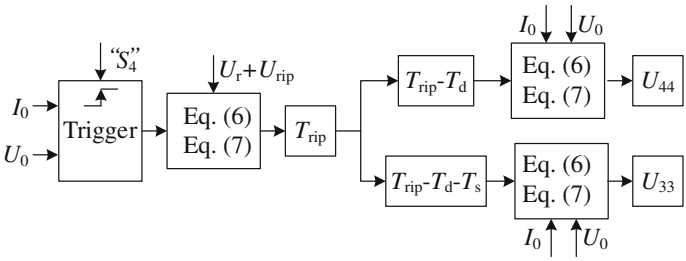

Fig. 11 The computations of U_{33}, U_{44} by chopper circuit equations

data p can be obtained by rounding $(T_2 + T_d)/T_s$, and the nearest sampling time to $t_1 + T_d$ is $T_3 = T_2 + T_d - p \times (T_2 + T_d)/T_s$, thus the initial voltage U_0 across the load at $t_1 + T_d$ can be estimated by

$$\frac{U_0 - U_{11}}{T_s + T_3} = \frac{U_{22} - U_{11}}{T_s} \tag{9}$$

where U_{11} and U_{22} are the sampled voltage values at $T_3 - T_s$ and T_3, respectively. The initial current I_0 through the superconducting magnet at $t_1 + T_d$ can be estimated by the similar method.

3.3.2 The Computations of the Critical Voltage Values by Chopper Circuit Equations

Applying the estimated initial current and voltage values (I_0, U_0) into (6) and (7), $U_R(t)$ during the current operation state can be computed and predicted. Assume that the permissible voltage ripple range is from $U_r - U_{\text{rip}}$ to $U_r + U_{\text{rip}}$, thus the time T_{rip}, when $U_R(t) = U_r + U_{\text{rip}}$, can be computed by (6) and (7) in the energy discharge state, and the digital control chip should output the state-switching signals at $T_{\text{rip}} - T_d$. As shown in Fig. 11, $U_R(t)$ at $T_{\text{rip}} - T_d - T_s$ and $T_{\text{rip}} - T_d$ are computed and defined as two critical voltage values (U_{33}, U_{44}) for state-switching judgement.

3.3.3 The Estimation of the State-Switching Time by Linear Interpolation Method

The sampled $U_R(t)$ is used to compare with U_{33} and U_{44}, and to predict the precise state-switching time. When $U_{33} \le U_R(t) \le U_{44}$, the time interval T_{sw} from the sampled time to $T_{\text{rip}} - T_d$ can be estimated by

$$\frac{U_{44} - U_R(t)}{T_{\text{sw}}} = \frac{U_{44} - U_{33}}{T_s} \tag{10}$$

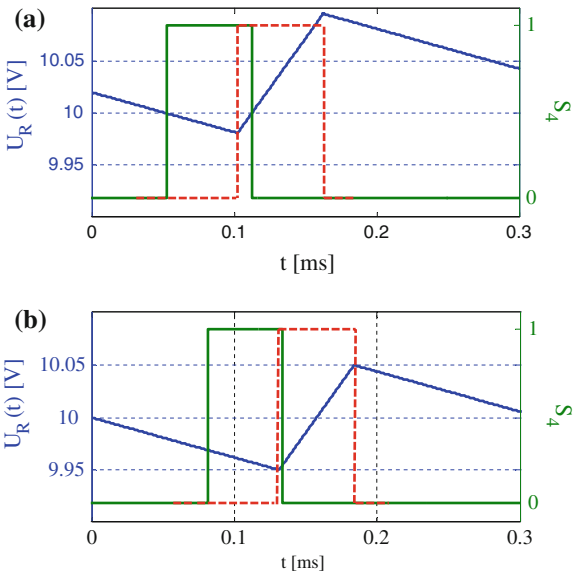

Fig. 12 $U_R(t)$ and "S_4" during the discharge-storage mode ($U_r = 10$ V, $U_{\text{rip}} = 0.05$ V, $T_d = 0.05$ ms). **a** with the conventional method; **b** with the improved method

Thus the digital control chip outputs the state-switching signals after T_{sw}, and finally makes the bridge-type chopper convert into storage state when $U_R(t) = U_r + U_{\text{rip}}$.

Figure 12 shows the voltage curve (blue line) across the external load and its corresponding digital control signal "S_4" for the switch S_4 by using the conventional and improved methods. If the turn-on and turn-off time delay of a switch is ignored, the practical state-switching control signal (red dotted line) corresponds to the voltage overshoots. However, if the improved method is applied, the digital control chip will output the state-switching control signal (green line) 0.05 ms before the time when $U_R(t)$ reaches 9.95 or 10.05 V, thus $U_R(t)$ can be precisely limited from 9.95 to 10.05 V.

4 Experimental Verification and Characteristics

4.1 Experimental Prototype Design

Figure 13 shows the schematic diagram of a unified energy exchange prototype for SMES study. Four Infineon N-channel MOSFETs with ultra-low turn-on resistance ($R_s \approx 0.65$ mΩ, under 100 A operation current) are introduced to develop the bridge-type chopper, with the power lines among the four MOSFETs formed by silvered copper bars. S_1, S_2, and, two reverse power diodes of S_2 and S_4 can be also used to form a conventional chopper for experimental tests and comparisons. The parameters of the reverse diode are $U_d \approx 0.65$ V and $R_d \approx 2.3$ mΩ. Thirty-two

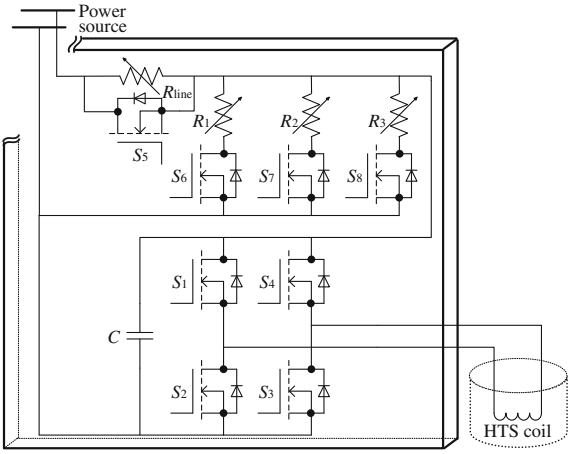

Fig. 13 The schematic diagram of the unified energy exchange prototype

Table 3 Specifications of the 0.2 H HTS coil

Parameter	Value
Coil structure	Solenoid type, three units in series
Coil frame	Reinforced fiber glass
Inner diameter	120 mm
Outer diameter	198 mm
Height	493 mm
No. of turns	3 × 748
Coil inductance	0.2 H
Critical current	>60 A at 77 K and self field
HTS wire used	Ag clad Bi-2223 tape, total length 1026 m

Nichicon conductive polymer aluminum solid electrolytic capacitors with ultra-low equivalent series resistance ($R_{esr} \approx 11$ mΩ) are connected in parallel to serve as the DC-link capacitor. The power-line resistor R_{line} is arbitrarily combined by three 0.5 Ω resistors. The power-load resistor R_{load} has three parallel resistor branches of R_1, R_2, and R_3. The available resistors in each branch are one 1 Ω resistor and two 2 Ω resistors, and can be controlled to connect or disconnect to the power-line resistor by a MOSFET.

The HTS coil used in the experiments is a 0.2 H HTS coil wound with Bi-2223 tapes. It consists of three solenoids in series for reducing the internal connections inside the HTS coil, and is operated under liquid nitrogen (LN_2) condition. The specifications of the HTS coil are shown in Table 3.

Based on the referred switching control requirements, a Micro-programmed Control Unit (MCU) was employed to build the digital control module of the system. As shown in Fig. 14, load voltage $U_R(t)$ and coil current $I_L(t)$ are sampled back to the MCU to determine the next output signals; the drive circuit mainly consisting of light coupling isolation devices to ensure the output signal from the

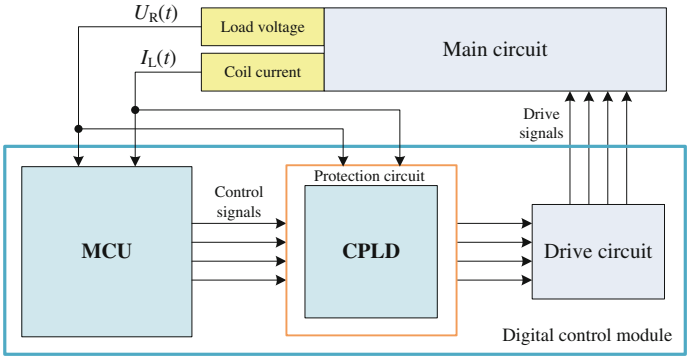

Fig. 14 A digital control module of the system

MCU can adequately drive the MOSFETs. The protection circuit is built based on CPLD. The protection function includes two parts: one is illegal logic protection for signals from the MCU; the other is overcurrent and overvoltage protection.

The main operation processes are described as follows: (i) Apply the power source to charge the DC-link capacitor through the power-line resistor, $U_R(t)$ increases gradually to the output voltage U of the power source; (ii) Close S_1, S_3 and S_5, the HTS coil is charged and $I_L(t)$ increases gradually to its preset initial value I_0; (iii) Open S_1, and then close S_2, the chopper is operated in the storage state; (iv) Open S_5, and then close one, two or three branched switches of S_6, S_7, and S_8, the corresponding branched resistors are connected to the power source through the power-line resistor; (v) The MCU and CPLD joint measurement and control unit are to implement the online voltage monitoring of $U_R(t)$ and further to change the next operation state of the chopper accordingly.

4.2 Experimental Verifications and Comparisons

4.2.1 Analysis on the Energy Absorption Characteristics

In the experiment, a DC power source $U = 15$ V is first applied to the power-line resistor $R_{\text{line}} = 0.5\ \Omega$ and power-load resistor $R_{\text{load}} = 0.25\ \Omega$. The power-load resistor is formed by three parallel branches of $R_1 = R_2 = 1\ \Omega$, $R_3 = 0.5\ \Omega$. Each branched resistor is operated at its rated voltage $U_r = 5$ V. Assume that R_2 and R_3 are disconnected from the time $t = 0$ s to $t = 6$ s, $U_R(t)$ will increase quickly to 10 V without SMES, and thus the remaining branched resistor R_1 is operated at a voltage swell state. If the SMES is applied, the 0.2 H HTS coil should be controlled to absorb the mean surplus power $P_{\text{su}} = 75$ W and the mean surplus current $I_{\text{su}} = 15$ A.

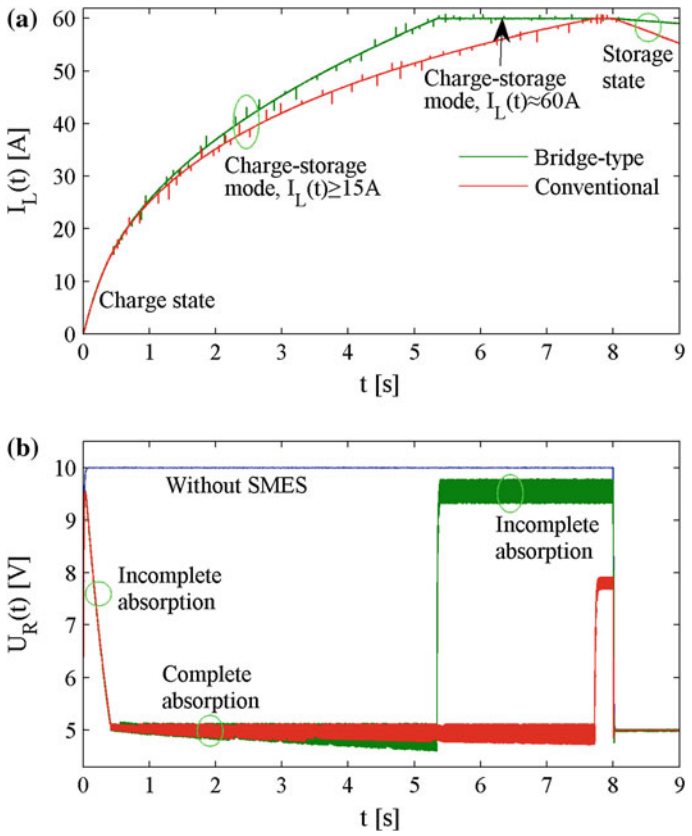

Fig. 15 The measured results of $I_L(t)$ and $U_R(t)$ during the whole energy absorption processes. **a** $I_L(t)$ versus t; **b** $U_R(t)$ versus t

Figure 15 shows the measured results of $I_L(t)$ and $U_R(t)$ during the whole energy absorption processes, which can be divided into three different segments. The first one is an incomplete absorption segment when $I_L(t) < 15$ A, both the bridge-type and conventional choppers will be operated at a charge state until $U_R(t)$ drops to 5 V again. The second one is a complete absorption segment when $15 \text{ A} \leq I_L(t) < 60$ A, the two choppers are operated at a charge-storage mode to maintain $U_R(t)$ around 5 V. Once $I_L(t)$ reaches its rated operation current $I_{\text{Lr}} = 60$ A, the third process enters into an incomplete absorption segment, and the surplus power cannot be absorbed completely. If an additional persistent current switch [26, 27] with nearly zero resistance is applied to connect with the HTS coil when its operation current reaches its rated value, the third process will be a zero absorption segment.

Figure 16 shows the measured results of $U_R(t)$ in the first incomplete absorption segment when $I_L(t) < 15$ A. If $I_0 < 15$ A, at the time $t = 0$, $U_R(t)$ will increase

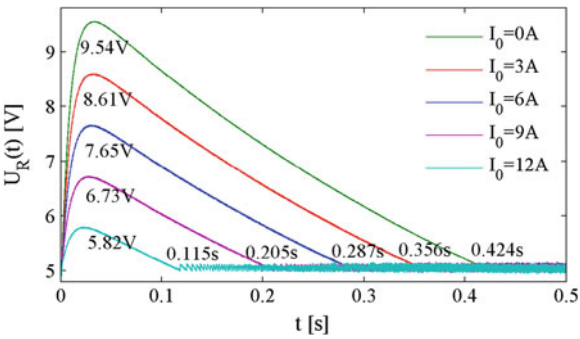

Fig. 16 The measured results of $U_R(t)$ when $I_0 < 15$ A

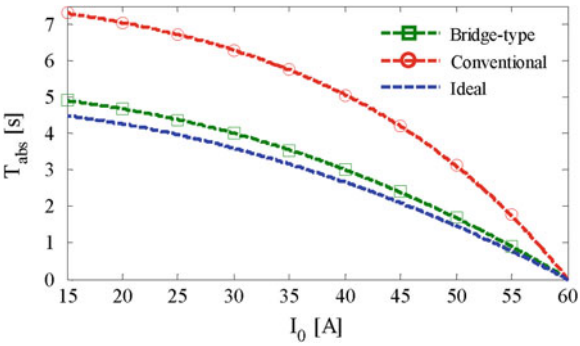

Fig. 17 The measured and calculated results of T_{abs} versus I_0

quickly to a peak voltage U_m, and then decreases gradually to 5 V after an incomplete absorption time duration T_m. Since the same MOSFETs S_1 and S_3 are used, both the bridge-type and conventional choppers have the same operation parameter in the incomplete absorption process.

In the following complete absorption segment, the maximum absorption time duration T_{abs} to absorb such a 75 W surplus power in the bridge-type chopper is shorter than that in the conventional one. As shown in Fig. 17, the measured results match well with the calculated results from the theoretical model, and the measured T_{abs} values in the bridge-type chopper are in very close proximity to the ideal values, so the bridge-type chopper has a higher energy utilization efficiency η than the conventional one. When $I_0 = 15$ A, the measured η values are about 91.5 and 61.9 % for the bridge-type and conventional chopper, respectively. However, for a practical SMES system with a determined I_{Lr}, the conventional chopper seems to be more suitable to achieve a longer T_{abs} to satisfy with the external absorption demands.

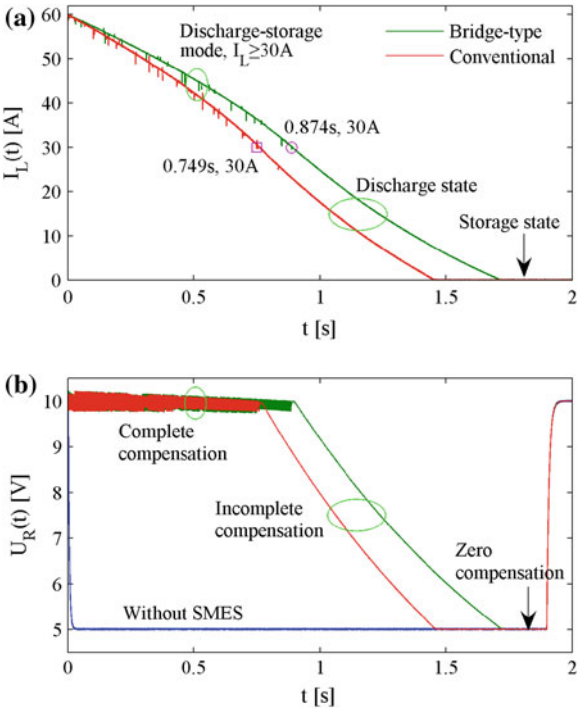

Fig. 18 The measured results of $I_L(t)$ and $U_R(t)$ during the whole energy compensation processes. **a** $I_L(t)$ versus t; **b** $U_R(t)$ versus t

4.2.2 Analysis on the Energy Compensation Characteristics

In the experiment, a DC power source $U = 15$ V is first applied to the power-line resistor $R_{\text{line}} = 0.5\ \Omega$ and power-load resistor $R_{\text{load}} = R_1 = 1\ \Omega$. The branched resistor R_1 is operated at its rated voltage $U_r = 10$ V. Assume that R_2 and R_3 are connected from the time $t = 0$ to 1.8 s, $U_R(t)$ will decrease quickly to 5 V without SMES, and thus the three branched resistors are operated at a voltage sag state. If the SMES is applied, the 0.2 H HTS coil should be controlled to compensate the mean shortfall power $P_{\text{sh}} = 300$ W and mean shortfall current $I_{\text{sh}} = 30$ A.

Figure 18 shows the measured results of $I_L(t)$ and $U_R(t)$ during the whole energy compensation processes, which can also be divided into three different segments. The first one is a complete compensation segment when $I_L(t) \geq 30$ A, both the bridge-type and conventional choppers are operated at a discharge-storage mode to maintain $U_R(t)$ around 10 V until $I_L(t)$ drops to 30 A. The second one is an incomplete compensation segment when $I_L(t) < 30$ A, the two choppers are operated at a discharge state to compensate a decreasing power. Once $I_L(t)$ drops to zero, the operation state of the two choppers should be converted into storage state to avoid the occurrence of reverse charge, and thus the third process enters into a zero compensation segment.

In the complete compensation segment, the maximum compensation time duration T_{com} to compensate such a 300 W shortfall power in the bridge-type

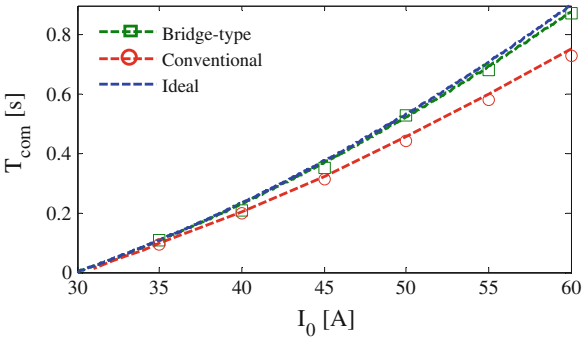

Fig. 19 The measured and calculated results of T_{com} versus I_0

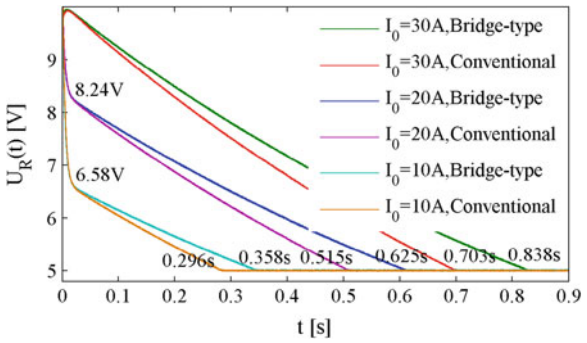

Fig. 20 The measured results of $U_R(t)$ when $I_0 \leq 30$ A

chopper is longer than that in the conventional one, as shown in Fig. 19. When $I_0 = 60$ A, the measured η values are about 97.1 and 83.2 % for the bridge-type and conventional chopper, respectively. Furthermore, if several MOSFETs are applied in parallel to serve as a power switch, both T_{com} and η can be further enlarged to approximately equal to that in an ideal chopper. However, the method to use several parallel power diodes cannot enlarge T_{com} and η effectively because of the inevitable power loss from the stationary voltage drop in the conventional chopper. Therefore, the bridge-type chopper has the potential to replace the conventional one in some low-voltage power applications like a SMES-based dynamic braking drive system of an AC motor [28]. Both the absorption and compensation efficiencies for kinetic energy of the motor will be much improved. The bridge-type chopper can also be directly applied to connect the HTS coil with DC bus in a micro grid (MG) [19]. Besides the significant improvement of practical energy exchange efficiency, the practical response time to absorb or compensate the electric energy will be reduced to microsecond level, which is very beneficial to enhance the power quality with the end-user.

Figure 20 shows the measured results of $U_R(t)$ in the incomplete compensation segment when $I_0 \leq 30$ A. If $I_0 < 30$ A, at the time $t = 0$ s, $U_R(t)$ will decrease quickly to a inflected voltage U_c, and then decreases gradually to 0 V after an

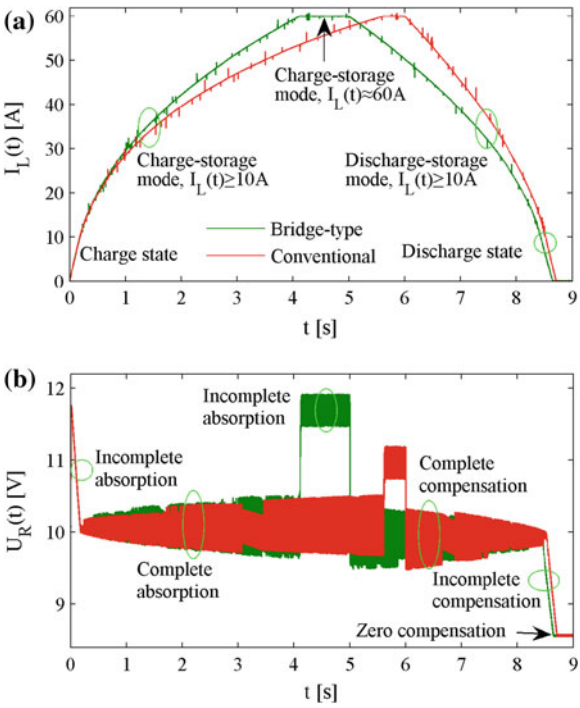

Fig. 21 The measured results of $I_L(t)$ and $U_R(t)$ during the whole energy exchange processes. **a** $I_L(t)$ versus t; **b** $U_R(t)$ versus t

incomplete compensation time duration T_c. The measured U_c values in the two choppers are similar, however, the bridge-type chopper will achieve a longer T_c than the conventional one.

4.2.3 Analysis on the Energy Exchange Characteristics

The energy absorption and compensation processes of the energy exchange prototype have been presented independently in Sects. 4.2.1 and 4.2.2. To further discuss the dynamic energy exchange characteristics, one branch and three branches of $R_1 = R_2 = R_3 = 1\ \Omega$ are connected with the power-line resistor $R_{\text{line}} = 0.5\ \Omega$ to achieve a power swell state and a power sag state, respectively. As shown in Fig. 21, the 0.2 H HTS coil should be controlled to absorb the mean surplus power $P_{\text{su}} = 100$ W until the time when $t = 5$ s in the bridge-type chopper or $t = 6$ s in the conventional chopper, and then to compensate the mean shortfall power $P_{\text{sh}} = 100$ W until the time when $t = 9$ s. The whole energy exchange processes can be divided into six different segments: (i) Incomplete absorption segment when $I_L(t) < 10$ A; (ii) Complete absorption segment when $10\ \text{A} \le I_L(t) < 60$ A; (iii) Incomplete absorption segment when $I_L(t) \approx 60$ A; (iv) Complete compensation segment when $I_L(t) \ge 10$ A; (v) Incomplete compensation segment when $0\ \text{A} < I_L(t) < 10$ A; (vi) Zero compensation segment when $I_L(t) = 0$ A.

Similarly, the dynamic energy exchange characteristics in all the energy absorption and compensation segments can be fully obtained by integrating the theoretical and experimental studies in Sects. 4.2.1 and 4.2.2. The available parameters and data curves mainly include: (i) U_m, T_m, U_c, and T_c in the incomplete absorption and compensation segments when $I_L(t) < 10$ A; (ii) T_{abs} and T_{com} in the complete absorption and compensation segments when $10\ \text{A} \le I_L(t) \le 60$ A; (iii) $I_L(t)$ and $U_R(t)$ at an arbitrary time; (iv) Transient voltage, current, consumed power curves of the power-line resistor and power electronic elements.

The above operation parameters and relevant relations probably follow several power and linear functions as follows: (i) Incomplete absorption segment, $U_m = -0.306I_0 + 9.514$, $T_m = -0.027I_0 + 0.435$; (ii) Complete absorption segment, $T_{\text{abs}} = -1.333 \times (I_0)^2 \times 10^{-3} + 4.8$ in the ideal chopper, $T_{\text{abs}} = -5.515 \times (I_0)^2 \times 10^{-2.234} + 5.157$ in the bridge-type chopper, $T_{\text{abs}} = -4.165 \times (I_0)^{2.945} \times 10^{-5} + 7.285$ in the conventional chopper; (iii) Complete compensation segment, $T_{\text{com}} = 3.333 \times (I_0)^2 \times 10^{-4} - 0.3$ in the ideal chopper, $T_{\text{com}} = 3.928 \times (I_0)^{1.957} \times 10^{-4} - 0.3054$ in the bridge-type chopper, $T_{\text{com}} = 6.336 \times (I_0)^{1.813} \times 10^{-4} - 0.3054$ in the conventional chopper; (iv) Incomplete compensation segment, $U_c = 0.171I_0 + 4.853$, $T_c = 0.024I_0 + 0.125$ in the bridge-type chopper, $T_c = 0.021I_0 + 0.08$ in the conventional chopper. The fitted linear and power functions have the potential to apply in practical SMES design and optimization for use in different power system applications. The proposed system also provides a feasible method to build a simple and economical test apparatus for the experimental evaluations of an SMES device before its practical applications.

Based the above theoretical and experimental results obtained, conclusions can be made as follows: As compared to the conventional chopper, the bridge-type one has higher energy utilization efficiency in various power end-user applications such as EVs, UPSs, DGs, and LVDC systems. What's more, the energy utilization efficiency can be further improved by introducing the MOSFETs with lower applicable voltage level or adopting the multi MOSFET in parallel connection method. However, similar methods cannot improve the efficiency significantly in the conventional chopper because of the inevitable power loss from the stationary voltage drop across the two power diodes. If one simply considers the practical energy exchange effects to satisfy with the external demands, a better application scheme is to use the charge-storage mode of the conventional chopper during the energy absorption process, and to use the discharge-storage mode of the bridge-type chopper during the energy compensation process. The scheme will integrate the advantages of the two choppers for achieving very long absorption and compensation time durations.

5 Development Status of Worldwide SMES Devices

In recent years, with the development of superconducting materials, especially HTS materials with promising strong-current applications in large-scale magnets, various SMES devices have been fabricated and tested for practical power grids.

Table 4 Worldwide development status of LTS SMES devices

R&D team	Materials	Energy level	Applications
Los Alamos Laboratory (USA)	NbTi	30 MJ	Damping the low frequency (0.35 Hz) [32]
University of Florida (USA)	NbTi	100 MJ	Damping the low frequency (0.2–3 Hz) [33]
American Superconductor (USA)	NbTi	1–5 MJ	Already successfully commercial applications [43]
National Nuclear Science Institute (Japan)	NbTi	1 MJ	UPS (500 kW, 1 s) [44]
Chubu Electric Power Company (Japan)	NbTi	7.34 MJ	Instantaneous voltage drop compensation [34]
	NbTi	20 MJ	Instantaneous voltage drop compensation [45]
Tokyo Institute of Technology (Japan)	NbTi	270 kJ	Power system stability [46]
Kyushu Electric Power Company (Japan)	NbTi	2.9 MJ	Power system stability [47]
Tsinghua University (China)	NbTi	0.3 MJ	Instantaneous voltage drop compensation [48]
Institute of Electrical Engineering, CAS (China)	NbTi	2 MJ	Pulsed power source [35]
Korean Electric Research Institute (Korea)	NbTi	3 MJ	UPS [36]
Bologna University (Italy)	NbTi	200 kJ	Power quality improvement [49]
Ansaldo Ricerche Spa (Italy)	NbTi	2.6 MJ	Protect the sensitive load [37]

The main LTS and HTS SMES devices worldwide are summarized in Table 4 and Table 5 [29–31].

Serious interests in SMES began in the early 1960s as reliable low-temperature superconductors (LTSs) became available. The practical feasibility of the SMES concept has been demonstrated with the world's first commercial 30 MJ NbTi SMES unit [32] used on the Pacific Intertie transmission line in the early 1980s. At this point in time, the LTS SMES technology is relatively mature and reliable; USA has developed several large-scale SMES devices, e.g., 30 MJ SMES in Los Alamos National Laboratory (LANL) [32], 100 MJ SMES in University of Florida [33], and has already achieved the primary process of commercialization. Other countries in the world have also developed several MJ-class LTS SMES devices, e.g., Chubu Electric Power Co. in Japan—7.34 MJ SMES [34], Chinese Academy of Sciences in China—2 MJ SMES [35], Korean Electric Research Institute in Korea—3 MJ SMES [36], Ansaldo Ricerche spa in Italy—2.6 MJ SMES [37], etc. The power system applications of the current LTS SMES devices include damping low-frequency oscillation in the interconnected grid, maintaining power system stability, compensating voltage dip, protecting critical load, etc. However, the high refrigeration loads, which is required to keep the LTS materials at 4.2 K, made the

Table 5 Worldwide development status of HTS SMES devices

Research and development team	Materials	Energy level	Applications
Chubu Electric Power Company (Japan)	Bi2212	1 MJ	Instantaneous voltage drop compensation [38]
	YBCO	2.4 GJ	Load fluctuation compensation [14]
Toshiba Company (Japan)	Bi2212	6.5 MJ	Fundamental study [50]
Institute of Electrical Engineering, CAS (China)	Bi2223	30 kJ	Fundamental study [51]
	Bi2223	1 MJ	Power quality improvement [39]
Huazhong University of Science and Technology (China)	Bi2223	35 kJ	Hydropower station experiments [52]
University of Electronic Science and Technology of China and Innopower (China)	Bi2223	1 kJ	Low-loss switching and digital control for micro grid applications [13, 29]
Korean Electric Research Institute (Korea)	Bi2233	600 kJ	Power system stability [41]
		2.5 MJ	Power system stability [53]
National Center for Scientific Research (France)	Bi2212	800 kJ	Pulsed power source [40]
ACCEL Instruments GmbH (Germany)	Bi2223	150 kJ	UPS [54]
Superconducting Technology Laboratory (Poland)	Bi2223	34.8 kJ	UPS [55]
Wollongong University (Australia)	Bi2223	2.48 kJ	Fundamental study [56]

LTS SMES uneconomical to practically operate. For LTS SMES further developments, the high refrigeration cost remains a significant barrier.

Immediately following the discovery of HTS materials in 1986, several studies looked into the feasibility of HTS SMES. Due to the anisotropy of 1G HTS tapes and immature HTS high-field magnet technology, the number of the worldwide HTS SMES devices is relatively few by comparison to LTS SMES devices, and the achieved capacities are limited to MJ-class, e.g., Chubu Electric Power Co. in Japan—1 MJ SMES [38], Chinese Academy of Sciences in China—1 MJ SMES [39], CNRS-CRTBT-LEG in France—0.8 MJ SMES [40], Korean Electric Research Institute in Korea—0.6 MJ SMES [41], etc. The HTS magnets in the above MJ-class HTS SMES devices are fabricated by 1G BSCCO tapes (Bi2212 or Bi2223), which have been considered as transitional materials for studying HTS magnet technology. With the continued development of HTS wires, the second generation (2G) YBCO tapes became more feasible, and their outstanding high-field properties make large-scale HTS SMES available, i.e., 2.4 GJ YBCO SMES [14]. Recently a new promising SMES technology based on MgB_2 tapes has been proposed to combine with liquid hydrogen (LH_2) for developing very compact hybrid ESSs, i.e., 48 GJ MgB_2 LIQHYSMES [42].

The continuous progresses of HTS materials and SMES devices have formed the firm base for the SMES developments and applications ranging from small to large scales in distribution to transmission power systems and future SGs. In addition, the suitable reduction of capital cost for SMES devices with the price

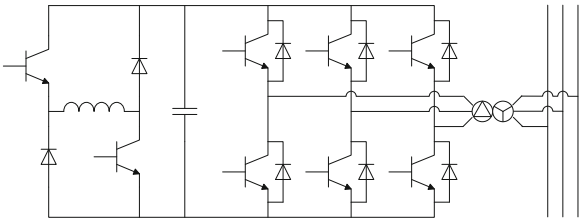

Fig. 22 Basic configuration of VSC-based SMES system

reduction of HTS conductors (BSCCO tapes for about 35 $/kA·m or below, YBCO tapes for about 15 $/kA·m or below), large-scale SMES devices will become economically available, and will play an important role in future SGs.

6 SMES Application Topologies and Performance Evaluations

With the development of micro grids (MGs) and smart grids (SGs), it is expected that combination of centralized power generation and distributed power generation for developing modern resource-saving and environment-friendly power systems will occur in future. The ultimate purpose is to satisfy the increased power quality requirements from modern power consumers. Fast response, high efficiency, large-scale energy storage systems (ESSs) play an important role for smart regulation and control in flexible AC transmission systems (FACTS) for power transmission, distributed flexible AC transmission systems (DFACTS) for power distribution, and widespread renewable energy sources (RESs) penetration and replacement of the current fossil-fuel power generation. This section summarizes the application topologies and evaluates the high-performance SMES devices for power grid applications.

6.1 Basic VSC and CSC Application Topologies

6.1.1 VSC-Based SMES

Figure 22, as an example, shows the basic configuration of a VSC-based SMES unit [57], which consists of a Wye-Delta transformer, a six-pulse pulse width modulation (PWM) rectifier/inverter using insulated gate bipolar transistor (IGBT), a two-quadrant DC–DC chopper using IGBT, and a superconducting coil or inductor. The PWM converter and the DC–DC chopper are linked by a DC-link capacitor.

The PWM VSC provides a power electronic interface between the AC power system and the superconducting coil. The control system of the VSC is shown in

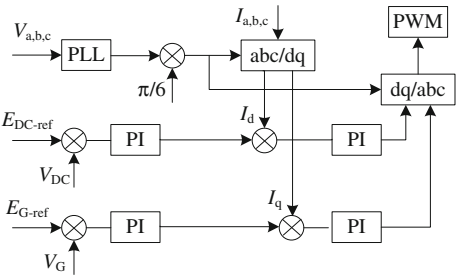

Fig. 23 Control system of the VSC

Fig. 23. The proportional-integral (PI) controllers determine the reference *d*- and *q*-axis currents by using the difference between the DC-link voltage E_{DC} and reference value E_{DC_ref}, and the difference between terminal voltage V_G and reference value V_{G_ref}, respectively. The reference signal for VSC is determined by converting *d*- and *q*-axis voltages which are determined by the difference between reference *d*–*q* axes currents and their detected values. The PWM signal is generated for IGBT switching by comparing the reference signal which is converted to a three-phase sinusoidal wave with the triangular carrier signal. The DC voltage across the capacitor is kept constant throughout by the six-pulse PWM converter.

The superconducting coil is charged or discharged by a two-quadrant DC–DC chopper. The DC–DC chopper is controlled to supply positive (IGBT is turned ON) or negative (IGBT is turned OFF) voltage V_{sm} to the SMES coil and then the stored energy can be charged or discharged. Therefore, the superconducting coil is charged or discharged by adjusting the average voltage V_{sm_av} across the coil which is determined by the duty cycle of the two-quadrant DC–DC chopper. When the duty cycle is larger than 0.5 or less than 0.5, the stored energy of the coil is either charging or discharging, respectively. In order to generate the PWM gate signals for the IGBT of the chopper, the reference signal is compared with the triangular signal.

6.1.2 CSC-Based SMES

Figure 24, as an example, shows the basic configuration of a current source converter-based (CSC-based) SMES unit. The DC side of CSC is directly connected with the superconducting coil, and its AC side is connected to the power line. A bank of capacitors connected to a CSC input terminal is utilized to buffer the energy stored in line inductances in the process of commutating direction of AC line current. Furthermore, the capacitors can filter the high-order harmonics of the AC line current. In the CSC, through regulating the trigger signals of the switching devices, the current in the superconducting coil can be modulated to generate controllable three-phase PWM current at the AC side. As the SMES system is inherently a current system, the transfer of both active and reactive powers between the CSC and power network is very fast.

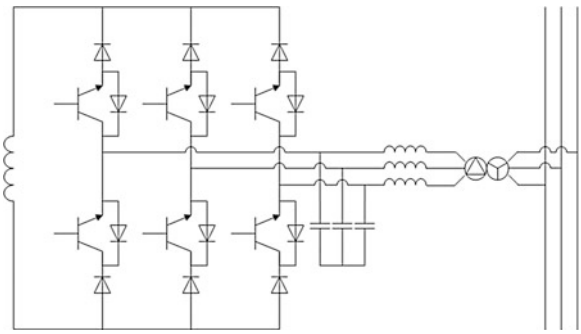

Fig. 24 SMES system with a CSC

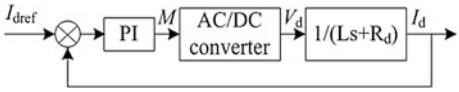

Fig. 25 Block diagram of the DC current control algorithm

In case of a 12-pulse CSC-based SMES, to improve the total harmonics distortion (THD) of the ac source currents, an optimal PWM switching strategy is used to minimize the 5th, 7th, 11th, and 13th harmonics. It has been proved that the 5th, 7th, 11th, and 13th harmonics can be minimized to zero with the modulation index ranging from 0.2 to 1. Compared to a 6-pulse CSC, the 12-pulse CSC has smaller voltage ripples on the dc side, which means a further reduction of the ac losses in the SMES coil.

For magnet training, a DC current I_d control algorithm is applied. The block diagram is shown in Fig. 25, where I_{dref} is the reference value of I_d, PI is a proportional-integral regulator, L is the inductance of the SMES coil, R_d is the resistance in the DC circuit, and V_d is the DC voltage. With the phase angle α being fixed to zero, the DC voltage is proportional to the modulation index M, which determines the charging rate.

6.2 Integrated Application Topologies in Power Grids

6.2.1 Application Topologies in Distributed Generators and Micro Grids

To reach widespread RESs penetration and replacement of the current fossil-fuel power generation, an innovative concept of micro grid (MG), which integrates several DGs and distributed ESSs, has been proposed to achieve large power quality improvements and comprehensive utilizations of various local DGs. A typical MG system with a SMES is shown in Fig. 26 [30, 31]. The generated power of the solar power system, wind power system, and hydro power system are

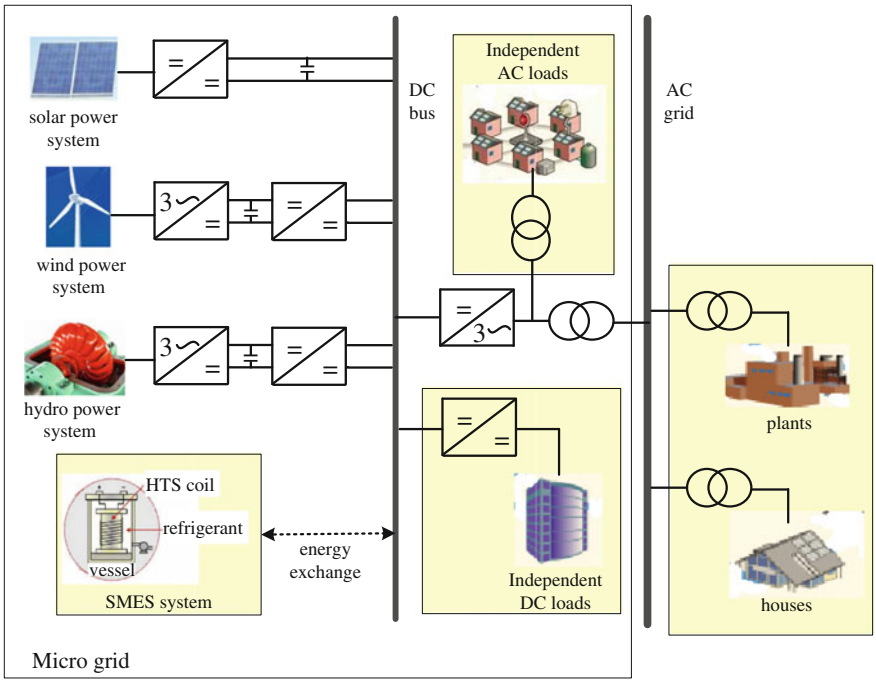

Fig. 26 A typical MG system with SMES

gathered in the DC bus through several power conversions. The SMES system carries out dynamic power exchange with the DC bus to maintain the power stabilization in DC bus. The MG system can be applied as a power supply for independent loads and grid loads.

There are three main technical advantages in the MG system with a SMES: (i) SMES with rapid response characteristics (ms level) can, such as voltage interrupt, instantaneous voltage dip, etc.; (ii) SMES with very large power output characteristics (MW level) can provide enough compensation power for DC bus; (iii) SMES with very high energy storage efficiency characteristics can improve the operation efficiency in the whole MG system.

6.2.2 Application Topologies in Transmission and Distribution Systems

To solve different power quality problems, e.g., voltage sag, voltage swells, voltage fluctuation, interruptions, harmonics, etc., various power conversions, compensation, and control devices have been introduced to regulate and control the transmission and distribution systems. The main solutions for various power

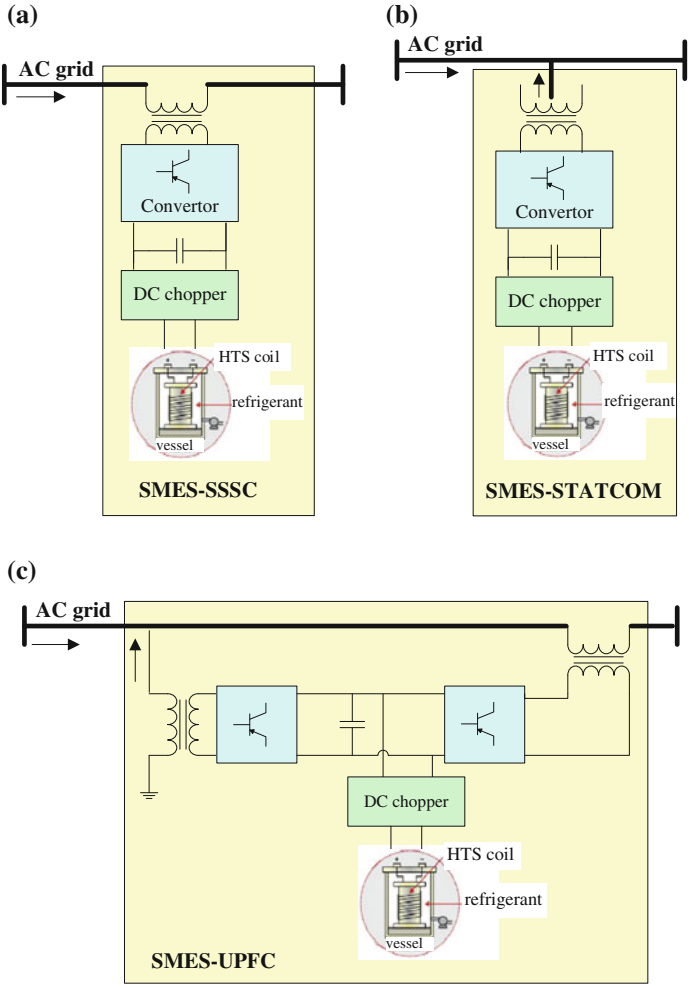

Fig. 27 Three typical FACTS/DFACTS with SMES. **a** SMES-SSSC; **b** SMES-STATCOM; **c** SMES-UPFC

quality problems include FACTS for the power transmission side and DFACTS for the power distribution side. Three basic FACTS and DFACTS devices, i.e., series-type static synchronous series compensator—SSSC, static synchronous compensator—STATCOM, unified power flow controller—UPFC, with a SMES unit in the device, are shown in Fig. 27. The integrated application schemes of SMES-FACTS/DFACTS in power transmission line (TL) and distribution line (DL) are shown in Fig. 28.

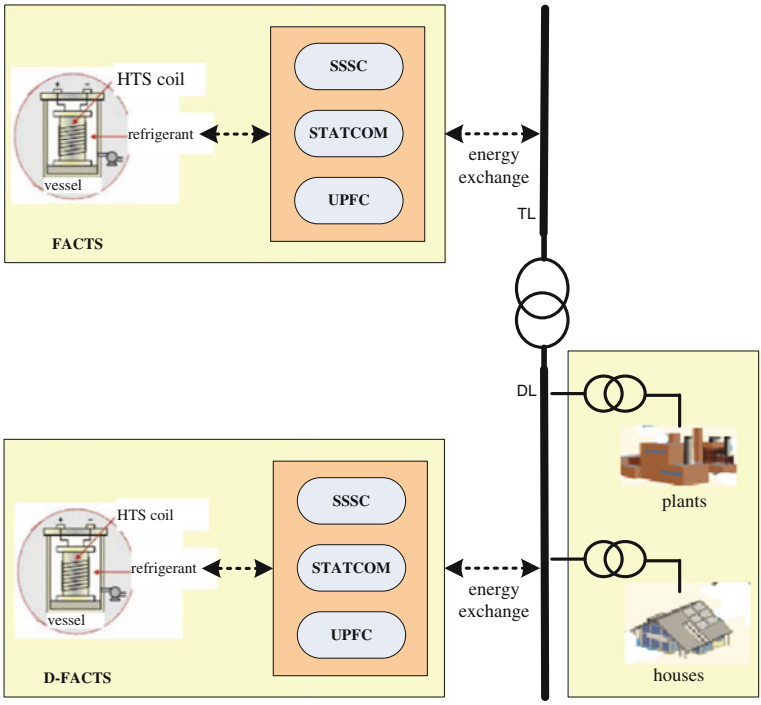

Fig. 28 The integrated application schemes of SMES-FACTS/DFACTS

6.2.3 Integrated Application Topologies in Smart Grids

Based on the above discussions, the prospect of SMES in future SG is proposed in Fig. 29. In addition to the traditional power generation plants including hydro power plants, thermal power plants, and nuclear power plants, various MGs or DGs using RESs will be widely installed in future SGs. With the dynamic power exchange and regulation from SMES or hybrid ESSs, MGs or DGs can be directly connected to the main power transmission and distribution lines (DLs). SMES-based FACTS and DFACTS devices can be further applied to carry out the whole power flow control for reaching the increasing power demands from modern power consumers (PCs). The real-time signals in the whole SG will be transmitted to the smart control center for data processing and finally achieving the integrated power management and control of FACTS, DFACTS, and MGs. As an auxiliary power management technology, the SMES-based UPS devices installed in the power terminals will guarantee the power quality for various PCs.

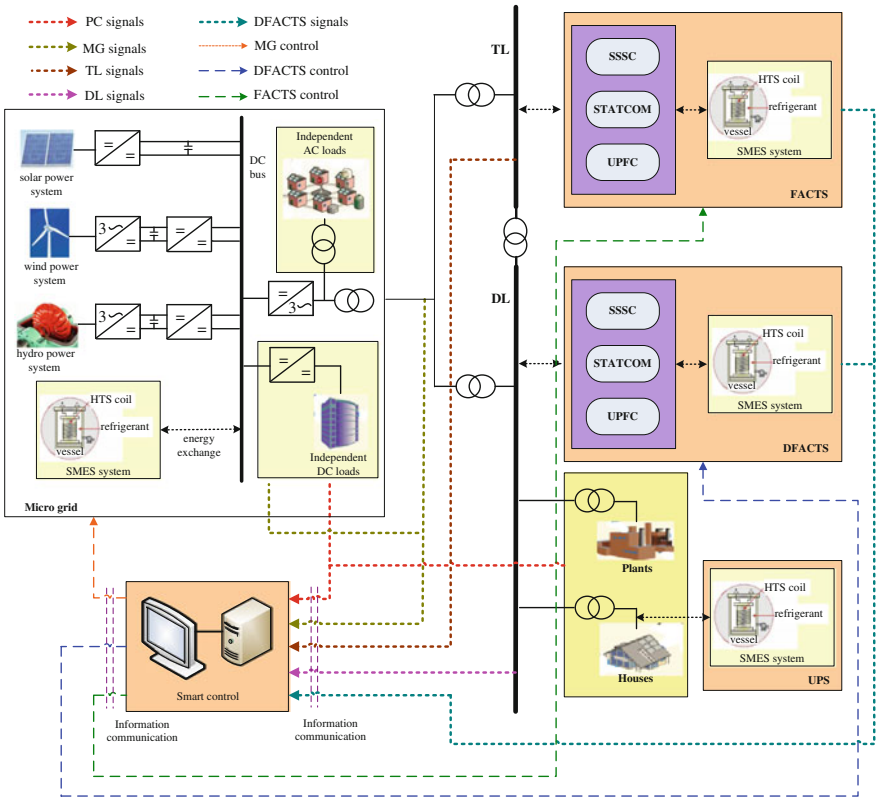

Fig. 29 The integrated application prospects of SMES in future smart grid

6.3 Applications of SMES in Power Grids

The application topologies and advantages of SMES for MGs, transmission and distribution systems are described in this section. The application scheme of hybrid ESSs with distributed SMES devices are proposed and discussed to combine the advantages from SMES devices and other conventional ESSs, and to achieve better performance in practical power applications. The integrated solutions for SGs are proposed with functions and application schemes of SMES devices.

6.3.1 Applications in Distributed Generators and Micro Grids

(1) *Application in wind power system*
The intermittence and unpredictable nature of the wind power cause voltage and power fluctuations. The bandwidth of the wind power fluctuations is

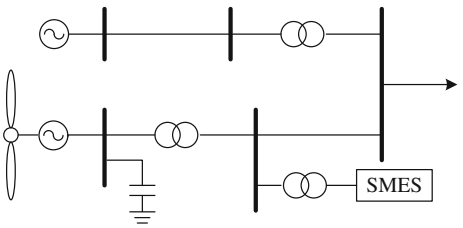

Fig. 30 A wind farm system integrated with an SMES unit

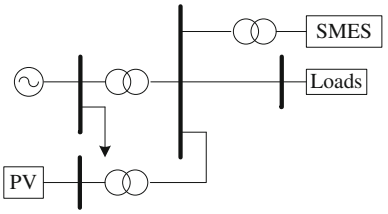

Fig. 31 Schematic diagram of a combined PV/SMES system

generally below 1 Hz, while the power system is more sensitive to the power fluctuations in the frequency region between 0.01 and 1 Hz. Therefore, it is necessary to smooth power fluctuations for large wind farms. Figure 30, as an example, shows a wind farm system integrated with an SMES unit, which consists of a power fluctuation suppression control module for a wind farm and a power control module for the SMES. The results obtained from the referred wind farm show that the SMES system can perform well with respect to the voltage fluctuation compensations [58].

(2) *Application in photovoltaic power generation*
Figure 31, as an example, shows the schematic diagram of a combined PV/SMES system. The PV generation system and the SMES system are joined by a common bus, which is connected to the utility grid. The results obtained with or without the modulation by the PV/SMES system show that the power generated by the SMES system can be able to satisfactorily smooth out PV power fluctuations [59]. Power generated from PV arrays can be completely utilized under different weather conditions and PV penetration can be increased to significant levels without causing side effects to the power system.

(3) *Application in hydroelectric power system*
Figure 32, as an example, shows a hydroelectric network integrated with a 10 MVA/20 MJ SMES device connected to an 11 kV bus in a hydro power station [45]. The SMES is operated to compensate power fluctuation generated by the metal rolling factory near the power station. The results of a compensation test for the load fluctuations show that the active power fluctuation load at the bus is effectively compensated, and the active power load of the generator is almost a constant after compensation by the SMES system.

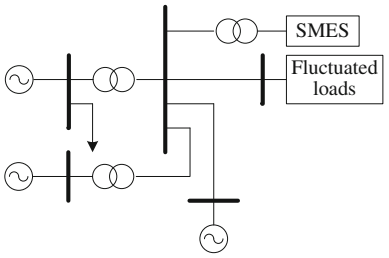

Fig. 32 A sample hydroelectric network integrated with an SMES unit

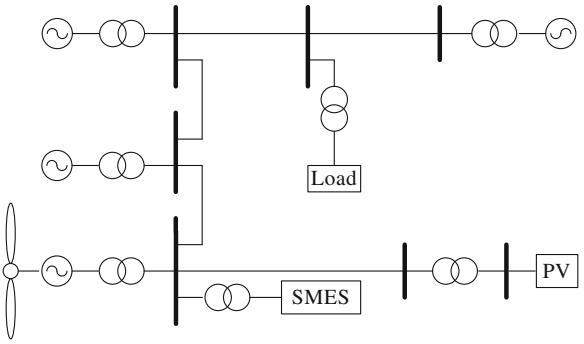

Fig. 33 A sample micro grid integrated with an SMES unit

(4) *Application in micro grids*
Figure 33 shows a micro grid (MG) integrated with a SMES unit. The sample system includes two diesel generators, one hydro generator, one wind generator, and one PV system. The SMES system is connected with the MG by a VSC [60]. The stability enhancement and minimization of frequency fluctuation of the MG can be achieved by using SMES and pitch control. Some SMES cases with different energy storage capacities and their compensation effects are discussed [60]. Simulation results show that the SMES is a very effective device for stabilization of the MG.

6.3.2 Applications in Flexible AC Transmission Systems

(1) *Application in power system dynamic stability improvement*
The application of SMES for dynamic stability improvement has been studied [61]. Take a three-machine and nine-bus power system, for example, as shown in Fig. 34. The SMES system was first located between buses 4 and 9 (nearer to bus 4); then, the faults obstacles were simulated with the SMES system placed at bus 7. A three-phase ground fault was made at $t = 175$ s for a period of 70 ms at different locations and the total performance of the system is simulated with or without the SMES system. The results show that the rotor speed is under control while the SMES system discharges into the system as

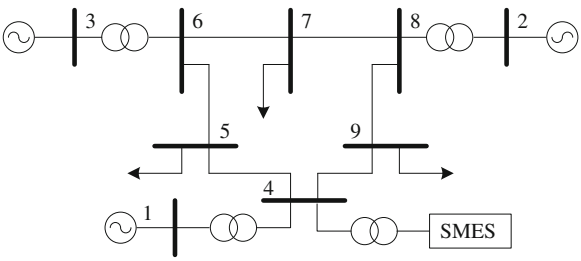

Fig. 34 A sample power system with an SMES to improve dynamic stability

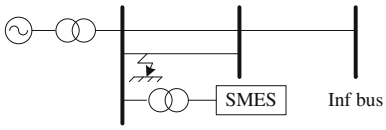

Fig. 35 Power system model with an SMES unit

the supply of both active and reactive power. An average active power of about 70 MW is discharged into the system during the fault at $t = 175$ s with a significant amount of reactive power being injected into the system simultaneously.

(2) *Application in power system transient stability improvement*
The application of SMES for transient stability improvement has been studied [62, 63]. The model system as shown in Fig. 35, as an example, consists of a synchronous generator and an infinite bus through a transformer and double circuit transmission line. In order to control the power balance of the synchronous generator during the dynamic period effectively, an SMES unit is located at the generator terminal bus. A fuzzy logic control method is applied to improve the transient stability and is also compared with that of a conventional PI-controlled SMES scheme. The simulation results of both balanced (three-phase-to-ground) and unbalanced (single-line-to-ground) faults demonstrate the effectiveness and validity of the SMES system for the transient stability improvements [63].

(3) *Application in power system active filter*
The passive filters have an increasing possibility of low degree harmonics and a limit to cover all harmonics current. However, the active filter system can reduce harmonics current at once without the problems of existing passive filter system. SMES is a very good promising source used in the active filter systems due to the high response time of charge and discharge. Figure 36, as an example, shows an SMES-based active filter system consisting of both series and shunt filter functions. The system is composed of a 3-phase DC–AC converter for compensation of harmonic current and three 1-phase DC–AC converters for compensation of voltage sag. Harmonic current from a nonlinear load was assumed for confirmation of the performance of the shunt active filter. If a shunt active filter energized by SMES is applied, the harmonic elements in the utility line current are fully compensated [64].

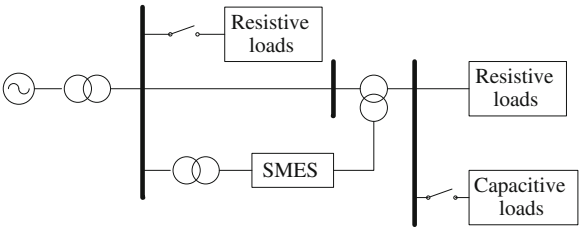

Fig. 36 Circuit topology of an SMES-based active filter system

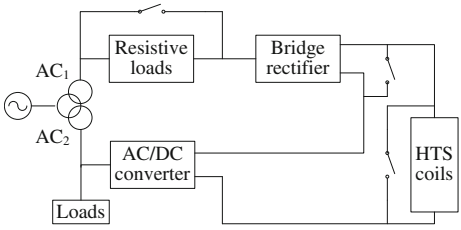

Fig. 37 Circuit topology of SMES-SFCL

(4) *Application in power system SMES–SFCL*
To make full use of the HTS coils for power system applications, a promising solution is to make the superconductivity device perform more than one function, e.g., SMES and SFCL (superconducting fault current limiter), thus we can take full advantage of the device and the cost of each function is reduced effectively. Figure 37 shows the circuit topology of a typical SMES-SFCL device [65]. The combined SMES–SFCL device acts as a SMES to the AC_1 system. It can alleviate voltage swells, sags, and even momentary outages. It also acts as a SFCL to the AC_2 system and can restrain the fault current by the large inductance of the superconducting coil. When the combined device reaches its steady state, a short circuit from phase A-to-ground occurs at 1.8 s and it lasts 0.08 s. DC current in the superconducting coil and current in phase A are both monitored. The results show [65] that the fault current is effectively limited, but the coil current does not rise very much because of the existence of the part of SMES.

7 Prospective SMES Applications Toward Smart Grids

7.1 Application Solutions of SMES in the Modern Power Systems

To cope with modern power systems, large-scale, medium-scale, and small-scale SMES devices with different energy storage capacity and power rating are demanded. In this section, four SMES units as shown in Table 6 are introduced to

Table 6 Specifications of four SMES units

Items	Scheme 1	Scheme 2	Scheme 3	Scheme 4
Coil structure	Toroid	Toroid	Solenoid	Solenoid
Stored energy	3.6 TJ	36 GJ	3.6 MJ	36 kJ
Rated power	100 MW	100 MW	1 MW	1 MW
Compensation time	~10 h	~6 min	~3.6 s	~0.036 s
Inductance	72 kH	18 kH	7.2 H	0.072 H
Rated current	10 kA	2 kA	1 kA	1 kA
Capital cost	3870.6 M$	387.1 M$	2.2 M$	0.1 M$

discuss and verify the application schemes and characteristics of SMES for power generation, transmission, distribution, and end-users.

7.1.1 Analysis on Daily Load Levelling

Daily load leveling refers to the use of electric energy stored in the large-scale ESSs during the time periods of low demand to supply peak demand. Large-scale pumped hydro storage (PHS) technology with a typical storage efficiency between 70 and 80 % is currently the commercial storage option for daily load leveling. It has been reported [66] that a TJ-class SMES device with high storage efficiency of ~90 % and no site limitation will be a promising solution in the future. Although the capital cost of a SMES device is more than that of a PHS device with the same capacity at present, SMES will reduce the annual operation cost for the same capital cost to 50–60 % of that of PHS, thus the overall life cycle cost of SMES may be lower than that of PHS.

Figure 38 shows a typical curve of a 3.6 TJ SMES device for daily load leveling: (i) During the low demand time periods, the 3.6 TJ SMES device in Scheme 1 is operated at energy charge state to absorb the surplus power $P_{\min} - P_{\text{demand}}$, and thus the base-load power plants can be operated efficiently at full power $P_{\min}$; (ii) During the peak demand time periods, the 3.6 TJ SMES device will be operated at energy discharge state to release the stored energy to compensate the shortfall power $P_{\text{demand}} - P_{\max}$ for satisfying the real-time load power demand P_{demand}, which reduces the need to draw an electricity from the peaking power plants or increase the grid infrastructures; (iii) During the medium-demand time periods, the practical electricity generated $P_{\text{generated}}$ can basically follow with the P_{demand}, and the 3.6 TJ SMES device is operated at energy storage state with nearly zero energy loss.

The energy practically stored in the 3.6 TJ SMES device fluctuates along with the dynamic energy exchange processes, and can be calculated by

$$E_{\text{SMES}}(t) = E_0 \pm \int_0^t P_r(t)\mathrm{d}t \tag{11}$$

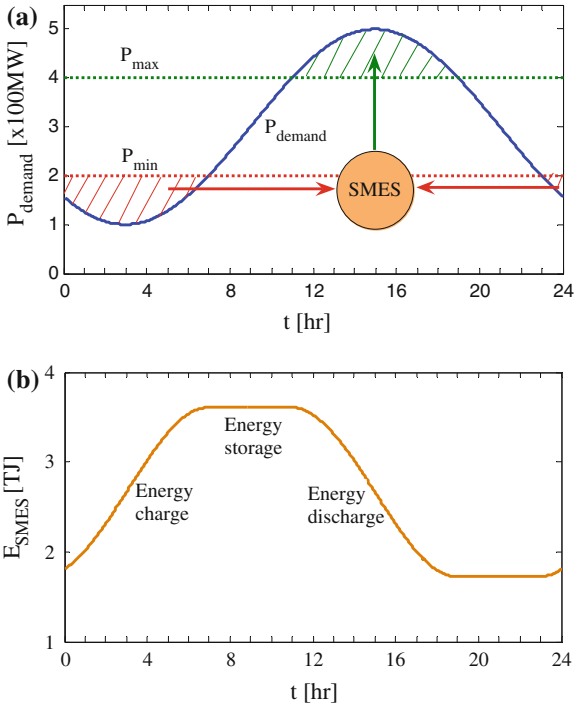

Fig. 38 The results of 3.6 TJ SMES for daily load leveling. **a** The power changes of daily demand and supply with SMES; **b** The energy changes of the 3.6 TJ SMES device

where E_0, initial stored energy; $P_r(t)$, the surplus or shortfall power. In the case of sinusoidal AC power and energy exchange, $P_r(t)$ approximately equals to the root mean square (RMS) power P_{RMS} due to the equivalence of the AC to DC power conversion, thus the absorbed or released energy equals to the product of P_{RMS} and time duration Δt.

Since the 3.6 TJ SMES device can be controlled to fully compensate the reference power demand when $I_{\mathrm{SMES}}(t)$ is greater than or equal to the RMS current I_{RMS}, the maximum compensation time duration can be calculated by

$$T_{\mathrm{comp}} = \frac{L}{2P_{\mathrm{RMS}}}\left(I_{\mathrm{max}}^2 - I_{\mathrm{RMS}}^2\right) \tag{12}$$

where I_{max} is the maximum allowable operation current through the HTS coil, which should be limited within its critical current to avoid the occurrence of quench.

Figure 39 shows the results of T_{comp} versus I_{max} with $L_{\mathrm{SMES}} = 72$ kH and $E_{\mathrm{SMES}} = 3.6$ TJ. For a specific coil inductance, T_{comp} is almost proportional to the square of I_{max}. For a specific energy storage capacity, T_{comp} increases rapidly with increment of I_{max} at first and then approaches a saturation value gradually. A reasonable parameter optimization should be achieved by considering the external power demands and development specifications of the HTS coil, e.g., the capital

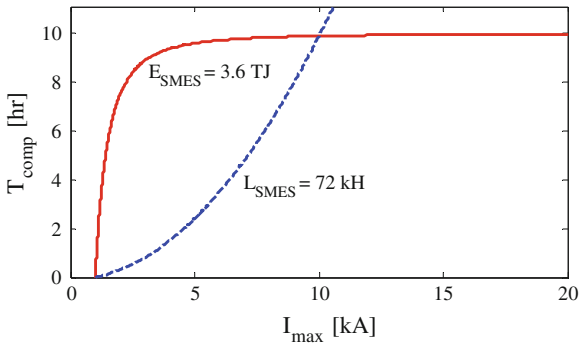

Fig. 39 T_{comp} versus I_{max} with $L_{SMES} = 72$ kH and $E_{SMES} = 3.6$ TJ

cost [67] for developing a large-scale HTS coil with large coil inductance, the refrigeration cost [68] for achieving a ultra-low operation temperature with high critical current. What is more, the coil structure should also be optimized to reduce the electromagnetic force and stray magnetic field for further improving the critical current and lessening the electromagnetic pollutions. The multipole solenoidal coil [33] and toroidal coil [14] are normally applied at present. Recently, three new kinds of force-balanced coil (FBC) [69], stress balanced coil (SBC) [70], and tilted toroidal coil (TTC) [71] have been introduced for large-scale coil developments.

7.1.2 Analysis on Load Fluctuation Compensation

As mentioned above, a TJ-class SMES or PHS device is available for daily load leveling. However, there are still some second-level or minute-level load fluctuations during the medium-demand time periods. A GJ class SMES device seems to be a more economical option for these load fluctuation compensation applications in the power transmission systems. Currently, two ongoing 2.4 GJ YBCO SMES [14] and 48 GJ MgB_2 SMES [42] projects are proposed to carry out the load fluctuation compensations from hundreds of MW to GW class.

Figure 40 shows the results of SMES for minute-level load fluctuation compensations. Since SMES has the shortest response time to absorb or release the electricity as compared to other ESSs, the introduction of the 36 GJ SMES device in Scheme 2 makes the dynamic compensation more effective and timely.

The relations between the capital cost and energy storage capacity in a SMES device are shown in Fig. 41, and the capital cost equations [67] for a solenoidal coil and toroidal coil can be approximatively expressed by Cost (M$) = 0.95 [Energy (MJ)]$^{0.67}$ and Cost (M$) = 2.04 [Energy (MJ)]$^{0.5}$.

The capital costs of the 3.6 TJ and 36 GJ SMES coils are 3870.6 and 387.1 M$, respectively. To reduce the capital cost and make better use of a SMES device, the SMES can be introduced to combine with other ESSs for forming a hybrid energy storage system (HESS). The HESS has very high reliability because the hybrid combinations of several ESSs can combine to use their advantages in full, but

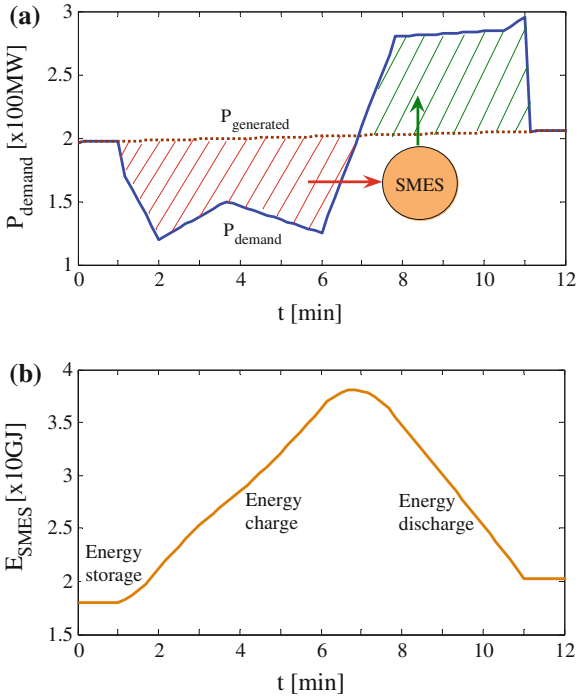

Fig. 40 The results of 36 GJ SMES for load fluctuation compensation. **a** The power changes of demand fluctuation and supply with SMES; **b** The energy changes of the 36 GJ SMES device

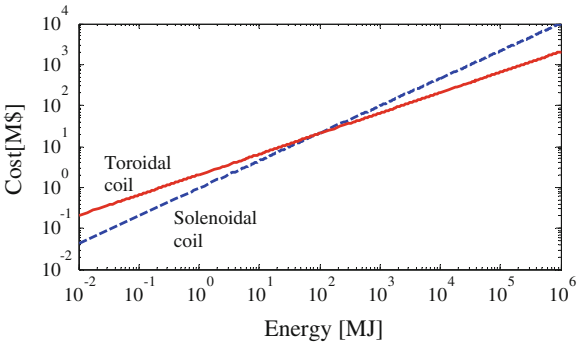

Fig. 41 Cost (M$) versus Energy (MJ) for solenoidal and toroidal coils

compensate for each other's disadvantages. A typical case is the LIQHYSMES storage unit (LSU) [42] consisting of 125 GWh LH_2 energy and 48 GJ SMES, which has the advantages of fast response speed, high power density, and high energy density. Therefore, the 36 GJ SMES device can be used not only for short-time load fluctuation compensations, but also for daily load leveling by combining with a large-scale PHS device. The above HESS concept provides an economical way for smart power generation and transmission management.

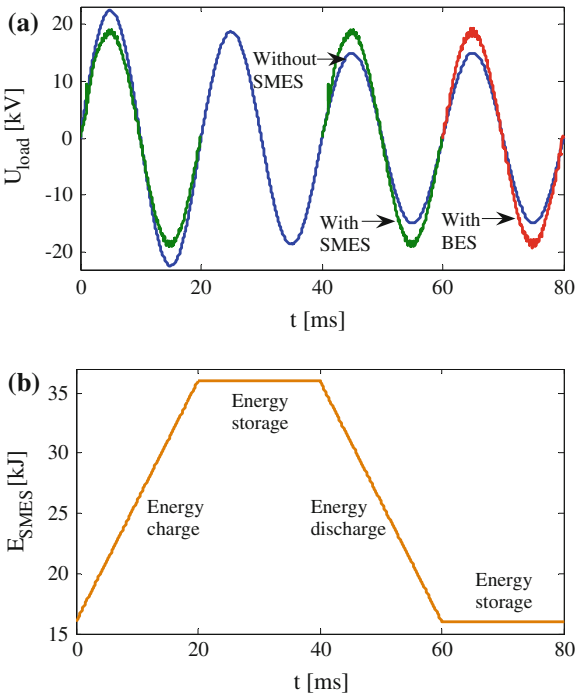

Fig. 42 The results of HESS for voltage fluctuation compensation. **a** The voltage changes of the load with HESS; **b** The energy changes of the 36 kJ SMES device

7.1.3 Analysis on Voltage Fluctuation Compensation

Since the power density of SMES is about 100 times higher than that of a redox flow battery, and about 10 times higher than those of a lead-acid battery and NaS battery [72], SMES can provide much larger exchanging power as compared to the battery energy storage (BES) for the same mass and volume. Moreover, the grid voltage fluctuations can be compensated within a quarter of power-frequency cycle because the response time of SMES is generally about 1–5 ms, however, the first cycle compensation cannot be practically achieved with BES. Therefore, a number of MJ-class and MW-level SMES devices [34–41] have been developed in the world for the studies of the potential replacement of BES in the power distribution systems.

According to (12), T_{comp} equals to several seconds for the MW-level fluctuation compensations if the 3.6 MJ SMES device in Scheme 3 is applied. To further enlarge T_{comp}, a larger energy storage capacity is needed. For instance, the 36 GJ SMES device in Scheme 2 can bring a very large T_{comp} of about 9 h, however, the high capital cost makes the scheme uneconomical. In view of the economy and practicability of the current SMES technology, some small-scale HESSs [13, 30, 31] have been studied and verified that the introduction of SMES with fast response speed and high power density can improve the dynamic performance of HESS, especially for solving ms-level power quality problems. Figure 42 shows the results of a typical SMES-BES HESS for voltage fluctuation compensations.

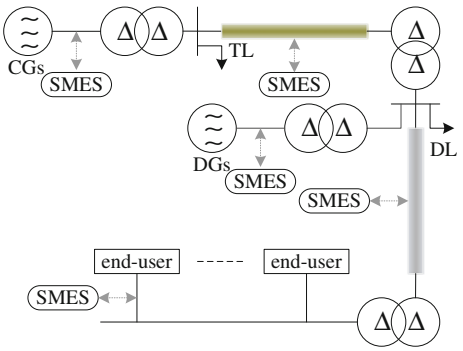

Fig. 43 The application prospects of SMES in future SGs

The 36 kJ SMES device in Scheme 4 is only applied to absorb or release 20 kJ electric energy to compensate the 1 MW voltage swell or sag within the first 20 ms, and then the BES will continue to carry out the voltage fluctuation compensations for a much longer time.

7.2 Application Prospects and Considerations of SMES in Future Smart Grid

The alternatives for the continued availability of a highly reliable and inexpensive power supply in future SGs include the deployment of clean coal generation, nuclear power generation, renewable energy generation, and other generation resources. Various ESSs can be used to allow increased capacity and stability to be derived from any given quantity of physical resources, and should be considered as a strategic choice that allows for optimum use of existing and new resources of all kinds. The overview and application analyses of the current SMES technology conclude that SMES has the significant potential to combine with, and even replace other ESSs in modern power systems. It is expected that the future SMES devices are not only essential to improve the power quality with small-scale or medium-scale energy storage capacity but also ensure the daily load leveling and overall reliability of the power systems with large-scale energy storage capacity.

7.2.1 Application Prospects of SMES in Future Smart Grids

Figure 43 shows the application prospects of SMES for future SGs [73]. The main SMES application schemes and their basic functions are described as follows: (i) SMES installed near the large-scale centralized generators (CGs) is used to balance the output power and to achieve daily load leveling; (ii) SMES installed in the transmission lines (TLs) is used to form FACTS devices for compensating the load fluctuations and maintaining the grid frequency stability; (iii) SMES installed

Table 7 Specification required for different applications

Items	Application schemes			
	CGs	TLs	DLs/DGs	UPSs
Stored energy	TJ class	10 GJ class	MJ class	10 kJ class
Rated power	0.1–1 GW	0.1–1 GW	1–10 MW	1–100 kW
Compensation time	1–10 h	1–10 min	0.1–1 s	0.1–10 s
Capital cost	1–10 G$	0.1–1 G$	1–10 M$	0.1–1 M$

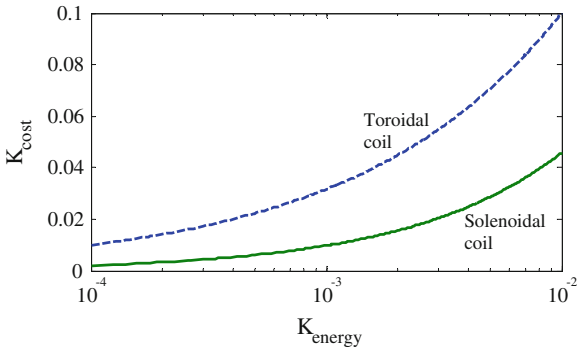

Fig. 44 K_{cost} versus K_{energy} with solenoidal coil and toroidal coil

in the distribution lines (DLs) is used to form DFACTS devices for improving the power quality; (iv) SMES installed near the DGs is used to reduce the impacts from the intermittent RESs and to facilitate the grid integration; (v) SMES installed near the power end-users is used to form SMES-based UPSs for enhancing the stability of electricity and protecting the critical loads.

The requirements of a single SMES unit in the above five application schemes are shown in Table 7. Besides the application solution of sole SMES with full energy storage scale, three additional application solutions of SMES should be considered in future SGs.

The first solution is to install a number of SMES devices with very high power rating and very low energy storage capacity near the commercial ESS devices for forming an SMES-based HESS. As compared to the application solution of sole SMES, SMES in a HESS is only used to compensate the initial fluctuations of electricity for a very short-time period. For instance, the 10 GJ class SMES can be used to carry out the daily load leveling for a few minutes before the initial operation of large-scale PHS, and to compensate some rapid load fluctuations during the whole day. The 10 kJ class SMES can be used to improve the power quality and stability for one or a few power-frequency cycles before the initial operation of medium-scale BES.

The HESS technology will greatly reduce the capital cost of ESSs in different power system applications. Figure 44 shows the results of K_{cost} versus K_{energy} with solenoidal coil and toroidal coil. K_{energy} is the ratio between the SMES energy storage capacity needed in a HESS and the energy storage capacity in a sole SMES.

Table 8 Comparisons of different SMES application solutions

Items	Advantages	Disadvantages
Sole SMES	Fast response speed High power density High storage efficiency Low control complexity	High capital cost
SMES-based HESS	Fast response speed High power density High energy density High reliability High economy	High system complexity High control complexity
DSMES	Fast response speed High power density High storage efficiency High mobility High expandability	High system complexity High control complexity
SMES-based DHESS	Fast response speed High power density High energy density High mobility High expandability High reliability High economy	High system complexity High control complexity

K_{cost} is the ratio between the SMES capital cost needed in a HESS and the capital cost in a sole SMES. It is noticed that $K_{\text{cost}} \approx 0.1$ when $K_{\text{energy}} = 0.01$ for large-scale toroidal coil developments, and $K_{\text{cost}} \approx 0.45$ when $K_{\text{energy}} = 0.01$ for medium-scale and small-scale solenoidal coil developments.

The second solution is to distribute several small-scale SMES units in different locations and to make all the SMES units work harmoniously by combined control of each SMES. This so-called distributed SMES (DSMES) technology has already been commercially deployed and operated [74]. The DSMES technology has the advantages of high mobility and high expandability because the SMES units in the trucks are easy to install in arbitrary locations once they arrives on site. The results reported [43] indicate that the DSMES technology behaves better in performance than the concentrated installation of a large-scale SMES unit.

The third solution is to combine the HESS and DSMES technologies and to distribute a number of HESS units in large, medium, and small scales for the power generation, transmission, distribution, and end-users. The distributed HESS (DHESS) technology having the advantages of both HESS and DSMES will provide very efficient stability and reliability of the whole power system.

The comparisons of different SMES application solutions are shown in Table 8. The three improved solutions utilize various ESS devices and technologies efficiently and enhance the flexibility and economy of SMES greatly. Therefore, it can be expected that SMES will be a flexible and efficient ESS option for smart power and energy managements in future SGs.

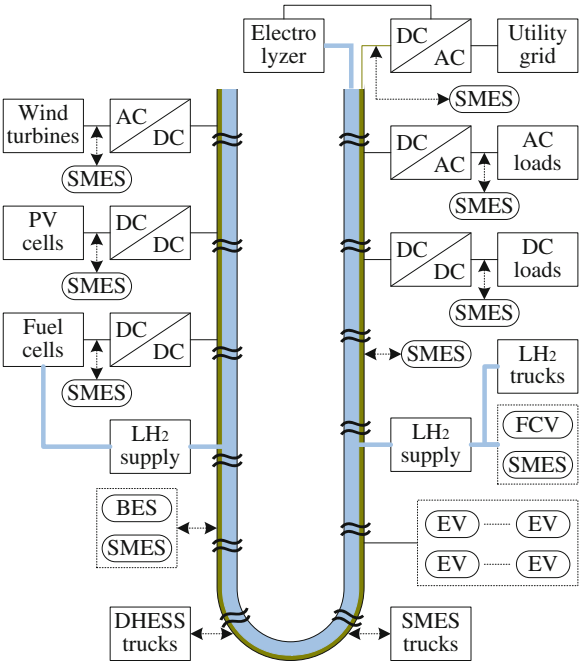

Fig. 45 Conceptual design of a superconducting DC distribution network

7.2.2 Conceptual Design of a Superconducting DC Distribution Network with Superconducting DC Cable and SMES Technologies

The resistive energy losses consumed on power transmission lines become enormous as the high-capacity of power demand is required by the dramatically expanding and developed society. HTS technology is an alternative way to resolve the conventional difficulties to achieve high efficiency in power transmissions [7, 8]. The superconducting DC cable with nearly zero energy loss is favorable for low-voltage and long-distance power transmission for future power end-users. Various SMES devices with different application schemes have the potential to further enhance the stability and reliability of the superconducting DC transmissions. Figure 45 shows the conceptual design of a superconducting DC distribution network with superconducting DC cable and SMES technologies. The superconducting DC distribution network is to implement the hybrid energy transfer of the hydrogen and electricity, which has been technically verified [75–77]. The LH_2 transferred can not only be used to provide hydrogen energy for the fuel cells (FCs) and FC vehicles (FCVs) [17], but also be used as the refrigeration fluid for cooling the superconducting DC cable and SMES devices, which can be developed by either HTS YBCO wires or MgB_2 wires.

The application schemes of SMES in the superconducting DC distribution network are described as follows: (i) SMES and HESS devices installed in the

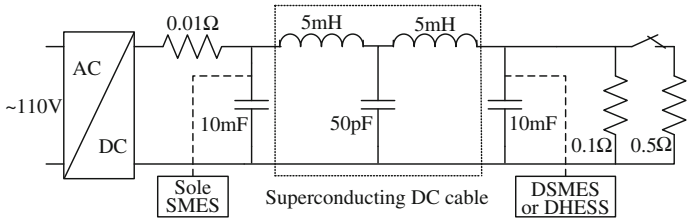

Fig. 46 An analytical case of the superconducting DC distribution network

cable terminal and middle parts are used to enhance the power transmission capacity and to maintain the voltage stabilization; (ii) DSMES and DHESS trucks with highly mobile and expandable characteristics are used to further improve the integrated performance of scheme (i) in arbitrary locations or time periods; (iii) SMES devices installed in the DC bus of local PV cells or FCs are used to maintain the output voltage stabilization for connecting with the DC distribution network and improving the reliability of electricity in off-grid loads; (iv) SMES devices installed near the on-grid loads are used to serve as fast response and high power UPSs; (v) SMES devices installed in FCVs are used to enhance the fast repeated charge–discharge performance and further to enhance the reliability of the vehicle-to-grid (V2G) [78] and vehicle-to-building (V2B) technologies [79].

The superconducting DC distribution network is able to operate with very high current density and very low voltage allowing direct connection of the generators to the local power end-users, eliminating the need for high voltage insulation and transformers. For the same power delivery as in the typical 110–1000 kV conventional transmission system, if a superconducting DC cable with the operation current ranging from thousands of amperes to tens of thousands of amperes is applied, the operation voltage might be greatly reduced to thousands of volts.

Figure 46 shows an analytical case of the superconducting DC distribution network. A 110 V rectified DC power source is applied to a 0.1 Ω load resistor through the superconducting DC cable. The energy lossy resistor from the relevant power electronic devices is assumed as 0.01 Ω. If an additional 0.5 Ω load resistor is connected in parallel from the time zero, the operation voltage across the two load resistors will decrease rapidly to about 83 V at first and then increase gradually to about 97 V, as shown in Fig. 47.

To maintain the practical operation voltage around their reference value of 100 V, three SMES application solutions are adopted. The first one is to install a 2 H/300 A sole SMES unit near the DC power source. The sole SMES unit can be used to compensate the dynamic load fluctuations in different superconducting DC cables, however, the inductive and capacitive reactance from the long-distance cable limits the practical response speeds. As shown in Fig. 47, there is still an inevitable voltage drop from 0 to about 0.24 s.

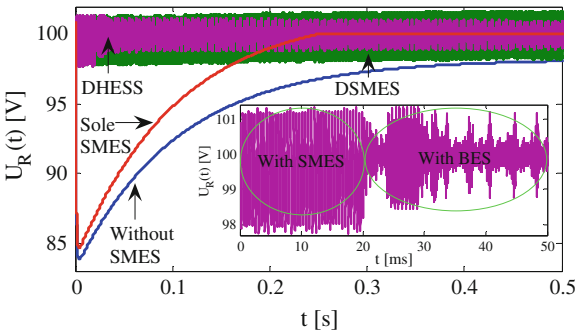

Fig. 47 The results of sole SMES, DSMES, and DHESS application solutions for a DC voltage sag compensation

The second one is to distribute several DSMES units in different cables or in different locations along a specific cable. The DSMES unit located at the terminal of a superconducting DC cable in Fig. 46 can be directly applied to compensate the voltage sag within several milliseconds, which results in an effective and timely voltage sag compensation process.

The third one is to combine the small-scale DSMES units with several local ESSs, e.g., BES, to form a DHESS. The DSMES unit is only applied to compensate the voltage sag within the first 20 ms, which reduces the energy storage capacity and capital cost of the DSMES units.

Acknowledgments The author thanks X. Y. Chen who assisted this work, and also the support from Y. Xin, Y. G. Guo, J. G. Zhu, and C. Grantham.

References

1. Jin JX, Zhang CM, Guo YG, Zhu JG (2007) Theory and operation principle of a HTS high Q resonant circuit. IEEE Trans Appl Supercond 17(2):2022–2025
2. Jin JX (2007) HTS energy storage techniques for use in distributed generation systems. Phys C 460–462:1449–1450
3. Jin JX (2007) High efficient DC power transmission using high-temperature superconductors. Phys C 460–462:1443–1444
4. Jin JX, Zheng LH, Guo YG, Zhu JG, Grantham C, Sorrell CC, Xu W (2012) High-temperature superconducting linear synchronous motors integrated with HTS magnetic levitation components. IEEE Trans Appl Supercond 22(5):5202617 (17 pages)
5. Jin JX, Zheng LH, Guo YG, Zhu JG (2011) Performance characteristics of an HTS linear synchronous motor with HTS bulk magnet secondary. IEEE Trans Ind Appl 47(6):2469–2477
6. Zheng LH, Jin JX, Guo YG, Xu W, Zhu JG (2012) Performance analysis of a double-sided HTSLSM for a HTS magnetic suspension system. IEEE Trans Magn 48(2):655–658
7. Jin JX, Zheng LH, Xu W, Guo YG, Zhu JG (2011) Influence of external traveling-wave magnetic field on trapped field of a high temperature superconducting bulk magnet in a linear synchronous motor. J Appl Phys 109(11):113913-1–113913-4
8. Jin JX, Zheng LH, Guo YG, Xu W, Zhu JG (2011) Analysis and experimental validation of an HTS linear synchronous propulsion prototype with HTS magnetic suspension. Phys C 471(1–2):520–527

9. Jin JX, Grantham C, Dou SX, Liu HK, Zeng ZJ, Liu ZY, Blackburn TR, Li XY, Liu HL, Liu JY (1997) Electrical application of high T_c superconducting saturable magnetic core fault current limiter. IEEE Trans Appl Supercond 7(2):1009–1012
10. Jin JX, Dou SX, Liu HK, Grantham C (1997) High voltage generation with a high T_c superconducting resonant circuit. IEEE Trans Appl Supercond 7(2):881–884
11. Jin JX, Dou SX, Grantham C, Liu HK (1995) Preparation of high T_c superconducting coils for consideration of their use in a prototype fault current limiter. IEEE Trans Appl Supercond 5(2):1051–1054
12. Chakraborty A (2011) Advancements in power electronics and drives in interface with growing renewable energy resources. Renew Sustain Energy Rev 15:1816–1827
13. Jin JX (2011) High temperature superconducting energy storage technologies: principle and application. Science Press, Beijing
14. Shikimachi K, Hirano N, Nagaya S, Kawashima H, Higashikawa K, Nakamura T (2009) System coordination of 2 GJ class YBCO SMES for power system control. IEEE Trans Appl Supercond 19(3):2012–2018
15. Pahlevaninezhad M, Drobnik J, Jain PK, Bakhshai A (2012) A load adaptive control approach for a zero-voltage-switching DC/DC converter used for electric vehicles. IEEE Trans Industr Electron 59(2):920–933
16. Kim HS, Ryu MH, Baek JW, Jung JH (2013) High-efficiency isolated bidirectional AC–DC converter for a DC distribution system. IEEE Trans Power Electron 28(4):1642–1654
17. Morandi A, Trevisani L, Negrini F, Ribani PL, Fabbri M (2012) Feasibility of superconducting magnetic energy storage on board of ground vehicles with present state-of-the-art superconductors. IEEE Trans Appl Supercond 22(2):5700106
18. Hamajima T, Amata H, Iwasaki T, Atomura N, Tsuda M, Miyagi D, Shintomi T, Makida Y, Takao T, Munakata K, Kajiwara M (2012) Application of SMES and fuel cell system combined with liquid hydrogen vehicle station to renewable energy control. IEEE Trans Appl Supercond 22(3):5701704
19. Kakigano H, Miura Y, Ise T (2012) Low-voltage bipolar-type DC microgrid for super high quality distribution. IEEE Trans Power Electron 25(12):3066–3075
20. Salomonsson D, Sannino A (2007) Low-voltage DC distribution system for commercial power systems with sensitive electronic loads. IEEE Trans Power Deliv 22(3):1620–1627
21. Furuse M, Fuchino S, Higuchi N, Ishii I (2005) Feasibility study of low-voltage DC superconducting distribution system. IEEE Trans Appl Supercond 15(2):1759–1762
22. Nakayama T, Yagai T, Tsuda M, Hamajima T (2009) Micro power grid system with SMES and superconducting cable modules cooled by liquid hydrogen. IEEE Trans Appl Supercond 19(3):2062–2065
23. Jin JX, Chen XY, Zhou X, Xu W, Zhang YC, Xin Y (2013) Development of a new bridge-type chopper for low-voltage SMES applications. In: 2013 IEEE energy conversion congress and exposition (ECCE), Denver, Colorado, USA, September 15, 2013, pp 5258–5265
24. Bibian S, Jin H (2000) Time delay compensation of digital control for DC switch mode power supplies using prediction techniques. IEEE Trans Power Electron 15(5):835–842
25. Bae BH, Sul SK (2003) A compensation method for time delay of full-digital synchronous frame current regulator of PWM AC drives. IEEE Trans Ind Appl 39(3):802–810
26. Tomita M, Murakami M, Nariki S, Sawa K (2002) Mechanical persistent current switch made of resin-impregnated bulk superconductors. Supercond Sci Technol 15(5):846–849
27. Hayashi H, Sannomiya T, Kimura H, Tsutsumi K, Yamashita Y, Kuboyama R, Sato S, Takeo M, Ishii T, Asano K, Okada S (2001) Connecting tests of superconducting persistent-current-switch in a type of current transformer to 1 kWh SMES system. IEEE Trans Appl Supercond 11(1):1904–1907
28. Yuan WJ, Xian W, Ainslie M, Hong Z, Yan Y, Pei R, Jiang Y, Coombs TA (2010) Design and test of a superconducting magnetic energy Storage (SMES) coil. IEEE Trans Appl Supercond 20(3):1379–1382

29. Chen XY, Jin JX, Ma KM, Wen J, Xin Y, Gong WZ (2008) High temperature superconducting magnetic energy storage and its power control technology. J Electr Sci Technol China 6(2):137–142
30. Chen XY, Jin JX (2011) Development and evaluation of superconducting magnetic energy storage techniques for smart grid. Appl Supercond Electromagnet 2(1):31–35
31. Jin JX, Xu W, Chen XY, Zhou X, Zhang JY, Gong WZ, Ren AL, Xin Y (2012) Developments of SMES devices and potential applications in smart grids. In: IEEE conference on innovative smart grid technologies Asia (ISGT Asia), Tianjing, China, 21–24 May 2012, pp 1569530679–1–6
32. Rogers JD, Schemer RI, Miller BL, Hauer JF (1983) 30-MJ superconducting magnetic energy storage system for electric utility transmission stabilization. Proc IEEE 71(9):1099–1107
33. Luongo CA, Baldwin T, Ribeiro P, Weber CM (2003) A 100 MJ SMES demonstration at FSU-CAPS. IEEE Trans Appl Supercond 13(2):1800–1805
34. Nagaya S, Hirano N, Moriguchi H, Shikimachi K, Nakabayashi H, Hanai S, Inagaki J, Ioka S, Kawashima S (2006) Field test results of the 5 MVA SMES system for bridging instantaneous voltage dips. IEEE Trans Appl Supercond 16(2):632–635
35. Wang QL, Dai YM, Zhao BZ, Song SS, Cao ZQ, Chen SZ, Zhang Q, Wang HS, Cheng JS, Lei YZ, Li X, Liu JH, Zhao SW, Zhang HJ, Xu GX, Yang ZM, Hu XN, Liu HY, Wang CZ, Yan LG (2010) Development of large scale superconducting magnet with very small stray magnetic field for 2 MJ SMES. IEEE Trans Appl Supercond 20(3):1352–1355
36. Kim HJ, Seong KC, Cho JW, Bae JH, Sim KD, Kim S, Lee EY, Ryu K, Kim SH (2006) 3 MJ/750 kVA SMES system for improving power quality. IEEE Trans Appl Supercond 16(2):574–577
37. Ottonello L, Canepa G, Albertelli P, Picco E, Florio A, Masciarelli G, Rossi S, Martini L, Pincella C, Mariscotti A, Torello E, Martinolli A, Mariani M (2006) The largest Italian SMES. IEEE Trans Appl Supercond 16(2):602–607
38. Nagaya S, Hirano N, Shikimachi K, Hanai S, Inagaki J, Maruyama K, Ioka S, Ono M, Ohsemochi K, Kurusu T (2004) Development of MJ-class HTS SMES for bridging instantaneous voltage dips. IEEE Trans Appl Supercond 14(2):770–773
39. Dai ST, Xiao LY, Wang ZK, Zhang JY, Zhang D, Hui D, Song NH, Zhang FY, Gao ZY, Wang YS, Lin LZ (2007) Design of a 1 MJ/0.5 MVA HTS magnet for SMES. IEEE Trans Appl Supercond 17(2):1977–1980
40. Tixador P, Bellin B, Deleglise M, Vallier JC, Bruzek CE, Pavard S, Saugrain JM (2005) Design of a 800 kJ HTS SMES. IEEE Trans Appl Supercond 15(2):1907–1910
41. Kim WS, Kwak SY, Lee JK, Choi KD, Jung HK, Seong KC, Hahn SY (2006) Design of HTS magnets for a 600 kJ SMES. IEEE Trans Appl Supercond 16(2):620–623
42. Sander M, Gehring R, Neumann H (2013) LIQHYSMES—a 48 GJ toroidal MgB_2-SMES for buffering minute and second fluctuations. IEEE Trans Appl Supercond 23(3):5700505
43. Howe JB (2001) Distributed SMES: a new technology supporting active grid management. Mod Power Syst 21(1):27–28
44. Mito T, Chikaraishi H, Kawagoe A, Maekawa R, Abe R, Baba T, Okumura K, Kuge A, Iwakuma M, Sumiyoshi F (2009) Summary of a 1 MJ conduction-cooled LTS pulse coil developed for 1 MW, 1 s UPS-SMES. IEEE Trans Appl Supercond 19(3):1999–2003
45. Katagiri T, Nakabayashi H, Nijo Y, Tamada T, Noda T, Hirano N, Nagata T, Nagaya S, Yamane M, Ishii Y, Nitta T (2009) Field test result of 10MVA/20 MJ SMES for load fluctuation compensation. IEEE Trans Appl Supercond 19(3):1993–1998
46. Hayashi H, Hatabe Y, Nagafuchi T, Taguchi A, Terazono K, Ishii T, Taniguchi S (2006) Test results of power system control by experimental SMES. IEEE Trans Appl Supercond 16(2):598–601
47. Nomura S, Kasuya K, Tanaka N, Tsuboi K, Tsutsui H, Tsuji-Iio S, Shimada R (2008) Experimental results of a 7-T force-balanced helical coil for large-scale SMES. IEEE Trans Appl Supercond 18(2):701–704
48. Zhu XG, Jiang XH (2007) 150 kVA/0.3 MJ current source type dynamic voltage compensation device. Power Electron Technol 41(1):1–3

49. Morandi A, Breschi M, Fabbri M, Negrini F, Penco R, Perrella M, Ribani PL, Tassisto M, Trevisani L (2008) Design, manufacturing and preliminary tests of a conduction cooled 200 kJ Nb–Ti μSMES. IEEE Trans Appl Supercond 18(2):697–700
50. Koyanagi K, Ohsemochi K, Takahashi M, Kurusu T, Tosaka T, Ono M, Ishii Y, Shimada K, Nomura S, Kidoguchi K, Onoda H, Hirano N, Nagaya S (2006) Design of a high energy-density SMES coil with Bi-2212 cables. IEEE Trans Appl Supercond 16(2):586–589
51. Wang QL, Dai YM, Song SS, Wen HM, Bai Y, Yan LG, Kim K (2008) A 30 kJ Bi2223 high temperature superconducting magnet for SMES with solid-nitrogen protection. IEEE Trans Appl Supercond 18(2):754–757
52. Shi J, Tang YJ, Zhou YS, Chen JL, Xu DH, Wang HL, Lu YF, Ren L, Wei B, Li JD, Cheng SJ (2007) Development of a conduction-cooled HTS SMES. IEEE Trans Appl Supercond 17(3):3846–3852
53. Kwak SY, Lee S, Lee S, Kim WS, Lee JK, Park C, Bae J, Song JB, Lee H, Choi K, Seong K, Jung H, Hahn SY (2009) Design of HTS magnets for a 2.5 MJ SMES. IEEE Trans Appl Supercond 19(3):1985–1988
54. Kreutz R, Salbert H, Krischel D, Hobl A, Radermacher C, Blacha N, Behrens P, Dütsch K (2003) Design of a 150 kJ high-T_c SMES (HSMES) for a 20 kVA uninterruptible power supply system. IEEE Trans Appl Supercond 13(2):1860–1862
55. Kozak J, Kozak S, Janowski T, Majka M (2009) Design and performance results of first polish SMES. IEEE Trans Appl Supercond 19(3):1981–1984
56. Hawley CJ, Gower SA (2005) Design and preliminary results of a prototype HTS SMES device. IEEE Trans Appl Supercond 15(2):1899–1902
57. Ali MH, Wu B, Dougal RA (2010) An overview of SMES applications in power and energy systems. IEEE Trans Sustain Energ 1(1):38–47
58. Liu CJ, Hu CS, Li X, Chen M, Xu DF (2008) Design of SMES control system for smoothing power fluctuations in wind farms. Autom Electr Power Syst 32(16):84–88
59. Tam KS, Kumar P, Foreman M (1989) Enhancing the utilization of photovoltaic power generation by superconductive magnetic energy storage. IEEE Trans Energy Convers 4(3):314–321
60. Jung HY, Kim AR, Kim JH, Park M, Yu IK, Kim SH, Sim K, Kim HJ, Seong KC, Asao T, Tamura J (2009) A study on the operating characteristics of SMES for the dispersed power generation system. IEEE Trans Appl Supercond 19(3):2028–2031
61. Padimiti DS, Chowdhury BH (2007) Superconducting magnetic energy storage system (SMES) for improved dynamic system performance. In: Power engineering society general meeting, 24–28 June 2007, pp 1–6
62. Zheng L, Ma WA (2000) Application of SMES system with a comprehensive control for enhancing transient stability. In: International conference on advances in power system control, operation and management, Oct. 30–Nov. 1, 2000, pp 225–229
63. Ali MH, Murata T, Tamura J (2005) A fuzzy logic-controlled superconducting magnetic energy storage (SMES) unit for augmentation of transient stability. In: International conference on power electronics and drives systems, 2005, vol 2, pp 1566–1571
64. Kim AR, Kim GH, Kim JH, Ali MH, Park M, Yu IK, Kim HJ, Kim SH, Seong KC (2008) Operational characteristic of the high quality power conditioner with SMES. IEEE Trans Appl Supercond 18(2):705–708
65. Zhu GP, Wang ZJ, Zhang GQ (2005) Research on a combined device SMES-SFCL based on multi-object optimization. IEEE Trans Appl Supercond 15(2):2019–2022
66. Nomura S, Shintomi T, Akita S, Nitta T, Shimada R, Meguro S (2010) Technical and cost evaluation on SMES for electric power compensation. IEEE Trans Appl Supercond 20(2):101–106
67. Green MA, Strauss BP (2008) The cost of superconducting magnets as a function of stored energy and design magnetic induction times the field volume. IEEE Trans Appl Supercond 18(2):248–251
68. Van Sciver SW (2001) Cryogenic systems for superconducting devices. Phys C 354(1–4):129–135

69. Nomura S, Chikaraishi H, Tsutsui H, Shimada R (2013) Feasibility study on large scale SMES for daily load leveling using force-balanced helical coils. IEEE Trans Appl Supercond 23(3):5700904
70. Nomura S, Yamagnta K, Watauabe N, Ajiki D, Ajikawa H, Koizumi E, Shimada R (2000) Experiment of HTS stress-balanced helical coil. IEEE Trans Appl Supercond 10(1):792–795
71. Fabbri M, Ajiki D, Negrini F, Shimada R, Tsutsui H, Venturi F (2003) Tilted toroidal coils for superconducting magnetic energy storage systems. IEEE Trans Magn 39(6):3546–3550
72. Kondoh J, Ishii I, Yamaguchi H, Murata A, Otani K, Sakuta K, Higuchi N, Sekine S, Kamimoto M (2000) Electrical energy storage systems for energy networks. Energy Convers Manag 41(17):1863–1874
73. Jin JX, Chen XY (2012) Study on the SMES application solutions for smart grid. Physics Procedia 36:902–907
74. Lee SJ (2007) Location of a superconducting device in a power grid for system loss minimization using loss sensitivity. IEEE Trans Appl Supercond 17(2):2531–2534
75. Bossel U (2006) Does a hydrogen economy make sense? Proc IEEE 94(10):1826–1837
76. Yamada S, Hishinuma Y, Uede T, Schippl K, Yanagi N, Mito T, Sato M (2010) Conceptual design of 1 GW class hybrid energy transfer line of hydrogen and electricity. J Phys Conf Ser 234:032064
77. Shintomi T, Makida Y, Hamajima T, Tsuda S, Miyagi D, Takao T, Tanoue N, Ota N, Munakata K, Miwa Y (2012) Design study of SMES system cooled by thermo-siphon with liquid hydrogen for effective use of renewable energy. IEEE Trans Appl Supercond 22(3):5701604
78. Liu H, Ning HS, Zhang Y, Guizani M (2013) Battery status-aware authentication scheme for V2G networks in smart grid. IEEE Trans Smart Grid 4(1):99–110
79. Pang C, Dutta P, Kezunovic M (2012) BEVs/PHEVs as dispersed energy storage for V2B uses in the smart grid. IEEE Trans Smart Grid 3(1):473–482

Multilevel Converters for Step-Up-Transformer-Less Direct Integration of Renewable Generation Units with Medium Voltage Smart Microgrids

Md. Rabiul Islam, Youguang Guo and Jianguo Zhu

Abstract For grid integration of renewable generation units, a power frequency transformer operated at 50 or 60 Hz is generally used to step-up the low output voltage (usually $\leq$690 V) to the medium voltage level (typically 6–36 kV). Because of the heavy weight and large size of the power frequency step-up transformer, the grid integration system can be expensive and complex for installation and maintenance. To achieve a compact and lightweight direct grid connection, a medium voltage multilevel converter may be an alternative approach. Different multilevel converter topologies with switching and control issues are analyzed for their medium voltage applications. The practical implementation issues are also reported in this chapter. It is expected that the medium voltage multilevel converter would have great potential for future renewable generation and smart microgrid applications.

Keywords Medium and large scale · Renewable power generation · Grid integration · Multilevel converters · Step-up-transformer-less

1 Introduction

The rapid increase in global energy consumption and the impact of greenhouse gas emissions have accelerated the renewable energy technology into a competitive area. Hence during the last decades, renewable energy resources have become an important part of the worldwide concern with clean power generation. Wind and solar energy has continued the worldwide success story as the wind and solar power development is experiencing dramatic growth. By 2012, there are over 282 GW of

M. R. Islam (✉) · Y. Guo · J. Zhu
Center for Electrical Machines and Power Electronics, University of Technology Sydney,
PO Box 123 Broadway, NSW 2007, Australia
e-mail: Md.Islam@uts.edu.auRabiulbd@hotmail.com

J. Hossain and A. Mahmud (eds.), *Large Scale Renewable Power Generation*,
Green Energy and Technology, DOI: 10.1007/978-981-4585-30-9_5,

wind power generation and over 102 GW photovoltaic (PV) generation installed worldwide and renewable power plants of more than 10 MW in capacity have now become a reality. These multi-megawatt renewable power systems cover large areas of land, and thus they are usually installed in offshore and remote areas, far from cities. For example, the land area covered by a 3.6 MW turbine can be almost 0.37 km^2, such that 54 turbines would cover about 20 km^2 of land area [1] and the 20 MW PV power plant would cover a land area of about 500,000 m^2.

Renewable energy source has very variable daily and seasonal patterns and consumer power demand requirements also have very different characteristics. Therefore, it is difficult to operate a stand-alone power system supplied from only one type of renewable energy resource unless there are appropriate energy storage facilities. If enough energy storage capacity is not available especially in medium-scale (0.1–5 MW) and large-scale (>5 MW) systems a grid connected renewable power generation may be the only practical solution. During the last few years, scientists and researchers have been introducing smart distribution grid called microgrid with distributed and renewable generation units, energy storages, and controllable loads. A medium voltage network feeder (e.g., 6–36 kV) is generally used to interconnect the renewable generation units.

Different power electronic converters have been developed using conventional topologies to fulfill the requirements of renewable generations. However, it is hard to connect the traditional converters to the grids directly, as the distortion in generated output voltages is high and a single switch cannot stand at grid voltage level. In this regard conventional systems having power frequency (i.e., 50 or 60 Hz) step-up transformer, filter, and booster not only increase the size, weight, and loss but also increase the cost and complexity of the system operation. For example, the weight and volume of a 0.69/33 kV, 2.6 MVA transformer are typically in the range of 6–8 tons and 5–9 m^3, respectively [1]. A liquid-filled 2 MVA step-up transformer uses about 900 kg of liquid as the coolant and insulator, which requires regular monitoring and replacement. These penalties are critical in offshore and remote area applications, where the costs of installation and regular maintenance are extremely high. Today, the industrial trend is to move away from these heavy and large size passive components to power electronic systems that use more and more semiconductor elements controlled by powerful processor so that smart operation is ensured.

In comparison with conventional two-level converters, multilevel converters present lower switching losses, lower voltage stress on switching devices, and better harmonic performance. These remarkable features enable the connection of renewable energy systems directly to the grid without using large, heavy, and costly power transformers and also minimize the input and output filter requirements. Although several multilevel converter topologies have been used in low voltage applications, most of the topologies are not suitable in medium voltage applications. Because of some special features, the number of components scales linearly with the number of levels, and individual modules are identical and completely modular in constriction and hence enable high-level number attainability; the modular multilevel cascaded (MMC) converter topology can be considered as a possible candidate for medium voltage applications [2].

The high number of levels means that medium voltage attainability is possible to connect the renewable generation units to the medium voltage grid directly and also to improve the output power quality. The component number and control complexity increase linearly with the increase in number of levels. Therefore, the optimal selection of number of converter levels is important for the best performance/cost ratio of the medium voltage converter systems. For example, the 19-level and 43-level converters are found optimal for an 11 kV and 33 kV systems, respectively [3]. Moreover, the multilevel converter requires a number of switching and control PWM signals, which cannot be generated by the available digital signal processor (DSP) because the available DSP at present only can provide about six pairs of PWM channels. In this instance, the field programmable gate array (FPGA) is the natural choice for medium voltage multilevel converters.

However, the MMC converter requires multiple isolated and balanced dc sources. In 2011, a high-frequency link operated at a few kHz to MHz was proposed to generate multiple isolated and balanced dc sources for MMC converter from a single source [3]. In 2013, a high-frequency link was developed and a comprehensive electromagnetic analysis was reported to verify the feasibility of the new technology [4]. Compared with the power frequency transformers, the high-frequency link has much smaller and lighter magnetic cores and windings, and thus much lower costs.

The chapter is organized as follows: The available multilevel converter topologies are presented in Sect. 2. Section 3 describes the procedure to select the multilevel converter topologies for medium voltage applications. The optimal selection of number of levels taking into account the specified system performance, control complexity, cost, and market availability of the power semiconductors for 33 kV converters are summarized in Sect. 4. The switching and control scheme for multilevel converter is presented in Sect. 5. Section 6 describes the experimental validation of the new concept by a scaled down prototype of 1 kV high-frequency link MMC converter. Finally, the chapter is concluded by brief remarks in Sect. 7.

2 Multilevel Converter Topologies

The multilevel converter is a power electronic circuit that can be operated in an inverter or rectifier mode. This chapter manly focuses on the inverter mode operation of the multilevel converters. In 1975, the concept of multilevel converter topology was proposed [5] and in the last few decades, several multilevel converter topologies have been patented [6, 7]. In order to achieve high voltage using low voltage switching devices, the multilevel converter topology uses a series of switching devices with low voltage dc sources. The proper control of the switching devices superimposes these multiple dc sources in a staircase form in order to achieve high voltage at the output.

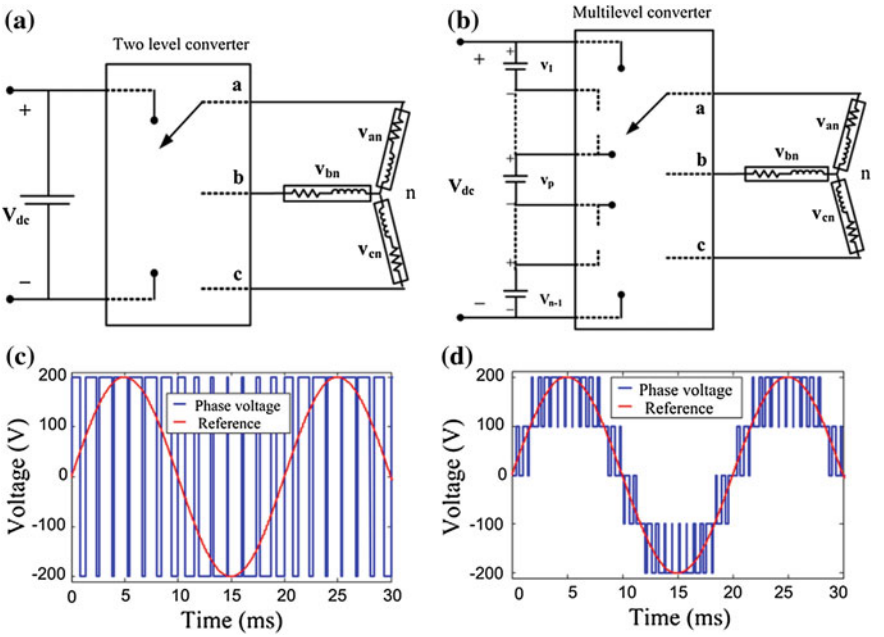

Fig. 1 Power converter circuit topologies and output phase voltage waveforms: **a** two-level converter topology, **b** multilevel converter topology, **c** voltage waveform of two-level converter, and **d** voltage waveform of 5-level converter

The renewable energy sources: wind turbine generators, solar PV arrays, and fuel cells can be used as the multiple dc voltage sources. With multilevel converter topology, the rated voltage of switching devices is much lower because the rated voltage of the switching devices depends on the rating of the dc voltage sources to which they are connected. A schematic circuit of a 3-phase 2-level conventional converter and a 3-phase m-level multilevel converter is shown in Fig. 1a, b. According to different switching states, it is possible to achieve high voltage level on output voltage by adding up the dc voltage sources compared with the 2-level inverters. According to Fig. 1c, it can be extracted that the quality of output voltage depends only on the sampling frequency, so higher sampling frequency means better voltage waveform. In case of multilevel converter output voltage waveform, as depicted in Fig. 1d, there is an additional factor to control the quality of output voltage waveform, i.e., the number of voltage levels.

Synthesizing a staircase output voltage, which is closer to sinusoidal voltage reference compared with 2-level converter output, allows reduction in harmonic content of voltage waveforms which leads to the size and cost reduction of the power conversion systems. Each level of the staircase consists of a few PWM pulses, as shown in Fig. 2.

The frequency of the carrier signal of the PWM generator can be adjusted to control the quality of the output waveform like 2-level converter. However, the

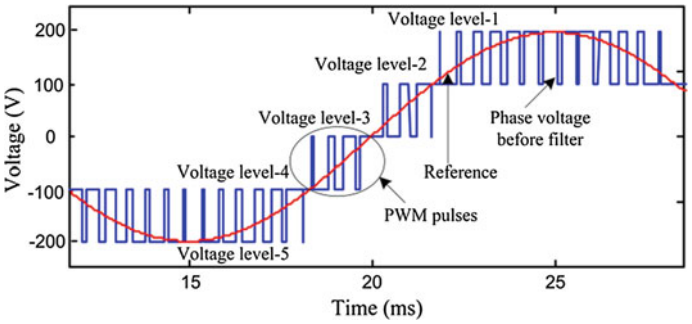

Fig. 2 Staircase output phase voltage waveform of a 3-phase 5-level converter

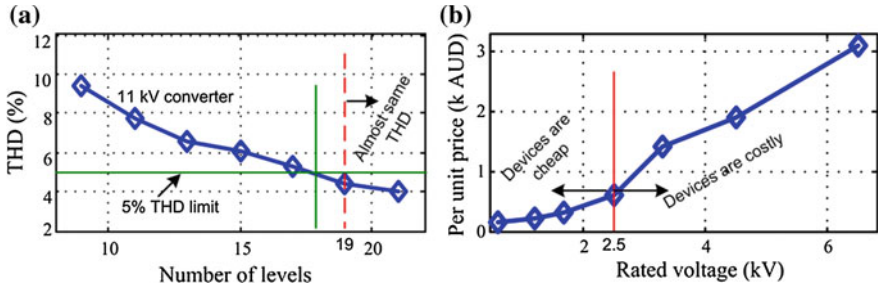

Fig. 3 Merits of multilevel converters: **a** THD of output voltages; possibility to design line filter-less converter, and **b** per unit price of IGBTs of 400 A; possibility to use cheap and mature semiconductors

number of levels of the staircase waveform mostly affects the quality of the output voltage waveform. Figure 3a plots the total harmonic distortions (THDs) of 11 kV converters with different number of converter levels.

Although the number of semiconductor devices increases with the number of converter levels, the high-level converter enables to use low voltage devices, which are not only cheap but also mature in technology. Figure 3b plots the per unit price of switching devices with a rated current of 400 A. Therefore, the semiconductor cost of multilevel converters is lower than the equivalent 2-level converters operating at the same rating. Total semiconductor cost of high-level multilevel converters is reported in Sect. 4.

The highest voltage rating of commercially available insulated gate bipolar transistor (IGBT) is 6.5 kV; suitable for 2.54 kV or lower voltage converter systems with traditional 2-level converter topology. Table 1a summarizes the voltage ratings of commercially available IGBTs, where ($V_{\text{com@100FIT}}$) is the device commutation voltage for a device reliability of 100 failures in time (FIT) due to cosmic radiation. The multilevel converter topology enables the possibility to develop medium and high voltage converters using commercially available

Table 1 Voltage handling capacity of (All are in kV)

(a) Available IGBTs		(b) Power converters		
Rated device voltage	$V_{com@100FIT}$	Device voltage rating	Number of levels	Line voltage (rms)
6.50	3.60	6.50	2	2.54
4.50	2.25	6.50	5	10.12
3.30	1.80	6.50	11	25.45
2.50	1.20	6.50	19	45.82
1.70	0.90	6.50	21	50.91

semiconductor devices. Table 1b summarizes the voltage handling capacity of 2-level and multilevel converters. Series connection of switching devices is a well-established method to develop medium voltage converter with 2-level converter topology. In order to reduce the effects of nonunique device characteristics and mismatch of driver circuit operations, the method uses snubber circuits and/or active gate controller, which increases switching losses.

The switching loss mostly depends on the commutation voltage of the switching devices, which can be much lower with multilevel converter topologies than that with 2-level converters. Moreover, multilevel converters require no switching aid circuits, which improve the commutation times. Therefore, multilevel converters give lower switching losses than that of 2-level converters. A power loss comparison between MMC converter and 2-level converter was analyzed and it was reported that the switching losses of MMC converters are much lower than 2-level series connected converters operating at the same conditions [8].

Three different major multilevel converter structures have been reported in the literature: neutral point clamped (NPC), flying capacitor (FC), and MMC converter with separate dc sources.

2.1 Neutral Point Clamped Converter

In order to increase the converter voltage rating without increasing the voltage rating of switching devices, the NPC converter topology was introduced in 1981 [9]. A 3-phase 5-level NPC converter circuit is shown in Fig. 4a.

A phase leg of a 5-level converter consists of four pairs of switching devices and three pairs of diode. Each switch in a pair works in complimentary mode and respective diodes pair provides access to the midpoint. If it is assumed that each auxiliary diode voltage rating is the same as the active switching device voltage rating, the number of diodes required for each phase will be (2m−4). An m-level NPC converter has an m-level output phase voltage and a (2m−1)-level output line voltage. Each of the three phases of the NPC converter shares a common dc-bus voltage, which has been subdivided by (m−1) capacitors into equal m-levels. Each phase leg of NPC converter requires (2m−2) active switching devices and the commutation voltage of each active switching device is (m−1) times lower than

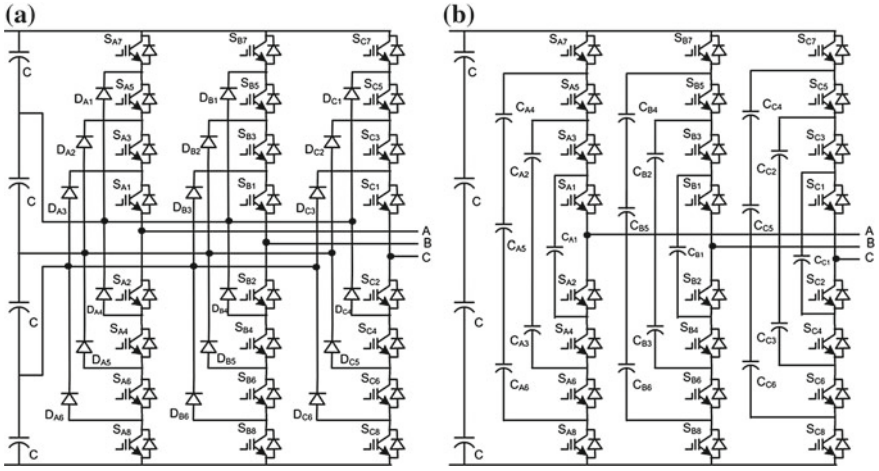

Fig. 4 Three-phase 5-level converter circuit with: **a** NPC topology, and **b** FC topology

Table 2 Switching states in a phase leg of the 5-level NPC converter

States	V_{an}	S_{A1}	S_{A2}	S_{A3}	S_{A4}	S_{A5}	S_{A6}	S_{A7}	S_{A8}
1	$2V_{dc}$	on	off	on	off	on	off	on	off
2	V_{dc}	on	on	on	off	on	off	off	off
3	0	on	on	on	on	off	off	off	off
4	$-V_{dc}$	on	on	off	on	off	on	off	off
5	$-2V_{dc}$	off	on	off	on	off	on	off	on

the total dc-bus voltage. Table 2 summarizes the five switching states for a phase leg of a 5-level NPC converter.

In 1998, the NPC converter-based high power ac motor drive system was proposed [10]. In 2002, another application of NPC converter for high power medium voltage variable speed motor drives was proposed [11]. The NPC converter has also attracted significant attention for an interface between a high voltage dc (HVDC) transmission line and an ac transmission line [12]. The NPC converter topology has the opportunity to connect the neutral point to middle point of the dc-link, reducing the ground leakage currents, which enables this topology to form back to back connection. Therefore, in the last few years, the back to back NPC converters have also been largely utilized in the grid interfacing of renewable energy sources such as wind turbine generators and solar PV arrays. In 2006, a back to back NPC three-level converter-based wind power system was proposed [13]. In 2013, improved control scheme has been proposed to improve the steady-state and transient operation of back-to-back NPC converter [14].

However, when the number of converter levels is sufficiently high, the number of diodes required will make the system impractical to implement. In addition to the requirement of several auxiliary diodes, the capacitor voltage balancing is one

Table 3 Switching states in a phase leg of the 5-level FC converter

States	V_{an}	S_{A1}	S_{A2}	S_{A3}	S_{A4}	S_{A5}	S_{A6}	S_{A7}	S_{A8}
1	$2V_{dc}$	on	off	on	off	on	off	on	off
2	V_{dc}	off	on	on	off	on	off	on	off
3	0	off	on	off	on	on	off	on	off
4	$-V_{dc}$	on	off	off	on	off	on	off	on
5	$-2V_{dc}$	off	on	off	on	off	on	off	on

of the notable drawbacks of NPC topology, which will be critical in high-level converters. Unbalanced capacitor voltages may cause distortions in output waveform and damage to switching devices due to over voltage breakdown of switching devices. For such a reason, many researchers are addressing their efforts in developing extra circuit and control algorithms [15], but still it is not more than 5-levels. Moreover, boost switch may limit the voltage and power rating of the converter. Therefore, this topology is not suitable for medium or high voltage applications, where higher number of levels are required.

2.2 Flying Capacitor Converter

In 1992, a new converter topology called FC converter was proposed [16]. The overall structure of FC converter can be comparable with that of the NPC converter except that the converter uses auxiliary capacitors, instead of using auxiliary diodes. The circuit topology of 3-phase 5-level FC converter is shown in Fig. 4b. A phase leg of a 5-level converter consists of four pairs of switching devices and three branches of capacitors. An m-level FC converter has an m-level output phase voltage and a (2 m−1)-level output line voltage. Each of the three phases of the FC converter may share a common dc-bus voltage similar to the NPC converter, which has been subdivided by (m−1) capacitors into equal m-levels. Each phase leg of FC converter requires (2 m−2) active switching devices and the commutation voltage of each active switching device is (m−1) times lower than the total dc-bus voltage. In addition to the (m−1) dc-bus capacitors, the m-level FC converter requires $(m^2-3\ m\ +\ 2)/2$ auxiliary capacitors per phase if the voltage rating of the capacitors is equal to that of the active switching devices. One of the possible combinations of the switching states for a phase leg of a 5-level converter is summarized in Table 3.

Due to some features, controllability of real and reactive power, and capability to ride through short duration outages and voltage sags, the FC voltage source converters have found their application in power system applications. In 2002, FC multilevel voltage source converter-based unified power flow controller was proposed [17]. In 2007, 3-level FC multilevel converter-based high voltage direct current power transmission system was presented [18].

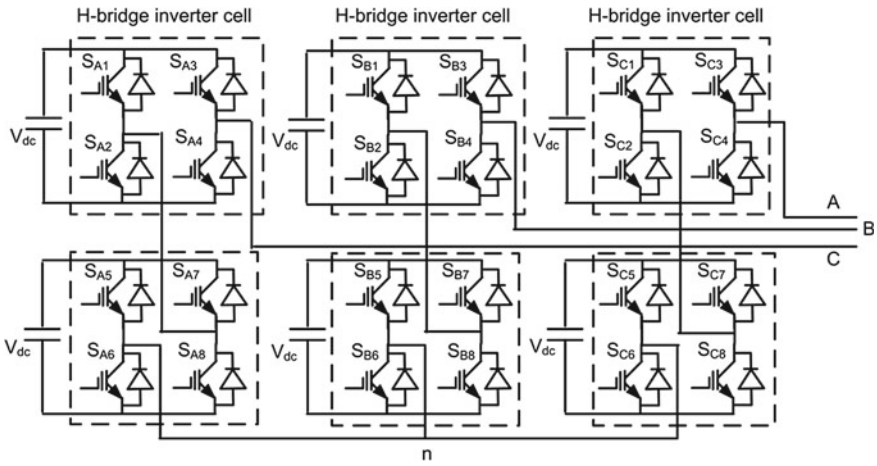

Fig. 5 Three-phase 5-level modular multilevel cascaded converter

However, the number of auxiliary capacitors required is quadratically related to the number of levels. When the number of converter levels is sufficiently high, the number of capacitors required will make the system impractical to implement. The large number of capacitors not only increases converter size and weight but also significantly reduces the lifetime of the converter. Due to regulation of capacitor voltages, the FC multilevel converter requires complex control strategies. Moreover, precharging of clamping capacitors with required voltage level may increase complexity and cost, and decrease the performances of the converter.

2.3 Modular Multilevel Cascaded Converter

In 1990, a single-phase MMC converter structure was presented for plasma stabilization applications [19] and in 1997, Robicon Corporation was presented a medium voltage high power 3-phase MMC converter for motor drive applications [20]. The complicated multi-winding phase-shifted power frequency transformer was used to deliver electric power to all the floating H-bridge inverter cells. In MMC converters, each phase leg consists of a series of modular single-phase full-bridge or H-bridge inverter cells. A 3-phase 5-level MMC converter circuit is illustrated in Fig. 5, which is wye connected. The 3-phase MMC converter can also be connected in delta.

Each isolated and balanced dc source is connected to a single-phase full-bridge or H-bridge inverter cell. The four switching devices of each H-bridge inverter cell can generate three different voltage outputs: $+V_{dc}$, 0, and $-V_{dc}$ by connecting the isolated dc source to the ac output. The proper control of the switching devices superimposes the voltage outputs of all the H-bridge cells of a phase in a staircase

Table 4 Switching states in a phase leg of the 5-level MMC converter

States	V_{an}	S_{A1}	S_{A2}	S_{A3}	S_{A4}	S_{A5}	S_{A6}	S_{A7}	S_{A8}
1	$2V_{dc}$	off	on	on	off	off	on	on	off
2	V_{dc}	off	on	on	off	on	off	on	off
3	0	on	off	on	off	on	off	on	off
4	$-V_{dc}$	on	off	off	on	off	on	off	on
5	$-2V_{dc}$	on	off	off	on	on	off	off	on

form in order to achieve high voltage at the converter output. Each H-bridge inverter cell contributes two voltage levels in output voltage. Similar to NPC and FC converters, an m-level MMC converter has also an m-level output phase voltage and a (2 m−1)-level output line voltage. As the NPC and FC multilevel converters, the MMC converter requires (2m−2) active switching devices per phase leg and the commutation voltage of each active switching device is (m−1) times lower than the total dc-bus voltage. Table 4 summarizes one of the possible switch combinations for a phase leg.

The component numbers of the MMC converters scale linearly with the number of levels, and individual modules are identical and modular in construction thereby enabling high-level number attainability. Furthermore, in the case of a fault in one of these modules, it is possible to replace it quickly and easily. Because of these special features the MMC converter topology has been considered as a possible candidate for medium and high voltage high power applications. In 1996, an MMC-based static synchronous compensator for reactive power control was presented [21] and in 1999, the converter was proposed for heavy duty electric and hybrid electric vehicles that have large electric motor drives [22]. A series of isolated batteries were used to deliver electric power to all the floating H-bridge inverter cells.

3 Selection of Multilevel Converter Topology

The main aim of this section is to find out a suitable converter topology, which can interconnect the renewable generation units to the grid directly by using mature semiconductor technology. A 5-level NPC, a 5-level FC, a 5-level MMC, an 11-level NPC, an 11-level FC, and an 11-level MMC converter topologies are considered for the comparison. The comparison is made in terms of number of semiconductors, semiconductor cost, THDs, filter size, and control complexity of the converters. The performance is analyzed and compared in the MATLAB environment. To generate switching pulses a level-shifted carriers-based switching scheme is used for NPC topologies and a phase-shifted carriers-based switching scheme is used for FC and MMC converter topologies with a carrier frequency of 1 to 2 kHz and modulation index of 0.8 to 0.90. The output voltage waveforms are shown in Fig. 6.

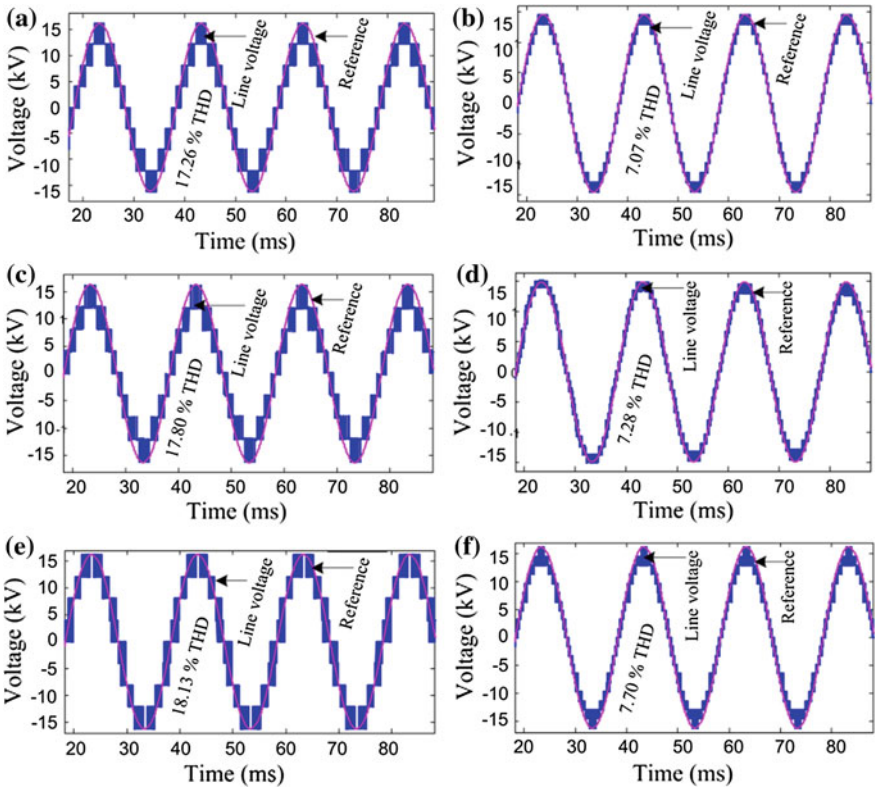

Fig. 6 Line voltages of 11 kV multilevel converters (no filter circuit in the system) with: **a** 5-level NPC converter topology, **b** 11-level NPC converter topology, **c** 5-level FC converter topology, **d** 11-level FC converter topology, **e** 5-level MMC converter topology, and **f** 11-level MMC converter topology

The output voltage waveform of 5-level NPC converter much more coincides with the reference sine wave as compared with other 5-level converters outputs. All 11-level converters output voltage waveforms are very close to the reference sine wave while NPC converter performance is better than the others. Moreover, from the output figures it is clear that increasing the level numbers means improving the converter performance. It is assumed that each blocking diode voltage rating is the same as the active device voltage rating. A total of 90 diodes are required for each phase of an 11-level NPC converter. This large number of diodes affects the reverse recovery of the clamping diodes which is a major design challenge in high voltage high-power systems. A list of the number of power components required for each converter topology is summarized in Table 5. As already stated, the availability of IGBT and diode modules is also considered when designing the converter. For the 5-level NPC, FC, and MMC converter topology, each IGBT switch is formed from the series connection of two 4.5 kV IGBTs so

Table 5 Cost and performance of different multilevel converters

Number of levels	5			11		
Topology	NPC	FC	MMC	NPC	FC	MMC
IGBTs	48	48	48	60	60	60
Diodes	18	–	–	54	–	–
Capacitors	–	18	–	–	135	–
Total comp.	66	66	48	114	195	60
THD (%)	17.26	17.80	18.13	7.07	7.28	7.70
Complexity	19	29	29	41	55	55
Total cost(AU$)	90961	117408	82027	115663	109545	82159

the number of IGBTs is 48. To enable a converter output phase current of 250 A, the simulation result is used to determine the current rating of the power semiconductors.

A total of 45 clamping capacitors are required for each phase of the 11-level FC converter. These large numbers of heavy and large size capacitors increase the converter size and cost and reduce the overall lifetime of the converter. The capacitor voltage balancing problem also becomes a challenging issue with this high level of component numbers. There are no blocking diodes or clamping capacitors in the MMC converter topology. The component numbers of this topology scale linearly with the number of levels. Hence, the overall number of components is much lower than that with other multilevel converter topologies. The individual modules are similar and totally modular in construction, which makes it easy to implement for any number of levels. The higher number of attainable levels provides more scope for reducing harmonics. The high number of levels means that it is possible to connect the converter to the medium voltage grid directly.

Table 5 also summarizes the THDs for different multilevel converter topologies. Among these three converter topologies, the NPC converter topology has the best harmonic performance. The harmonic performance of the MMC converter topology is not as good as that of the NPC converter topology. The harmonic content decreases rapidly with increasing number of levels. This means that by increasing the levels of the converter, it is possible to keep the output voltage total harmonic distortion to less than, or equal to 5 % (according to IEEE1547 and IEC61727). Among these converters, the 11-level MMC converter is the low cost high performance converter and it is suitable for the connection of medium voltage grid directly. The price data quoted for the semiconductor devices and capacitors were collected from the Galco Industrial Electronics and Farnell catalogs where devices were chosen from the same family so that it was possible to fit with requirements. The IGBTs chosen are with integrated freewheel diodes and hence these diodes do not appear in costing. The current rating of most devices is selected on the basis of simulation results.

Table 5 also summarized the estimated cost of different converter topologies. The number of semiconductors increases with the number of levels but the variation in cost is small because the price of the lower rated device is comparatively

Table 6 Comparison of different multilevel converter topologies

Number of levels	5			11		
Topology	NPC	FC	MMC	NPC	FC	MMC
Performance	0.92	0.97	1	0	0.02	0.06
Complexity	0	0.28	0.28	0.61	1	1
Cost	0.25	1	0	0.95	0.78	0.003
Total index	1.17	2.25	1.28	1.56	1.80	1.063

much lower. Because of the lower voltage and current requirements, the total semiconductor cost of the 11-level MMC converter is lower than that of all other topologies. The number of arithmetic and logic operations (ALOs) for switching section is calculated through the MATLAB/Simulink environment. The number of ALOs is used to compare the complexity of the converters, as summarized in Table 5.

Based on the performance, control complexity, and semiconductor cost, an overall comparative study is carried out among the converter topologies. If y is the given value, $y_{\min}$ the minimum value, and $y_{\max}$ the maximum value in a group of data, the normalized index value can be calculated as

$$I_d = \frac{y - y_{\min}}{y_{\max} - y_{\min}}. \tag{1}$$

Table 6 summarizes the index values of Table 5. For lower level number converters NPC converter topology may be the best choice. But for higher level number converters MMC converter topology may be the best choice. Moreover, in MMC converter the individual modules are identical and completely modular in construction. Thus, in the case of a fault in one of these modules, it is possible to replace it quickly and easily. Therefore, MMC is the proper converter topology to design a medium voltage converter for step-up transformer-less direct grid connection of renewable generation systems.

4 Selection of Number of Converter Levels

The component number and control complexity increase linearly with the increase of level number. Therefore, optimal selection of number of converter level is important for the best performance/cost ratio of the converter system. Each H-bridge inverter cell commutation voltage of a 15-level topology-based 33 kV inverter is 3,467 V, which may be supported by the 6.5 kV IGBT. Thus, at least 15-level topology is required to design a 33 kV converter. The output power quality of 55-level inverter is good enough to feed into the 33 kV ac grid directly. The cheap 1.7 kV IGBT can be used to design 55-level converter. Therefore, 15-level to 55-level MMC topologies can be considered for a 33 kV converter system.

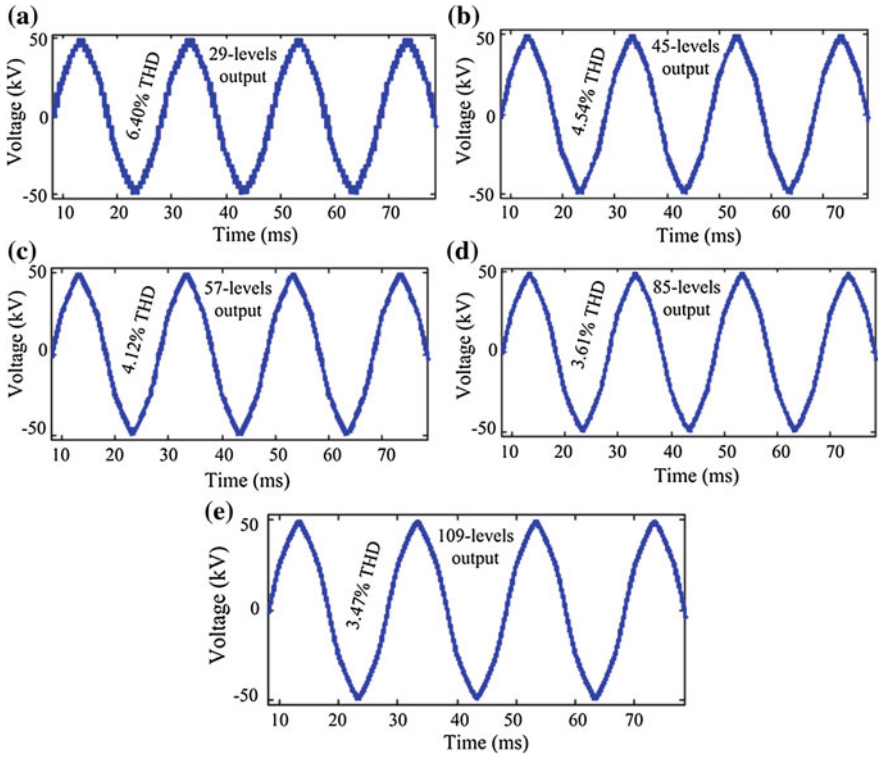

Fig. 7 Line voltages of 33 kV MMC converter (no filter circuit in the converter system) with: **a** 15-level converter topology, **b** 23-level converter topology, **c** 29-level converter topology, **d** 43-level converter topology, and **e** 55-level converter topology

The device voltage utilization factor (DVUF); ratio of commutation voltage of respective commutation cells (V_{com}) and ($V_{com@100FIT}$), are counted in the design process. Higher DVUF is essential for cost-effective design, since semiconductor cost is the significant figure in medium voltage converter applications. In order to ensure cost-effective design, the converters with level numbers of 15, 23, 29, 43, and 55 for a 33 kV converter were considered for the further analysis. These converter systems have been designed and analyzed in the MATLAB/Simulink environment. Figure 7 shows the simulated output voltage waveforms of 15, 23, 29, 43, and 55 level MMC converters. The number of ALOs for switching section and cost of semiconductors are calculated. The number of ALOs is used to compare the complexity of the converters.

The THDs are calculated through the MATLAB/Simulink environment. Table 7 summarizes the calculated data for a 33 kV converter with different number of levels. The component number and control complexity increase linearly

Table 7 Comparison of number of levels for a 33 kV system

Number of levels	15	23	29	43	55
IGBTs	84	132	168	252	324
THDs (%)	6.40	4.54	4.12	3.61	3.47
Cost(AU$)	25,8552	237,600	229,992	141,200	110,030
ALOs	77	121	154	231	297

Table 8 Overall comparison of number of levels for a 33 kV system

Number of levels	15	23	29	43	55
Performance	1.00	0.36	0.22	0.04	0.00
IGBTs cost	1.00	0.85	0.80	0.20	0.00
Complexity	0.00	0.20	0.35	0.70	1.00
Total index	2.00	1.41	1.37	0.94	1.00

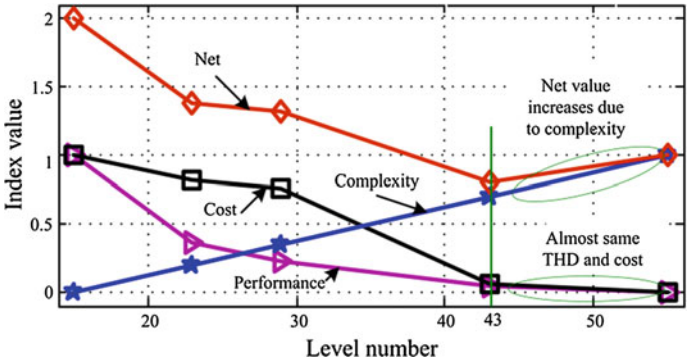

Fig. 8 Graphical presentation of converter parameters with number of levels

with the increase of level number. Moreover, there is no significant output power quality improvement and semiconductor cost reduction for converters with more than 43-level systems. Therefore, the 43-level MMC converter may be considered for a 33 kV converter system. The output power quality of 43-level converter system is good enough to feed the converter output into the medium voltage grid directly (i.e., no step-up transformer or line filter circuit is required). Equation (1) is used to calculate the normalized values of the three significant parameters: performance, complexity, and cost of the converters. Table 8 summarizes the index values of Table 7. Based on the index values, overall performance graphs are plotted and shown in Fig. 8, showing that the total index value is the lowest for 43-level converter, which is the optimal level number for 33 kV systems.

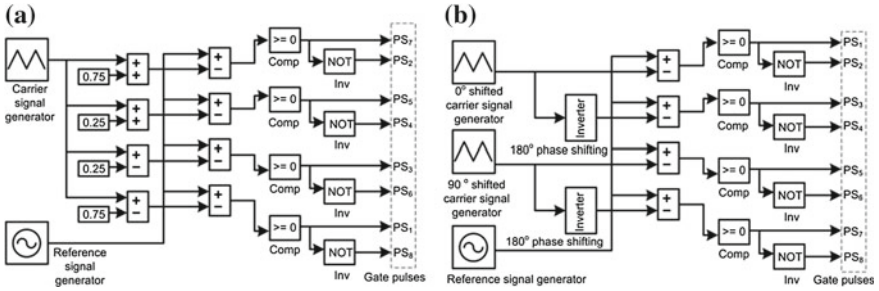

Fig. 9 Switching controllers for multilevel converters with: **a** level-shifted technique for NPC converter, and **b** phase-shifted technique for FC and MMC converters

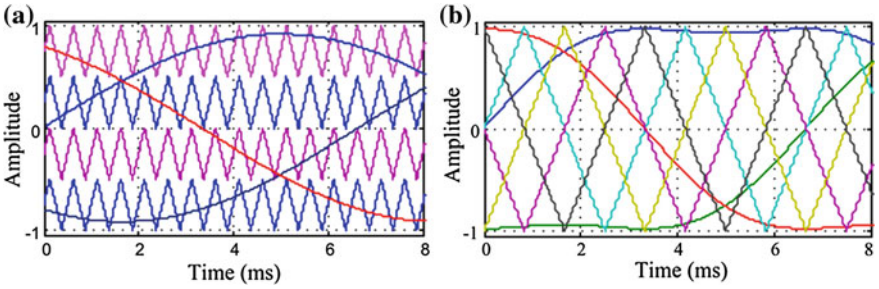

Fig. 10 Switching schemes for multilevel converters with: **a** level-shifted technique for NPC converter, and **b** phase-shifted technique for FC and MMC converters, third-harmonic-injected references

5 FPGA-Based Switching Controller

A phase-shift or level-shift can be introduced between the carrier signals of contiguous cells to produce a phase-shifted or level-shifted switching pattern between them. In this way, when connected together a staircase multilevel waveform is synthesized. For m-level converter, (m−1) phase-shifted or line-shifted carriers are needed. The phase-shifted carriers are specially conceived for FC [23] and MMC [24] converters and level-shifted carriers are especially useful for NPC converter. Figure 9 shows the basic block diagram of switching controller.

One compare unit is used for each half-bridge of the H-bridge inverter cell or each pair of active switching devices; the compare units compare the carrier signal with a reference signal. Each compare unit generates one switching signal for the top switching device. The inverted form of this switching signal drives the bottom switching device. The four carrier signals and the three reference signals as required by the 3-phase 5-level multilevel converter are shown in Fig. 10.

The performance of DSP is limited by the clock rate, and the number of useful operations per clock. In addition, the available DSP at present only can provide

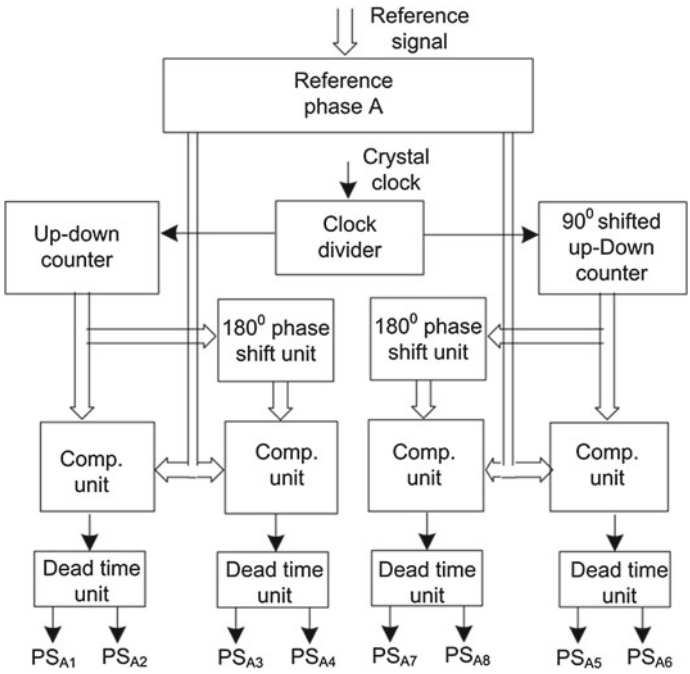

Fig. 11 Basic block diagram of digital switching controller for 5-level converter (a phase leg)

about six pairs of PWM channels, which is clearly insufficient for multilevel inverter systems (e.g., a 3-phase 5-level modular multilevel inverter requires 24 PWM signals). In this chapter, a fully digital switching control scheme is developed and implemented with an Xilinx XC3S500E FPGA. The most common software such as the MATLAB/Simulink and Xilinx ISE-based design technique is used to develop the switching controller, which may save the development time and cost of the switching controller. Figure 11 shows the basic block of the digital switching controller. In this technique, the switching control scheme with target system is modeled in the MATLAB/Simulink environment first.

After having achieved satisfactory performance from the Simulink, the updated model is used for behavioral modeling of the switching controller in the Xilinx ISE environment. The behavioral simulation results were observed, and they were found highly consistent with the Simulink results. After having acquired satisfactory simulation results, the design was implemented and verified with timing simulation. Before connecting with the target system, the gate signals were measured and they were found highly consistent with the Simulink results and the theoretical values.

In total, three reference signals are required, one for each phase leg. A look-up table (LUT) is used to generate the reference signals, which makes the control circuit totally digital and integrated. Including the inverted carrier signals, a total

of four carriers are able to generate four gate pulses when comparing them with a reference signal. The other four gate pulses can be generated by just inverting these four gate pulses with a consideration of the deadtime. In this project, 9-bit up-down counters are used to generate phase-shifted carrier signals. An LUT is actually a set of memory locations which contains the sampled values of a desired analog signal. The frequency of the sine wave can be increased by skipping entries in the sine LUT as the angular resolution depends on the number of entries, for a cycle. If A is the amplitude of the reference signal, δ the phase angle, L the number of entries, and i varies from 0 to (L-1), the sample value can be calculated as

$$S_R(i+1) = A \times \sin\left(\frac{360}{L} i + \delta\right). \tag{2}$$

In order to keep the output span positive between 0–A, the sample value stored in the LUT can be expressed as

$$S_{\mathrm{LUT}}(i+1) = \frac{A}{2} + \frac{A}{2} \times \sin\left(\frac{360}{L} i + \delta\right). \tag{3}$$

The clock divider may determine the frequency of the reference signals. For example, if there are 256 entries in the LUT, to generate a 50 Hz reference signal from 256 entries using the 50 MHz clock, the clock divider value k is given by

$$k = \frac{50 \times 10^6\, Hz}{256 \times 50\, Hz} = 3906.25. \tag{4}$$

The sample values of the reference signals can be calculated from Eq. (3). The reference signals for phases A, B, and C can be generated by considering the values of δ as 0°, 120°, and −120°, respectively. A very high speed integrated hardware description language (VHDL) code-based program is used to create the LUT, which contains the sine reference.

6 High-Frequency Link MMC Converter

The MMC converter requires multiple isolated dc sources that must be balanced, and therefore its application is not straightforward, especially in medium- and large-scale renewable power generation applications. Although it is well reported that the above limitation is not major in solar PV and fuel cell applications, grid connected medium or large-scale generation may suffer from some critical problems. In 2012, by combination of a few quasi-Z source inverters into an MMC converter, a medium voltage PV inverter was proposed [25], where the quasi-Z source inverters generate dc supplies for the floating H-bridge cells of the MMC converter. The proposed converter system does not have electrical isolation

between PV array and medium voltage grid. Multiple isolated high-frequency link-based medium voltage PV inverter topology was proposed [26], where the high-frequency link generates dc supplies for the MMC converter. In these proposed systems, the voltage balancing is the challenging issue, since each module is connected to a PV array through separate dc/dc converter. In 2012, a common dc-linkbased PV inverter was proposed [27]. Although this design may reduce the voltage balancing problem in grid side, the generation of common dc-link voltage from different PV arrays makes the converter operation complex and limits the range of operation of the maximum power point tracker (MPPT).

In 2008, a multi-coil modular permanent magnet generator-based medium voltage MMC converter was proposed to eliminate the step-up transformers of wind turbine generators [28]. This multi-winding generator generates multiple dc supplies for all the H-bridge cells of the MMC converter, which requires a special winding arrangement (still large weight and volume due to power frequency operation) and complicated control strategies. An improved control strategy was proposed and verified on an almost similar generator converter system [29]. In 2010, another approach to eliminate the step-up transformers of wind turbine generators with medium voltage MMC converter was proposed [30]. A few 6-phase generators are placed in the wind turbine nacelle to generate multiple dc supplies for all the H-bridge inverter cells of the MMC converter. However, these approaches require special modular generators or multiple traditional generators to generate isolated multiple dc supplies for all the H-bridge inverter cells of the MMC converter, and introduce electrical isolation problem between generator and grid.

On the other hand, compared with the conventional transformers operated at the power frequency, the high-frequency transformers have much smaller and lighter magnetic cores and windings, and thus much lower costs, which have already been widely used in the low voltage applications. Operated at 1.2 kHz, the weight and size of a 3 MW transformer can be less than 8 % of an equivalent 50 Hz unit [31]. Therefore, advanced magnetic material-based common high-frequency link may be the natural choice to generate multiple isolated and balanced dc supplies for the MMC converter. To verify the feasibility of the new concept of generation of balanced multiple sources from single source with a high-frequency link, a comprehensive preliminary analysis was reported in [32]. A high-frequency link MMC medium voltage converter is developed for step-up-transformer-less direct grid integration of renewable sources. Figure 12 shows high-frequency link MMC medium voltage converter for direct grid integration of solar PV arrays.

This converter can also be well applicable in wind turbine generator systems with the replacement of PV array MPPT circuit by a rectifier circuit. The common magnetic-link generates multiple isolated and balanced dc supplies for the modular MMC from a single or multiple renewable sources. The grid electrical isolation and voltage unbalance problems are solved through the common high-frequency link. The high-frequency link MMC medium voltage converter-based grid integration system will have the following advantages: (i) no requirement of special or

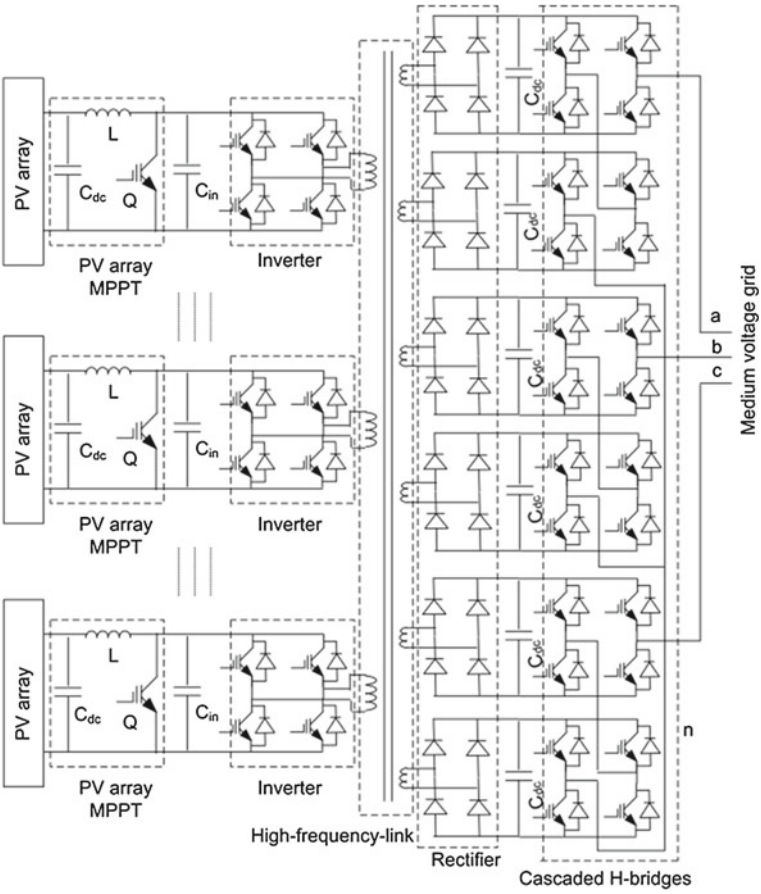

Fig. 12 High-frequency link MMC converter-based direct grid connection of PV arrays

multiple generators for wind turbine generator systems, (ii) wide range of MPPT operation for PV systems, (iii) inherent dc-link voltage balance due to common magnetic-link, (iv) direct gird connection without using step-up transformer, (v) overall compact and lightweight system, and (vi) inherently minimizing the grid isolation problem through high-frequency link. To verify the feasibility of the high-frequency link MMC converter, a scaled down 1.73 kVA laboratory prototype system with 3-phase 5-level MMC converter is developed, which converts 210 V dc (PV array voltage) into 3-phase 1 kV rms 50 Hz ac. Metglas amorphous alloy 2605S3A- and 2605SA1-based 10 kHz magnetic links are developed to generate the isolated and balanced 6 dc supplies for the 3-phase 5-level MMC converter. As measured, before the filter circuit, the 9-level output line voltage waveform contains about 19.3 % THDs and after the filter it is reduced to less than

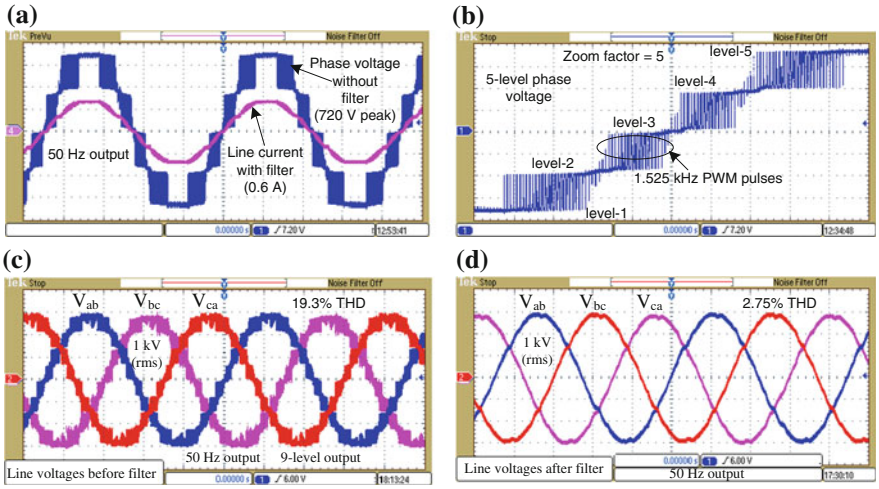

Fig. 13 Measured output voltage and current waveforms of a scaled down prototype 1 kV high-frequency link MMC converter: **a** phase voltage and line current, **b** zoomed phase voltage, **c** line voltage before LC filter circuit, and **d** line voltage after filter circuit

3 %. Each level of the output voltage contains a number of PWM pulses. The measured voltage and current waveforms of scaled down prototype converter are shown in Fig. 13.

7 Conclusion

The MMC converter would be the natural choice to design medium voltage power converters for step-up-transformer-less grid integration of renewable generation units. A common high-frequency magnetic link can be considered to generate multiple isolated and balanced dc supplies for all the H-bridge inverter cells of MMC converter, which automatically minimizes the voltage imbalance problem. The leakage currents and safety problems will also be solved inherently due to electrical isolation provided by the high-frequency link. Although the additional windings and rectifiers may increase the loss of the high-frequency link MMC converter, it is still similar to a 2-level converter-based traditional system, because the use of an MMC converter can eliminate three main parts, i.e., 2-level converter, line filter, and power frequency step-up transformer, from the classical system. Moreover, the elimination of heavy and large step-up transformer and line filter will enable large amount of cost savings in installation, running, and maintenance of renewable power generation systems. Regardless of the type of power transmission system, the medium voltage converter is equally applicable in high voltage ac (HVAC) or HVDC system.

References

1. Islam MR, Guo YG, Zhu JG (2012) A transformer-less compact and light wind turbine generating system for offshore wind farms. In: 2012 IEEE international conference on power and energy, Kota Kinabalu, Malaysia, 2–5 Dec 2012, pp 605–610
2. Islam MR, Guo YG, Zhu JG (2011) Performance and cost comparison of NPC, FC and SCHB multilevel converter topologies for high voltage applications. In: Proceedings of international conference on electrical machines and systems, Beijing, China, 20–23 Aug 2011, pp 1–6
3. Islam MR, Guo YG, Zhu JG (2011) H-bridge multilevel voltage source converter for direct grid connection of renewable energy systems. In: 2011 IEEE PES innovative smart grid technologies Asia (ISGT), Perth, Australia, 13–16 Nov 2011, pp 1–7
4. Islam MR, Guo YG, Zhu JG (2013) A medium frequency transformer with multiple secondary windings for medium voltage converter based wind turbine power generating systems. J Appl Phys 113(17):17A324–17A324-3
5. Baker RH, Bannister LH (1975) Electric power converter. US Patent 3 867
6. Peng FZ, Lai JS (1997) Multilevel cascade voltage-source inverter with separate dc source. US Patent 5 642 275
7. Aiello MF, Hammond PW, Rastogi M (2001) Modular multi-level adjustable supply with series connected active inputs. US Patent 6 236 580
8. Massoud AM, Finney SJ, Williams BW (2004) Multilevel converters and series connection of IGBT evaluation for high-power, high-voltage applications. In: Second international conference power electronics, machines and drives, University of Edinburgh, UK, 31 Mar–2 Apr 2004, pp 1–5
9. Nabae A, Takahashi I, Akagi H (1981) A new neutral-point clamped PWM inverter. IEEE Trans Ind Appl IA-17:518–523
10. Manjrekar MD, Lipo TA (1998) A hybrid multilevel inverter topology for drive applications. In: Thirteenth annual applied power electronics conference and exposition, Anaheim, California, 15–19 Feb 1998, pp 523–529
11. Corzine K, Familiant Y (2002) A new cascaded multilevel H-bridge drive. IEEE Trans Power Electron 17(1):125–131
12. Lai JS, Peng FZ (1996) Multilevel converters—a new breed of power converters. IEEE Trans Ind Appl 32(3):509–517
13. Portillo RC, Prats MM, Leon JI, Sanchez JA, Carrasco JM, Galvan E, Franquelo LG (2006) Modeling strategy for back to back three-level converters applied to high power wind turbines. IEEE Trans Ind Electron 53:1483–1491
14. Alepuz S, Calle A, Monge SB, Kouro S, Wu B (2013) Use of stored energy in PMSG rotor inertia for low voltage ride through in back to back NPC converter based wind power systems. IEEE Trans Ind Electron 60:1787–1796
15. Nami A, Zare F, Ghosh A, Blaabjerg F (2010) Multi-output dc–dc converters based on diode clamped converters configuration: topology and control strategy. IET Trans Power Electron 3(2):197–208
16. Meynard TA, Foch H (1992) Multi-level conversion: high voltage choppers and voltage-source inverters. In: 23rd annual IEEE power electronic specialists conference, Madrid, 29 Jun–3 Jul 1992, pp 397–403
17. Xu L, Agelidis VG (2002) Flying capacitor multilevel PWM converter based UPFC. IEE Proc Electr Power Appl 149(4):304–310
18. Xu L, Agelidis VG (2007) VSC transmission system using flying capacitor multilevel converters and hybrid PWM control. IEEE Trans Power Delivery 22(1):693–701
19. Marchesoni M, Mazzucchelli M, Tenconi S (1990) A nonconventional power converter for plasma stabilization. IEEE Trans Power Electron 5(2):212–219
20. Hammond PW (1997) A new approach to enhance power quality for medium voltage ac drives. IEEE Trans Ind Appl 33(1):202–208

21. Peng FZ, Lai JS, McKeever JW, VanCoevering J (1996) A multilevel voltage-source inverter with separate DC sources for static var generation. IEEE Trans Ind Appl 32(5):1130–1138
22. Tolbert LM, Peng FZ, Habetler TG (1999) Multilevel converters for large electric drives. IEEE Trans Ind Appl 35(1):36–44
23. Meynard TA, Foch H (1998) Electronic device for electrical energy conversion between a voltage source and a current source by means of controllable switching cells, US Patent 5737201 A
24. Hammond P (1997) A new approach to enhance power quality for medium voltage drives. IEEE Trans Ind Appl 33(1):202–208
25. Sun D, Ge B, Peng FZ, Haitham AR, Bi D, Liu Y (2012) A new grid-connected PV system based on cascaded H-bridge quasi-Z source inverter. In 2012 IEEE international symposium on industrial electronics, Hangzhou, China, 28–31 May 2012, pp 951–956
26. Choi H, Zhao W, Ciobotaru M, Agelidis VG (2012) Large-scale PV system based on the multiphase isolated dc/dc converter. In: 3rd IEEE international symposium on power electronics for distributed generation systems, Aalborg, Denmark, 25–28 Jun 2012, pp 801–807
27. Kouro S, Fuentes C, Perez M, Rodriguez J (2012) Single dc-link cascaded H-bridge multilevel multistring photovoltaic energy conversion system with inherent balanced operation. In: 38th annual conference on IEEE industrial electronics society (IECON 2012), Montreal, QC, Canada, 25–28 Oct 2012, pp 4998–5005
28. Ng CH, Parker MA, Ran L, Tavner PJ, Bumby JR, Spooner E (2008) A multilevel modular converter for a large, light weight wind turbine generator. IEEE Trans Power Electron 23(3):1062–1074
29. Yuan X, Chai J, Li Y (2012) A transformer-less high-power converter for large permanent magnet wind generator systems. IEEE Trans Sus Energy 3(3):318–329
30. Deng F, Chen Z (2010) A new structure based on cascaded multilevel converter for variable speed wind turbine. In: 36th annual conference on IEEE industrial electronics Society, Glendale, AZ, USA, pp 3167–72
31. Prasai A, Yim JS, Divan D, Bendre A, Sul SK (2008) A new architecture for offshore wind farms. IEEE Trans Power Electron 23(3):1198–1204
32. Islam MR, Guo YG, Zhu JG (2012) A medium-frequency transformer with multiple secondary windings for grid connection through H-bridge voltage source converters. In: Proceedings of international conference on electrical machines and systems , Sapporo, Japan, 21–24 Oct 2012, pp 1–6

A Review of Interconnection Rules for Large-Scale Renewable Power Generation

Tareq Aziz, Tapan K. Saha and Nadarajah Mithulananthan

Abstract Around the world penetration levels of renewable-based power into power systems have been increasing rapidly over the last few years. In the year 2011, almost half of the estimated 208 GW of newly added electric capacity was reported from renewable-based generation. Wind and solar photovoltaic (PV) generators accounted for almost 40 % and 30 % of new renewable capacity, respectively, followed by hydropower. Besides rooftop and small-scale systems, the trend toward very large-scale wind farms and ground-mounted PV systems continued to play an important role. It is evident that renewable-based generation will be comparable to conventional power generation in the coming decades. Therefore, many transmission system operators (TSOs) and regulators around the world have come up with interconnection rules/codes to request these volatile renewable resource-based power plants to have more or less the same operating competence as conventional power plants. Depending on system characteristics and renewable penetration levels, the level of requirements imposed by these grid codes are getting more stringent over time to ensure the common aim of secured and reliable power system operation. This chapter presents a comprehensive study of the grid interconnection rules set by various TSOs and regulators for large renewable-based power plants. A brief discussion explaining the necessity of grid codes has been presented in the beginning, followed by a list of principal static and dynamic operation issues usually addressed in existing grid codes. A comparative study has then been carried out to compare various rules among grid codes around

T. Aziz (✉)
Department of Electrical and Electronic Engineering, Ahsanullah University of Science and Technology, Dhaka, Bangladesh
e-mail: aziz.tareq@gmail.com; taziz@ieee.org

T. K. Saha · N. Mithulananthan
Power and Energy Systems Research Group, School of Information Technology and Electrical Engineering, The University of Queensland, Brisbane QLD, Australia
e-mail: saha@itee.uq.edu.au

N. Mithulananthan
e-mail: mithulan@itee.uq.edu.au

J. Hossain and A. Mahmud (eds.), *Large Scale Renewable Power Generation*, Green Energy and Technology, DOI: 10.1007/978-981-4585-30-9_6,

the globe. The study focuses on the primary concerns such as active and reactive power regulations under static operation, active and reactive power response during and after faults, and fault ride-through requirements imposed by the codes. A useful discussion on future trends for synchronizing diverse grid codes has also been presented. The contents of this chapter will be helpful for regulators as well as for renewable-based generator manufacturers to form better frameworks, which will ultimately result in secure system operation with increased penetration of large-scale renewable generation.

Keywords Renewable power plants · Large-scale integration · Grid code · Transmission system operators · Continuous operation · Low voltage ride through · High voltage ride through

1 Introduction

Standard interconnection rules for renewable-based generators are a comparatively recent policy innovation to accelerate the growth of clean energy supply [1]. Grid code regulations were primarily developed by transmission system operators (TSOs)/regulators to summarize both privileges and responsibilities of all generation units/customers connected to the transmission system. Developing such codes also promoted competition in power generation and supply, hence ensuring reliability and efficiency of power generation, transmission, and distribution [2].

As the level of penetration of renewable energy-based generation was insignificant compared to fossil fuel-based generation systems, earlier grid standards did not include rules for wind and solar power plants. However, the situation has altered over the last few years as number of countries around the world have observed a remarkable rise in the quantity and capacity of renewable power plants (RPPs) included into their electricity networks [3].

As a global trend for exploration of clean and renewable power, wind power generation has drastically increased in the generation scenarios of many countries and is set for additional growth over the coming years. Global wind power plant (WPP) installations reached approximately 283 GW by the end of 2012, resulting in the greatest capacity additions of any renewable-based technology. As in 2011, more new capacities were added in developing countries and emerging markets than in the countries listed in the Organization for Economic Co-operation and Development (OECD). With improvements in wind power interconnection policies and economics, the United States and China together accounted for nearly 60 % of the global market in 2012, followed distantly by Germany, India, and the United Kingdom. Renewable resources accounted for almost 70 % of addition to existing electricity generation capacity in European Union in the year 2012. Majority of these additions were from wind power and solar photovoltaic (PV). Germany remained the largest wind power market in Europe in 2012. Besides the

domination of large wind turbines and farms, the small-scale (<100 kW) wind industry also continued to mature in 2012 [4].

Solar PV grew the fastest of all renewable technologies during the period from 2006 to 2012. The operating capacity of PV plants increased by an average of 58 % annually, followed by concentrating solar-thermal plant (CSP), which increased almost 37 % annually over this period from a small base of 367 MW. Almost 30 GW of PV operating capacity was added in 2012, mounting the total global capacity to approximately 100 GW. This was led by Europe, with significant additions in Asia late in the year. The trend toward large-scale ground-mounted systems continued, while small-scale rooftop systems continued to play a significant role. From the end of 2007 through 2012, total global capacity of CSP grew at an average annual rate of 43 %. In 2012, with an addition of 970 MW CSP in Spain, the total global capacity was doubled relative to the 2011 capacity and reached 2,550 MW [4].

Increased share of RPP is starting to affect the structure and management of Europe's electricity system and is increasingly facing barriers that include direct competition with conventional electricity producers and saturation of local grids. It is just a matter of time that the same phenomenon might be observed by other systems where capacities of RPPs are becoming comparable to existing large-scale power plants. Therefore, several TSOs/regulators around the world have come up with newly developed grid standards requesting the RPPs to have essentially similar operating capabilities as conventional plants. Other TSOs are also engaged in revising their grid codes. This chapter explains the basic needs of developing new grid codes for RPPs under changing generation scenario. Different features in principal grid codes developed by various TSOs for integrating large RPPs are also explained. The authors believe that the discussion presented in this chapter would facilitate TSOs to assess their present requirements versus requirements set by other TSOs and would also assist generator manufacturers to develop grid code compatible RPP units.

2 Necessity of Grid Connection Rules

The grid impact of an RPP depends on a number of factors such as technology of the plant, interconnection features/capabilities, and penetration level. The challenging features of RPP can be summarized as follows [5].

2.1 Variability and Uncertainty of Resources

Unlike customary nonrenewable resources, the output of solar, wind, and some hydro generation units fluctuates according to the availability of the primary resources (solar irradiance, wind velocity, and water head) that cannot be practically

stored. These resources are considered variable and hence the output of RPP changes according to their availability. As a result, plant output from an RPP becomes variable and less predictable than a conventional plant [6]. The intermittent and random characteristics of wind and PV power result in difficulties to attain reliable energy balance and resource assurance. As wind power peaks usually occur at load off-peak, the situation is exacerbated with widespread integration of wind turbines [7]. It adversely influences the real power balance of the system and causes severe system frequency problems under certain circumstances.

2.2 Location of Plant

Because of the availability of resources, RPPs are often located in distant regions and hence require long transmission lines to deliver power to load centres. For example, it can be mentioned that large-scale PV plant requires enormous land area for harnessing enough power from solar irradiation. Similar justification is applicable for large-scale integration of wind turbines too. In offshore wind plants with lengthy submarine AC cables, high charging currents necessitate the injection of a large amount of apparent power. Quick and large variation of wind output causes swift changes in system voltages as well as in tie line flows. This phenomenon can ultimately lead to voltage instability issues and endanger the security of the power system [5].

2.3 Generation Technologies and System Condition

Generation technologies behind each RPP influence the voltage and frequency regulation capabilities, harmonic emissions, and protection coordination [8]. Integration of large WPPs in a weak power system results in inadequate dispatch and balancing capabilities.

In order to address the above technical disputes while responding to the pressure of accommodating increased clean power sources, TSOs have to modify traditional planning methods and operational practices. The foremost attitude is that, wherever feasible, RPPs should have practical potentials comparable to conventional generators to support secured operation of the power system [8]. The principal grid codes discussed in the present study have been presented in the next section.

3 Grid Codes in Study

This chapter presents a detailed study on the international rules and regulations imposed by TSOs/regulators on large RPPs. Primarily, the codes corresponding to the countries with significant RPP penetration are considered. According to [4], the top countries for nonhydro renewable power capacity at the end of 2012 were China, United States, and Germany, followed by Spain, Italy, and India. At the end of 2012, the EU had the maximum amount of nonhydro renewable-based generation. Most of that capacity came from solar PV and wind and it was recorded as approximately 44 % of the global total. Along with codes of the mentioned countries, parts of the UK, Canadian, and Australian grid codes have also been taken into account.

Design of grid rules and their applications are dictated by the size of the RPP unit. In order to increase utility confidence with RPPs at distribution levels, industry organizations such as IEEE and Underwriters Laboratories (UL) began to develop standards that enabled safe and reliable interconnection of generators to the grid. However, with increasing size of generation, direct interconnection at transmission level was required and hence rules were being developed by different TSOs and regulators [1]. The present study is focused on the technical regulations relating to large RPPs connected to transmission systems. Though regulations such as fault level contribution, power quality, and anti-islanding protection are mostly considered for small RPPs connected to distribution systems [9, 10], they have also been discussed in brief in Sect. 4.2. Table 1 lists the principal grid codes proposed by different TSOs/regulators in the top RPP integrating countries.

Along with the codes practised in the countries mentioned earlier, grid codes in Denmark have been chosen due to the high penetration level of wind power. The Irish grid code is also selected because of its unique system nature [22, 23].

4 Principal Technical Issues in Grid Interconnection

The purpose of outlining the requirements of a generic grid code is to provide a suggestion of the technical specifications, which should be satisfied by a generic RPP when connected to the system [23]. The technical terms of grid codes are divided into two major classes—static and dynamic requirements. Among these two classes, the static part of each code consists of issues related to continuous operation of generation units. Voltage and reactive power control, power factor requirements, frequency requirements, and power quality are some of the common issues, which are addressed. The dynamic part of the codes considers issues regarding the operation of RPPs during fault sequences and disturbances in the grid.

Table 1 Principal international grid codes

Code title	TSO/Regulator	Country	Date of proposal
FERC order No. 661-A, interconnection for wind energy [11]	Federal energy regulatory commission (FERC)	USA	December, 2005
Technical rule for connecting wind farm to power system [12]	China electric power research institute (CEPRI)	China	December, 2005
Netzanschlussregeln Hoch- u. Höchstspannung [13]	Energy on (E.ON)	Germany	August, 2003
Datos a incluir en la solicitud de acceso a la red de transporte para centrales de generación fotovoltaica [14]	Red eléctrica de españa(REE)	Spain	November, 2007
Codice di trasmissione, dispacciamento, sviluppo e sicurezzadella rete [15]	Terna	Italy	December, 2006
Indian electricity grid code (IEGC) [16]	Central electricity regulatory commission	India	April, 2006
Regulation TF 3.2.5, wind turbines connected to grids with voltages above 100 kV [17]	Elkraft/Eltra	Denmark	December, 2004
EirGrid grid code WFPS1- wind farm power station grid code provisions [18]	EirGrid	Ireland	October, 2009
Grid code[19]	National grid electricity transmission (NGET)	UK	September, 2010
Wind power facility technical requirements [20]	Alberta electric system operator (AESO)	Canada	November, 2004
National electricity rules [21]	Australian energy market commission (AEMC)	Australia	September, 2010

4.1 Static Regulations

The first part of the grid code focuses on the static requirements. A few of these requirements contain time limits or operate within fixed time frames. The values are, however, still constant within the mentioned time frames and hence semi-static regulations are included in this static analysis. Normally, these requirements are specified at the point of common coupling (PCC) of the RPPs [23].

4.1.1 Reactive Power and Voltage Regulation

Voltage regulation in a power system is dependent on flow of reactive power as well as on short circuit capacity and impedance of the network. By operating in a wide range of power factors, conventional generation units have traditionally provided reactive power to support system voltage. Voltage regulators on their excitation systems provide the primary voltage control function. However, lack of this capability leads to problems such as depressed voltages and excessive voltage

fluctuations, which have been found common with many old wind turbines. Another important parameter that influences voltage at PCC is tap-changing operation of on-load tap changer transformers. The speed of response of the tap changer, the size of the first step, and those of subsequent steps are all relevant parameters that influence the voltage at PCC of RPP [24].

In general, there are three common reactive power control modes for RPPs [8]:

(a) Fixed reactive power mode: As specified by TSO/regulator, reactive power flow at certain set point is maintained.
(b) Fixed power factor mode: In this mode, the ratio between active and reactive power is maintained. This mode is common for small-scale generators connected at the distribution level.
(c) Voltage set-point control mode: Necessary reactive power is injected at PCC to regulate the voltage magnitude.

The reactive power generation capability of the RPPs at PCC is defined by power factor regulation. With the development of converter technology, the doubly fed induction generator (DFIG) wind turbines have come up with both capacitive and inductive reactive power capabilities according to active power output. With increased rating of the grid side converter, full-converter based variable speed wind turbines offer even wider range of reactive power capability compared to DFIG turbines [25]. By using additional Static Var Compensator (SVC), STATic COMpensator (STATCOM), and other reactive support equipment at the plant level, reactive power capability of wind and solar plants can be further enhanced.

Power factor requirements and reactive power capabilities are more or less similar in the reviewed grid codes. Table 2 illustrates these requirements.

Power factor requirements in countries such as USA, China, Denmark, and Australia are relatively simple. The RPPs are requested to operate within the range specified by capacitive and inductive power factor. For example, in Australia WPPs must be able to continuously operate at their rated output power within the range of 0.93 capacitive to 0.93 inductive power factor [21]. However, this set of requirements is applicable only to Automatic Access Standard formulated by AEMC. The minimum access standard does not allow supply or absorption of reactive power at PCC. Some grid codes consider the variation in voltage level while fixing power factor/reactive power requirements at PCC. German grid code for WPPs is one such example [13].

In Germany, the reactive power requirements for WPPs consist of two parts. WPPs with ratings less than 100 MW have similar reactive power requirement as in other grid codes. These WPPs need to be operated within the range of 0.95 capacitive to 0.95 inductive power factor. However, reactive power requirement for the WPPs with ratings over 100 MW is voltage dependent [13].

Figure 1 illustrates the reactive power requirements of each turbine in WPPs over 100 MW in size. The power factor range changes from 0.925 capacitive–0.95 capacitive at minimum operating voltage to 0.95 inductive–0.925 capacitive at the

Table 2 Power factor/reactive power requirement

Country or region	PF requirements
USA	0.95 leading to 0.95 lagging [11]
China	0.97 lagging to 0.97 leading [12]
Germany	For a rated active power capacity <100 MW: 0.95 lagging to 0.95 leading and For a rated active power capacity >100 MW: Power factor is voltage dependent [13]
Spain	0.98 leading to 0.98 lagging without any penalty [14]
Italy	0.95 lagging to 0.95 leading [15]
India	0.95 lagging to 0.95 leading [16]
Denmark	At full production: Q/Prated = 0 to Q/Prated = 0.1 and At zero production: From Q/Prated = −0.1 through a straight line to Q/Prated = 0 [17]
Ireland	At full production: 0.95 lagging to 0.95 leading, For active capacity from 100 % production to 50 % production: 32.6MVAr per 100 MW installed, From 50 % production to idle: 0.95 lagging to 0.95 leading [18]
UK	0.95 lagging to 0.95 leading [19]
Canada	0.90 lagging to 0.95 leading [20]
Australia	0.93 lagging to 0.93 leading [21]

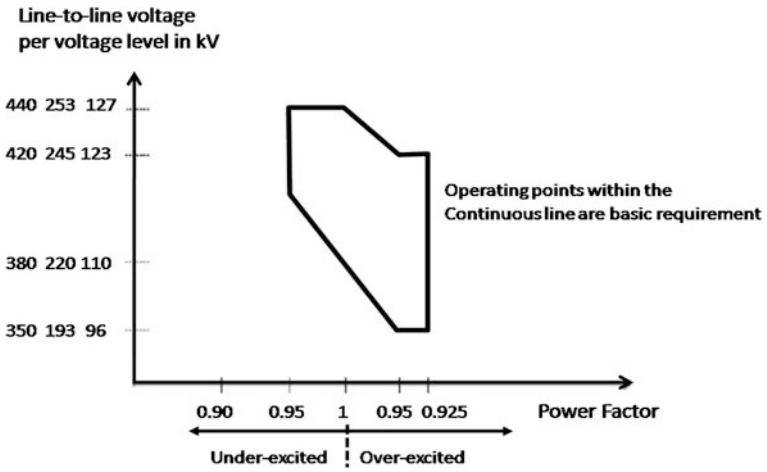

Fig. 1 Power factor requirements for wind farms above 100 MW, German grid code [13]

full power factor operation. The power factor requirement is from inductive 0.95–1.0 at the maximum operating voltage [13].

In Spain, the WPP with reactive power capability is paid an additional bonus, whereas a lack of reactive power to maintain the mentioned power factor at PCC results in a penalty. Bonus or penalty is calculated as a percentage of a reference tariff expressed in €/MWh [26].

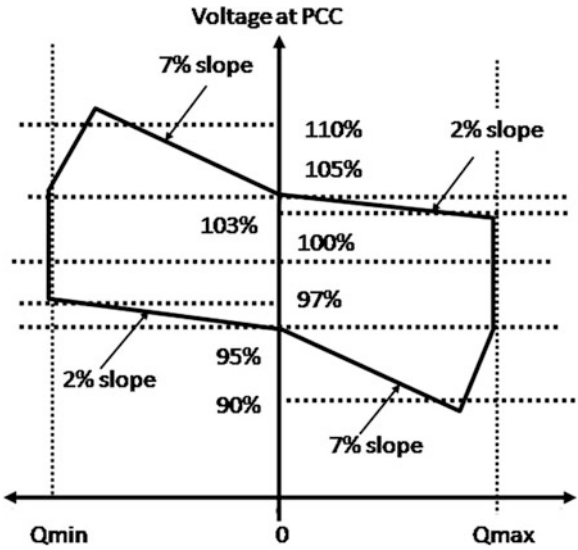

Fig. 2 Voltage-reactive power envelope in UK code for voltage levels >33 kV [19]

In Canada, the reactive power requirements for WPPs are specified under continuous as well as dynamic operating conditions. WPPs need to be operated within the power factor range of 0.9 capacitive to 0.95 inductive under steady state. For dynamic conditions, power factor ranges from 0.95 capacitive to 0.985 inductive. The Canadian grid code also demands WPPs to be incorporated with voltage set-point control mode [27]. With a step change in the voltage set-point, the voltage control loop should be adjusted to attain 95 % of the reference reactive power within 0.1–1 s [20]. Besides the Canadian grid code, wind plants in the UK connected to a line rated 33 kV or above are required to contribute to voltage control with a predefined reactive power–voltage droop characteristic as shown in Fig. 2. In case of an unexpected voltage variation in grid, the WPP is required to start reacting within 200 ms and should provide at least 90 % of the required reactive power within 1 s. After 2 s from the event, the fluctuations in the reactive power output should be limited within ± 5 % of the target value [19].

4.1.2 Continuous Voltage Operating Range

Table 3 illustrates the continuous voltage operating requirements for RPPs in reviewed grid codes. The RPPs are asked to operate within the continuous operating voltage range as mentioned in Table 3. At specified continuous operation range, the voltages inside the RPPs must be within the tolerable voltage range of their constituent components.

Table 3 Continuous voltage operating range at PCC of RPP

Country or region	Voltage operating requirement
USA	±10 % [11]
China	−3 to +7 % [12]
Germany	220 kV −13 to +12 %, 400 kV −8 to +10 % [13]
Spain	132 kV ±10 % [14]
Italy	–
India	400 kV −10 to +5 %, 220 kV −9 to +11 %, 132 kV −9 to +10 %, 110 kV −12.5 to +10 % [16]
Denmark	150 kV −3 to +13 % [17]
Ireland	220 kV −9 to +12 % [18]
UK	132 and 275 kV ±10 %, 400 kV −10 to +5 % [19]
Canada	Provided by TSO [20]
Australia	±10 % [21]

4.1.3 Frequency Operating Requirement

System events that embrace load-generation mismatches often result in transient fluctuations of system frequency. Mechanical failures of generators, abrupt load changes, or loss of line in the transmission system are a few of the reasons behind such anomalies. The rate and depth of frequency fluctuations and the time for the frequency to return to its pre-event nominal value are affected by the dynamics of the generation mix.

In the presence of a large share of RPP such as WPP, this load-generation mismatch issue is obvious during simultaneous light load and high wind periods. Due to economic consideration, fewer synchronous generators will be operating, which would consequently reduce the overall grid inertia.

Table 4 shows the frequency operating requirements for RPPs in the reviewed codes.

In general, the TSOs request the generators' primary frequency control to maintain the continuous frequency limit at PCC. Some TSOs require wind plants to be equipped with an inertia emulation system to support system frequency following a major frequency event [28]. The design considerations for inertial response emulation include: (a) the optimal amount of power that can be drawn from the rotating masses; (b) the duration of the momentary injection; and (c) the duration of the speed and energy recovery phase. Several frequency control techniques reported in research and in practice can be found in [29–32].

Almost all the grid codes state that some power ramp rate limitation or active power curtailment should be used to control frequency deviation at the wind farm level. The Irish grid and the connected WPPs can be taken as a good example for this control. Due to weak interconnection with the neighboring systems, the Irish grid faces notorious frequency variation on a regular basis. Therefore, the Irish

Table 4 Continuous frequency operating range in principal grid codes

Country or region	Frequency requirements
USA	Not specified [11]
China	Continuous operating range 49.5–50.5 Hz, No more than 2 Min for 50.5–51.0 Hz, No more than 10 Min for 48.0–49.5 Hz [12]
Germany	Continuous operating range 47.5–51.5 Hz [13]
Spain	Continuous operating range 49.5–50.5 Hz [14]
Italy	Continuous operating range 47.5–51 Hz [15]
India	Continuous operating range 47.5–51.5 Hz [16]
Denmark	30 Min for 50.5–52.0 Hz and 49.5–47.5 Hz [17]
Ireland	60 Min for 50.5–52.0 Hz and 49.5–47.5 Hz [18]
UK	Continuous operating range 47.5–52 Hz, 20 s for <47.5 Hz [19]
Canada	Refer to western electricity coordinating council (WECC) requirement [20]
Australia	Continuous operating range 47.0–52.0 Hz [21]

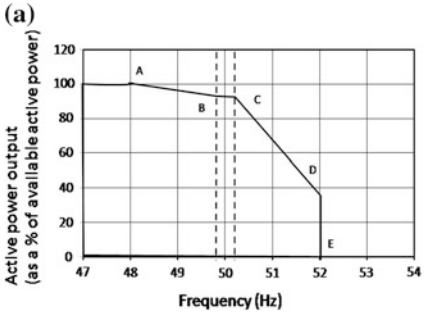

(b)

Operating Point	Frequency (Hz)	Active Power (% of available active power)	
		Capacity>10 MW	5MW< Capacity< 10MW
A	47.0 - 51.0	50 - 100	100
B	49.5 - 51.0	50 - 100	100
C	49.5 - 51.0	50 - 100	100
D	50.5 - 52.5	20 - 100	20-100
E	50.5 - 52.5	0	0

Fig. 3 **a** Power-frequency response curve and **b** Power-frequency regulations in Irish code [18]

grid code demands WPPs to control active power as close to real-time as possible according to the response curve described in Fig. 3. The rate of response should be 1 % of rated power per second for each online wind turbine generator (WTG) [18]. Other European grid codes also contain similar requirements [8].

4.2 Power Quality

The power system needs to run in a stable state and be able to deliver power to consumers at an acceptable quality. Harmonics and flicker at PCC are two major power quality disturbances, which need to be taken care of while harnessing power through RPPs. Sources, which contributes in harmonics injection in RPP include [33]:

Table 5 THD at planning level in UK code [35]

System voltage at PCC	THD limit (%)
400 V	5
6.6, 11 and 20 kV	4
22 to 400 kV	3

(a) Generator technology—Wind turbines utilizing static power converters and modern power converters used in bulk PV applications inject harmonics.
(b) Dynamic reactive power compensation equipment—SVCs and STATCOMs also inject harmonics into the grid.
(c) Collector system feeders—In offshore WPPs, long AC submarine cables set off critical resonances with the power system at relatively low frequencies.
(d) Electric grid itself—The impedance of grid is a function of loading level and switching state in the grid. The worst case network impedance needs to be assumed while determining the contribution of WPP to the harmonic voltage distortion at PCC [8].

In the United States and Canada, the IEEE Standard 519 [34] sets out the quality of power that an electric utility is expected to deliver to the customer at PCC. Section 5 of Chapter "HVDC Transmission for Offshore Wind Farms" of IEEE Standard 519 recommends that as a percentage of the nominal fundamental frequency voltage in the utility service, the voltage distortion limits should not exceed 5 % for the total harmonic distortion (THD), and 3 % for any individual harmonic. The Danish grid code sets a more stringent rule where it demands THD to be less than 1.5 % and distortion factor (DF) for an individual harmonic to be less than 1 %. Engineering Recommendation G5/4 defines the harmonic requirements in UK and Scotland. Summary of UK THD limits at planning level are given in Table 5. Details of allowable harmonic voltages at various levels can be found in [35].

Flicker is fluctuation in the system voltage and it can produce noticeable changes in light output. In many cases, flicker becomes annoying and objectionable. Step changes in transmission system voltage can occur due to switching in and out of lines, cables, capacitors, transformers, and other generating plant. In a solar plant, abrupt change in the irradiance and power output of the facility occurs due to passing clouds. This results in noticeable flicker. Variations in WTG power output due to variation in wind speed, tower shadowing, wind shear or gradient, blade pitching, and WTG start and stop operations are few reasons, which cause flicker in a wind farm [36]. Flicker is only a concern for distribution interconnections in areas of the system where fault currents are very low, i.e., in weak systems [10].

IEEE Standard 1453 [37] has primarily adopted IEC 61000-4-15 [38] to provide uniformity to international standards. Short-term flicker (Pst) is measured as a weighted average of the flicker contribution over 10 min, whereas long-term flicker value (Plt) is measured as a weighted average of the flicker contribution

Table 6 IEEE standard 1453 adopted Pst and Plt in MV, HV, and EHV power systems [37]

Flicker measurement	Planning levels	
	MV (1 to 35 kV)	HV–EHV (above 35 kV)
Pst	0.9	0.8
Plt	0.7	0.6

over 2 h [23]. The recommended values of Pst and Plt at planning levels are given in Table 6.

According to the Danish grid codes Pst and Plt values should be limited to 0.30–0.20, respectively. Among European grid codes, it is primarily the Danish code, which mentions restrictive regulations regarding flicker. The German and Irish codes do not mention anything on flicker [25].

4.3 Dynamic Regulations During and After Disturbances

Reliability of the interconnected power system is greatly affected by system disturbances. System disturbances include asymmetrical or symmetrical faults on transmission system elements. Dynamic regulations also consider associated switching to clear the faulted elements and other system elements. It is expected that transition to the acceptable, new steady state is stable and fast enough after such disturbances. Along with control and protection units, generation units play a significant role in providing satisfactory dynamic performance [6].

4.3.1 Low Voltage Ride Through

Unless the conventional synchronous generators are physically disconnected from the system due to disturbance, they can be defined as riding through [6]. When a fault occurs in an electric network, the supply voltage drops to a lower level until the protection devices detect the faulty region and isolate it from the rest of the network [3]. Depending on the type and location of the fault, RPPs experience a voltage sag condition at PCC and consequently get disconnected from the grid. The disconnection of RPPs under such voltage anomalies is not acceptable when renewable energy constitutes a large share of the total generation. Thus, modern grid codes demand large RPPs to continue their uninterrupted operation according to given voltage–time profiles under different fault conditions. Specifications related to undervoltage are usually identified as low voltage ride-through (LVRT).

Figure 4 shows LVRT requirement according to FERC Order 661-A as an example. The curve in Fig. 4 represents a boundary within which voltage at PCC is expected to be held. That means a WPP shall remain connected to the transmission

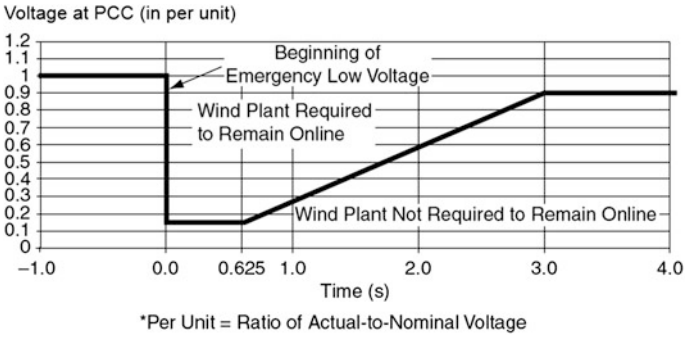

Fig. 4 LVRT requirement proposed for WPPs in FERC 661-A [39]

system under the fault conditions when the voltage measured at PCC remains above the solid line for any fault in the network [39].

LVRT capability curves proposed in international grid codes are somewhat similar to Fig. 4. However, quantitative features of those curves may vary from one TSO/regulator to another. Table 7 lists the important parameters of LVRT requirements in the principal grid codes considered in the present study.

The German grid code has no regulations for asymmetrical voltage sags, but demands ride-through capability for three-phase faults with the PCC voltage drop to zero for the maximum duration of 150 ms, followed by voltage recovery to 0.8 p.u. within 1.5 s. In USA, the older version of German LVRT curve has been adopted by FERC. Minimum voltage for this curve is 0.15 p.u for 0.625 s and the voltage recovery period is set at 3 s [11]. Similar requirements can be observed with EirGrid in Ireland [18]. The Spanish grid code requires WPPs to endure three-phase faults with PCC voltage down to 0.2 p.u. for 0.15 s, followed by the voltage recovery to 0.85 p.u. during the next 1 s. On the other hand, for two-phase faults, continuous operation of WPPs is requested at 0.6 p.u. for the maximum duration of 0.5 s [14]. The Indian grid code has varying fault clearing times with different nominal voltages at PCC. At 400 kV, fault clearing time is set at 100 ms, whereas at 220 and 66 kV the clearing times are set at 160 and 300 ms, respectively [16]. In Australian code, WPPs must remain connected for symmetrical as well as for asymmetrical faults with the voltage drop to 0 p.u. for 140 and 400 ms, respectively. The supply voltage has got to return to 0.7 p.u. in 2 s and 0.8 p.u. in 10 s [21].

4.3.2 High Voltage Ride Through

Voltage swell conditions at PCC can occur due to switching off large loads, energizing capacitor banks, or faults in the grid [40]. In order to ride through such a condition, a requirement known as high voltage ride through (HVRT) has been recently added in the grid codes of Germany, Spain, Denmark, and Australia. In USA, WECC sets high voltage boundary for all kinds of RPPs [41]. Figure 5

Table 7 LVRT criteria in grid codes

Country or region	Technology addressed	During fault		Fault clearance		Reference
		Vmin (p.u.)	Tmax (s)	Vmin (p.u.)	Tmax (s)	
USA	WPPs	0.15	0.625	0.9	3	[11]
China	WPPs	0.2	0.625	0.9	3	[12]
Germany	WPPs	0.0	0.15	0.9	1.5	[13]
Spain	WPPs	0.2	0.15	0.85	1	[14]
Italy	WPPs	0.2	0.5	0.75	0.8	[15]
India	WPPs	0.15	0.16	0.9	3	[16]
Denmark	WPPs	0.25	0.15	0.75	1	[17]
Ireland	WPPs	0.15	0.625	0.9	3	[18]
UK	Tidal, wave, wind, geothermal, or similar plants. Wind, wave, and solar units are referred to as intermittent power sources	0.15	0.14	0.8	1.2	[19]
Canada	WPPs	0.0	0.15	0.75	2	[20]
Australia	All technologies	0.0	0.4	0.7	2	[21]

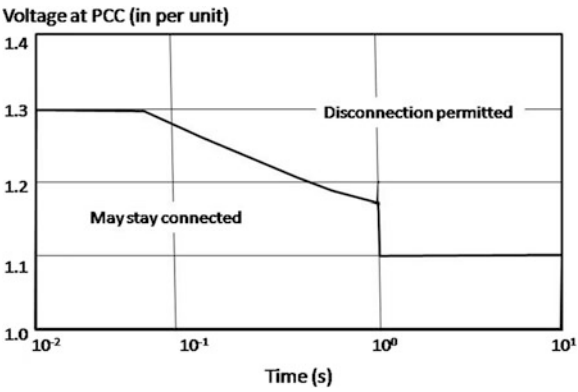

Fig. 5 HVRT requirement in Australia [21]

shows the HVRT requirement according to the Australian grid code. Table 8 lists the HVRT requirements for other grid codes in quantitative form. It is obvious that the Australian and Spanish grid codes have the most challenging HVRT regulations that insist WPPs to withstand voltage swell of 1.3 p.u [14, 21].

4.3.3 Reactive Current Injection During Fault

Along with LVRT and HVRT capability curves, a few grid codes demand reactive current support at PCC during the fault period and/or fast active power recovery after the clearing of a fault. These rules are enforced by TSOs/regulators to utilize

Table 8 HVRT requirements in available grid codes

Country or region	During swell condition		Reference
	Vmax (p.u.)	Tmax (s)	
USA (WECC)	1.2	1	[41]
Germany	1.2	0.1	[13]
Spain	1.3	0.25	[14]
Denmark	1.2	0.2	[17]
Australia	1.3	0.07	[21]

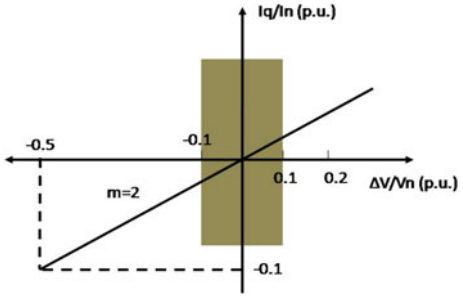

Fig. 6 Reactive current injection requirement in German code [13]

the control potential of new WPPs to support stability during and after system faults. Grid codes of Germany, Spain, UK, and Australia define such regulations on the reactive power response during faults. The Australian grid code demands that if the voltage at PCC drops below 90 %, WPPs must provide capacitive reactive current of at least 4 % of their maximum continuous current for each 1 % reduction in the PCC voltage [21]. Figure 6 shows the reactive current injection rule in the German grid code, which has a similar regulation to the Australian code. However, in the German code, WPP requires the injection of 2 % reactive current for each percent reduction in the PCC voltage [13]. The British and Spanish codes state that WPPs must produce their maximum reactive current during a voltage dip at PCC due to grid fault [14, 19]. Some grid codes also specify the active power recovery time after the fault. The active power recovery requirement in the Irish grid code is stated as-"WTG must be able to provide at least 90 % of its maximum active power within 1 s of the system voltage recovering to the normal operating range" [18].

4.3.4 Repetition of Faults

A distinctive disturbance attribute has been included in the Danish grid code where TSO demands WPPs in operation irrespective of quick repetition of faults. Generally such repetition is the result of unsuccessful line reclosing [6, 17]. According to that code, a wind turbine generation unit must have sufficient capacity to meet

the above mentioned requirements. According to the Danish code, the WPP must have the capacity to withstand the following three independent sequences [23]:

(a) Minimum two single-phase ground faults within 2 min;
(b) Minimum two two-phase short circuits within 2 min;
(c) Minimum three-phase short circuits within 2 min.

5 Grid Codes for Large-Scale PV Plants

A thorough investigation of existing grid codes around the world shows inadequate sets of rules developed for solar PV generation plants [42]. This is also noticeable from Table 7. The reason behind such deliberate development of PV grid codes is that PV generation has developed in a different way, starting with very small units on rooftops connected to the local secondary distribution system. Therefore instead of TSO, the distribution system operators were the first to adopt standards to welcome inverter-based PV generation. Especially, IEEE Std. 1547–2003 [43], has been the established standard governing the connection of distributed resources including PV plants with aggregate capacity of 10 MVA or less at primary or secondary distribution voltage levels in USA. FERC Order 661-A [11] was the first rule to directly impact the interconnection of large RPPs in the transmission system. However it was primarily developed only for WPP integration. On July 2, 2010, the California Independent System Operator Corporation (CAISO) filed [44] with FERC for revisions of its tariff relating to interconnection requirements related to both WPPs and solar PV plants [45]. The TSOs that have incorporated separate rules for large-scale PV integration include—State Grid Corporation of China (China, 2011), CEI (Italy, 2006) and REE (Spain, 2010). Section 3 of Chapter "Frequency Control and Inertial Response Schemes for the Future Power Networks" of Spanish grid code P.O. 12.2 has provided a few guidelines on operating voltage range and control of PV integrated systems. However, this is still in draft form [46]. Several other joint utility groups have drafted similar codes including power factor, voltage support, LVRT, frequency ride through, real power ramping, and curtailment capabilities for PV plants. It is expected that most of these regulations will ultimately be adopted in some form for large-scale PV plants in coming years [45].

6 Summary and Future Trend

As can be seen from the above sections, every grid code reflects the technical features of the individual transmission network. Every network has its own unique technical features to deal with and these special features influence the grid code. The static part of grid code has shown a number of significant aspects including reactive power requirements at PCC as well as continuous voltage and frequency

operating range. It has been observed from Table 2 that in several countries such as Germany, Denmark, and Ireland reactive power is ordered based on the amount of real power generation. In other countries, power factor/reactive power requirements have not been related to real power generation. Continuous voltage operation range has been found to be dependent on voltage level of PCC in Germany, India and UK. In other countries, permitted range of voltage deviation has been found mostly to be ± 10 %. RPPs are required to run continuously between 47 and 52 Hz in Australia and this is the widest frequency range of continuous operation among all the countries discussed. The analysis of the dynamic regulations has shown that (except for UK) a WPP under no circumstances is permitted to trip during the first 150 ms of voltage drop due to a nearby fault. Along with WPP other technologies have also been considered in LVRT requirements of UK and Australia. However, HVRT requirements have been defined in only a few countries including Germany, Spain, Denmark, and Australia.

A thorough analysis of the most recent drafts of international grid codes reveals that more rigorous requirements for RPPs are anticipated to be in place in the upcoming years. In particular, WPPs will be enforced to provide the following support to the grid–inject reactive power during faults, imitate synchronizing power feature, and damp power oscillations. TSOs in Germany, Spain, UK, and Australia have already included reactive power injection features in their updated codes. Recent development with variable-speed wind turbines boost flexible reactive power control capability, which is decoupled to their output active power. Hence, TSOs can willingly rely on those WPPs to further maintain the network voltage stability [47, 48].

Because of the back-to-back converter connection to the grid, variable speed wind turbines as well as solar PV plant operation is fundamentally decoupled from the rest of the grid [49]. In a system with a large share of converter based plants, the lack of synchronizing power results in a reduction of total inertia of the system. To address this problem, some TSOs strongly propose WPPs to have inertia response similar to that of conventional synchronous generators. REE in Spain is an example TSO in this regard. Followed by Denmark, Spain had the highest penetration of wind electricity consumption (15.9 %) among EU countries in 2011 [50]. Spanish regulations on the inertia response set by REE are as follows [14]:

(a) The gains of proportional-integral (PI) controller must be set in a way that the active power output can vary by 5 % within 50 ms. It can be mentioned that an extra PI controller has to be fitted in the WPP control scheme, which acts on the input and changes the output power consequently suppressing the frequency variations [51];
(b) In order to support WPPs, energy storage devices must be used. These devices must inject or absorb at least 10 % of the output active power for 2 s;
(c) Dead-band of frequency variations is equal to ± 10 mHz; and
(d) Inertia response must be disabled for voltage sags below 0.85 p.u.

Ireland and New Zealand are also expected to include similar requirements in their grid codes in the near future.

7 Conclusions

This chapter has revealed the necessity for developing grid standards in integrating RPPs into existing transmission networks. A variety of technical issues such as reactive and real power control, voltage and frequency ride through, and frequency and inertial response have been found to be addressed in the existing international grid codes. However, these regulations are subject to continuous changes. HVRT and reactive power support during the fault period are two major additions in grid codes over the last few years. The authors believe that the comprehensive comparison of principal grid codes presented in this chapter would be beneficial for network operators as well as for manufacturers of RPPs. This study would help new TSOs to develop their requirements and compare them with the requirements set by the TSOs in countries with a large share of renewable power. However, it is worth mentioning that each TSO should develop its own grid codes depending on the availability of renewable resources in the region, strength of existing network, and local utility practices.

References

1. The Clean Energy-Environment Guide to Action: Policies, Best Practices, and Action Steps for States (2006). Available: www.epa.gov/statelocalclimate/resources/action-guide.html
2. Zhu Y, Brown D (2012) Transmission planning studies for grid code compliance. In: IEEE Power and Energy Society General Meeting. San Diego, USA
3. Mohseni M, Islam SM (2011) Comparing technical connection requirements for large wind power plants. In: IEEE Power and Energy Society General Meeting. Detroit, USA
4. Renewables 2013 Global Status Report (2013). Edited by REN21, c/o UNEP, France
5. Ni M, Yang Z (2012) By leaps and bounds: lessons learned from renewable energy growth in China. IEEE Power and Energy Magazine, pp 37–43
6. Ellis A, Walling R, Zavadil B, Jacobson D, Piwko R (2012) Special assessment: interconnection requirements for variable generation. NERC, Atlanta
7. Dudurych IM, Rogers A, Aherne R, Wang L, Howell F, Lin X (2012) Safety in numbers. IEEE Power and Energy Magazine, 10(2):62–70
8. El Itani S, Joós G (2012) Advanced wind generator controls: meeting the evolving grid interconnection requirements. Advances in wind power. Available: cdn.intechopen.com/pdfs/41127/InTech-Advanced_wind_generator_controls_meeting_the_evolving_grid_interconnection_requirements.pdf
9. Mohseni M, Islam SM (2011) International regulations on the transient response of large wind power plants. In: 37th Annual Conference on IEEE Industrial Electronics Society
10. International Grid Code Comparison (IGCC-list) Available: www.gl-group.com/pdf/IGCC_list.pdf
11. FERC Order No. 661-A, Interconnection for wind energy [Online]. Available: www.ferc.gov
12. Technical Rule for Connecting Wind Farm to Power System [Online]. Available: www.cwpc.cn
13. Netzanschlussregeln Hoch-u. Höchstspannung [Online]. Available: www.tennettso.de/site/binaries/content/assets/transparency/publications/grid-connection/tennet-nar2012ger.pdf
14. Datos A Incluir En La Solicitud De Acceso A La Red De Transporte Para Centrales De Generación Fotovoltaica [Online]. Available: www.aeeolica.es

15. Codice di Trasmissione, Dispacciamento, Sviluppo e Sicurezzadella Rete. Terna – G.U.R.I. 2005
16. Indian Electricity Grid Code [Online]. Available: www.powermin.nic.in
17. Regulation TF 3.2.5. Wind turbines connected to grids with voltages above 100 kV [Online]. Available: www.energinet.dk
18. EirGrid Grid Code WFPS1- Wind Farm Power Station Grid Code Provisions [Online]. Available: www.eirgrid.com
19. The Grid Code [Online]. Available: www.nationalgrid.com
20. Wind Power Facility Technical Requirements [Online]. Available: www.aeso.ca
21. National Electricity Rules Version 51, Australian Energy Market Commission (AEMC) 2012
22. Comech MP, García-Gracia M, Arroyo SM, Guillén MÁM (2011) Wind farms and grid codes. From turbine to wind farms—technical requirements and spin-off products. Available: cdn.intechopen.com/pdfs/14825/InTech-Wind_farms_and_grid_codes.pdf
23. Christiansen W, Johnsen DT (2006) Analysis of requirements in selected Grid Codes. Technical university of Denmark (DTU). Available: www.frontwind.com/Analysis%20of%20the%20requirements%20in%20selected%20Grid%20Codes.pdf
24. Piwko R, Meibom P, Holttinen H, Shi B, Miller N, Chi Y, Wang W (2012) Penetrating insights. IEEE Power and Energy Magazine, 10(2):44–52
25. Wu Q, Xu Z, Ostergaard J (2010) Grid integration issues for large scale wind power plants (WPPs). In: IEEE Power and Energy Society General Meeting
26. Rodriguez JM, Alonso O, Duvisonand M, Domingez T (2008) The integration of renewable energy and the system operation: the special regime control centre (CECRE) in Spain. In: IEEE power and energy society general meeting
27. Mohseni M, Islam SM (2012) Review of international grid codes for wind power integration: Diversity, technology and a case for global standard. Renew Sustain Energy Rev 16(6): 3876–3890
28. Hydro-Québec TransÉnergie (2009) Transmission provider technical requirements for the connection of power plants to the Hydro-Quebec transmission system
29. Chang-Chien LR, Yin YC (2009) Strategies for operating wind power in a similar manner of conventional power plant. IEEE Trans Energy Convers 24(4): 926–934
30. Doherty R, Mullane A, Nolan G, Burke DJ, Bryson A, O'Malley M (2010) An assessment of the impact of wind generation on system frequency control. IEEE Power and Energy Society, 25(1):452–460
31. Gautam D, Goel L, Ayyanar R, Vittal V, Harbour T (2011) Control strategy to mitigate the impact of reduced inertia due to doubly-fed induction generators on large power systems. IEEE Trans Power Syst 26(1):214–224
32. El Itani S, Dernbach M, Kosbab M (2012) Supplementary grid functions in DFIG wind turbines to meet Québec's frequency requirements. In: CIGRÉ Canada conference 2012
33. Feltes J, Hendriks R, Stapleton S, Voelzke R, Lam B, Pfuntner N (2012) Twixt land and sea. IEEE Power and Energy Magazine, 10(2):53–61
34. IEEE Std 519–1992 (1993) IEEE recommended practices and requirements for harmonic control in electrical power systems
35. Electricity services association limited (2001) Engineering Recommendation G5/4. London
36. Mueller D, Camm EH (2012) Power quality standards for utility wind and solar power plants. In: IEEE PES Transmission and Distribution Conference and Exposition (T&D). Orlando, USA
37. IEEE Std 1453–2004 (2005) IEEE recommended practice for measurement and limits of voltage fluctuations and associated light flicker on ac power systems
38. IEC 61000-4-15 (2010) Electromagnetic compatibility (EMC) – testing and measurement techniques – flicker meter – functional and design specifications
39. Richard Piwko NM, Thomas Girard R, MacDowell J, Clark K, Murdoch A (2010) Generator fault tolerance and grid codes. IEEE Power and Energy Magazine pp 18–26
40. Aziz T, Saha TK, Nadarajah M (2012) Analysis and mitigation of transient overvoltage with integration of small scale power-electronic interfaced DG. In: IEEE Power and Energy Society General Meeting

41. Wind Generation Task Force1 (2007) The Technical Basis for the New WECC Voltage Ride-Through (VRT) Standard [Online]. Available: www.wecc.biz/library/Documentation%20Categorization%20Files/Guidelines/Voltage%20Ride%20Through%20White%20Paper.pdf
42. International Grid Code Comparison List [Online]. Available: www.gl-group.com/pdf/IGCC_list.pdf
43. IEEE Std 1547–2003 (2003) IEEE standard for interconnecting distributed resources with electric power systems
44. California Independent System Operator Corporation (2010) Tariff amendment to modify interconnection requirements applicable to large generators and request for waiver. FERC docket No. ER10-1706-000
45. Schauder C (2011) Impact of FERC 661-A and IEEE 1547 on photovoltaic inverter design. In: IEEE Power and Energy Society General Meeting
46. Garc′ıa-Gracia Miguel, El Halabi Nabil, Ajami Hassan, Comech Mar′ıa Paz (2012) Integrated control technique for compliance of solar photovoltaic installation grid codes. IEEE Trans Energy Convers 27(3):792–798
47. Kayikci M, Milanovic JV (2007) Reactive power control strategies for DFIG based plants. IEEE Trans Energy Convers 22(2):389–396
48. Konopinski RJ, Vijayan P, Ajjarapu V (2009) Extended reactive capability of DFIG wind parks for enhanced system performance. IEEE Trans Power Syst 24(3):1346–1355
49. Yazdani A, Iravani R (2010) Voltage-sourced converters in power systems: modeling, control, and applications. Wiley, Oxford
50. The European Wind energy association (2012) Wind in power: 2011 European statistics
51. Kayikci M, Milanovic JV (2009) Dynamic contribution of DFIG-based wind plants to system frequency disturbances. IEEE Transactions on Power Systems 24(2):859–867

Resiliency Analysis of Large-Scale Renewable Enriched Power Grid: A Network Percolation-Based Approach

A. B. M. Nasiruzzaman and H. R. Pota

Abstract Recent trend of integrating renewable energy into the power grid poses new challenges like power quality, voltage stability, etc. Due to the intermittent behavior of the renewable energy sources power flow pattern changes continuously throughout the grid which adds more complexity to the grid monitoring and control task. Although the percentage of renewable energy consumption is low in Australia, the electricity generation sector shares a large proportion of the total renewable usage and the usage rate is increasing every year. The constant increase of generation in the existing transmission network creates a huge burden on the system and frequent large-scale contingencies are expected. The trouble encountered in analyzing systems like power grid is that individual behavior of its components is reasonably well understood. It is designed to behave collectively in an orderly fashion but sometimes it shows chaotic, confusing attitude, and sometimes behave destructively like when blackout occurs. Complex network theory provides an alternative but promising platform to analyze networked system like power grid where traditional approach fails to provide solution. In this chapter, a complex network framework-based network resiliency (percolation) analysis has been presented. A topological model of transmission level Australian National Electricity Market (NEM) with projected renewable integration has been simulated. The effects of random and targeted removal of transmission lines or substations on the network structure and functionality have been analyzed. A fast and simple algorithm to analyze percolation on large-scale power grid has also been addressed.

Keywords: Complex network · Cascading failure · Blackout · Percolation

A. B. M. Nasiruzzaman (✉) · H. R. Pota
School of Engineering and Information Technology, The University of New South Wales, Canberra, ACT 2612, Australia
e-mail: nasiruzzaman@ieee.org

H. R. Pota
e-mail: H.Pota@adfa.edu.au

J. Hossain and A. Mahmud (eds.), *Large Scale Renewable Power Generation*, Green Energy and Technology, DOI: 10.1007/978-981-4585-30-9_7,

1 Introduction

Power systems play an indispensable role in modern society. However, there have been several large-scale blackouts in recent years in spite of technological progress and huge investments in system reliability and security. For instance, in August 1996, more than 4 million people in several western states of the USA were out of the power service [1].

In August 2003, a historic blackout was triggered in the power grid of the United States and Canada, which disconnected 61,800 MW of power to an area spanning most of the north-eastern states of the USA and two provinces of Canada, totally containing more than 50 million people [2]. Besides, in the summer and autumn of the year 2003, several large-scale blackouts happened, such as London blackout in the UK, Sweden–Denmark blackout and Italy blackout, etc. [2].

Prevention of large-scale outages is attributed to the security assessment and monitoring system. Recent series of blackouts occurring all over the world shows that the system designated for prevention of blackouts is not working well, which stimulates researchers to seek solutions from alternative means. Recently advances of research in complex network field have attracted the interest of researchers of the power grid to model and analyze the century old power grid under the complex network framework.

In case of a power system, the number of possibilities to be analyzed is huge. Suppose we want to analyze the consequence of every line getting tripped with faults in several locations in the Australian power grid. It is just too complicated, time-consuming, and does not make any sense. So, first of all, from some topological characteristics of the network we have to find few cases which we should study in depth. The number of contingency is too large, somehow we have to decide which contingencies are important and which are not. Complex network framework can be used for this purpose.

If the network structure is known, several measures or matrices could be developed, which can identify particular features of the network. Social scientists have used several centrality measures [3–6] to explain a person's influence within a network. Among these centralities most widely used measures are degree centrality, betweenness centrality, and closeness centrality. To analyze the vulnerability of the power grid or to measure which nodes are more important within a power network, these centrality approaches were used by researchers [7–10]. Some of this research considered the power grid as an abstract network and neglected concrete engineering features, whereas some literature studies considered various features like impedance or admittance of various lines.

Network percolation-based analysis has been carried out in case of the power system [5, 11]; Ref. [5] provided an excellent generalized framework for resiliency analysis for a networked system, but did not consider important vulnerability characteristics for the power system. The theoretical analysis of [11], although promising for planning operation of the power grid, but cannot be used for

dynamic security assessment and monitoring systems, due to negligence of various operating parameters while modeling the power grid.

In this chapter, a percolation-based approach is devised to analyze the resiliency of the power grid. A fast algorithm is formulated to facilitate percolation analysis of large-scale power grids. Various standard IEEE test systems are simulated along with the Australian test system to simulate percolation in real power grids. An analysis of the effect of large-scale renewable energy penetration on the percolation threshold, which is an indicator of network robustness, is carried out at the end.

The rest of the chapter is organized as follows: Sect. 2 discusses the power system model for percolation-based analysis. Section 3 deals with basics of percolation process. Sections 4–6 concern about various centrality measures of the power system. Section 7 provides simulation results, while Sect. 8 concludes the chapter.

2 System Model

In order to analyze the electric power using the network percolation approach, the first thing to do is to construct a graph from the system model [12]. From the perspective of network theory, a graph is an abstract representation of a set of objects, called nodes or vertices, where some pairs of the objects are connected via links or edges.

To portray the assemblage of various components of the power system, engineers use single-line or one-line diagrams, which provide significant information about the system in a concise form [13]. Power is supplied from the generator nodes to the load nodes via transmission and/or distribution lines. The principle of constructing a graph from the single-line diagram of the power grid is described as follows [14]:

- all impedances between a bus and neutral are neglected,
- all transmission and/or distribution lines are modeled except for the local lines in plants and substations,
- all transmission lines and transformers are modeled as weighted lines, the weight is equal to the optimum power flowing in the network, and
- parallel lines between buses are modeled as equivalent single lines.

A power system network is represented by a graph $G = (V, E, W)$ comprising of a set V, whose elements are called vertices or nodes, a set E of ordered pairs of vertices, called edges or lines. An element $e = (x, y)$ of the edge set E, is considered to be directed from x to y; where y is called the head, and x is called the tail of the edge. A set W, whose elements are weights of the edge set elements. There exists a one-to-one correspondence between set E and set W. In this model, we consider the transmission line impedances in pu as weights of the edges between nodes.

Table 1 System data for simple 5 bus system

From bus	To bus	R in pu	X in pu	½ Bin pu
1	2	0.20	0.6110	0.030
1	3	0.08	0.1123	0.025
2	3	0.60	0.5139	0.020
2	4	0.06	0.5663	0.020
2	5	0.04	0.1155	0.015
3	4	0.10	0.5727	0.010
4	5	0.08	0.2725	0.25

Fig. 1 Simple 5 bus system

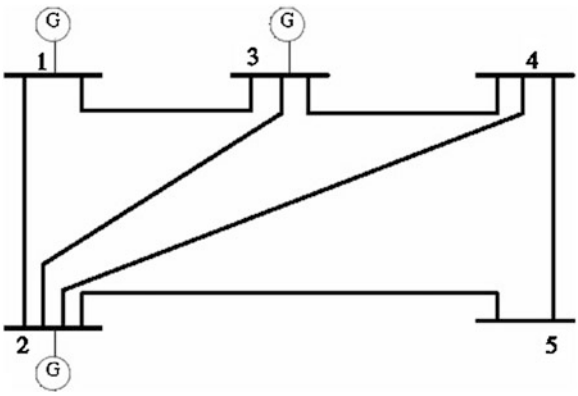

A simple example of 5 bus system [15] is used in this chapter to illustrate various concepts of complex network in the power system. Figure 1 depicts the system with 5 bus bars, and 7 links connecting them. We can model the system as a graph which contains 5 nodes/vertices, which correspond to the slack, voltage-controlled, and load bus bars of the original system. The transmission lines can be represented by the 7 links/edges which connects various nodes. The system data are given in Table 1.

For the network in Fig. 1, $V = \{1, 2, 3, 4, 5\}$, $E = \{(1, 2), (1, 3), (2, 3), (2, 4), (2, 5), (3, 4), (4, 5)\}$, and $W = \{0.20 + j0.61, 0.08 + j0.11, 0.60 + j0.51, 0.06 + j0.57, 0.04 + j0.12, 0.10 + j0.57, 0.08 + j0.27\}$.

3 Percolation and Network Resiliency

The dynamic evolution encountered in a fully connected network, where any node is connected to every other nodes within the network, by removing components from the system, either in a random fashion or following some logic, is called network percolation [5]. The percolation process is divided into two subgroups, depending on the type of component being removed. In case of the power system,

most cascades initiates from malfunctioning of transmission lines or links, but sometimes it is not edges in the network that fail but the vertices, i.e., substations or bus bars in the grid. In order to distinguish these two types of failure involved in the percolation phenomena, we could outline them as edge percolation on one hand and vertex percolation on the other. Historically, in fact, these processes are called bond percolation and site percolation. This nomenclature has been derived from research, in the field of physics and mathematics, on percolation process. In this chapter, we will consider a percolation process, which involves both edge and node removal, consistent with transmission lines tripping and out-of-service substations due to low-voltage or other reasons.

There is more than one way in which vertex or edge removal can be modeled in a power grid. In the simplest form, the components could be removed in a random fashion. We could, for example, take away some specified fraction of the vertices chosen uniformly at random from the entire power grid. This is the most commonly studied form of percolation. There, of course, are many feasible alternatives. One commonly used alternative removal scheme consists of removing vertices or edges according to a centrality measure, e.g., degree centrality or betweenness centrality. For example, components can be removed in order of betweenness from the highest to the lowest. The targeted removal of vertices according to their degree proved to be an effective vaccination strategy for the control of diseases.

By tradition, the probability involved with parameterizing the percolation process is called the occupation probability, ϕ, which is a probability that a bus or line is functional or present in the power grid. Thus, if the power grid is fully functional with all the components operating then the occupational probability $\phi = 1$, no elements are nonfunctional or have been removed, and $\phi = 0$ is an indication that no elements are occupied which may happen when there is a large blackout totally containing the entire grid.

An example of site percolation process is demonstrated in Fig. 2 for IEEE 30 bus test system with 30 nodes and 43 edges. In Fig. 2a, all vertices are present or occupied, they are connected together via transmission lines or edges into a single connected component. Now, if we concentrate on other panels in the same figure, a snapshot of the percolation process is observed. In Fig. 2b, 24 out of 30 vertices are functional, represented by grey color nodes, giving an occupation probability of $\phi = 0.80$. Six nonfunctional nodes knocks down 12 adjacent edges, the removed transmission lines are represented by light grey-colored edges. The remaining vertices still compose a single connected component through the intact edges. Figure 2c shows a situation during the percolation process, where more vertices along with associated edges have been removed, and the remaining vertices are no longer connected together. The vertices are split into two small components. In Fig. 2d, all vertices have been removed and the network collapses.

The process that is demonstrated in this small example is a typical percolation behavior. When ϕ is large, close to unity, the vertices tend to be connected together forming a giant connected component spanning most the grid. As the occupation probability decreases, for some reason or the other, the cohesiveness of

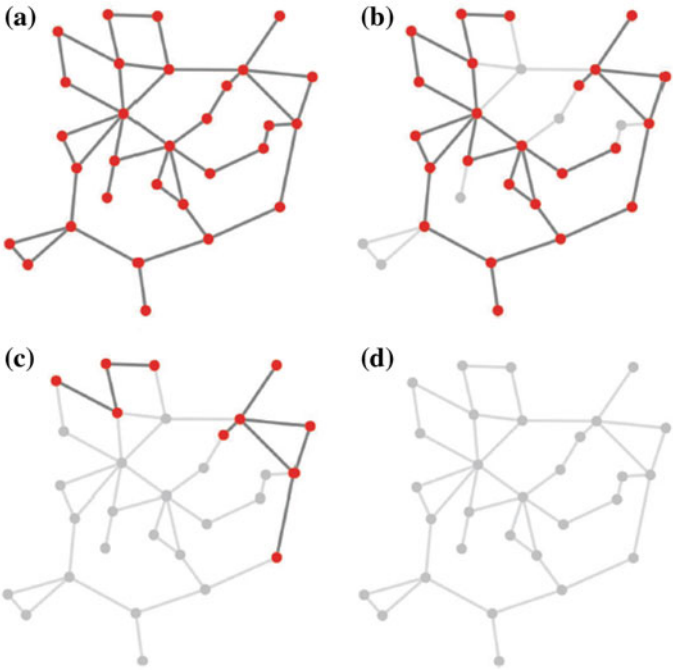

Fig. 2 An example of the site percolation process in the IEEE 30 bus test system for various values of occupation probability ϕ. *Red vertices* are functional nodes of the system, whereas *grey vertices* are nonfunctional. *Light watermark-like color*, in case of edges, denotes edges that have been removed, and *dark colored edges* represent those that are still present in the grid

the grid decreases, and the grid can no longer function as a single entity and collapses into various small components. The process can be understood in a reverse fashion, when the occupation probability, ϕ is low many small components exist in the network, and with the increase in the occupation probability small components are merged together to form a single large connected component, occupying the whole network.

Evolution of the power grid can be thought of as the building dynamics of the connected components in the network. In the early days of the electricity generation, generators supplied local areas only building a locally distributed small-connected components spanning various regions of a continent. As the technology flourished, with the invent of transformer, long distance power transmission was made possible. The grid began to form expand in size and number of components and finally giving rise to a massive machine running in unison with hundreds of thousands of components connected altogether.

Interconnection has many benefits such as fewer generation capacity required as a reserve for peak load and spinning reserve, economical and reliable energy generation and transmission to name a few. But the advantages come with a great adversity of large-scale blackouts, where small initial failure in amplified and

large-scale cascades are propagated through the system. This process of cascading can be compared with the percolation phenomenon. Generally, the power grid runs as a single component with every substations and transmission lines fully functional, resembling the percolation process sub case as shown in Fig. 2a and $\phi = 1$. Failure of a single transmission line or substation produces stress on the system because the load of the failed component is shifted upon the occupied ones. During a much stressed condition, the system operating in a heavily loaded condition, the shift of load may exceed the safe operating limit of some components and those may fail consequently, exerting even more stress on the grid. This chain of event continues and the grid in broken down with small connected components serving only local loads, similar to the percolation phenomenon with the occupation probability, $0 < \phi < 1$. In an extremely bad condition, the process of cascading proceeds even further giving birth to entire system collapse, as in the percolation process with $\phi = 0$.

The creation and demise of the giant component during the percolation process is known as a percolation transition. The point at which the percolation transition occurs is called the percolation threshold. The threshold value of the occupation probability suggests different aspects of grid robustness and vulnerability. Larger values of ϕ in the percolation threshold indicate the system is more vulnerable than the system with lower critical occupational probability, ϕ_{cr}. Removal of very few nodes breaks the cohesiveness of the grid and makes the system nonfunctional, where ϕ_{cr} is very high. Lots of components, within the grid, have to run properly in order to maintain the functionality of this type of system. On the other hand, systems with low critical occupational probability show a great degree of robustness. In order to reduce the functionality of these types of networks, lots of components have to be taken out, making the system less vulnerable to random attacks.

In percolation studies the term "component" is used to indicate the connected portion of the unaffected network, whereas "cluster" refers to the components that exist in the network after and during the breakdown process. In this chapter, we will use the term "component" to refer to connected group of vertices (substations, bus bars, generators, and loads) on the original network before any vertices or edges have been removed and "cluster" to refer to those after removal.

Delivery of electricity to the consumer end is the function of the overall power grid. Power companies and consumers are mainly concerned about providing sufficient power to the consumers, not the connectivity of the grid after failure. As it turns out, the nature in which the power grid is evolved gives the power grid sufficient robustness to deliver local power even if there is a cascade going on within the system. The total capacity of the connected generators within the disconnected area must be greater than the local load demand in order to maintain the balance of consumed and generated power.

Figure 3 illustrates the situation in case of a two cluster power grid. Both cluster 1 (C1) and cluster 2 (C2) are capable of maintaining the local load demands, but the use of a simple topological measure gives a different picture. C1 contains 252 nodes and 458 links, whereas the second cluster C2 has 183 vertices and 253 links.

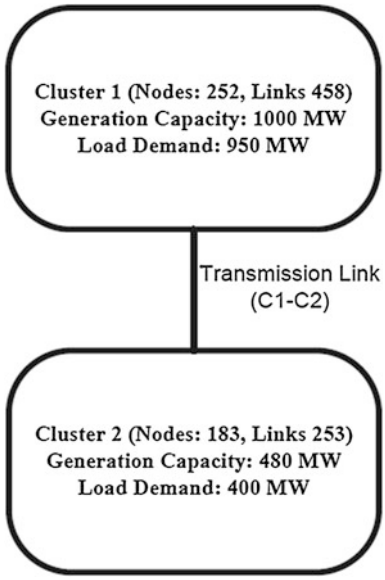

Fig. 3 Disadvantage of using size of largest cluster for power grid vulnerability analysis

The load and generation capacity of the two clusters are 950, 1,000 MW, and 400, 480 MW, respectively. Removal of C1–C2 transmission link makes the size of the largest component to shrink to 0.57, almost 40 % loss of the system functionality, but both of the clusters have ample reserve to supply local demand. Hence, size of largest cluster may not be a good indication of topological vulnerability [16].

Researchers have proposed many alternative definitions of network robustness which are described below:

Loss of load for any disconnected cluster i, ΔL_i, is [16]:

$$\Delta L_i = \begin{cases} D_i - C_i & \text{if } D_i > C_i \\ 0 & \text{if } D_i \leq C_i \end{cases} \tag{1}$$

where, C_i and D_i are the capacity of the generators and the demand of loads in the ith cluster while the cascade is in progress. The loss of load for the whole system, LOL, can be calculated as follows:

$$\text{LOL} = \frac{1}{D} \sum_{i=1}^{s} \Delta L_i \tag{2}$$

where, D is the total load demand before the failure.

The grid demanded load, GDL, is the sum of the power generated from all the generators g_i, $i = 1, 2, \ldots, N_G$:

$$\text{GDL} = \sum_{i=1}^{N_G} g_i. \tag{3}$$

The grid received load, GRL, is the sum of power received at load nodes $l_i, i = 1, 2, \ldots, N_L$:

$$\text{GRL} = \sum_{i=1}^{N_L} l_i. \tag{4}$$

The grid lost load, GLL, is obtained from the difference of the GDL, and the GRL:

$$\text{GLL} = \text{GDL} - \text{GRL}. \tag{5}$$

The grid service efficiency, GSE, is obtained from the ratio of two powers—the GRL, to the GDL [17, 18]:

$$\text{GSE} = \frac{\text{GRL}}{\text{GDL}}. \tag{6}$$

In this chapter, we have used size of largest cluster along with grid service efficiency as a network performance indicator.

4 Measure of Connectivity-Degree Centrality

Degree centrality is the simplest form of centrality measures for networks. Although it is very simple, it has a great significance. It represents the connectivity of a node to the network [19]. Individuals who have more links with other persons are more connected to the network in the sense that they have more resource, access of information than others. A nonsocial network example is the use of citation counts in the evaluation of scientific papers. The number of citations of a paper can be regarded as its impact on research [20]. For example, node 2 in Fig. 1 is adjacent to four other nodes, it's degree is four. In a 5 node graph, any node can be adjacent to only remaining four nodes. So, this node has got highest connectivity. In some literature studies, degree centrality is defined as:

$$C_D(k) = \frac{deg(k)}{n-1} \tag{7}$$

where, $deg(k)$ is the degree of node k. In case of electrical network, the power flowing in the adjacent links of the node in concern can be regarded as a degree of the node and the definition of the electrical degree centrality can be given as:

$$C_D^E(k) = \frac{\sum_{k \sim t} P_{kt}}{n-1} \tag{8}$$

where, $k \sim t$ indicates that node k are t are connected. P_{kt} indicates the power flowing in line connected in between nodes k and t. Table 2 shows the degree centrality of simple 5 bus system in Fig. 1 using classical and proposed approach.

Table 2 Degree centrality for network in Fig. 1

Bus	$C_D(k)$	$C_D^E(k)$
1	0.50	21.58
2	1.00	42.33
3	0.75	16.13
4	0.75	40.13
5	0.50	15.80

5 Measure of Independence-Closeness Centrality

This approach of centrality measure is based upon the degree to which a node is close to all other nodes in the network [3]. Figure 4 shows closeness in a classical sense and to illustrate the idea of electrical closeness centrality, Fig. 5 is drawn to show the closeness of various nodes of the simple 5 bus system in Fig. 1 in terms of electrical distance found in Table 1. It is clear from Fig. 5 that node 2 is adjacent to three other nodes (nodes 1, 3 and 4) in terms of electrical distance, while nodes 1, 3, and 4 being adjacent to two nodes. Node 5 is adjacent to one node only. So node 2 is the closest to other nodes than the rest of the nodes in the network.

In the social network theory, closeness is a sophisticated measure of centrality. It is defined as the mean geodesic distance (i.e., the shortest path) between a vertex k and all other vertices reachable from it [21]. In mathematical form, the closeness centrality of a vertex k, $C_C(k)$ in a network of n vertices is given by:

$$C_C(k) = \frac{\sum_{t \in V \backslash k} d(k,t)}{n-1} \tag{9}$$

where, $d(k,t)$ being the shortest path length between vertices k and t. This definition of closeness centrality gives a measure of distance of particular vertex from other vertices. So, some researchers have used the reciprocal of the shortest path to quantify closeness centrality as follows:

$$C_C(k) = \frac{1}{\sum_{t \in V \backslash k} d(k,t)}. \tag{10}$$

The electrical closeness centrality was defined as [10]:

$$C_{C_z}(k) = \frac{n-1}{\sum_{t \in V \backslash k} d_z(k,t)} \tag{11}$$

where, $d_z(k,t)$ is taken as the shortest electrical distance between nodes k and t. Resistance was neglected since they considered only transmission systems; but in order to generalize the concept in both transmission and distribution system we cannot neglect resistance of the network lines, which is a significant portion of the line impedance in case of distribution lines. The numerator was taken as $n-1$.

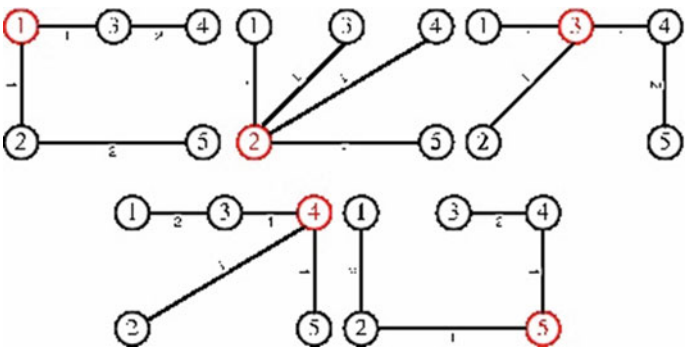

Fig. 4 Classical closeness of various nodes of the simple 5 bus system

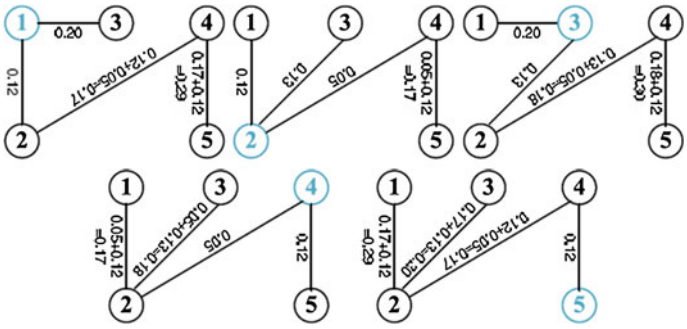

Fig. 5 Electrical closeness based on line impedance of various nodes of simple 5 bus system

This was adopted in (9) to average the distance, but when it comes in the numerator it just scales the parameter. So, in this chapter, we propose our electrical closeness centrality as:

$$C_C^E(k) = \frac{1}{\sum_{t \in V \setminus k} d(k,t)} \tag{12}$$

where, $d(k,t)$ is the weight of the shortest electrical path from node k to all other nodes t reachable from k.

Table 3 shows the closeness centrality of simple 5 bus system in Fig. 1 in classical as in (10) and proposed approach.

The independence of a node is determined by the closeness centrality of the node [3]. In Fig. 1, node 2 is in direct contact with nodes 1, 3 and 4. It must depend upon node 4 to communicate with node 5. So, node 5 needs only one relayer to communicate with all other nodes of the network. On the other hand, node 1 needs node 2 to communicate with node 4 and both need 2 and 4 to communicate with

Table 3 Closeness centrality for network in Fig. 1

Bus	$C_C(k)$	$C_C^E(k)$
1	0.17	1.28
2	0.25	2.13
3	0.20	1.23
4	0.20	1.92
5	0.17	1.14

node 5. So we can say that node 2 is more independent than node 1. So closeness centrality can be used to quantify independence of various nodes within an electrical power grid.

6 Measure of Control of Communication-Betweenness Centrality

This type of centrality is based upon the frequency with which a node falls between pairs of other nodes on the shortest or geodesic paths connecting them [3]. This idea is illustrated by 10 possible shortest paths in the network of Fig. 1 as shown in Fig. 6. Node 2 comes four times between other points in the six geodesics. Node 4 comes three times. So node 2 is more central in terms of betweenness.

The betweenness centrality $C_B(k)$ for vertex k is computed as follows [21]:

1. Find the shortest path set of the network.
2. Find out the fraction of the shortest path containing node k for each pair of vertices.
3. Sum this fraction over all pairs.

Mathematically,

$$C_B(k) = \sum_{s=1}^{n} \sum_{t=1}^{n} \frac{\sigma_{st}(k)}{\sigma_{st}}, s \neq t \neq k \in V \tag{13}$$

where, σ_{st} is the number of shortest paths from s to t, and $\sigma_{st}(k)$ is the number of shortest paths from s to t that pass through a vertex k.

As in closeness centrality the shortest paths for an electrical network can be calculated from the line impedance, and the power flowing in the line is taken as a measure of betweenness [14]. The electrical betweenness centrality of a node k in a network of n nodes is defined as:

$$C_B^E(k) = \sum_{s=1}^{n} \sum_{t=1}^{n} \frac{P_{st}(k)}{P_{st}}, s \neq t \neq k \in V \tag{14}$$

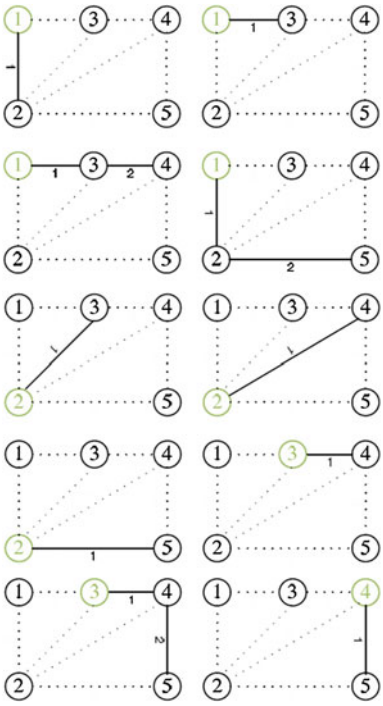

Fig. 6 Illustration of betweenness in 10 possible shortest path set of the test system

where, P_{st} is the maximum power flowing in the shortest electrical path between buses s and t, and $P_{st}(k)$ is the maximum of inflow and outflow at bus k within the shortest electrical path between buses s and t. Figure 7 illustrates the concept of electrical shortest path and shows 10 possible geodesics in the simple 5 bus test system.

Table 4 shows the betweenness centrality of simple 5 bus system in Fig. 1 using classical and proposed approach (Tables 5, 6, and 7).

7 Simulation Results

Network percolation can be implemented in many ways. In this chapter, we have implemented a method which is computationally efficient making it applicable for on line processing of information while cascade in progress. The process of percolation can be implemented as follows:

1. Consider an empty network.
2. Initialize $c = 0$, where c represents the number of cluster in the network.
3. Choose the order of addition of vertices in the empty network.

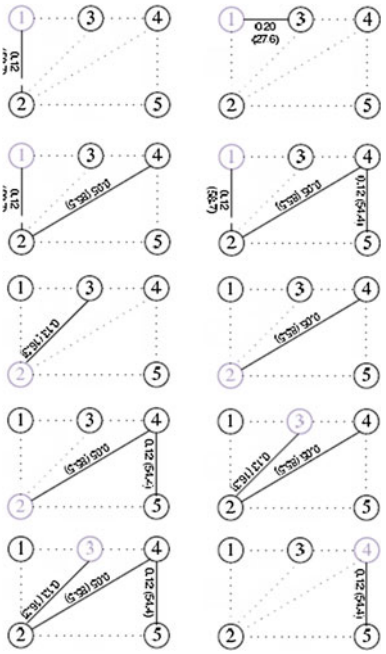

Fig. 7 Ten possible shortest path set in terms of electrical distance in simple 5 bus system

Table 4 Betweenness centrality for network in Fig. 1

Bus	$C_B(k)$	$C_B^E(k)$
1	$\frac{0}{10}$	$\frac{0}{670}$
2	$\frac{1}{10}$	$\frac{192}{670}$
3	$\frac{1}{10}$	$\frac{0}{670}$
4	$\frac{1}{10}$	$\frac{93.3}{670}$
5	$\frac{0}{10}$	$\frac{0}{670}$

Table 5 Top ten critical nodes according to degree centrality of various standard IEEE test systems

30 Bus	$C_B^E(k)$	57 Bus	$C_B^E(k)$	118 Bus	$C_B^E(k)$
2	12.5841	1	7.9668	12	12.2114
6	9.2330	4	5.3512	69	5.6372
1	9.0528	2	4.9898	70	5.1916
4	7.0180	3	4.4910	80	4.8233
3	5.7375	15	3.9604	7	4.7227
5	3.7382	6	3.5725	11	4.7200
10	2.4665	17	3.4561	32	4.4156
9	2.3013	24	2.9787	46	4.1532
7	2.2122	23	2.0769	75	3.8160
12	2.1811	13	2.0628	34	3.2639

Table 6 Top ten critical nodes according to closeness centrality of various standard IEEE test systems

30 Bus	$C_C^E(k)$	57 Bus	$C_C^E(k)$	118 Bus	$C_C^E(k)$
6	2.2366	14	1.7785	65	3.0553
4	2.1676	13	1.7596	68	3.0249
28	2.0587	46	1.7399	116	2.9884
8	2.0438	47	1.7120	81	2.9366
3	2.0108	48	1.7042	38	2.8773
9	2.0029	15	1.6993	64	2.8353
10	1.9662	38	1.6775	69	2.8298
7	1.9069	11	1.6663	80	2.8158
12	1.8110	3	1.6167	66	2.8119
21	1.7877	12	1.6149	30	2.7189

Table 7 Top ten critical nodes according to betweenness centrality of various standard IEEE test systems

30 Bus	$C_B^E(k)$	57 Bus	$C_B^E(k)$	118 Bus	$C_B^E(k)$
2	0.6117	1	0.6117	12	0.7030
1	0.5546	2	0.4862	7	0.4331
6	0.3114	17	0.4142	11	0.4310
4	0.3103	3	0.3380	2	0.3431
3	0.2972	15	0.2271	3	0.0780
5	0.1668	16	0.1427	6	0.0629
7	0.0547	4	0.1398	14	0.0350
8	0.0490	6	0.0566	117	0.0340
9	0.0420	14	0.0544	13	0.0286
10	0.0406	5	0.0498	4	0.0219

4. According to the order add next vertex to the network, and increase c by one.
5. Label the vertex with label c. This number represents the cluster of the vertex.
6. Investigate edges attached to the vertex one after another.
7. If the vertex at the other end of the edge has been added earlier, add the edge to the network.
8. Examine the cluster label of the vertices at either end of the edge.
9. If the cluster labels are the same, do nothing.
10. If the labels are different, choose one of the clusters and re-label all its vertices to have the same label as the other cluster.
11. Update the cluster size record to be equal to the sum of the sizes of the two parent clusters.
12. Repeat from step 4, until all the vertices have been added.

The test systems used for the percolation analysis are standard IEEE test systems [22] and the Australian power grid [23]. Figure 8 is the topological representation of the Australian power grid. The Australian power grid operated under the National Electricity Market (NEM) is the world's longest interconnected

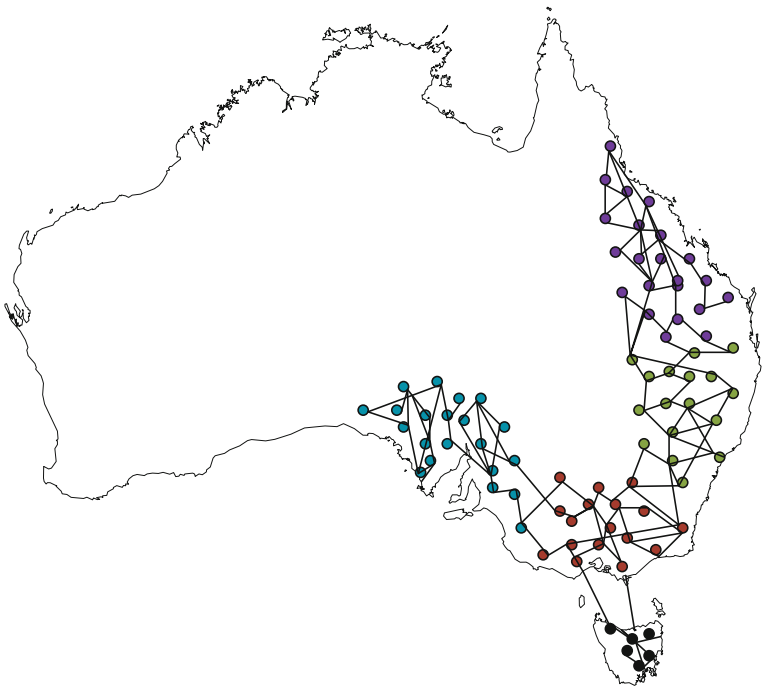

Fig. 8 Topological representation of the Australian electricity grid

power system that runs for more than 5,000 km from Port Douglas in Queensland to Port Lincoln in South Australia and supplies more than 10 billion electricity annually to meet the demand of more than 8 million end users [23]. NEM interconnects five regional market jurisdictions including Queensland, New South Wales, Victoria, South Australia, and Tasmania.

Figure 9 is the result of percolation process carried out in the Australian test system, with random node and line removal. The results shown are averaged over 1,000 random simulations. It is clear from the result that GSE is a good measure of network robustness, since although the network seems to breaks down around $\phi = 0.6$ in case of largest cluster-based analysis; but the network can perform well beyond that point since the percolation threshold is around $\phi = 0.5$ as shown in Fig. 8.

Next, the penetration levels of renewable are varied for the Australian test system and percolation thresholds are calculated. It is found that, as given in Table 8, the threshold increases with increase of penetration, which implies increased vulnerability of the power grid with large-scale penetration of excess energy in the existing grid. Afterwards, nodes and edges are removed from the system according to various centrality measures, and it is found that network is

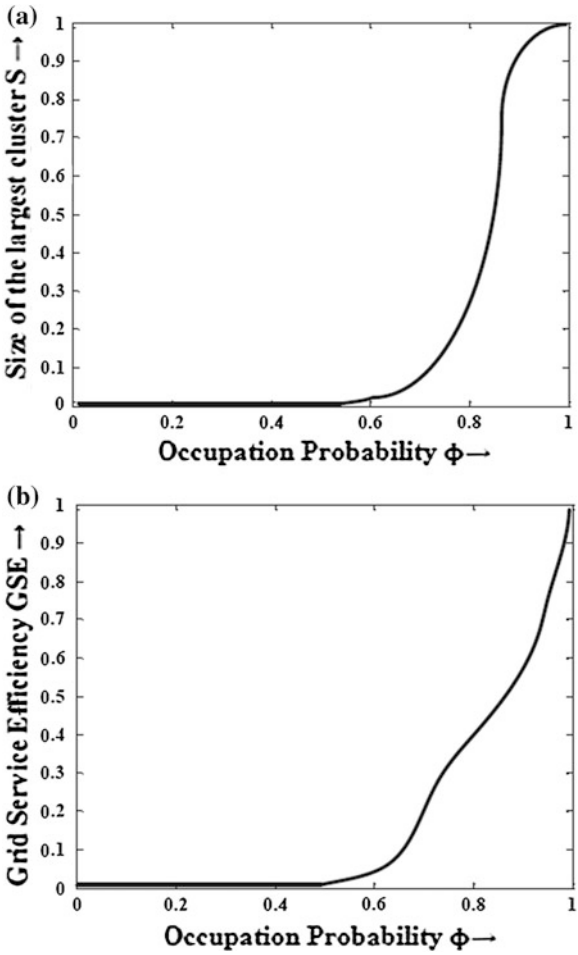

Fig. 9 Percolation in the Australian test system

Table 8 Percolation threshold for various penetration levels

Penetration (%)	Threshold
0	0.5
10	0.55
25	0.65
50	0.72
70	0.80

hampered much is betweenness-based attacks are carried out on the system. This result, shown in Fig. 10, gives us an opportunity to allocate our resources to regularly monitor and service critical elements.

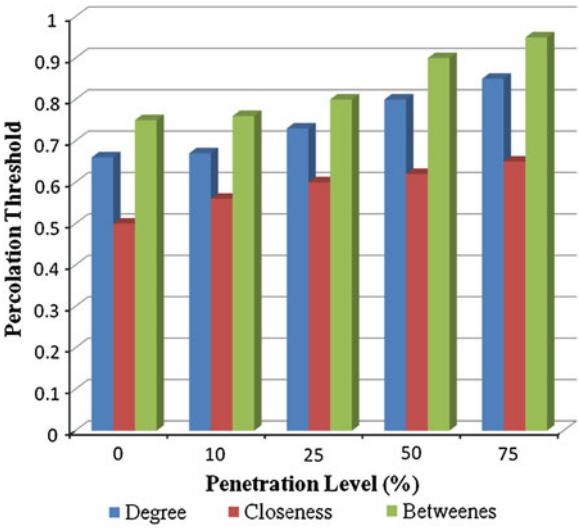

Fig. 10 Relation of percolation threshold with centrality measure

8 Chapter Summary

This chapter provides a novel approach of network resiliency analysis of the power grid, employing complex network framework-based percolation method. An efficient algorithm is used to assess the vulnerability of the Australian power grid with large-scale renewable generation capacities. Our analysis finds that, although renewable energy have many advantages, and the target is to incorporate more and more renewable within the grid, but increased penetration caused vulnerability in a greater scale. Also, it is found that betweenness-based targeted attack reduces the functionality of the system to a great extent. Preventive measures should be taken so that critical components could be protected in order to ensure secure operation of the power grid.

References

1. Kosterev DN, Taylor CW, Mittelstadt WA (1999) Model validation for the august 10, 1996 WSCC system outage. IEEE Trans Power Syst 14(3):967–979
2. Andersson G, Donalek P, Farmer R, Hatziargyriou N, Kamwa I, Kundur P, Martins N, Paserba J, Pourbeik P, Sanchez-Gasca J, Schulz R, Stankovic A, Taylor C, Vittal V (2005) Causes of the 2003 major grid blackouts in North America and Europe, and recommended means to improve system dynamic performance. IEEE Trans Power Syst 20(4):1922–1928
3. Freeman LC (1979) Centrality in social networks: i conceptual clarification. Soc Netw 1(3):215–239
4. Girvan M, Newman MEJ (2002) Community structure in social and biological networks. Proc Natl Acad Sci USA 99(12):7821–7826

5. Newman MEJ (2005) A measure of betweenness centrality based on random walks. Soc Netw 27(1):39–54
6. Rajasingh I, Rajan B, Florence IsidoD (2009) Betweeness-centrality of grid networks. In: Proceedings of IEEE ICCTD'09, Kota Kinabalu, Malaysia, pp 407–410
7. Gorton I, Huang Z, Chen Y, Kalahar B, Jin S, Chavarría-Miranda D, Baxter D, Feo J (2009) A high-performance hybrid computing approach to massive contingency analysis in the power grid. In: Proceedings of IEEE e-Science'09, Oxford, UK, pp 277–283
8. Hines P, Blumsack S (2008) A centrality measure for electrical networks. In: Proceedings of IEEE Hawaii international conference on system sciences'08, Waikoloa, HI, pp 1–8
9. Torres A, Anders G (2009) Spectral graph theory and network dependability. In: Proceedings of IEEE DepCos-RELCOMEX'09, Brunów, Poland, pp 356–363
10. Wang Z Scaglione A, Thomas RJ (2010) Electrical centrality measures for electric power grid vulnerability analysis. In: Proceedings of IEEE CDC'10, Atlanta, GA, pp 5792–5797
11. Xiao H, Yeh EM (2011) Cascading a percolation-based analysis. In: IEEE international conference on communications workshops (ICC)
12. Chen G, Dong ZY, Hill DJ, Zhang GH (2009) An improved model for structural vulnerability analysis of power networks. Physica A Stat Mech Appl 388(19):4259–4266
13. Stevenson WD (1982) Elements of power system analysis. Mcgraw-Hill Book Company, New York
14. Nasiruzzaman ABM, Pota HR (2011) Transient stability assessment of smart power system using complex networks framework. In: Proceedings IEEE PESGM'11, Detroit, MI, pp 1–7
15. Saadat H (2002) Power systems analysis of Mcgraw-Hill series in electrical and computer engineering. McGraw-Hill, New York
16. Wang K, Zhang B, Zhang Z, Yin X, Wang B (2011) An electrical betweenness approach for vulnerability assessment of power grids considering the capacity of generators and load. Physica A: Stat Mech Appl 390(23â€“24):4692–4701
17. Zio E, Piccinelli R (2010) Randomized flow model and centrality measure for electrical power transmission network analysis. Reliab Eng Syst Saf 95(4):379–385
18. Zio E, Piccinelli R, Delfanti M, Olivieri V, Pozzi M (2012) Application of the load flow and random flow models for the analysis of power transmission networks. Reliab Eng Syst Saf 103:102–109
19. Lewis TG (2011) Network science: theory and applications. Wiley, Hoboken
20. Newman M (2009) Networks: an introduction. OUP, Oxford
21. Centrality, Retrieved 23 Aug 2013. http://en.wikipedia.org/wiki/Centrality
22. IEEE power system test case archieve, Retrieved 23 Aug 2013. http://www.ee.washington.edu/research/pstca
23. National transmission network development plan, Retrieved 23 Aug 2013. http://www.aemo.com.au/Electricity/Planning/National-Transmission-Network-Development-Plan

Frequency Control and Inertial Response Schemes for the Future Power Networks

F. Gonzalez-Longatt

Abstract Future power systems face several challenges: (i) the high penetration level of renewable energy from highly variable generators connected over power converters, (ii) several technologies for energy storage with very different time constants, some of them using power converters as an interface to the grid, and (iii) a pan-European transmission network facilitating the integration of large-scale renewable energy sources and the balancing and transportation of electricity based on underwater multi-terminal high voltage direct current (MTDC) transmission. All of them have an element in common, high power converters that decouple the new energy sources from the pre-existent AC power systems. During a system frequency disturbance, the generation/demand power balance is lost, the system frequency will change at a rate initially determined by the total system inertia. However, future power systems will increase the installed power capacity (MVA) but the effective system inertial response will stay the same nowadays, because the new generation units based on power converters creates a decoupling effect of the real inertia and the AC grid. The result is deeper frequency excursions of system disturbances. A considerable reduction in the ability to overcome system frequency disturbances is expected, the inertia response may be decreased. The aim of this chapter is to present the fundamental aspects of system frequency control and inertial response schemes for the future power networks.

Keywords Frequency controller · Frequency stability · Future power networks · Power system · Protection scheme · Wind turbine generator

F. Gonzalez-Longatt (✉)
Faculty of Engineering and Computing, Coventry University, Priory Street, Coventry CV6 3FG, United Kingdom
e-mail: fglongatt@fglongatt.org

J. Hossain and A. Mahmud (eds.), *Large Scale Renewable Power Generation*, Green Energy and Technology, DOI: 10.1007/978-981-4585-30-9_8,

1 Introduction

Electrical power systems have been developed, over more than 50 years, to deliver electricity to the end users. This approach requires to use a vital infrastructure to link the producers of the electric energy and the consumers [1]. This approach of power systems design and operation has served their purpose with great success for many decades mainly because they were developed to meet the needs of large and predominantly carbon-based energy producers located remotely from the load centers. Nowadays, governments around the world are striving toward three key issues:

- **Climate change**. The climate conference in Kyoto for the first time had internationally binding targets for the reduction of greenhouse gases like carbon dioxide, methane, nitrous oxide, hydro fluorocarbons, and sulfur hexafluoride until 2012 by 5.2 % compared to 1990. The United Nations Climate Change Conference was held in Cancun in 2010 [1], and it agreed only to continue the implementation of the Kyoto Conference without setting new targets for the period after 2012. However, the *European Union* (EU) has been seriously committed to CO_2 reduction. In 2007, it agreed to the target triple of *supply, competitiveness, environment*, to reduce the CO_2 emissions by 2020 by at least 20 % compared to 1990. Several scientific works argue that this would not be sufficient to limit the effect of warming process in reach heating of the atmosphere within 2 °C. For this reason, the EU considered to increase the reduction target to 30 % by 2020. By 2040, emissions are to be reduced by 60 %. With the use of appropriate technologies, no CO_2 should be emitted any more by the power generation industry by 2050 [2]. Reducing the greenhouse gas emissions by 80 % is the specific target of the UK government by 2050 [3]. This target on the country's emission reduction targets is defined in the Climate Change Act 2008 [4]. De-carbonizing the power sector is the key factor to reach this objective, and will enable further low-carbon choices in the transport sector (e.g., plug-in hybrid and electric vehicles) and in buildings (electric heat pumps).
- **Energy security**. Over the coming decades, governments around the world face the daunting challenge of meeting the energy needs of a growing and developing world population while mitigating the impacts of global climate change. Security of supply is an important goal of energy policy in many countries around the world. The importance of energy security derives from the critical role that energy plays in all aspects of everyday and business life [5]. As demand for resources rises within today's turbulent global markets, supply chain vulnerability is becoming a significant issue. Global sourcing has created more complex and increasingly risky supply chains. Severe energy security has serious implications for social, environmental, and economic well-being. The conversion of the centralized power generation structures with the consumption of mostly imported primary energy like coal, oil, gas, and uranium to more decentralized renewable power plant systems opens the chance of reducing the import dependence from fossil energy sources. Europe as a whole is a major

importer of natural gas. Although second to Norway as a supplier to Europe, Russia remains one of Europe's most important natural gas suppliers. Europe's natural gas consumption is projected to grow while its own domestic natural gas production continues to decline. Increasing energy efficiency is clearly the most cost-effective part of the energy revolution. Overall, in the EU the possible energy savings by energy efficiency measures and in the energy conversion process of coal, oil, gas, and uranium to electricity and heat are twice as much the energy generation potential of renewables. The EU Directive on the *Energy Performance of Buildings* (EPBD) [6] provides the guidelines for the reduction of 40 % of the total energy consumption in the EU. This is also true for the electricity consumption. The European Commission published in 2011 a proposal for a Directive on Energy Efficiency in order to achieve the 20 % saving goal of the EU until 2020, where a broad mix of measures are proposed. The UK government has been working on energy security for years, making sure consumers can access the energy they need at prices that are not excessively volatile. It has been reached by a combination of its liberalized energy markets, firm regulation, and extensive North Sea resources. The Department of Energy & Climate Change of UK is actively working in several aspects to guarantee that the energy system has adequate capacity and is diverse and reliable [7].

- **Economic development**. Development of the electric power system must contribute to growth and minimize costs to the consumer. A right balance between investing in generation, nongeneration balancing technologies (i.e. storage, demand-side response, and interconnection), and network assets is necessary. In addition, efficient operation of the power systems is critical to maximizing the efficient use of assets across the system. When conventional power is substituted by wind power, the avoided cost depends on the degree to which wind power substitutes each of three components—fuel cost, O&M costs, and capital. The economic competitiveness of wind power generation will depend on short-term prediction, and specific conditions for budding into short-term forward and spot markets at the power exchange. Some calculations demonstrate that although wind power might be more expensive than conventional power today, it may nevertheless take up a significant share in investors' power plant portfolios as a hedge against volatile fossil fuel prices [8]. Continuing research and development work is needed in order to ensure wind power is to continue reducing its generation costs for sustainable economy growth.

Whilst current networks presently, fulfill their function, they will not be sufficient to meet the future challenges as described above. These challenges require technical, economic, and policy developments in order to move toward lower carbon generation technologies as well as higher efficiency devices and systems.

The radical changes that power systems are undergoing will change the landscape of the future power networks; they face several technical challenges characterized by:

a. **High penetration levels of renewable energy from highly variable generators connected over power converters**. Changes in generation portfolio of power systems will be occurring at a time when the demand on the system is expected to increase significantly. If the environmental targets that are being imposed on the operation of power systems are to be met then large scale, more than 50 GW, renewable generation must become commonplace in the future power system. Wind generation, either onshore or offshore, is currently the primary scalable renewable generation technology that is commercially available. The future targets for installing wind power in GB are: total of 26 GW (9 GW onshore and 17 GW offshore) of wind generation by 2020 and 47 GW (10 GW onshore and 37 GW offshore) of wind generation by 2030 [9]. The very fast development of fully rated converter wind turbine generator offers both enlarged capabilities and lower price per MW capacity. Increasing the penetration levels of power converter-based wind power will produce a displacement of traditional synchronous generation services without offering equivalent technical performance.
b. **Technologies for energy storage with very different time constants, some of them use power converters as an interface to the grid**. One of the greatest challenges of operating a power system is that electrical energy cannot be directly stored. Power systems must keep a balance between power generation and demand in the system in real time. This balance will become complex in the future power systems due to issues such as high variability provided by renewable energy resources. *Electricity storage system* (ESS) enables electricity that is generated at a point of low demand to be used at a time of high demand and allows the operator to capture the difference between prices at their peak and trough. Large-scale storage (*bulk*) is connected to the transmission system and tends to have relatively large power output and long periods over which that power can be provided. Storage systems can also operate on a smaller scale (*distributed*) connected to the distribution network. Energy storage technologies have the potential to support the future system integration. Preliminary analysis in UK suggests an additional storage could be installed in the range of 1–29 GW under certain future scenarios by 2050, of which distribution storage is estimated to dominate the bulk storage, due to the savings from avoided distribution network costs [10]. There are several technologies already commercially available for distributed and bulk ESSs. However, they are technically and/or economically very different between them, and there is expectation for radically different and new technologies. Technologies will respond accordingly to provide a secure and an economical operation; they have a very different time response and interface to power system creating a complex situation in terms of operation and control.
c. **A pan-European transmission network facilitating the integration of large-scale renewable energy sources and the balancing and transportation of electricity based on underwater multiterminal high voltage direct current (MTDC) transmission**. Interconnection allows connected markets to import and export electricity according to the market prices on either side of the

interconnector. Increased amounts of interconnection have the potential to bring savings to the system where connected markets have different generation and/or demand profiles to trade. In such circumstances, interconnection could result in generation capacity being dispatched more efficiently and reducing the total generation capacity required. The existing power grid in Europe is a highly interconnected system, spanning the whole of Continental Europe with connections to neighboring systems, e.g., in Scandinavia (Nordel), the UK, and Russia. The current structure of this meshed, supranational system was largely influenced by available generation technologies. The UK electricity network is connected to the systems in France (National Grid and Réseau de Transport d'Electricité, 2 GW), Northern Ireland (IFA, 2 GW), and the Netherlands (BritNed, 1 GW) through "interconnectors," with others under construction or planned. Potential future interconnector opportunities include interconnectors between UK and Belgium (Nemo Link), Norway (2 GW), France, Denmark, and Iceland. HVDC has become a technology of increasing relevance to modern power systems, especially for interconnections and integration of power coming from renewable resources. There are several advantages to the use of HVDC system, but two of them are found suitable for massive deployment in the future power systems: it allows a high efficiency on the bulk power transmission over long distances and it provides a very high controllability in terms of power flows maximizing the integration of variable power coming from renewable energy resources. The use of HVDC for interconnections enables to isolate electrically the neighboring systems, it allows connecting power systems that are not synchronized or do not even have the same frequency. However, this advantage comes with an issue, HVDC links offer no natural response to a frequency deviation or support for frequency control, affecting the power system security.

All technical challenges described above have an element in common; high power converters that decouple the new energy sources from the pre-existent AC power systems (see Fig. 1).

In basic works, the frequency in power systems represents the balance between generated power and demanded power. During a system frequency disturbance the generation/demand power balance is lost, and the system frequency will change at a rate initially determined by the total system inertia. However, future power systems will have a *frequency response* (FR) very different from actual systems. The future power system will increase the installed power capacity (MVA) but the effective system inertial response will stay the same nowadays, this is because the new generation units based on power converters creates a decoupling effect of the real inertia and the AC grid. The result is deeper frequency excursions of system disturbances. A considerable reduction in the ability to overcome system frequency's disturbances is expected, the inertia response may be decreased. The inertial response of the system might be negatively affected with devastating consequences for system security and reliability.

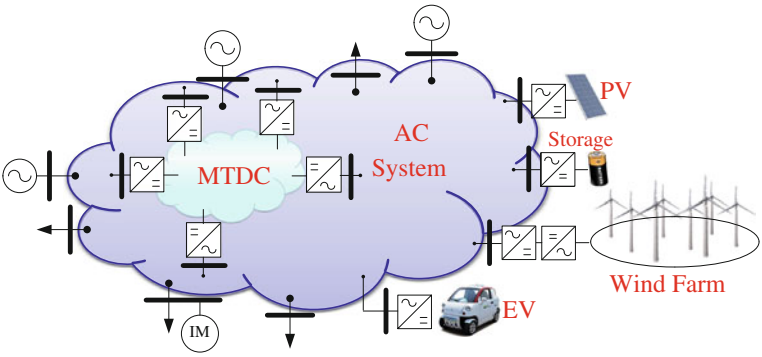

Fig. 1 General representation of a future power system

The objective of this chapter is to present the fundamental aspects of system frequency control and inertia response schemes for the future power networks. This chapter is developed not to be intended as a generic case of all possible future scenarios and technologies, instead it focuses on the expected development to the UK system. The organization of the chapter is as follows. Section 2 presents the main concepts of *system frequency response* (SFR) in the classical power system. Section 3 presents the controller used to enable FR on wind power, details of wind turbine, wind farm, and power system level are presented. Commercial experiences on synthetic inertia and inertia requirements in several countries are presented in Sect. 4. Section 5 presents a general overview of the main control strategies used in order to enable FR of offshore wind power connected using multiterminal HVDC systems. Section 6 closes the chapter with the main conclusions and perspectives of future work.

2 System Frequency Response

The electric frequency in a power system (system frequency, f) is a measure of the rotation speed of the synchronized generators. Changes in generation/demand will produce changes on the system frequency (speed of generators). System frequency is a continuously changing variable that is determined and controlled by the second-by-second (real time) balance between system demand and total generation.

A change in active power demand at one point of a network is reflected throughout the system by a change in electric frequency. Therefore, system frequency provides a useful index to indicate system generation and load imbalance.

Considering a system frequency disturbance condition (active power imbalance between generation and demand), the generator-demand dynamic relationship between the incremental mismatch power and the frequency can be expressed by an equivalent form of the swing equation. If demand is greater than generation, the frequency falls while if generation is greater than demand, the frequency rises.

The electrical devices connected to a synchronous power system are designed to operate at this system's nominal frequency (f_0), it is assumed to be 50 Hz as in the ENTSO-E Continental Europe system [11] (former UCTE) and UK [12].

Generally, deviations from this desired value arise due to imbalances between the instantaneous generation and consumption of electric power, which has an accelerating or decelerating effect on the synchronous machines. These small deviations on electric frequency are a normal result of stochastic variations in loads and should not affect the behavior of any component in the network. The electrical power system must be able to cope with those changes.

Frequency control is responsible for balancing real-time changes in load and generation that occur in a power system and ensuring that the frequency is approximately nominal throughout any period of time. The frequency control is responsible for helping to ensure frequency stability, which is defined as "*the ability of a power system to maintain steady frequency following a severe system upset resulting in a significant imbalance between generation and load*" [13]. Frequency stability analysis concentrates on studying the overall system stability for sudden changes in the generation-load balance (system frequency disturbance). In addition, the frequency control is responsible for limiting the frequency deviation that occurs after a large system frequency disturbance to the power balance in the system, e.g., the loss of a generator, the sudden disconnection of transmission line, as well as then returning the frequency to the nominal value within the required time. This task is accomplished using occasional *frequency control services*.

The SFR can be classified into two categories: *Frequency Response* (FR) *Dynamic* and *Non Dynamic Frequency Response*. The dynamic FR is continuously provided to manage the normal second by second changes on the system (i.e., small changes on demand). The nondynamic FR is usually a discrete service triggered at a defined frequency deviation.

Frequency control practices differ significantly between the various transmission system operators in the world. Responsibility of frequency control is managed in GB by National Grid PLC [12], though the procurement and despatch of *frequency response services*, under *normal operation conditions* the frequency is maintained at $f_0 = 50$ Hz within operational limits of ± 0.2 Hz. In an abnormal event (instantaneous loss of 1,320 MW of generation), the maximum allowed system frequency deviation is $\Delta f_{\max} = -0.8$ Hz. Figure 2 shows the main control thresholds and operational limits in terms of the absolute frequency magnitude that are used by National Grid (UK).

A representative example of the system frequency behavior following a frequency disturbance, (i.e., loss of generation or connection of a large load), is shown in Fig. 3. Numerical values depicted in Fig. 3 are related to the illustrative case of frequency control in GB.

Immediately after the disturbance, the system frequency starts dropping (region 1–2 of Fig. 3) at a rate mainly determined by the total inertia of the system (summation of the inertia constant of all generators and spinning loads). For occasions that the frequency drops greater than -0.20 Hz, some generating plants

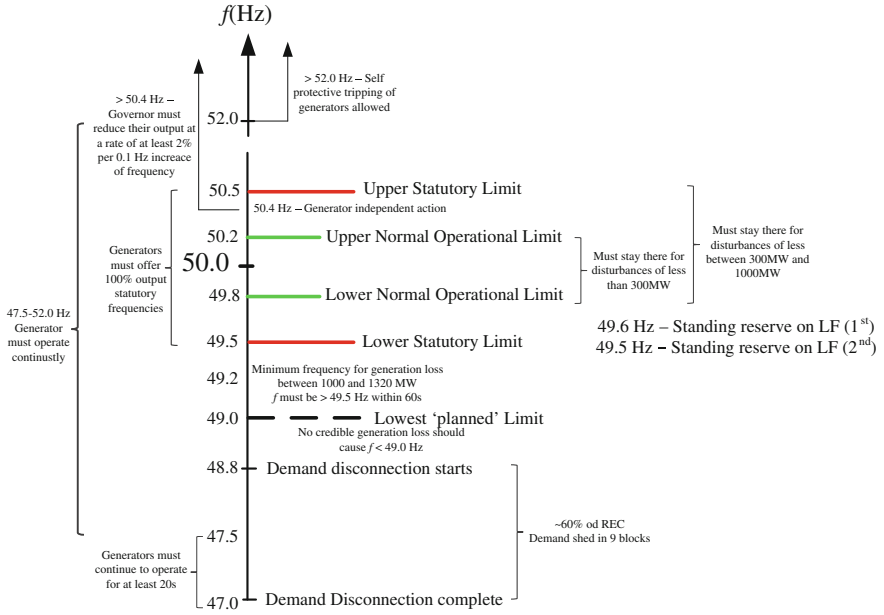

Fig. 2 The main frequency thresholds and operating limits defined as part of GB frequency control practices. Figure based on information from the NGC grid code [14]

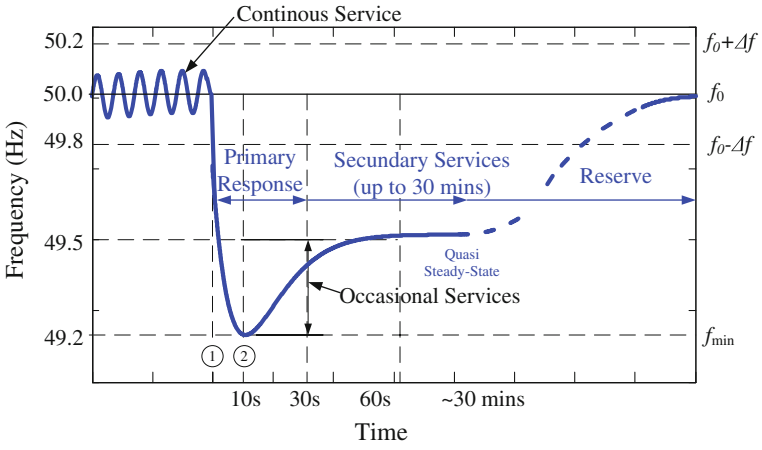

Fig. 3 Typical SFR based on a system frequency disturbance including numerical references to GB frequency control system

are contracted to provide FR. The response is classified as an *occasional service* and has two parts: *primary response* and *secondary response*. Primary and secondary response are defined as the additional active power that can be delivered

from a generating unit that is available at 10 and 30 s, respectively, after an event and that can be sustained for a further 20 s and 30 min respectively [14].

The primary response is provided by two mechanisms: *Inertia response* and *Governor Action*. The inertia response of *fast primary response* is related to a natural FR on synchronous generator. On an event of frequency reduction, the speed of synchronous generator also reduces and some of the kinetic energy stored in the rotating mass is released as an electrical energy. This is a very fast and natural response of synchronous generator directly connected to the grid and it is related to the rate of chance of frequency. A frequency controller named governor produces the governor action. An automatic droop control loop in governor acts on change in frequency and increases mechanical power on prime-mover to increase the generator output. This is a slower response and depends on main governor's characteristic and time response of prime-mover.

The *frequency control system* consists of two main parts: the *primary* and *secondary control*. *Tertiary control* is additional and slower than primary and secondary frequency control.

The primary control refers to control actions that are done locally (on the power plant level) based on the set-points for frequency and power. The objective of the primary control is to maintain the balance between generation and load. This balance can be reached at post-disturbance steady-state frequency different from the nominal frequency (especially on governor including droop characteristic). The control task is shared by all generators participating in the primary frequency control irrespective of the location of the disturbance.

Following a system frequency disturbance, the system will not be able to return to the nominal frequency on its own, without additional action. The secondary frequency control, also called *Load Frequency Control* (LFC), adjusts power set points of the generators in order to compensate for the remaining frequency error after the primary control has acted. The purpose of secondary control actions is to restore the system frequency to the nominal set point and ensure that any tie-line flows in the system are at their contracted level. LFC can also be performed manually as in the Nordel powers system, the ENTSO-E Continental Europe interconnected system, an automatic scheme is used, which can also be called *Automatic Generation Control* (AGC).

The tertiary control acts after the system frequency has been returned to, or very near to, the nominal value. The task of tertiary control depends on the organizational structure of a given power system and the role that power plants play in this structure [15]. It is different to primary and secondary control because it does not deal directly with controlling the frequency. It is not discussed here.

Following a large system frequency disturbance (e.g., large generation loss), a power system's frequency may drop quickly if the remaining generation no longer matches the load demand. Significant loss of generating the plant without adequate system response can produce extreme frequency excursions outside the working range of plant. Depending on the size of the frequency deviation experienced, *emergency control* and *protection schemes* may be required to maintain power system frequency.

If the frequency control system cannot restore the system frequency and the power system operators may follow an emergency control plan such as *under-frequency load shedding* (UFLS). UFLS is a widely used last resort against large low frequency events that may cause cascading outages and even the disconnection of parts of a system. The UFLS strategy is designed to rapidly balance the demand of electricity with the supply and to avoid a rapidly cascading power system failure. Allowing normal frequency variations within expanded limits will require the coordination of primary control and scheduled reserves with generator load set points [16]; for example *under-frequency generation trip* (UFGT), *over-frequency generation trips* (OFGT), or *over-frequency generator shedding* (OFGS) and other frequency-controlled protection devices.

Several performance indicators may be used to describe and to evaluate the FR. Figure 4 shows a typical and idealistic SFR (secondary and tertiary controls are not included) where the main performance indicators are depicted:

(i) *Maximum frequency gradient* ($[df/dt]_{\max}$) as observed by ROCOF (*Rate-Of-Change-Of-Frequency*) relays (line *A*).
(ii) *Maximum frequency deviation* ($f_{\max}$) as observed by under-frequency relays (point *B*) is defined as the absolute frequency deviation from nominal frequency (f_0).

Both these quantities shall be kept as small as possible to prevent relays from tripping *df/dt*.

(iii) *Frequency nadir* ($f_{\min}$) measures the minimum post contingency frequency (point *B*).
(iv) *Frequency nadir time* ($t_{\min}$) is the time it takes for the response to reach its nadir.
(v) *Quasi-steady-state deviation* (Δf_{ss}) is the deviation between the nominal frequency value and the final value. The term "quasi" is used because a steady-state analysis is performed on a dynamical system. Though, the dynamics considered are slow enough to allow such a definition. The quasi-steady state is usually defined with the help of a maximum gradient that the frequency should not exceed.

Mainly by the following aspects defines the magnitude of the dynamic maximum frequency deviation ($\Delta f_{\max}$) in a classical power system:

(i) The amplitude and development over time of the system frequency disturbance.
(ii) The kinetic energy of rotating machines in the system.
(iii) The number of generators subject to primary control and primary control reserve and how it is between these generators.
(iv) The dynamic characteristics of the machines (including controllers).
(v) The dynamic characteristics of loads, particularly the self-regulating effect of loads.

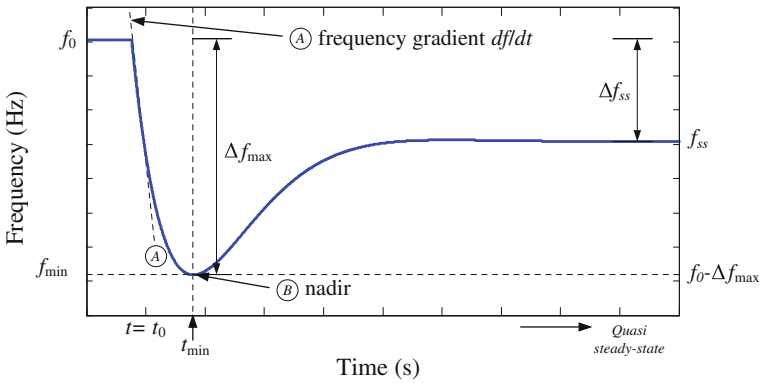

Fig. 4 SFR considering primary control and showing the main performance indicators

The quasi-steady-state frequency deviation is governed by the amplitude of the disturbance and the network power-frequency characteristic, which is influenced mainly by the following aspects:

(i) The droop characteristic included on all generators subject to primary frequency control in the synchronous area.
(ii) The sensitivity of power demand consumption to variations in system frequency.

3 Frequency Response of Wind Power

The SFR of future power system is different to the traditional power systems. The massive penetration level of wind power on the power system represents a change from the large-scale interconnected power system design and operation. Wind power generation causes some synchronous generator to be de-committed, and some to be dispatched down to lower power level, it reduces the system inertia. The electromechanical behavior of wind power generators differs fundamentally from that of conventional synchronous generators. Frequency stability and control is a particularly significant issue in future power systems.

Despite the seemingly large variety of utility scale wind turbine technologies in under development, there is an agreement about four basic technologies [17]:

(i) *Type 1*: *Fixed Speed Wind Turbines* (FSWT) using *Singe Cage Induction Generators* (SCIG) (see Fig. 5a).
(ii) *Type 2*: *Variable Speed Wind Turbine* (VSWT) using *Wound Rotor Induction Generator* (WRIG) (see Fig. 5b).
(iii) *Type 3*: VSWT using *Doubly Fed Induction Generator* (DFIG) (see Fig. 5c).
(iv) *Type 4*: VSWT with *Full Rated Converter* (FRC) interface (see Fig. 5d).

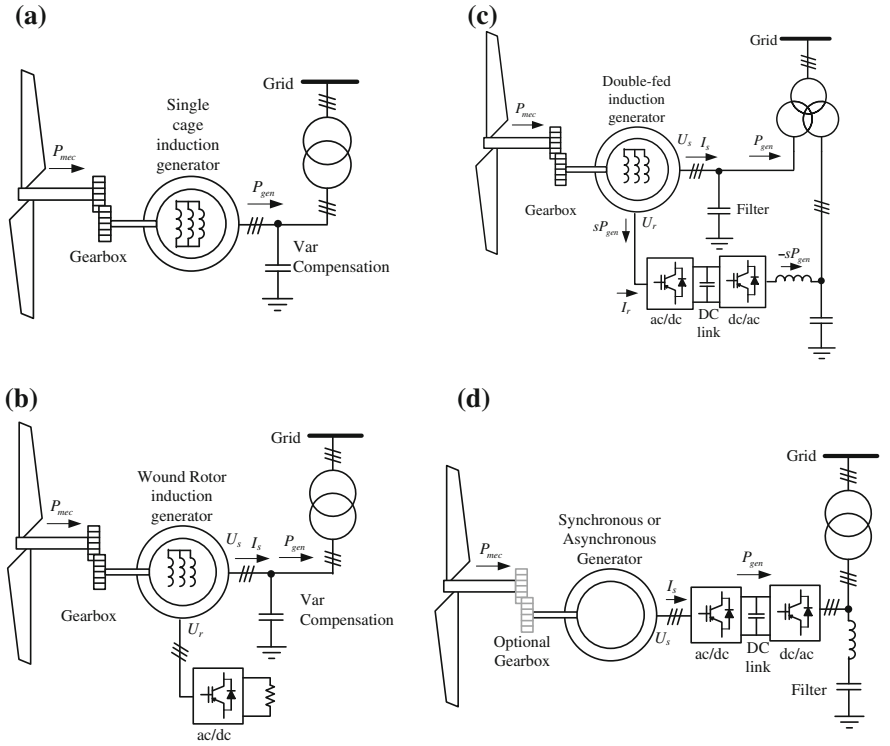

Fig. 5 Schematic representation of four basic wind turbine generator technologies. **a** WTG Type 1, **b** WTG Type 2, **c** WTG Type 3, **d** WTG Type 4

Wind Generation Modelling Group (WGMG) of the *Western Electricity Coordinating Council* (WECC) and *Working Group on Dynamic Performance of Wind Power Generation* of IEEE Power System Dynamic Performance Committee have developed and provided specification of generic model for these technologies [17].

Future development in the wind turbine industry will most probably to be focused on a gradual improvement of already known technology. It seems that both *Type 3* and *Type 4* may still dominate and be very promising wind turbine technologies for large wind farms. Wind turbine *Type 4* is a VSWT generator where the output of the generator is passed through the power converter to the grid. There are two types of generators used in these technologies: *Electrically Excited Synchronous Generators* (EESG) and *Permanent Magnet Synchronous Generator* (PMSG), and they look very promising wind technologies.

These wind power generation technologies employ power electronic converters, which electrically decoupled the electric generator and its electromechanical behavior from the power system frequency, and they cannot automatically contribute to system frequency.

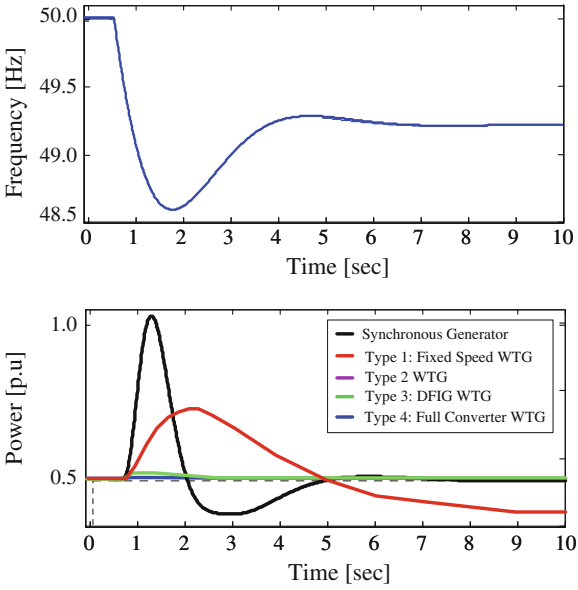

Fig. 6 Frequency response for synchronous generator and several WTG Types

The FR of a WTG depends on mainly on the type of technology. Figure 6 shows the response on active power production for several WTG technologies for a typical system frequency disturbance.

WTG based on *Type 1* and *Type 2* technologies are directly connected to the grid. FR of these technologies has different characteristic compare with the synchronous generator. They are capable to naturally release kinetic energy stored on their rotating parts (blades, gearbox, generator, etc.) during a system frequency disturbance, they have inertial response [18, 19].

Considering the frequency disturbance shown on Fig. 6, sudden frequency drop, the rotor of *Type 1* WTG does not change instantaneously because of the inertia of the wind turbine. However, the power production of this type of technology allows an increase of active power production as consequence of changes on the rotational speed. The active power contribution of *Type 1* WTG is higher compared with other WTG technologies, however, it still below FR provided by a classical synchronous generator. *Type 2* WTG uses a generator, which is an induction generator with provisions for adjusting its rotor resistance, during system frequency disturbance the active power output is kept at its previous disturbance set value by an adequate adjust of the rotor resistance controller. The FR of this type of WTG is negligible.

Type 3 and *Type 4* WTGs are VSWT which use a generators electronically controller and/or electronically connected to the grid. *Type 3* and *Type 4* WTG do not naturally provide FR. Traditional solutions for this issue are: reduce wind penetration during low system load, modify reserve policy, more static reserve at times of high wind and low system inertia. However, future power systems require

maximize power production from wind power, as consequence more effective solutions has been developed: modify existing technology and include of supplementary control loop in the WTGs.

FR, inertia and governor response, can be emulated on generators electronically controller and/or electronically connected to the power system adding a supplementary control, this approach is discussed in next section.

4 Controller Used for Frequency Response in Wind Power

Frequency control in power systems is usually formed of primary and secondary control. Future power system will require an active participation of wind power generation on the primary and secondary frequency control. Although generators electronically controller and/or electronically connected to the grid do not provide FR, this capability can be obtained by adding a supplementary control to the power converters.

Several control schemes can be drawn to enable the wind power generation to provide FR, it can be divided into three-level hierarchy [20]:

(i) Wind turbine controller.
(ii) Wind farm controller.
(iii) Power system level controller.

Local control at wind turbine level is used to provide primary frequency control and other additional auxiliary services then wind farm level controller allows coordination between the central and local control in order to achieve the desired generation for the system. Power system level controllers are used for secondary frequency control; it provides better system frequency behavior by the coordination between the AGC and the wind farms.

4.1 Wind Turbine Level Controllers

Wind turbine level controllers are local controllers added to the VSWT subsystems in order to enable transiently support the frequency (see Fig. 7). They can enable the primary frequency control by two strategies: *inertial controller* and *governor controller*.

4.1.1 Inertia Controller

Under system frequency disturbance conditions (active power imbalance between generation and demand), the generator-demand dynamic relationship between the

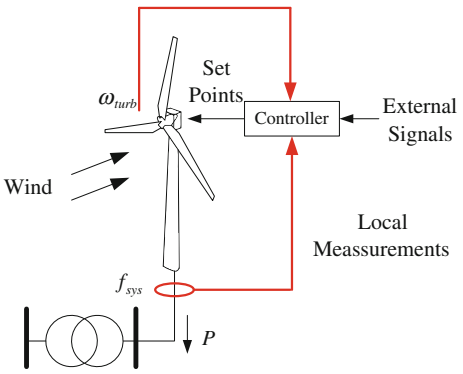

Fig. 7 Representative scheme of control interactions at wind turbine level

incremental mismatch power (Δp_i) and the frequency (f_i) can be expressed at i-th synchronous generator as:

$$\frac{2H_i}{f_0}\frac{df_i}{dt} = p_{m,i} - p_{e,i} = \Delta p_i \qquad i = 1, 2, \ldots, N \tag{1}$$

where:

$p_{m,i}$ is the mechanical power of prime mover in p.u.,

$p_{e,i}$ is the electrical power in p.u.,

Δp_i is the load generation imbalance in p.u.,

H_i is the inertia constant in seconds of i-th generator, H_i is given in seconds and is a measure of the time that a rotating generator can provide rated power without any input power from the turbine.

f_i is the frequency in Hz,

f_0 is its rated value, and

df_i/dt is the frequency change in Hz/s.

This is a simplified version of the swing equation, considering damping effect to be small during the event. Now, it is simple to understand frequency behavior of a traditional power system during a system frequency disturbance using (1). If demand is greater than generation ($p_{e,i} > p_{mi}$, $\Delta p_i < 0$), the frequency falls ($df_i/dt < 0$) while if generation is greater than demand, the frequency rises ($df_i/dt > 0$).

The same reasoning that is used in mechanics to introduce the concept of center of mass can be invoked for the definition of a *frequency of inertia center* (COI). This frequency is denoted by f_{COI} and corresponds to the inertia-weighted average of all generator frequencies:

$$f_{\mathrm{COI}} = \frac{\sum_{i=1}^{N} H_i f_i}{\sum_{i=1}^{N} H_i} = \frac{1}{H_T}\sum_{i=1}^{N} H_i f_i \tag{2}$$

where H_T is the total inertia of the system.

In a highly meshed power system, all units can be assumed to be connected to the same bus, representing the COI of the system and assuming further

simplifications, they can even be condensed into one single equivalent unit. A summation of all Eq. (1) for the N generators in the system yields:

$$2\sum_{i=1}^{N}\frac{H_i}{f_0}\frac{df_i}{dt}=\sum_{i=1}^{N}\left(p_{m,i}-p_{e,i}\right)\qquad i=1,2,\ldots,N. \tag{3}$$

Assuming a strong coupling of the generation units following quantities can be defined:

$$f_{\mathrm{COI}}=\frac{\sum_{i=1}^{N}H_i f_i}{\sum_{i=1}^{N}H_i}\qquad \text{Center of Inertia Frequency}$$

$$S_T=\sum_{i=1}^{N}S_{N,i}\qquad \text{Total rating}$$

$$H_T=\frac{\sum_{i=1}^{N}H_i S_{N,i}}{\sum_{i=1}^{N}S_{N,i}}\qquad \text{Total system inertia}$$

$$P_m=\sum_{i=1}^{N}P_{m,i}\qquad \text{Total mechanical power}$$

$$P_e=\sum_{i=1}^{N}P_{e,i}\qquad \text{Total electrical power}$$

The principal frequency dynamics of the system can be described by the nonlinear differential equation:

$$\frac{2H_T}{f_0}\frac{df_{\mathrm{COI}}}{dt}=p_m-p_e=\Delta p\qquad i=1,2,\ldots,N. \tag{4}$$

During a system frequency disturbance the system frequency will change at a rate initially determinate by the *total system inertia* (H_T).

The contribution of the total system inertia of one load or generator (H_i) depend if the system frequency causes change in its rotational speed and, then, its *kinetic energy*.

$$H_i=\frac{1}{2}\frac{J_i\omega_{sm}^2}{S_{\mathrm{base}}}. \tag{5}$$

The power associated with this change in kinetic energy is fed or taken from the power system and is known as the *inertial response*. It must be noticed inertial response is dominated during the initial frequency change, at the very beginning this is dominant dynamic process, however, after a very short time period where the kinetic energy is released governor control start to made a dominant presence in the FR. Figure 8 shows a representative FR provided by a synchronous

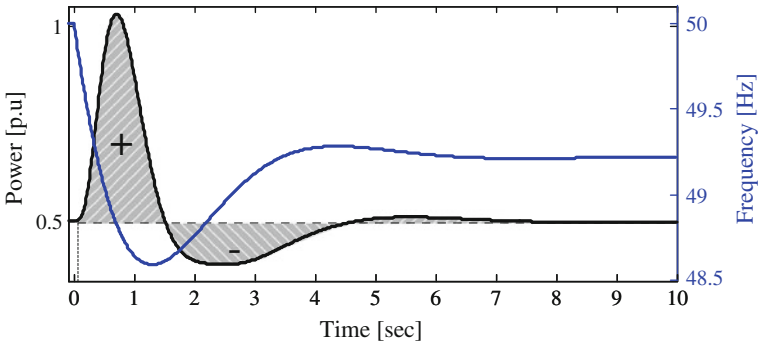

Fig. 8 Representative frequency response of a synchronous generator

Table 1 Typical data for a 3 MW WTG

Drive train concept	Generator type	Rated speed (rpm)	Generator rotor inertia (Kg/m^2)
Double fed 3-stage gear	Wound rotor asynchronous 6-pole	1,200	250
Low speed full converter (LSFC) direct drive	Permanent magnet, multipole	14	40.5
Medium speed full converter (MSFC) 2-stage gear	Permanent magnet 14-pole	400	510
High speed full converter (HSFC) 3-stage gear	Permanent magnet 6-pole	1,600	115

generator and change in the energy is depicted on the shadow area below the active power response.

The objective of the inertia control is to enable temporarily increase power output during frequency disturbance. This control requires some sort of energy storage to be able to increase the power production. The concept is therefore easily applicable to WTG, which have a reasonably large amount of kinetic energy stored in the rotating parts. The inertia control allows the converter and other subsystem in the WTG to extract the stored inertial energy from the moving part on WTGs: blades, gearbox, generator, etc. Table 1 shows typical values of generator rotor inertia for 3 MW modern variable speed WTG.

Considering per unit values, the inertia constant of a wind turbine generator is in the order of 2.0–6.0 s, which is comparable to traditional synchronous generation with various types of turbines and a resulting inertia constant in the range of 2.0–10.0 s. It explains why this controller is typically designed for an energy contribution of a very short duration (i.e., first 10.0 s of frequency disturbance).

The inertia controller can be created in several ways, there are two basic approaches:

(i) Releasing "*Hidden Inertia*"
(ii) *Fast Power Reserve Emulation*.

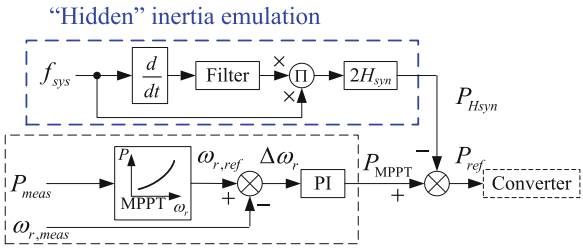

Fig. 9 Releasing hidden inertia controller

4.1.2 Releasing "Hidden Inertia"

A VSWT can emulate FR similar to the inertial response provided by synchronous generator by implementing an inertial controller. This controller is a simple control loop added on the power converter controller, it creates an active power control signal (inertial power P_{Hsyn}) following a version of the swing Eq. (4) [18, 21, 22]:

$$P_{\text{Hsyn}} = 2H_{\text{syn}} f_{\text{sys}} \frac{\mathrm{d}f_{\text{sys}}}{\mathrm{d}t} \tag{6}$$

where H_{sys} express the synthetic or emulated inertia (sec) and f_{sys} system frequency in per unit. Implementation of releasing hidden inertia controllers is depicted in Fig. 9.

The WTG can quickly store and release a large amount of kinetic energy in the rotating masses because of the power electronic converter, due to a large amount of inertia and wide rotational speed. The inertia controller helps to reduce the maximum frequency change rate and increases the transient frequency nadir. Comparison with FSWT and conventional generators, the inertia controller releases considerably larger kinetic energy.

4.1.3 Fast Power Reserve Emulation

The *fast-power reserve emulation* controller is designed to provide a short term constant power, and it can provide FR for a short period of time [23–25]. The fast-power reserve (P_{Hsyn}) is derived from a simple integration of kinetic energy stored in the wind turbine rotor:

$$P_{\text{Hsyn}} t = \frac{1}{2} J_{\text{syn}} \left(\omega_{r,0}^2 - \omega_{r,f}^2 \right) \tag{7}$$

where t ($t < t_{\max}$) is the lasting time of the fast-power reserve since the beginning of the frequency disturbance, $\omega_{r,\,0}$ is the initial rotational speed and $\omega_{r,\,\text{f}}$ is the rotor rotational speed corresponding to t.

This controller acts on the reference rotational speed creating an artificial change on the rotational speed to allow release kinetic energy from the wind turbine rotor. The change on the rotational speed ($\omega_{r,\,\text{ref}}$) is obtained as:

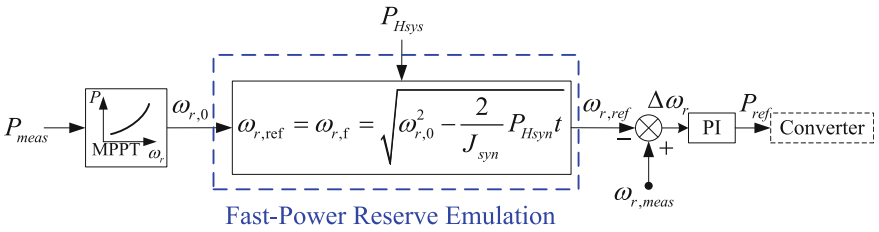

Fig. 10 Fast-power reserve emulation controller

$$\omega_{r,ref} = \omega_{r,f} = \sqrt{\omega_{r,0}^2 - \frac{2}{J_{\mathrm{syn}}} P_{\mathrm{Hsyn}} t}. \tag{8}$$

A general scheme for the fast-power reserve emulation controller is depicted on Fig. 10.

The fast power reserves provides FR for a short period and save time for other slower generators to participate in the frequency control.

4.2 Governor Response Controller

The objective of the primary control is to maintain the balance between generation and load. It corresponds to a proportional controller (*P*-controller) based on the classical control theory. The governor provides the control between frequency and generation power in a generator participating in primary frequency control. The governor of a generator provides the governor response and it is expected to be available within a few seconds (depending on intrinsic time contestants) after system frequency disturbance.

The governor control refers to control actions that are done locally (on the power plant level) based on the set-points for frequency and power. The actual values of these can be measured locally, and deviations from the set values results in a signal that will influence the valves, gates, servos, etc. in a primary-controlled power plant, such that the desired active power output is delivered. In primary frequency control, the control task of priority is to bring the frequency back to (short term) acceptable values. However, there remains an unavoidable frequency control error because the control law is purely proportional. Also, this controller cannot have an integral component because the integrators of different power plants could start "competing" each other for power production shares, which can lead to an unpredictable and unreasonable distribution of power generation on the available plants.

The control task is shared by all generators participating in the primary frequency control irrespective of the location of the disturbance.

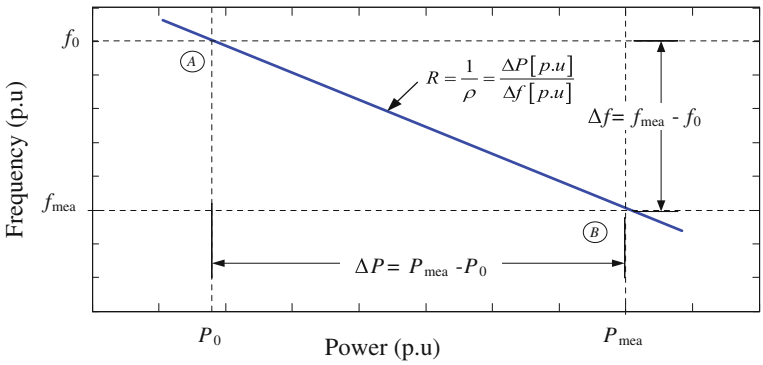

Fig. 11 Frequency droop characteristic

The steady-state properties of the governor controller is defined by the *permanent droop* (ρ), which define is defined as the change in frequency (Δf), normalized to the nominal frequency (f_0), divided by the change in power output (ΔP), normalized to a given power base, (P_{base}).

$$\rho = \frac{\Delta f[p.u]}{\Delta P[p.u]}. \tag{9}$$

The inverse of the droop is R and it is referred to as *the stiffness of the generator*.

$$R = \frac{1}{\rho} = \frac{\Delta P[p.u]}{\Delta f[p.u]}. \tag{10}$$

The *droop controller* is described by a steady-state frequency characteristic as shown on Fig. 11. It produces an active power change that is proportional to the frequency deviation.

Frequency droop control can be included as a control loop in modern wind turbines based on generators electronically controller and/or electronically connected to the power system. Figure 12 shows an implementation of the frequency droop control for a converter-based VSWT [22, 26, 27].

The droop control in WTG emulates the similar frequency droop characteristic to the synchronous generators. However, the power increase (ΔP) during a sudden drop on system frequency must be obtained from the kinetic energy of the rotation parts of WTG, it causes a decrease on rotational speed due to the *Maximum Power Point Tracking* (MPPT) operation. The support of steady-state frequency requires extra steady-state power to reduce the frequency deviation; this extra-power is provided in long term from the prime-mover in classical generation units.

Droop controller has not high impact on the initial ROCOF after frequency disturbance but largely influences the frequency nadir. However, decrease on rotational speed on wind turbines equipped with droop controllers may not be

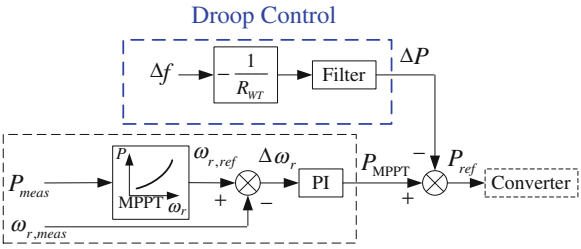

Fig. 12 Frequency droop control for VSWT

avoided because extra wind speed cannot be obtained, for this reason droop controller require support of other wind turbine components to avoid turbine stall by rotational speed falling too low. This issue can be solved using two approaches:

(i) *Stopping Frequency Droop Contribution.*
(ii) *De-loading the wind turbine.*

Frequency droop controller can be equipped with a triggering system to allow finish the action control on time to avoid a potential stall condition on the wind turbine. This triggering off system is similar to one use in fast power reserve emulation. This solution is easily implemented; however, its real benefit is on doubt because power contribution will be interrupted creating a potential risk of frequency disturbance.

Another solution is to use the droop controller combined with a *de-loading control*. De-loading the wind turbine is a technique that enables it to operate a lower operation point (speed-power) instead of the optimal provided by the MPPT controller. This operation condition saves the available power in the wind as reserves. This controller is described in the next section.

4.2.1 De-loading Control

When the wind speed is below the rated value ($v_w < v_{w,0}$), traditional VSWT, always operate on the MPPT condition with the *constant blade pitch angle* ($\beta = \beta_{\min}$). This operation mode allows extracting power from the wind energy as much as possible. The maximum power-tracking curve is shown in Fig. 13. The MPPT curve is given is used to define the power reference at any rotor speed for the active power control of VSWT.

Usually, the pitch angle of the wind turbine is equal to zero during the MPPT operation condition while the wind speed is below the rated value. If the wind speed increases and exceeds the rated value, the pitch angle starts to increase to keep the active power output on its rated value [28, 29].

The operation of WTG at MPPT condition allows the active power output has reached the maximum value at the instant wind speed. However, there are no power reserves from the wind turbine, and using the kinetic energy from the rotor mass of the wind turbine can only give a short-term frequency droop control.

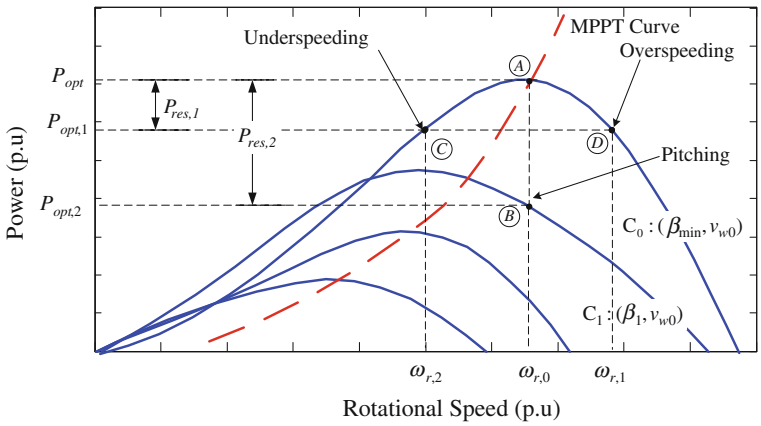

Fig. 13 MPPT curves and de-loading possibilities: **a** Over-speeding and **b** Pitching

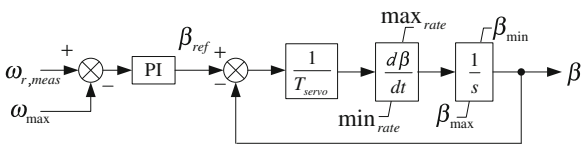

Fig. 14 Scheme for a traditional pitch angle controller

The de-loading control can enable wind turbines to save some active power as reserves. The active power production in a VSWT can be controlled acting on pitch angle (β) and rotational speed (ω), as consequence, the de-loading operation can be realized by two ways: (i) *pitch control* (pitching action) and (ii) *over-speeding control.*

a. Pitching Control.

Assuming a constant wind speed (v_{w0}) and constant rotational speed ($\omega_{r,0}$) the active power of a VSWT can be reduced from the MPP (point *A*, Fig. 13) by regulating the pith angle $\beta_{\min}$ to a large value β_1 (point *B*), this new operative condition allows a power reserve ($P_{\text{res, 2}} = P_{\text{opt}} - P_{\text{opt, 2}}$). This action is known as *pitching* and a modification on the pith angle controller is required to modify the pitch angle-rotational speed characteristic (move from curve C_0 to C_1 on Fig. 13).

A representative scheme of a traditional pitch angle controller is shown on Fig. 14, it acts when the rotational speed is above the maximum value for a high wind speed condition.

Traditional pitch angle controller must be modified to allow pitching, one approach includes a proportional integral control for pitch angle control, it avoids the use of a mechanical characteristics look-up table, usually needed to identify the required pitch angle and reference speed that would lead to the required response [30]; this implementation is depicted in Fig. 15.

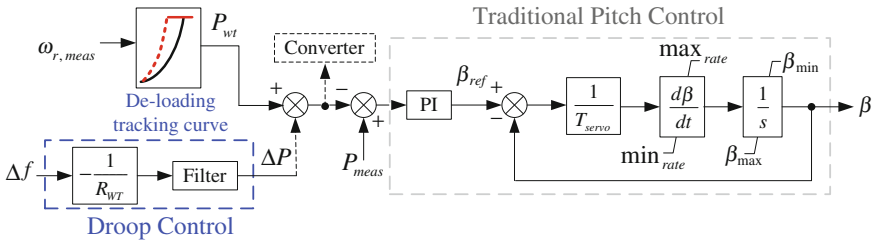

Fig. 15 Modified angle controller including pitching controller

One important aspect of the pitching approach is that response of pitch angle controller is slow because the mechanical time constant of pitch angle controller.

The pitching approach provides sufficient reserves for systems and save investment of the reserves and storages; however, this control strategy requires a careful market evaluation, or it can be adopted only a few hours per year. The de-loading operation of wind turbines without any financial incentive to provide this power reserves service produce loss of annual revenues for wind park developers will be reduced. This approach is always preferable to the disconnection of wind generators in specific operational conditions because of the lack of operational security in the system.

This control strategy should be performed through a hierarchical control approach, it allows the coordination of the activation of the adoption of de-load margins, definition of droop settings, and other control parameters of the WTG. A hierarchical control approach allows to *transmission system operator* (TSO) to send requests, to be transformed in control settings by the wind generation dispatch centers, that finally will interact with the wind parks and wind turbines in the field.

The de-loading approach involves a set of other problems, like the identification of the needed volume of de-load margins for a given set of operating conditions in a system, which requires further research.

b. Rotational Speed Control.

Assuming a constant wind speed (v_{w0}) and constant pitch angle ($\beta_{\min}$) the active power of a VSWT can be reduced from the MPP (point *A*, Fig. 13) by increasing the rotational speed over the MPPT speed ($\omega_{r,1} > \omega_{r,0}$, point *D*), this action is known as *over-speeding*. This is a more convenient operation than pitching action when the rotational speed is below the maximum value, and it can protect the pitch blade of wear and tear compared for low wind speeds.

Decreasing the rotational speed below the MPPT speed (under-speeding) is one more de-loading alternative. However, this alternate forces the WTG operation at lower rotational increasing risk of stalling. On the other hand, over-speeding operation allows more kinetic energy stored in the blade as consequence if the WTG is equipped with inertia controller the FR is improved.

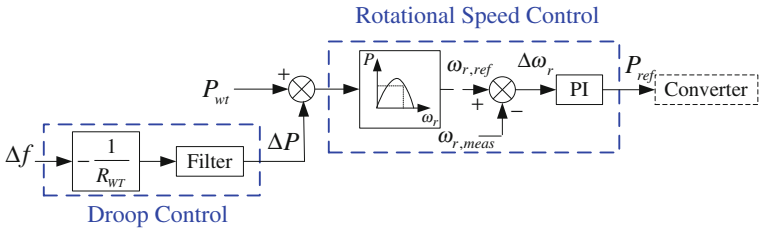

Fig. 16 Rotational speed control for VSWT

Figure 16 shows a general scheme for a rotational speed controller for a VSWT.

The over-speeding operation of VSWT has the advantages to provide sufficient reserves for systems and save investment of the reserves and storages although the wind energy may be partially lost if changes on speed produce stall. The wind power regulation is faster than the thermal power regulation due to the PWM control technology and the power system will be more stable than MPPT condition.

4.3 Wind Farm Level Controller

The effective frequency support from WTG requires a coordination of all individual frequency controllers installed inside the wind farm, as a consequence a *hierarchical structure of control* is used. Two major control system are defined at wind farm level:

(i) *Central control* and
(ii) *Local control*.

The main objective of the central control is to control active power of the whole wind farm (P_{WF}) by sending out set points to all wind turbines. Local control ensures the set-points at wind turbine level are reached and sends back information about of generation capabilities to the central controller.

The massive use of *energy storage systems* (EES) is expected on the future power systems for several reasons; one of them is to support the massive integration of wind power. Two ESS configurations can be used for wind farms:

(i) *Large agregated EES*.
(ii) *Small distributed ESS*.

There are several technical and economic differences between technologies EES used by each configuration. Large aggregated EES often are directly connected to the power system based on the external and nonwind technologies like batteries, compressed air, and pumped hydro for the whole wind farm. Small distributed ESS is a local solution located on terminal of the wind turbine or inside it (typically connected across DC link). Batteries [31], super-capacitors [32], and

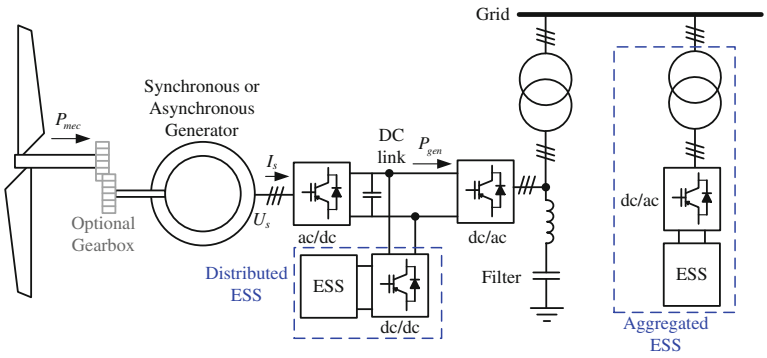

Fig. 17 Representative scheme of distributed ESS and aggregated ESS

flywheels [33, 34] are the main technologies used as small distributed ESS in wind farms. The choice of ESS depends on the demands of the control process. From the point of view of reaction time, distributed ESS is typically faster than large aggregated ESS energy storage devices. Fast- and medium-term ESS are suitable tor frequency control [35]. A generic scheme of small-distributed ESS on VSWT is shown on Fig. 17.

The central controller receives an active power control signal from the system operator $\left(P^*_{WF}\right)$ and produce two sets of individual signals: (a) *Power command signals for wind turbine controller* $\left(P_{\text{cmd},i}\right)$ in order to de-load wind turbine based on local data (MPPT, v_w, etc.), (b) *Power command signals to distributed ESS controller* $\left(P^*_{\text{ESS},i}\right)$. Feedback signals from each individual wind turbine are taken to the central controller to provide an online monitoring and control system. Also, the central controller acts on the aggregated ESS to ensure an overall control (see Fig. 18).

The active power set point of the wind farm $\left(P^*_{WF}\right)$ must be appropriately allocated to each wind turbine and ESS units by the wind farm central control, following a power balance:

$$P_{WF} = P_{WT,\text{total}} + P_{WF,\text{losses}} + P_{\text{ESS,total}} \tag{8.11}$$

where $P_{WT,\text{total}}$ is the total active power command for the wind turbines and $P_{\text{ESS,total}}$ is the total active power command by the ESS. The internal power losses in the wind farm $\left(P_{WF,\text{losses}}\right)$ are assumed negligible for simplicity.

An important aspect is the distribution scheme of individual active power command for wind turbines $\left(P_{\text{cmd},i}\right)$ and ESS $\left(P^*_{\text{ESS},i}\right)$. This is an area that still open for research because there are several aspects to be included. The distribution scheme must consider several important aspects affecting the power production inside the wind farm wake effect, random wind speed, etc.

Incentive mechanism must be defined to encourage wind farm proprietary to provides frequency support services, de-loading wind turbines is an technical

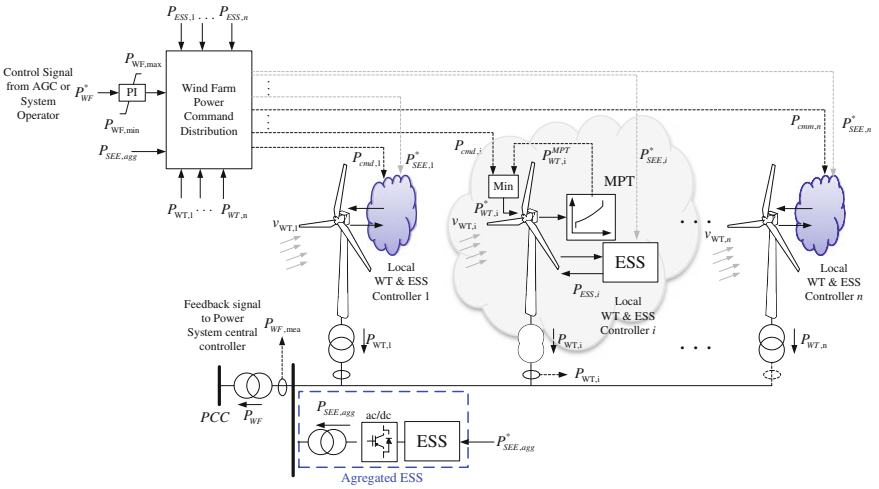

Fig. 18 Wind farm controller for considering wind turbine level frequency controllers

aspect with financial impact, however, not all wind turbines in the wind farm are necessary to operate at de-loading mode. In fact, migration to more on-line market controls can allow central control of wind farm an optimal decision of how many wind turbines inside a wind farm should be de-loaded in order to cope with a security risk and responding to economic signals provided by the market.

ESS capability and economic benefits should be carefully investigated. Modern ESS has limited frequency support due to the little capacity of batteries, super-capacitor, flywheel, etc., and very low time response of hydro-pump, CAES, etc. ESS may reduce the system frequency excursion for a relatively short period of time, however, ESS cannot influence the steady-state frequency. Therefore, conventional power plants and wind power must be rectified to support long-term frequency control. Consideration about security and risk must be carefully examined during the recharge period of ESS to avoid a frequency stability event.

4.4 Power System Level Controller

Frequency support from wind power at wind turbine level and wind farm level are aspects well documented. However, there are few studies focus on the power system level frequency control considering wind power penetration. Massive penetration of wind power is expected in future power systems, as consequence frequency control must be provided.

The main controllers used for primary frequency control in wind turbines and wind farm are presented in the previous sections and the tertiary control is not taken into account.

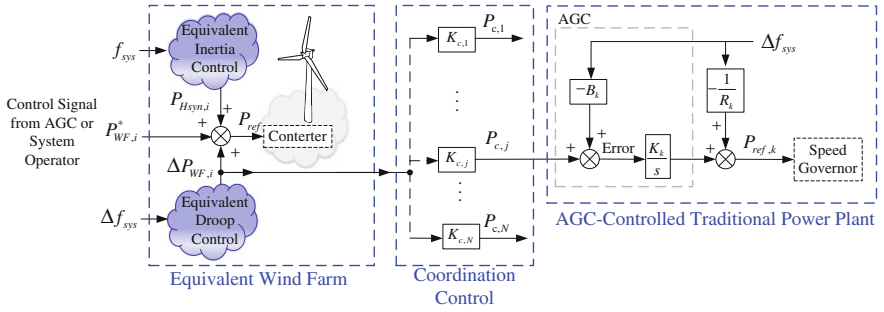

Fig. 19 Power system level control: wind-traditional power plant coordination

The power system level controller is a slow global controller related to quasi-steady state processes ($\sim$30 min) of secondary frequency control. The objective of this controller is to restore the frequency to rated frequency, it is reached by adjusting the set-point of power generation at power plant with capability of modify its power dispatch. This section presents a description of a power system level controller based on the coordination between wind power generation and traditional generation. This pseudo-AGC controls the traditional power plants to be aware of the frequency control support provided by the wind farms as soon as possible. A wind farm including inertial and droop controllers are enough to provided system frequency support and improve the frequency stability but an coordinated power system control can provided an even better frequency behavior. Figure 19 shows a power system level control; equivalent model of the *i*-th wind farm participating on frequency control is depicted.

A *coordination control* is used as interface between the wind farms with participation on frequency support an traditional power plants. During a frequency disturbance, the inertial response provided by the wind farm with inertial controller helps to modify the maximum frequency change rate and nadir, it has been discussed in previous sections. These indicators of quality in system frequency may be improved in future power system by the coordination between wind farm with FR capability and AGC-controlled traditional power plants. The droop power ($\Delta P_{WF,\ i}$) provided but the *i*-th wind farm participating in frequency support is divided by the coordination control following the rule as follows:

$$P_{c,j} = K_{c,j}\Delta P_{WF,i} \tag{12}$$

$$\sum_{j=1}^{N_c} K_{c,j} = 1 \qquad 0 \le K_{c,j} \le 1 \tag{13}$$

where $P_{c,j}$ is the coordination control signal, $K_{c,j}$ is the participation factor for each traditional power plant supporting the wind farm. In a highly competitive environment, as expected in future power system, this participation factor is a time-dependent variable and must be calculated dynamically.

The coordination signals ($P_{c,\ j}$) modify the *AGC error* which is similar to the *area control error* (ACE) and the traditional power plants receive an appropriate signal of the power imbalance since the very beginning. This coordinated control provides an early frequency support from the traditional power plants and the system frequency can be controlled and recovered back to the nominal frequency faster than the no coordinated control condition. The coordinated control presented is based on the same principle as the tie bias control, but the AGC error uses the coordination control signal ($P_{c,\ j}$) instead of the lie line power deviation.

5 Synthetic or Artificial Inertia

Modern WTGs use power electronics converters to enable variable speed operation in order to capture wind energy over a wide range of speeds. However, these converters isolate the rotational speed from the system frequency so WTG based on back-to-back AC–DC–AC converters offer no natural response to system frequency [36]. The adjective *natural* is included on the previous sentence because some manufacturers have started to integrate controllers on modern WTGs in order to provide inertial response (and governor response on some cases) for large, short-duration frequency deviations.

The wind turbine industry has created several names for this control system that enable inertial responses on a WTG [37, 38]: *Artificial, Emulated, Simulated, or Synthetic Inertia*.

Examples of synthetic inertia controlled commercially available for WTG are: General Electric WindINERTIA™ [39, 40], ENERCON Inertia Emulation [41], Vestas, GE, etc.

ENERCON's solution to contribute on frequency changes and especially to drops is named ENERCON® Inertia Emulation™. This is an inertia controller, which uses the kinetic energy stored in the wind turbine rotor to temporarily provide extra amount of power (P_{increase}). The minimum power of the WEC to enable Inertia Emulation™ is 4 % of rated power (P_{rated}) and the maximum increase reached is 10 % of the nominal power for a maximum duration of 10 s. No stalling is triggered after the action of the Inertia Emulation™ system and the WEC gets twice the activation time, before a further activation is allowed. Figure shows a representative results of Inertia Emulation™ system.

Figure 20 shows a measurement of an ENERCON E-82/2 MW with Inertia Emulation, which was operating at partial load ($\sim$34 % rated power) where the active power output was temporarily increased by $\sim$10 % rated power to in total 44 % rated power without an increase in wind speed [42].

During the last few years, some TSOs and manufacturer have shown interest and collaborated to enable synthetic inertia in wind power generation.

ENERCON have cooperated with Hydro Québec and simulated frequency support controllers in the power system of Quebéc [43]. Hydro Québec was early

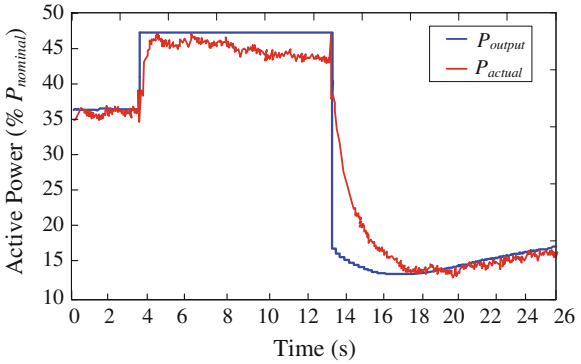

Fig. 20 Sample measurement of the power performance of an ENERCON® WEC with Inertia Emulation™ [42]

to require that a wind power plant must have an inertia emulation system that acts on major frequency deviations with a performance "*at least as much as does the inertial response of a conventional synchronous generator whose inertia (H) equals 3.5 s*." A somewhat different definition of the requirements is then developed in cooperation with ENERCON and REpower. A controller defined with power increase, power decrease, and time for these actions is found to be a better option than requiring an equivalent inertia.

National grid (UK) has studied FR and synthetic inertia during the last few years and its *Frequency Response Technical Sub-Group Report* [44] recommended the fast FR instead of synthetic inertia. The active power reserve shall be fully available in 5.0 s and sustained for at least a further 25.0 s.

ENTSO-E Draft Requirements for Grid Connection [11, 45] stated that a type C unit (a synchronous generating unit or power park module connected below 110 kV and with a maximum capacity above 10 MW) without natural inertia may be required to provide synthetic inertia. The grid operator in cooperation with the TSO "*shall have the right to require a power generating facility to deliver an equivalent performance by an increase of active power related to the rate of change of frequency*".

Table 2 shows a general overview of inertia requirements for several countries around the world, it is clear that there are various opinions regarding synthetic inertia, how to define it, and what to require. The uncertainty leads to dissatisfaction among the wind turbine manufacturers. A problem is that general requirements are not easily defined as the entire system has to be taken into account. Different systems with different types of production and wind power penetration have different needs.

Currently, no grid code contains real tangible requirements—only few loose indications, and the inertia has not been reported as implemented in any commercial project yet. Together this seems to indicate that the need is not there currently.

Table 2 Overview of inertia requirements—year 2011 [46]

Country/state	Requirement	Comment
REE-Spain	No formal requirement	REE encourage development but does not foresee a need for this for the Spanish mainland fora long time
Hydro Quebec-Canada	Equivalent response as would have been provided by a synchronous machine with a inertia constant, $H = 3.5$ s	Basically undefined
Ercot-Texas USA	No formal requirement	Have been under discussion for a number of years
National Grid-UK	No formal requirement A current draft suggest a primary control with +10 % over 5 s, and 1 s max delay time	NGET has been studied this for the last 2–3 years
Ireland	No formal requirement	Have been studied and so far been concluded not critical
Denmark	Similar to Hydro-Quebec	Same as for HQ
ENTSO-E Draft EU Grid code	The TSO shall have the right to require an equivalent delivery related to the rate of change of frequency	Basically undefined

6 Enabling the HVDC System to Deliver Frequency Response

There are several challenges that de future power systems will face in coming future. One of them is meets rising energy requirements in a manner that is sustainable, secure, and competitive. There is no single answer for this situation; however, there are several aspects to consider regarding primary resource [47, 48]: (i) greater energy efficiency and conservation, (ii) increased use of resources that are secure, indigenous, sustainable, clean, and competitive.

A potentially realistic solution for this situation is the use of a primary energy source, which is a clean, and fuel cost-free, wind power. This resource is enormous in the Europe's offshore and the amount available is able to meet Europe's demand seven times over. There are 150 GW on offshore wind projects are already at various stages of planning and development. The North Sea has a vast potential for renewable energy generation: offshore wind power, tidal and wave energy.

High Voltage Direct Current (HVDC) systems are more flexible than their AC counterparts and it offers distinct advantages for the integrating offshore wind farms to inland grid system. The *Voltage Source Converter* (VSC) HVDC transmission system enable fast and flexible control active and reactive power, and can alleviate the propagation of voltage and frequency deviations due to wind variations in wind strength. It seems advances on technologies open the door for VSC HVDC systems at higher voltage and higher power range, which is making *multi-terminal HVDC* (MTDC) system a technical possibility [47].

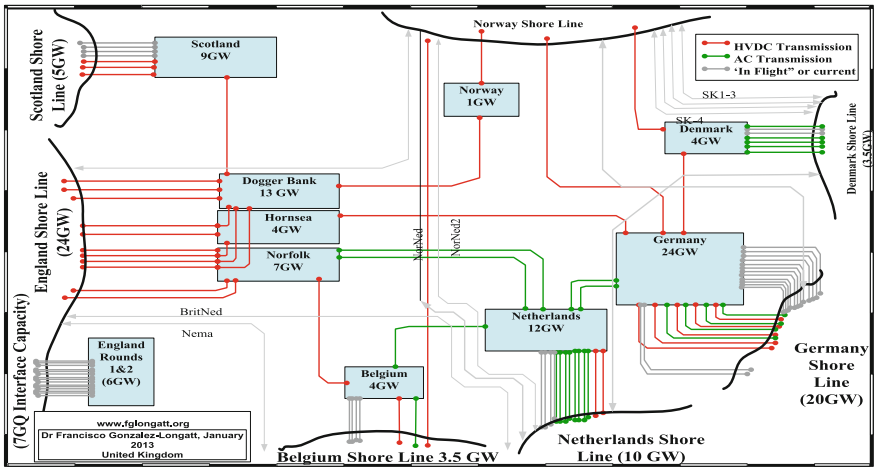

Fig. 21 2030 possible optimized integrated offshore network development [48]

Wind power evolution in Northern Europe is foreseen to continue in the future with development of large-scale wind power on far offshore. Integration scheme of these wind farms to the onshore grids would grow from point-to-point connection to a transnational multiterminal network where the transmission capacity serves both to evacuate the wind power and to facilitate power trading between countries.

Supergrid will be the transmission backbone of Europe's decarbonized power sector. It will facilitate the trading of electricity across and it will strengthen security of supply [49].

Although the Supergrid has gotten much attention, it cannot be built yet. Many Supergrid topologies have been proposed or studied by different organizations [50–52]. Regulatory and policies aspects have been defined: A single planner (European Network of Transmission System Operators for Electricity, Entso-e), a single operator (ISO), a single grid code (Entso-e), and a single European regulator (ACER). However, North Sea Supergrid can probably not be built as a planned and optimally structure [48].

The main reason, independently planned projects would be coupled together, leading to a rather grown network, comprising several DC and AC voltage levels and maybe different frequencies. The 2030 Possible optimized integrated offshore network development based on results of Entso-e is depicted on Fig. 21. It is based on the national target in terms of offshore wind power for North Sea national, scenario 2030, it was created by *European Wind Energy Association* (EWEA), and depicted in Fig. 22. Large offshore DC links in excess of several gigawatt may have several capabilities to enhance the grid stability [53].

The *Supergrid* will be built out in phases, initially connecting the current crop of offshore wind generators to existing networks. As a first step, (Phase 1) nodes will be built in the North Sea using 2015 technology to cluster offshore wind

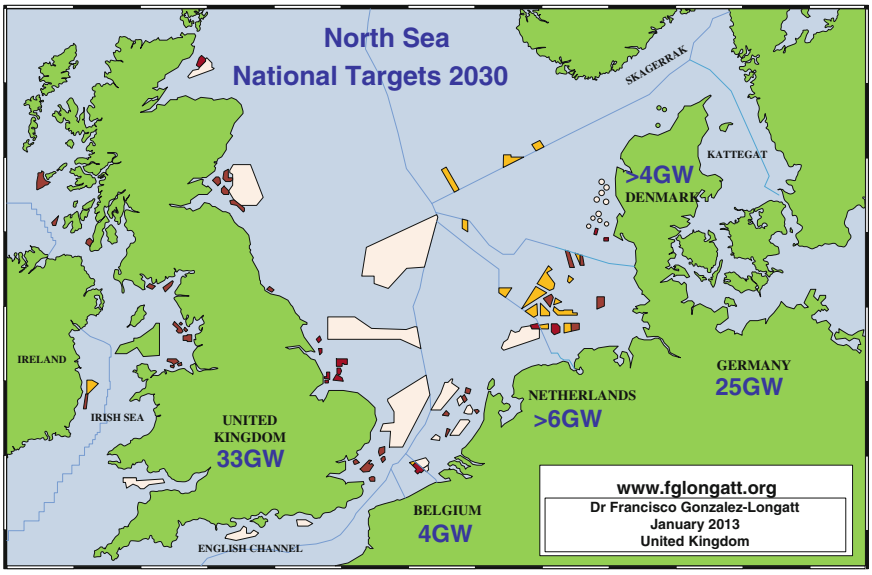

Fig. 22 North Sea National Target in terms of offshore wind power

generation for bulk delivery. Figure 23 shows a proposal scheme for Phase 1 of *Supergrid.*

A *benchmark test system for the Phase I of Supergrid is introduced on* [48], the proposal of such a test system is based on information publicly available on the scenario presented above for 2020–2025.

In this system, the energy from wind generation clusters off the east coast of the UK will be collected at *SuperNodes* at Firth of Forth, Dogger Bank/Hornsea and Norfolk Bank which will be connected together and interconnected with the German and Belgian North Sea clusters and Norwegian Hydro Power. The network then will deliver this power to the existing networks at terminals at Glasgow, Hull and Zeebrugge and nodes at London and Southern Germany (or North Rhine Westphalia)—see Table 3 and Fig. 24.

In order to develop offshore transmission system for this massive international infrastructure, reliability, and security of supply will be the main focus. Among those, fast reactive power response, power reversal, active and reactive power modulation, and fault ride through need to be carefully considered. FR is also another important element, which is done by fast power injection from the DC link, in case of a loss of generation unit at onshore, the frequency may be restored.

Frequency support from wind turbines and wind farms have been described in previous section, and it has been demonstrated its positive impact on SFR on future power systems. Massive offshore wind farms connected to the grid using HVDC must be enabled to provide frequency support to the AC power system.

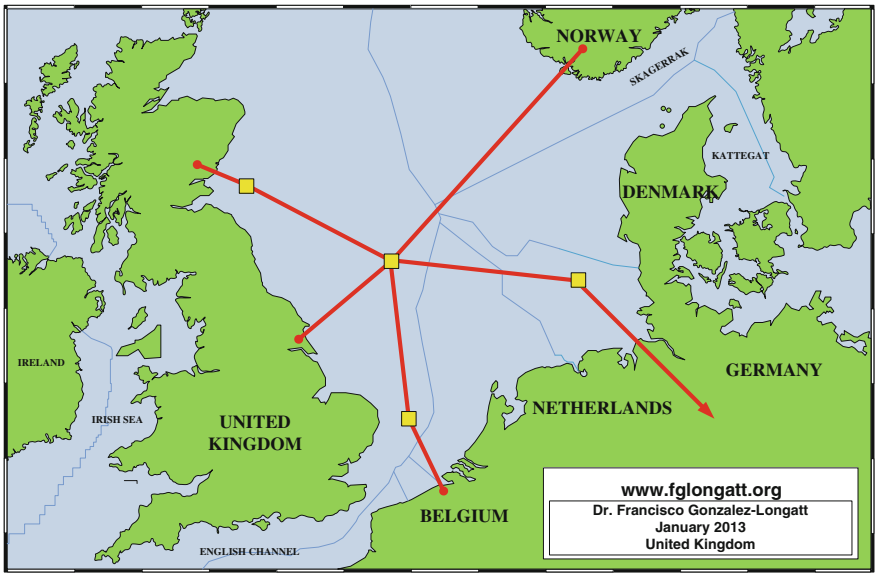

Fig. 23 Supergrid Phase I [54]

Table 3 Interconnection and node capacities for Phase 1 of Supergrid [54]

Connection	Capacity (GW)
Dogger-Germany Offshore	10.0
Dogger-Norfolk Bank	5.0
Dogger-Firth of Forth	5.0
Dogger-Norway	5.0
Germany Offshore-Munich	10.0
London-Norfolk Bank	5.0
Norfolk Bank-Belgium Offshore	2.0
Nodes	
Belgium Offshore	2.0
Dogger-Hornsea	10.0
Germany Offshore	10.0
Norfolk Bank	5.0
Munich	10.0
Firth of Forth	5.0

Several publications have addressed the issue of frequency support from offshore wind farms connected via HVDC systems. Most of them based on point-to-point HVDC connections, where the frequency control is enabled by a control loop on the VSC-HVDC stations (see Fig. 25).

Small DC voltage variations are caused by fluctuations of power injected into the DC transmission lines. Hence, by operating the main grid side HVDC terminal

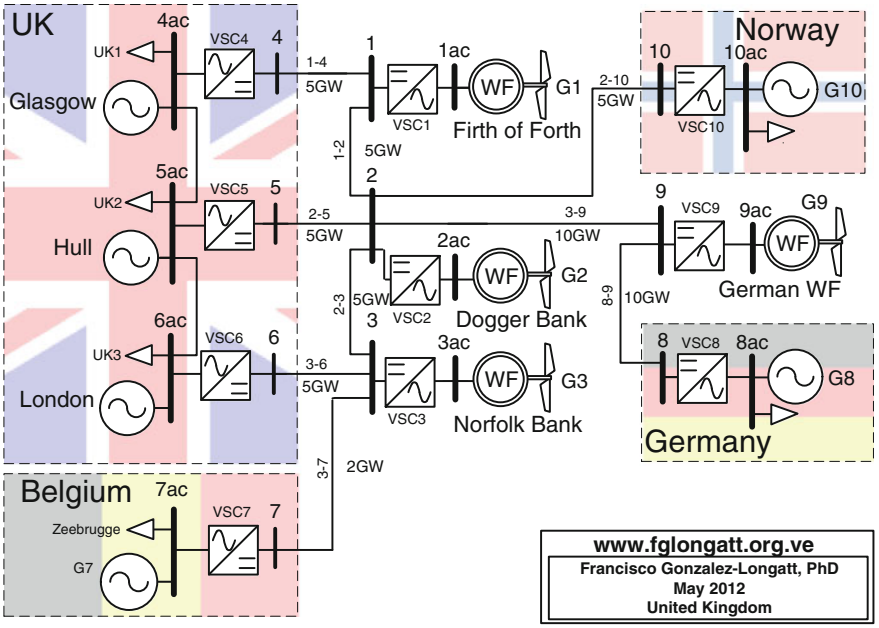

Fig. 24 Basic structure of the benchmark test system for Phase I of *Supergrid* project [48]

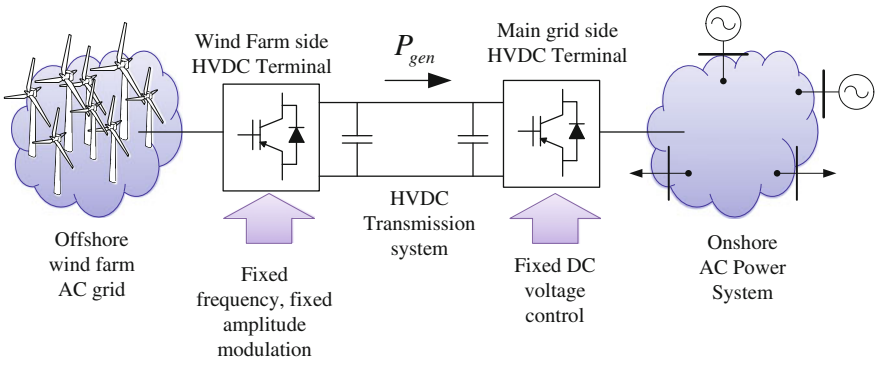

Fig. 25 Schematic representation of an Offshore wind farm connected to AC power system using point-to-point HVDC system. Operation mode on HVDC terminals shows frequency support enabled

in *DC voltage control mode*, the wind farm power fluctuations would result in immediate and equal changes in power flow via the DC transmission line. The frequency support of the main AC grid is based on local frequency measurements at the collection grid and the artificial frequency coupling of the collection grid and the main grid is achieved by implementation of *DC voltage controllers* [55].

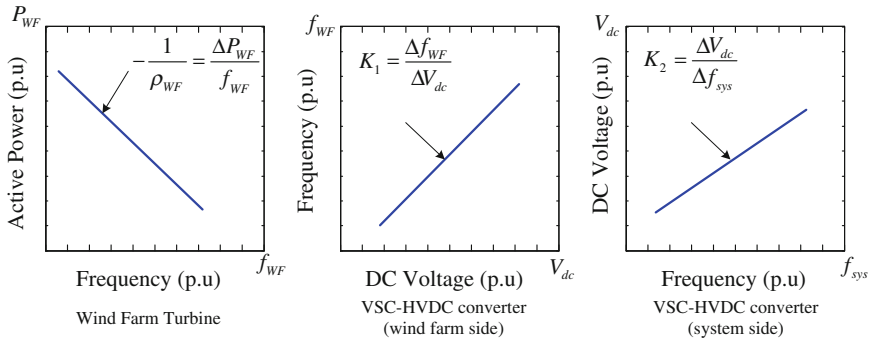

Fig. 26 Characteristic curves of the wind turbine generation, wind farm frequency and HVDC transmission voltage for frequency support

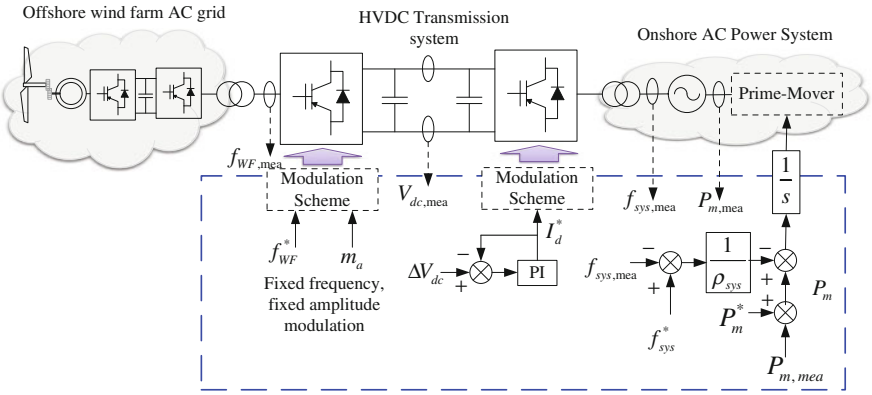

Fig. 27 Wind farm + HVDC controller to enable system frequency support

The desired characteristic curves of the wind turbine generation, wind farm frequency and HVDC transmission voltage, are shown in Fig. 26.

The HVDC system is used to create a coupling between wind farm and the AC system, it should be noted that in order to get this desired frequency droop characteristics, the wind turbine should operate with some power margin (or reserve) below the maximum attainable. The schematic of the control strategy including the droop relations is shown in Fig. 27.

Other control schemes reported in the literature including to enable HVDC to delivery in inertial response and primary frequency control [56, 57]. An innovative scheme includes inertia emulation control system using the exercising the electrostatic energy stored in DC shunt capacitors of the HVDC system to emulate inertial contribution [58].

There are several publications that deal with the primary frequency control of multiarea power system considering multiterminal HVDC systems [59, 60].

Almost all of them use a control scheme where DC contributions are used to achieve the primary frequency control. A combination of DC voltage droop control and frequency droop control are used at converter terminals. It allows a bidirectional interaction of multiterminal HVDC and AC grids thereby responding to variations in power unbalances in both systems (as reflected by DC voltage and frequency deviations).

7 Conclusions

Future power systems face several challenges: (i) the high penetration level of renewable energy from highly variable generators connected over power converters; (ii) several technologies for energy storage with very different time constants, some of them using power converters as an interface to the grid; and (iii) a pan-European transmission network facilitating the integration of large-scale renewable energy sources and the balancing and transportation of electricity based on underwater MTDC transmission. All of them have an element in common, high power converters that decouple the new energy sources from the pre-existent AC power systems. During a system frequency disturbance, the generation/demand power balance is lost, the system frequency will change at a rate initially determined by the total system inertia. However, future power systems will increase the installed power capacity (MVA) but the effective system inertial response will stay the same nowadays, this is because the new generation units based on power converters creates a decoupling effect of the real inertia and the AC grid. The result is deeper frequency excursions of system disturbances. A considerable reduction in the ability to overcome system frequency's disturbances is expected, the inertia response may be decreased. The inertial response of the system might be negatively affected with devastating consequences for system security and reliability.

References

1. UN (2011) The conference of the parties. The Cancun agreement. FCCC/CP/2010/7/Add.1, Decision 1/CP.16, The Cancun agreements: outcome of the work of the Ad Hoc working group on long-term cooperative action under the convention. Decision [1/CP.16]. http://unfccc.int/resource/docs/2010/cop16/eng/07a01.pdf. Accessed 15 March 2011
2. EUREL Electrical Power Vision 2040 for Europe. www.eurel.org/home/…/EUREL-PV2040-Full_Version_Web.pdf (Online)
3. GOV.UK (2011) Policy reducing the UK's greenhouse gas emissions by 80 % by 2050. https://www.gov.uk/government/policies/reducing-the-uk-s-greenhouse-gas-emissions-by-80-by-2050
4. Legislation.gov.uk (2008) Climate Change Act 2008. http://www.legislation.gov.uk/ukpga/2008/27/contents
5. Winzer C (2012) Conceptualizing energy security. Energy Policy 46:36–48

6. EU (2009) Directive 2002/91/EC of the European Parliament and of the Council of 16 December 2002 on the energy performance of buildings. http://eur-lex.europa.eu/LexUriServ/LexUriServ.do?uri=OJ:L:2003:001:0065:0071:EN:PDF
7. DECC (2013) Department of energy & climate change. https://www.gov.uk/government/organisations/department-of-energy-climate-change
8. EWEA (2012) Factsheets: wind power economy. http://www.ewea.org/fileadmin/ewea_documents/documents/press_releases/factsheet_economy2.pdf
9. DECC (2011) Planning our electric future: a white paper for secure affordable and low carbon electricity. https://www.gov.uk/government/publications/planning-our-electric-future-a-white-paper-for-secure-affordable-and-low-carbon-energy
10. CarbonTrust (2012) Strategic assessment of the role and value of energy storage systems in the UK low carbon energy future. http://www.carbontrust.com/media/129310/energy-storage-systems-role-value-strategic-assessment.pdf
11. ENTSO-e (2012) European network of transmission system operators for electricity: operation handbook. https://www.entsoe.eu/publications/system-operations-reports/operation-handbook/
12. NG (2013) The Grid Code: Issue 5 Revision 3—2 April 2013. http://www.nationalgrid.com/uk/Electricity/Codes/gridcode/gridcodedocs/
13. Kundur P, Paserba J, Ajjarapu V, Andersson G, Bose A, Canizares C et al (2004) Definition and classification of power system stability IEEE/CIGRE joint task force on stability terms and definitions. IEEE Trans Power Syst 19:1387–1401
14. Erinmez IA, Bickers DO, Wood GF, Hung WW (1999) NGC experience with frequency control in England and Wales-provision of frequency response by generators. In: Power Engineering Society 1999 Winter Meeting, IEEE, vol 1, pp 590–596
15. Machowski J, Bialek JW, Bumby JR (2008) Power system dynamics: stability and control, 2nd edn. Wiley, Oxford
16. Bevrani H (2009) Robust power system frequency control: robust techniques, 1st edn. Springer, New York
17. Ellis A, Kazachkov Y, Muljadi E, Pourbeik P, Sanchez-Gasca JJ (2011) Description and technical specifications for generic WTG models—a status report. In: Power systems conference and exposition (PSCE), 2011 IEEE/PES, pp 1–8
18. Ekanayake J, Jenkins N (2004) Comparison of the response of doubly fed and fixed-speed induction generator wind turbines to changes in network frequency. IEEE Trans Energy Convers 19:800–802
19. Muljadi E, Gevorgian V, Singh M, Santoso S (2012) Understanding inertial and frequency response of wind power plants. In: Power electronics and machines in wind applications (PEMWA), 2012 IEEE, pp 1–8
20. Yuan-Zhang S, Zhao-Sui Z, Guo-jie L, Jin L (2010) Review on frequency control of power systems with wind power penetration. In: 2010 international conference on power system technology (POWERCON), pp 1–8
21. Holdsworth L, Ekanayake JB, Jenkins N (2004) Power system frequency response from fixed speed and doubly fed induction generator-based wind turbines. Wind Energy 7:21–35
22. Morren J, De Haan SWH, Kling WL, Ferreira JA (2006) Wind turbines emulating inertia and supporting primary frequency control. IEEE Trans Power Syst 21:433–434
23. Ping-Kwan K, Pei L, Banakar H, Ooi BT (2009) Kinetic energy of wind-turbine generators for system frequency support. IEEE Trans Power Syst 24:279–287
24. Teninge A, Jecu C, Roye D, Bacha S, Duval J, Belhomme R (2009) Contribution to frequency control through wind turbine inertial energy storage. IET Renew Power Gener 3:358–370
25. Ullah NR, Thiringer T, Karlsson D (2008) Temporary primary frequency control support by variable speed wind turbines—potential and applications. IEEE Trans Power Syst 23:601–612
26. Jeong Y (2011) Comparison and testing of active power control strategies for grid-connected wind turbines. In: Colorado School of Mines, Division of Engineering

27. Duval J, Meyer B (2009) Frequency behavior of grid with high penetration rate of wind generation. In PowerTech, 2009 IEEE Bucharest, pp 1–6
28. Cao Z, Wang X, Tan J (2012) Control strategy of large-scale DFIG-based wind farm for power grid frequency regulation. In: 31st Chinese control conference (CCC) 2012, pp 6835–6840
29. Vidyanandan KV, Senroy N (2013) Primary frequency regulation by deloaded wind turbines using variable droop. IEEE Trans Power Syst 28:837–846
30. de Almeida RG, Peas Lopes JA (2007) Participation of doubly fed induction wind generators in system frequency regulation. IEEE Trans Power Syst 22:944–950
31. Jiang Q, Gong Y, Wang H (2013) A battery energy storage system dual-layer control strategy for mitigating wind farm fluctuations. IEEE Trans Power Syst 28:3263–3273
32. Chowdhury MM, Haque ME, Gargoom A, Negnevitsky M (2012) A direct drive grid connected wind energy system with STATCOM and super-capacitor energy storage. In: 2012 IEEE international conference on power system technology (POWERCON), pp 1–6
33. Wang L, Yu JY, Chen YT (2011) Dynamic stability improvement of an integrated offshore wind and marine-current farm using a flywheel energy-storage system. IET Renew Power Gener 5:387–396
34. Islam F, Al-Durra A, Muyeen SM (2013) Smoothing of wind farm output by prediction and supervisory-control-unit-based FESS. IEEE Trans Sustain Energy PP:1–9
35. Lubosny Z, Bialek JW (2007) Supervisory control of a wind farm. IEEE Trans Power Syst 22:985–994
36. Gonzalez-Longatt FM (2012) Effects of the synthetic inertia from wind power on the total system inertia: simulation study. In: 2012 2nd international symposium on environment friendly energies and applications (EFEA), pp 389–395
37. Gonzalez-Longatt F (2012) Impact of synthetic inertia from wind power on the protection/control schemes of future power systems: simulation study. In: 11th international conference on developments in power systems protection (DPSP) 2012, pp 1–6
38. Gonzalez-Longatt F, Chikuni E, Stemmet W, Folly K (2012) Effects of the synthetic inertia from wind power on the total system inertia after a frequency disturbance. In: Power engineering society conference and exposition in Africa (PowerAfrica), IEEE 2012, pp 1–7
39. Miller N, Clark K, Walling R (2009) WindINERTIA: controlled inertial response from GE wind turbine generators. In: Presented at the 45th annual Minnesota power systems conference, Minneapolis, Minnesota, 2009
40. Miller NW, Clark K, Shao M (2011) Frequency responsive wind plant controls: Impacts on grid performance. In: Power and energy society general meeting, 2011 IEEE, pp 1–8
41. Wachtel S, Beekmann A (2009) Contribution of wind energy converters with inertia emulation to frequency control and frequency stability in power systems. In: Presented at the 8th international workshop on large-scale integration of wind power into power systems as well as on transmission networks for offshore wind farms, Bremen, Germany, 2009
42. ENERCON (2011) WindBlast. ENERCON Magazine for wind energy Issue 03 | 2010. www.enercon.de, http://www.enercon.de/p/downloads/Windblatt_0310_engl.pdf
43. Brisebois J, Aubut N (2011) Wind farm inertia emulation to fulfill Hydro-Quebec's specific need. In: Power and energy society general meeting, 2011 IEEE, pp 1–7
44. NG (2012) Frequency response technical sub group. http://www.nationalgrid.com/uk/Electricity/Codes/gridcode/workinggroups/freqrespTSG/
45. ENTSO-e (2011) ENTSO-E draft requirements for grid connection. https://www.entsoe.eu/index.php?id=42&no_cache=1&tx_ttnews%5btt_news%5d=106
46. Christensen PW, Tarnowski GC (2011) Inertia for wind power plants—state-of-the-art review—year 2011. In: Presented at the 10th international workshop on integration of wind power in power systems, Århus, Denmark, 2011
47. Gonzalez-Longatt F, Roldan JM (2012) Effects of DC voltage control strategies of voltage response on multi-terminal HVDC following a disturbance. In: 47th international universities power engineering conference (UPEC) 2012, pp 1–6

48. Gonzalez-Longatt F, Roldan JM, Charalambous CA (2012) Solution of AC/DC power flow on a multiterminal HVDC system: illustrative case supergrid phase I. In: 47th international universities power engineering conference (UPEC) 2012, pp 1–7
49. FOSG (2011) Friends of the supergrid. http://www.friendsofthesupergrid.eu/
50. Rudion K, Orths A, Eriksen PB, Styczynski ZA (2010) Toward a Benchmark test system for the offshore grid in the North Sea. In: Power and energy society general meeting, 2010 IEEE, pp 1–8
51. D. Foundation. Clean power from deserts—the DESERTEC concept for energy, water and climate security. www.desertec.org/downloads/articles/trec_white_paper.pdf
52. Vrana TK, Torres-Olguin RE, Liu B, Haileselassie TM (2010) The North Sea super grid—a technical perspective. In: 9th IET international conference on AC and DC power transmission (ACDC) 2010, pp 1–5
53. Bangar A, Hamidi V (2012) Control strategy requirements for connection of offshore windfarms using VSC-HVDC for frequency control. In: 10th IET international conference on AC and DC power transmission (ACDC) 2012, pp 1–6
54. FOSG (2010) Friends of supergrind. Position paper on the EC communication for a European infrastructure package. http://www.friendsofthesupergrid.eu/documentation.aspx
55. Haileselassie TM, Torres-Olguin RE, Vrana TK, Uhlen K, Undeland T (2011) Main grid frequency support strategy for VSC-HVDC connected wind farms with variable speed wind turbines. In: PowerTech, 2011 IEEE Trondheim, pp 1–6
56. Zhixin M, Lingling F, Osborn D, Yuvarajan S (2010) Wind farms With HVDC delivery in inertial response and primary frequency control. IEEE Trans Energy Convers 25:1171–1178
57. Pipelzadeh Y, Chaudhuri B, Green TC (2012) Inertial response from remote offshore wind farms connected through VSC-HVDC links: a communication-less scheme. In: Power and energy society general meeting, 2012 IEEE, pp 1–6
58. Jiebei Z, Campbell BD, Grain AP, Roscoe JA (2011) Inertia emulation control of VSC-HVDC transmission system. In: 2011 international conference on advanced power system automation and protection (APAP), pp 1–6
59. Haileselassie TM, Uhlen K (2010) Primary frequency control of remote grids connected by multi-terminal HVDC. In: Power and energy society general meeting, 2010 IEEE, pp 1–6
60. Hendriks RL, Paap GC, Kling WL (2007) Control of a multiterminal VSC transmission scheme for connecting offshore wind farms. In: European wind energy conference, Milan, Italy, 2007

Active Power and Frequency Control Considering Large-Scale RES

Elyas Rakhshani and Pedro Rodriguez

Abstract Renewable energy sources (RES) like wind and PV are dependent on weather conditions and geographic location and as results their stochastic behavior can significantly influence power systems performance. These effects will be more relevant in case of large-scale penetration of RES. Therefore, modern power plants based on RES should both deliver power as conventional generators and contribute to support the grid services by providing ancillary services and in this way applications of advanced technology are very important to reach this goal. Active power and frequency controls are known as essential ancillary services that should be provided by generation units in large power plants. Therefore, controlling this type of grid interactive power plants is critical issue to achieve large-scale integration of RES in distributed power systems. In consequence, it is necessary to take advantages of new technologies and advanced control concepts in order to configure more intelligent and flexible generation systems, which should be able to improve the performance and stability of grid. A brief review on conventional active power/frequency control issues and complete investigation on adapted scenarios of active power/frequency control considering liberalized markets, high penetration of RES and coexistence of AC and DC networks will be explained in this chapter.

Keywords Active power · Frequency control · Automatic generation control · Advanced optimal control · Deregulated power market

E. Rakhshani (✉) · P. Rodriguez
ABENGOA Campus Palmas Altas, Building G, Energia Solar 1 St 41014 Seville, Spain
e-mail: elyas.rakhshani@research.abengoa.com

P. Rodriguez
Technical University of Catalonia (UPC) GAIA Building, Rambla Sant Nebridi S/n 08222 Terrassa-Barcelona, Spain
e-mail: prodriguez@ee.upc.edu; pedro.rodriguez@research.abengoa.com

J. Hossain and A. Mahmud (eds.), *Large Scale Renewable Power Generation*, Green Energy and Technology, DOI: 10.1007/978-981-4585-30-9_9,

1 Introduction

Energy is a very important issue all around the world and during the last few decades, energy demands increased rapidly. Beside all problems related to coal energy, the new trends in the world are to increase the application of renewable energy sources to provide more green electrical energy. The concept of deregulation and competition in power market of energy is another important issue that forced the scientists to think more about the challenges related to modification of conventional large-scale power system [1].

Solar power is a type of energy with great future potential. As reported by EPIA (European Photovoltaic Industry Association), the world cumulative installed solar energy capacity was 22,900 MW in 2009, a change of 46.9 % compared to 2008. Renewable type electricity will be faced with a remarkable growth by 2030 [2, 3]. This suggests RE could participate in several ancillary services like frequency support and play important roles in transition to a sustainable energy economy. However, in order to have more DGs systems as a major source of energy, advanced development of technologies are very important.

These days we are facing with growth and extension of AC systems and as result with more complexity and more stability problems. In new scenarios of modern power system with high penetration of renewable energy sources (RES), the role of advanced technologies will be so important. For example, HVDC can essentially improve the reliability of complex interconnected systems. Furthermore, HVDC is a kind of firewall against cascading disturbances and in this way, it prevents blackouts. For these reasons, in some parts of the world, HVDC or hybrid interconnections, consisting of AC and DC interconnections, became already the preferred solution. The first commercial application of HVDC was between the Swedish mainland and the island of Gotland in 1954 [4]. Since then, there has been a huge increase in the application of HVDC transmission.

Based on this brief introduction, that is clear the future power system is a very challenging issue with high penetration of RES, DC transmission, and high complexity. Scientists and engineers have intensified their research efforts during the last decade to change such pessimistic electrical scenario. Technological advances, such as the use of modern power processing systems, energy storage and control techniques in high-power systems, as well as some last decade socioeconomic factors, such as the large-scale penetration of renewable energy sources, the generalized liberalization of electrical markets and the strategic importance dispensed to the security in supply, have led to a reformulation of the conventional power systems, moving toward a more flexible distributed generation scheme.

The organization of the chapter is as follows: Section 2 presents the conventional story for frequency/active power control with a complete model of automatic generation control (AGC) for active power control and Sect. 3 presents adapted scenarios considering market environment for adapting the conventional model of AGC model in the deregulated environment of power system. Detailed model of AGC considering the effects of renewable resources like PV and also the effects

of adding the HVDC links on the active power responses will be discussed and presented. Then new applications of advanced control concepts for active power and frequency control issues will be presented in Sect. 4. It should be noted that to have a better understanding for each concept of this chapter; several simulation examples with different scenarios are presented. Finally, Sect. 5 closes the chapter with the main conclusions and possible solutions for modern future power system.

2 Conventional Scenario in Active Power Control

The frequency of the system is dependent on active power balance and any mismatch between load and generation will be reflected into the system with changing the frequency [4]. The control of generated power and frequency in large-scale power systems is commonly referred as load–frequency control (LFC).

2.1 Primary Active Power/Frequency Control

As frequency is a common factor throughout the system, a change in active power demand at one point is reflected throughout the system (Fig. 1). This issue is mainly related with LFC concept.

Primary frequency control is a very well-known concept in power system studies [4–8]. As shown in Fig. 2, the first reaction of speed governors of generation units will be reflected to primary control or load frequency control. At this stage, the system will try to stabilize load change and contingencies. As shown in this figure, later by applying secondary supplementary frequency control the steady state error of frequency will be covered to the desired values [6].

2.2 Supplementary Higher Level Control

In addition to primary control, another higher level control which is known as AGC will be applied to ensure the area absorbs its own load change and also to maintain net interchanges and frequency at their schedule values.

2.2.1 Area Control Error

The area control error (ACE) will present the imbalance of generated power and load demands within the control area. By means of ACE, any power/frequency mismatched though the interconnected system will be checked. ACE could be a linear combination of frequency deviation and net interchange [7, 8].

$$\mathrm{ACE}_i = \Delta P_{\mathrm{tie},ij} + \beta_i \Delta f \tag{1}$$

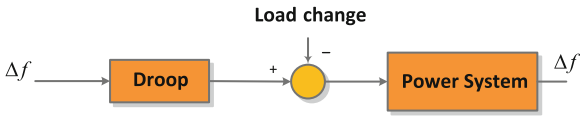

Fig. 1 The droop governor model for load–frequency effects

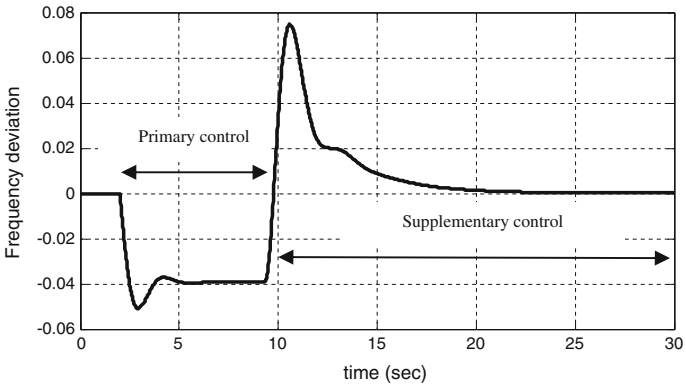

Fig. 2 Frequency deviation responses (Hz) in primary and supplementary controls

where $\Delta P_{\text{tie},ij}$ is deviation of transmitted power between areas and β_i is the frequency bias of each area. Frequency bias could be calculated as follows:

$$\beta_i = \frac{1}{R_i} + D_i \tag{2}$$

while R_i is the droop characteristic of generation units and D_i is the load-damping constant.

2.2.2 Area Participation Factor

Area participation factor (APF) is another important signal for doing the AGC though the supplementary control. In fact, if there will be more than one generation unit in one area or if some generation unit cannot participate in AGC, there is a possibility to manage their participation by means of participation factor. In each area, the sum of participation factors is equal to 1 [7].

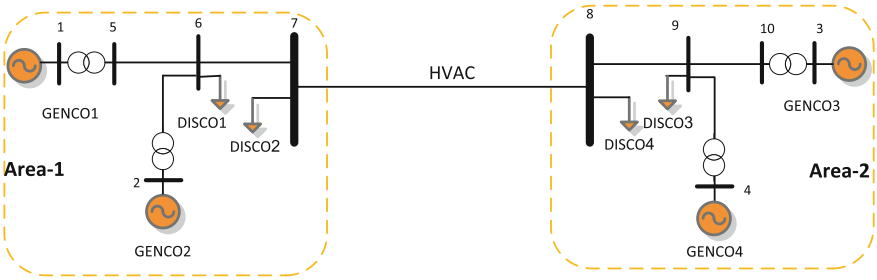

Fig. 3 Two area model for dynamic analysis of interconnected systems

2.2.3 Control of Interconnected Multi-Area Systems

Automatic generation control is one of the main functions of Energy Management Systems (EMS) and controlling of frequency, generated power, and transmitted power through the transmission lines are the most important responsibilities of AGC in multiarea interconnected power system.

A typical system for this type of analysis is a modified two-area interconnected system [4] as shown in Fig. 3. Two generation companies (GENCO) and two distribution companies (DISCO) as loads have been considered for each area.

A proper control strategy for active power/frequency issue is shown in Fig. 4. A low-order linearized model could be used for modeling the load-generation dynamics. The relationships between power deviations and frequency deviation are as follows [4]:

$$\Delta P_m(s) - \Delta P_L(s) = 2Hs\Delta f(s) + D\Delta f(s) \tag{3}$$

where ΔP_m is generated power deviation, ΔP_L is load change, H is the inertia constant of the system ($M_{\text{sys}} = 2H$) in second and D is the load damping coefficient. For modeling the interconnections between N areas, the tie-line power change between area i and the rest of area could be presented as [7, 8]:

$$\Delta P_{\text{tie},ij} = \sum_{\substack{j=1 \\ j \neq i}}^{N} \Delta P_{\text{tie},ij} = \frac{2\pi}{s}\left[\sum_{\substack{j=1 \\ j \neq i}}^{N} T_{ij}\Delta f_i - \sum_{\substack{j=1 \\ j \neq i}}^{N} T_{ij}\Delta f_j\right] \tag{4}$$

where T_{ij} is the synchronizing coefficient between areas. For two-area system with two generation units in each area, the s-domain could be like this:

$$\Delta F_1(s) = \frac{1}{D_{\text{sys},1} + sM_{\text{sys},1}}\left(\Delta P_{m1} + \Delta P_{m2} - \Delta P_{d1} - \Delta P_{\text{tie},12}\right) \tag{5}$$

$$\Delta F_2(s) = \frac{1}{D_{\text{sys},2} + sM_{\text{sys},2}}\left(\Delta P_{m3} + \Delta P_{m4} - \Delta P_{d2} + \Delta P_{\text{tie},12}\right) \tag{6}$$

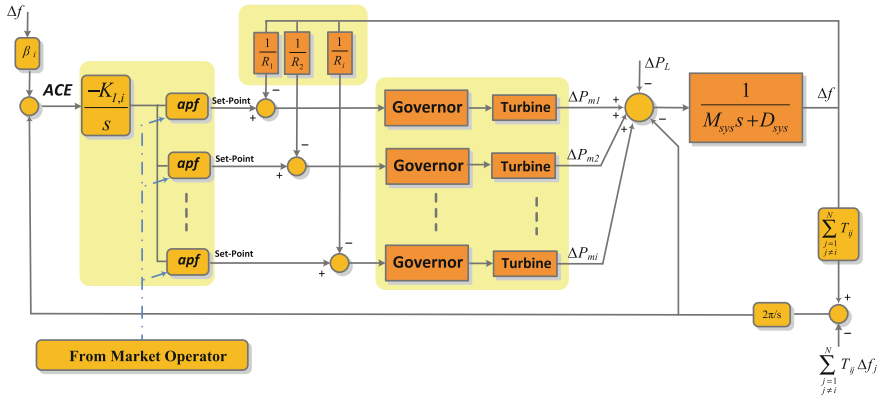

Fig. 4 Frequency control strategy for dynamic analysis of interconnected systems

where ΔP_m is deviation of generated power by each unit and ΔP_d is any local load change as disturbance. Relationship between output power deviation and frequency could be as follows:

$$\Delta P_{m1}(s) = \frac{1}{1 + sT_{T-G,1}}\left[\text{apf}_1 K_{I,1} \int \text{ACE}_1 - \frac{1}{R_1}\Delta F_1(s)\right], \tag{7}$$

$$\Delta P_{m2}(s) = \frac{1}{1 + sT_{T-G,2}}\left[\text{apf}_2 K_{I,1} \int \text{ACE}_1 - \frac{1}{R_2}\Delta F_1(s)\right], \tag{8}$$

$$\Delta P_{m3}(s) = \frac{1}{1 + sT_{T-G,3}}\left[\text{apf}_3 K_{I,2} \int \text{ACE}_2 - \frac{1}{R_3}\Delta F_2(s)\right], \tag{9}$$

$$\Delta P_{m4}(s) = \frac{1}{1 + sT_{T-G,4}}\left[\text{apf}_4 K_{I,2} \int \text{ACE}_2 - \frac{1}{R_4}\Delta F_2(s)\right]. \tag{10}$$

The AC transmitted power deviation for two-area system will be like this:

$$\Delta P_{\text{tie},12}(s) = \frac{T_{12}}{s}\left[\Delta F_1(s) - \Delta F_2(s)\right]. \tag{11}$$

2.3 Multi Machine Four-Area Power System Example

In order to show the performance of AGC in a multimachine system, a general scenario for detailed model of 12-bus test system (Fig. 5) is performed in Simpower/MATLAB software. Complete data and parameters of this 12-bus benchmark are

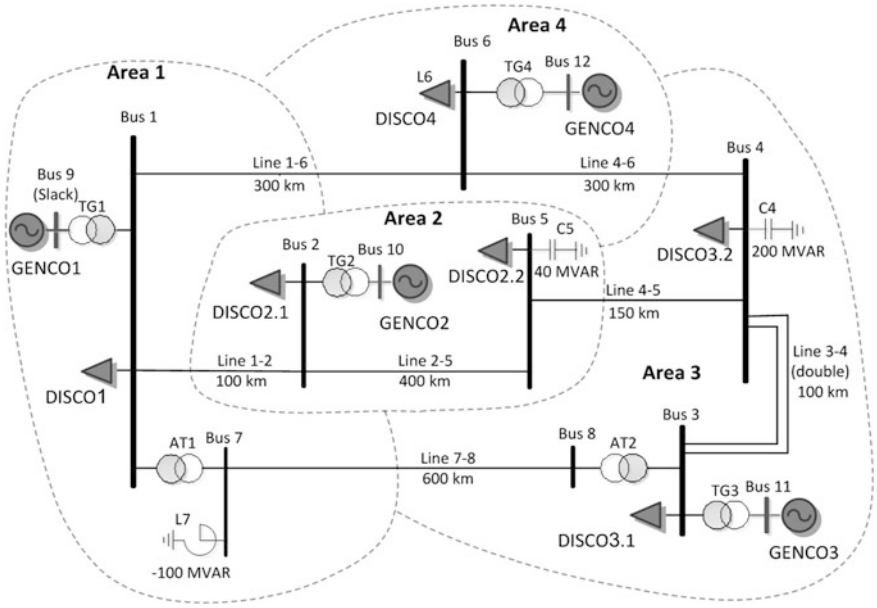

Fig. 5 12-bus multimachine test system with four areas

given in appendix of this chapter. As explained before, the steady state error in frequency and transmitted power could not be solved by primary local frequency control. So another type of higher level control based on AGC should be implemented. Based on the defined standard for frequency regulation, the response of this higher level control will be slower than those local controllers, so AGC will be completed after starting the actions of primary frequency controllers.

The system responses for this example are presented in Figs. 6, 7, and 8. In order to check the performance of AGC control strategy, it is assumed that after 250 s a large step load reduction around 7 % p.u. is happened for demanded load of DICSO3.1 in third area. As shown in Figs. 6 and 7, by decreasing the demanded load, the frequency start to increase, while by acting of AGC both frequency and scheduled transmitted power could remain on their scheduled values.

Usually, with using this supplementary control action in AGC strategy, perturbation in any area should be responded with the nearest units, mainly with all the units in the same area and some in the neighbors. As shown in Fig. 8, load iation in area 3 is responded with GENCO3 in the same area by decreasing its output.

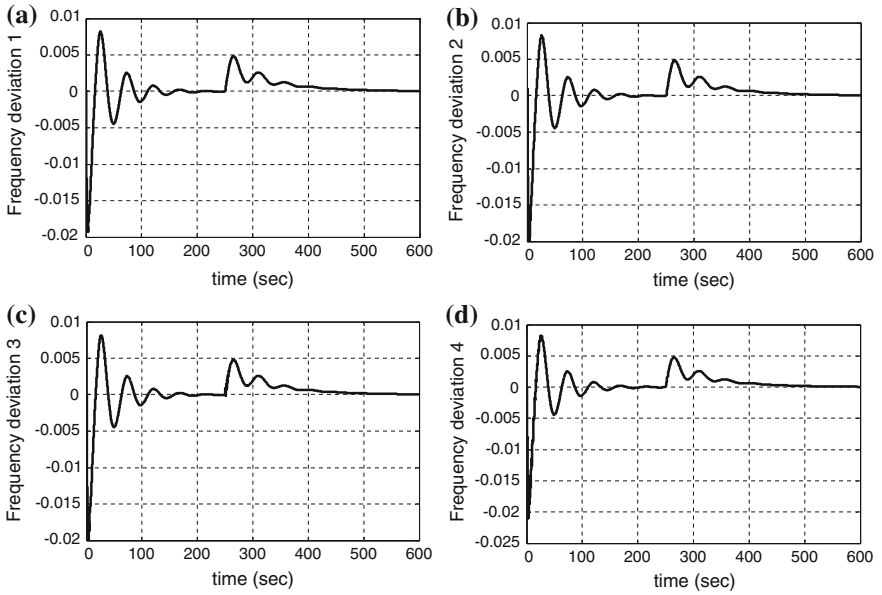

Fig. 6 Frequency deviations for step load change at 250 s (Hz): **a** area 1, **b** area 2, **c** area 3, **d** area 4

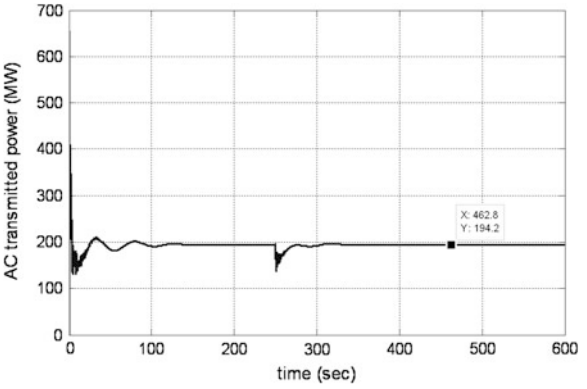

Fig. 7 Tie-line power deviation from bus 7 to 8 (MW)

3 Adapted Scenarios

As explained in the introduction of this chapter, the main trends of modern future power system will be through three main adaption which will be related to market activities, RES penetration with advanced technology and AC/DC transmissions.

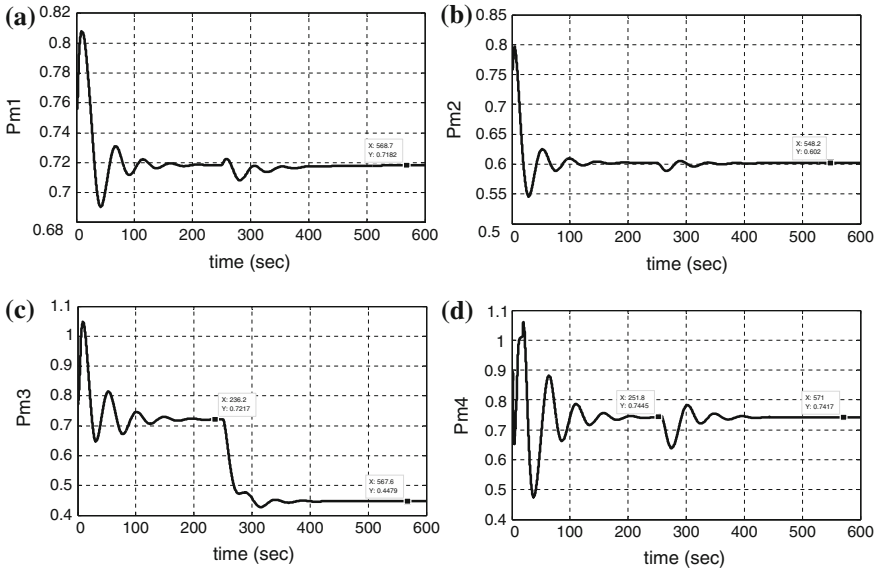

Fig. 8 Output power deviations of generation units (p.u.): **a** GENCO1, **b** G ENCO2, **c** GENCO3, **d** GE NCO4

So in this section, the modeling and control issue of active power and frequency control will be presented based on deregulated scenarios of power market, RES modeling and HVDC effects on dynamics responses of large system.

3.1 Power/Frequency Control in Market Environment

In order to have more competition in power industry, it is necessary to modify and adapt the conventional models by adding the market signals for performing complete scenarios by evaluating the effects of bilateral contracts of market on active power control and dynamics of interconnected power system.

3.1.1 AGC Market Review

The electric power industries worldwide have undergone considerable changes especially from vertical structure to full deregulated entities [9, 10]. In the competitive environment of power system, the vertically integrated utility (VIU) no longer exists. Deregulated system will consist of Generation Companies (GENCOs), Distribution Companies (DISCOs), transmission companies (TRANSCOs), and independent system operator (ISO) [11–13]. In the deregulated power system, competition is the main goal of energy privatization. In this way, access to the transmission system and the

possibility of presenting ancillary services are some of the main issues in the market environment. The AGC service and related transactions in market will be supervised by an independent system operator (ISO) and transmission system operator (TSO) [10]. In the deregulated environment, we will have a lot of independent power producer like DGs and in this kind of environment DC interconnections like VSC-HVDC are very important to act as a corridor to transfer power based on possible scenarios, which will discussed by the next following sections.

3.1.2 Active Power/Frequency Control in Market

In the deregulated scenario of active power control for interconnected systems, any GENCO in any area may supply any DISCOs in its user pool and DISCOs in other areas through tie-lines between areas. In other words, for restructured system having several GENCOs and DISCOs, any DISCO may contract with any GENCO in another control area independently. This case is called as "bilateral transactions." The transactions have to be implemented through an independent system operator. The impartial entity, ISO, has to control many ancillary services, one of which is AGC. In deregulated environment, any DISCO has the liberty to buy power at competitive prices from different GENCOs, which may or may not have contract in the same area as the DISCO. Based on the idea presented in [11], the concept of an "augmented generation participation matrix" (AGPM) to express the possible contracts in AGC system will be used. The AGPM shows the participation factor of a GENCO in the load following contract with a DISCO. The number of rows and columns of AGPM matrix is equal to the total number of GENCOs and DISCOs in the overall power system, respectively. So, the AGPM structure for a large-scale power system with N control areas is given by [14]:

$$\mathrm{AGPM} = \begin{bmatrix} \mathrm{AGPM}_{11} & \cdots & \mathrm{AGPM}_{1N} \\ \vdots & \ddots & \vdots \\ \mathrm{AGPM}_{N1} & \cdots & \mathrm{AGPM}_{NN} \end{bmatrix} \tag{12}$$

where

$$\mathrm{AGMP}_{ij} = \begin{bmatrix} \mathrm{gpf}_{(s_i+1)(z_j+1)} & \cdots & \mathrm{gpf}_{(s_i+1)(z_j+m_j)} \\ \vdots & \ddots & \vdots \\ \mathrm{gpf}_{(s_i+n)(z_j+1)} & \cdots & \mathrm{gpf}_{(s_i+n_i)(z_j+m_j)} \end{bmatrix}.$$

For $i,j = 1,\ldots, N$ and

$$s_i = \sum_{k=1}^{j-1} n_i, z_j = \sum_{k=1}^{i-1} m_j, s_1 = z_1 = 0. \tag{13}$$

In the above, N is the number of areas, n_i and m_i are the number of GENCOs and DISCOs in area i and gpf_{ij} refers to "generation participation factor" and

shows the participation of GENCO_i in the total load following requirement of DISCO_j based on the possible contract. The sum of all entries in each column of an AGPM is unity. The diagonal submatrices of AGPM correspond to local demands and off-diagonal submatrices correspond to demands of DISCOs in one area on GENCOs in another area. The details and block diagram of the generalized AGC scheme for a two-area deregulated power system are shown in Fig. 9 dashed lines show interfaces between areas and the demand signals based on the possible contracts. These new information signals are absent in the traditional LFC scheme.

As there are many GENCOs in each area, the AC signal has to be distributed among them due to their ACE participation factor in the LFC task by the following equations [14]:

$$d_i = \Delta P_{\text{Loc},i} + \Delta P_{di}. \tag{14}$$

It means that the total load changes d_i will consist of total contracted demand ($\Delta P_{\text{Loc},i}$) and total un-contracted load changes of area as disturbance (ΔP_{di}).

$$\Delta P_{\text{Loc},i} = \sum_{j=1}^{m_i} \Delta P_{Lj-i}, \Delta P_{di} = \sum_{j=1}^{m_i} \Delta P_{ULj-i} \tag{15}$$

$$\zeta_i = \sum_{\substack{k=1 \\ K \neq i}}^{N} \Delta P_{\text{tie},ik,\text{sch}} \tag{16}$$

where ζ_i is the scheduled tie-line power flow deviation and then:

$$\Delta P_{\text{tie},ik,\text{sch}} = \sum_{j=1}^{n_i} \sum_{t=1}^{m_k} \text{apf}_{(s_i+j)(z_k+t)} \Delta P_{Lt-k} - \sum_{t=1}^{n_k} \sum_{j=1}^{m_i} \text{apf}_{(s_k+t)(z_i+j)} \Delta P_{Lj-i} \tag{17}$$

$$\Delta P_{\text{tie},i,\text{error}} = \Delta P_{\text{tie},i,\text{actual}} - \zeta_i \tag{18}$$

$$\Delta P_{m,k-i} = \rho_{ki} + apf_{ki} \sum_{j=1}^{m_i} \Delta P_{ULj-i}, k = 1, 2, \ldots, n_i \tag{19}$$

where ΔP_{ULj-i} is the un-contracted demands and $\Delta P_{m,k-i}$ is the scheduled total power generation of a GENCO_k in area i that should track the demand of DISCOs based on market contracts and:

$$\rho_{ki} = \sum_{j=1}^{N} \left[\sum_{i=1}^{m_j} \text{apf}_{(s_i+k)(z_j+t)} \Delta P_{Lt-j} \right]. \tag{20}$$

Also the error signal in Eq. (18) is used to generate its ACE signals in the steady state as follows:

$$\text{ACE}_i = \beta_i \Delta f_i + \Delta P_{\text{tie},i,\text{error}}. \tag{21}$$

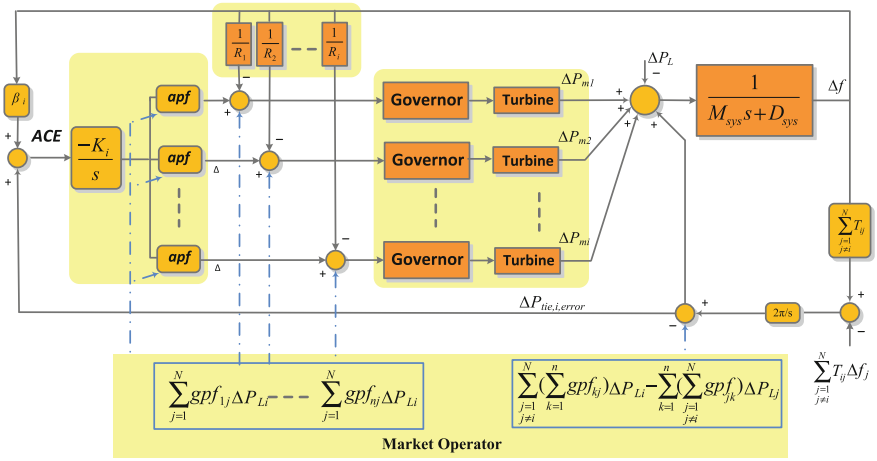

Fig. 9 Modified model of AGC control in a deregulated environment

Based on this type of matrix definition, it is possible to adapt the conventional scenarios to modified model presented in Fig. 9 for dynamic analysis of large complex interconnected systems.

3.1.3 Multi Machine Two-Area Example Considering Power Market Contracts

In order to show the market effects on AGC system in multimachine system and to evaluate the manner of implementing market contracts on the system, a two-area power system shown in Fig. 3 is implemented. Complete data and parameters of implemented two-area benchmark are given from [4] and [14].

The whole power system structure can be considered as a pool of DISCOs and GENCOs when each GENCOs can contract with any DISCOs based on their negotiable bilateral policies. The concept of AGPM could define any type of bilateral contracts for any complex interconnected system with several GENCO and DISCOs. In this example, DISCOs have the freedom to have a contract with any GENCO in their or other areas. So all the DISCOs contract with the GENCOs for power base on following AGPM:

$$\text{AGPM} = \begin{bmatrix} 0.5 & 0.25 & 0 & 0.3 \\ 0.2 & 0.25 & 0 & 0 \\ 0.0 & 0.25 & 1 & 0.7 \\ 0.3 & 0.25 & 0 & 0 \end{bmatrix}.$$

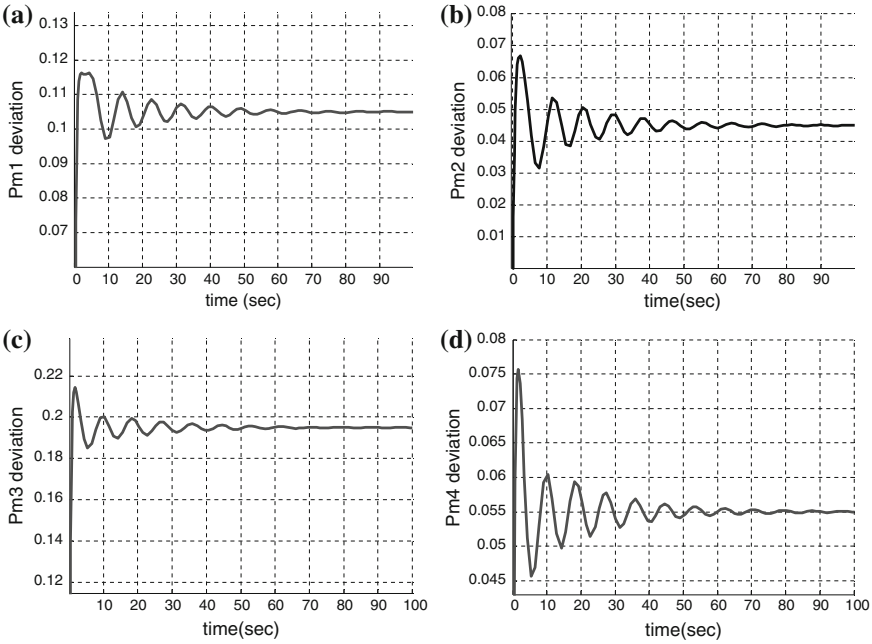

Fig. 10 Output power deviations of generation units (p.u.): **a** GENCO1, **b** GENCO2, **c** GENCO3, **d** GENCO4

It is also considered that each DISCO demands 0.1 p.u. total power from GENCOs as defined by entries in AGPM and each GENCO participate in ACE as defined by following apfs:

$$\text{apf}_1 = 0.75, \quad \text{apf}_2 = 0.25$$

$$\text{apf}_3 = 0.50, \quad \text{apf}_4 = 0.50.$$

As shown in Fig. 10, the actual generated powers of the GENCOs properly reach the desired contracted values in the steady state as given by Eq. (19):

$$\Delta P_{m1} = 0.105\,\text{p.u. MW}, \quad \Delta P_{m2} = 0.045\,\text{p.u. MW}$$

$$\Delta P_{m3} = 0.195\,\text{p.u. MW}, \quad \Delta P_{m4} = 0.055\,\text{p.u. MW}.$$

The off diagonal blocks of the AGPM correspond to the contract of a DISCO in one area with a GENCO in another area. As Fig. 11 shows, the tie-line power flow properly converges to the specified value of Eq. (17) in the steady state, i.e., $\Delta P_{\text{tie1}-2,\ \text{scheduled}} = -0.\ 05$ p.u.

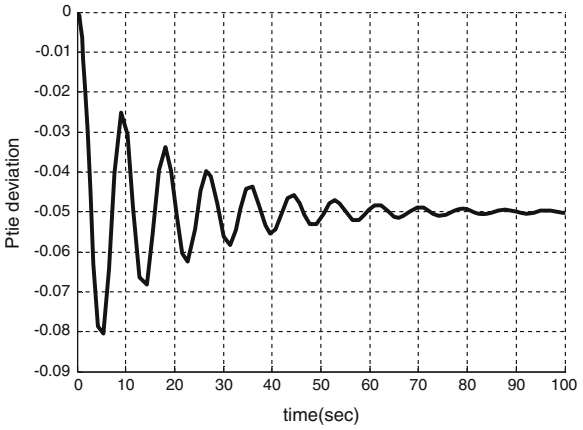

Fig. 11 Tie-line power deviation between two areas (p.u.)

3.2 Power/Frequency Control with Res Penetrations

Modern power system are making fundamental changes in conventional structures while high penetration of renewable resource with different type of AC/DC interconnections though the market policies are the main focus of research these years.

Renewable energy has reached high penetration levels especially in the USA and Europe, with some big PV power plants in the range of 250 MW in the USA, while these levels will continue to rise at least in the next several years. So there is a possibility to participate them for ancillary services like frequency support at the transmission level of interconnected power system. But in parallel, they could have negative effects on the system since RES could increase uncertainties during abnormal conditions and act as an additional source of disturbance. There is a lack of inertia by high penetrated systems especially in case of PV power plants and also the stochastic nature of RES is another issue that should be added to the dynamic modeling of large-scale power systems. The main question is that in high penetration of RE power plants, for how much the balancing uncertainties will be increased? Naturally it is known that fluctuations in PV or Wind output are largely uncorrelated to load. This implies that the additional uncertainty introduced by PV power does not add linearly to the uncertainty of predicting the load.

3.2.1 Adapted Active Power Control Models

Managing the new technologies in deregulated system is more difficult than conventional generation management due to their primary resources, most of them are not fully controllable and highly stochastic that eventually will have various impacts, like steady state or transient effects, on the large power system. There is a need for more study and research to see all negative and positive effects of large-scale PV system on the grid by proposing adapted models for modeling the effects

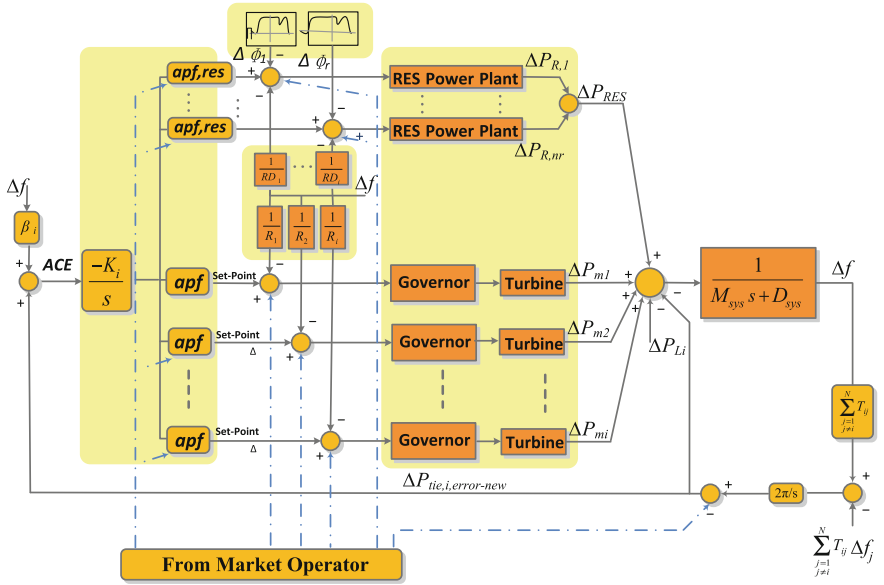

Fig. 12 Modified model of AGC control considering RES

of RES on the system [15, 16]. The adapted model for active power/frequency control is presented in Fig. 12. Based on this model, the main difference between modellng of conventional model and updated model with RES is in two main signals which are related to dynamic impacts of stochastic nature of RES in the local disturbances ($\Delta\Phi$) and tie-line power changes ($\Delta P_{\text{tie,RES}}$):

$$\Delta P_{\text{tie,RES}} = \sum \left(P_{\text{tie,RES-actual}} - P_{\text{tie,RES-schedule}}\right). \tag{22}$$

Then the new tie-line power deviation could be as follows:

$$\Delta P_{\text{tie},i,\text{error-new}} = \Delta P_{\text{tie},i,\text{error}} + \Delta P_{\text{tie,RES}}. \tag{23}$$

As result, the ACE signal should be updated as follows:

$$\text{ACE} = \beta_i + \Delta P_{\text{tie},i,\text{error-new}}. \tag{24}$$

By considering the effects of primary and supplementary frequency control in Fig. 12, the system frequency deviation will be as follow:

$$\Delta f_i(s) = \frac{1}{M_{\text{sys}}s + D_{\text{sys}}} \left[\sum_{k=1}^{n} \Delta P_{mk}(s) + \Delta P_{\text{RES}}(s) - \Delta P_{Li}(s) - \Delta P_{\text{tie},i,\text{error-new}}(s)\right] \tag{25}$$

$$\Delta P_{\mathrm{RES}}(s) = \sum_{r=1}^{nr} \Delta P_{R,r}(s) \tag{26}$$

$$\Delta P_{R,r}(s) = \Delta \Phi_r(s).G_{\mathrm{RES}} + \Delta P_{c,p}(s) - \frac{\Delta f_i(s)}{RD_r} \tag{27}$$

where $p = 1{:}nr + n$, n is the number of conventional generators, nr is the number of renewable power plants, G_{RES} is the transfer function defining the dynamic behavior of RES and $\Delta P_{c,p}(s)$ is the set-points for contributing each unit for active power/frequency support.

Note that RD_r is the droop of RES power plants. This value will be different from conventional ones and depend on the type of power plant higher values could be assigned [17].

Usually small-scale renewable resources like PV especially without any reserve or storage devices could not contribute in AGC services and output response will be like this:

$$\Delta P_r(s) = \Delta \Phi_r(s).G_{\mathrm{RES}} + \Delta P_{c,p}(s). \tag{28}$$

At this condition, grid feeding type PV power plant with fixed output based maximum power point tracking (MPPT) cannot contribute in primary frequency control and based on market policies and physical capacity, they are implemented. But by using advance technologies and storage devices in large-scale PV power plant a complete participation in primary and also secondary frequency control is feasible. In fact, applying a normal grid feeding PV power plant based on MPPT for a fixed maximum power output will reduced the flexibility for active power and frequency regulation [18, 19]. In order to solve this problem, a kind of pseudo power point tracking or kind of coordination is necessary to prepare PV power plant to do its responsibility as a normal part of the grid for contributing in frequency control services. It is also worthy to mention that, conventionally, inverters frequency with using Phase Locked Loop (PLL) control will follow the frequency of grid and it will not appropriate for system stability especially in the abnormal conditions. The new concept of virtual synchronous generator (VSG) presents solutions which control the inverter to behave like a synchronous generator. In this concept, a short-term storage system will be combined by renewable resources with a suitable control mechanism for its power electronics converters [20]. Also adding energy storage system (ESS) will reduce the overall losses. The ESS will be charged by the power difference between the local maximum PV power and the local command PV power at day time. Also in case of modern wind turbines with the capability of pith control, they could change their output in real time for contributing in frequency support.

Characteristic of WTG's Output Power

The mechanical output power of wind turbine could be written as:

$$P_W = C_p(\lambda, \beta)\left(\frac{1}{2}\rho A_r V_W^3\right) \tag{29}$$

$$\lambda = \frac{R_{\text{blade}}\omega_{\text{blade}}}{V_W} \tag{30}$$

where ρ is the air density is assumed to be 1.25 kg/m^3, V_W is the wind speed, A_r is the swept area of blades assumed to be 1735 m^2 and C_p is a non-dimensional curve of power coefficient as a function of tip speed ratio λ and blade pitch angle β. The overall performance of a wind turbine depends on the construction and the orientation of the blades [21]. One important parameter is the pitch angle which is the angle between the cord line of the blade and the plane of rotation.

Characteristic of PV Output Power

The output power of PV plants could be determined by the following equation:

$$P_{PV} = \eta S \Phi[1 - 0.005(T_a + 25)] \tag{31}$$

where η is the conversion efficiency of the PV array usually by using new advanced technologies could reach up to 25 %. S is also the measured area of PV array, Φ is the solar radiation around 1,000 W/m^2 and T_a is ambient temperature in degree Celsius. It is assumed that T_a is almost constant and then P_{PV} will be proportional with solar radiationΦ. Based on this assumptions the suitable transfer function could be made [21]. Note that for normal PV power plant without additional facilities like batteries or virtual synchronous processor, it would be possible to consider a first order transfer function. But by considering VSG concept which consists of PV and energy storage devices, two-order or much more complex transfer functions could be chosen.

3.2.2 Multimachine Two-Area Example Considering RES Effects

In order to evaluate the effects of RES power plants with and without droop actions, two different scenarios are simulated. In the first scenario, one multi MW PV power plant is added to the first area of presented model in Fig. 13. In this part of simulation, the effects of PV power plant under load step change and huge sunlight drop will be evaluated. Based on the technological issues, two different PV plants with/without the ability of droop participation are also considered. Then in order to show the positive effects of wind power plant for improving the

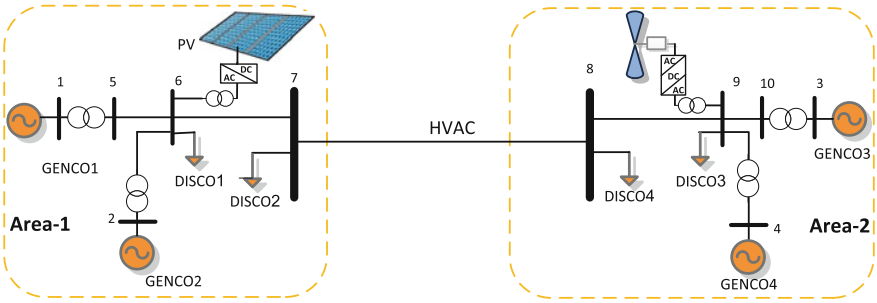

Fig. 13 Two-area model for dynamic analysis of interconnected systems

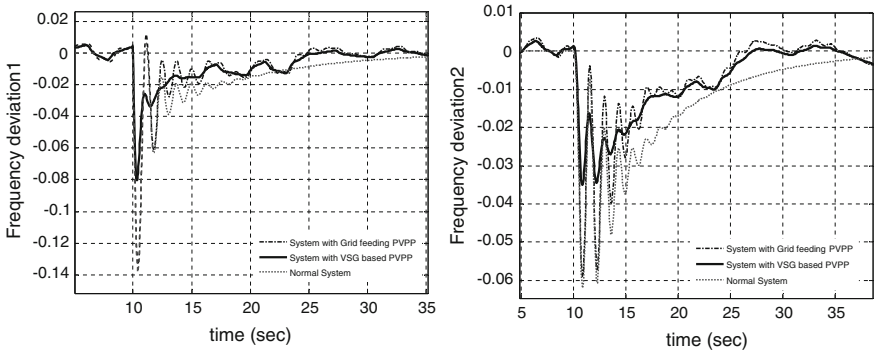

Fig. 14 Frequency deviations after load step change at 10 s (Hz)

oscillations of second area, the last scenario is simulated by considering another RES like a wind power plant in the second area.

Simulation of Two-Area Power System with PV Power Plant

In this simulation, it is assumed there is just one PV power plant in area 1 with two simultaneous contingencies at 10 and 50 s. The first one is related to one step load change around 0.1 p.u. in first area and the second one is related to reduction of generated power in PV power plant due to 50 % of sunlight drop for a period of 20 s. Based on the explanations in previous part, two different PV power plants are considered, one without the ability of participating in primary frequency (droop) control which will be based on a fixed output (MPPT based) grid-feeding PV power plant and the other type is an equipped PV power plant with energy storage or VSG based power plant which has the ability of droop/primary frequency control in real-time application. The effects of these different PV power plants on load variations of large interconnected power system are depicted in Figs. 14, 15,

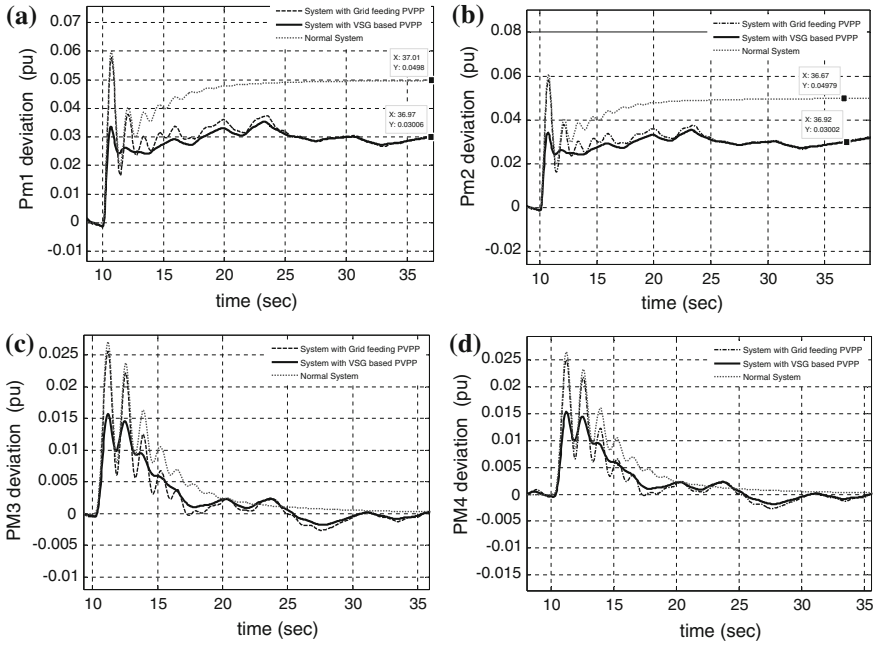

Fig. 15 Output power after load step change at 10 s: **a** GENCO1, **b** GENCO2, **c** GENCO3, **d** GENCO4

16, 17, 18 and 19. It should be noted that, in the simulations, the response of systems with RES like PV and Wind are compared to the normal system (the system of Fig. 3 without RES). Frequency responses in both areas are depicted in Fig. 14. In this figure, a normal system without RES are compared with the system including RES generations. Based on the result, it is obvious that using renewable resource with fixed output (Grid feeding type) without droop action will just improve the settling time of the system but after using more facilitated PV plants (like VSG-based PV) with the ability of droop/primary frequency control, there is a huge improvement in the dynamic of first overshoot of the system. Note that, small variation in the steady state response is because of the stochastic nature of the RES inputs.

The output power generations of each unit are depicted in Figs. 15 and 16. As shown in these figures, all conventional generators and PV power plant in the first area are participating on load variation (0.1 p.u. in area 1). The steady state values for each generation unit are related to assigned participation factors as follows:

$$\mathrm{apf}_1 = 0.03, \mathrm{apf}_2 = 0.03, \mathrm{apf}_{,PV1} = 0.04$$

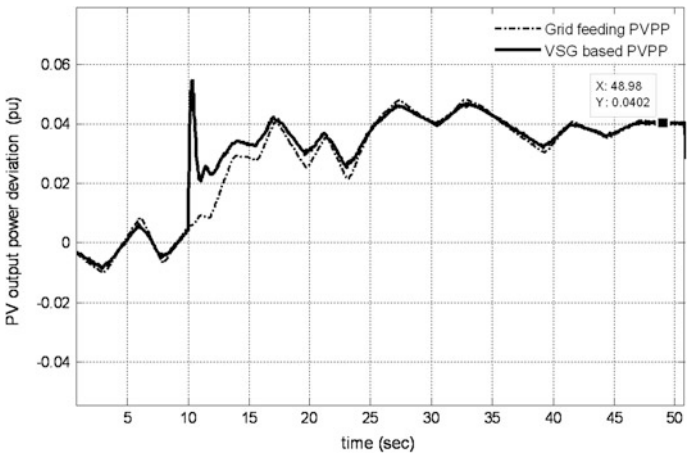

Fig. 16 Output power of PV power plant

Fig. 17 Irradiation (W/m^2)

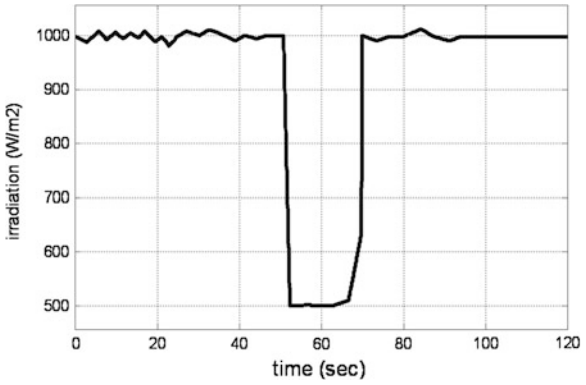

As shown in Fig. 15, the actual generated powers of the GENCOs properly reach their desired contracted values for area 1 as given by Eq. (19). That is,

$$\Delta P_{m1} = 0.03\,\text{p.}u.\,\text{MW}$$

$$\Delta P_{m2} = 0.03\text{p.u. MW}$$

$$\Delta P_{PV1} = 0.04\text{p.u. MW}$$

Also as shown in Figs. 15 and 16, with using energy storage with advanced technology, smoother responses against input variations is accessible.

The second contingency was related to 50 % drop in the sunlight (Fig. 17) which make a huge decrease at the output of PV power plant. The output generations of all units in area 1 are presented in Fig. 18. Based on the results, by reduction of power in PV output, conventional generators will try to compensate the PV part.

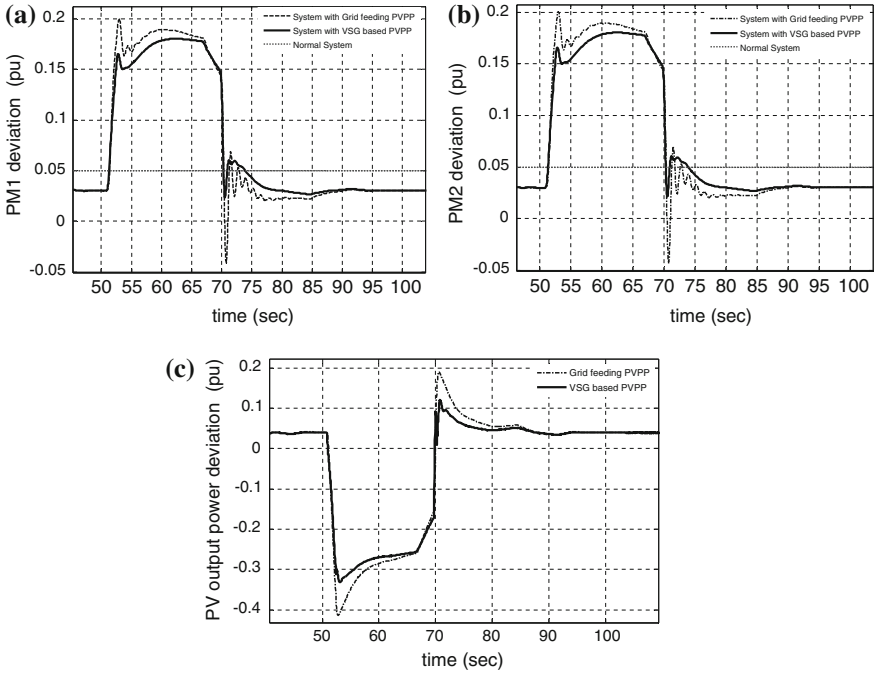

Fig. 18 System response after 50 % drop of sunlight: **a** GENCO1 output, **b** GENCO2 output, **c** PV plant output

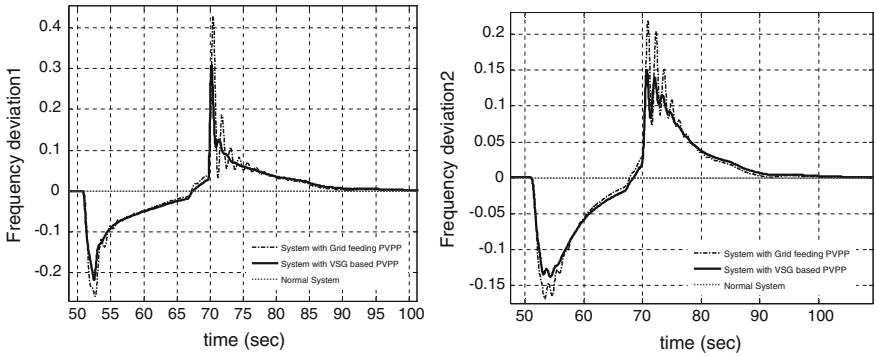

Fig. 19 Frequency deviation after huge reduction of PV plant output at 50 s

As shown in Fig. 19, there is a huge frequency drop in the system and it is because of high penetrations of renewable sources mixing with conventional plants. This drop could be improved by using some reserve or energy storage. The amount of stored energy is a very important key in this issue.

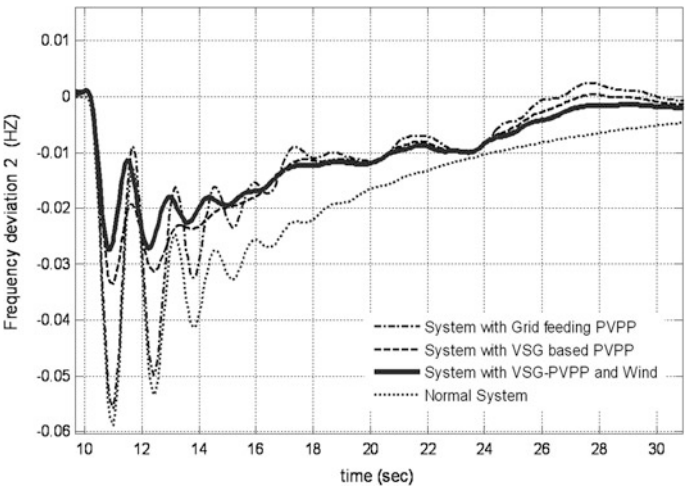

Fig. 20 Frequency deviations in area 2 after load step change at 10 s (Hz)

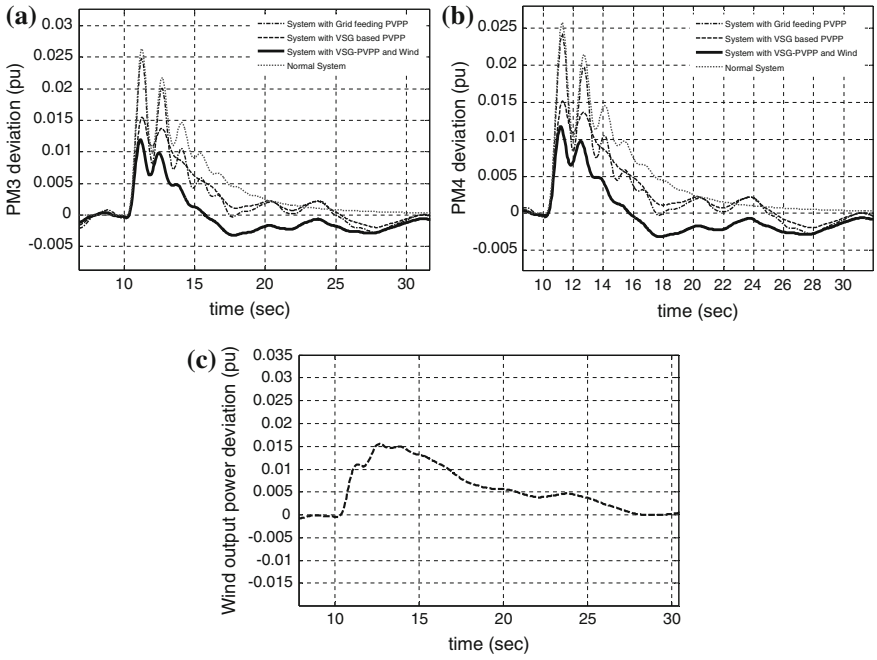

Fig. 21 Output power variations in area 2 after load change in area 1 at 10 s (p.u.): **a** GENCO3 output, **b** GENCO4 output, **c** Wind power plant output

Simulation of Two-Area Power System with Both PV and Wind Power Plants

In this scenario, in order to check the effects of wind generation on electromechanical oscillation in second area, the same simulation as previous case is considered just by adding a new wind power plant at bus nine in area 2. Based on simulation results, the main effects of wind power plant will be appeared in the related second area. The frequency deviation and output power deviations of all components in area 2 are presented in Figs. 20 and 21, respectively. As shown in Fig. 20, the first overshoot of frequency deviation is improved by adding wind power plant in second area.

In Fig. 21, the output variation of all related units in area 2 (GENCO3, GENCO4, and Wind power plant) are depicted. Based on these results, by participating of wind power plant in load step contingency, another improvement is clear in the generated output power variations.

3.3 Power/Frequency Control with AC/DC Transmission Lines for Interconnected Systems

In the future of modern power system with high penetration of renewable resources and deregulations, various applications of AC/DC interconnection arepredictable. In case of active power and frequency control, it would be also necessary to adapt conventional model based AC interconnection by adding the model of HVDC lines for better evaluations on system performance considering DC lines. By taking the advantages of the fast power control capability in HVDC systems together with the implementation of a supplementary controller to modulate the DC power transfer, based on an AC system signal, it is feasible to simultaneously achieve the main objectives of the AGC [22, 23]. In this section, for improve the LFC performance and avoiding HVAC limitations a new supplementary modulation controller for a bi-directional VSC-HVDC system is proposed [24].

3.3.1 Modified Model

In modern power system, to have better stability and proper control on dynamic behavior of active power and frequency, interconnections between neighboring areas will be important strategy. Sometimes these interconnections will be between asynchronous areas or there will be very large distance between generation and load centers which will lead to installation and operation of HVDC systems. Also in case of power market and liberalization of power system, we need secure corridors to transfer power for a very long distance. HVDC technology will be a very good candidate to face up with these problems. In order to show the

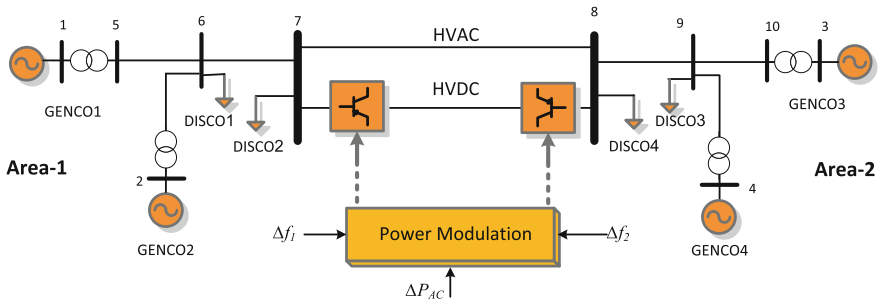

Fig. 22 Tow-area system with AC/DC links

effects of HVDC links on modeling and control of active power for interconnected power systems, a new parallel DC link is considered as shown in Fig. 22.

The main effect of this new DC link will appear in the equations related to tie-line power deviation by additional state which is related to DC transmitted power.

$$\Delta P_{\text{tie},12,\text{total}}(s) = \Delta P_{\text{AC}} + \Delta P_{\text{DC}} \tag{32}$$

where ΔP_{AC} is the old AC tie-line power explained in previous sections. Note that transmitted power consists of AC and DC power and ACE signal will affect by new parameters.

$$\int \text{ACE}_1(s) = B_1 \Delta F_1(s) + \Delta P_{\text{DC}}(s) + \Delta P_{\text{AC}}(s) \tag{33}$$

$$\int \text{ACE}_2(s) = B_2 \Delta F_2(s) - \Delta P_{\text{DC}}(s) - \Delta P_{\text{AC}}(s) \tag{34}$$

$$\Delta P_{\text{DC}}(s) = \frac{1}{1 + sT_{\text{DC}}} \Delta x_{\text{DC}}(s) \tag{35}$$

where T_{DC} is time constant of the HVDC unit and Δx_{DC} is the modulated control signal in supplementary power modulation controller (SPMC) of modified AGC control strategy.

Supplementary Power Modulation Controller for the HVDC Link

A new designed bi-directional power modulation controller is proposed to control the dc power flow through the VSC-HVDC link in a two-area interconnected power system. The DC link in this case, thanks to the use VSC-HVDC technology, acts as a bi-directional line that includes two converter stations, one performing as a rectifier at the sending side, and the other performing as an inverter at the receiving end. The block diagram of the supplementary power modulation controller for modeling the VSC-HVDC in AGC power system is shown in Fig. 23.

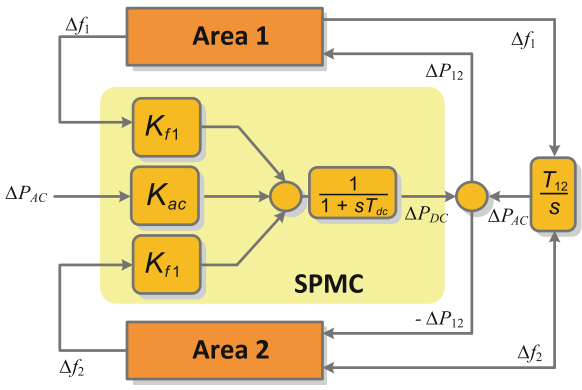

Fig. 23 Schematic diagram of applied SPMC in AC/DC systems for AGC

This controller modulates both frequency and active power by processing the frequency signal obtained from local measurements. The objective is to improve the electromechanical oscillation especially during load changes.

It should be noted that, the power flow through the VSC-HVDC link is modulated based on the sensed frequency at the two AC sides of the dc link and also based on the rate of change of the AC power flow between the control areas where the VSC-HVDC end buses are located.

The dynamics of HVDC power electronic parts is neglected because the time constant of electronic parts is much smaller than those involved in dynamic analysis of large-scale power system. The DC power flow through each HVDC-link is represented as a load at the converter buses. Supplementary Modulation Controller (SMC) is designed to improve the performance of power system during load changes and also to increase the ability of steady state power transferring between two AC systems.

A major feature of such SMC is that they utilize signals obtained from local measurements to synthesize the control signal to damp critical modes [25].

If the frequency deviations are sensed, it can be used as a control signal to the VSC-HVDC unit to control the power flow by changing the duty cycles of bi-directional converters, as explained in [22]. It is assumed that the VSC-HVDC is bi-directional and as a result the frequency in each area must be sensed. The feedback scheme is constructed using two measurable signals, frequency deviations for each area and the power deviation in the AC tie-line transmission link. The proposed coordinated control for this kind of HVDC can be written as follows:

$$\Delta x_{\mathrm{DC}} = K_{f1}\Delta f_1 + K_{f2}\Delta f_2 + K_{\mathrm{AC}}\Delta P_{\mathrm{AC}}. \tag{36}$$

Considering that Δx_{DC} is the control signal for the DC link while K_{f1}, K_{f2} and K_{DC} are control gains should be defined by additional tuning algorithms.

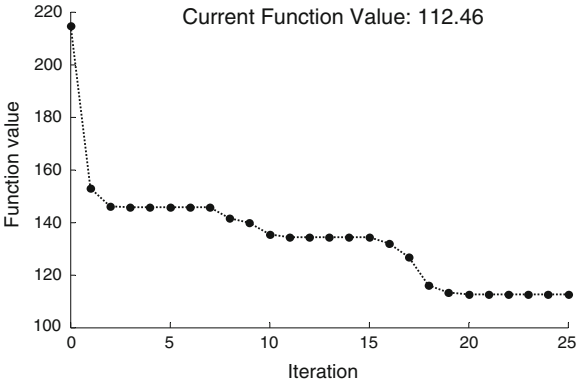

Fig. 24 Performance index for classical FMINCON algorithm

Table 1 Tuned values by classical FMINCON

Parameters	GA
K_{f1}	0.29
K_{f2}	0.038
K_{AC}	5.07
Fitness value	112

Parameters Tuning for SPMC

Optimal tuning of modulation controllers for LFC and tie power control could be done by various methods like conventional algorithms or using genetic algorithm (GA) and simulated annealing (SA) algorithms which will explain in the next section. In optimization methods, the first step in parameters tuning is defining a performance index for optimal search. Here, the proper performance index used for optimization is defined by the Integral of Time multiply Absolute Error (ITAE) of the frequency deviation and ACE of both areas and tie-line power deviation. Accordingly, the objective function J is set to be:

$$J = \int_0^\infty t(|\Delta f_1| + |\Delta f_2| + \Delta|\Delta \mathrm{ACE}_1| + |\nabla \mathrm{ACE}_2| + \left|\Delta P_{\mathrm{tie},12,\mathrm{total}}\right|)\mathrm{d}t. \tag{37}$$

Based on this objective function, the optimization problem can be stated as minimize J subject to these positive parameters:

$$\begin{gathered} K_{f1}^{\min} \le K_{f1} \le K_{f1}^{\max} \\ K_{f2}^{\min} \le K_{f2} \le K_{f2}^{\max} \\ K_{\mathrm{AC}}^{\min} \le K_{\mathrm{AC}} \le K_{\mathrm{AC}}^{\max} \\ \left(K_{f1}, K_{f2}, K_{\mathrm{AC}}\right) \ge 0. \end{gathered} \tag{38}$$

The final goals are control of frequency and inter-area tie power with good oscillation damping and also obtaining a good performance under all operating

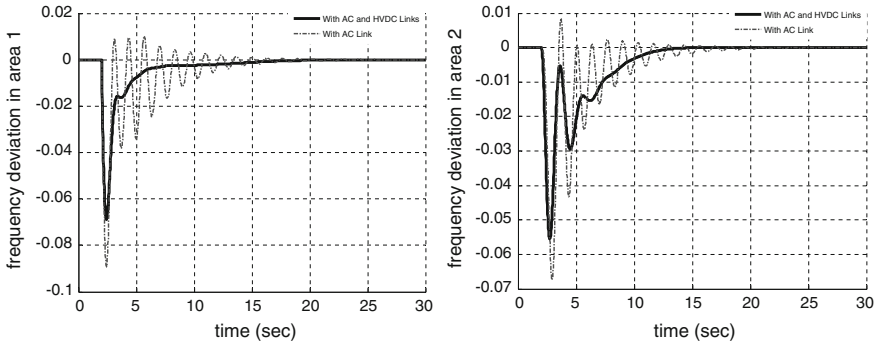

Fig. 25 Frequency response of both areas (Hz)

Fig. 26 Tie-line power deviation

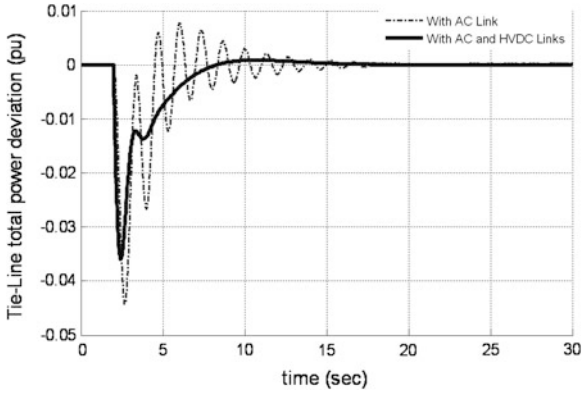

conditions with various load demands. A classical FMINCON solver in MATLAB software which is based on Sequential Quadratic Programming (SQP) algorithm could be used for obtaining the initial results. The gradients of the objective and constraint functions are provided as the user-defined functions. As shown in Fig. 24, after 25 iterations acceptable values were obtained.

The controller values obtained from the design of the power modulation controller are given in the Table 1.

3.3.2 Multi Machine Two-Area Power System Example

In this section, presented model in Fig. 3 is modified by adding one HVDC link in parallel with AC line and a new simulation with the same parameters as before is performed. It is assumed that the load in area 1 is suddenly increased about 0.03 p.u. at t = 5 s and all generators participate in LFC defined by the following apf:

$$\begin{aligned} \text{apf}_1 &= 0.75, \quad \text{apf}_2 = 1 - \text{apf}_1 = 0.25 \\ \text{apf}_3 &= 0.50, \quad \text{apf}_4 = 1 - \text{apf}_3 = 0.50 \end{aligned}.$$

The frequency deviations of two areas are presented in Fig. 25. It is clear that the initial system with standard AC link has a huge oscillation wile applying proposed tuned AC/DC interconnection will improve the dynamic responses of the system. In fact, by adding HVDC link, dynamic responses are improved effectively, and the frequency deviations of all areas are quickly driven back to zero.

Also as shown in Fig. 26, the magnitude of the oscillations in tie-line power and frequency deviations is damped by the HVDC link. This result clearly confirms the positive effects of HVDC link to improve the dynamic stability and also the capacity of transmission between two areas.

Based on the simulation results and comparisons between HVAC transmissions and HVDC systems it has been stated that the use of HVDC transmission lines in parallel with HVAC transmission lines increases the strength and the dynamic stability of frequency and transmitted power. It is clear that by means of the proposed model, a bi-directional power flow control is available and also because the DC-interconnection provides an adequate power exchange, reduction of frequency deviations for tested system will be achieved if the control gain is tuned properly.

4 Application of Advanced Control Concepts in Active Power Control

Applying various types of renewable power plants with different characteristics will increase the complexity and number of state variable that should be control in a large-scale interconnected systems. Advanced control technology should be designed to address these types of necessity. On the other hand, in practical environment, one of the main observed problems in the control of AGC systems is the limitation to access and measurement of state variables. In order to solve this problem, an optimal output feedback method as an advanced LQR controller could be proposed. In the output feedback method, only the measurable state variables within each control area are required to use for feedback. But in order to improve dynamic performance and better design for this controller, concept of intelligent regulator is added to the LQ regulators and as a result the PSO-based LQ output feedback regulator and ICA-based LQ output feedback are proposed to calculate the global optimal gain matrix of controller intelligently [26, 27].

4.1 Design of Advanced LQR Control for LFC System

The design of optimal control systems is an important function of control engineering. The purpose of design is to realize a system with practical components that will provide the desired operating performance [28]. In this section, in order to improve the dynamic performance of system and for more accuracy and better design for conventional LQR controller, intelligent techniques are added to find the global optimal gain matrix.

4.1.1 Overview of Optimal Output Feedback

The power system model, which explained in previous sections, consists of a set of equations which describe models of generators, inertia, loads, RES units, and their associated controls. A linearized model of this system could usually obtained by a proper linearization around their operating point [4]. The generalized form of state space representation of power system could be as follows:

$$\Delta \dot{x} = A\Delta x + B\Delta u \tag{39}$$

$$\Delta y = C\Delta x. \tag{40}$$

For this extracted state space system, the output feedback control law is [28]:

$$u = -K \cdot y. \tag{41}$$

The objective of this regulator for the system may be attained by minimizing a performance index (J) of the type:

$$J = \frac{1}{2}\int [x^T(t)Qx(t) + u^T(t)Ru(t)]\mathrm{d}t. \tag{42}$$

By substituting Eqs. (41) into (39), the closed-loop system equation is:

$$\dot{x} = (A - \mathrm{BKC})x = A_c x. \tag{43}$$

This dynamical optimization may be converted to an equivalent static one that is easier to solve as follows. A constant, symmetric, positive-semi definite matrix P can be defined, as:

$$\frac{\mathrm{d}(x^T Px)}{\mathrm{d}t} = -x^T(Q + C^T K^T \mathrm{RKC})x \tag{44}$$

$$J = \frac{1}{2}x^T(0)Px(0) - \frac{1}{2}\lim_{t\to\infty} x^T(t)Px(t). \tag{45}$$

Assuming that the closed-loop system is stable so that x(t) vanishes with time, this becomes:

$$J = \frac{1}{2}x^T(0)Px(0). \tag{46}$$

If P satisfies (44), then Eq. (43) could be used to see that:

$$-x^T\left(Q + C^T K^T \mathrm{RKC}\right)x = \frac{\mathrm{d}(x^T Px)}{\mathrm{d}t} = \dot{}^T Px + x^T P\dot{x} = x^T(A_c^T P + PA_c)x \tag{47}$$

$$g \equiv A_c^T P + PA_c + C^T K^T \mathrm{RKC} + Q = 0. \tag{48}$$

If Eq. (46) be written as:

$$J = \frac{1}{2}tr(PX) \tag{49}$$

where the $n \times n$ symmetric matrix X is defined as:

$$X = E\{x(0)x^T(0)\} \tag{50}$$

The best K could be selected, to minimize (42) subject to the constraint (48) on the auxiliary matrix P. For solving, Lagrange multiplier approach will be used and the constraint will be adjoined by defining this Hamiltonian:

$$H = tr(PX) + tr(gS). \tag{51}$$

Now to minimize (49), partial derivatives of H with respect to all the independent variables P, S and K must be equal to zero.

$$0 = \frac{\partial H}{\partial S} = A_c^T P + PA_c + C^T K^T \mathrm{RKC} + Q \tag{52}$$

$$0 = \frac{\partial H}{\partial P} = A_c S + SA_c^T + X \tag{53}$$

$$0 = \frac{1}{2}\left(\frac{\partial H}{\partial K}\right) = \mathrm{RKCSC}^T - B^T \mathrm{PSC}^T. \tag{54}$$

To obtain the output feedback gain K with minimizing the (42), these three coupled Eqs. (52), (53), and (54) must be solved simultaneously. The first two of these are Lyapunov equations and the third is an equation for the gain K.

If R is positive definite and is nonsingular, then (54) may be solved for K [28]:

$$K = R^{-1}B^T \mathrm{PSC}^T(\mathrm{CSC}^T)^{-1}. \tag{55}$$

Various methods may be used to solve these equations, such as iterative methods [26]. But as shown in Fig. 27, the PSO and ICA algorithms are used to find the global optimal gain matrix.

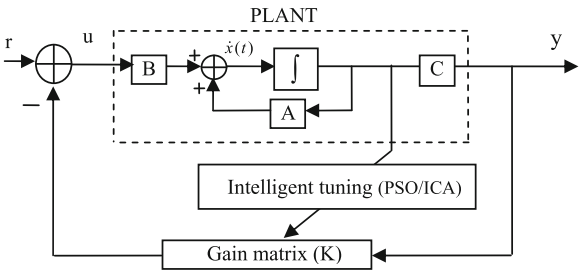

Fig. 27 Closed loop system with the proposed LQR output feedback controller

4.1.2 AWPSO Algorithm

PSO is a population-based heuristic search technique which imitates finding food principle of bird swarm [29]. A swarm consists of a set of particles where each particle represents a potential solution within the search space. Particles are then flown through the hyperspace, where the position of each particle is changed according to its own experience and that of its neighbors. Let $\vec{x}_i(t)$ denotes the position of particle P_i in hyperspace, at time step t. The position of P_i is then changed by adding a velocity $\vec{v}_i(t)$ to the current position as:

$$\vec{x}_i(t) = \vec{x}_i(t-1) + \vec{v}_i(t). \tag{56}$$

The velocity vector drives the optimization process and reflects the socially exchange information. Velocity update equation is as follows:

$$v_i(t) = \omega v_i(t-1) + c_1 r_1 (P_{bi} - x_i(t-1)) + c_2 r_2 \big(P_g - x_i(t-1)\big) \tag{57}$$

where ω is the inertia weight, c_1 and c_2 are positive constants and r_1 and r_2 are random numbers obtained from a uniform random distribution function in the interval [0, 1]. The parameters $\vec{P}_{bi}$ and $\vec{P}_g$ represent the best previous position of the i-th particle and position of the best particle among all particles in the population, respectively [29].

The inertia weight controls the influence of previous velocities on the new velocity. Large inertia weights cause larger exploration of the search space while smaller inertia weights focus the search on a smaller region. Typically, PSO started with a large inertia weight, which is decreased over time. But for more adaption, the following formula is used to change the inertia weight at each generation:

$$\omega = \omega_0 + r(1 - \omega_0) \tag{58}$$

where ω_0 is the initial positive constant in the interval [0, 1] and r is random number obtained from a uniform random distribution function in the interval [0, 1].

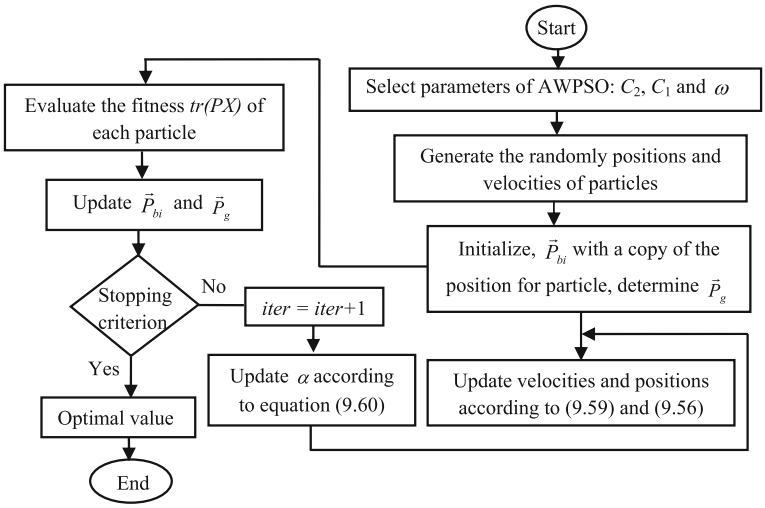

Fig. 28 Flowchart of the proposed AWPSO technique

The suggest range for ω_0 is [0, 0.5], which make the weight ω randomly varying between ω_0 and 1. As shown in Fig. 28, to improve the performance of the PSO, Mahfouf [29] proposed an Adaptive Weighted PSO (AWPSO) algorithm, in which the velocity in (57) is modified as follows:

$$v_i(t) = \omega v_i(t-1) + \alpha[c_1 r_1(P_{bi} - x_i(t-1)) + c_2 r_2\big(P_g - x_i(t-1)\big)]. \tag{59}$$

The second term in Eq. (60) can be viewed as an acceleration term, which depends on the distances between the current position $\vec{x}_i(t)$, the personal best $\vec{P}_{bi}$ and the global best $\vec{P}_g$. The acceleration factor α is defined as follows:

$$\alpha = \alpha_0 + \frac{t}{T} \tag{60}$$

where t is the current generation, T denotes the number of generations and the suggest range for α_0 is [0.5, 1].

As can be seen from Eq. (59), the acceleration term will increase as the number of iterations increases, which will enhance the global search ability at the end of run and help the algorithm to jump out of the local optimum.

4.1.3 Imperialist Competitive Algorithm

Imperialist competitive algorithm (ICA) is proposed by Caro Lucas et al. [30], and it is inspired by imperialist competition. ICA is a socio-politically motivated optimization algorithm which is similar to many other evolutionary algorithms,

and starts with a random initial population or empires. Each individual agent of an empire is called country and the countries are categorized into two types; colony and imperialist state that collectively form empires. Imperialistic competitions among these empires form the basis of the ICA. During this competition, weak empires collapse and powerful ones take possession of their colonies. Imperialistic competitions converge to a state in which there exists only one empire and its colonies are in the same position and have the same cost as the imperialist [30].

With an N-dimensional optimization problem, a country is a $1 \times N$ array. This array is defined as follow is:

$$\text{Country} = [P_1, P_2, P_3, \ldots, P_N]. \tag{61}$$

Now from optimization point of view, algorithm should find the optimal solution of the problem and solution with the least cost value, when:

$$\text{cost} = f(\text{country}) = f(P_1, P_2, P_3, \ldots, P_N). \tag{62}$$

To form the initial empires, the colonies are divided among imperialists based on their power. To proportionally divide the colonies among imperialists, the normalized cost of an imperialist is defined by [30]:

$$C_n = c_n - \max_i\{c_i\} \tag{63}$$

where c_n is the cost of the nth imperialist and C_n is its normalized cost. Then the normalized power of each imperialist is defined by:

$$P_n = \left| \frac{C_n}{\sum_{i=1}^{N} C_i} \right|. \tag{64}$$

And the initial number of colonies ($N.C._n$) of an empire is:

$$N.C._n = \text{round}\{p_n.N\}. \tag{65}$$

It is clear that bigger empires have greater number of colonies while the weaker ones have less. In each term of ICA, the following operations are carried out:

- **Assimilation of Colonies**: Colonies of each imperialist are assimilated to their respective imperialist. Assimilation is formulated as following:

$$x_{\text{col}}^{\text{new}} = x_{\text{col}}^{\text{old}} + \beta r \otimes (x_{\text{imp}} - x_{\text{col}}^{\text{old}}) \tag{66}$$

where β is assimilation factor, and r is a vector, and its elements are uniformly distributed random numbers in [0,1]. x_{imp}, $x_{\text{col}}^{\text{old}}$ and $x_{\text{col}}^{\text{new}}$ are position of imperialist, old position of colony, new position of colony, respectively. For more information about deviation, refer to [30].

- **Revolution of colonies**: In this step, selected colonies of every imperialist are changed randomly, or revolved. Revolution is applied to a colony, with a probability of p.

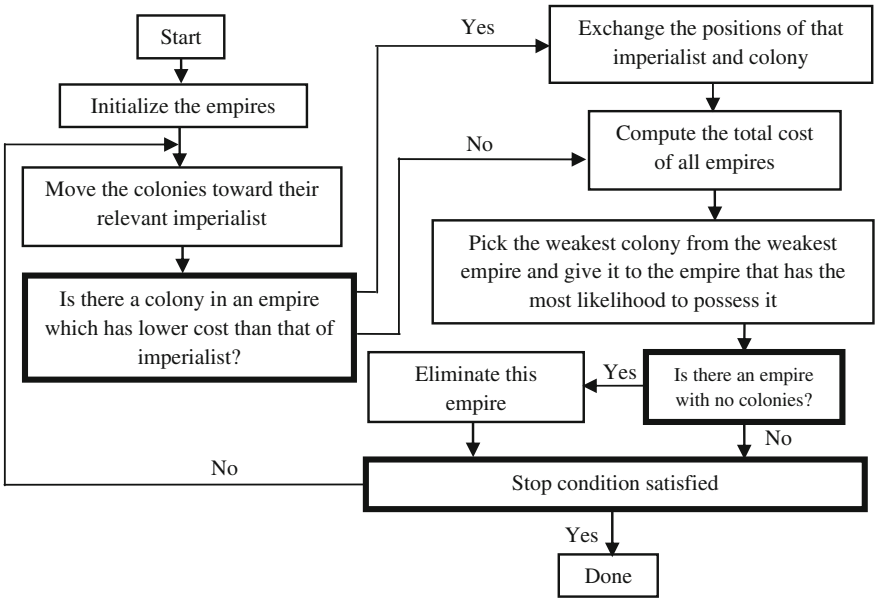

Fig. 29 Flowchart of the ICA algorithm

- **Exchange with best colony**: If after assimilation and revolution steps, there are colonies which are better than their respective imperialists, the imperialist is exchanged with its best colony.
- **Imperialist competition**: Weakest imperialist among others, loses its weakest colony. One of other imperialists will capture the lost colony, randomly. An imperialist without colony will collapse.

As shown in Fig. 29, the mentioned steps are carried out, while stop conditions are not satisfied.

4.2 General Examples for Advanced Control Applications

The state space model for explained AGC models can be obtained to extract the required state matrices as shown in Fig. 27. By means of this advanced control techniques, it would be possible to analysis huge systems with several state variables just in matrix definitions. Then for better tuning intelligent methods will be applied. The proposed controllers are tested on two-area AGC power system, and a complete comparison between proposed output feedback controllers with AWPSO, with PSO, with Imperialist Competitive Algorithm (ICA) and

Table 2 PSO parameters

Parameters	GA
Population size	50
C_1	1.8
C_2	1.8
ω_0	0.4
ω_{max}	0.9
Number of iterations	100

Table 3 ICA parameters

Parameters	GA
Initial countries	50
Initial imperialists	8
Revolution rate	0.35
α	2
Number of iterations	100

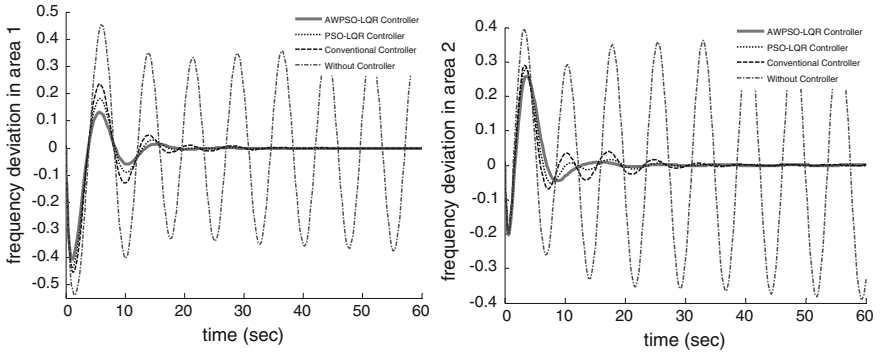

Fig. 30 Frequency deviation in area 1 and 2 (Hz)

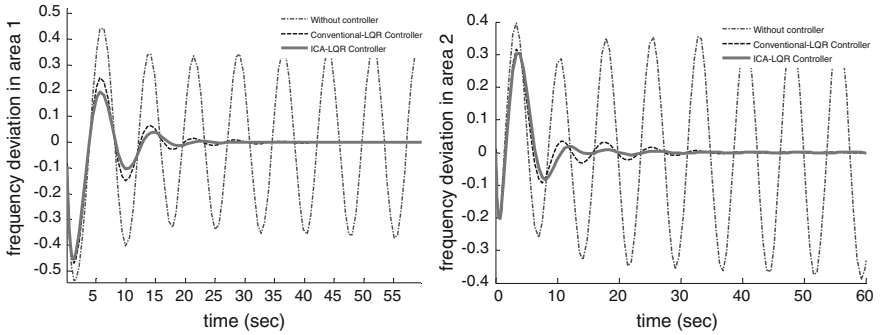

Fig. 31 Frequency deviation in area 1 and 2 (Hz)

conventional output feedback controller are presented. In Tables 2 and 3, defined parameters for PSO and ICA algorithms are presented.

As shown in Figs. 30 and 31, using this method, the frequency deviation of each area and the tie-line power have a good dynamic response in comparing with conventional controller. Using the proposed intelligent methods, the frequency deviation of all areas is quickly driven back to zero and has a good dynamic response.

5 Summary

In this chapter, modified models for analyzing the effects of RES and DC links on active power and frequency support issue in large-scale power system under power market scenarios are presented. Based on the simulation results, combination of RE sources like PV and wind will be so useful in reliability of system. In fact, their aggregation and combination can reduce the overall variability of the power produced, with all the resulting benefits in terms of improved capacity credit and improved effectiveness in the reliability of the system. Technological advances, such as the use of modern power processing systems, energy storage, and control techniques in high-power systems are very important. Also by means of global RE integration and competitive markets, it would be necessary to equip the network with several DC interconnections at high voltage level between the areas. It is necessary to do more investigation in VSC-HVDC link as a bi-directional gate and application of the last technologies in power electronics interfaces. However, more frequent use of such HVDC applications with advanced power electronic devices can be expected in the future to fulfil the requirements in deregulated power system. The results of last section of this chapter, demonstrate that proposed intelligent controller improved the dynamic response of system faster than conventional controller and provides a control system that satisfied the load frequency control requirements. It was obvious that intelligent control for coordination between RES and reserve/stored energy, certainly plays a significant role. It will not be possible to integrate large amounts of RESs into the conventional power systems without intelligent control and regulation of systems.

Appendix A

Below are listed 12-bus System parameters [31]: line data in Table A.1, transformers data in Table A.2, bus data in Table A.3, and generators data in Table A.4.

Table A.1 System data

Bus	V (kV)	Type	P_{gen} (MW)	P_{load} (MW)	Q_{load} (MW)	Q_{shunt} (MVAR)	V (p.u.)
1	230	PQ	_	300	186	_	_
2	230	PQ	_	250	121	_	_
3	230	PQ	_	350	115	_	_
4	230	PQ	_	300	186	200	_
5	230	PQ	_	100	48	40	_
6	230	PQ	_	150	49	_	_
7	345	PQ	_	_	_	−100	_
8	345	_	_	_	_	_	_
9	15.5	SL	_	_	_	_	1.00
10	15	PV	400	_	_	_	1.01
11	18	PV	270	_	_	_	1.01
12	13.8	PV	330	_	_	_	1.02

Table A.2 Line data (Sbase = 100 MVA)

Line from–to	Length (km)	R (p.u.)	X (p.u.)	B (p.u.)
1–2	100	0.01131	0.08998	0.18377
1–6	300	0.03394	0.26995	0.55130
2–5	400	0.04530	0.35990	0.73510
3–4	100	0.01144	0.09110	0.18261
3–4	100	0.01144	0.09110	0.18261
4–5	150	0.0170	0.13500	0.27570
4–6	300	0.03394	0.26995	0.55130
7–8	600	0.01590	0.17210	3.28530

Table A.3 Transformer data (Sbase = 100 MVA)

From-to bus	MVA capacity	V_1 /V_2 (kV)	X (%)	Vector group
1–7	500	230/345	13	YY
1–9	800	230/15.5	12	YD
2–10	700	230/15	12	YD
3–8	500	230/345	13	YY
3–11	400	230/15	10	YD
6–12	500	230/13.8	11	YD

Table A4 Generator data

Name	Bus	Number of units	Total MVA capacity	V_{nom} (kV)	M (s)	D
GENCO1	9	6	750	15.5	10.0128	0
GENCO2	10	4	640	15	8.3213	0
GENCO3	11	2	388	18	6.9344	0
GENCO4	12	3	474	13.8	6.6722	0

References

1. Solangib KH, Islamb MR, Saidura R, Rahimb NA, Fayazb H (2011) A review on global solar energy policy. Renew Sustain Energy Rev 15:2149–2163
2. Hoffmann W (2006) PV solar electricity industry: market growth and perspective. Solar Energy Mater 90(18–19):3285–3311
3. EPIA report (2011) Solar generation 6, solar photovoltaic electricity empowering the world
4. Kundur P (1994) Power system stability and control. MacGraw-Hill, New York
5. Wood AJ, Wollenberg BF (1984) Power generation, operation, and control. Wiley, New York
6. Saadat H (1994) Power system analysis. McGraw-Hill, New York
7. Bevrani H (2009) Robust power system frequency control. Springer, New York
8. Machowski J, Bialek JW, Bumby JR (2008) Power system dynamics—stability and control, 2nd edn. Wiley-IEEE Press, Oxford
9. Lai LL (2001) Power system restructuring and deregulation: trading, performance and information technology. Wiley, New York
10. Shahidehpour M, Yamin H, Li Z (2001) Market operations in electric power system: forecasting, scheduling and risk management. Wiley, New York
11. Bevrani H, Mitani Y, Tsuji K (2004) Robust decentralized LFC design in a deregulated environment. Energy Convers Manage 45:2297–2312
12. Kumar J, Kah-Heo NG, Sheble G (1997) AGC simulator for price-based operation, Part 1: a model. IEEE Trans Power Syst 12(2):527–532
13. Donde V, Pai A, Hiskens IA (2001) Simulation and optimization in a AGC system after deregulation. IEEE Trans Power Syst 16(3):481–489
14. Rakhshani E, Sadeh J (2010) Practical viewpoints on load frequency control problem in a deregulated power system. Energy Convers Manage 51(6):1148–1156
15. Morel J, Bevrani H, Ishii T, Hiyama T (2010) A robust control approach for primary frequency regulation through variable speed wind turbines. IEEJ Trans Power Syst Energy 130(11):1002–1009
16. Bevrani H, Daneshfar F, Daneshmand PR (2010) Intelligent power system frequency regulation concerning the integration of wind power units In: Wang LF, Singh C, Kusiak A (eds) Wind power systems: applications of computational intelligence. Springer book series on green energy and technology. Springer, Heidelberg, pp 401–437
17. Datta M, Senjyu T, Yona A, Funabashi T, Kim C-H (2011) A frequency-control approach by photovoltaic generator in a PV-diesel hybrid power system. IEEE Trans Energy Convers 26(2):559–571
18. Datta M, Senjyu T, Yona A, Funabashi T, Chul-Hwan K (2009) A coordinated control method for leveling PV output power fluctuations of PV–diesel hybrid systems connected to isolated power utility. IEEE Trans Energy Convers 24(1):153–162
19. Mercier P, Cherkaoui R, Oudalov A (2009) Optimizing a battery energy storage system for frequency control application in an isolated power system. IEEE Trans Power Syst 24(3):1469–1477
20. Rodriguez P, Ignacio Candela J, Luna A (2013) Control of PV generation systems using a synchronous power controller. In: Proceedings of the IEEE energy conversion congress and exposition, ECCE, USA
21. Lee DJ, Wang L (2008) Small-signal stability analysis of an autonomous hybrid renewable energy power generation/energy storage system Part I: time-domain simulations. IEEE Trans Energy Convers 23(1):311–320
22. Du C, Agneholm E, Olsson G (2008) Use of VSC-HVDC for industrial system having onsite generation with frequency control. IEEE Trans Power Delivery 23(4):2233–2240
23. Preece R, Milanovic JV, Almutairi AM, Marjanovic O (2012) Damping of inter-area oscillations in mixed AC/DC networks using WAMS based supplementary controller. IEEE Trans Power Syst 28(2):1160–1169

24. Rakhshani E, Luna A, Rouzbehi K, Rodriguez P, Etxeberia-Otadui I (2012) Effects of VSC-HVDC on load frequency control in multi-area power system. In: IEEE energy conversion congress and exposition, ECCE, pp 4432–4436
25. Padiyar KR (2009) Facts controller in power transmission and distribution. New Age International Ltd., India
26. Rakhshani E (2012) Intelligent linear-quadratic optimal output feedback regulator for a deregulated automatic generation control system. Electr Power Compon Syst 40:513–533
27. Rakhshani E, Sadeh J (2010) Reduced-order observer control for two-area LFC system after deregulation. Control Intell Syst 38(4):185–193
28. Lewis FL, Syrmos VL (1995) Optimal control. Prentice Hall, Englewood Cliffs (Chapter 4)
29. Mahfouf M, Chen M, and Linkens DA (2004) Adaptive weighted particle swarm optimization (awpso) of mechanical properties of alloy steels. In: 8th international conference on parallel problem solving from nature (PPSN VIII), Birmingham, UK
30. Atashpaz E, Lucas C (2007) Imperialist competitive algorithm: an algorithm for optimization inspired by imperialistic competition. In: IEEE congress on evolutionary computation, Singapore, pp 4661–4667
31. Adamczyk A, Teodorescu R, Rodriguez P (2010) Adaption of 12-bus system for wind power integration studies. In: Proceedings of the 9th international workshop on large-scale integration of wind power into power systems

Impact of Large Penetration of Correlated Wind Generation on Power System Reliability

Carmen L. T. Borges and Julio A. S. Dias

Abstract Power system reliability evaluation measures the system's ability to properly and continually supply the demand under uncertain conditions. The large penetration of wind power generation, which is an intermittent energy source, introduces some major challenges for maintaining the system reliability level. In order to deal with uncertainties, nonsequential or sequential Monte Carlo simulation (MCS) may be used for probabilistic reliability evaluation. Power systems are composed by components that may be accurately modeled by independent random variables and also by time-varying energy sources and loads, which are represented by time series. These time series can be statistically correlated, both spatially and temporally, and disregarding the dependencies that may exist between them may produce an incorrect reliability evaluation. This chapter presents a model for representing statistically dependent time-varying variables (wind, solar, river inflows, load, etc.) in nonsequential MCS-based reliability evaluation. The results show that the model can correctly represent the effects of statistical dependence, what is normally achieved by sequential simulation, but requiring as little computational effort as the nonsequential simulation. This facility gains importance nowadays with the large penetration of wind generation that is being observed all over the world, both onshore and offshore.

Keywords Reliability evaluation · Wind generation · Time-varying load · Correlated variables · Nonsequential Monte Carlo simulation

C. L. T. Borges (✉)
Department of Electrical Engineering, Federal University of Rio de Janeiro, Rio de Janeiro, Brazil
e-mail: carmen@nacad.ufrj.brs

J. A. S. Dias
PSR, Rio de Janeiro, Brazil
e-mail: alberto@psr-inc.com

J. Hossain and A. Mahmud (eds.), *Large Scale Renewable Power Generation*, Green Energy and Technology, DOI: 10.1007/978-981-4585-30-9_10,

1 Introduction

Power systems reliability evaluation measures the system's ability to fulfil its function of properly attending the customer demand under uncertainty conditions. In order to deal with uncertainties, the probabilistic reliability evaluation can be performed by two distinct representations of the system. In the state space representation, the system states are randomly sampled by nonsequential Monte Carlo simulation (MCS). In the chronological representation, the states are sequentially sampled to simulate system operation by sequential MCS.

Sequential MCS tends to produce more accurate results in the presence of time-varying elements, such as load curves and wind generation, because the time series are explicitly represented and therefore the correlation and statistical dependency between them are preserved [1–3]. However, sequential MCS has a high computational cost and can become prohibitive for practical large systems.

On the other hand, nonsequential MCS has a much lower computational cost but the representation of time-varying elements is not straightforward. Some hybrid simulation models have been proposed [4, 5] in order to obtain the accuracy of sequential MCS with a computational cost similar to nonsequential MCS, but still requiring extra computation time.

Nonsequential MCS-based models do not consider the statistical dependence between time series because the system states are obtained by sampling the state space based on the hypothesis that the events are independent. However, disregarding some dependencies, which may exist between wind generations located at different sites and/or time-varying loads, for example, may produce incorrect reliability indices. The dependence representation has been applied to systems with at most two wind series [6] or without consideration of time-varying load [7]. A model applicable to several time series has been initially presented in [8] and further evolved in [9]. Although efficient and precise, the model efficiency is sensitive to the number of time-varying elements considered.

Therefore, this chapter presents a flexible and an efficient model for representation of any number of statistically dependent time-varying elements (wind, solar, river inflows, load, etc.) in nonsequential MCS-based reliability evaluation. The model can correctly represent the effects of statistical dependence and correlation on the reliability indices, what is normally achieved by sequential simulation, but requiring as little computational effort as the nonsequential simulation.

The organization of the chapter is as follows: Sect. 2 presents the conventional approach for reliability evaluation using nonsequential MCS; Sect. 3 introduces the influence of correlated time-varying elements; Sect. 4 proposes a model for representation of time-varying elements in nonsequential MCS; Sect. 5 presents the results obtained with the proposed model and Sect. 6 contains the main conclusions.

2 Reliability Evaluation by Non-sequential MCS

The calculation of the reliability indices in nonsequential MCS can be summarized by evaluating Eq. (1):

$$\overline{E}(F) = \frac{1}{N}\sum_{i=1}^{N} F\left(\underline{x}^i\right) \tag{1}$$

where N is the number of simulated states, F is the test function for calculating the indices for each system state x^i and $\overline{E}(F)$ is the estimate of the annual reliability indices.

The system states are obtained by combining the states of all system components. For a system with m components, a system state can be represented by the random vector $x = [x_1, x_2, \ldots, x_k, \ldots, x_m]$ where x_k represents the state of the kth component.

Sampling the component state is done by applying the Inverse Transformation (IT) method to the cumulative distribution function (CDF) of the component operating states. Considering a component modeled by n states, this is done by generating a random number U_k uniformly distributed between [0, 1] and then identifying its state x_k by (2), where $P_i = P(x_k \leq i)$:

$$x_k = \begin{cases} 1 & \text{if } 0_k \leq P_1 \\ 2 & \text{if } P_1 < U_k \leq P_2 \\ \vdots & \vdots \\ n & \text{if } P_{n-1} < U_k \leq 1 \end{cases} \tag{2}$$

The models usually used by nonsequential MCS assume that the states of the components are statistically independent and therefore, the probability of occurrence of each system state is given by the product of the probability of each component state. Defining $P(x_k)$ as the probability of occurrence associated with the kth component, the probability of the ith system state $P(x^i)$ is calculated by (3):

$$P\left(\underline{x}^i\right) = p_i = \prod_{k=1}^{m} P(x_k) \tag{3}$$

However, as will be discussed in the next section, this approach is incorrect when there are statistically dependent components, as is the case of multiple correlated wind generations, for example.

3 Correlated Time-Varying Elements

Power systems are composed by components whose states may be accurately represented by independent random variables (transmission lines, transformers, generators, etc.) and also by time-varying elements (wind, loads, river inflows,

etc.) that are represented by time series. These time-varying elements can be statistically correlated and therefore the consideration of statistical independence becomes invalid. The correlation between variables can be both spatial and temporal, and in general these two effects are observed. This feature is not a problem for sequential MCS, where the time series are explicitly represented. However, in nonsequential MCS, it can become a challenge for obtaining indices with an acceptable level of accuracy. Therefore, an appropriate approach is required for a correct representation of the correlation between them in nonsequential MCS.

When a single time-varying element is represented, as in the case of the aggregated system load curve [10] or one wind generation [11], nonsequential MCS can be directly applied because this single variable is statistically independent from the others and therefore Eq. (3) remains valid. However, when two or more time-varying elements are represented, the assumption of statistical independence cannot always be accepted. This problem is well known in the representation of different load curves in multi-area systems [12]. This question gains a new dimension nowadays with the strong incorporation of wind generation that is being observed all over the world. For a correct representation, it is necessary to consider that there may be correlation between wind time series of the different wind farm sites or even between these wind series and the load curves.

Consider, at first, two different time-varying elements which could be two wind time series, for example, and assume that random variable x_1 represents the state of the first element and x_2 represents the state of the second. Equation (3) can be rewritten by separating the terms related to the two variables as (4):

$$p_i = P(x_1, x_2) \cdot \prod_{k=3}^{m} P(x_k) \tag{4}$$

If x_1 and x_2 are not statistically independent, $P(x_1,x_2)$ can be more generally written as (5):

$$P(x_1, x_2) = P(x_1|x_2) \cdot P(x_2) \tag{5}$$

Therefore, the probability of the ith state of the system can be written as (6):

$$p_i = P(x_1|x_2) \cdot P(x_2) \cdot \prod_{k=3}^{m} P(x_k) \tag{6}$$

This relation can be extended for the consideration of several statistically dependent time-varying elements. For the particular case of three dependent variables, it can be written based on the Chain Rule as (7):

$$P(x_1, x_2, x_3) = P(x_1|x_2, x_3) \cdot P(x_2|x_3) \cdot P(x_3) \tag{7}$$

And therefore, the probability of the *i*th state of the system can be written as (8):

$$p_i = P(x_1|x_2, x_3) \cdot P(x_2|x_3) \cdot P(x_3) \cdot \prod_{k=4}^{m} P(x_k) \tag{8}$$

In [8, 9], a model has been proposed for considering the correlation between any numbers of time series in nonsequential MCS. The model is based on explicitly obtaining the conditional probability distribution functions by a recursive algorithm. However, the computational efficiency of the model depends on the number of dependent variables and therefore its applicability is affected when several wind generations are present in the system. This chapter presents a more flexible model to overcome this constraint and also maintain the computational efficiency.

4 Model for Time-Varying Variables Representation

The proposed model consists in representing the w time-varying variables $v_1, v_2, \ldots, v_w$ by one single random variable V_T in the simulation process and to adopt a multiple states Markov model to represent it. Each state of this variable corresponds to one combination of states of the time-varying variables, and therefore the state of each one can be written as a function of V_T by (9):

$$\begin{cases} v_1 = F_{v1}(V_T) \\ v_2 = F_{v2}(V_T) \\ \quad \vdots \\ v_w = F_{vw}(V_T) \end{cases} \tag{9}$$

where F_{v1}, $F_{v2}, \ldots, F_{vw}$ are functions that map $v_1, v_2, \ldots, v_w$ from V_T.

For example, considering three time-varying variables *Load* (P_L), *Wind1* (V_1) and *Wind2* (V_2) that can be individually represented by three different states, a Markov model of 27 states for V_T may be constructed where each state corresponds to one of the possible combinations of P_L, V_1 e V_2, as shown in Fig. 1.

To enhance the efficient of the model for application to any number of time-varying variables, the time series are clustered into the most representative states in order to prevent that a large number of states is required to represent V_T. However, this is not a requirement of the model and it could be used without any clustering. The k-means technique is used to perform the statistical clustering of the time series, but other techniques may be used as well [13]. Thus, based on the w clustered time series $v_{1c}, v_{2c}, \ldots, v_{wc}$, the Markov model for V_T is obtained by the algorithm shown in Fig. 2.

After applying this algorithm, a Markov model of V_T with N_T states is available, similar to the one shown in Fig. 1, where each state of V_T represents a unique combination of the time-varying variables $v_{1c}, v_{2c}, \ldots, v_{wc}$.

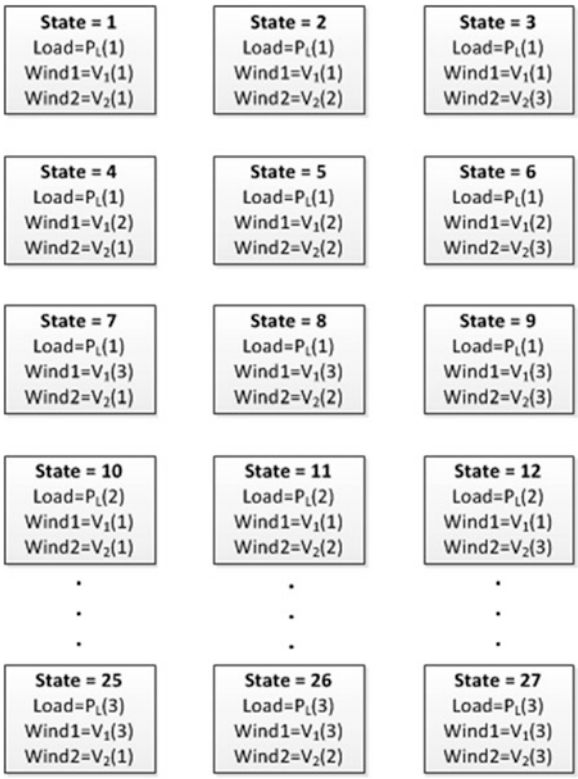

Fig. 1 State space of V_T for three time-varying variables

From this model, the transition rates between the states of V_T may be calculated and then used to obtain the transition intensity matrix A [14] that is used to calculate the stead state probabilities of each state of V_T. Having the steady state probabilities of all states of V_T, sampling a state is done by applying the IT method to the CDF of V_T in a similar way as described for the independent components. From generating a random number U_k uniformly distributed between [0, 1], the state of V_T is obtained by (10), where $P_i = P(V_T \leq i)$.

$$V_T = \begin{cases} 1 & \text{if } 0 \leq U_k \leq P_1 \\ 2 & \text{if } P_1 < U_k \leq P_2 \\ \vdots & \vdots \\ N_T & \text{if } P_{N_T-1} < U_k \leq 1 \end{cases} \tag{10}$$

The conceptual algorithm for composite reliability evaluation by nonsequential MCS considering correlated time-varying variables is shown below:

(1) Sample the state of each independent component by (3);
(2) Sample the state of V_T by (10);
(3) Identify the state of each time-varying variable by (9);

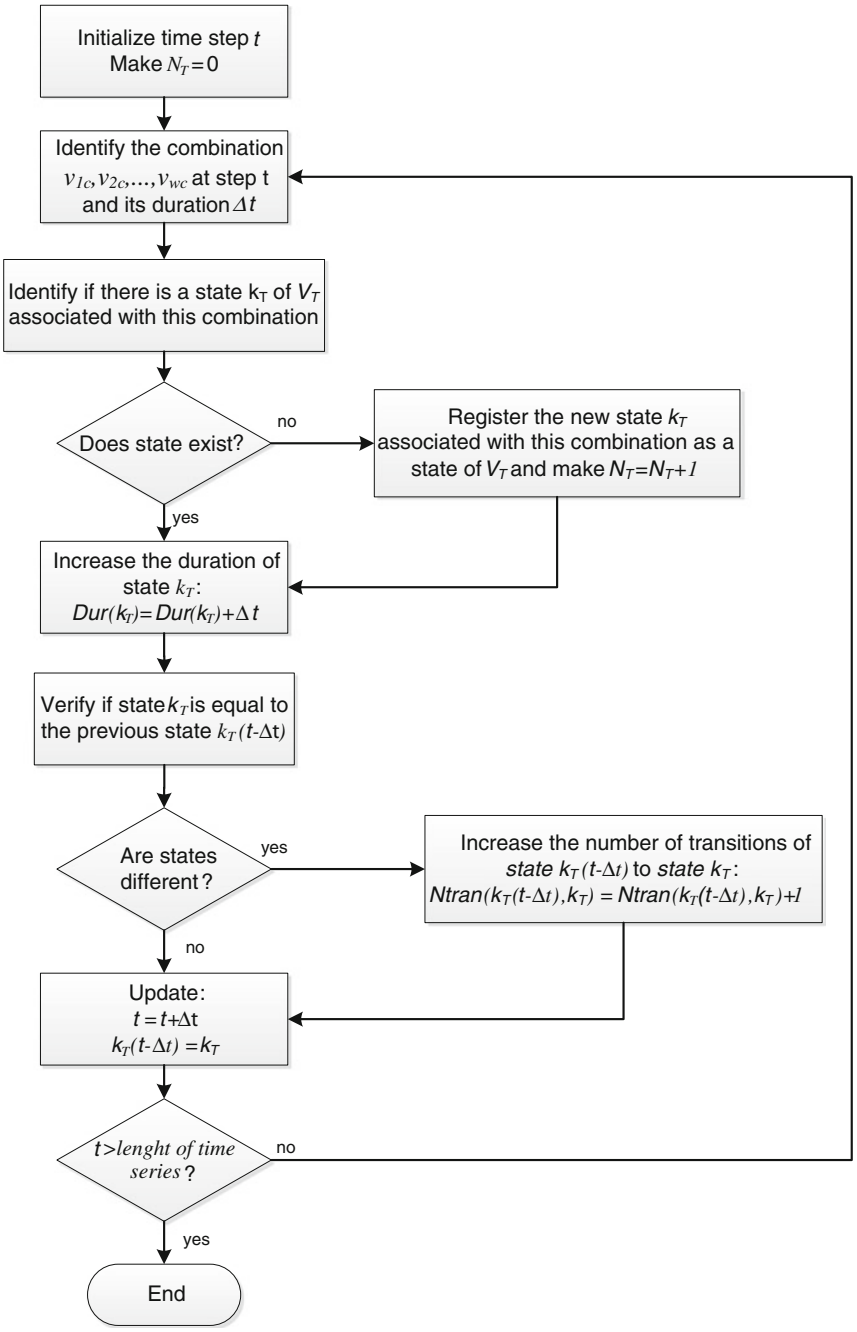

Fig. 2 Obtaining the Markov model for V_T

(4) Configure the system state x based on the sampled states of the independent components and the time-varying variables;
(5) Calculate the value of the test functions $F(x)$ that are defined for evaluating each reliability index;
(6) Update the reliability indices estimates $\overline{E}(F)$ based on the results of step 5;
(7) If the coefficients of variation of the indices (α) are less than an acceptable tolerance, stop the simulation; otherwise, return to step 1.

The main reliability indices calculated in nonsequential simulation for composite generation and transmission systems are the loss of load probability (LOLP, %), the expected power not supplied (EPNS, MW) and the loss of load frequency (LOLF) (occurrences). From these indices, others may be derived, such as the expected energy not supplied (EENS, MW h), the loss of load duration (LOLD, h), etc.

5 Results

To evaluate the model presented in this chapter, a modified version of the IEEE reliability test system (RTS) [15], shown in Fig. 3, is used. The original generation, composed of thermal, hydro, and nuclear units with installed capacity of 3,405 MW, is enlarged by the addition of three wind power plants, whose details are summarized in Table 1. The wind power plant WP-SE was added to busbar 1, WP-NE was added to busbar 2 and WP-S was added to busbar 7 of Fig. 3.

The characteristics of the wind time series Southeast (SE), Northeast (NE), and South (S) are described in [11]. The forced outage rate (FOR) and mean time to repair of the wind (MMTR) turbine/generator group are equal to 4 % and 97 h, respectively. The system load is represented by the time series described in [15]. The original load curve has been increased by 10 % leading to an average annual load of 1,862 MW.

The correlations between the wind time series and the load are shown in Table 2.

It can be seen that the wind series are not independent, although the correlation between them is small. However, the correlation between the wind series and the load is more significant, especially with the NE wind. As will be shown in the results, correlations of this magnitude are enough to produce completely incorrect evaluations if the independent approach is adopted. The higher the correlation the more incorrect are the results, except for the case when the time series are fully correlated, in which case they may be treated as one.

The simulations have been performed using the computational model *RelSim* developed in [16]. It was adopted a maximum coefficient of variation (α) of 3 % for all reliability indices. For all studies, the indices LOLP, EPNS, and LOLF were obtained by sequential MCS, considered as reference, and by nonsequential MCS using the independent and the proposed approaches, for sake of comparison.

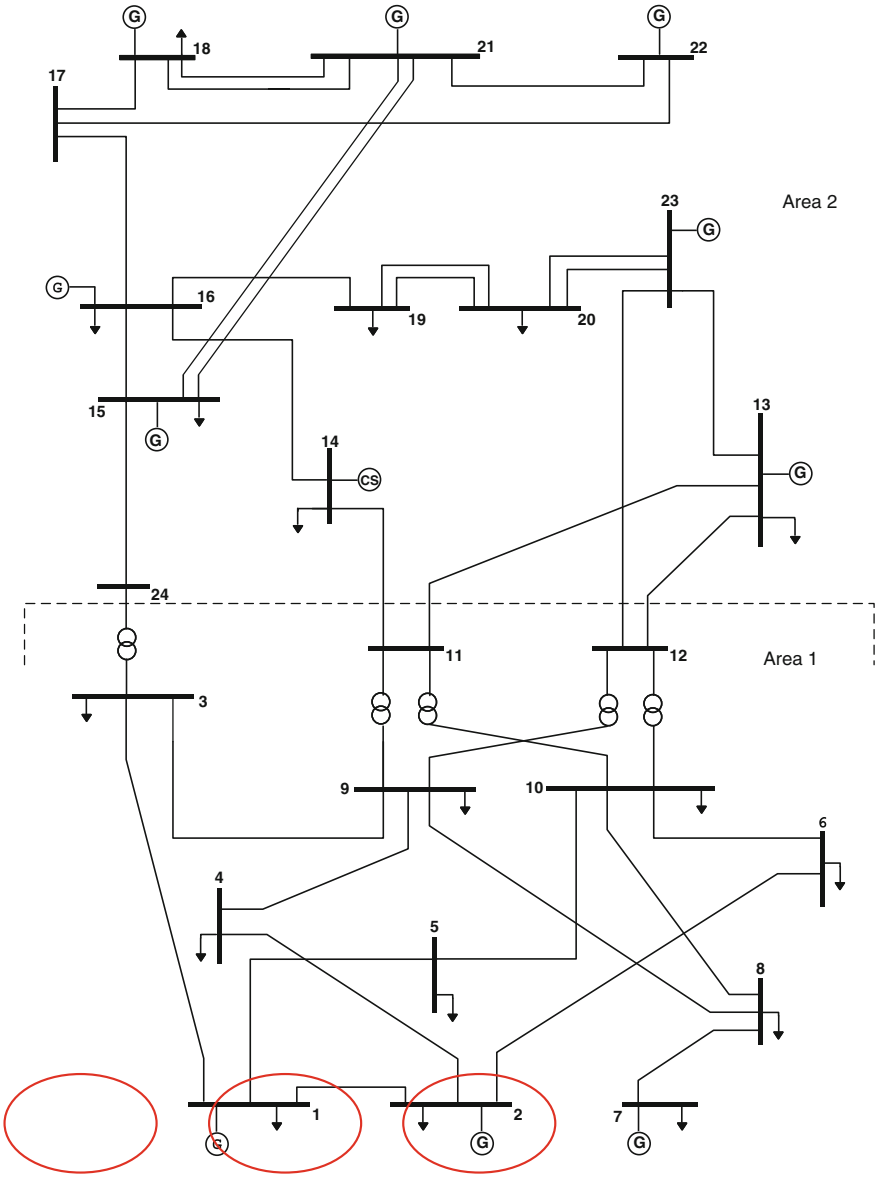

Fig. 3 RTS system

5.1 Case 1: Variable Load and No Wind Farm

As a reference to evaluate the impact of the connection of wind power plants to the system, the reliability indices considering the time-varying load and no wind

Table 1 Wind power plants characteristics

	WP-SE	WP-NE	WP-S
Installed capacity	75 MW	55 MW	50 MW
Number of turbines	50 × 1.5 MW	50 × 1.1 MW	50 × 1.0 MW
Wind time series	Southeast (SE)	Northeast (NE)	South (S)
Average wind speed	6.59 m/s	7.58 m/s	7.00 m/s
Capacity Factor	0.34	0.30	0.21

Table 2 Correlation between time series

	Time series		
	Wind SE × Wind NE	Wind SE × Wind S	Wind NE × Wind S
Correlation	0.054	0.042	0.135
	Wind SE × Load	Wind NE × Load	Wind S × Load
Correlation	0.172	0.337	0.125

generation are shown in Table 3. The indices where obtained by sequential MCS (Table 4).

First of all, it can be noticed the improvement of the system reliability by the addition of wind generation. Taking the sequential simulation results for comparison with the previous case, the connection of the two wind farms reduced the LOLP of 1 %, the EPNS of 2.26 MW, and the LOLF of 21.96 occurrences. However, due to the intermittent nature of wind generation, as well as transmission constraints, the reliability benefit is not as large as the generation capacity added to the system (130 MW or 3.67 %).

In order to evaluate the precision of the models, the confidence intervals for the indices obtained by sequential MCS with 95 % confidence are shown in Table 5 and the errors between the indices obtained by the models in relation to the sequential MCS are shown in Table 6.

Regarding the independent approach, it can be noted that the indices obtained are not accurate, showing the inadequacy of such a model to represent correlated time-varying variables. This is evident by the fact that they are not within the confidence intervals of the indices calculated by sequential MCS and that the percentage errors are higher than the coefficient of variation adopted for all indices.

On the other hand, all the indices obtained by the proposed model for all numbers of clusters are within the respective confidence intervals. Regarding the percentage errors, the improvement in the accuracy of the proposed model with increasing number of clusters is clear, especially for the EPNS index, with all indices errors being less than the coefficient of variation with 350 groups.

The computational performance of the proposed model is much better than the sequential simulation (up to 41.4 times faster). It is important to emphasize that the computational cost for obtaining the proposed Markov model is already

Table 3 Reliability indices—Case 1

LOLP	EPNS	LOLF
5.39 %	9.67 MW	80.11 cc

Table 4 System reliability indices—Case 2

Model	LOLP (α_{LOLP})	EPNS (α_{EPNS})	LOLF (α_{LOLF})	Time (number of states)
Sequential	4.39 (0.021)	7.41 (0.029)	58.15 (0.017)	6 h:54 min (2,369,218)
Independent	4.55 (0.018)	7.07 (0.023)	54.12 (0.030)	12 min (65,352)
Proposed 125 clusters	4.31 (0.020)	6.98 (0.029)	61.27 (0.030)	10 min (53,452)
Proposed 250 clusters	4.36 (0.018)	7.12 (0.024)	59.36 (0.030)	13 min (67,452)
Proposed 350 clusters	4.44 (0.016)	7.51 (0.022)	59.20 (0.030)	15 min (72,602)

Table 5 Sequential MCS indices confidence intervals—Case 2

Limit	LOLP	EPNS	LOLF
Lower	4.21	6.97	56.16
Upper	4.58	7.84	60.13

Table 6 Errors in relation to sequential MCS—Case 2

Model	LOLP (%)	EPNS (%)	LOLF (%)
Independent	3.62	4.57	6.93
Proposed 125 clusters	1.84	5.82	5.37
Proposed 250 clusters	0.73	3.86	2.08
Proposed 350 clusters	1.16	1.34	1.81

incorporated in the computing time reported. The increase in the number of clusters does not burden the model efficiency significantly. For example, doubling the number of clusters (125–250) requires only 30 % additional processing time, while multiplying it by 2.8 (125–350) implies in only 50 % extra time.

Therefore, it can be concluded that the proposed model with 350 clusters is as accurate as the sequential simulation and requires a computational effort of the same order as the independent approach, which is completely inaccurate.

5.2 Case 3: Constrained Transmission Network

In order to extend the evaluation of the proposed model, another modification to the RTS system has been done, which consists in reducing by half the maximum capacity of transmission lines. The objective is to examine how a more constrained transmission network would impact on the accuracy and efficiency of the model.

The results obtained for this case are shown in Table 7, the confidence intervals for the indices obtained by sequential MCS with 95 % confidence in Table 8 and

Table 7 System reliability indices—Case 3

Model	LOLP (α_{LOLP})	EPNS (α_{EPNS})	LOLF (α_{LOLF})	Time (Number of states)
Sequential	9.23 (0.019)	18.12 (0.030)	113.80 (0.017)	3 h:26 min (1,024,920)
Independent	11.35 (0.016)	19.05 (0.024)	132.40 (0.030)	5 min (28,706)
Proposed 125 clusters	8.81 (0.015)	17.27 (0.020)	112.00 (0.030)	9 min (43,452)
Proposed 250 clusters	9.08 (0.013)	17.91 (0.017)	111.30 (0.030)	12 min (56,402)
Proposed 350 clusters	8.99 (0.012)	17.96 (0.017)	115.68 (0.030)	14 min (62,252)

Table 8 Sequential MCS confidence intervals—Case 3

Limit	LOLP	EPNS	LOLF
Lower	8.88	17.05	110.67
Upper	9.58	19.18	116.92

Table 9 Errors in relation to sequential MCS—Case 3

Model	LOLP (%)	EPNS (%)	LOLF (%)
Independent	22.90	5.13	16.34
Proposed 125 clusters	4.53	4.69	1.58
Proposed 250 clusters	1.60	1.16	2.20
Proposed 350 clusters	2.58	0.88	1.65

the errors between the indices obtained by the models in relation to the sequential MCS are shown Table 9.

Initially it is interesting to notice how this modification has impacted on the reliability of the system, with all the indices becoming more than twice the values of the previous case. This serves to highlight the importance of the transmission system in composite reliability evaluation.

The results of the independent model are even worse than those obtained for the previous case. The percentage errors are very high, especially for the LOLP and LOLF indices, showing again that this approach fails to estimate the indices correctly.

In general, the results of the proposed model showed the same good behavior observed previously, with all indices being within the interval of confidence of the indices calculated by sequential MCS. The only exception is the LOLP index for 125 clusters that was out of range for a small difference.

The percentage errors remained also low, confirming the validity of the proposed model for a transmission constrained network. An interesting observation is that the use of 250 clusters to represent the time series is enough in this case to obtain indices with errors smaller than the coefficient of variation. Although the indices with 350 clusters have been calculated, it would not be necessary to increase the number of groups beyond 250 clusters.

Table 10 System reliability indices—Case 4

Model	LOLP	EPNS	LOLF	Time
Sequential	3.98	6.65	57.05	8 h:28 min
Proposed 125 clusters	4.10	6.70	61.20	12 min
Proposed 250 clusters	3.87	6.64	58.70	15 min
Proposed 350 clusters	4.01	6.57	56.88	17 min

Table 11 Errors relative to sequential MCS—Case 4

Model	LOLP (%)	EPNS (%)	LOLF (%)
Proposed 125 clusters	3.14	0.87	7.27
Proposed 250 clusters	2.79	0.11	2.89
Proposed 350 clusters	0.93	1.16	0.30

The good computational performance of the proposed model is also confirmed in this case. Considering 250 clusters, it was 17.17 times faster than the sequential simulation and obtains indices as accurate as it.

5.3 Case 4: Three Wind Farms and Variable Load

In order to evaluate the impact of a larger penetration level of wind generation on the system reliability and also to explore the performance of the model for a larger number of time-varying variables, the reliability indices were calculated considering the connection of the third wind farm WP-S to the system with the original transmission network and using the same time-varying load.

The results obtained for this case are shown in Table 10 and the errors between the indices obtained by the models in relation to the sequential MCS are shown in Table 11. The coefficients of variation off all indices are smaller than 3 %.

The accuracy of the proposed model is again confirmed for this case with three different wind farms and variable load. The percentage errors in relation to the sequential simulation are low for all indices, except for the LOLF index when using 125 clusters.

In terms of computational performance, the proposed model has demonstrated to be very efficient even with an increased number of time series. Considering the most time-consuming simulation (with 350 clusters), it was about 30 times faster than the sequential simulation. An interesting characteristic to be highlighted is the little extra computation time required by the proposed model due to the addition of another wind generation, what can be seen by comparing with the simulation time required by Case 2.

The addition of a new wind farm has slightly reduced the reliability indices in relation to Case 2, but not proportionally to the amount of added generation capacity. The addition of 50 MW of WP-S has increased the wind generation

penetration level from 3.67 % (Case 2) to 5.02 % in terms of installed capacity and from 6.98 to 9.66 % in terms of load demand. However, the EPNS and LOLP indices have only reduced by 0.76 MW and 0.41 %, respectively. These effects are due to the intermittency of wind generation and consequently low capacity factor, and must be taken into consideration when planning a larger penetration of wind generation.

6 Conclusions

This chapter proposed a model for representing statistically dependent time-varying variables in nonsequential MCS. The model was used to evaluate the reliability of a system in which there is temporal dependence between four temporal variables (three winds and the load).

The results showed that the model can correctly represent the effect of statistical dependence, what is normally achieved by sequential simulation. The independent model was also applied and proved to be incorrect when the time series correlation values are significant.

The proposed model to represent statistical dependence is a good alternative to deal with multiple time-varying elements in nonsequential simulation with a reduced computational effort. This facility gains importance nowadays with the large penetration of wind generation that is being observed all over the world, both onshore and offshore.

References

1. Billinton R, Chen H, Chajar R (1996) A sequential simulation technique for adequacy evaluation of generating systems including wind energy. IEEE Trans Energy Convers 11(4):728–734
2. Wangdee W, Billinton R (2006) Considering load-carrying capability and wind speedcorrelation of WECS in generation adequacy assessment. IEEE Trans Energy Convers 21(3):734–741
3. Xie K, Billinton R (2009) Considering wind speed correlation of WECS in reliability evaluation using the time-shifting technique. Electr Power Syst Res 79(4):687–693
4. Melo JCO, Pereira MVF, Silva AML (1993) Evaluation of reliability worth in composite systems based on pseudo-sequential Monte Carlo simulation. IEEE Trans Power Syst 9(3):1318–1326
5. Silva AML, Manso LAF, Mello JCO, Billinton R (2000) Pseudo-chronological simulation for composite reliability analysis with time varying loads. IEEE Trans Power Syst 15(1):73–80
6. Billinton R, Gao Y, Karki R (2009) Composite system adequacy assessment incorporating large-scale wind energy conversion systems considering wind speed correlation. IEEE Trans Power Syst 24(3):1375–1382
7. Vallée F, Lobry J, Deblecker O (2007) Impact of the wind geographical correlation level for reliability studies. IEEE Trans Power Syst 22(4):2232–2239

8. Dias JA, Borges CLT (2012) Representation of wind and load correlation in non-sequential Monte Carlo reliability evaluation. In: 12th international conference on probabilistic methods applied to power systems
9. Dias JA, Borges CLT (2012) Representation of wind and load correlation in non-sequential Monte Carlo reliability evaluation. In: Billinton R et al (eds) Reliability and risk evaluation of wind integrated power systems, reliable and sustainable electric power and energy systems management. Springer, India
10. Véliz FFC, Borges CLT, Rei AM (2010) A comparison of load models for composite reliability evaluation by non-sequential Monte Carlo simulation. IEEE Trans Power Syst 25(2):649–656
11. Leite AP, Borges CLT, Falcão DM (2006) Probabilistic wind farms generation model for reliability studies applied to Brazilian sites. IEEE Trans Power Syst 21(4):1493–1501
12. Justino TC, Borges CLT, Melo ACG (2012) Multi-area reliability evaluation including frequency and duration indices with multiple time varying load curves. Int J Electr Power Energy Syst 42(1):276–284
13. Jain AK, Dubes RC (1988) Algorithms for clustering data. Prentice-Hall Inc, New Jersey
14. Billinton R, Allan R (1996) Reliability evaluation of power systems. Plenum, New York
15. Ieee RTS (1979) Task force of APM subcommittee. IEEE reliability test system. IEEE PAS 98(6):2047–2054
16. Dias JA, Borges CLT (2010) Object oriented model for composite reliability evaluation including time varying load and wind generation. In: 11th international conference on probabilistic methods applied to power systems
17. Billinton R, Gao Y (2008) Multistate wind energy conversion system models for adequacy assessment of generating systems incorporating wind energy. IEEE Trans Energy Convers 23(1):163–170

HVDC Transmission for Offshore Wind Farms

Raymundo Enrique Torres Olguin, Alejandro Garces and Gilbert Bergna

Abstract Large-scale wind energy expansion is limited by factors such as the land use and the visual impact of facilities on land. Offshore wind energy can overcome the above-mentioned limitations. In addition, wind velocity is higher and more constant offshore than onshore. This chapter will present an overview of different topologies for grid integration of offshore wind farms. Special emphasis is made on the offshore grid topologies and types of power electronic converters.

Keywords Offshore wind energy · HVDC transmission · Offshore grid · Line-commutated converters · Voltage source converters · Modular multilevel converters

1 Introduction

Nowadays, the two main challenges in the energy sector are to assure the energy security and to meet the environmental goals [1]. In the recent years, many countries have prioritized the use of renewable energy sources on their agenda in order to ensure the energy security while helping to preserve our environment [2].

R. E. Torres Olguin (✉)
Sintef Energy Research, Trondheim, Norway
e-mail: raymundo.torres-olguin@sintef.no

A. Garces
Department of Electric Power Systems, Universidad Tecnológica de Pereira, Pereira, Colombia
e-mail: alejandro.garces@utp.edu.co

G. Bergna
Département d'Electrotechnique et de Systèmes d'Energie, École Supérieure d'Électricité, Paris, France
e-mail: gilbert.bergnadiaz@supelec.fr

J. Hossain and A. Mahmud (eds.), *Large Scale Renewable Power Generation*, Green Energy and Technology, DOI: 10.1007/978-981-4585-30-9_11,

Among renewable energy sources, wind energy is highlighted because of its enormous development in the last years. Nowadays, wind energy can be categorized as a mature technology, but the large-scale expansion is limited by factors such as the land use and the visual impact of facilities on land. The development of the offshore wind energy industry can overcome the above-mentioned limitations. Moreover, offshore wind resources are abundant in some regions and in general, wind conditions are better offshore than onshore, i.e., the average wind speed is higher and less turbulent. However, offshore installations are more costly compared to onshore facilities. The unit cost of energy can be decreased by increasing the rating and efficiency of offshore wind farms (OWFs), and hence, most of the research in the field is related to these two aspects. For these reasons, one of the greatest challenges is the transmission of large amounts of energy over long distances [3].

For interconnecting the wind farms there are two alternatives: high-voltage alternating current (HVAC) and high-voltage direct current (HVDC) [3, 4]. Today, HVAC is chosen in most of the projects located at a relatively short distance to the shore [4]. HVAC has an important limitation, the HVAC cables. This type of cables has a high capacitance per length, so in addition to the delivery electrical current, there is a capacitive current. This capacitive current is fluctuating every half cycle, and is utilizing part of the total current delivery capability. In other words, HVAC long cables require excessive reactive power [5]. This reactive power can be absorbed by using reactive shunt compensation, but this is at the expense of the investment and operating costs [5]. For offshore applications, HVDC becomes a more attractive solution in terms of investment and operating costs as the distance from the shore increases. The break-even point between HVAC and HVDC may vary from 60 to 100 km [6].

Currently, there are two HVDC technologies available in the market: LCC-based HVDC and VSC-based HVDC. LCC uses thyristors, which are line commutating devices, whereas VSC uses insulate-gate bipolar gate transistors (IGBT), which are self-commutating devices [7]. Although the LCC is the most widespread HVDC technology around the world, most studies on the grid integration of OWFs have been focused on VSCs because of their beneficial features of the ability to have independent control of active and reactive power, an external commutating source voltage is not required for the proper operation, VSC is able to supply passive grids, and reduced footprint compared with LCC-based HVDC systems [8–11]. The use of LCC for grid integration OWFs has been briefly studied. It has been neglected mainly because of the large footprint, and the external commutation voltage needed for its operation. However, LCC has the lowest power losses and the lowest cost among converters for HVDC. Moreover, LCC-based HVDC is very suitable for the transmission of bulk power, and its reliability and availability have been demonstrated for many years.

This chapter deals with configurations of HVDC systems on OWFs. Different technologies and topologies are exposed and analyzed from the stand point of losses and reliability. The chapter is organized as follows: in Sect. 2 the main challenges for offshore wind energy are presented. Next, in Sect. 3, different grid

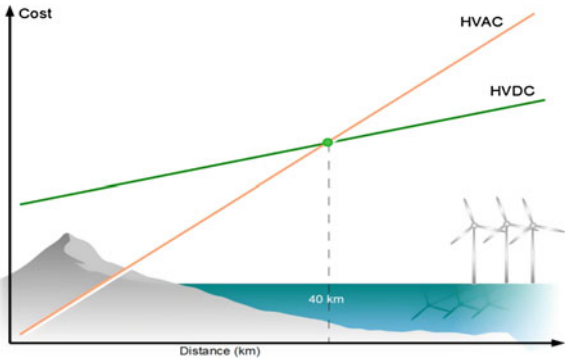

Fig. 1 Comparison between HVDC and HVAC for offshore wind applications

topologies are exposed. After that, the type of converter more suitable for each topology is analyzed in Sect. 4. The main types of HVDC systems are presented in Sects. 5 and 6, followed by the new trends on HVDC systems in Sect. 7. A brief review of the cable technologies is presented in Sect. 8. Finally, conclusions are presented in Sect. 9.

2 Challenges of Offshore Wind Energy

Offshore wind energy has several advantages compared to conventional onshore-based wind facilities, i.e., less visual impact and auditory contamination, reduced user conflicts, and high-power capability [12]. These characteristics allow the use of wind turbines with high-power ratings and customized power electronic converters as will be presented later in this chapter. Turbines up to 10 MW are planned for offshore applications [13].

Most of the future wind farms are expected to be placed at deep water offshore due to the better conditions of wind in terms of magnitude and constancy in such places. Transmitting power at long distances is certainly a challenge that must overcome considering a trade-off between efficiency and investment cost. In these conditions HVDC transmission is the most cost-effective alternative as shown in Fig. 1. The break-point between HVAC and HVDC is not unequivocal defined and depends on many factors including the type of HVDC technology and the cable to be used [14]. A break-point of 40 km is accepted for submarine cables. Most future OWFs are expected to be placed beyond this distance.

Despite the constant development of the HVDC technology in the last decade, it must to be adapted to certain specific conditions of offshore facilities. In particular for the grid integration of OWF, HVDC faces new challenges such as:

- *Footprint*. The weight and the space occupied by the HVDC stations have a significant impact on investment costs.
- *Efficiency*. Offshore projects can be more affordable minimizing power losses in the system.

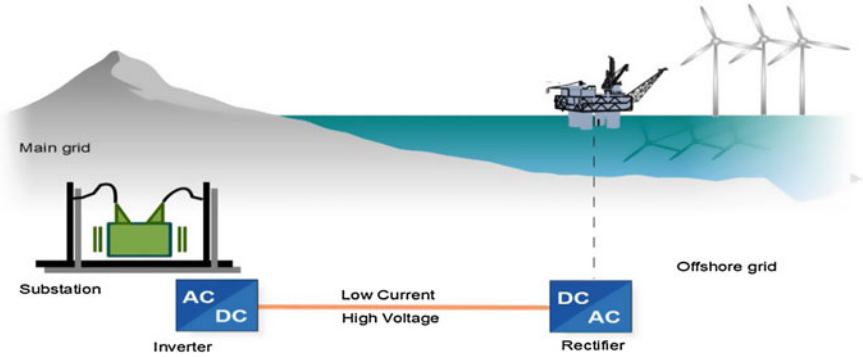

Fig. 2 Schematic representation of HVDC transmission for offshore wind farms

- *Reliability*. The cost of non-harvested energy due to unavailability of the transmission system can be crucial to make a profitable offshore project.
- *Harsh environment*. There is a limited access for maintenance.

For instance, power density and power-to-weight ratio must be carefully considered during the design of the components to be placed offshore in order to reduce investment and operative costs. On one hand, investment costs are directly related to the power-to-weight ratio due to the platforms required to support the components placed offshore. On the other hand, operative costs are related to the transportation of spare parts from shore during maintenance. The latter aspect imposes additional requirements in terms of reliability of the offshore components as will be presented later in Sect. 4

A conventional HVDC transmission approach is shown in Fig. 2. It consists of three main components: a rectifier, a submarine cable, and an inverter. Submarine cables deal with high capacitive effect which must be considered in transient studies. The rectifier and the inverter are usually based on the same type of technology. Their principal difference is in the control and operation rather than the component itself. Nevertheless, new hybrid topologies can be used due to the unidirectional characteristic of the power and the aforementioned requirements of offshore wind energy.

3 Offshore Grid: AC Versus DC Topologies

HVDC transmission is the most cost-effective solution for offshore wind energy when there are large distances to the mainland. This transmission could be done in a conventional way in which the HVDC link interconnects two separated grids. However, new and fascinating alternatives are possible for offshore wind energy [15]. Many of these are based on the DC grid concept which arises naturally in the case of the wind energy since it requires AC/AC converters.

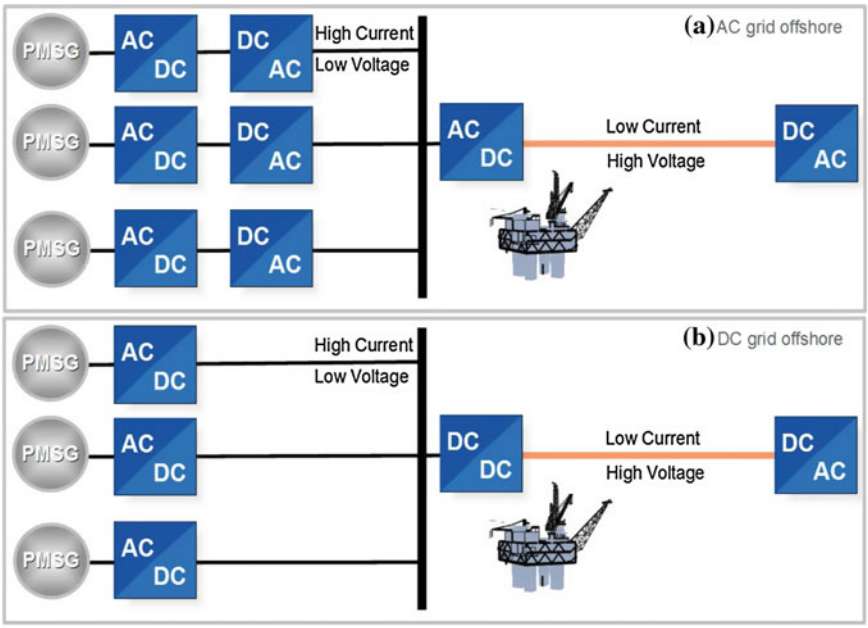

Fig. 3 Possible configurations for offshore grids: **a** AC grid, **b** DC grid

Any wind turbine must be equipped with a power electronic converter in order to control its rotational speed and hence, extract maximum power from the wind. An AC/AC converter is the most used alternative. However, many of the AC/AC converters have an intermediate DC conversion stage. It means what is called an AC/AC converter is in reality an AC–DC–AC converter as shown in Fig. 3a. It is possible to eliminate the last stage of conversion by using a DC grid as shown in Fig. 3b. This concept is called DC grid topology.

A DC grid could be a more efficient solution since it increases the utilization of cables offshore. In AC systems under ideal sinusoidal waveforms, cables must carry both active and reactive power. Needless to say reactive power increases the current and consequently transmission losses. However, total losses are given not only because of the transmission losses but also because of the efficiency of the converters themselves. In a DC grid, transformers are replaced with DC/DC converters. Different topologies have been proposed to increase the efficiency of these converters as will be studied in Sect. 4.

Permanent magnet synchronous generator (PMSG) is the most promising technology for OWFs with DC grids. A PMSG requires a full converter for its integration to the grid. A gearbox is not required with this technology if the machine is properly designed using high number of poles. Therefore, efficiency, reliability, and power density are increased by the use of PMSG.

Every DC/DC converter in a DC grid configuration must increase the voltage level in order to permit long distance power transmission. This allows different DC

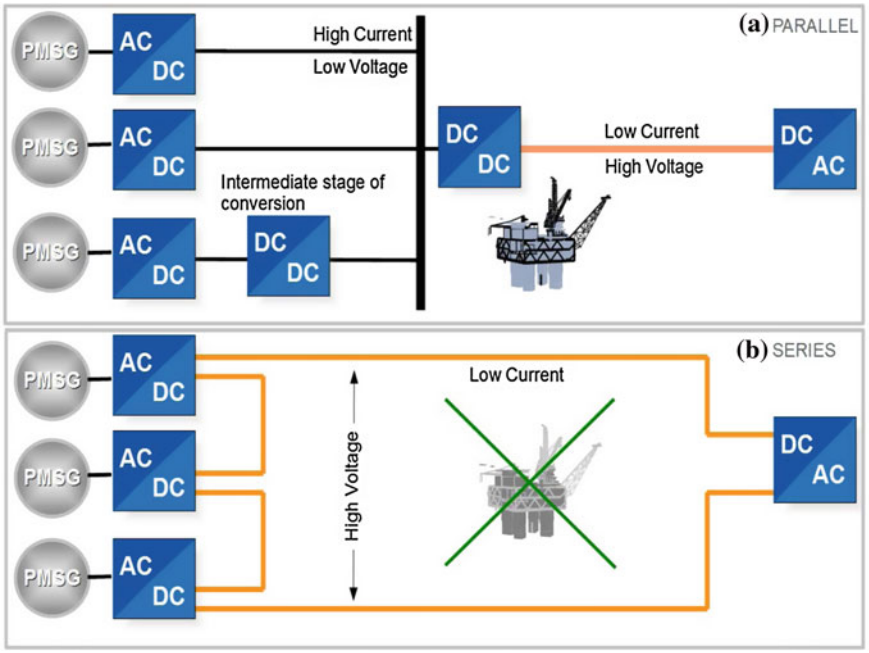

Fig. 4 Possible configurations for DC grids: **a** parallel connection, **b** series connection

grid configurations. A simple DC grid with parallel connection is shown in Fig. 4a. In this configuration, the DC/DC converter must increase the DC voltage from the generation level, usually less than 1 kV, to transmission level. A DC grid could have one or several stages of DC/DC conversion emulating the way it is done in conventional AC grids. This option is also shown in Fig. 4a.

In Fig. 4b, the high voltage required by the efficient is achieved by connecting turbines in series [16]. In this type of configuration, both the offshore grid and the transmission have the same low current. Therefore, efficiency is highly increased. In addition, the centralized DC/DC converter is not required allowing the elimination of the supporting platform. This affects the investment cost. Reliability is not compromised since the transmission distance is the same and hence, the probability of fault is similar to conventional HVDC transmission.

4 Different Concepts for the Energy Conversion System in Offshore Wind Energy

Each concept of HVDC transmission and offshore grid is directly related to the type of energy conversion system in the side of the generators. Double fed induction generators are the most common alternative for mainland wind farms.

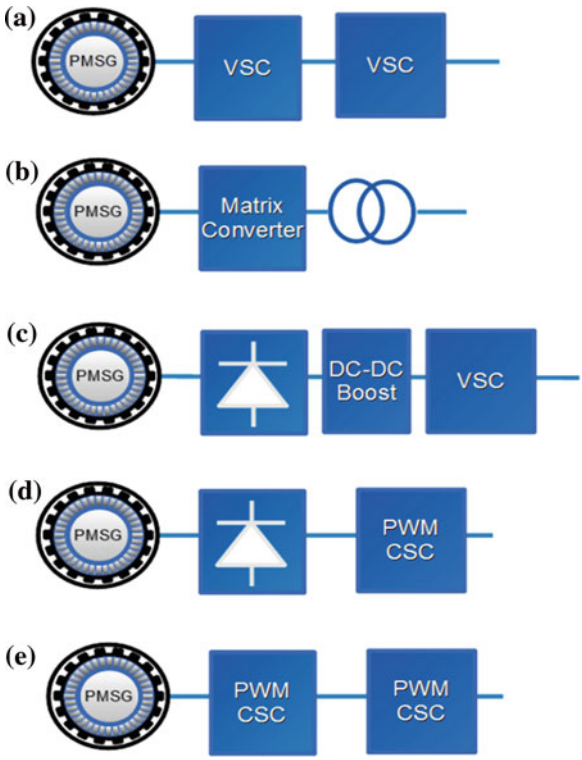

Fig. 5 Configurations for grid integration of PMSG in AC grids: **a** back-to-back configuration with VSC, **b** matrix converter, **c** full-bridge diode rectifier with DC converter, **d** full-bridge diode rectifier with PWM-CSC, **e** back-to-back configuration with PWM-CSC

However, for offshore wind energy is the PMSG the most suitable option, especially on DC grids offshore. PMSGs require a full converter to be integrated to the main grid. Different type of converters can be used according to the type of offshore grid.

In the case of AC grids as the one shown in Fig. 3, the PMSG must to be integrated using AC/AC converters. Different configurations have been proposed as shown in Fig. 5. They come from voltage source-based converters to current source-based converters. Back-to-back configuration with voltage source converters (VSCs) is the most common type of technology (see Fig. 5a). It permits to control the active and reactive power in both sides of the converter. Therefore, it can be used with both PMSG and induction machines. A second alternative is the matrix converter (see Fig. 5b). It is an AC/AC converter without intermediate stage of DC conversion. It can control voltage in the input and current on the output. Consequently, the machine and power factor can be directly controlled. Among its advantages is the reduced size high reliability. PMSG can be integrated though a full-bridge diode rectifier as shown in Fig. 5c and d. In both cases, the output voltage varies according to the wind velocity and hence VSC cannot be used directly on the output. Consequently, the converter must be integrated though an intermediate stage of DC/DC conversion. Another alternative is to use pulse

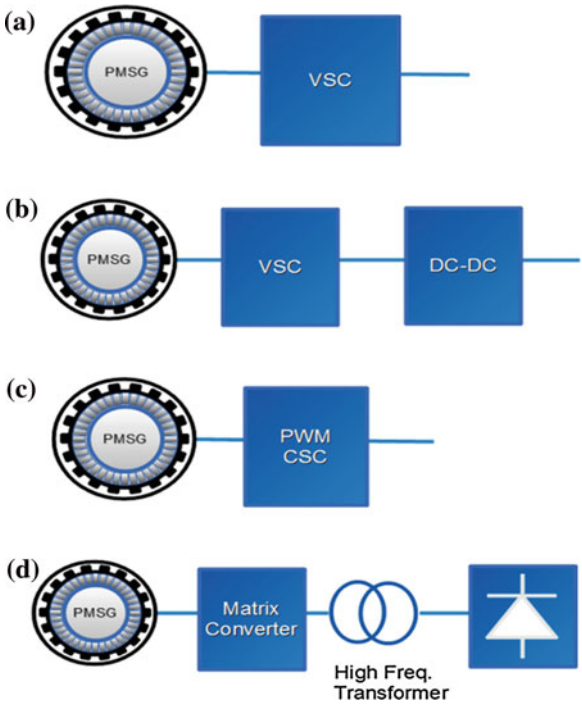

Fig. 6 Configurations for grid integration of PMSG in DC grids: **a** VSC, **b** high-frequency link with matrix converter, **c** VSC with DC/DC converters, **d** PWM-CSC

width modulated current source converter (PWM-CSC). Last option is promising due to the high efficiency of the diode rectifier and the high reliability of the PWM-CSC. Finally, a back-to-back configuration with PWM-CSC is also an option as shown in Fig. 5e.

In the case of parallel DC grid, the topology of the converter depends on the type of connection, i.e., series or parallel. For parallel connection, the converters based on VSCs are the most suitable. A classic VSC as shown in Fig. 6a is enough for controlling the machine. However, it could be required a DC/DC converter in order to step-up the output voltage as shown in Fig. 6b.

In series connection, the most suitable technology is the current source convert as shown in Fig. 6c. This converter can control the machine based on the current shared by the all the converters connected in series. The output voltage varies according to the wind velocity. Finally, a configuration based on reduced matrix converter (RMC) and high-frequency transformer is shown in Fig. 6d. This topology operates in a very similar way as the PWM-CSC. However, the high-frequency transformer increases the voltage and permits galvanic isolation.

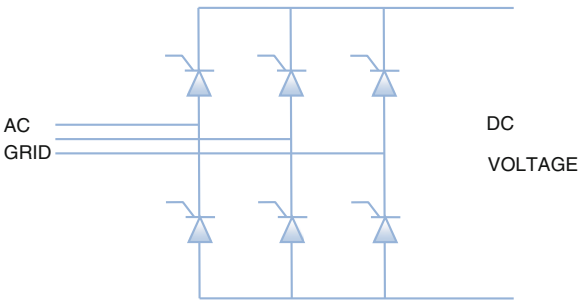

Fig. 7 Six-pulse line-commutated converter

5 Line-Commutated Converters for HVDC Transmission in Offshore Wind Energy

HVDC based on line-commutated converters uses a set of thyristor valves usually connected in a 6-pulse or 12-pulse configurations as shown in Fig. 7. A thyristor is a solid-state semiconductor device which is able to conduct the current flow if the anode voltage is more positive than the cathode voltage, similar to a diode, but additionally requires a positive voltage applied to the gate terminal. The conduction process cannot be initiated without a current of proper polarity to the gate. It is important to remark, that the gate only is able to control the thyristor turn-on. Once the conduction process has started, the valve will continue to conduct until the current through it drops to zero and the reverse voltage bias appears across the thyristor.

LCC HVDC is a technology very suitable for the transmission of bulk power, and its reliability and availability have been demonstrated for many years on land installations. Moreover, it could be cheaper than others transmission systems for power ratings of hundreds of megawatts [6]. Line-commutated converters have several advantages, e.g., simplified control and reduced number of sensors, reduced costs, lower conduction and switching losses, and robust and reliable operation.

However, the use of LCC for grid integration of marine energy parks has been neglected mainly because:

- *Space requirements*. LCC HVDC requires passive filters for its proper operation and this increases the footprint of the installations which implies enormous offshore platforms.
- *AC voltage for the commutation*. LCC HVDC needs an external commutating source voltage for the proper operation. This means that the LCC is unable to supply passive loads and it does not have start-up capability.
- *Susceptibility to ac disturbances*. LCC HVDC is highly susceptible to AC network disturbances which results in a commutation failure [14].
- A LCC consumes reactive power in both sides of the system.
- High harmonic contents.

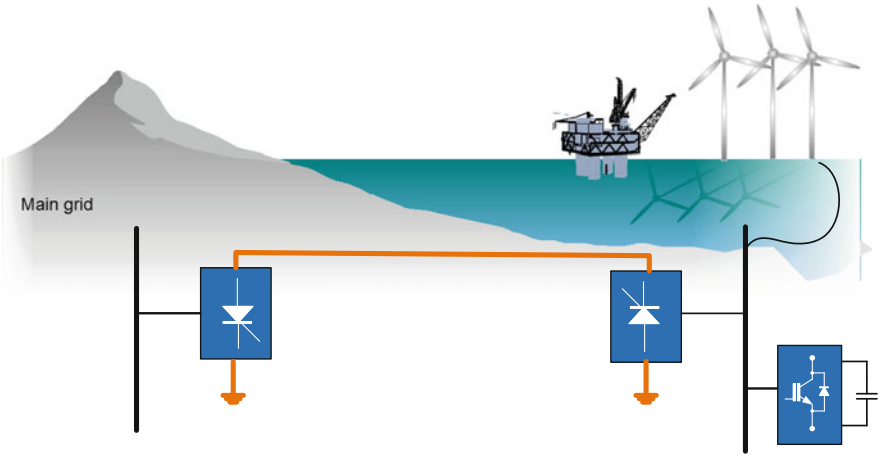

Fig. 8 Diagram of the wind farm connection using LCC-based HVDC transmission

In the literature there have been the following concepts using LCC HVDC. In [4, 17–19], it is proposed to use either a synchronous compensator or a static var compensator (STATCOM) to provide the necessary commutation voltage required for the operation of the LCC HVDC. STATCOM is set at the offshore station as shown in Fig. 8. Moreover, the STATCOM can provide reactive power compensation for the grid during steady state, dynamic, and transient condition.

In [20], it is proposed to use back-to-back PWM converter at each variable speed turbine to provide the reactive power demand using a frequency controller to regulate the firing angle or DC-link current to control the power flow of an OWF.

6 Voltage Source Converter for HVDC Transmission in Offshore Wind Energy

Voltage source converter (VSC)-based HVDC transmission uses self-commutated devices. The latest converters are built using series IGBT with antiparallel diodes; however, they can be built using gate turn-off thyristors (GTO) or Integrated gate-commutated thyristors (IGCT). The commutation can be achieved independently of the AC system so the operation differs considerably from those based on LCC. A VSC is shown in Fig. 9.

The main advantages of this type of converter are:

- External commutating source voltage is not required for the proper operation. Contrary to LCC-based HVDC systems which are unable to operate without an AC voltage for the commutation.
- IGBTs or similar work in a higher switching frequency range, so there is with much lower harmonic distortion in VSC-based than LCC-based HVDC systems, though with higher power losses.

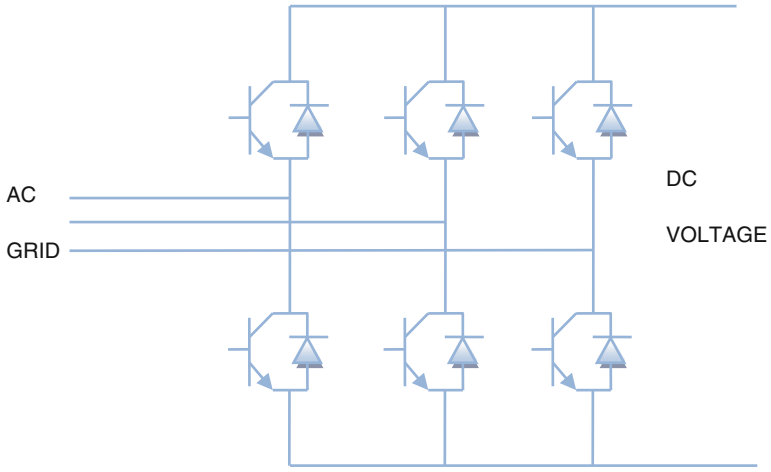

Fig. 9 Voltage source converter

- The ability to have independent control of active and reactive power. LCCs need passive filters to supply the reactive power demand intrinsic to their operation.
- VSC is able to supply passive grids. This feature is important for the integration of OWF since is related with the start-up capability and the ability to establish an AC grid.
- Reduced footprint compared with LCC-based HVDC systems. The large footprint in LCC systems is caused by AC filtering that is needed for proper operation.

The cost and switching losses in this type of converter are higher than in a line-commutated converter. However, its high controllability compensates these drawbacks. Active and reactive power can be controlled in the converter and therefore, power quality issues are reduced. Therefore, the converter itself can be used to maintain unity power factor or for reactive power injection to the grid.

Most of the research on the grid integration of OWF using HVDC has been focused on the VSC HVDC [21] which is shown in Fig. 10. Some papers have focused on the economic feasibility [22]. In [14] a comparison of AC and DC transmission options is presented. It is concluded that the VSC-based HVDC is the more affordable option when the OWF is above 100 MW and it is located to more than 90 km. Several others have been focused in the control strategies [23–26]. Some papers have been focused on the impact on the power systems [27]. The use of multiterminal configurations have been extensity studied [28–33]. Many papers have been studied the fault response of the VSC [10, 32, 34].

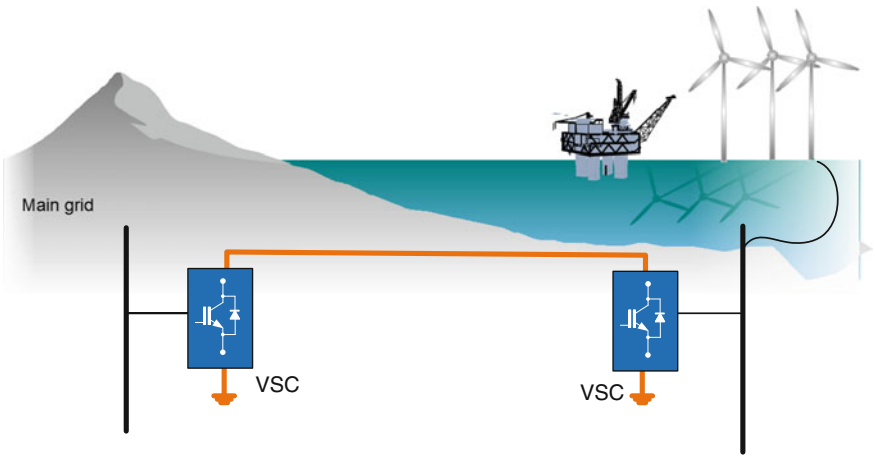

Fig. 10 Diagram of the wind farm connection using VSC-based HVDC transmission

7 New Trends on HVDC Transmission for Offshore Wind Energy

7.1 Hybrid Topologies

An alternative which has been poorly studied is to build a hybrid HVDC using a self-commutated converter, and a line-commutated converter. This hybrid topology takes advantages from force-commutated converters, i.e., VSC, as well as line-commutated converters, i.e., LCC. In the case of offshore applications, an increase in efficiency and a reduction in cost are expected.

Grid integration of OWFs in [35, 36] are presented a configuration consisting of a VSC located at offshore and an LCC located onshore as shown in Fig. 11. In [35] the corresponding control strategy is stated, which is verified through numerical simulations of several conditions including: the start-up and AC faults. In [35, 37] a multiterminal approach was presented. In [38], it is proposed a hybrid with an offshore LCC and an onshore VSC. The required commutation voltage and the relatively large footprint of the offshore LCC stations are major obstacles to the implementation of this concept.

In [39] and [40], a configuration is proposed, which consists of diode-based rectifier and LCC in the same HVDC link. The concept is aimed to reduce the power losses and installation costs. A control strategy is proposed both in steady state and during transients. The concept is shown in Fig. 12.

Among current source converters some are made with self-commutating devices, denoted in this work as PWM-CSC. To date, the use of PWM-CSC has not been contemplated for HVDC applications. In [41] is presented a new hybrid configuration consisting of an LCC and a PWM-CSC as shown in Fig. 12.

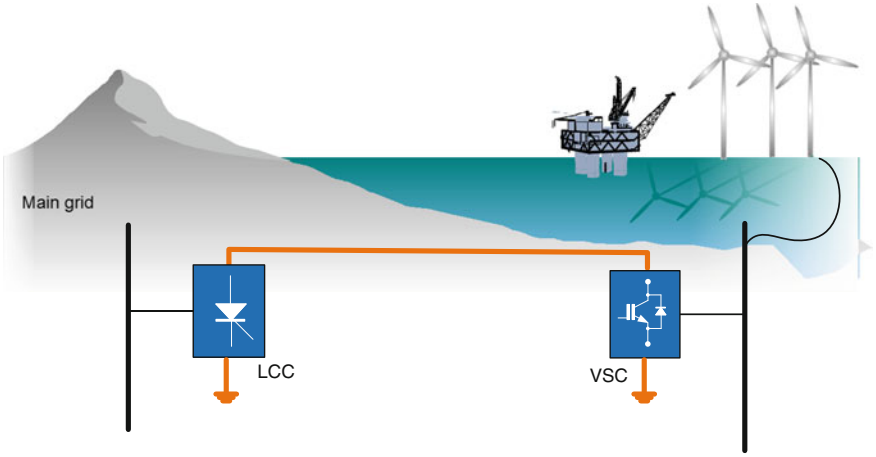

Fig. 11 Diagram of the wind farm connection using a hybrid between a VSC and an LCC

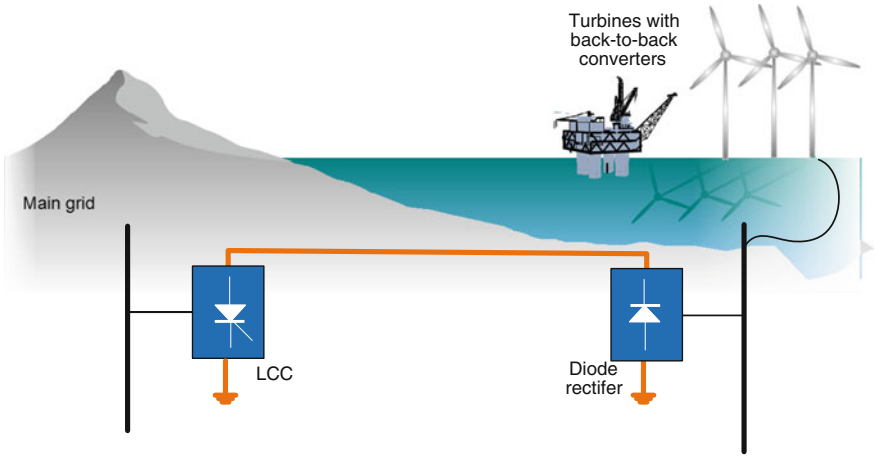

Fig. 12 Diagram of the wind farm connection using a hybrid between a diode rectifier and an LCC

In onshore applications, LCC is connected to the main grid, while the PWM-CSC is connected to an OWF at offshore side. The potential benefits of this concept include: low power losses, simple AC voltage controller, and good response to AC and DC faults. Moreover, PWM-CSC and LCC are both current sourced converters and the coupling between them can be effortlessly done.

Another option was proposed in [16]. This grid topology presents different stages of conversion. The first stage of conversion is required for controlling the generators. The second and third stages of conversion are step-up DC/DC converters. The last stage of conversion is the onshore converter for grid integration of

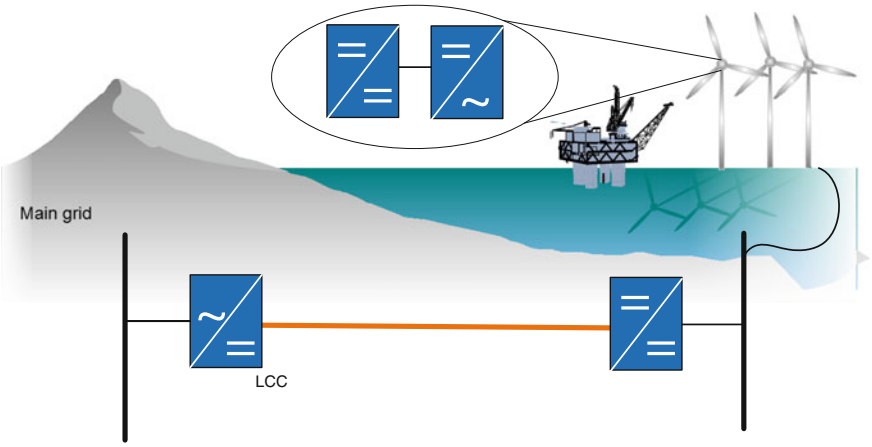

Fig. 13 Diagram of the wind farm connection using DC/DC converters

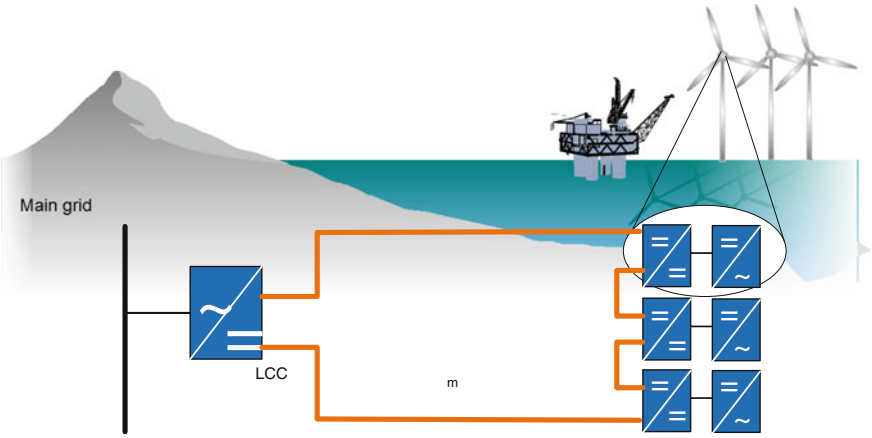

Fig. 14 Diagram of the wind farm with series connection

the wind farm as shown in Fig. 13. A novel DC/DC converter with a three-phase high-frequency transformer is required in this kind of topology. Another similar concept is the dispersed converter concept with series connection [16]. This topology is schematically shown in Fig. 14.

In [16], it was found that series connection leads to the lowest grid losses. However, the total losses are not competitive with DC parallel connections due to the losses in the converters. As a consequence of that, the efficiency of the converter must be improved in order to make series connection a practical alternative.

In [42], it is proposed to use an RMC which transforms the three-phase voltages and currents in a square wave, high-frequency single-phase output. A high-frequency

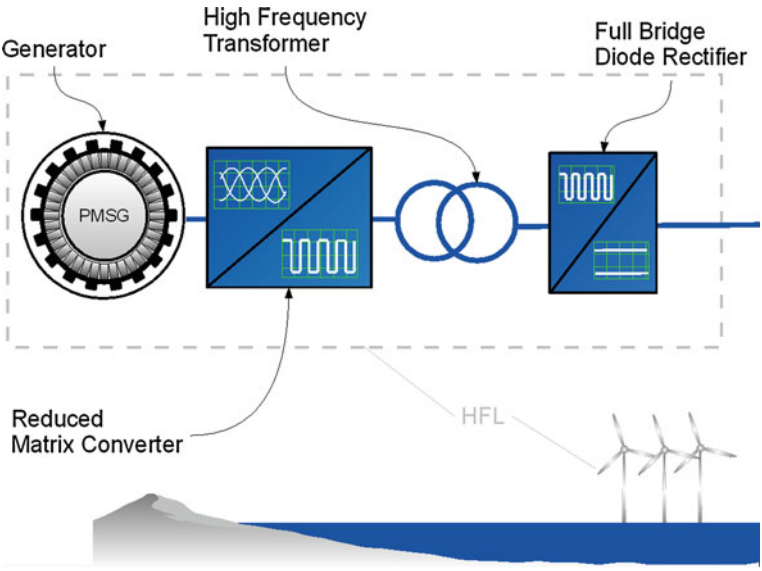

Fig. 15 Reduced matrix converter

transformer is used for galvanic isolation and to raise the output voltage. A full-bridge diode rectifier is used as an AC/DC converter to connect the conversion system with the output DC grid. The schematic is shown in Fig. 15.

7.2 Modular Multilevel Converter

Considering the shortcomings of the classic technologies (line-commutated converters) for multiterminal operation, it is highly probable that the first developments of the "renewable energy electricity highway" or the so-called Super-Grid will be using VSCs. Among the different topologies of this type of converters, the modular multilevel converter (MMC) introduced by Prof. Marquardt in [43] is the most promising power converter for high-voltage/high-power applications [44–46].

The MMC is the only converter in the multilevel family that presents at the same time a modular design while having only two DC terminals suitable for HVDC transmission. Its topology allows a smooth and nearly ideal sinusoidal output voltage which requires little or no filtering at all. It is able to operate at lower switching frequencies; hence the converter losses are closer to the LCC technology [44, 45, 47]. Its modular design may lead to a reduced production cost and easier maintenance. Moreover, it has high scalability allowing a simple adjustment to the maximum voltage by increasing or reducing the number of submodules; and finally it has the ability to continue its operation in spite of module failure, and could be operated without the need of a transformer [48].

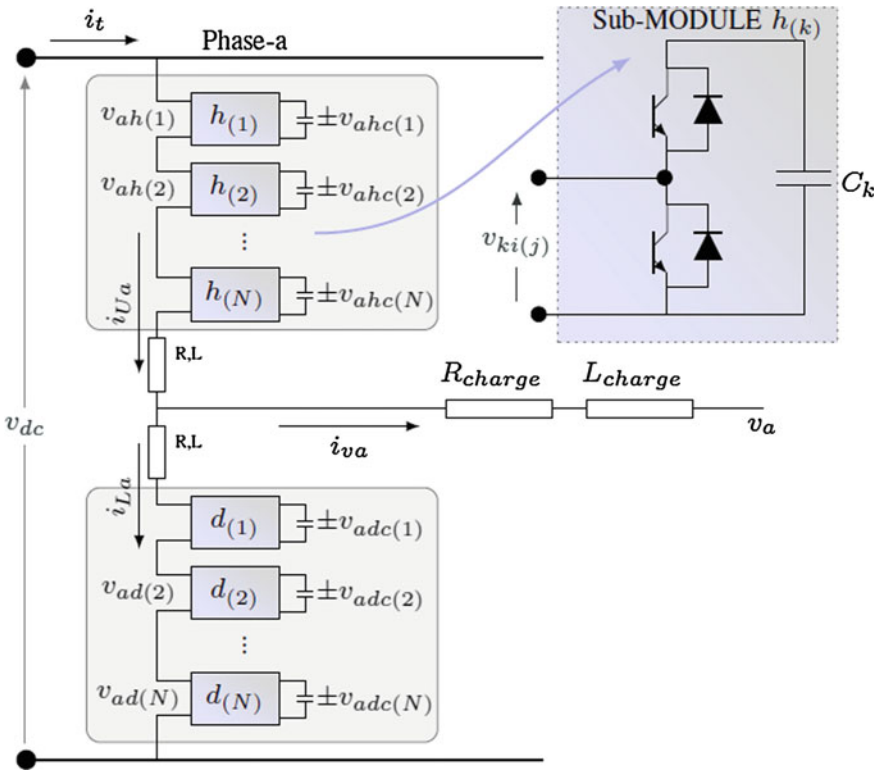

Fig. 16 MMC topology

The MMC three-phase structure is shown in Fig. 16. The converter is formed by "*n*" sub-modules of which half of them are placed in the upper "arm" and the other half on the lower "arm." Each sub-module is composed of two switches (IGBT + diode), and basically allows two effective states: (1) a short-circuit or (2) the appearance of the capacitor voltage between the sub-module terminals. The converter needs two-arm inductances in order to compensate voltage unbalances between the sum of the upper and lower "multi-valves" voltages in one phase (created by all the sub-modules), and the DC source.

The currents of the upper and lower arms may be decomposed in two independent terms each: One half of the current that will flow into the AC grid/load, and an additional current called circulating or differential current that does not flow into the load but stays "trapped" inside both arms of the converter, and contributes to the DC current by means of its average value. In equations:

$$i_{\mathrm{Uk}} = i_{\mathrm{diff_k}} + \frac{i_{\mathrm{vk}}}{2} \tag{1}$$

$$i_{\mathrm{Lk}} = i_{\mathrm{diff_k}} - \frac{i_{\mathrm{vk}}}{2} \tag{2}$$

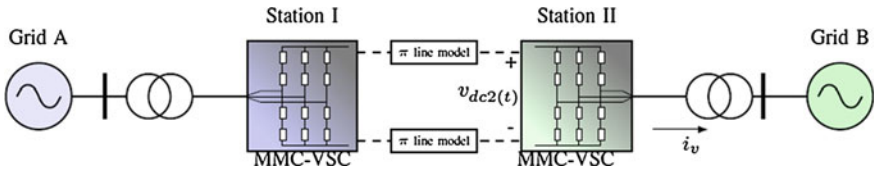

Fig. 17 MMC-based HVDC configuration

Although the MMC topology may appear quite simple, the control task of balancing the energy stored in the capacitors while performing a stable power transfer between the DC and AC terminals is rather complex. Basically, it can be divided into two control stages: On the one hand, a fast balancing algorithm is implemented independently in each arm that will ensure that every capacitor will have practically the same voltage waveform. To do so, one must measure and sort all capacitors in the arm, and depending on the direction of the current flowing in such arm, the algorithm will select among all capacitors of the arm, the "n" most appropriate capacitors to be inserted, knowing that "n" will be given by the controller at an upper stage. On the other hand, and at a superior regulation stage, a control technique is implemented to equally distribute the energy between the arms of the converter.

Thanks to the fact that the MMC operates with two ideally independent currents, two degrees of freedom are at our disposition when designing a control scheme, instead of one as is usually the case with more traditional converters. The load current is typically used to control the active power of the AC grid, while the differential current is free to be used to balance and equally distribute among each arm, the average of the energy stored in the converter.

Control methods have been proposed in order to accomplish this second task based on accurate analytical models of the MMC in state space representation (see [47, 49]). Some of the control strategies have been implemented by means of a coordinate transform, where instead of controlling the differential current in its natural phase "abc" coordinates, it has been controlled in the stationary "$\alpha\beta 0$" or even in the rotating "dqo" coordinates, which result from Clarke's or Park's respective transform (e.g., [50–52]).

Nonetheless, it seems to be getting clear that there are significant disadvantages when the control is not designed in the natural "abc" phase coordinates (unlike classical converters) since the complete phase-independent control of the converter state variables is not possible, hence the MMC potential will not be fully exploited. In [53] a control scheme in "abc" coordinates based on mathematical optimization by means of Lagrange's multipliers was presented to overcome this obstacle, by extending the work previously done in [54, 55].

Furthermore, such promising results were extended to the MMC-HVDC case, shown in Fig. 17, under unbalance operation in [56]. With this controller the MMC acts as a "power oscillation firewall" as it absorbs the power fluctuations coming from the AC side and caused by the unbalance operation, yielding a constant

power output at the DC terminals in spite of the unbalance. This is particularly useful in HVDC multiterminal applications, since the terminal that is being operated under unbalanced conditions will not influence the rest of the terminals, at least not through the DC grid.

Classic converters could achieve such conditions by means of their AC load current. Nonetheless, the MMC achieves such operation by means of the differential current, leaving the load current free to attend a different task; e.g., balancing the currents at the AC side during the unbalance voltage operation. This was presented in [52, 56] using a coordinate transform; while in [57], it was achieved with natural phase "abc" coordinates, allowing full independent control of the averaged phase variables of the converter.

8 Cable Technologies

Nowadays, there are three types of DC cables available in the market:

- Self-contained fluid filled cables
- Mass-impregnated cables
- Extruded insulation cables

Self-contained fluid filled (SCFF) cables have as insulation system consisting of a paper impregnated with a low-viscosity fluid. The cable has a central duct where the fluid is maintained under pressure allowing it to reach to the insulator. Since fluid is in constant circulation, hydraulic and pumping stations are essential. However, the possibility of occurrence of oil leakage is a potential risk for the SCFF cables [58].

Mass-impregnated (MI) cables have as insulator a high-density paper impregnated in a high-viscosity fluid. This type does not require fluid pressure supplying. So, MI cables may be installed in a very long length without the large oil duct system.

Extruded cables use cross-linked polyethylene (XLPE) as insulator. This option has attractive features such as: (i) XPLE cables are lighter than MI or SCFF since having better insulation properties so less insulation is needed. (ii) XLPE cables have smaller banding radius than MI and SCFF so to install and to transport is relatively easy. (iii) As MI cables, XPLE cables do not need an oil duct system, so there is not risk of oil leakage [58].

AC cables, XLPE type, up to 200 MW to 150 kV have been successfully installed for submarine applications [5]. However, as was mentioned above the cable distance is limited by the reactive power demand, which is the product of the capacitive characteristic of the cable. This limitation can be overcome with the assistance of reactive compensation on both sides of the cable, but the cost of installing more platforms to locate such compensation makes it unaffordable. LCC HVDC uses MI-insulated cables, which are made from copper with high-density

oil-impregnated paper as an insulator. It is also possible to use SCFF cables. XLPE cables have been only applied for HVDC with VSC technology. XLPE are made using a solid dielectric instead of pressurized liquid or oil-impregnated paper. XLPE cable has insulation degradation to voltage polarity reversal, therefore it is not recommended for HVDC with LCC technology [59].

9 Final Remarks

Nowadays, wind energy can be categorized as a mature technology, but the large-scale expansion is limited by factors such as the land use and the visual impact of facilities on land. The development of the offshore wind energy industry can overcome the above-mentioned limitations. One of the greatest challenges is the transmission of large amounts of energy over long distances.

For interconnecting the OWFs there are two alternatives: HVAC and HVDC. Today, HVAC is chosen in most of the projects located at a relatively short distance to the shore since HVAC cables have a high capacitance per length, which require excessive reactive power and this reduces the total current delivery capability.

For offshore applications, HVDC becomes a more attractive solution in terms of investment and operating costs as the distance from the shore increases. There are two HVDC technologies: LCC-based HVDC and VSC-based HVDC. Most studies on the grid integration of OWFs have been focused on VSC. However, LCC has the lowest power losses and the lowest cost among the converter for HVDC. This chapter has presented several concepts that used LCC and other types of devices that can be used for the grid integration of OWFs.

References

1. Agency IE et al. (2004) Energy security and climate change policy interactions: an assessment framework
2. W. E. Council (2013) Available: http://www.worldenergy.org/
3. Kirby N et al (2002) HVDC transmission for large offshore wind farms. Power Eng J 16:135–141
4. Xu L, Andersen BR (2006) Grid connection of large offshore wind farms using HVDC. Wind Energy 9:371–382
5. Kling W et al (2008) Advanced transmission solutions for offshore wind farms. In: Power and energy society general meeting-conversion and delivery of electrical energy in the 21st century, IEEE, pp. 1–6
6. Negra NB et al (2006) Loss evaluation of HVAC and HVDC transmission solutions for large offshore wind farms. Electr Power Syst Res 76:916–927
7. Kim C-K et al (2009) HVDC transmission: power conversion applications in power systems. Wiley, New York
8. Andersen B et al (2002) Topologies for VSC transmission. Power Eng J 16:142–150

9. Flourentzou N et al (2009) VSC-based HVDC power transmission systems: An overview. IEEE Trans Power Electron 24:592–602
10. Feltes C et al (2009) Enhanced fault ride-through method for wind farms connected to the grid through VSC-based HVDC transmission. IEEE Trans Power Syst 24:1537–1546
11. Zhang L et al (2011) Modeling and control of VSC-HVDC links connected to island systems. IEEE Trans Power Syst 26:783–793
12. Snyder B, Kaiser MJ (2009) Ecological and economic cost-benefit analysis of offshore wind energy. Renew Energy 34:1567–1578
13. Natarajan A. An overview of the state of the art technologies for multi-MW scale offshore wind turbines and beyond. WIREs Energy Environ. doi:10.1002/wene.80
14. Bresesti P et al (2007) HVDC connection of offshore wind farms to the transmission system. IEEE Trans Energy Convers 22:37–43
15. Garces A (2012) Design, operation and control of series-connected power converters for offshore wind parks. PhD Thesis, Norwegian University of Science and Technology, Tronheim
16. Meyer C (2007) Key components for future offshore dc grids. Shaker, Aachen
17. Bozhko SV et al (2007) Control of offshore DFIG-based wind farm grid with line-commutated HVDC connection. IEEE Trans Energy Convers 22:71–78
18. Foster S et al (2008) Control of an LCC HVDC system for connecting large offshore wind farms with special consideration of grid fault. In: Power and energy society general meeting-conversion and delivery of electrical energy in the 21st century, IEEE, pp. 1–8
19. Li R et al (2006) Grid frequency control design for offshore wind farms with naturally commutated HVDC link connection. In: 2006 IEEE international symposium on industrial electronics, pp. 1595–1600
20. Li R et al (2008) Frequency control design for offshore wind farm grid with LCC-HVDC link connection. IEEE Trans Power Electron 23:1085–1092
21. Spahic E, Balzer G (2005) Offshore wind farms—VSC-based HVDC connection. In: Power Tech, 2005 IEEE Russia, pp. 1–6
22. Morton AB et al (2006) AC or DC? Economics of grid connection design for offshore wind farms. In: The 8th IEE international conference on AC and DC power transmission, 2006. ACDC 2006, pp. 236–240
23. Feltes C, Erlich I (2007) Variable frequency operation of DFIG based wind farms connected to the grid through VSC-HVDC link. In: Power Engineering Society General Meeting, IEEE, pp. 1–7
24. Kong DC, Zhang XP (2010) Modelling and control of offshore wind farm with VSC-HVDC transmission system. In: 9th IET international conference on AC and DC power transmission, 2010. ACDC, pp. 1–6
25. Rios B, Garcia-Valle R (2010) Dynamic modelling of VSC-HVDC for connection of offshore wind farms. In: 9th IET international conference on AC and DC power transmission, ACDC, pp. 1–4
26. Gomis-Bellmunt O et al (2011) Control of a wind farm based on synchronous generators with a central HVDC-VSC converter. IEEE Trans Power Syst 26:1632–1640
27. Spahic E, Balzer G (2007) Impact of the VSC HVDC connection of large offshore wind farms on power system stability and control. In: Power Tech, IEEE Lausanne, pp. 207–212
28. Lie X et al (2008) Multi-terminal DC transmission systems for connecting large offshore wind farms. In: Power and energy society general meeting—conversion and delivery of electrical energy in the 21st century, IEEE, pp. 1–7
29. Da Silva R et al (2010) Power delivery in multiterminal VSC-HVDC transmission system for offshore wind power applications. In: Innovative smart grid technologies conference Europe (ISGT Europe), IEEE PES, pp. 1–8
30. Jin Y et al (2010) Multi-terminal DC wind farm collection and transmission system internal fault analysis. In: 2010 IEEE international symposium on industrial electronics (ISIE), pp. 2437–2442

31. Giddani OA et al (2010) Grid integration of offshore wind farms using multi-terminal DC transmission systems (MTDC). In: 5th IET international conference on power electronics, machines and drives (PEMD 2010), pp. 1–6
32. Jin Y et al (2010) Multiterminal DC wind farm collection grid internal fault analysis and protection design. IEEE Trans Power Deliv 25:2308–2318
33. Haileselassie TM, Uhlen K (2010) Frequency sensitivity analysis of ac grids connected to MTDC grid. In: 9th IET international conference on AC and DC power transmission, ACDC, pp. 1–5
34. Arulampalam A et al (2010) Fault Ride Through operation of a DFIG wind farm connected through VSC HVDC. In: International conference on industrial and information systems (ICIIS), pp. 520–525
35. Torres-Olguin RE et al (2012) Offshore wind farm grid integration by VSC technology with LCC-based HVDC transmission. IEEE Trans Sustain Energy 3:899–907
36. Wulue P et al (2006) Hybrid multi-terminal HVDC system for large scale wind power. In: Power systems conference and exposition, PSCE'06. IEEE PES, pp. 755–759
37. Xia C et al (2011) Integrating wind farm to the grid using hybrid multiterminal HVDC technology. IEEE Trans Ind Appl 47:965–972
38. Honglin Z et al (2008) Grid integration of DFIG-based offshore wind farms with hybrid HVDC connection. In: International conference on electrical machines and systems, 2008. ICEMS 2008, pp. 2579–2584
39. Blasco-Gimenez R et al (2010) Distributed voltage and frequency control of offshore wind farms connected with a diode-based HVdc link. IEEE Trans Power Electron 25:3095–3105
40. Blasco-Gimenez R et al (2011) Diode-based HVdc link for the connection of large offshore wind farms. IEEE Trans Energy Convers 26:615–626
41. Torres-Olguin RE et al (2013) Integration of offshore wind farm using a hybrid HVDC transmission composed by the PWM current-source converter and line-commutated converter. IEEE Trans Energy Convers 28:125–134
42. Garces Ruiz A (2012) Design, operation and control of series-connected power converters for offshore wind parks. Norwegian University of Science and Technology
43. Lesnicar A, Marquardt R (2003) An innovative modular multilevel converter topology suitable for a wide power range. In: Power tech conference proceedings, IEEE Bologna, vol 3, p. 6
44. Marquardt R (2010) Modular multilevel converter: an universal concept for HVDC-networks and extended DC-bus-applications. In: Power electronics conference (IPEC), 2010 International, pp. 502–507
45. Glinka M, Marquardt R (2005) A new AC/AC multilevel converter family. IEEE Trans Ind Electron 52:662–669
46. Ahmed N et al (2011) Prospects and challenges of future HVDC SuperGrids with modular multilevel converters. In: Proceedings of the 2011-14th European conference on power electronics and applications (EPE 2011), pp. 1–10
47. Antonopoulos A et al. (2009) On dynamics and voltage control of the modular multilevel converter. In: 13th European conference on power electronics and applications, EPE'09, pp. 1–10
48. Solas E et al (2010) Modulation of modular multilevel converter for HVDC application. In: Power electronics and motion control conference (EPE/PEMC), 2010 14th International, pp. T2-84–T2-89
49. Harnefors L et al (2013) Dynamic analysis of modular multilevel converters. IEEE Trans Ind Electron 60:2526–2537
50. Qingrui T et al (2011) Reduced switching-frequency modulation and circulating current suppression for modular multilevel converters. IEEE Trans Power Deliv 26:2009–2017
51. Bergna G et al (2013) An energy-based controller for HVDC modular multilevel converter in decoupled double synchronous reference frame for voltage oscillation reduction. IEEE Trans Ind Electron 60:2360–2371

52. Qingrui T et al (2012) Suppressing DC voltage ripples of MMC-HVDC under unbalanced grid conditions. IEEE Trans Power Deliv 27:1332–1338
53. Bergna G et al (2012) A generalized power control approach in ABC frame for modular Multilevel Converters based on mathematical optimization. In: Energy conference and exhibition (ENERGYCON), 2012 IEEE International, pp. 158–165
54. Akagi H et al (2007) Instantaneous power theory and applications to power conditioning, vol 31. Wiley, New York
55. Garces A et al (2012) A generalized compensation theory for active filters based on mathematical optimization in ABC frame. Electr Power Syst Res 90:1–10
56. Bergna G et al (2012) Mitigating DC-side power oscillations and negative sequence load currents in modular multilevel converters under unbalanced faults-first approach using resonant PI. In: IECON 2012-38th annual conference on IEEE industrial electronics society, pp. 537–542
57. Bergna JASG, Berne E, Egrot P, Vannier JC, Molinas M (2013) Generalized ABC frame differential current control ensuring constant DC power for modular multilevel converters under unbalanced operation. In: European power electronics conference EPE, Lille, France
58. Stijn C (2010) Steady-state and dynamic modelling of VSC HVDC systems for power system Simulation. PhD dissertation, Katholieke University Leuven, Belgium
59. Murata Y (2011) HVDC XLPE cable systems applicable for higher temperature and polarity reversal operation. Presented at the 8th international conference on insulated power cables, Versailles, France, 19–23 June 2011

Wind Farm Protection

Waqar A. Qureshi and Nirmal-Kumar C. Nair

Abstract Transmission system operation with wind generators has been well analyzed for issues like forecasting, reliability, control, power quality, and fault ride through (FRT) impacts following large-scale integration. However, there are still no standardized protection schemes for wind farms such as those practiced for the protection of conventional generation plants. Wind generators' collective response under high penetration scenarios needs special attention especially under abnormal operations such as grid disturbances and faults. During abnormal grid situations like faults, protection requirements for wind farms depend on a variety of factors. Different wind generation technologies exhibit different dynamic characteristics compared to conventional synchronous generator plants. Network characteristics and their interaction with available wind technologies also impact the fault behavior. This chapter first comprehensively reviews the integration characteristics and criteria for three different wind generator technologies connected to high voltage (HV) transmission systems. Aspects such as selection of time step and impact of additional controls such as crowbar protection are also discussed with their possible impacts on fault current estimation. A case study in DIgSILENT® PowerFactory has been developed to assess and compare the fault response of wind generator technology types. The response of each WTG type is generalized and analyzed in time domain to determine the number of electrical frequency cycles before the fault current reaches to steady-state value. Based on the estimated number of cycles and in the scenario of weaker interconnecting grids, protection schemes performance and protection relay operation are mainly assessed for each wind turbine generator (WTG) type. Technical challenges and difficulties are also highlighted before concluding.

W. A. Qureshi (✉) · N.-K. C. Nair
Department of Electrical and Computer Engineering, Science Centre,
University of Auckland, 38 Princes Street, Building 303, Auckland 1142, New Zealand
e-mail: w.qureshi@auckland.ac.nz

N.-K. C. Nair
e-mail: n.nair@auckland.ac.nz

J. Hossain and A. Mahmud (eds.), *Large Scale Renewable Power Generation*,
Green Energy and Technology, DOI: 10.1007/978-981-4585-30-9_12,

Keywords Wind generators · Low voltage ride through

1 Introduction

The protection practices for wind farms are not standardized. This chapter first reviews the general existing protection practice at wind farms. A brief comparison has been made between conventional generation and wind farm layout to further explore the protection design in each case. The chapter discusses a number of factors effecting fault current or its calculation for different wind generator technologies types as highlighted in earlier chapters. In order to investigate possible issues with existing protection schemes in case of a large wind farm, a specific case study representing a weak grid scenario has been established. This case study, thereafter, is assessed for all the four types of wind generator technologies at the same time. Through dynamic analyses using DIgSILENT® PowerFactory, comparative fault behavior analyses are achieved. Using results from the case study, the protection performance of each individual WTG type is investigated. Challenges to wind technology modeling and standardization efforts are also highlighted in this chapter.

2 Conventional Generator Layout

Figure 1 illustrates the philosophy of conventional generator layout and its connection to the power system. A conventional generator normally generates at a relatively higher voltage level compared to wind farms, for instance 11–15 kV, thus directly connecting to a medium voltage (MV) level bus as shown in the figure. The voltage is further stepped up through a high voltage (HV) transformer to connect to grid through HV transmission link. The actual arrangement for relatively smaller generation units may vary but large conventional generation units generally follow this arrangement.

3 Wind Farm Layout

Figure 2 illustrates the philosophy of wind farm layout and its connection to the grid. A wind farm comprises multiple wind units varying from a few to hundreds in number. Each WTG normally generates at a relatively lower voltage (LV) level compared to wind farms, for instance 400 or 690 V; thus directly connecting to an LV level bus called collector feeder as shown in Fig. 2. Each collector feeder may have one or few units connected to it in parallel. The voltage from these collector feeders is then collected to collector bus to achieve aggregated power from all

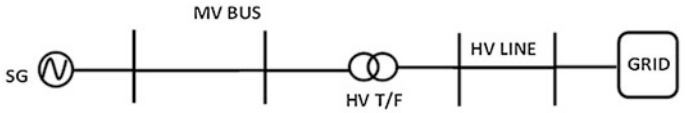

Fig. 1 Conventional generation interconnection with grid

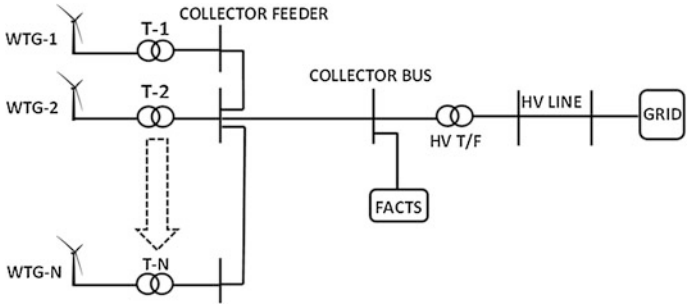

Fig. 2 Wind farm interconnection with grid

turbines at the same time. Collector bus voltage is then further stepped up through HV transformer to connect it to grid through HV transmission link. The flexible alternating current transmission systems (FACTS) devices such as static VAR compensators (SVCs) and static synchronous compensator (STATCOMs) are generally connected at the collector bus but they may vary in location in the real practice. The actual arrangements differ but most of the installed wind farms globally follow this arrangement.

4 Wind Farm and Conventional Generation Protection

Figure 3 explains the philosophy of conventional generator protection and its protection zones. A large conventional generator is protected through the standard protection philosophy of unit generation protection scheme. In the above case it is easier to establish coordination among generator, transformer, and transmission protection because of limited or single unit of generation. Conventional generators even have the capability of supplying reactive power and the inertia is also an inherent capability. Because of the reactive support and having higher short-circuit strength, they have higher FRT capability and they can satisfy almost any FRT criteria established in any part of the world.

If wind farms are compared to conventional generators, they will require different and varied protection requirements. Since a single wind farm usually consists of several wind units and these units are connected together to collector bus through collector feeders. Reactive support is also a separate unit and is normally

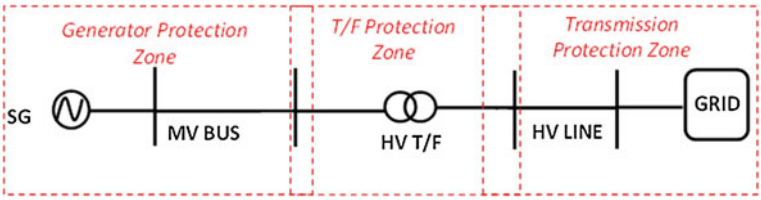

Fig. 3 Conventional generation protection

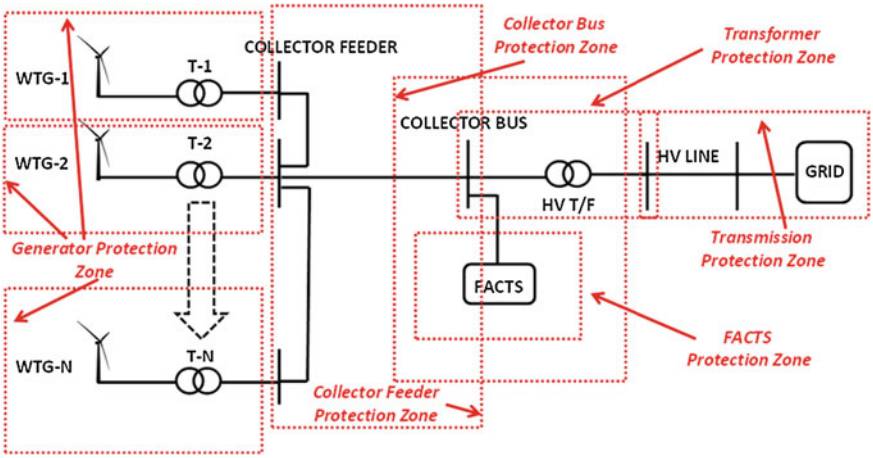

Fig. 4 Wind farm protection

connected to collector bus. The collector bus voltage is stepped up in order to connect to transmission system as shown in Fig. 4. In thisarrangement, protection requirements are different from normal conventional generator as each wind unit is provided with generator protection and also has the collector feeder protection. The coordination of transmission protection with entire unit protection configuration requires additional effort and care.

5 FRT Criteria, Protection, and Control Coordination

In the context of FRT capability, undervoltage and overvoltage protection relays must operate accurately to achieve ride through and ensure safety of the wind farm. The safety of the wind units is also important as wind farm operating on extended envelope requirements cannot afford any malfunctioning of these relays.

In addition to voltage envelope requirement for abnormal operation, grid codes also demand wind farms to operate on extended voltage and frequency limits

during normal operation. These requirements have been well-defined in some of the grid codes and are to be satisfied even at the expense of active power [1]. Robust control design of the wind farm can help achieve these requirements. Not all available technologies meet these requirements, thus requiring additional control blocks, demanding certain protection requirements.

All the above-mentioned expectations from large wind farms have a direct impact on the fault response of the wind units while riding through the faults and participating in market services at the same time. Increasing penetration of larger wind farms using different WTGs raises questions on system protection schemes. The literature review identifies that this aspect requires much more attention. Ongoing research for large-scale wind integration is around standardization of practices followed in transmission systems and exploring new options for control that will support the grid. Normal system operation with wind has been well studied with issues like forecasting, reliability, power quality, transient stability, and FRT impacts following large-scale wind integration [2]. However, there are no standard protection schemes for wind farms, yet are available like those available for conventional generation plants. Wind generators collective response has not been discussed much especially under abnormal operations such as grid disturbances and faults.

Reference [3] discusses impacts of distributed generation on protective device coordination, but focuses on distribution system rather than transmission system. In [4, 5] the author has analyzed the performance of conventional protection schemes used for a 225 MW wind farm and some issues such as disconnection of whole generation in case of fault in a single wind generator is highlighted. This leads toward investigation and design of new intrawind farm protection schemes and better coordination strategies for future integrations. Reference [6] discusses the earth fault protection for decentralized wind power plants. Overcurrent protection based on a particular model and testing facility for Type-1, 2, and 3 wind farms has been discussed but only from the modeling validation viewpoint [7]. The importance and necessity of overvoltage and overvoltage lightning protection has also been identified based on a Chinese case study but not emphasizing over any particular WTG or its protection issues [8]. Some of the potential WTG faults and their effective management through the IEC 61850 perspective and control viewpoint is discussed in [9–11]. In order to assess accurate protection settings, realistic wind farm models are required. These models should closely represent the dynamic behavior of connected wind farms. Accuracy of the machine model, ability of the model to be used to carry out balanced and unbalanced studies, type of the model based on its differential equation order, and accurate transfer functions of the control blocks are essentially required.

There is a need to carry out detailed system short-circuits and fault studies under various operating scenarios. Though short-circuit models for WTGs have been proposed in a few publications, standardization of relaying schemes is still a work in progress. These studies require wind farm modeling and all fault calculations and protection relay settings would thereby be influenced by the models.

Terminal voltage, stator, and rotor current magnitude during a fault are influenced by the model type [12].

The next section presents a case study developed in DIgSILENT® PowerFactory to carry out comparative analyses of dynamic fault behavior of all four mentioned WTG arrangements from a grid interface perspective. The impacts of each WTG arrangement on protection operation and performance for distance, differential, and overcurrent protection are explored and discussed in detail as the scope of this chapter.

6 Case Study

6.1 Network Under Study

Fault current response of WTGs depends on the following factors;

- Short-circuit strength of WTG technology;
- Distance of WTG from PCC;
- System protection schemes;
- Voltage level of connection point; and
- System characteristics at that particular network region.

For weak system conditions, an individual distant wind farm connected to an HV system has been selected as case study in the scope of this chapter. To understand the response of each of the WTG technologies, a case study has been developed to carry out a comparative study for different WTG types. The network used for this case study is shown in Fig. 5. All the WTG types are connected under the same network conditions to provide a fair basis of comparison. All the models of this network are developed in DIgSILENT® Power Factory, and are lumped aggregated models. A strong external network having large short-circuit strength has been modeled but this has been separated by two long transmission lines. This is an attempt to create a weak network, as there is no conventional generation near the wind farms and the external infinite grid is separated by transmission lines. FSIG (Types-1 & 2) and DFIG (Type-3) wind farms are stepped up to a 0.69/33/220 kV voltage level to connect to point of common coupling (PCC). Full-scale frequency converter (FSFC) (Type-4) is stepped up to 0.4/33/220 kV voltage level to be connected to PCC. The voltage is further stepped down for transmission. Network and generators parameters are given as shown in the Appendix Tables A.1, A.2, A.3, and A.4. However, the system parameters are given in Table A.5 in Appendix A.

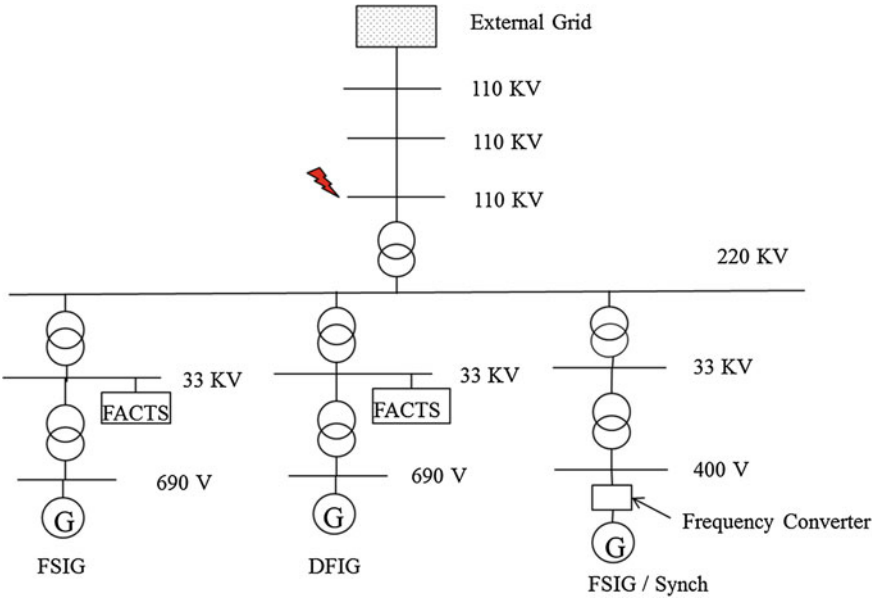

Fig. 5 Case study for comparative fault study

7 Wind Integration Dynamic Fault Studies

7.1 Model Order Impact on Fault Current or Voltage

The model-related difference in the machine short-circuit behavior is primarily caused by disregarding stator flux transients in the reduced third-order model. However, ignoring the term is only suitable for slow variations and control under limited conditions. It is concluded that the third-order model should not be used for effective fault analysis. The results of the test cases show that the crowbar protection settings also have significant influence on the DFIG short-circuit model. The short-circuit model is useful for grid operator to determine whether it meets the requirements of recently proposed grid codes. Wherever possible, fifth-order model should be used to conclude accurate fault current values. The concept has been discussed in this co-authored publication [12].

7.2 Time Step Impact on Fault Current or Voltage

The selection of ideal time step is also a very important factor. If the time step is too short it might result in some abrupt values within one cycle of the electrical frequency and peak current values obtained through such results may cause protective devices to underestimate the fault. This may result in inefficient

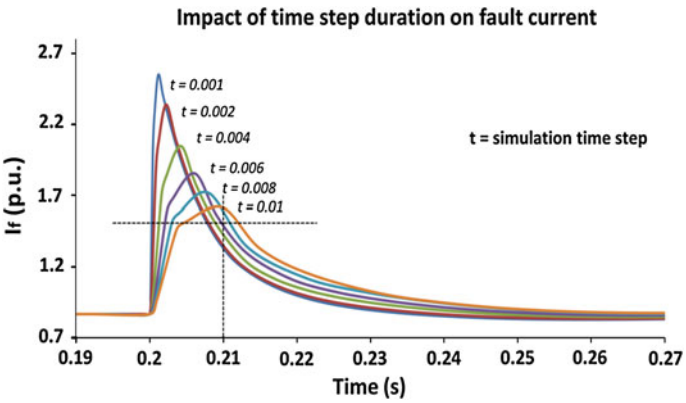

Fig. 6 Impact of time step duration on fault current

performance of the protective relays. In order to understand the impact of time step on fault current magnitudes for protection configuration, the Type-3 model as discussed above in this chapter was observed under similar network and fault condition scenario. The time step for this simulation was varied from 0.001–0.01 s in a manner illustrated in Fig. 6.

It could clearly be observed that the peak current is directly dependent on the time step duration.Protection relays and devices are configured based on these peak short-circuit currents obtained from simulation results. Thus, in order to assess the protection performance, reasonable time step duration should be selected to improve protection performance. For the above-mentioned case study, time step duration has been selected as $t = 0.01$ s. This is because of the fact that during 10 ms which is half of the electrical frequency cycle, it is rare that any protection device may detect the fault and fault current would eventually come down to a magnitude shown by crossed dotted lines.

The selection criteria for the time step would be determined by the specific control and protection application of the system. For instance, a system does not consider high magnitude but short-duration current spikes would be less concerned about choosing a shorter time step. Applications requiring/functioning based on high magnitudes even of shorter durations, must catch such peaks, thus requiring a time step to be as short as possible. For HV transmission protection, a shorter time step may be preferred and for a local distribution system a longer time step may be suitable because of its short calculation/simulation duration.

7.3 Crowbar Impact on Fault Current or Voltage

Besides the model order type time step duration, other controls within WTG or wind farm may have direct impacts on fault current calculations. A commonly

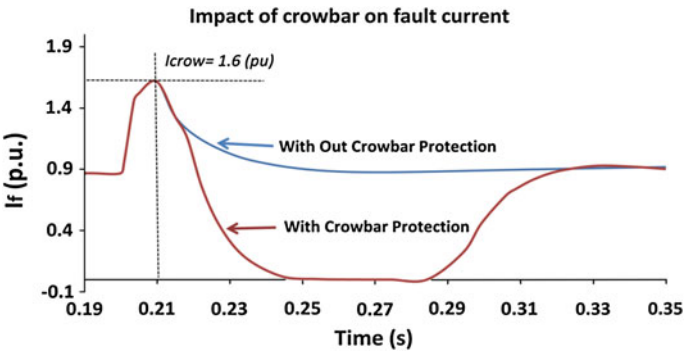

Fig. 7 Impact of crowbar duration on fault current

used and proposed technique is a bypass resistor known as crowbar resistor which is connected to rotor terminal to improve FRT capability for Type-3 which is discussed in several Refs. [13–17]. Bypass technique not only improves the FRT capability but also protects the rotor from being damaged. However, when the crowbar is connected, a Type-3 behaves more like a conventional induction generator, thus compromising the control performance [18, 19]. This technique has its own merits and demerits. While performing the analysis, it is important to identify all the internal controls and protection functions which could interact with your fault current calculations. To explain this phenomenon, Type-3 (DFIG)-based machines having similar network condition and parameters are discussed in Section 6.1 of chapter "Probabilistic Modeling and Statistical Characteristics of Aggregate Wind Power", where a specific scenario was simulated.

This scenario involves enabling and disabling the crowbar protection within the DFIG model. The crowbar protection was set to operate if the fault current exceeded 1.6 pu in magnitude. Both the fault current profiles for Type-3 machine have been recorded as reported in Fig. 7.

From Fig. 7, it is worth noticing that with crowbar protection the fault current significantly drops down to a negligible value in two electrical frequency cycles. In such cases, Type-3 machines may have severe impacts on protection relay operation during the fault. The details about protection performance in scenarios of 'with crowbar protection' and 'without crowbar protection' have further been explored in the following sections.

7.4 Comparative Fault Analysis for WTGs

In this case study, a three-phase fault on 110 kV busbar has been simulated as indicated in Fig. 5. The fault duration is 400 ms with zero impedance. The purpose of this dynamic fault study is to understand the behaviors of large wind farms with

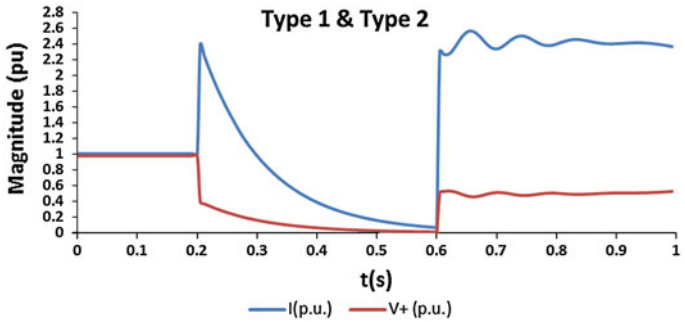

Fig. 8 Fault response of Types-1 and 2 (IG) wind farms

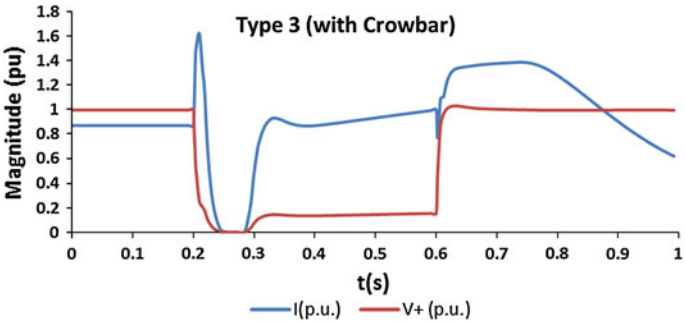

Fig. 9 Fault response of Type-3 WTG with crowbar

regard to the WTG technology used. Thus, the resultant fault current and voltage from each generator collector bus have been recorded. To understand the responses from each of the wind generator types, similar fault scenarios have been created for each WTG type, while the wind farm is connected to the same PCC. One type of wind farm is connected at a time. The purpose of developing scenarios of weak and independent connections is to investigate the future possibility of having only wind farms connected to PCC, because wind is a resource that is limited to specific parts of geographical regions. If a wind farm of some wind technology isconnected to a grid location then it is very unlikely to have conventional generation in the same region. The fault current contribution and positive sequence voltages have been recorded. The results are illustrated as shown in Figs. 8, 9, 10, and 11.

The normal operations of wind generator types have been well understood. These wind farms may not have a direct impact on each other in the case of normal operation. Their interaction in a case of abnormal operation such as a system fault or any frequency event remains unidentified unless that region faces a similar situation. As FRT criteria are in place it becomes important to investigate these wind farms for system security and voltage stability issues to overcome severe

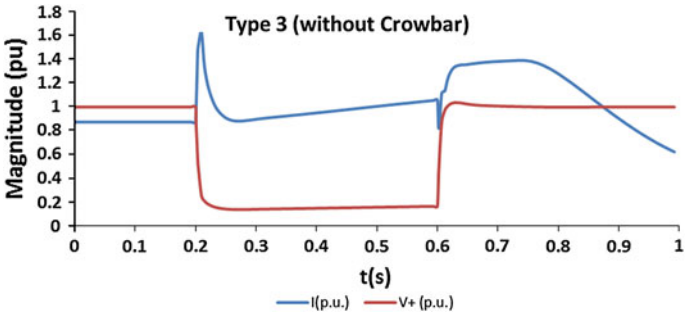

Fig. 10 Fault response of Type-3 WTG without crowbar

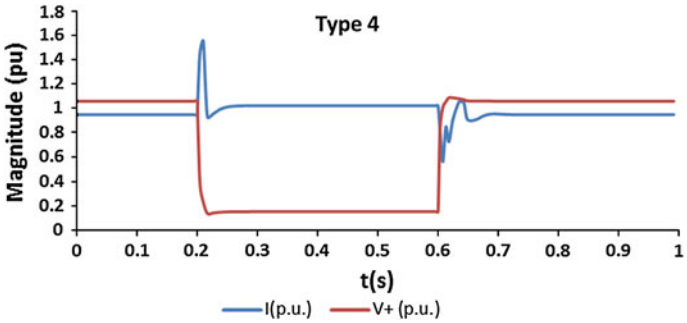

Fig. 11 Fault response of Type-4 WTG

situations through special protection schemes. Since wind farm interactions may also impact the fault response of any particular wind farm to the system, it is essential to understand a standard response of a generator connected independently to a grid. Based on the simulation results, Fig. 8 represents the pu current and voltage response of Types-1 and 2 WTGs. It is worth noticing that Type-1 and 2 are being treated the same due to the fact that rotor resistance is fixed during simulation. Figures 9 and 10 represent similar responses in pu (per-unit) for Type-3 with and without crowbar action, respectively. Figure 11 shows the response from Type-4 WTGs.

8 Significance of Results

Based on the results obtained from Figs. 8, 9, 10, and 11, the fault response of each generator type can be approximated as shown in Fig. 12.

Type-1 and 2 WTGs have been widely available technologies for large-scale wind units and they are normally modeled as a voltage source behind the locked

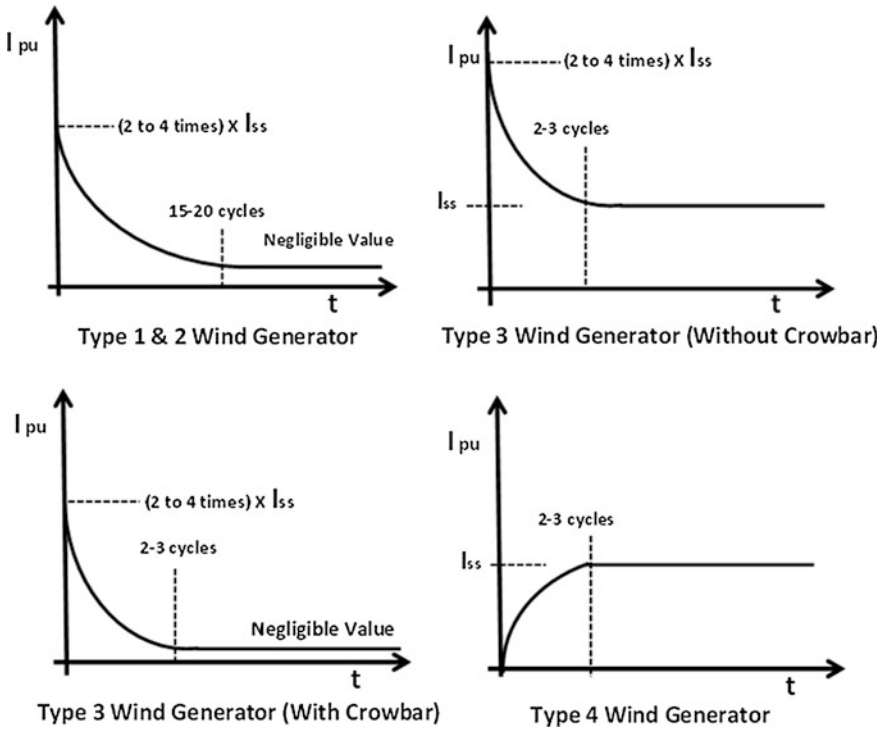

Fig. 12 Generalized fault current response of wind generators

rotor impedance. The response is not ideal as a 'short-circuit' current source. Typically, the induction generator contributes to the initial three-phases short-circuit current at generator terminals fault, supplying balanced short-circuit currents that normally are 2–4 times the generator rated current. This short-circuit current quickly decays, and typically may be neglected past a few hundred milliseconds (300–400 ms) after the short-circuit inception, depending on the size and design of the induction generator. However, Fig. 9 shows that the initial short-circuit current is close to 2.5 times the WTG rated current and decays quickly, similar to the typical induction response.

In terms of modeling aspects, Type-1, 2, and 3 WTGs initially behave as a voltage source. Their equivalent circuit can be represented as shown in Fig. 13a. However, after a very short time because of the presence of rotor and grid side converter control action, the response of Type-3 WTG differs from Types-1 and 2 and matches the response of Type-4 WTG which is a constant current source response. At that time, the equivalent circuit of Types-3 and 4 may be represented as shown in Fig. 13b.

Type-3 WTG transient response quickly decays from the initial short-circuit current of a magnitude of 2–4 times the rated current, as a typical squirrel cage

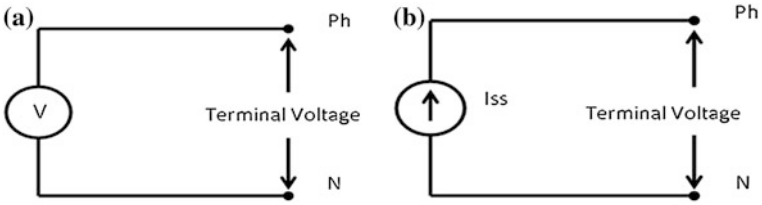

Fig. 13 **a** Equivalent circuit of Types-1, 2, and 3 immediately after fault, **b** equivalent circuit of Types-3 and 4 during the fault

machine, to the limited steady-state current value in the range of 1–1.5 times the generator rated current (I_{ss}). The decaying time is typically a few tens of milliseconds (40–60 ms). After a few cycles, these WTGs behave as an ideal current source that supplies continuously balanced constant current to the three-phase short-circuit [6]. WTGs equipped with DFIG type respond to the above model only if the generator rotor electronic converter is adequately sized or if the generator system is technically equipped to withstand the short-circuit current without any additional controls such as crowbar action or any special protection scheme in place to trip DFIG to guarantee electronic devices self-protection. However, this may not be true if the DFIG operation is altered by the introduction of crowbar or other control action. If crowbar is activated, Type-3 WTG response matches with Type-2 WTG but fault current decays even faster than Type-2 WTGs. By contrast, DFIG current response as shown in Fig. 12 shows that current reaches a much lower value than the rated value.

Figure 11 shows that Type-4 WTG current builds up to 1.6 times that of the steady-state current but it is worth noticing that it immediately goes back to steady-state value in less than one cycle. This is such a short duration for protection and control activation and so can be ignored here. Such a peak could be due to limitations in modeling full-scale frequency converter-based WTG. It can also be observed in Fig. 11 that fault current through FSFC reaches to a steady value very quickly. This response entirely depends on the converter capability and models being used for dynamic studies. Generally, in case of Type-4 WTG, the initial short-circuit current is around 25 % of the rated current and this builds up in 2–4 cycles to reach a rated value of constant current (I_{ss}) [6].

The next section onward focuses on finding possible issues with relay performance for the various protection types. The most commonly used protection type in case of large wind farms are distance, differential, and overcurrent schemes. These schemes have some minimum sensitivity requirements to detect the fault and operate relays. Most of the modern relays require a minimum current magnitude (I_{min}) to carry out these calculations and operate relay. If the current to the relay is lesser than its minimum required value, relay may not operate and fault could remain unattended.

As mentioned earlier, each WTG is connected to the grid with no conventional generation in the vicinity. In addition, the grid is separated by a long transmission

network, thus creating the situation of a weak grid. In such a case, there are two possible issues. If a wind unit does not supply enough fault current as expected, then relay might not operate. Let us examine each of the protection type and their possible issues for all four WTG types. It is worth repeating that the system is a radial one with a single wind farm feeds the fault. The argument revolves around a relay operation where the minimum required current known as pick up current (I_p) is being fed through WTG only.

8.1 Type-1 and 2 WTGsProtection Performance

Distance relays operate based on measured impedance value from relaying point to fault location. These impedances are calculated based on ratios of phase to ground voltages of each phase and phase currents. Initial fault current from Type-1 and 2 WTGs is much larger than the rated value so the minimum required or pickup current to operate distance protection is easily achieved; thus, distance relay connected to such wind farms may not have any issues in sensing the fault. However, the fault current decays to a much lower value in a period of a few cycles. This means distance relay for Zone 2 and Zone 3 protections may not adequately function.

Differential protection schemes are not used for all types of transmission levels, being used mostly for HV lines or some of the critical lines. In case of differential protection, Type-1 and 2 WTGs are capable enough to feed in sufficient current at the initial stages of the fault to get protection activated.

For overcurrent protection, Type-1 and 2 WTGs may easily supply enough fault current to get overcurrent relay activated and operated. However, the coordination may be the main concern. Normally, overcurrent protections are used as back-up protection, or if used as main protection, they are delayed to coordinate with differential and distance protection relays, resulting in overcurrent relay waiting for a few hundred milliseconds before the operation. During this waiting period, the fault current of Type-1 and 2 WTGs may have decayed to a much lower value, causing overcurrent protection to fail to operate.

With the presence of FACTS, typically used to improve voltage response, there exist more uncertainties estimating a fault current magnitude of the Types-1 and 2-based wind farms. FACTS devices have some advanced controls which may play a role in achieving fault current response from WTG feeder terminal.

8.2 Type-3 WTG Protection Performance

In the absence of crowbar action, distance protection is unlikely to face any issues with Type-3 WTG collective response as the initial current magnitude is large enough to get distance relays operated for Zone-1 protection. After a few cycles,

the current response quickly decays to a rated value, capable of achieving Zone 2 and Zone 3 protection activation. Differential protection may not have any problems depending on Type-3 WTG collective response. The initial current should be able to activate the differential protection scheme. However, an overcurrent protection scheme may face issues due to protection coordination delays and the decaying response of such WTGs.

As discussed earlier, this response may be altered through the insertion of a crowbar with the rotor circuit, intentional trips, or any other control/protection action within a WTG. The distance protection, differential protection, and even an overcurrent protection may have detection issues if the crowbar is activated. As shown in Fig. 12, the current response of Type-3 becomes negligible within few cycles as soon as the crowbar action takes place. Either crowbar action is to be delayed or other control strategies used to ensure reliable operation of protection devices. Some turbine manufacturers are employing advanced controls such as advanced grid options 2(AGO2) in VESTAS made turbines. Certain Type-3 WTG may also require FACTS devices having some impact on collective fault current response from collector feeder similar to Type-2 WTG-based wind farms.

8.3 Type-4 WTG Protection Performance

If protection schemes are solely dependent on collective current response of Type-4 WTG, in case of a weak grid situation, then protection operation is an important concern. The initial current response from standard Type-4 WTG is not significant. The fault current magnitude increases within a few tens of milliseconds (30–40 ms) reaching to a value of the rated current magnitude (I_{ss}). If such WTG is not supported through some additional advanced control features then distance, differential, and overcurrent protection schemes are most likely to have functional problems.

With the response shown in Fig. 11, Type-4 WTG may not be able to supply enough current for Zone-1 protection to operate. Differential protection may also have problems as the fault current may take some time to achieve its rated value, and overcurrent protection may hardly detect the faults because it is difficult to detect normal and abnormal current magnitudes, with the magnitude of fault current supplied by Type-4 WTG.

Nowadays, it is being claimed that modern Type-4 WTGs are far more capable than other wind technologies but these claims are still to be verified through testing and validation for certain fault situations other than simulation platforms. Significant advancement is not achieved in this direction as unsymmetrical and detailed models of Type-4 WTGs are still awaited to be available for research and study purpose.

Table 1 Summary of protection performance issues for WTG technologies

WTG technology	Protection schemes		
	Distance protection	Differential protection	Overcurrent protection
Types-1 and 2	May have sensing issues in Zone-2 and Zone-3	No known issues	May not have issues as main scheme but could have issues as backup scheme
Type-3	No known issues	May have issues while crowbar protection is activated	May have issues while crowbar protection is activated
Type-4	May have detection issues for Zone-1 at higher voltages	May have detection issues at higher voltages	May have detection issues for smaller clearance time

8.4 Summary of WTG Protection Performance

On basis of the above results, the protection performance of three main schemes against four different WTG technology types has been summarized as shown in Table 1.

9 Summary

This chapter reviews the existing literature related to wind farm protection and identifies important aspects worth considering for the design of protection for the various WTG types. It discussed the interconnection of wind units to the grid through multiple hierarchies and identifies possible areas where protection system or relays could be installed. Later, in this chapter a case study involving Type-1–Type-4 type WTGs is carried out, recording the fault current data for each type during a similar fault condition. Results obtained from the mentioned case study, developed in DIgSILENT® PowerFactory, have been utilized to analyze the fault behavior of four common WTG types. WTG type equivalent short-circuit models are presented to form the basis of comparative fault behavior study. The responses have been then generalized to an extent and compared to analyze their impacts on protection operation and performance under a weak grid interconnection. Distance, differential, and overcurrent protection operation and performance have been assessed for each WTG type. The chapter further identifies impacts on fault current because of three major aspects of modeling. These aspects include mechanical model order type, time step, crowbar protection, and additional controls. All these aspects have significant impact to achieve the correct current magnitudes for protection relay configuration. Practical challenges and implementation issues identified can be addressed by improving cooperation among wind generators, transmission system operators, and researchers.

Appendix A:

Table A.1 Parameters for FSIG and DFIG generators

Parameter	Representation	Value
Rated voltage	V	0.69 kV
Rated power	Pm	2 × 20 MW
Rated power factor	pf	0.8799
Efficiency	η	98 %
Nominal frequency	fm	50 Hz
Nominal speed	Nm	1,485 rpm
No. of pole pairs	N	2
Stator resistance	Rs	0.00889 pu
Stator reactance	Xs	0.1
Rotor resistance	Rr	0.1022388 pu
Rotor reactance	Xr	0.1017394 pu
Magnetizing reactance	Xm	3.1198 pu
SVC rating	Q	23 Mvar

Table A.2 Parameters for DFIG converter

Parameter	Representation	Value
d-Axis current gain	Kd	0.05
d-Axis time constant	Td	0.013
q-Axis current Gain	Kq	0.05
q-Axis time constant	Tq	0.013
Max rotor current for crowbar	MaxIr	1.3 pu
Crowbar bypass time	Tbypass	0.06 s
Additional rotor crowbar resistance	Ra'	0.1 pu

Table A.3 Parameters for FSFC

Parameter	Representation	Value
Rated AC voltage	Vac	0.4 kV
Rated DC voltage	Vdc	1 kV
Rated power	Pm	40 MVA
Short-circuit impedance	Zsc	10 %
Copper loss	Pc	120 kW
AC voltage set point	Set Vac	1.05 pu
DC voltage set point	Set Vdc	1.00 pu
Chopper rating	Ich	40,000 A
Reactive power limits	±Q	±0.4 pu

Table A.4 Parameters for synchronous

Parameter	Representation	Value
Rated voltage	V	33 kV
Rated power	Pm	40 MW
Power factor	Pf	0.8
Bus type	Type	PV
Reactive power rating	Qm	20 Mvar
Bus voltage	Vb	1.05 pu
Nominal frequency	fm	50 Hz
d-Axis syn. reactance	Xd	2 pu
q-Axis syn. reactance	Xq	2 pu
Transient reactance	Xd'	0.3 pu
d-Axis subtransient reactance	Xd''	0.2 pu
q-Axis subtransient reactance	Xq''	0.2 pu
Leakage reactance	Xl	0.1 pu
Acceleration time constant	Ta	10 s

Table A.5 Network parameters

Parameter	Representation	Value
Maximum short-circuit power	Sk' max	9,999 MVA
Minimum short-circuit power	Sk'' min	150 MVA
Reactance to resistance ratio	X/R	10
Resistance ratio	R0/R1	0.1
Reactance ratio	X0/X1	1
Impedance ratio	Z2/Z1	1
Acceleration time constant	Ta	9,999 s

References

1. Tsili M, Papathanassiou S (2009) A review of grid code technical requirements for wind farms. IET Renew Pow Gen 3(3):308–332
2. Wind Generation Investigation Project (WGIP) (2005) [cited 2013 23 January]; Available from: http://www.ea.govt.nz/our-work/programmes/pso-cq/wgip/
3. Girgis A, Brahma S (2001) Effect of distributed generation on protective device coordination in distribution system. In Large Engineering Systems Conference on Power Engineering
4. Kawady T et al (2008) Dynamic modeling of Al-Zaafarana wind farm for protection applications. In 12th International Middle-East Power System Conference
5. kawady TA, Mansour N, Taalab A (2008) Performance evaluation of conventional protection systems for wind farms. in IEEE Power and Energy Society General Meeting
6. Achleitner G et al (2007) Overall protection in decentralized wind power plants and decentralized grids. In Clean Electrical Power, ICCEP '07. International Conference on. 2007
7. Comech MP, Montanes MA, Garcia MG (2008) Overcurrent protection behavior before wind farm contribution. In the 14th IEEE Mediterranean Electrotechnical Conference
8. Tianwen Y, Niansheng X, Rongxing J (2009) The Over-voltage protection Of wind turbine generators. In World Non-Grid-Connected Wind Power and Energy Conference, 2009. WNWEC 2009

9. Musunuri S (2009) Protection requirements for a large scale wind park. in Power Systems Conference, PSC '09. 2009
10. Hunt R et al (2010) Wind Farm Protection Using an IEC 61850 Process Bus Architecture, In DistribuTech Conference & Exposition
11. Cardenas J et al (2010) Wind farm protection using an IEC 61850 process bus architecture. In 10th IET International Conference on Developments in Power System Protection
12. Zhao S, Qureshi WA, Nair NK-C (2011) Influence of DFIG Models on Fault Current Calculation and Protection Coordination. in IEEE PES General Meeting 2011, Detroit, USA
13. Bing X, Fox B, Flynn D (2004) Study of fault ride-through for DFIG based wind turbines. In Proceedings of the 2004 IEEE International Conference on Electric Utility Deregulation, Restructuring and Power Technologies
14. Morren J, de Haan SWH (2005) Ridethrough of wind turbines with doubly-fed induction generator during a voltage dip. IEEE Transactions on Energy Conversion 20(2):435–441
15. Jayanti NG et al (2006) Optimising the rating of the UPQC for applying to the fault ride through enhancement of wind generation. In Proceedings of the 41st International Universities Power Engineering Conference
16. Seman S, Niiranen J, Arkkio A (2006) Ride-through analysis of doubly fed induction wind-power generator under unsymmetrical network disturbance. IEEE T Power Syst 21(4):1782–1789
17. Hansen AD, Michalke G (2007) Fault ride-through capability of DFIG wind turbines. Renew Energ 32(9):1594–1610
18. Dittrich A, Stoev A (2005) Comparison of fault ride-through strategies for wind turbines with DFIM generators. In European Conference on Power Electronics and Applications
19. Erlich I, Winter W, Dittrich A (2006) Advanced grid requirements for the integration of wind turbines into the German transmission system. In IEEE Power Engineering Society General Meeting

Wind Power Plants and FACTS Devices' Influence on the Performance of Distance Relays

L. A. Trujillo Guajardo and A. Conde Enríquez

Abstract The continuous growth in power demand in the electric power system allowed the development of various power electronics-based schemes for compensation and optimization of transmission systems. The converter-based systems like wind power plants (doubly fed induction generator or DFIG scheme), flexible AC transmission systems (FACTS) devices such as static synchronous compensator (STATCOM), unified power flow controller (UPFC), and series compensator are power electronics-based equipment, so the inclusion of the converter-based systems in the power transmission system generates frequency components that affects the performance of the distance relays, the relays have constant pickup values which will be exposed to these new power system conditions causing fault detection problems. The modern power converters generate a wide spectral band of frequency components which compromise the quality of the energy delivered, which affects the operation of the electric power grid, power consumers, and relay protection systems. Relay operation should be established using only the fundamental signal components at the nominal frequency because these are proportionately affected by the fault location. The main purpose of the conventional digital filters in distance relays is to estimate the fundamental frequency phasor of the electric input signals required by the relay, but when frequency components as interharmonics or subharmonics exist in the voltage and current signals, the conventional digital filters as Cosine or Fourier will cause an error in the fundamental frequency phasors estimate, and by consequence an error in the estimate of apparent impedance, this will compromise the performance of the distance relay causing underreach or overreach (fault detection problems). This book chapter is intended to present the effect and compensation of nonfiltered frequency components, such as interharmonics

L. A. Trujillo Guajardo (✉) · A. Conde Enríquez
Facultad de Ingeniería Mecánica y Eléctrica, Universidad Autónoma de Nuevo León (UANL), Av. Universidad S/N Ciudad Universitaria 66451,
San Nicolás de los Garza, NL, Mexico
e-mail: luistrujillo84@gmail.com

A. Conde Enríquez
e-mail: con_de@yahoo.com

J. Hossain and A. Mahmud (eds.), *Large Scale Renewable Power Generation*,
Green Energy and Technology, DOI: 10.1007/978-981-4585-30-9_13,

and subharmonics in the performance of conventional distance relays. Prony method is implemented as a filtering technique as a solution of the apparent impedance measurement error due to nonfiltered frequency components; simulated cases and real fault events are evaluated to validate the proposed distance relay algorithm.

Keywords Wind power plant · STATCOM · UPFC · Series compensation · Distance relay · Prony

1 Introduction

Converter-based systems like wind power plants DFIG schemes (doubly fed induction generator) which are the most common wind turbine schemes use a wound rotor induction generator which is controlled by a back-to-back power converter. The stator of a doubly fed induction generator (DFIG) is connected to the grid directly, while the rotor of the generator is connected to the grid by electronic converters through slip rings. Self-commutated converter systems, such as IGBT-based switching converters, are normally used for this type of system. The DFIG normally uses a back-to-back converter, which consists of two bidirectional converters sharing a common dc link, one connected to the rotor and the other one to the grid [1, 2]. Another converter-based system known as flexible AC transmission systems (FACTS) devices, such as static synchronous compensator (STATCOM) which is used for parallel compensating of reactive power and, its inductive or capacitive current can be controlled independent of system AC voltage using a voltage source converter (48 pulse VSC), a coupling transformer, and controls [3]. The STATCOM injects a reactive current into the system to correct the voltage sag and swell [3]. The unified power flow controller (UPFC) is the most versatile and complex of the FACTS devices. UPFC which consists of a series and a shunt converter connected by a common DC link capacitor can simultaneously perform the function of transmission line real/reactive power flow control in addition to UPFC bus voltage/shunt reactive power control. The shunt converter of the UPFC controls the UPFC bus voltage/shunt reactive power and the DC link capacitor voltage. The series converter of the UPFC controls the transmission line real/reactive power flows by injecting a series voltage of adjustable magnitude and phase angle. The interaction between the series injected voltage and the transmission line current leads to real and reactive power exchange between the series converter and the power system [3]. The fixed series compensator (FSC) reduces the electric distance of a transmission line allowing an increment in the power transfer capability, it comprises capacitors banks and parallel metal oxide varistors (MOVs), triggered spark-gap, and a bypass switch (Circuit Breaker). The MOVs protect the capacitors bank from overvoltages during and after transmission system failures. The triggered spark-gap protects the MOVs

against excessive energy absorption and the bypass switch (Circuit Breaker), in turn, protects the triggered spark-gap. Three high-voltage disconnecting switches serve to integrate the FSC into and isolate it from the transmission line [4]. The devices described are power electronics-based equipment, where its operating characteristics interacting with the power system during a fault condition could lead in a power quality issue in the voltage and current signals causing a mal-operation of a distance relay, so the inclusion of the converter-based systems in the power transmission system generate frequency components as interharmonics and subharmonics [5–11]. The quality of the voltage and current signals are now a significant problem for the electric power system which affects the operation of the electric power grid, power consumers, and manufacturers of electric-electronic equipment. The main problem in the quality of current and voltage signals is caused by the inclusion of equipment that its operation is based on power electronics; this is the main reason why certain requirements are necessary for a good quality of the energy in the electric power system.

The input voltage and current signals required by the distance relay are expected to be purely sine with an assigned amplitude and frequency. The modern power converters generate a wide spectral band of frequency components which compromise the quality of the energy delivered, and by consequence there's an increment in the power losses and the reliability of the electric power system is reduced [9].

In some cases, the large-scale power converter schemes generate in addition to the typical operational harmonics of an ideal power converter, noncharacteristic frequency components as interharmonics and subharmonics will greatly deteriorate the power quality of the voltage and current signals [9–11].

The estimation of the frequency components is very important in the power system protection schemes, that is why the characterization of these frequency components allows to compensate measurement errors in the electric protection system, such as distance relay. The frequency components as interharmonics and subharmonics could not be rejected by the distance relay digital filters (Cosine or Fourier filter) [12–15]. The main purpose of the conventional digital filters in distance relays is to estimate the fundamental frequency phasor of the electric input signals required by the relay, but when frequency components as interharmonics or subharmonics exist in the voltage and current signals, the conventional digital filters as Cosine or Fourier will cause an error in the fundamental frequency phasors estimate [13], and by consequence an error in the estimate of apparent impedance; this will compromise the performance of the distance relay causing underreach or overreach (fault detection problems) [16–19].

The Prony method is a good alternative to obtain the correct apparent impedance measurement by estimating the fundamental frequency voltage and current phasors [20].

The main contribution of this chapter is the implementation of Prony method as a filtering technique in distance relay algorithms; hence, an apparent impedance measurement error due to nonfiltered frequency components (generated by the interconnection of wind power plants and FACTS devices in the power grid) when

conventional digital filters (Fourier or Cosine) are used is compensated. The solution is presented and is validated using simulated and real fault events.

The organization of the chapter is as follows: in Sect. 2 the model of conventional distance relay and the effect of nonfiltered frequency components is presented; in Sect. 3 the fundamental frequency phasor estimation error is characterized due to the impact of converter-based systems in the performance of distance relays. In Sect. 4 a proposed distance relay algorithm using Prony method as filtering technique is presented as a solution of the error in the fundamental frequency phasor estimation in conventional distance relays due to nonfiltered frequency components in the voltage and current input signals. Then in Sect. 5 an evaluation of the proposed algorithm is performed using simulated and real fault events. Finally Sect. 6 closes the chapter with the main conclusions of this work.

2 Distance Relay Modeling

The distance relay operation is based on the amplitude or phase comparison of two input signals, operation and polarization, to determine the trip condition.

The distance relay models could have an amplitude or phase comparator that responds to the magnitude or phase angle displacement between input signals [12]. The input signals of an amplitude or phase comparator are obtained using the electric signals measured by the instrument transformers and design constants. The model of the distance relay is shown in (1).

$$\begin{aligned} S_O \text{ or } S_1 &= k_1\angle\alpha_1 \cdot V_r\angle 0^{\circ} + Z_{R1}\angle\theta_1 \cdot I_r\angle - \varphi_r \\ S_R \text{ or } S_2 &= k_2\angle\alpha_2 \cdot V_r\angle 0^{\circ} + Z_{R2}\angle\theta_2 \cdot I_r\angle - \varphi_r \end{aligned} \tag{1}$$

where S_1 and S_2 are the input signals to establish the trip signal; $\bar{k}_1$ and $\bar{k}_2$ are the constants for the design; $\bar{Z}_{R1}$ is the replica impedance of the protected transmission line; and $\bar{Z}_{R2}$ is the impedance multiplied by the current, resulting in a polarization voltage; $\bar{I}_r$ and $\bar{V}_r$ are the electric input signals which are estimated by the phasor estimation technique (Fourier filter or Cosine filter) to obtain the fundamental frequency phasor [13].

In Fig. 1 the amplitude and phase comparator for distance relays are shown. The amplitude comparator performs a comparison of the operation $|\overline{S}_O|$ and restriction $|\overline{S}_R|$ signals. When the following criteria $|\overline{S}_O| > |\overline{S}_R|$ are established, the relay will send a trip signal. The phase comparator has a similar operation but it needs the phase angle displacement of the operation $\bar{S}_1$ and polarization $\bar{S}_2$ signals to perform a comparison $\left(\beta = \arg\left(\overline{S}_1/\overline{S}_2\right)\right)$. When β is within the limits of β_1 and β_2 ($-\beta_1 < \beta < \beta_2$), the relay will send a trip signal.

The phase relays are required for the detection of phase-to-phase faults; an important aspect in the distance relay design is that the correct values of $\bar{I}_r$ and $\bar{V}_r$

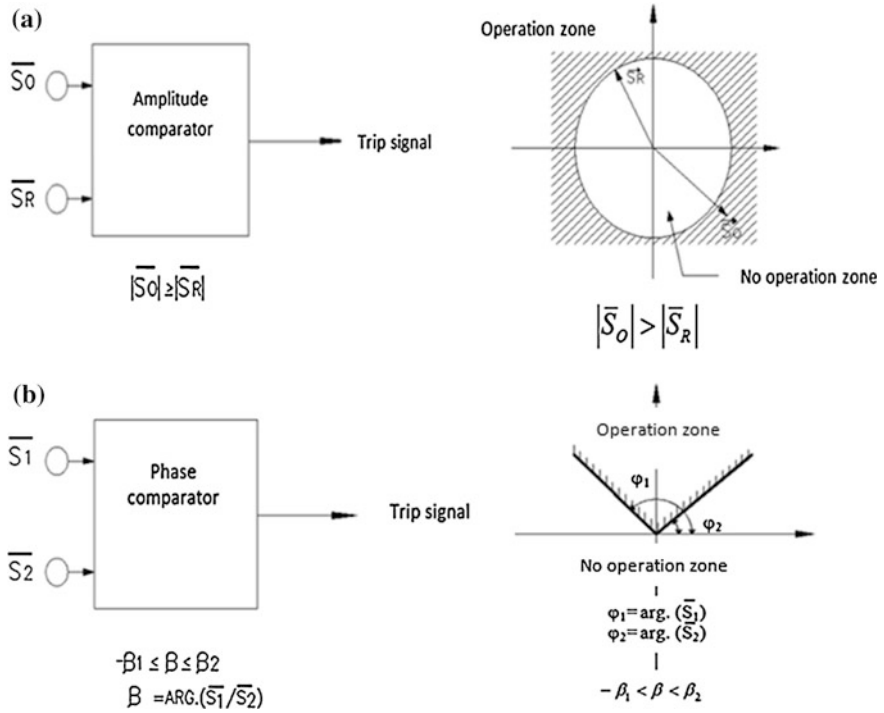

Fig. 1 Distance relay signal comparators. **a** Amplitude comparator. **b** Phase comparator

Table 1 Electric input signals for distance relay unit

Unit Phase	Voltage (V_r)	Current (I_r)
(AB)	$V_{an}-V_{bn}$	I_a-I_b
(BC)	$V_{bn}-V_{cn}$	I_b-I_c
(CA)	$V_{cn}-V_{an}$	I_c-I_a

have to be selected. In Table 1 the electric input signals that correspond to phase distance relay units are presented.

In Fig. 2 the Mho operation characteristic is presented in a tridimensional space of the impedance plane through time, the time is represented by the one cycle window length displacement. The estimated fundamental phasors of voltage and current are used for the relay (phase relay unit). The typical sampling time used in input signals V_r and I_r is 16–32 samples per cycle [13, 21]; then these signals are used (see Table 1) to form the operation characteristic and the phase comparator scheme; in this study the Mho characteristic is evaluated.

It is necessary to incorporate two stages of filtering to eliminate the unwanted frequency components as noise, harmonics, and DC component as these frequency

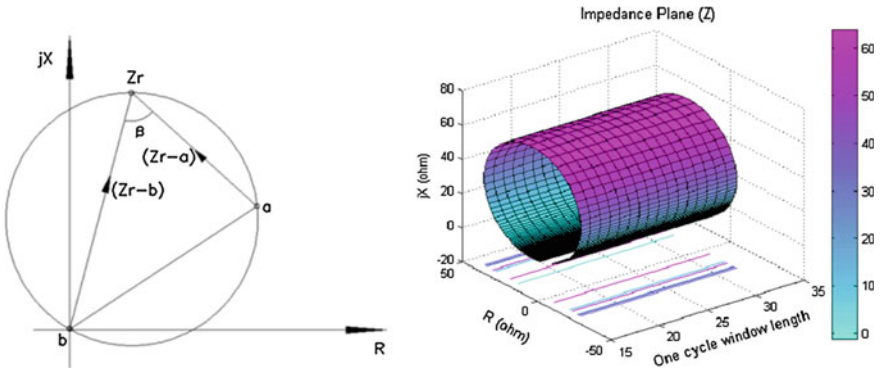

Fig. 2 Mho operation characteristic (fundamental frequency)

Fig. 3 Distance relay structure for input signals processing

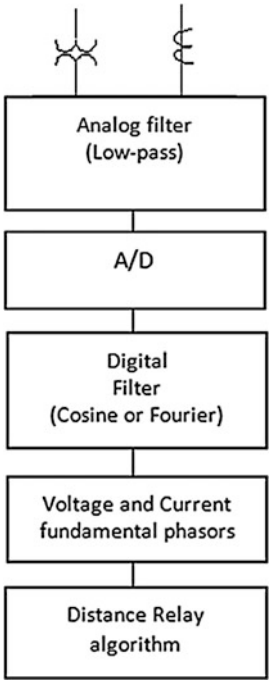

components are considered as a source of error that could affect the selectivity of the relay (see Fig. 3).

There are two filter stages, analog and digital, that are intended to reduce the operation time in fault detection. Generally, the analog filter used is a Butterworth filter of second or fourth order with a cut-off frequency of 360 Hz (see Fig. 4); this filter is preferred because it has flat response in passband and decreasing monotonic in stopband [22].

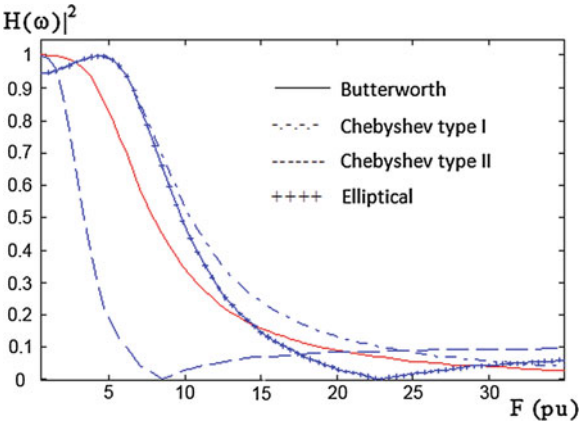

Fig. 4 Frequency response of analog filters

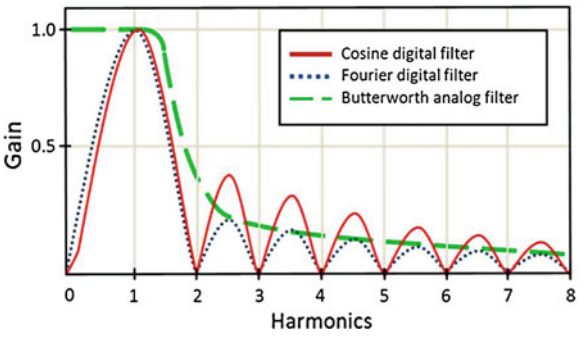

Fig. 5 Analog and digital filter frequency response used in distance relays

After the analog filter stage, there is the process of digitalization of the analog signal; the increment in the sampling frequency allows a substantial increment in the signal resolution, but the microprocessor burden is increased. The "aliasing" effect reduction is obtained by tuning between analog and digital filter allowing an overlap of the filter frequencies. It is possible to remove analog filter by an oversampling of the signal.

The digital filtering is performed with *Finite Impulse Response* (FIR) filters, because there is no recursion, i.e., the output depends only from the input and not from past values of the output. The memory of the previous conditions of the signal does not have a benefit in obtaining the fault condition by the distance relay. Also, the *Infinite Impulse Response* (IIR) filter produce in general a phase angle distortion, opposite to FIR filters. This condition allows that their frequency response has natural zeros in the harmonic frequencies allowing a rejection of these frequency components (see Fig. 5).

The distance relay algorithms used for the fundamental frequency component estimation of voltage and current signals so apparent impedance estimation could be obtained use the Fourier or Cosine filter (see Fig. 6). In studies performed for

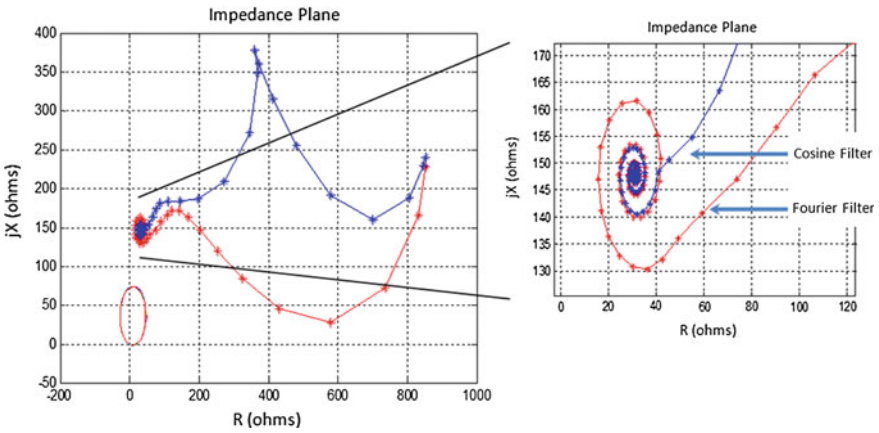

Fig. 6 Impedance trajectory comparison using Cosine and Fourier filter

the evaluation of digital filters [23] for the estimation of the fundamental component, the Cosine filter presented good results in the rejection of the DC component during the fault period as it can be seen in Fig. 6 [23].

The distance relay model is based on the fundamental frequency phasor, but due to the digital filters used in distance relays errors in the fundamental frequency phasor estimate are present due to the existence of interharmonics and/or subharmonics in the voltage and current signals during the fault period (see Fig. 7). When these frequency components are present, the digital filter generates an error in the fundamental frequency phasors estimates of voltage and current. The distance relay model needs an estimate of the fundamental frequency phasors of voltage and current during the fault period, so an estimate of the apparent impedance can be calculated by the relay, but with the increment of power electronics equipment or series compensation used to have a more dependable transmission system. This type of equipment generates frequency components that the common digital filters as Fourier and Cosine cannot reject.

Due to the fact that distance relay algorithms that use Fourier and Cosine filters generate an error in the fundamental frequency phasors estimation of voltage and current signals, a characterization of the problem using the distance relay model in (1) is represented in (2) as follows:

$$S_1 = k_1\angle\alpha_1\left[V_{h1}e^{j\theta_{Vh1}} + \overbrace{\sum V_i e^{j\theta_{Vi}} + \sum V_s e^{j\theta_{Vs}}}^{\text{Error in estimation}}\right] + Z_{R1}\angle\theta_1\left[I_{h1}e^{j\theta_{Ih1}} + \overbrace{\sum I_i e^{j\theta_{Ii}} + \sum I_s e^{j\theta_{Is}}}^{\text{Error in estimation}}\right] \quad (2)$$

$$S_1 = k_1\angle\alpha_1\left[V_{h1}e^{j\theta_{Vh1}} + \sum V_i e^{j\theta_{Vi}} + \sum V_s e^{j\theta_{Vs}}\right] + Z_{R1}\angle\theta_1\left[I_{h1}e^{j\theta_{Ih1}} + \sum I_i e^{j\theta_{Ii}} + \sum I_s e^{j\theta_{Is}}\right]$$

where $h1$ = fundamental frequency; i = interharmonics, $i > 1$; and s = subharmonics, $s < 1$. The graphical representation of the error in the estimate is presented in Fig. 8. When these kind of frequency components are present in the voltage and

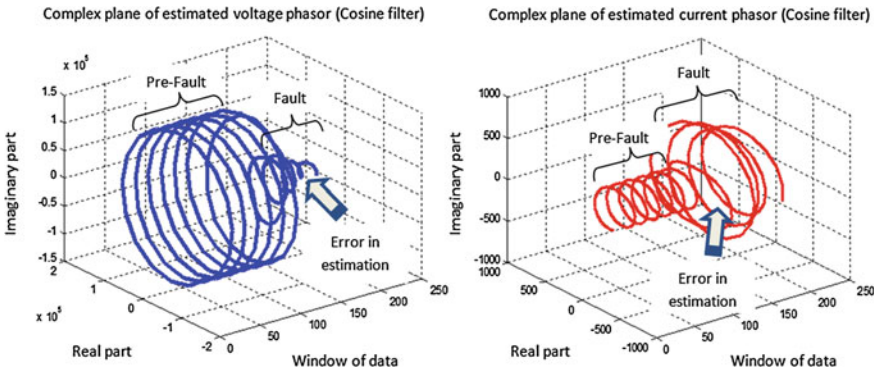

Fig. 7 Estimated fundamental frequency phasors of voltage and current using Cosine filter when interharmonics and subharmonics are present in the voltage and current signals during fault period

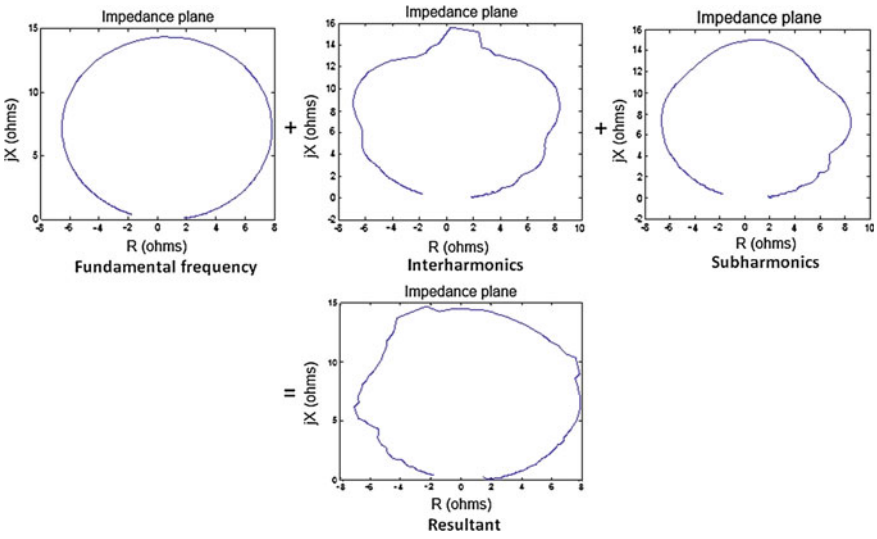

Fig. 8 Graphical representation of the error in apparent impedance estimation using digital filters

current signals, an error in the fundamental frequency phasors of voltage and current will cause an error in the operation characteristic. The operation characteristic is formed by the comparison signals in (1), which at the same time requires the voltage and current phasors and from (2) the resultant operation characteristic is formed (see Fig. 8).

The operation scheme for a distance relay is described as follows:

(1) Define the operational characteristic and select the design constants and the settings of the distance relay. This process is made offline and is defined by the manufacturer of the relay.
(2) The electric input signals measured online from the instrument transformers (voltage and current) are used to estimate the fundamental phasor component.
(3) With the fundamental phasor component estimated, the comparison signals are formed and the trip condition is evaluated.
(4) The trip condition criterion is then performed to generate a trip signal.

3 Impact of Converter-Based Systems in the Performance of Distance Relay

This section describes the model of the DFIG scheme, STATCOM, UPFC, and Series Compensation in the power grid for protection systems analysis.

3.1 Wind Power Plant (DFIG Scheme)

In this particular case, a proposed model of a DFIG scheme is presented to perform the protection system analysis. The control loops and elements that show slow response times in the DFIG scheme when compared with the distance relay response times are considered as constants. This is due to the fact that in a fault condition in the power grid, these elements will not impact on the distance relay operation.

In accordance with the time response of each block of DFIG detailed model scheme [5, 6], a reduction of the system has been made according to the considerations recommended in [24]. In the pitch angle controller, the time response of a change in speed to compensate for the wind speed up or speed down to optimize the turbine speed is in the range of 1–3 Hz (20 cycles of fundamental frequency) due to the size and weight of the blades, so the pitch angle is considered as a constant. In the rotor speed controller, the time response of a change in wind speed is in the range of 20 Hz. It should be mentioned that a change in wind speed causes a change of rotor speed and during a grid fault the rotor speed controller will not respond. Therefore, the time response of the speed control is not considered due to the time of fault detection of distance relays is 1–2 cycles.

The voltage terminal controller in DFIG detailed model represents the reactive power capacity of the wind power plant during a voltage dip or an external fault in the power system, although not every wind power plant has this configuration. For example, in Germany and Spain their grid codes for interconnecting wind power

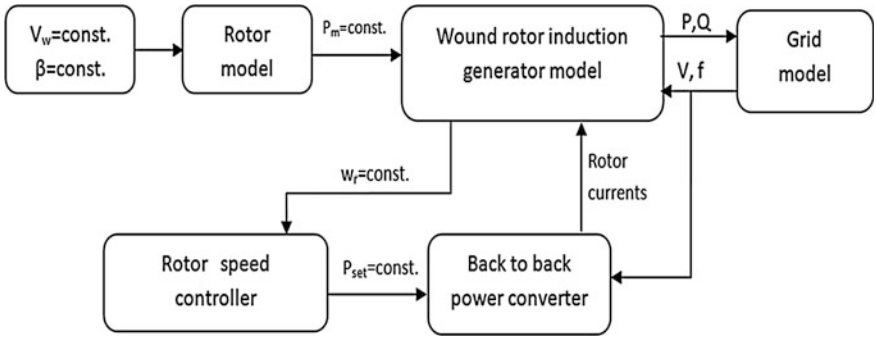

Fig. 9 Proposed model structure of DFIG scheme for analysis of operation of distance relays

plants to the power system specify that the wind power plants should have reactive power compensation of 100 % of capacity of the wind power plant during an external fault in the power system [25]. It should be mentioned that during an external fault, the time response of the reactive power compensation control is about 15 cycles [26], and the reactive power compensation will not affect the operation of the distance relay due to the slow time response when it is compared to the distance relay response to the fault.

In Fig. 9 the proposed model scheme for the DFIG for protection system analysis is presented. The pitch angle β; the wind speed *Vw*; the mechanical power generated by the wind *Pm*; and the active and reactive power references required by the power converter *Pset* and *Qset* are considered constants. This is due to the dynamic responses of these variables being too slow in comparison with the response time of the distance relays.

3.2 Test System

In this section, a test system is shown in Fig. 10 to evaluate the distance relay operation using Matlab/Simulink. The system consists of a wind power plant with DFIG discrete model scheme represented as a single equivalent turbine interconnected to a 60 Hz power system, with a two phase fault applied at 80 % in the transmission line [27]. The response of the wind power plant during an external fault is evaluated in the impedance plane by the measurement of voltage and current signals in the bus B of the test system. By using these signals as the input signals in the distance relay algorithm, the apparent impedance measurement can be evaluated.

The system parameters of the test system for the evaluation of the detailed and proposed model are shown in Table 2.

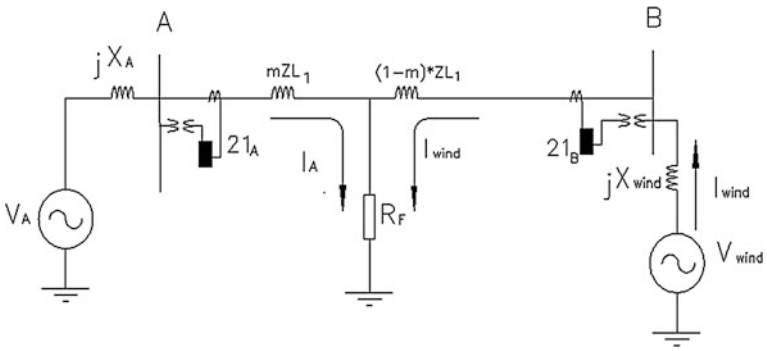

Fig. 10 One-line diagram of the test system

Table 2 System parameters

Test system parameters	Values
Source A reactance	jXA = 35 Ω
Source wind power plant reactance	jXwind = 6*27.54 Ω
Active power generation of wind power plant	Pwind = 9 MW
Transmission system voltage level	V = 120 kV
Line impedance Z_{L1}	Z_{L1} = 82.4/_73.7° Ω
Fault resistance	Rf = 2 Ω
Wind speed	Vw = 15 m/s

3.2.1 Measured Signals

The voltage and current signals measured at bus B of the test system are shown in Fig. 11. For the wind power plant proposed model, the sampling rate of the signals is 32 samples per cycle. A two phase to ground fault is applied in the transmission line at 0.03 s over a duration of 100 ms. The two phase to ground fault is analyzed due to the fact that is nonsymmetrical and has a major impact on the response of the power converter [1, 5, 6].

The frequency spectrum of the voltage and current signals is calculated during the fault period. The frequency components detected during the fault are shown in Tables 3 and 4 for the detailed and simplified model, respectively. It can be seen that low frequency components (subharmonics) and interharmonics have been detected. The frequency components are not filtered by the digital filters of the distance relays and this becomes an error in the apparent impedance measurement which leads a fault detection problem (underreach/overreach) [27]. The frequency spectra of the signals using the detailed and simplified model are shown in Fig. 12.

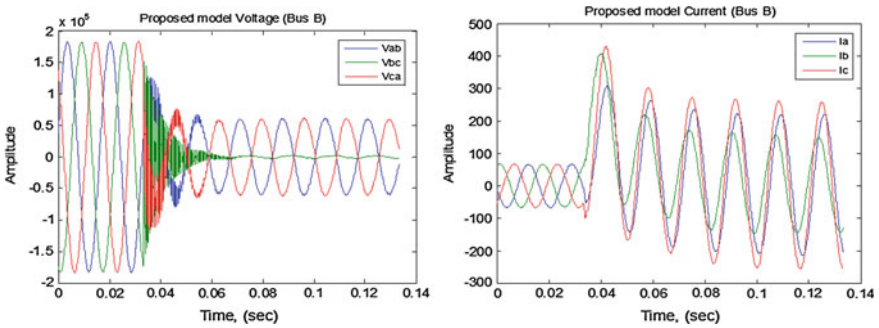

Fig. 11 Voltage and current signals of bus B for a two phase fault on the transmission line

Table 3 Dominant frequencies of voltage signal (detailed and simplified model)

Frequency (Hz)	Harmonic order	Detailed model amplitude	Simplified model amplitude
60.00	1.00	63,770.00	60,736.33
33.75	0.56	4,162.00	3,968.8
78.75	1.31	3,377.00	3,213.19
180.00	3.00	1,856.00	1,764.61

Table 4 Dominant frequencies of current signal (detailed and simplified model)

Frequency (Hz)	Harmonic order	Detailed model amplitude	Simplified model amplitude
60.00	1.00	264.9	251.28
0.00	0.00	31.24	28.75
33.75	0.56	15.17	15.44
78.75	1.31	16.00	14.23
180.00	3.00	3.64	2.46

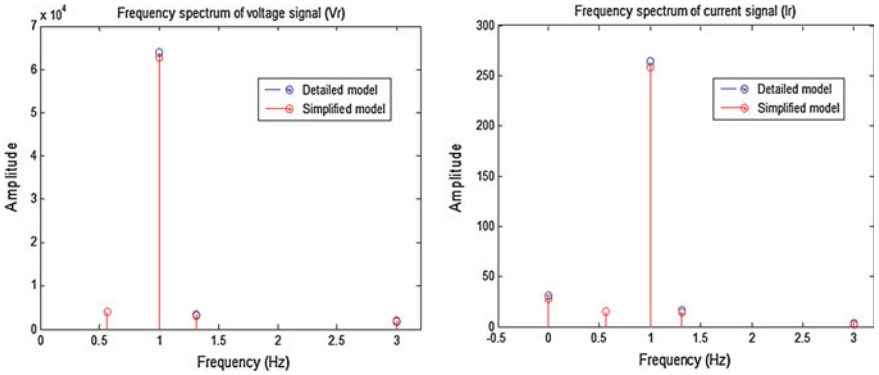

Fig. 12 Frequency spectrum of voltage (V_r) and current (I_r) signals at bus B

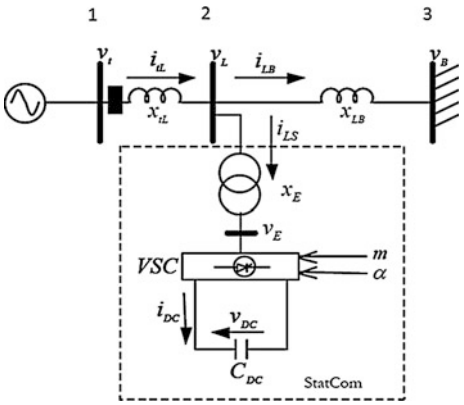

Fig. 13 Model of STATCOM in the power system

3.3 STATCOM

The STATCOM voltage magnitude control is based on pulse width modulation (PWM), where there are two control inputs: m is the modulation ratio and α is the voltage phase angle of the STATCOM. There is only reactive power exchange between the STATCOM and the power system that is being evaluated.

In Fig. 13 v_t is the terminal voltage at the generator, v_L is the voltage at system bus where the STATCOM is connected, v_B is the voltage at system infinite bus, $v_E = mkv_{\mathrm{DC}}\angle\alpha$ is the voltage at converter terminals, v_{DC} is the voltage at capacitor, and k is the ratio between AC and DC voltage depending on the converter structure of the STATCOM [3].

3.3.1 Test System

In this section, a test system using STATCOM discrete model as a compensator is shown in Fig. 14 to evaluate the distance relay operation. A simulation is performed using Matlab/Simulink applying a three phase fault at 0.25 s with duration of 150 ms and a fault resistance of 2 Ω at 80 % of the transmission line (L2_75 km), the voltage level is 500 kV, and a line impedance of 30.9/_84.8° Ω.

3.3.2 Measured Signals

The voltage (V_r) and current (I_r) signals for the phase distance unit evaluated (BC) at B2 bus are obtained from voltage and current signals in Fig. 15 and the sampling rate of the signals is 32 samples per cycle.

The frequency spectra of the signals are shown in Fig. 16. The frequency components detected during the fault are shown in Tables 5 and 6 for the voltage (V_r) and current (I_r) signals, it can be seen that low frequency components (subharmonics) have been detected.

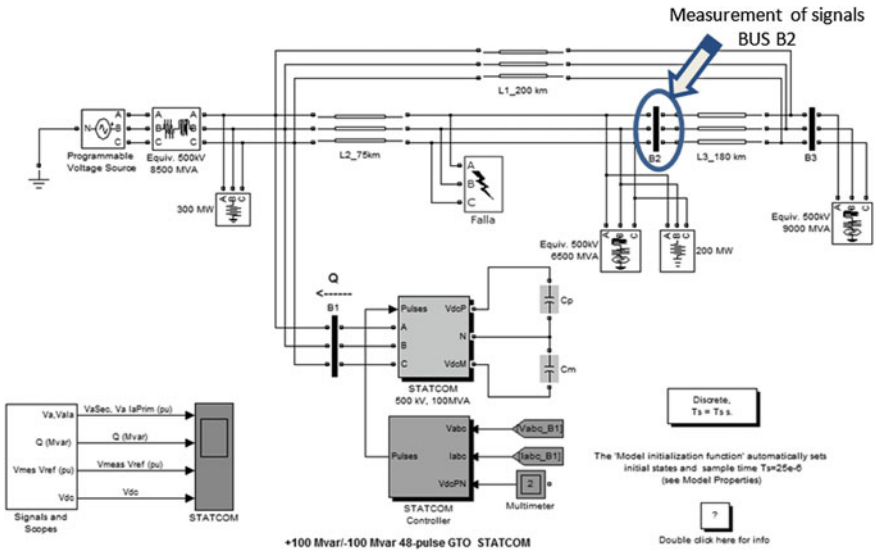

Fig. 14 Test system using STATCOM

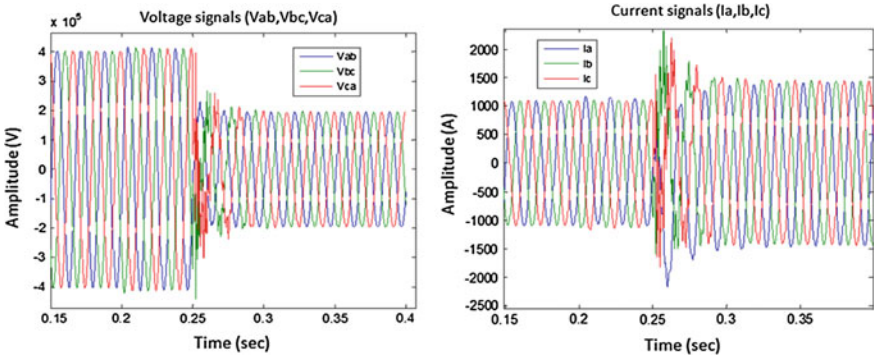

Fig. 15 Voltage and current signals of bus B2 for a three phase fault on the transmission line

3.4 UPFC

The basic principles of UPFC operation are already well established in the open literature [3, 28, 29]. Figure 17 shows a single line system configuration of a general UPFC. The UPFC is composed of two back-to-back self-commutated, voltage source converters (VSC) operated from a common dc link capacitor. The converters are coupled to the network via a shunt (exciting) and series (boosting) transformer.

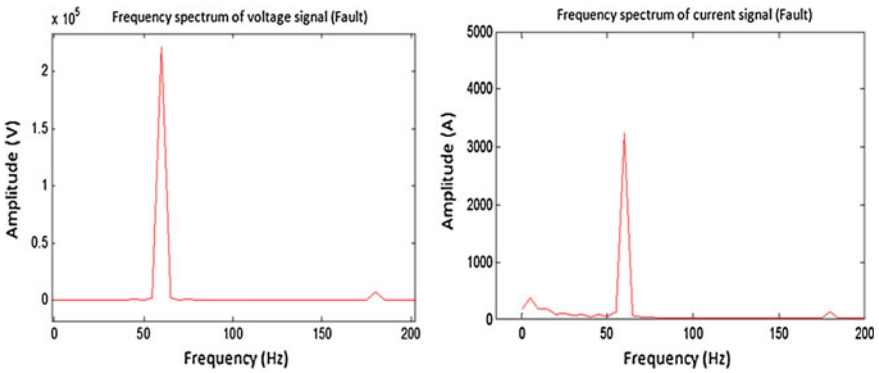

Fig. 16 Frequency spectrum of voltage (V_r) and current (I_r) signals at bus B2

Table 5 Dominant frequencies of voltage signal (bus B2)

Frequency (Hz)	Harmonic order	Amplitude
45	0.75	1,239.69
60	1	221,901
180	3	7,280

Table 6 Dominant frequencies of current signal (bus B2)

Frequency (Hz)	Harmonic order	Amplitude
0	0	166.58
5	0.083	373.78
10	0.16	157.51
15	0.25	169.71
60	1	3,241.86
180	3	121.35

The series VSC is used to generate a fundamental frequency voltage with variable magnitude and phase angle which is added to the AC transmission line by the series connected boosting transformer. Hence, the series VSC acts as a combination of voltage regulator, variable series compensator, and phase shifter. This VSC can internally generate or absorb reactive power at its AC terminal and only the active power has to be supplied at its DC input terminal from the AC power system. This power exchange results in either the discharge or overcharge of the DC link capacitor. To maintain the capacitor voltage at the required value, and assure proper operation of the series VSC, the shunt converter is used to regulate the amount of active power drawn from the AC system at the common DC link terminal. In addition, this shunt VSC has the capability of controlling the reactive power at its AC terminal; independently the active power is transferred to (or from) the DC terminal [3, 28, 29].

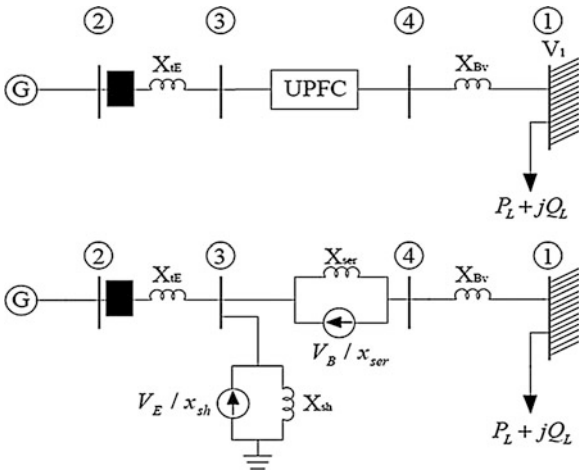

Fig. 17 Model of UPFC in the power system

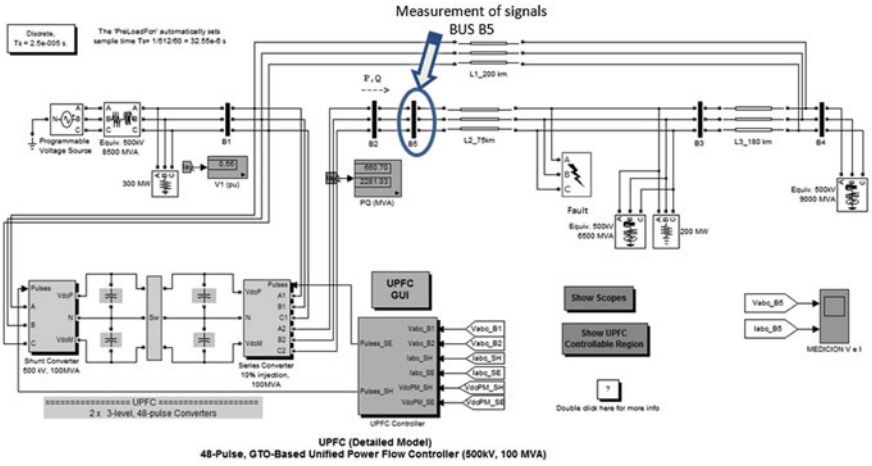

Fig. 18 Test system using UPFC

3.4.1 Test System

A test system using UPFC discrete model is shown in Fig. 18 to evaluate the distance relay operation. A simulation is performed using Matlab/Simulink applying a three phase fault at 0.65 s with duration of 150 ms and a fault resistance of 2 Ω at 80 % of the transmission line (L2_75 km), the voltage level is 500 kV, and a line impedance of 30.9/_84.8° Ω.

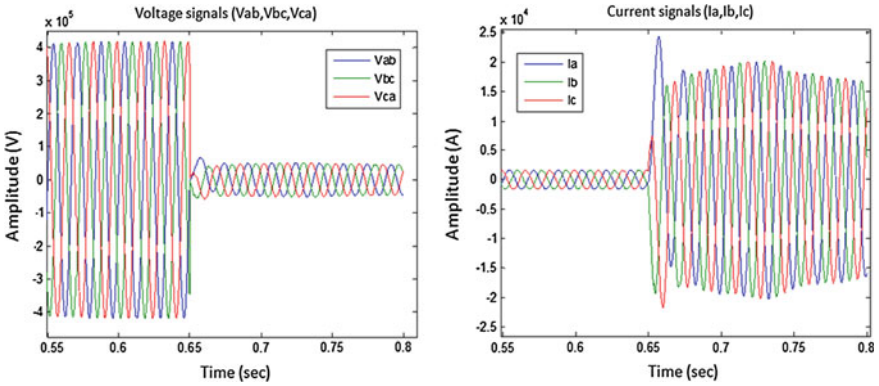

Fig. 19 Voltage and current signals of bus B5 for a three phase fault on the transmission line

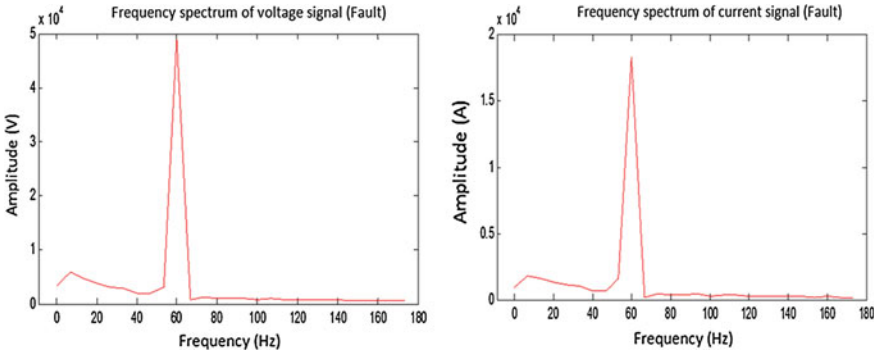

Fig. 20 Frequency spectrum of voltage (V_r) and current (I_r) signals at bus B5

3.4.2 Measured Signals

The voltage (V_r) and current (I_r) signals for the phase distance unit evaluated (BC) at B5 bus are obtained from voltage and current signals in Fig. 19 and the sampling rate of the signals is 32 samples per cycle.

The frequency spectra of the signals are shown in Fig. 20. The frequency components detected during the fault are shown in Tables 7 and 8 for the voltage (V_r) and current (I_r) signals, it can be seen that a low frequency component (subharmonic) has been detected.

Table 7 Dominant frequencies of voltage signal (bus B5)

Frequency (Hz)	Harmonic order	Amplitude
5	0.083	5,820
60	1	48,995

Table 8 Dominant frequencies of current signal (bus B5)

Frequency (Hz)	Harmonic order	Amplitude
0	0	898.5
5	0.083	1,821
60	1	18,319

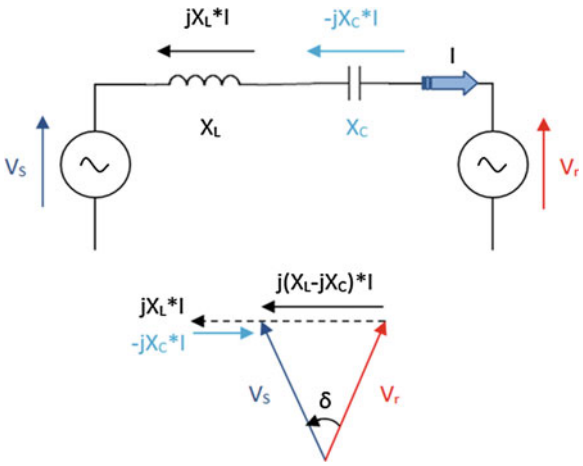

Fig. 21 Series compensation model in the power system

3.5 Series Compensation

The model of the series compensation in the power system is shown in Fig. 21, when a series capacitor ($-jX_C$) is installed in a transmission line, the electric distance of the transmission line will be reduced allowing an increment in the power transfer capability of the line.

When a fault occurs in the series compensated line, an error in the fundamental frequency phasor estimates of voltage and current signals appears due to the line characteristic (RLC resonant circuit), potentially generating low frequency components (subharmonics) [13, 30]. Subsequently, interharmonics and subharmonics generate an error in the fundamental frequency phasors of the voltage and current signals required by the distance relay, giving rise to apparent impedance estimation errors and, as a consequence, an error in the fault detection (underreach/overreach) [31–34].

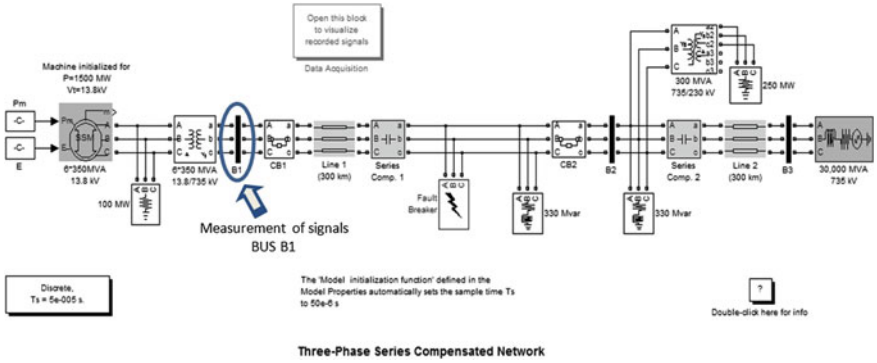

Fig. 22 Series compensation test system

Table 9 Test system parameters

Test system parameters	Values
Transmission system voltage level	V = 735 kV
Line impedance Z_L	$Z_L = 123.6/\_84.8^o\ \Omega$
Series capacitor reactance jX_C	$jX_C = 61.8\ \Omega$
Fault resistance	Rf = 2 Ω

3.5.1 Test System

In this section, a test system is shown in Fig. 22 to evaluate the distance relay operation using Matlab/Simulink. The system consists of a series compensated line scheme using a discrete model. A single phase to ground fault is applied at 100 % of the line. The response of the series compensation scheme during the fault period is evaluated in the impedance plane by the measurement of voltage and current signals in the bus B1 of the test system. By using these signals as the input signals in the distance relay algorithm, the apparent impedance measurement can be evaluated.

The system parameters for the test system for the evaluation of the distance relay at a series compensated line scheme are shown in Table 9.

3.5.2 Measured Signals

The voltage and current signals measured at bus B1 of the test system are shown in Fig. 23, the sampling rate of the signals is 32 samples per cycle. A single phase to ground fault in phase A is applied in the transmission line at 0.05 s over duration of 150 ms. The single phase to ground fault is analyzed using voltage and current signals (V_r and I_r) of the phase distance relay unit (AB), see Fig. 23.

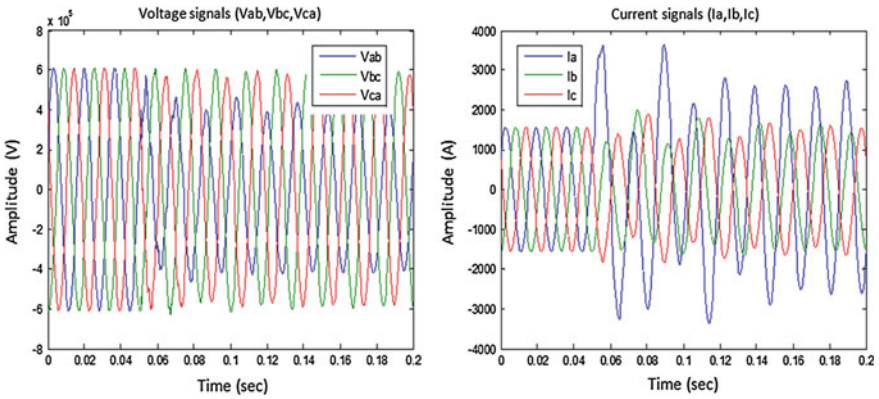

Fig. 23 Voltage and current signals of bus B1 for a single phase fault on the series compensated transmission line

Table 10 Dominant frequencies of voltage signal (bus B1)

Frequency (Hz)	Harmonic order	Amplitude
20	0.33	12,126.96
30	0.5	14,810.59
60	1	417,259.56

Table 11 Dominant frequencies of current signal (bus B1)

Frequency (Hz)	Harmonic order	Amplitude
0	0	11.37
15	0.25	132.64
20	0.33	301.58
30	0.5	491
60	1	2,642.69

The voltage and current signals measured at bus B1 of the test system are shown in Fig. 23. Their frequency spectrum is calculated during the fault period. The frequency components detected during the fault are shown in Tables 10 and 11, it can be seen that low frequency components (subharmonics) have been detected. The frequency components are not filtered by the digital filters of the distance relays (see Fig. 5) and this becomes an error in the apparent impedance measurement which leads to a fault detection problem (underreach/overreach). The frequency spectra of the signals are shown in Fig. 24.

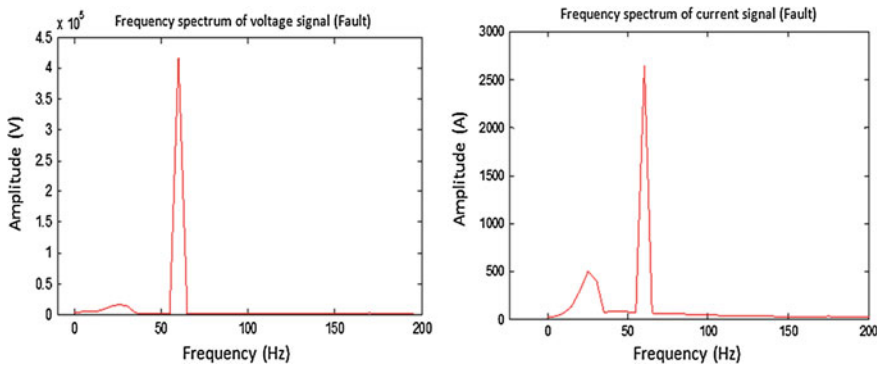

Fig. 24 Frequency spectrum of voltage (V_r) and current (I_r) signals at bus B1

3.6 Effect of Input Signals with Nonfiltered Frequency Components in Distance Relay Impedance Estimation

In Sect. 3 is presented a brief description and test systems to acquiring the voltage and current input signals for the distance relay for each converter-based system evaluated, and it has been showed that converter-based systems inject asynchronous frequency components to the power grid, and this generates an error in the fundamental frequency phasor estimation of the voltage and current signals required by the distance relay, giving rise to apparent impedance estimation errors and by consequence affects the reach and the operation time of the distance relay. A distorted operation characteristic allows to evaluate the reach error in the distance relay, where the reach error percentage is calculated using the Cosine conventional digital filter to obtain the tridimensional estimated mho operation characteristic, then the reach error is calculated using the pickup value of zone 1 and the reach value obtained from the tridimensional operation characteristic during the first one cycle window data with fault values only. The fault impedance trajectory in the impedance plane allows to evaluate the operation time of the relay. In this section, the operation performance of the conventional distance relay is evaluated in reach and operation time using Cosine digital filter. It should be mentioned that a phase distance relay unit is evaluated with a pickup value of protection zone 1 of 80 % of the line impedance and that a down sampling to 16 samples per cycle of the signals is performed.

3.6.1 Wind Power Plant (DFIG Scheme)

The simulated case data is presented in Sect. 3.1 and the voltage and current signals used for the analysis are from Fig. 11. In Fig. 25 the Mho characteristic is presented in a tridimensional space of the impedance plane using the voltage and

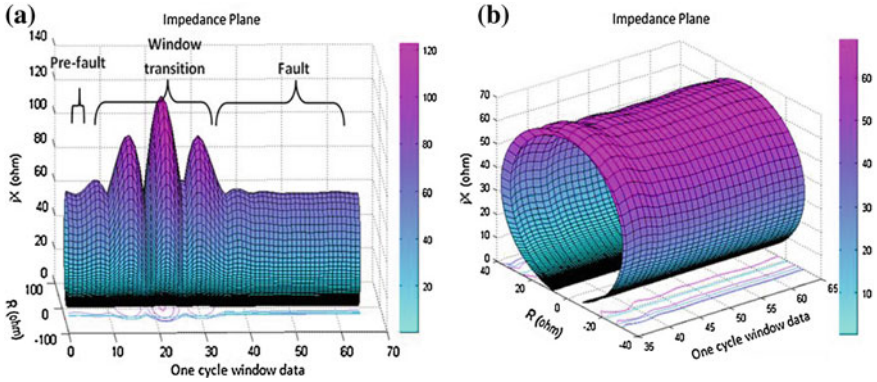

Fig. 25 Operation characteristic of a Mho distance relay at bus B. **a** *Side view* indicating transition stages. **b** Fault period

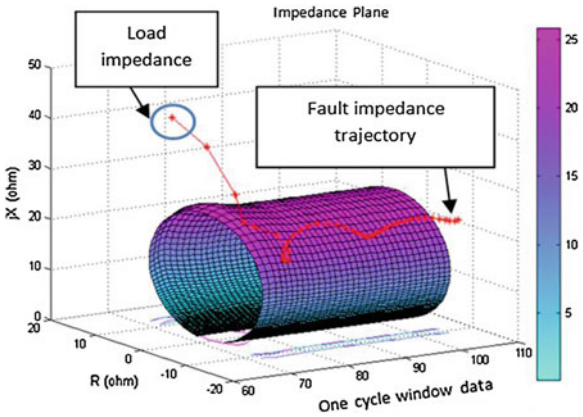

Fig. 26 Operation characteristic of a Mho distance relay at bus B2 during fault period

current signals (V_r and I_r). A reach error of the relay due to the frequency components (subharmonics and interharmonics) can be observed in Fig. 25b, the reach error percentage of the distance relay is 5.7 % in the test system of Fig. 10. The relay could not operate at this fault condition due to the frequency components of the input signals in Fig. 12.

3.6.2 STATCOM

The simulated case data is presented in Sect. 3.2 and the voltage and current signals used for the analysis are from Fig. 15. A reach error of the relay due to the frequency components (subharmonics) can be observed in Fig. 26, the reach error

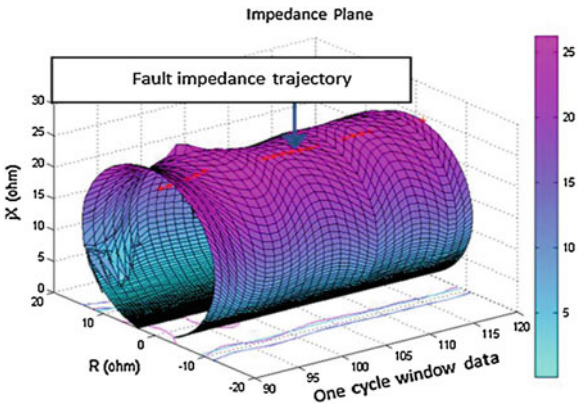

Fig. 27 Operation characteristic of a Mho distance relay at bus B5 during fault period

percentage of the distance relay is 3 % in the test system of Fig. 14. The relay operates in 2.5 cycles at this fault condition due to the frequency components of the input signals in Fig. 16.

3.6.3 UPFC

The simulated case data is presented in Sect. 3.3 and the voltage and current signals used for the analysis are from Fig. 19. A reach error of the relay due to the frequency components (subharmonics) can be observed in Fig. 27, the reach error percentage of the distance relay is 2.19 % in the test system of Fig. 18. The relay operates in 2.7 cycles at this fault condition due to the frequency components of the input signals in Fig. 20.

3.6.4 Series Compensation

The simulated case data is presented in Sect. 3.4 and the voltage and current signals used for the analysis are from Fig. 23. A reach error of the relay due to the frequency components (subharmonics) can be observed in Fig. 28, the reach error percentage of the distance relay is 15.8 % in the test system of Fig. 22. The relay operates in 2.8 cycles at this fault condition due to the frequency components of the input signals in Fig. 24.

3.6.5 Real Fault Event I (Wind Power Plant)

In this section, a real fault event of a wind power plant interconnected to the power system is evaluated. The real fault event corresponds to a 230 kV transmission line with an impedance of 75/_82.4^{o} Ω, the transmission line is interconnected with La

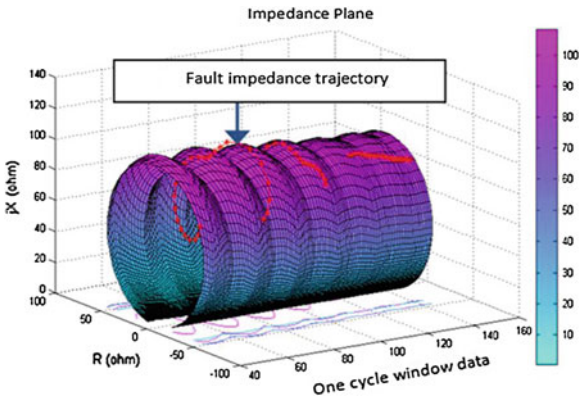

Fig. 28 Operation characteristic of a Mho distance relay at bus B1 during fault period

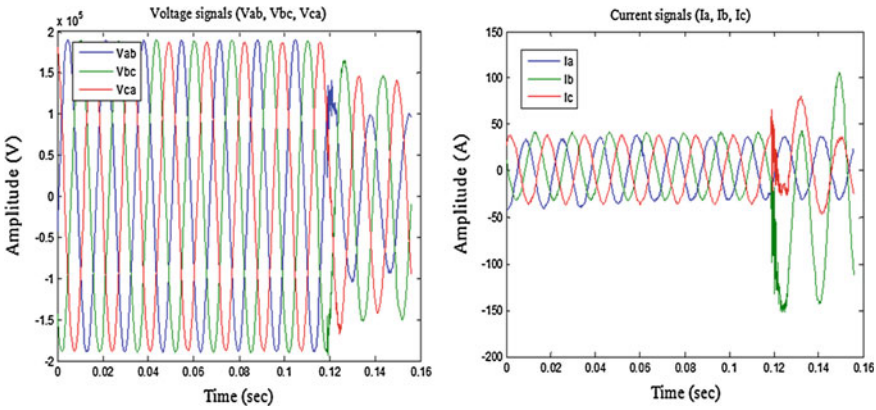

Fig. 29 Recorded fault event I (voltage and current signals)

Venta II wind power plant in Oaxaca, México with an approximate 100 MW generation capability. The power system frequency is 60 Hz, and the sampling frequency of the recorded signals is 128 samples per cycle (see Fig. 29). There is no record of operation of protection relays, so this analysis only focuses on the reach error caused by the unfiltered frequency components.

The Mho characteristic of the relay is presented in a tridimensional space of the impedance plane using the Cosine filter to estimate the phasors of voltage and current, so the reach error of the relay could be calculated (see Fig. 30). An error in the Mho characteristic is observed during the window transition and during the fault period. The reach error in the relay at this fault event is 5.8 % during the fault period compared with the fundamental characteristic.

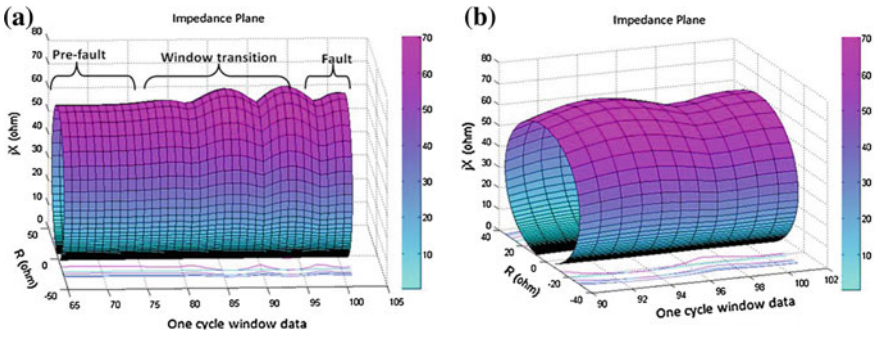

Fig. 30 Mho operation characteristic (fault event I). **a** *Side view* indicating transition stages. **b** Fault period

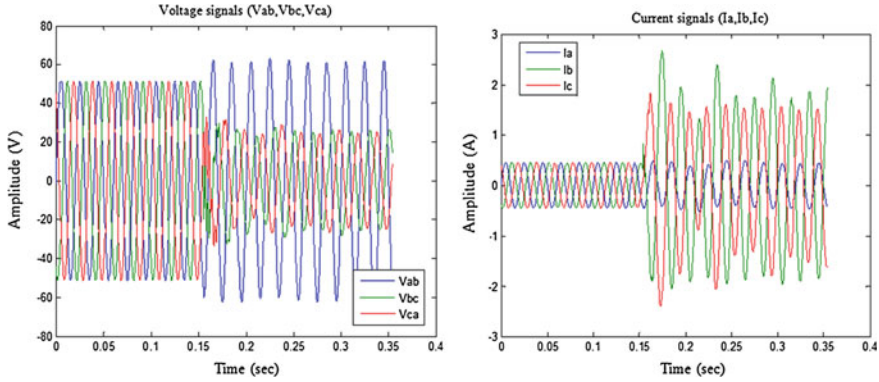

Fig. 31 Recorded fault event II (voltage and current signals)

3.6.6 Real Fault Event II (Series Compensation)

The actual fault event record was provided by ERLPhase Power Technologies Ltd and corresponds to a two phase (BC) ground fault in a 230 kV series compensated transmission line with an impedance of 10/_84.8° Ω; the power system frequency is 50 Hz and the recorded signal sampling frequency is 96 samples per cycle (see Fig. 31). It should be noted that the signal values are referenced to the secondary winding of the instrument transformers.

In Fig. 32, the Mho characteristic of the relay is shown in the tridimensional space of the impedance plane, where an error in the Mho characteristic is observed during the window transition and during the fault period. The relay reach error at this fault event is 16.17 % during the fault period, and the relay operate in 2.5 cycles at this fault condition due to the existence of low frequency components (subharmonics) in the input signals.

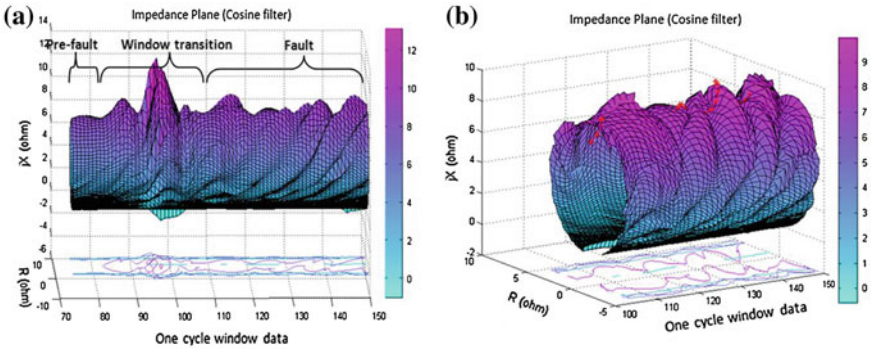

Fig. 32 Mho operation characteristic (fault event II). **a** *Side view* indicating transition stages. **b** Fault period

4 Proposed Distance Relay Algorithm Using Prony Method as a Filtering Technique

In this section, the proposed distance relay algorithm using the Prony method is presented.

4.1 Prony Method

The Prony method has been studied as a power quality analysis tool [35–37] obtaining good results in comparison with FFT, also it has been used in power system stability studies [38]. The proposed algorithm for distance relay using Prony method estimates the signals parameters (amplitude, frequency, phase angle, and damping factors) using one cycle window of data, so the real fundamental frequency of the voltage and current signals can be extracted during the first fault period and that the error in the phasor estimates (see Sect. 2) could be reduced.

The Prony method is a signal processing technique based on signal estimation where a signal $y(t)$ is considered and its samples $[y(1)\ y(2)\ldots y(n)]$ are obtained using a sampling frequency f_s. The Prony model approximates the sampled data with the following linear combination of N complex exponentials:

$$y(t) = \sum_{n=1}^{N} A_n e^{\sigma_n t} \cos(2\pi f_n t + \theta_n) \tag{3}$$

$$y_M = \sum_{n=1}^{N} B_n \lambda_n^M \tag{4}$$

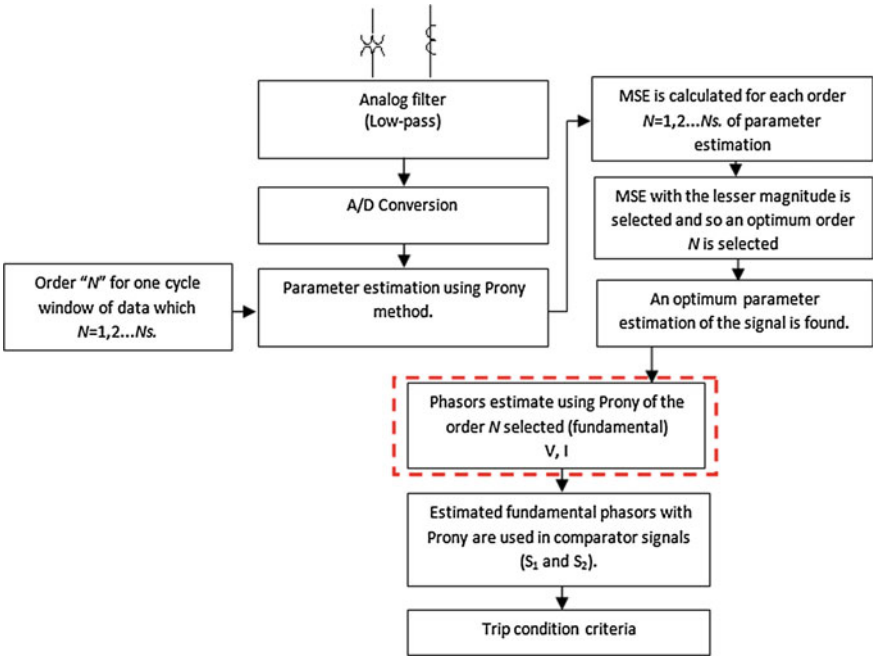

Fig. 33 Proposed distance relay algorithm using Prony method

The signal $y(t)$ in (3) has four elements: Magnitude A_n, damping factor σ_n, frequency f_n, and the phase angle θ_n. Each exponential term with different frequency is a unique signal mode of the original signal $y(t)$. So, using the Euler theorem and total time $t = \mathrm{MT}$, where M is the length of the signal and T is the time between samples, Eq. (3) can be rewritten as (4). From (4) the parameters of the signal $y(t)$ can be found as it is mentioned in the Prony method literature [35–37].

So that the Prony method can be implemented in distance relay algorithm is necessary to obtain the order N of the linear prediction model (LPM). The order is obtained evaluating the mean square error (MSE) for one cycle window of data of $N = 1, 2 \ldots Ns$, where Ns is the samples per cycle in a window data. The MSE for each value of N is calculated and the MSE of lesser magnitude is selected for the corresponding N value, so this value of N is the optimum estimate of the model signal parameters. The proposed distance relay algorithm is shown in Fig. 33, and is intended to estimate the real signal parameters during the first fault period.

In Fig. 34 the Prony phasor magnitude of estimated fundamental phasors and the phase angle estimated with Prony are calculated and the compensated phasors are formed, the compensated phasors are used as the fundamental phasors in the distance relay model.

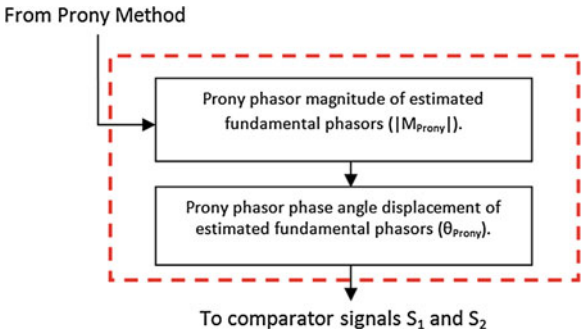

Fig. 34 Prony method as filtering technique for distance relay

4.1.1 Formulation

The formulation of the proposed distance relay algorithm using the Prony estimated phasors is presented as follows:

$$\begin{aligned} S_1 &= k_1\angle\alpha_1 \overbrace{\left[V_{P1}e^{j\theta_{V_{P1}}}\right]}^{\text{Prony phasor estimation}} + Z_{R1}\angle\theta_1 \overbrace{\left[I_{P1}e^{j\theta_{I_{P1}}}\right]}^{\text{Prony phasor estimation}} \\ S_2 &= k_2\angle\alpha_2\left[V_{P1}e^{j\theta_{V_{P1}}}\right] + Z_{R2}\angle\theta_2\left[I_{P1}e^{j\theta_{I_{P1}}}\right] \end{aligned} \tag{5}$$

where $P1$ is the fundamental component estimated with Prony. For the analysis of the proposed algorithm the Mho characteristic will be evaluated. The distance relay model for a Mho characteristic is

$$\begin{aligned} S_1 &= k_1\angle\alpha_1\left[V_{P1}e^{j\theta_{V_{P1}}}\right] + Z_{R1}\angle\theta_1\left[I_{P1}e^{j\theta_{I_{P1}}}\right] \\ S_2 &= k_2\angle\alpha_2\left[V_{P1}e^{j\theta_{V_{P1}}}\right] \end{aligned} \tag{6}$$

where $Z_{R2}\angle\theta_2 = 0$ in (5) for a Mho characteristic, so the distance relay model for the Mho characteristic is as shown in (6).

5 Analysis of Proposed Distance Relay Algorithms

The proposed algorithm presented in Sect. 4 is validated using voltage and current signals of the simulated cases presented in Sect. 3 and using signals from real fault events, it should be mentioned that a phase distance relay unit is evaluated with a pickup value of protection zone 1 of 80 % of the line impedance and that a down sampling to 16 samples per cycle of the signals is performed.

In Sect. 3 a characterization of the problem in distance relay performance due to converter-based systems is presented. Due to asynchronous frequency components in the input signals (Voltage and Current), the conventional distance relays that uses Fourier or Cosine digital filter generates an error in the fundamental

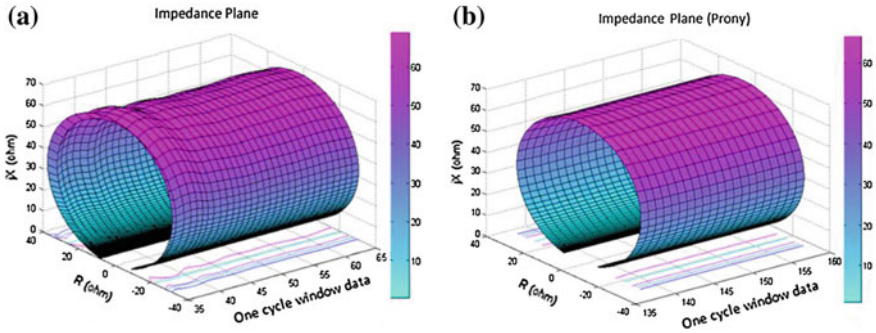

Fig. 35 Dynamic Mho operation characteristic during fault period (wind power plant). **a** Using conventional distance relay algorithm. **b** Using the Prony method as compensation algorithm

frequency phasor estimate and by consequence a reach error of the distance relay. In this section, the reach error compensation results and operation times of the proposed distance relay algorithm (Using Prony Method) for each of the test systems and real fault events of Sect. 3 are presented using the Mho operation characteristic.

5.1 Reach Error Compensation (Wind Power Plant)

In this section, the Mho characteristic is presented in a tridimensional space of the impedance plane using the voltage and current signals (V_r and I_r) of the test system in Sect. 3.1. A reach error of the relay due to the frequency components (subharmonics and interharmonics) can be observed in Fig. 35a, the reach error percentage is calculated using the Cosine conventional digital filter to obtain the tridimensional estimated Mho operation characteristic, then the reach error is calculated using the pickup value of zone 1 and the reach value obtained from the tridimensional operation characteristic during the first one cycle window data with fault values only.

In Fig. 35 the Mho operation characteristic of a conventional distance relay using Cosine filter is compared with the proposed distance relay algorithm.

The reach error during the first fault period (first one cycle window data with fault values only) of the distance relay in Fig. 35a is 5.7 % (maximum deviation of Fig. 35a compared with the fundamental characteristic of Fig. 2) in the test system of Fig. 10. In contrast the reach error using the Prony proposed algorithm is 0.02 % in Fig. 35b. The operation time (fault detection) using the Cosine filter could not generate a trip signal, so the fault could not be detected. The operation time of Prony proposed algorithm is 0.75 cycles, so the fault is detected.

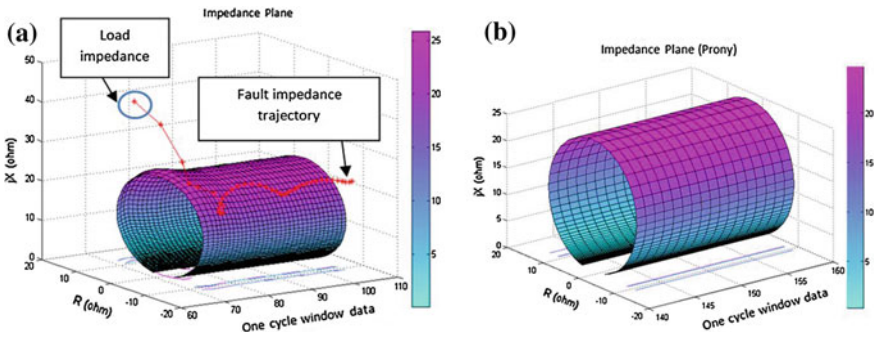

Fig. 36 Dynamic Mho operation characteristic during fault period (STATCOM). **a** Using conventional distance relay algorithm. **b** Using the Prony method as compensation algorithm

5.2 Reach Error Compensation (STATCOM)

In Fig. 36 the results of the comparison of the conventional distance relay using Cosine filter and proposed Prony algorithm is evaluated.

The reach error calculated during the fault period in Fig. 36a is 3 %. The reach error in Fig. 36b is 0.035 % using the Prony proposed algorithm. The operation time is 0.36 cycles for the proposed Prony algorithm. By comparison, with the Cosine filter, the operation time is 2.5 cycles and the reach error is 3 %; there is reach error compensation on the distance relay performance and also a reduction in the operation time.

5.3 Reach Error Compensation (UPFC)

In Fig. 37 the Mho operation characteristic of a conventional distance relay using Cosine filter is compared with the proposed distance relay algorithm.

The reach error during the fault period in Fig. 37a is 2.19 %. The reach error in Fig. 37b is 0.01 % using the Prony proposed algorithm. The operation time is 1.63 cycles for the proposed Prony algorithm. By comparison, with the Cosine filter, the operation time is 2.7 cycles and the reach error is 2.19 %; there is reach error compensation in the distance relay performance and also a reduction in the operation time.

5.4 Reach Error Compensation (Series Compensation)

In Fig. 38 it could be observed that the distortion of the Mho characteristic is of greater magnitude for the Series compensation compared with the other converter-based systems, this is due to the nonfiltered low frequency components that are

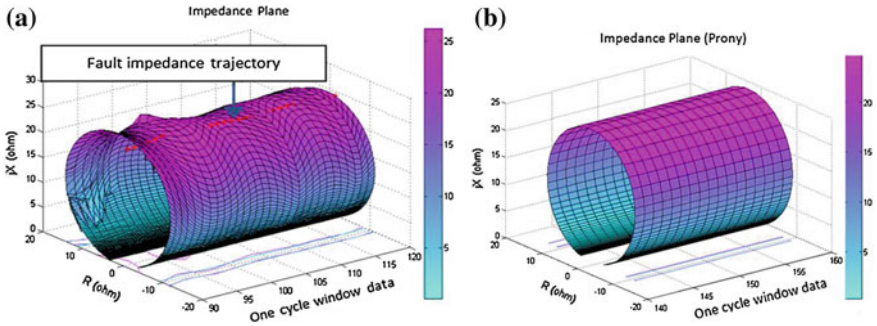

Fig. 37 Dynamic Mho operation characteristic during fault period (UPFC). **a** Using conventional distance relay algorithm. **b** Using the Prony method as compensation algorithm

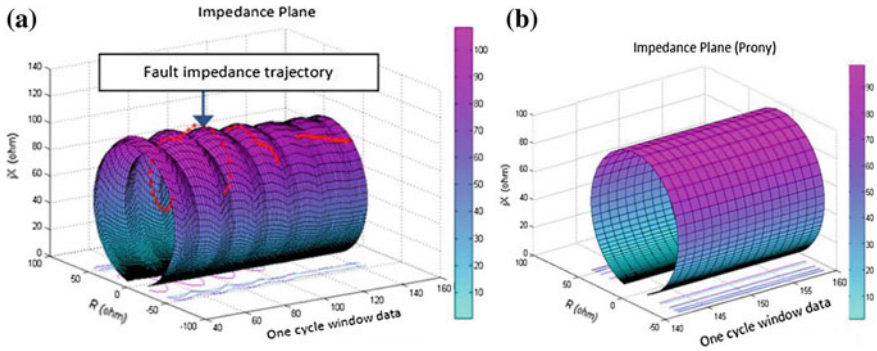

Fig. 38 Dynamic Mho operation characteristic during fault period (series compensation). **a** Using conventional distance relay algorithm. **b** Using the Prony method as compensation algorithm

primarily generated by the resonant circuit RLC of this type of compensation system during the fault period, also the error is greater due to the frequency response of the Cosine filter (see Fig. 5). When low frequency components exist in the input signals needed by the distance relay, the estimate of the fundamental frequency phasor will not be accurate, giving rise to a greater error in the apparent impedance estimation (see Fig. 38a) and by consequence could affect the performance of the distance relay.

In this case the reach error during the fault period in Fig. 38a is 15.8 %. The reach error in Fig. 38b is 0.09 % using the Prony proposed algorithm. The operation time is 1.43 cycles for the proposed Prony algorithm. By comparison, with the Cosine filter, the operation time is 2.8 cycles and the reach error is 15.8 %.

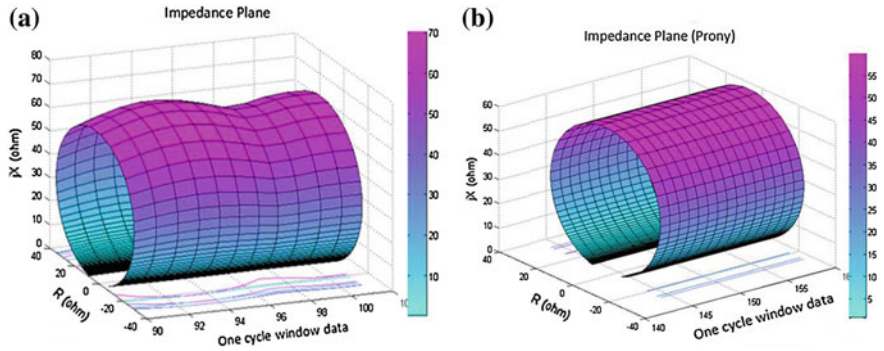

Fig. 39 Dynamic Mho operation characteristic during fault period (real fault event I). **a** Using conventional distance relay algorithm. **b** Using the Prony method as compensation algorithm

5.5 Reach Error Compensation (Real Fault Events)

This section assesses the real fault events I and II presented in Sects. 3.5 and 3.6 using the current and voltage signals recorded to validate the proposed algorithms. This section presents the results of reach error compensation in the Mho operation characteristic and operation time of a distance relay for real fault events using Prony proposed distance relay algorithm.

5.5.1 Real Fault Event I (Wind Power Plant)

In Fig. 39 the Mho operation characteristic of a conventional distance relay is compared with the Prony proposed distance relay algorithm.

The reach error during the fault period in Fig. 39a is 5.8 %. The reach error in Fig. 39b is 0.09 % using the Prony proposed algorithm. The operation time is 0.92 cycles for the proposed Prony algorithm. The operation time (fault detection) using the Cosine filter could not generate a trip signal, so the fault could not be detected. These results confirm that the use of the Prony proposed distance relay algorithm leads to a reduction in the relay reach error and, therefore, a reduction in the operation time.

5.5.2 Real Fault Event II (Series Compensation)

In Fig. 40 the Mho operation characteristic of a conventional distance relay is compared with the proposed distance relay algorithm.

The reach error calculated during the fault period in Fig. 40a is 16.17 %. The reach error in Fig. 40b is 0.66 % using the Prony proposed algorithm. The operation time is 0.87 cycles for the proposed Prony algorithm. By comparison, with

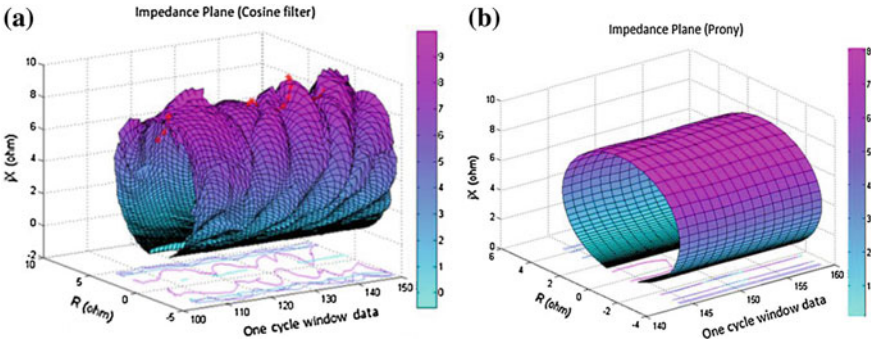

Fig. 40 Dynamic Mho operation characteristic during fault period (real fault event II). **a** Using conventional distance relay algorithm. **b** Using the Prony method as compensation algorithm

Table 12 Fault detection operation time of distance relay algorithms

Event	Operation time (cycles)		% Error in operation time	
	Cosine	*Prony*	Cosine	*Prony*
Wind power plant	Could not operate	0.75	Could not operate	25[a]
STATCOM	2.5	0.36	150	64[a]
UPFC	2.7	1.63	170	62.5
Series compensation	2.8	1.43	180	43
Real fault event I	Could not operate	0.92	Could not operate	8[a]
Real fault event II	2.5	0.87	150	13[a]

[a] The percentage error in operation time in cycles indicates an improvement in the operation time because the fault detection is established in less than one cycle

Table 13 Reach error of distance relay algorithms

Event	% Reach error (cosine filter)	% Compensated reach error (proposed distance relay algorithm)
		Prony
Wind power plant	5.7	0.02
STATCOM	3	0.035
UPFC	2.19	0.01
Series compensation	15.8	0.09
Real fault event I	5.8	0.09
Real fault event II	16.17	0.66

the Cosine filter, the operation time is 2.5 cycles and the reach error is 16.17 %. These results confirm that the use of the Prony proposed distance relay algorithm leads to a reduction in the relay reach error and, therefore, a reduction in the operation time.

6 Summary of Results

The time of fault detection of digital distance relays are approximately 2–4 cycles [13], so the error in the operation time is evaluated during the first cycle during the fault period. This means that the results of the reduction of the error in the operation time using the proposed algorithm represent a good result; because the fault detection is performed in a time less than one cycle for the simulated case (see Table 12). Also the error compensation in the apparent impedance estimation is done during the fault period (see Table 13). Using the proposed algorithm, a malfunction of the distance relay can be prevented (underreach/overreach).

7 Conclusions

Converter-based systems as wind power plants, FACTS devices (STATCOM and UPFC), and series compensators are used nowadays to fulfill the power grid requirements, as optimization of generated power, voltage regulation, increment of power transfer capabilities, and stability. By continuing to use relays with conventional digital filters for the protection of transmission lines that have interconnected converter-based systems such as wind power plants, FACTS, series compensation, or where a transmission line has two sections, overhead and then underground, it could lead to a fault detection problem.

The proposed distance relay algorithm could be used as an alternative for the compensation of the error generated in the apparent impedance estimation during fault period, this is caused by the nonfiltered frequency components as interharmonics and subharmonics that affects the fundamental frequency phasor estimation when conventional digital filters as Cosine or Fourier are used.

This power electronics-based systems generate asynchronous frequency components that could compromise the distance relay performance during a fault condition. The frequency components generated by converter-based systems in the power system were evaluated in the performance of the distance relay, a solution for this issue (apparent impedance error estimation) described in this chapter is proposed by using Prony proposed algorithm. The proposed algorithm showed good results during the fault period and the estimation times considering one cycle data window are acceptable (1.03 cycles for the proposed algorithm). The estimation time is obtained by measuring the algorithm execution time in Matlab.

References

1. Chen Z, Guerrero JM, Blaabjerg F (2009) A review of the state of the art of power electronics for wind turbines. IEEE Trans Power Electron 24(8):1859–1875
2. Blaabjerg F, Liserre M, Ma K (2012) Power electronics converters for wind turbine systems. IEEE Trans Ind Appl 48(2):708–719

3. Hingorani NG, Gyugyi L (1999) Understanding FACTS concepts and technology of flexible ac transmission systems. IEEE Press, New York
4. Oliveira ALP (2008) Fixed series compensation protection evaluation using transmission lines faults simulations. In: IEEE/PES transmission and distribution conference and exposition: Latin America, pp 1–6
5. Heier S (2006) Grid integration of wind energy conversion systems. Wiley, Hoboken
6. Ackerman T (2005) Wind power in power systems. Wiley, New York
7. Kasztenny B (2001) Distance protection of series compensated lines problems and solutions. GE power management, Markham, Ontario, Canada L6E 1B3. http://store.gedigitalenergy.com/faq/Documents/Alps/GER-3998.pdf
8. Altuve HJ, Mooney JB, Alexander GE (2008) Advances in series-compensated line protection. Technical report SEL. https://www.selinc.com/WorkArea/DownloadAsset.aspx?id=3540
9. Testa A (2007) Interharmonics: theory and modeling. IEEE Trans Power Deliv 22(4):2335–2348
10. Leonowicz Z (2011) Assesment of power quality in wind power systems. In: 10th international conference on environment and electrical engineering (EEEIC), pp 1–3
11. Leonowicz Z (2010) Analysis of sub-harmonics in power systems. In: 9th international conference on environment and electrical engineering (EEEIC), pp 125–127
12. Cook V (1985) Analysis of distance protection. Wiley, New York
13. Phadke AG, Thorpe JS (2009) Computer relaying for power systems. Research Studies Press Ltd, Wiley, New York
14. Van Cor Warrington AR (1978) Protective relays their theory and practice. Springer, London
15. Ziegler G (2008) Numerical distance protection principles and applications. Siemens AG, Wiley, Berlin
16. Krause G (2011) From turbine to wind farms-technical requirements and spin off products. In: Krause G (ed) Distance protections in the power system lines with connected wind farms, 1st edn. InTech, Croatia
17. Srivastava S, Shenoy UJ et al (2013) Impedance seen by distance relays on lines fed from fixed speed wind turbines. Int J Emerg Electr Power Syst 14:17–24
18. He L, Chen-Ching L (2013) Impact of LVRT capability of wind turbines on distance protection of AC grids. In: IEEE PES innovative smart grid technologies (ISGT), pp 1–6
19. De Rijcke S, Pérez PS, Driesen J (2010) Impact of wind turbines equipped with doubly-fed induction generators on distance relaying. In: IEEE power and energy society general meeting, pp 1–6
20. Lobos T, Rezmer J, Schegner P (2004) Parameter estimation of distorted signals. In: Proceedings of ieee power tech conference, vol 4 no 1, pp 1–5, Bologna
21. Leite EP (2010) Matlab-modelling, programming and simulations. In: Leite EP (ed) Simulation of numerical distance relays, 1st edn. Intech, Sciyo, Lybia
22. Proakis JG, Manolakis DG (2006) Digital signal processing. Prentice hall, Upper Saddle River
23. EO Schweitzer, Hou D (1993) Filtering for protective relays. WESCANEX. In: Proceedings of ieee communications, computers and power in the modern environment conference, pp 15–23
24. Ljung L (1994) Modeling of dynamic systems. Prentice Hall, Englewood
25. Iov F, Hansen AD et al (2007) Mapping of grid faults and grid codes. Riso National Laboratory, Technical University of Denmark, Roskilde Denmark. http://orbit.dtu.dk/fedora/objects/orbit:79876/datastreams/file_7703139/content
26. Seman S, Niiranen J (2006) Ride through analysis of doubly fed induction wind power generator under unsymmetrical network disturbances. IEEE Trans Power Syst 21(4):1782–1789
27. IEEE Standard C37.113-1999 (2002) IEEE guide for protective relay applications to transmission lines. IEEE, New York
28. Gyugyi L (1992) A unified power flow control concept for flexible AC transmission systems. IEE Proc C Gener Transm Distrib 139(4):323–331

29. Gyugyi L, Schauder CD, Williams SL et al (1995) The unified power flow controller: a new approach to power transmission control. IEEE Trans Power Deliv 10(2):1085–1097
30. Joe Perez Understanding subharmonics. ERLPhase power technologies. Winnipeg MB, Canada. http://www.erlphase.com/downloads/application_notes/Understanding_Sub_Harmonics.pdf
31. Fotuhi-Firuzabad M, Billinton R, Faried SO (2000) Subtransmission system reliability enhancement using a thyristor controlled series capacitor. IEEE Trans Power Deliv 15(1):443–449
32. Lee GE, Goldsworthy DL (1996) BPA's Pacific AC intertie series capacitors: experience, equipment & protection. IEEE Trans Power Deliv 11(1):253–259
33. Swann DE, Larsen EV, Piwko RJ (1993) Major benefits from thyristor controlled series capacitors. Power Technol Int. CODEN: PTEIE 8:109–112
34. Johnson RK, Torgerson DR, Renz K, Thumm G, Weiss S (1993) Thyristor control gives flexibility in series compensated transmission. Power Technol Int. CODEN: PTEIE 8:99–103
35. Leonowicz Z (2006) Parametric methods for time–frequency analysis of electric signals. Politechnika Wrocławska. Wroclaw University of Technology, Poland
36. Qi L, Qian L, Woodruff S, Cartes D (2007) Prony analysis for power system transients. EURASIP J Adv Signal Process 1–12
37. Meunier M, Brouaye F (1998) Fourier transform, wavelets, prony analysis: tools for harmonics and quality of power. In: 8th international conference on harmonics and quality of power ICHQP, pp 71–76
38. Hauer JF, Demeure CJ, Scharf LL (1990) Initial results in prony analysis of power system response signals. IEEE Trans Power Syst 5(1):80–89

Protection Schemes for Meshed VSC-HVDC Transmission Systems for Large-Scale Offshore Wind Farms

J. Yang and J. E. Fletcher

Abstract This chapter discusses network protection of high-voltage direct current (HVDC) transmission systems for large-scale offshore wind farms where the HVDC system utilizes voltage-source converters. The multi-terminal HVDC network topology and protection allocation and configuration are discussed with DC circuit breaker and protection relay configurations studied for different fault conditions. A detailed protection scheme is designed with a solution that does not require relay communication. Advanced understanding of protection system design and operation is necessary for reliable and safe operation of the meshed HVDC system under fault conditions. Meshed-HVDC systems are important as they will be used to interconnect large-scale offshore wind generation projects. Offshore wind generation is growing rapidly and offers a means of securing energy supply and addressing emissions targets whilst minimising community impacts. There are ambitious plans concerning such projects in Europe and in the Asia–Pacific region which will all require a reliable yet economic system to generate, collect, and transmit electrical power from renewable resources. Collective offshore wind farms are efficient and have potential as a significant low-carbon energy source. However, this requires a reliable collection and transmission system. Offshore wind power generation is a relatively new area and lacks systematic analysis of faults and associated operational experience to enhance further development. Appropriate fault protection schemes are required and this chapter highlights the process of developing and assessing such schemes. The chapter illustrates the basic meshed topology, identifies the need for distance evaluation, and appropriate cable models, then details the design and operation of the protection scheme with simulation results used to illustrate operation.

J. Yang (✉)
School of Engineering and Applied Science, Aston University, Birmingham B4 7ET, UK
e-mail: j.yang8@aston.ac.uk

J. E. Fletcher
School of Electrical Engineering and Telecommunications, The University of New South Wales UNSW, Sydney, NSW 2052, Australia
e-mail: john.fletcher@unsw.edu.au

J. Hossain and A. Mahmud (eds.), *Large Scale Renewable Power Generation*, Green Energy and Technology, DOI: 10.1007/978-981-4585-30-9_14,

Keywords Voltage source converter (VSC) · High voltage direct current (HVDC) · Fault overcurrent protection · Meshed multi-terminal DC network · Wind power generation

1 Introduction

A High-Voltage Direct Current (HVDC) "Supergrid" is an ambitious concept, primarily aimed at wind power integration that utilizes a meshed HVDC grid to connect multiple offshore wind farms to onshore substations [1, 2]. The supergrid concept can be realized using voltage source converter (VSC) technology operating at HVDC. Such technology is flexible and can be used with weak AC system connections. The meshed topology enhances system reliability, which is indispensable for transmission networks with a large contribution from offshore wind generation. Networks with loops are common in traditional AC transmission power grids, because they are relatively economical compared to the double-line systems and more reliable than radial systems without backup. The potentially large capacity of wind power integrated into AC grids requires the transmission systems to be much more reliable due to its influence on the whole electricity system. If the concept of supergrid progresses to reality for multiple wind farm connection and integration to onshore systems, issues related to the meshed topology should be considered in advance, especially for the untried high-power DC operation scenario.

Due to the lack of existing multi-terminal high-power DC systems and their operational experience, there is no currently established protection scheme developed for application to the VSC-based high-power DC scenario. In order to solve the DC system protection problem, radial multi-terminal DC VSC-based overcurrent protection for wind power generation has been published by the authors [3], which is the basis of the work in this chapter. As mentioned, there is little work on VSC-based DC system switchgear configuration for protection. However, for large-scale offshore DC wind farms with HVDC power transmission, proper DC switchgear configuration is indispensable. Therefore, this chapter will further deal with the protection design of meshed networks at the transmission level. Former fault analysis of VSC-cable systems will be summarized and applied. The DC switchgear applied is a uni-directional current-blocking power electronic circuit breaker (CB). The key protection issues to realize protection reliability and selection of this meshed DC network are defined and discussed with a consequent CB tripping strategy.

The chapter is organized as follows. In Sect. 2, the multi-terminal DC system is introduced along with possible topologies. A typical network section is proposed for study. DC fault characteristics are summarized and applied in Sect. 3. With fault current frequency analysis, the DC cable modeling issue is discussed with

comparisons via simulation. DC switchgear options and their allocation are presented in Sect. 4 followed by a detailed protection strategy design. Illustrative examples and PSCAD/EMTDC simulations are provided in Sect. 5.

2 Multiterminal Meshed DC Wind Farm Network

Nowadays, multiterminal DC wind farm topologies that have been researched are mainly radial [4, 5]. However, a meshed connection is required for future reliable HVDC power transmission [2]. DC system protection research is still focusing on specific converter topologies or control under fault conditions [6]. There is currently no reported work on the network level protection of such systems.

2.1 Meshed Multiterminal DC Wind Farm Topology

The topology with loops is commonly used in traditional AC power transmission systems because of its balance between economic costs and reliability. The high-power DC transmission network will need to achieve the highest standard of reliability and availability. If the supergrid concept is to be realised for multiple offshore wind farm connections and integration to different onshore AC grids, the protection issues related to the meshed system must be addressed. For the collection grid, the reliability can also be enhanced by introducing redundant cables, but usually, the system will operate in open-loop which leaves all the redundant cables as backup in case of faults occurring in cables or devices used during normal operation. If many wind farms are connected together with multiple onshore connections, the transmission system should be optimal and have a loop, or be meshed. Power flows in this network can be much more flexible with a more even utilization of cable resources, which is one of the most expensive investments. However, this meshed topology makes the protection relay coordination and switchgear system significantly more complex.

One main problem for a complex loop/meshed system is that the power flow cannot be predicted accurately. The power flow varies as the system condition changes, for example, wind speed oscillations that result in power fluctuations, or possible power flow direction changes due to switch-in or switch-out of wind farms. Special attention to the loop cables between wind farms is required because of the bi-directional load flow on them. Therefore the possible normal power flow oscillations and direction changes need to be excluded to make the relay setting simpler and accurate in operation. Apart from that, mature protection and relay coordination techniques of meshed AC distribution and transmission systems [7–9] may be adopted for application to DC systems.

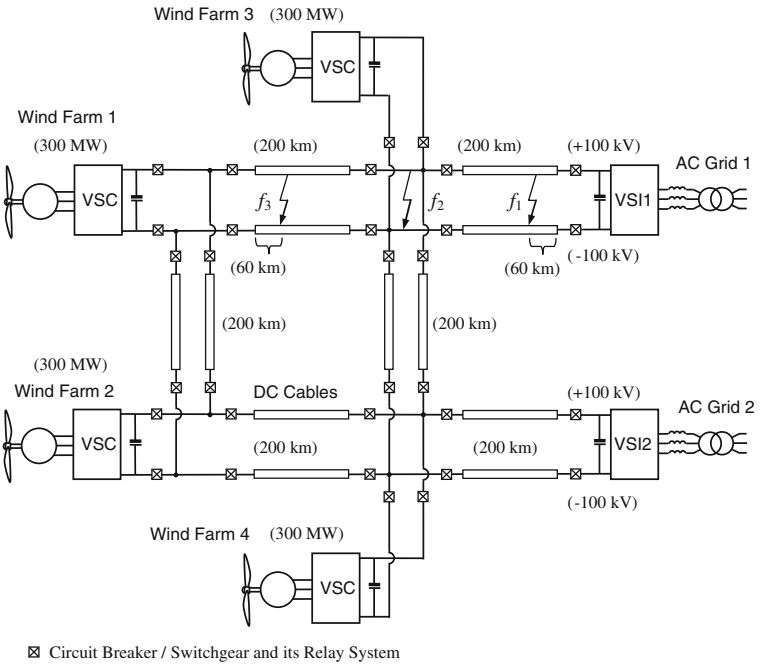

Fig. 1 A typical section of multiterminal DC transmission system for the concept supergrid

2.2 Supergrid Section for Protection Test Study

The DC topology investigated is a multi-terminal VSC-HVDC system connecting large-scale wind farms. A typical section of this meshed DC supergrid with possible switchgear allocation for protection test is shown in Fig. 1. All the AC/DC rectifiers and DC/AC inverters are sinusoidal pulse-width-modulation (SPWM) VSCs connected with DC cables (lengths as shown). No more detailed DC wind farm collection grids are shown, only the transmission system with converters or centralized step-up DC/DC converters illustrated as VSCs. Each wind farm is represented by an equivalent wind turbine-permanent magnet synchronous generator (PMSG) set in which maximum-power-point-tracking (MPPT) is fulfilled by the AC/DC VSC. The rectifier VSC and voltage source inverter (VSI) control schemes are that of a single PMSG direct-driven wind power generation system [10]. The four wind farms are all of 300 MW rating each—1200 MW in total—and connected to a $\pm$100 kV DC loop with two parallel cables to two separate onshore AC grid connection stations.

This example transmission section is made according to the following assumptions: (1) Each node has a connection to a wind farm or onshore inverter platform to AC grid substation; (2) The loop here is symmetrical with connections to two AC grids; (3) There might not be real DC bus conductors allocated in an

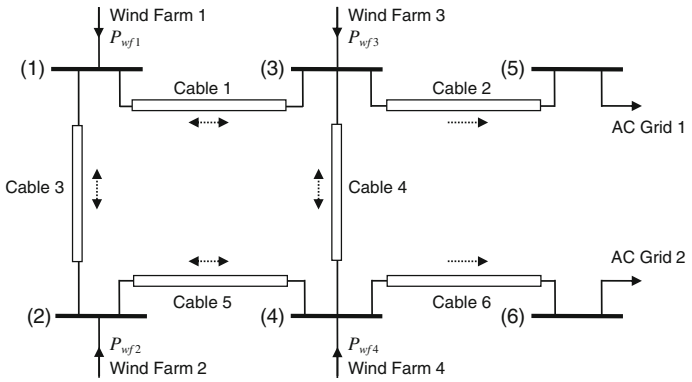

Fig. 2 Single-line diagram shows system nodes, cable connections, and power flow directions

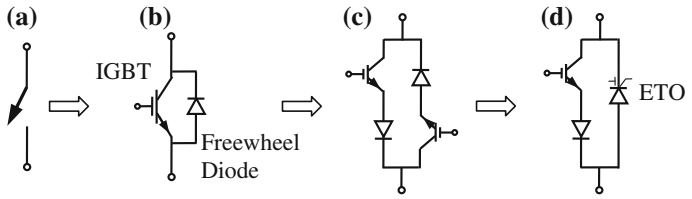

Fig. 3 Illustration of VSC switch configuration for fault tolerant function: **a** switch symbol; **b** traditional IGBT/diode switch; **c** bi-directional IGBT/diode-series fault tolerant switch; **d** bi-directional IGBT/ETO parallel fault tolerant switch

offshore environment, but the node with more than two connections is considered to be a DC bus where bus faults can occur (shown as fault f_2 in Fig. 1).

This network is simplified to a single-line diagram, Fig. 2, for node/cable numbering and possible power flow directions indicated with dotted arrows. The Cables 1, 3, 4 and 5 are defined as loop cables; while Cables 2 and 6 are radial cables. It is the bi-directional loop Cables 1, 3, 4, 5 that complicate the protection coordination.

IGBT-based VSCs have freewheel diodes—as shown in Fig. 3b—which will be destroyed by the overcurrent that occurs during DC-link discharge. Fault tolerant converters can be applied to avoid allocating a large number of DC CBs. The main idea is to replace those passive diodes with self-turn-off power electronic devices, like another IGBT/diode series branch (Fig. 3c) or emitter turn-off devices (ETOs) [11] (Fig. 3d). Furthermore, a thyristor-based dedicated high-power DC/DC transformer that can isolate fault currents is proposed in Jovcic and Ooi [12]. However, in terms of a network, this means all the converters need to be totally immune from DC faults. During the development of the network, at this stage, with mostly conventional VSCs, it is economically infeasible. Therefore, protection scheme design is still necessary in the development of multi-terminal DC transmission networks.

Table 1 Frequency of fault currents

Fault condition	Phase	Description	Frequency
Short-circuit fault	I	DC-link capacitor discharging, natural response	$\omega^2 = \frac{1}{LC} - \left(\frac{R}{2L}\right)^2$
	II	Cable inductance discharging, natural response	N/A
	III	Grid side current feeding, forced response	$\omega^2 = \frac{1}{LC} - \left(\frac{R}{2L}\right)^2$
Ground fault	I	Transient phase, natural response	$\omega_s = 2\pi f_s$
	II	Steady-state phase, forced response	$\omega_s = 2\pi f_s$

f_s the synchronous frequency; C DC-link capacitance; R, L the equivalent resistance and inductance for faulted cable

3 DC Fault Analysis for Large-Scale Meshed Systems

Detailed fault analysis of a VSC-based radial system using a π-model for the cable is illustrated in this section. The faults are mainly short-circuit faults and ground faults both on positive and negative cables. The IGBTs of VSCs can be blocked for self-protection during faults, leaving the reverse diodes exposed to the DC-link discharge overcurrent. To solve the complete response of this nonlinear circuit, different time periods are defined with expressions of both the DC-link voltage collapse and cable overcurrent. There are three stages established for this nonlinear system. The frequency characteristics are provided in Table 1 for the following cable modeling comparison.

In essence, DC bus faults use the same circuit analysis but require different relay coordination, especially for the uni-directional current-blocking CBs. A distance evaluation protection method is used here, with a new coordination strategy presented for the meshed topology.

3.1 Appropriate Cable Modeling for DC Fault Analysis

For large-scale offshore wind farms with HVDC power transmission, detailed and appropriate DC cable models are required for accurate transient analysis. In this section, the multi-layered submarine distributed cables are analyzed because they are used in practice for large-scale onshore/offshore wind power integration. Overhead line models are not investigated.

(1) *Existing Cable Models*

There are several cable models available for circuit analysis and computer simulation. Theoretically, the distributed single-conductor cable model is represented by partial derivative equations in time and distance as the original mathematical model. Furthermore, to separate distance and time dependency, the travelling wave model analysis [13] is performed for steady-state solution under ideal sinusoidal signals.

For transient response simulations, there are four common models. The most common and simple is the π-equivalent model. The Bergeron model is a progression

of the simple π-model. It accurately represents the distributed L and C, but with a lumped R to simulate cable power loss. They are accurate at a specified frequency and are suitable for studies where a certain frequency is important (e.g., for AC relay studies) [14]. The frequency dependent model in mode represents the frequency dependence of all parameters (not just at the specified frequency as in the Bergeron model). The problem of a frequency dependent transformation matrix can be overcome by formulating the model directly in the phase domain (without diagonalization) [14], which results in the frequency-dependent phase model. It also represents the frequency dependence of all parameters as in the mode model, and produces the most accurate transient responses.

Therefore, the choice of cable model mainly depends on the frequency range of the study. Appropriate cable models will be chosen for the DC fault protection analysis with simulation comparison as verification of the π-model analysis.

(2) *Fault Current Frequency*

Traditional fault analysis and solutions for AC distribution and transmission systems are well understood and have led to mature technologies. To clarify the analysis for traditional AC system fault conditions, the capacitor discharging part in the AC fault analysis is introduced here as a reference.

In the IEEE Standard 551 (2006)—"Recommended practice for calculating short-circuit currents in industrial and commercial power systems" [15]—the normal capacitor discharging currents from power factor correction capacitors or harmonic filters have been considered in ANSI or IEC calculation procedures. Even for conservative models with larger sized capacitors, the result is still that capacitor discharge currents will have no effect on circuit breaker fault clearing operations. Therefore the standard still does not recommend that capacitors be added to system simulations with detailed cable model for breaker duty calculations. Because of the low capacitance value, the stresses associated with capacitor discharge currents have high-frequency components. Hence the simulations provided are with the most detailed model—frequency-dependent model in phase—for breaker duty determinations.

However, with a large DC-link capacitor, the frequency is much lower for high power DC systems—in terms of several Hz. Therefore if appropriate simple π-model parameters are chosen, this will be precise enough for fault current calculation. To test the accuracy of the π-model for fault transient response simulation, the first phase of DC-link capacitor discharge is simulated using PSCAD/EMTDC. The most detailed frequency dependent phase model in PSCAD/EMTDC is applied as comparison, which includes all the conductor layers: copper core, sheath, and armor. Detailed cable physical data and underground environment data can be found in Mura et al. [16]. The corresponding lumped π-model parameters for simulation comparison are listed in Table 2. An ideal DC voltage source is connected to a resistance load through cables. A short-circuit fault is applied across the load to produce a transient response in the system.

With appropriate *RLC* parameters (calculated according to Ametani [17]), the π-model simulation results are close enough to the accurate cable model as shown

Table 2 Cable π-model parameters

Parameter	Value
Resistance r	0.005 Ω/km
Inductance l	0.5 mH/km
Rated voltage	200 kV
Cable length	15 km
DC-link capacitor	10 mF
Initial current	4 kA

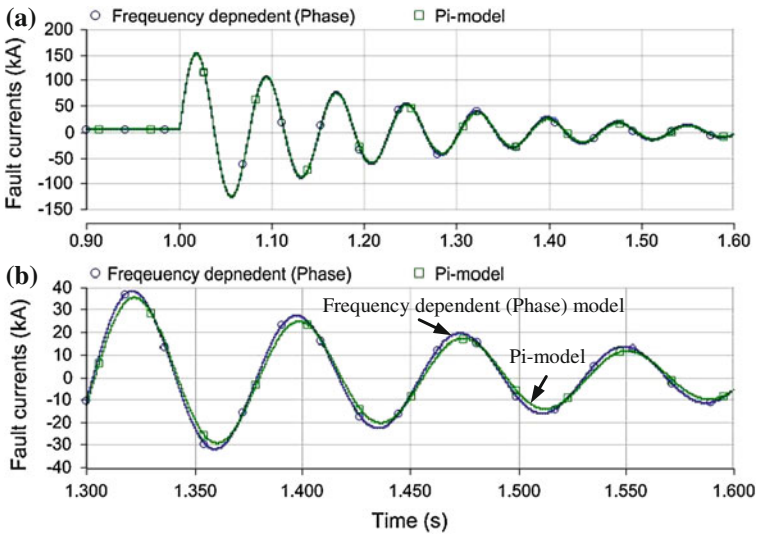

Fig. 4 A comparison between the frequency dependent phase model and the π-model of the cable during a DC fault

in Fig. 4a. Figure 4b shows some minor current differences between the two simulation results. This is due to the various frequency components in the over-current which sees a frequency-independent set of π-model parameters resulting in calculation error. However, the difference is only perceptible toward the end of the fault. The first wavefront can be fitted exactly the same as that with a detailed model, which is adequate for accurate protection relay setting and configuration.

3.2 DC Bus Fault

When the fault distance estimated from the relay point is zero, the fault can be considered as occurring on the DC bus (which is at the same electrical point as the relay in terms of the equivalent circuit), an example is shown in Fig. 1 (fault f_2). Since there is no node with more than one output connection in a radial system, for CB

coordination, DC bus faults are the same as cable faults. However, for meshed systems, a DC fault is severe especially at a location with multiple output connections, i.e., the DC bus. That means at least three CBs (one for input-side and two for output-side) are involved and the coordination for uni-directional DC CBs is necessary for their selective operation. This design process will be discussed in the following section.

4 Protection Scheme for Meshed DC Systems

According to the analysis in Sect. 3, the protection scheme design depends on the fault characteristics and the type of CB applied. The key issue is the strategy of a selective but reliable CB coordination method. The proposed protection coordination is realized by distance evaluation without communication between distant relays. The CB fault tripping requirements are: (1) The DC current and voltage are required to be continuously monitored during system operation. (2) When overcurrent is detected, the equivalent fault distance is evaluated rapidly using a voltage difference comparison method. (3) The assessed distance will be used to compare with the relay preset values to decide when and whether to trip the CB.

4.1 High-Power DC Switchgear Allocation

High-power DC switchgear is still under development with few mature commercial products. The traditional mechanical structured CB used in AC systems cannot be applied due to the slow fault isolation speed and the requirement of zero-crossings in the fault current. Therefore, power electronic devices are used to quickly block fault currents, such as IGBT and gate turn-off thyristors (GTOs). Generally, CBs of this kind are called solid-state CBs (SSCBs). One option includes a paralleled mechanical switch S_p as an auxiliary switch for lower loss during normal operation, a metal-oxide-varistor surge arrester MOV_{CB}, and power electronic blocking device PE_{CB}, Fig. 5a. The PE_{CB} block can be a parallel or series topology. Figure 5b, c realise bi-directional current block functions. Sometimes, a series inductance L_{CB} and a switch S_s are used as a fault current limiter and to provide an obvious electrical isolation point for the network operator, i.e., as a disconnecter. This CB topology can be seen as device redundancy to enhance reliability, as a comparison with topology redundancy.

The technical challenges for high-power DC CBs are the current isolation capability of power electronic devices, their high costs and their losses. Although some fault tolerant converters can reduce the allocation of CBs, as long as the development of this DC network includes traditional VSCs, reliable system protection relies on DC CBs. At this stage, in terms of device number, it is still economical to allocate DC CBs. Multi-IGBT devices could be used in series or parallel connection to increase the voltage or current ratings, particularly for high-overcurrent situations.

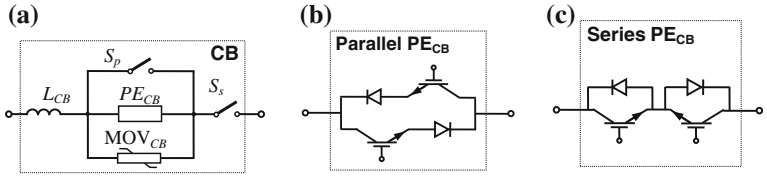

Fig. 5 A DC CB option: **a** DC CB configuration; **b** parallel connected bi-directional PE block; **c** series connected bi-directional PE block

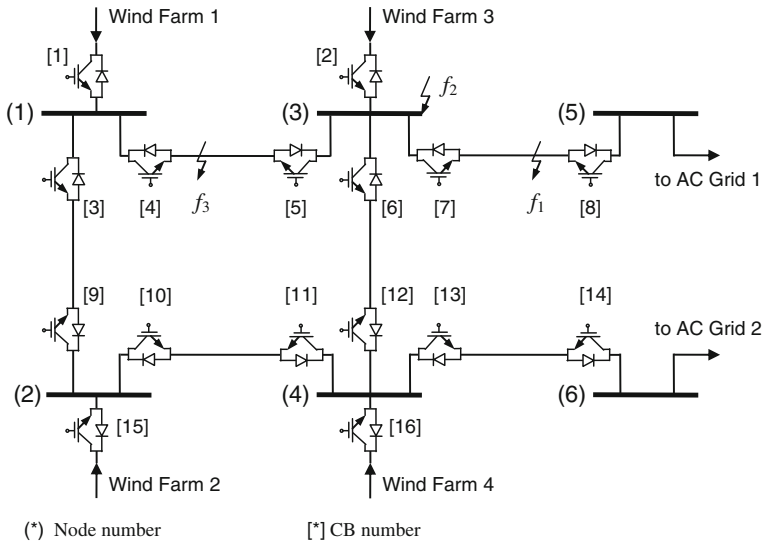

Fig. 6 DC CB allocation and numbering for relay configuration and coordination

The DC switchgear allocation is shown in Fig. 6 for the six-node test system. Uni-directional current-blocking DC CBs are used. This is a trade-off option considering both economic costs and function. The CB at each cable end has only one IGBT for fault current blocking but the two CBs can cooperate to isolate faults that occur between them on the cable. This requires only half the number of power electronic devices for fault current cut-off compared to the fully functioned bi-directional CBs, with half the loss but with a reduction in functionality. This CB allocation and configuration will influence the coordination strategy design. If bi-directional functionalised CBs are used, the multi-loop coordination strategy of the AC system can be applied to this DC loop protection analysis [7, 8].

The operating state of the wind farm depends on the wind resource conditions. The power acquired from a large wind turbine is variable but normally varies over at time period of seconds. Simulation of variable wind speed conditions have been performed using the wind profile shown in Fig. 7. In the simulation, the whole wind farm is exposed simultaneously to the wind profile which is the most severe case of power flow and current variation on the cable. The wind model applied is

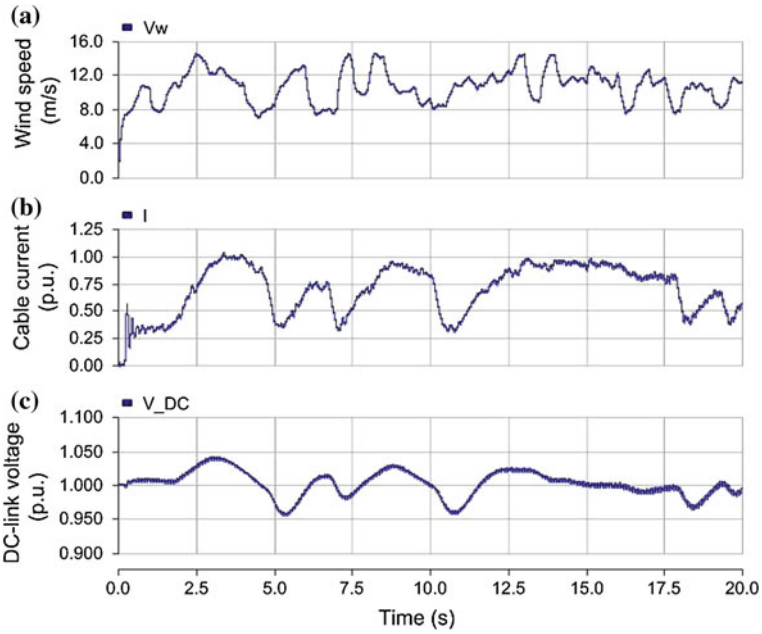

Fig. 7 DC cable current and voltage responses under wind speed fluctuation: **a** wind speed (ms^{-1}); **b** cable current (p.u.); **c** inverter DC-link voltage (p.u.)

from PSCAD/EMTDC with gusts, noise and a rated speed of 12 ms^{-1}. The shear and tower effects which result in a flicker power quality problem [18] are not considered. This will not influence the protection system operation.

The results in Fig. 7 show that: (1) There can be steep current increase and decrease; (2) DC-link voltage fluctuation is not as dramatic as under fault conditions. Aggregation of wind turbine output reduces the fluctuation effect. Hence the power fluctuation due to changes in wind conditions will not influence the relay system performance as long as the rate of change of current is not utilized for fault detection. The DC fault currents are always extreme where overcurrent occurs in milliseconds and is distinct enough from normal fluctuations for fault identification.

The power flow calculation for this linear system will obey basic physical principles, which will not need a specific algorithm for the convergence of results, like those commonly used for nonlinear AC systems. In this DC system, all the power sources can be calculated separately to estimate current flow according to the superposition theorem. Therefore the theoretical power flow results can be calculated almost instantaneously which is helpful for the real-time decision process. Figure 8 shows a power increase due to a change in system operation. There are high rates of change of current in some cables which reinforces the need to not use rate of change of current in the decision-making process.

Another issue is the exclusion of current harmonics due to the modulation method of the converters [16]. The harmonics are with known high-order

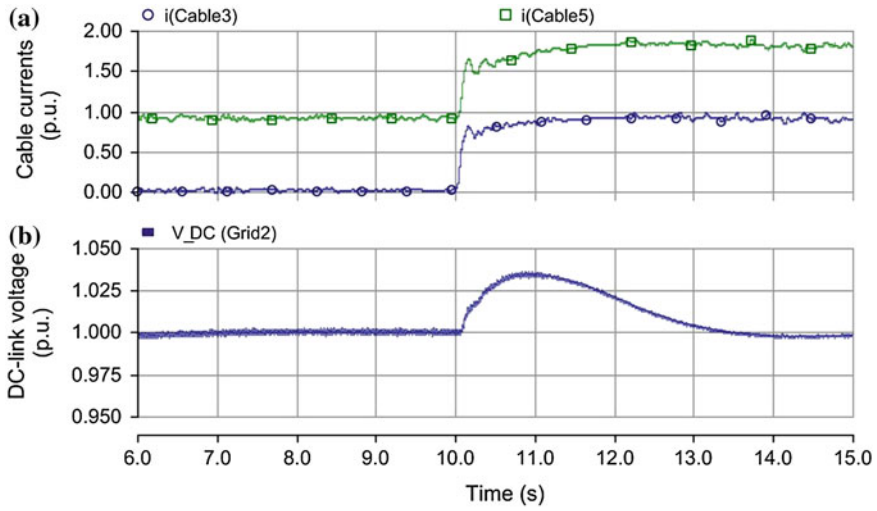

Fig. 8 DC cable current and voltage responses under sudden power increase: **a** cable currents (p.u.); **b** inverter DC-link voltage (p.u.)

frequencies and can be eliminated from the method used to detect faults via frequency detection. Hence, only in the low frequencies given in Table 1, current and DC-link voltage amplitude and direction changes will the signals be used to detect fault conditions.

4.2 DC CB Relay Coordination Relations

For a very complex multi-loop network, it is necessary to describe the relay coordination relations by definition of the dependency degrees [8, 9]. The primary protection relay set (PPRS), primary protection dependency degree (PD), and backup protection dependency degree (BD) are defined as functional dependency [8].

Protection setting of relay $R_{[x]}$ depends on the relay setting $R_{[i]}, R_{[j]}, \ldots, R_{[n]}$ to realise coordination. Then $\{R_{[i]}, R_{[j]}, \ldots, R_{[n]}\}$ is called the PPRS. Number n is defined as PD. According to the cooperation principle between primary protective relays and backup protective relays, the protection relay $R_{[2]}$ should cooperate with $R_{[1]}$, i.e., the setting value of $R_{[2]}$ must be calculated in terms of the setting value of $R_{[1]}$. Moreover, the time delay of the backup $R_{[2]}$ must avoid the most serious diode freewheel phase (short-circuit fault phase II in Table 1). Analogically, $R_{[3]}$ cooperates with $R_{[2]}$, $R_{[m]}$ cooperates with $R_{[m-1]}$, and $R_{[1]}$ cooperates with $R_{[m]}$ as a loop. Consequently, the cooperation relations among protective relays $R_{[i]}, R_{[j]}, \ldots, R_{[m-1]}\ R_{[m]}$ result in a circulation. BD is the relay number which can

Table 3 Relay coordination relations and coordination dependency degrees

Relay	PPRS	PD	BD
[1]	∅	0	2
[2]	∅	0	3
[3]	{[10], [15]}	2	1
[4]	{[2], [6], [7]}	3	1
[5]	{[1], [3]}	2	2
[6]	{[11], [13], [16]}	3	2
[7]	AC grid 1	1	2
[8]	{[2], [5], [6]}	3	0
[9]	{[1], [4]}	2	1
[10]	{[12], [13], [16]}	3	1
[11]	{[9], [15]}	2	2
[12]	{[2], [5], [7]}	3	2
[13]	AC grid 2	1	2
[14]	{[11], [12], [16]}	3	0
[15]	∅	0	2
[16]	∅	0	3

∅ empty set

act as backup for others. Table 3 shows the PPRS, PD, and BD of all the relays in the example section network in Fig. 6.

These dependency degrees are used to determine the Minimum loop-Breaking Point Set (MBPS) for multi-loop systems to be broken down to radial systems, then the simple distance coordination method can be carried out to realize selection. If DC/DC isolation transformers are applied [12], the system can be automatically separated into radial sub-networks. But this requires reliable DC/DC transformers and additional device costs and power losses will be incurred.

4.3 Protection Scheme

The steps of the protection scheme are defined as follows and are illustrated in Fig. 9.

(1) *Relay setting preparation*. At the planning stage, the overcurrent threshold i_{th} and voltage drop threshold v_{th} are set. In this section, i_{th} is chosen as 2.1 p.u. to avoid tripping during normal operation when power flow could be 2.1 p.u. due to a previous CB trip (assume normal operation can be up to 1.05 p.u. for each wind farm). The voltage drop threshold is $v_{th} = 0.5$ p.u. for the DC-link voltage.

(2) *Real-time monitoring*. For each wind resource sampling period (e.g. 1 s), calculate the system power flows and measure relay point current and voltage amplitudes for each sampling period (e.g. 50 μs) as state monitoring. The measurement equipment should have a short sample period to ensure the

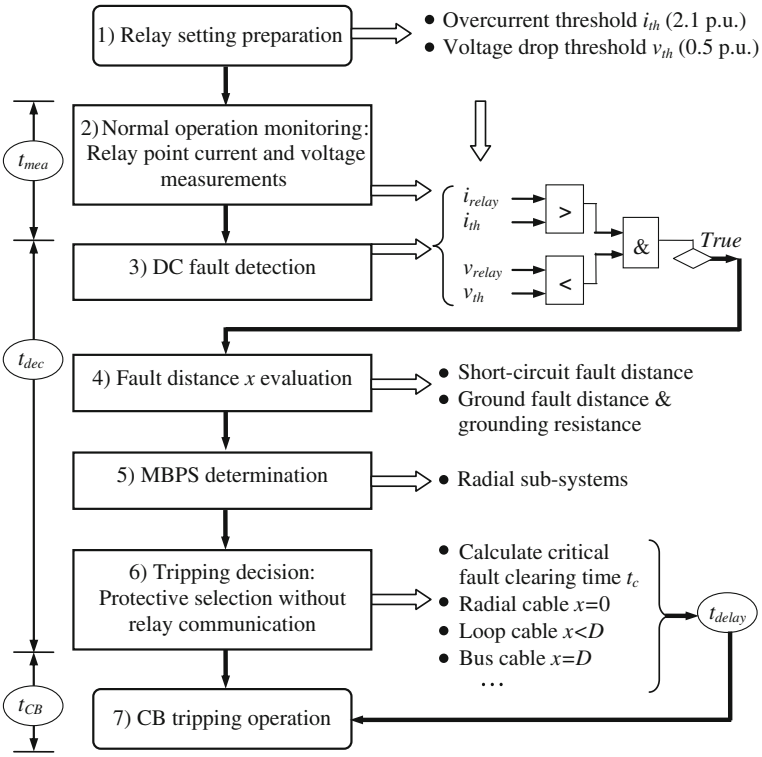

Fig. 9 The proposed DC meshed network protection flowchart

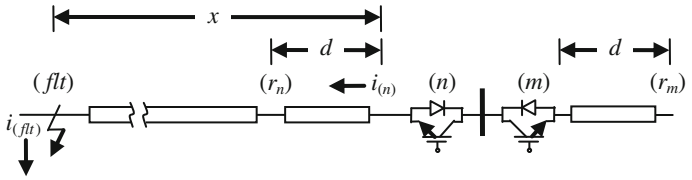

Fig. 10 Distance evaluation with two voltage divider measurements

relays have enough sampling points to deal with fault detection and tripping operation.

(3) *Real-time fault detection*. The abrupt change of currents and DC-link voltage collapse are compared with the preset threshold values. Practically, this will take at least one current and voltage sampling time-step to complete.

(4) *Real-time distance evaluation*. After the fault is detected, a distance calculation is performed using voltage comparison. A reference relay voltage sensor unit (r_i) is equipped for the relative voltage calculation, it is located near the main relay point on the same section of cable, as shown in Fig. 10, to avoid

long-distance communication issues. Voltage dividers are used for voltage measurements. The distance between them is known as d, so the fault distance measured from this reference is

$$x = \mathrm{d}\, v_{(n)} / \left(v_{(n)} - v_{(r_n)}\right). \tag{1}$$

(5) *Real-time MBPS determination*. The multi-loop breaking-points are chosen with the BD relation of the minimum distance relay points as the start. Then the system is separated into radial branches with the MBPS.

(6) *Tripping decision*. If a fault is detected from step (3), a corresponding relay delay time for the CB will be applied. At this stage a decision is made as to whether the fault is in the protection region of this CB. It will trip after a given delay time as backup protection, or immediately as primary protection. Firstly, the critical time t_c (for short-circuit fault phase II in Table 1) is calculated at each relay point as the tripping period upper limit. In respect of the evaluated distance x, the critical time is

$$t_c = \frac{\pi - \arctan(V_0 C\omega' / (V_0 C\delta - I_0))}{\omega'} \tag{2}$$

where $\omega' = \sqrt{\omega_0^2 / x - \delta^2}$, $\omega_0 = \sqrt{\delta^2 + \omega^2}$, $\delta = R/(2L)$, $\omega^2 = 1/(LC) - [R/(2L)]^2$. C, R, and L are the DC-link capacitance, fault-length DC cable equivalent π-model resistance and inductance respectively. The values of V_0 and I_0 used are from real-time measurement one time-step before the fault detection. This critical time t_c will be used to set the upper limit of relay delay time for backup CBs.

(7) *CB tripping operation*. After waiting the consequent time delay, the CB trips with IGBT block and possible disconnecter operation. The time for the CB to extinguish the fault current is designated as t_{CB}.
The total protection clearing time includes the measurement time t_{mea}, decision and evaluation time t_{dec}, resulting delay time t_{delay}, and CB time t_{CB}, as shown in Fig. 9. Again this has to be completed before the appropriate critical time t_c. The selection decision step without relay communication is described in detail as follows.

4.4 Protective Selection without Relay Communication

To avoid the use of communication between distant relays, the selection is realised by the following assumptions and measurement allocations.

(1) The CBs just connected to one radial cable or a wind farm will operate immediately only when their evaluated distance x is exactly or almost zero. The DC-chopper system across the wind farm DC-link must then operate to absorb all the generated power to avoid an overspeed condition. Meanwhile the wind farm needs to be stopped. If x is not zero, it will always wait for

a delay time for the primary cable protection to operate and form a possible new power transmission route around the loop.

(2) If the CB at one end of the cable detects exactly the cable length D as fault distance, this means the fault has occurred at the DC bus connected to other end of this cable. This CB will trip immediately because the CB near the DC bus cannot block fault current by itself due to the reverse diode of the CB in which reverse current flows. This is the main difference from AC protection, where the CB near an AC bus is the fastest primary protection. However, this depends on the accuracy of distance evaluation algorithm, especially for a ground fault with grounding resistance. Hence an accurate and efficient fault distance evaluation method is required.

(3) If the value of the evaluated distance is negative then the fault did not occur on this cable so the system will wait for a delay time (as shown the CB relay point (m) in Fig. 10, for the fault (*flt*), $v_{(m)} < v_{(r_m)}$, hence evaluated distance $x = \mathrm{d}\, v_{(m)} \big/ \left(v_{(m)} - v_{(r_m)}\right) < 0$).

Three examples of protection coordination for typical fault conditions are shown in detail in Table 4 to illustrate the decision process. (1) For a cable fault f_3 occurring in a loop, Fig. 1, the absolute distance range is used to categorize all the relay points, where D is the cable length (e.g. 200 km in Fig. 1). (2) For each of the absolute distance categories, the "+" distance relays are the primary protections relays because the fault is detected within their protection range. For others in this category, those only connected to a VSC source are in the second order, because if the primary protection CBs fails to trip, it can be seen as a bus fault, where the VSC definitely needs to be tripped. (3) The others in this category are ranked as the third order.

This ordering process continues until all the categories are sorted to yield the trip order table. These rules are the same as for a radial cable fault like f_1. However, for DC bus fault, it is different, as the CB near the faulted DC bus cannot isolate fault current as it flows through freewheel diodes. Therefore if a relay evaluates a distance equal to the cable length, D, its CB has primary priority, e.g. relay $R_{[4]}$, $R_{[8]}$, and $R_{[12]}$ in Table 4 under the condition of bus fault f_2.

Communication may be needed for CB relays at the same DC bus but because they are physically close such communication is practical. A cable ground fault with a large resistance is not as serious as a short-circuit fault and a time delay is tolerable. But a ground fault on the DC bus can be precisely detected even without accurate grounding resistance evaluation. For example, it is easy for relay $R_{[2]}$ to identify a bus fault, f_2, when the ground distance evaluation is exactly the same as that evaluated by $R_{[5]}$, $R_{[6]}$, and $R_{[7]}$ The cable length inductance ratio with typical grounding resistance can be used as a reference for a fuzzy decision. For instance, evaluated distance from $R_{[4]}$ may not be exactly D, but 1.5 D. However, it still needs to trip first as the primary protection.

Table 4 Protective order selection without relay communication

Loop cable fault f_3					Radial cable fault f_1					Bus fault f_2				
Absolute distance	Distance sign	Radial source only	CB relay	Result tripping order	Absolute distance	Distance sign	Radial source only	CB relay	Result tripping order	Absolute distance	Exact distance	Radial source only	CB relay	Result tripping order
$\|x\| \leq D$	+	N/A	[4] [5]	1	$\|x\| \leq D$	+	N/A	[7] [8]	1	$\|x\| \leq D$	$x = 0$	√	[2]	1
	N/A	√	[1] [2]	2		N/A	√	[2]	2		$x = D$	N/A	[4] [8] [12]	2
	−	×	[3] [6] [7]	3		−	×	[5] [6]	3		$x = 0$	×	[5] [6] [7]	3
$D < \|x\| \leq 2D$	N/A	√	[8] [15] [16]	4	$D < \|x\| \leq 2D$	N/A	√	[1] [16]	4		$x = -D$	√	[1] [16]	4
			[9] [10] [11] [12] [13]	5				[3] [4] [11] [12] [13]	5		$x = -D$	×	[3] [11] [13]	5
$2D < \|x\| \leq 3D$	N/A	√	[14]	6	$2D < \|x\| \leq 3D$	N/A	√	[14] [15]	6	$D < \|x\| \leq 2D$		√	[14] [15]	6
						−		[9] [10]	7			×	[9] [10]	7

Table 5 PMSG parameters

Parameter	Value
Rated power P_n	300 MW
Rated output voltage V_{sn}	99 kV
Rated frequency f_g	50 Hz
Pole pair no. P_p	100
Phase resistance	0.068 p.u.
Phase inductance	0.427 p.u.

Table 6 VSC parameters

Parameter	Value	
	Wind farm VSC rectifier	AC grid VSC inverter
Rated power	300 MW	600 MW
DC voltage	±100 kV	±100 kV
DC-link capacitance	10 mF	20 mF
Choke inductance	18 mH	22 mH
Transformer voltages	99/96 kV	96/110 kV

5 DC Wind Farm Protection Simulation Results

A simulation system of the proposed Supergrid section is modeled in PSCAD/EMTDC. Network parameters of the system are shown in Fig. 1. The PMSG and VSC parameters are provided in Tables 5 and 6. A detailed frequency-dependent phase cable model is employed in the simulations. The same DC cable π-model parameters in Table 2 are used for critical tripping time t_c calculations. The proposed protection scheme is applied to this specific DC wind farm system to show the protection results. The faults simulated are short-circuit faults and ground faults at the three selected points in Fig. 1 and Table 4. After the faults occur, the VSC IGBTs are blocked for self-protection. The per unit power calculation uses 600 MW as the base value for each grid-side VSI connected to an AC grid. Finally in Sect. 2, the aforementioned cable modeling comparison is also performed on this system for a short-circuit fault.

5.1 DC Radial Cable Short-Circuit/Ground Fault Condition

A short-circuit and a positive-side metallic ground fault are applied at f_1 (60 km from VSI1) at $t = 10.0$ s. Figures 11 and 12 are the fault overcurrents without protection. In Fig. 11, the total short-circuit fault current for VSI1 side $i_{(\text{fault})}$ reaches more than 210 kA—up to 70 times of the rated value (3.0 kA for 600 MW wind power transmitted in ±100 kV voltage level). The main contribution comes from the discharge of the DC-link capacitor. After the capacitor discharge phase,

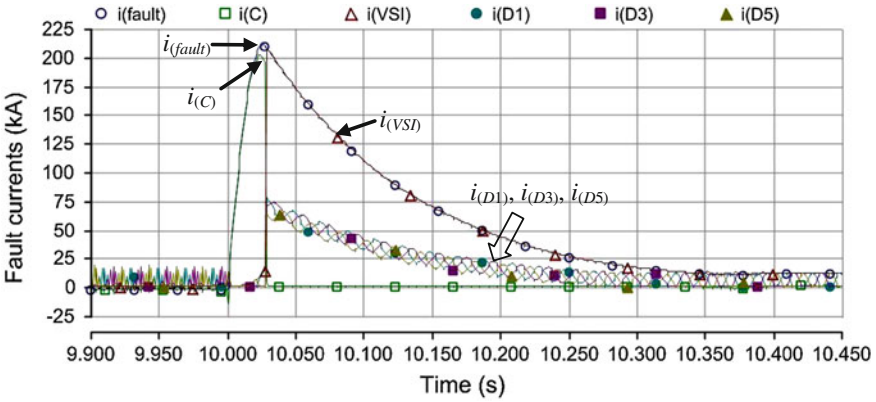

Fig. 11 Short-circuit fault currents flow through the fault point f_1 $i_{(\text{fault})}$, DC-link capacitor $i_{(C)}$, voltage source inverter $i_{(\text{VSI})}$, and conducting freewheel diode currents $i_{(D1)}$, $i_{(D3)}$, $i_{(D5)}$. Note that the VSI freewheel diode currents share VSI current equally

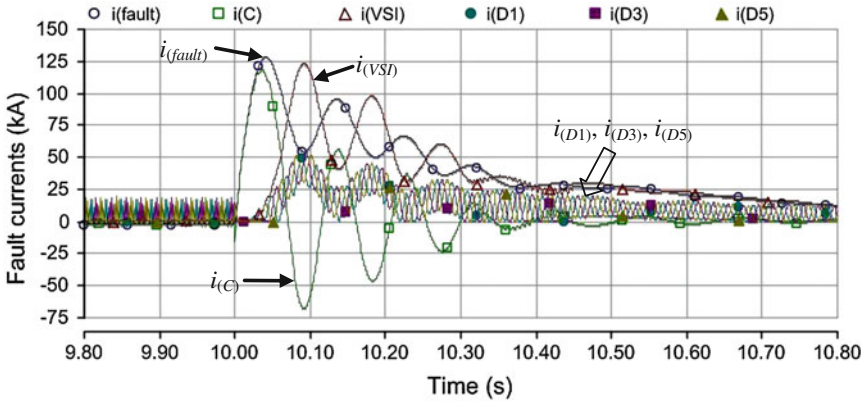

Fig. 12 Ground fault currents flow through the fault point f_1 $i_{(\text{fault})}$, DC-link capacitor $i_{(C)}$, voltage source inverter $i_{(\text{VSI})}$, and its three-phase diodes $i_{(D1)}$, $i_{(D3)}$, $i_{(D5)}$

the most vulnerable component—diodes—suffer during the freewheel phase (short-circuit phase II in Table 1). The diode freewheel overcurrent phase happens after 28 ms, with abrupt VSI current $i_{(\text{VSI})}$ distributed in the three phase diodes $D1$, $D3$, and $D5$ as $i_{(D1)}$, $i_{(D3)}$, and $i_{(D5)}$. This abrupt overcurrent is about 5 times normal (from 15 to 75 kA). This has the most serious impact on the VSC-HVDC system and will immediately destroy the converter. At the same time, the AC-side grid currents will feed into the fault through VSI1 freewheel diodes, which results in the oscillation and absorption of active and reactive power from the AC grids (shown in Fig. 13).

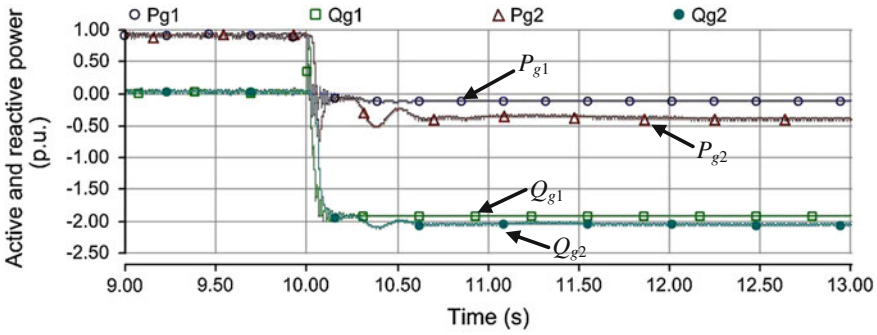

Fig. 13 Active powers (P_{g1}, P_{g2}) and reactive powers (Q_{g1}, Q_{g2}) of the two grid-side VSIs under short-circuit fault f_1 without CB protection

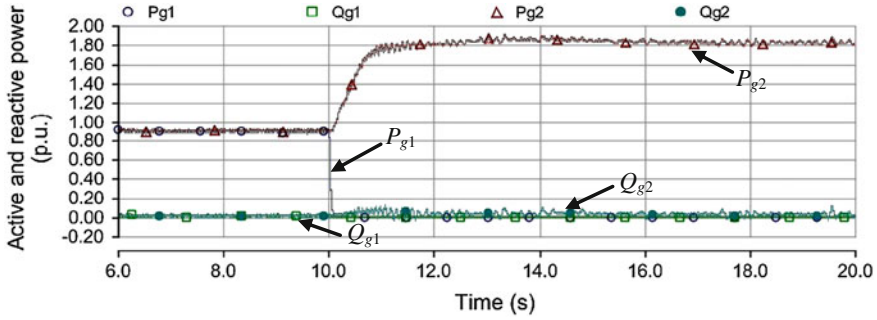

Fig. 14 Active powers (P_{g1}, P_{g2}) and reactive powers (Q_{g1}, Q_{g2}) of the two grid-side VSIs under short-circuit fault f_1 with CB protection

For the positive cable ground fault, although it is metallic, the fault current is not as serious as the short-circuit condition—up to 125 kA in Fig. 12, as the fault current loop has the transformer winding as a current limiter. Furthermore, there is no severe overcurrent through the freewheel diode. The diode currents increase gradually.

With immediate $CB_{[7]}$ and $CB_{[8]}$ tripping to clear the fault, and other CBs as backup protections for coordination, the system will still operate with all the power flows to AC Grid 2, P_{g2} about 1.80 p.u.—twice the value before fault, 0.90 p.u. (shown in Fig. 14). The system will experience a transient period of 2 s and then reach a new steady-state. There will be no overcurrents that threaten the system devices and all the wind farms still operate to supply power to the AC Grid 2.

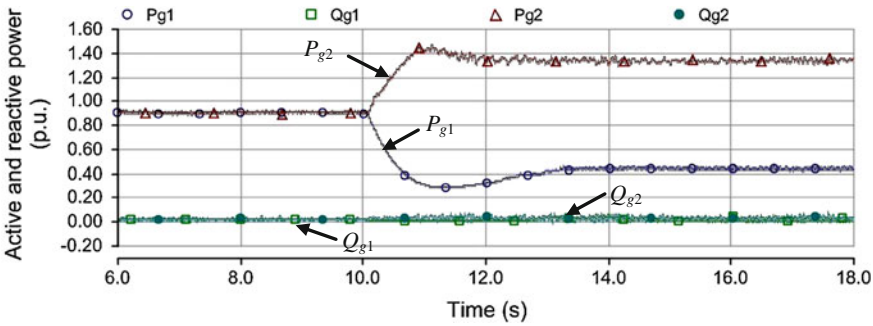

Fig. 15 Active powers (P_{g1}, P_{g2}) and reactive powers (Q_{g1}, Q_{g2}) of the two grid-side VSI under short-circuit fault f_3 with CB protection

5.2 DC Loop Cable Short-Circuit/Ground Fault Condition

The fault overcurrents for this fault location are not shown; they are similar to the previous radial cable condition. Here the normal operation condition is introduced. Because the network is symmetrical, for normal operation, there is no power flowing in the two link-cables (Cables 3 and 4 in Fig. 2), i.e., they are in stand-by condition. When the fault f_3 occurs on Cable 1, the power from Wind Farm 1 can flow from Cable 3. The tripping of $CB_{[4]}$ and $CB_{[5]}$ will separate the network as two radial branches: The power of Wind Farm 3 flows to AC Grid 1; while the power from the other three flows to AC Grid 2. Simulation results in Fig. 15 show that the active power of AC Grid 1, P_{g1}, reduces to half of that before fault (from 0.90 to 0.45 p.u.). For AC Grid 2, the active power increases to 1.35 p.u., that is 3 × 0.45 p.u. It also takes about 3 s to reach the new state. During this process, the DC-link voltages of VSI1 and VSI2 are still in control, without large reactive power fluctuations.

5.3 DC Bus Short-Circuit/Ground Fault Condition

The DC bus fault f_2 with four connections through $CB_{[2]}$, $CB_{[5]}$, $CB_{[6]}$, and $CB_{[7]}$ will result in the tripping of the four CBs as shown in Table 4: $CB_{[2]}$, $CB_{[4]}$, $CB_{[8]}$, and $CB_{[12]}$. The protection performance of the resultant AC grid power flow is shown in Fig. 16. The only cable connection—Cable 2 has to be tripped from $CB_{[8]}$ hence no power is delivered to AC Grid 1. At the same time, Wind Farm 3 has to be curtailed until the bus fault is cleared. However, the other three wind farms (1.35 p.u. in total) still have a cable route (Cable 3–Cable 5–Cable 6) for power transmission to AC Grid 2.

The three cables (Cables 1, 2, and 4) connected to DC $Bus_{(2)}$ will be protected from the tripping of $CB_{[4]}$, $CB_{[8]}$, and $CB_{[12]}$. Hence their relay current measurements are scaled to 50 μs division (the simulation time-step) as shown in

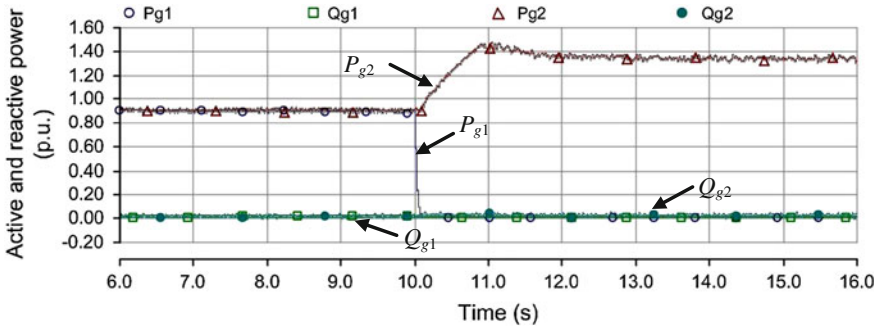

Fig. 16 Active powers (P_{g1}, P_{g2}) and reactive powers (Q_{g1}, Q_{g2}) of the two grid-side VSI under short-circuit bus fault f_2 with CB protection

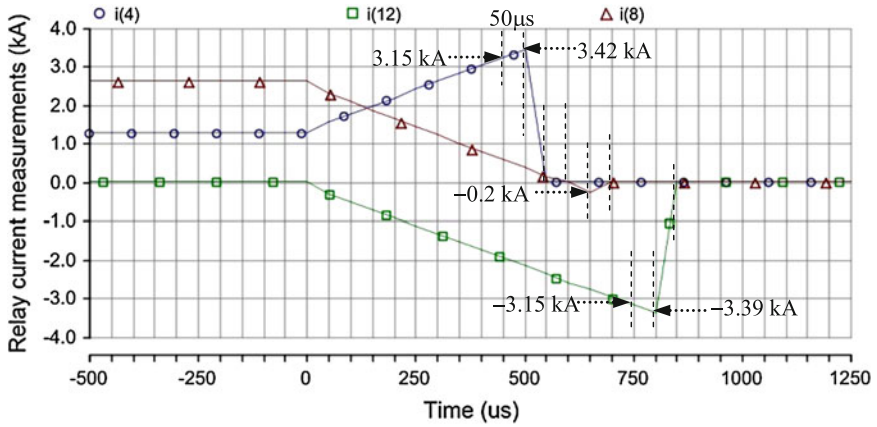

Fig. 17 Relay current measurements under DC bus short circuit fault f_2 condition: relay $R_{[4]}$ current $i_{(4)}$, relay $R_{[12]}$ current $i_{(12)}$, and relay $R_{[8]}$ current $i_{(8)}$

Fig. 17 to observe the tripping decision procedure. The overcurrent relay threshold is set to be 2.10 p.u. (3.15 kA) for relay $R_{[4]}$ and $R_{[12]}$. The positive power flow direction is defined as: from $R_{[4]}$ to $R_{[5]}$ for Cable 1; from $R_{[6]}$ to $R_{[12]}$ for Cable 4. Therefore, in Fig. 17, it takes about 450 μs for $R_{[4]}$ current $i_{(4)}$ to reach the trip value and then the tripping decision is simulated to be one time-step, i.e. 50 μs. Then the current increases to 3.42 kA, which is tolerable for the system for a short period of 50 μs. The CB fault current extinguishing time t_{CB} is also chosen to be 50 μs. The DC circuit breaker simulated is a self-defined PSCAD model of a uni-directional IGBT/diode switch, with gate control from the relay system. The actual minimum extinction time for the IGBT is set as 50 μs in this case, which is adequate for commercial IGBT devices. Hence in total it takes 500 μs to actually extinguish the fault current, much less than the freewheel effect time $t_c = 54$ ms for the fault distance of 200 km (calculated from Table 2).

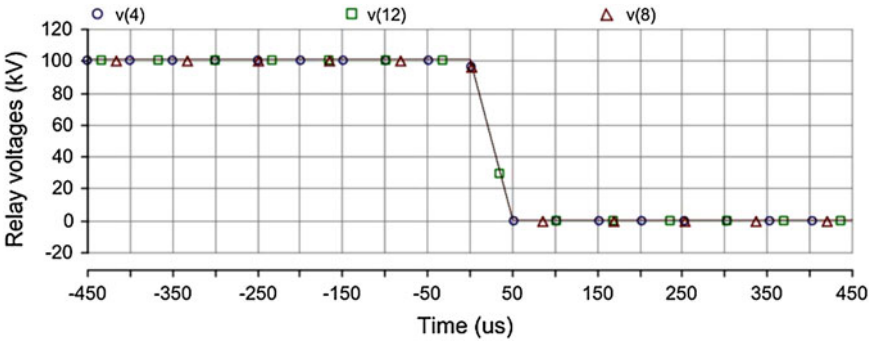

Fig. 18 Relay voltage measurements under DC bus short circuit fault condition: relay $R_{[4]}$ voltage $v_{(4)}$, relay $R_{[12]}$ voltage $v_{(12)}$, and relay $R_{[8]}$ voltage $v_{(8)}$

For Cable 4, the power flows in the negative direction, and the overcurrent $i_{(12)}$ reaches –3.15 kA after 750 μs and then reaches a maximum of –3.39 kA. Hence in total it takes 800 μs (including the tripping decision time which is one time-step, 50 μs) to actually extinguish the fault current, still well below the calculated critical time t_c.

For Cable 2, the normal power flow is only in one direction toward the AC Grid 1. Therefore, as long as the directional element in relay $R_{[8]}$ detects negative current, it will send signal for CB tripping. In Fig. 17, after crossing-zero, the negative current reaches –0.20 kA in one time-step, and then $CB_{[8]}$ immediately operated after $t_{CB} = 50$ μs.

The DC voltage measurements as the other detection criterion are shown in Fig. 18. All three voltages collapse to zero rapidly within 50 μs. This also proves that the main protection is based on overcurrent detection, hence the term overcurrent distance protection.

5.4 Cable Modeling Comparison

Simulation results of the cable short-circuit fault, f_1, with both the detailed model and the simple π-model are shown in Fig. 19. The results with the two models are close, except that some high frequency components in the diode currents have a phase delay due to the single inductance value in the π-model. However, the diode freewheel overcurrent period and fault overcurrent amplitude are close to the analysis and to the t_c calculation. The ground fault simulation results are not compared here because there is no abrupt change in diode current and the current oscillation pattern is similar to the example given in Fig. 4.

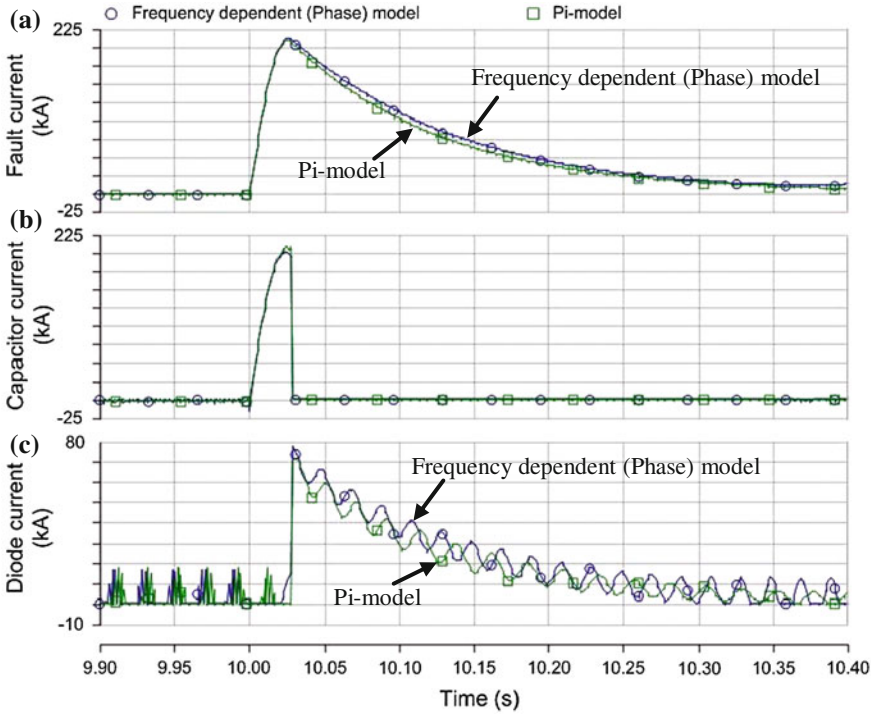

Fig. 19 DC wind farm fault current simulation comparison with the two cable models: **a** the total cable fault currents; **b** DC-link capacitor discharging currents; **c** VSC diode freewheel currents (Phase-*a* diode)

6 Conclusions

This chapter discusses the design of a protection scheme for a meshed HVDC network topology for offshore wind power grid integration. Key issues are introduced and possible solutions are presented based on a proposed typical network section. DC circuit breakers are allocated and configured with an appropriate coordination strategy. This protection scheme is defined and detailed as several steps. Simulation results of three typical fault conditions illustrate and verify the design concept.

The offshore DC transmission network with onshore AC grid connections may have multiple and hybrid loops. For instance, one AC transmission cable connecting the two AC grid onshore substations in Fig. 1 will form a hybrid loop with both AC and DC connections. The AC and DC system breaker coordination should be considered due to the significant difference in operation time, as indeed does the protection influence on other AC CBs located in the vicinity of the onshore substations. Moreover, accurate and fast distance evaluation and grounding resistance assessment methods are required for real-time coordination application.

References

1. Gordon S (2006) Supergrid to the rescue. Power Eng 20(5):30–33
2. Ackermann T (2002) Transmission system for offshore wind farms. IEEE Power Eng Rev 22:23–27
3. Yang J, Fletcher JE, O'Reilly J (2012) Short-circuit and ground fault analysis and location in VSC-based dc network cables. IEEE Trans Ind Elect 59(10):3827–3837
4. Bresesti P, Kling WL, Hendriks RL, Vailati R (2007) HVDC connection of offshore wind farms to the transmission system. IEEE Trans Energy Convers 22(1):37–43
5. Jovcic D, Strachan N (2009) Offshore wind farm with centralised power conversion and DC interconnection. IET Gener Transm Distrib 3(6):586–595
6. Li X, Song Q, Liu W, Rao H, Xu S, Li L (2013) Protection of non permanent faults on DC overhead lines in MMC-based HVDC systems. IEEE Trans Power Deliv 28(1):483–490
7. Anderson PM (1999) Power system protection. IEEE Press, New York
8. Lu F (2005) Novel method for determining the optimal coordination sequence of directional relays in a complicated multi-loop power network based on coordination relationships between relays. J Auto Electr Power Syst 29:24
9. Yue Q, Lu F, Yu W, Wang J (2006) A novel algorithm to determine minimum break point set for optimum cooperation of directional protection relays in multiloop networks. IEEE Trans Power Deliv 21(3):1114–1119
10. Chinchilla M, Arnaltes S, Burgos JC (2006) Control of permanent-magnet generators applied to variable-speed wind-energy systems connected to the grid. IEEE Trans Energy Convers 21(1):130–135
11. Baran ME, Mahajan NR (2007) Overcurrent protection on voltage-source-converter-based multiterminal DC distribution systems. IEEE Trans Power Deliv 22(1):406–412
12. Jovcic D, Ooi BT (2010) Developing DC transmission networks using DC transformers. IEEE Trans Power Deliv 25(4):2535–2543
13. Liu X, Osman AH, Malik OP (2009) Hybrid travelling wave/boundary protection for monopolar HVDC line. IEEE Trans Power Deliv 24(2):569–578
14. Gustavsen B, Irwin G, Mangelrod R, Brandt D, Kent K (1999) Transmission line models for the simulation of interaction phenomena between parallel ac and dc overhead lines. Paper presented at the international conference on power systems transients, Budapest, Hungary, pp 20–24
15. IEEE Standard 551 (2006) Capacitor contributions to short-circuit currents (Chap. 7). In: IEEE recommended practice for calculating short-circuit currents in industrial and commercial power systems
16. Mura F, Meyer C, De Doncker RW (2010) Stability analysis of high-power dc grids. IEEE Trans Ind Appl 46(2):584–592
17. Ametani A (1980) A general formulation of impedance and admittance of cables. IEEE Trans Power App Syst PAS-99(3):902–910
18. Hu W, Chen Z, Wang Y, Wang Z (2009) Flicker mitigation by active power control of variable-speed wind turbines with full-scale back-to-back power converters. IEEE Trans Energy Convers 24(3):640–649

Control of Emerging Brushless Doubly-Fed Reluctance Wind Turbine Generators

Sul Ademi and Milutin Jovanovic

Abstract This chapter is concerned with field-oriented control (FOC) and vector control (VC) of a promising brushless doubly fed reluctance generator (BDFRG) technology for large-scale grid-connected wind turbines. The BDFRG has been receiving increasing attention because of the low capital and operation and maintenance costs afforded by the use of partially rated power electronics and the high reliability of brushless construction, while offering performance competitive to its well-known slip-ring counterpart, a doubly fed induction generator (DFIG). The two parameter independent control schemes have been developed for a custom-designed BDFRG fed from a conventional "back-to-back" IGBT converter. The preliminary studies have evaluated and compared the algorithms under the maximum torque per inverter ampere (MTPIA) conditions allowing the improved efficiency of the generator–converter set and thus the entire wind energy conversion system.

Keywords Wind power · Brushless · Doubly fed machines · Control

1 Introduction

The brushless doubly fed generators (BDFGs) have been considered as a reliable, cost-effective candidate for wind turbines [1–10], which have traditionally been served by a wound rotor induction machine either with a controllable external

S. Ademi (✉) · M. Jovanovic
Faculty of Engineering and Environment, Northumbria University,
Newcastle upon Tyne NE1 8ST, UK
e-mail: sul.ademi@northumbria.ac.uk

M. Jovanovic
e-mail: milutin.jovanovic@northumbria.ac.uk

J. Hossain and A. Mahmud (eds.), *Large Scale Renewable Power Generation*,
Green Energy and Technology, DOI: 10.1007/978-981-4585-30-9_15,

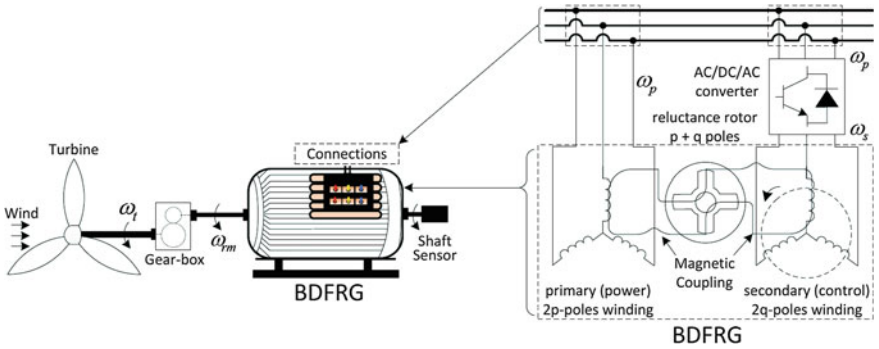

Fig. 1 A conceptual diagram of the variable speed WECS with BDFRG

resistance in the rotor circuit or operated in a doubly fed slip power recovery mode (DFIG) [11]. In these applications, where only a limited variable speed capability is required (e.g., typically, a 2:1 range or so around the synchronous speed [2, 6, 12]), the BDFG has retained the DFIG cost benefits of using a smaller inverter (e.g., around 25 % of the machine rating), but with higher reliability and maintenance-free operation by the absence of brush gear.

The BDFG has two standard stator windings of different applied frequencies and pole numbers, unlike the DFIG. The primary (power) winding is grid-connected, and the secondary (control) winding is supplied from a bi-directional power converter. A BDFG reluctance type (Fig. 1), the brushless doubly fed reluctance generator (BDFRG) [1–6], appears to be more attractive than its "nested" cage rotor form, the brushless doubly fed induction generator (BDFIG) [7–10, 13]. This preference has been mainly attributed to the prospect for higher efficiency [3] with simpler modeling and control[1] associated with the BDFRG cageless rotor of similar design to that of a modern synchronous reluctance machine [14–16]. However, the BDFG rotor must have half the total number of stator poles to provide the rotor position-dependent magnetic coupling between the stator windings, a prerequisite for the torque production [1, 4].

In light of the recently introduced grid codes requiring wind turbines to stay online and provide reactive power support for voltage recovery rather than being disconnected under faulty conditions, another important BDFG merit is the seemingly superior low-voltage fault ride through (LVFRT) capability to the DFIG. It has been shown that, owing to relatively large leakage inductances and thus lower fault current levels, the LVFRT of the BDFIG may be accomplished safely without a crowbar circuitry, and with the higher operating stability as well as the lower cost grid integration [17, 18]. These potential LVFRT performance

[1] Field-oriented control of the primary reactive power and electromagnetic torque is inherently decoupled in both the BDFRG and DFIG [20], but not in the BDFIG [8, 10, 26].

advantages over the DFIG can be carried over to the BDFRG featuring the leakage reactance values of the same order as the BDFIG.

Various control strategies[2] have been developed for the BDFRG over the years including scalar control [2, 19], field-oriented control (FOC) [2, 19, 20], direct torque control [5, 19], torque and reactive power control [21, 22], and direct power control [23]. Although a comparative analysis of these control methods has been partly made in [19] (and more detailed for the DFIG in [24]), to the best knowledge of the authors, no similar study has been reported specifically on FOC versus VC, and there has been no published work on true vector control (VC) of the BDFRG. The most likely reason is the misconception amongst the two terms (FOC/VC) which have been often interchangeably used to indicate the same control approach despite their quite distinctive meanings [25]. In the BDFRG case, the "FOC/VC" are commonly being referred to as the primary winding flux/voltage-oriented control, respectively, by analogy to the stator flux/voltage-oriented control of the DFIG.

The fact is that with a proper selection of the reference frames, the two popular control techniques become very similar in nature and dynamic response, especially with larger machines of lower resistances. Nevertheless, they have clear differences and performance trade-offs to be pointed out in this paper using the maximum torque (power) per inverter ampere (MTPIA) strategy [1, 2, 16] as a ground for their comparison on a large custom-designed 2 MW BDFRG [6]. The rationale behind looking at this particular control objective is the efficiency gain that can be achieved by reducing both the secondary winding copper and inverter switching losses [1, 2]. Extensive realistic simulation results taking into account the usual practical effects (e.g., transducers' DC offset, noise in measurements, and a four-quadrant power converter model with space-vector PWM) are presented to support the discussions.

2 Dynamic Model

The underlying principles of the FOC and VC algorithms can be better understood by having a closer insight into the space-vector theory and unusual torque producing mechanism of the BDFRM [4]. Assuming motoring convention and using standard notation, the BDFRM model in arbitrary rotating $d - q$ reference frames can be represented as [4]:

[2] A good literature review on control of the BDFIG can be found in [7–10, 18], and of the DFIG in [24, 27].

$$\left.\begin{aligned}
\underline{v}_p &= R_p\underline{i}_p + \left.\frac{d\underline{\lambda}_p}{dt}\right| = R_p\underline{i}_p + \left.\frac{d\underline{\lambda}_p}{dt}\right|_{\theta_p \text{ Const}} + j\omega_p\underline{\lambda}_p \\
\underline{v}_s &= R_s\underline{i}_s + \left.\frac{d\underline{\lambda}_s}{dt}\right| = R_s\underline{i}_s + \left.\frac{d\underline{\lambda}_s}{dt}\right|_{\theta_s \text{ Const}} + j\omega_s\underline{\lambda}_s \\
\underline{\lambda}_p &= L_p\left(\underbrace{i_{pd} + ji_{pq}}_{\underline{i}_p}\right) + L_{ps}\left(\underbrace{i_{sd} - ji_{sq}}_{\underline{i}^*_{sm}}\right) \\
\underline{\lambda}_s &= L_s\left(\underbrace{i_{sd} + ji_{sq}}_{\underline{i}_s}\right) + L_{ps}\left(\underbrace{i_{pd} - ji_{pq}}_{\underline{i}^*_{pm}}\right)
\end{aligned}\right\} \quad (1)$$

The above flux equations can be manipulated to:

$$\underline{\lambda}_p = \underbrace{L_p i_{pd} + L_{ps} i_{sd}}_{\underline{\lambda}_{pd}} + j \cdot \underbrace{(L_p i_{pq} - L_{ps} i_{sq})}_{\underline{\lambda}_{pq}} \quad (2)$$

$$\underline{\lambda}_s = \underbrace{\sigma L_s i_{sd} + \lambda_{ps_d}}_{\underline{\lambda}_{sd}} + j \cdot \underbrace{(L_s i_{sq} + \lambda_{ps_q})}_{\underline{\lambda}_{sq}} = \sigma L_s \underline{i}_s + \underbrace{\frac{L_{ps}}{L_p}\underline{\lambda}^*_p}_{\underline{\lambda}_{ps}} \quad (3)$$

where the primary and secondary winding are denoted by "p" and "s" respectively, $\sigma = 1 - L_{ps}^2/(L_p L_s)$ is the leakage factor, and λ_{ps} is the primary flux linking the secondary winding (i.e., the mutual flux linkage). The definitions of the 3-phase self ($L_{p,s}$) and mutual (L_{ps}) inductances can be found in [4, 14].

The fundamental angular velocity relationship for the electromechanical energy conversion in the machine with p_r rotor poles and $\omega_{p,s} = 2\pi f_{p,s}$ applied frequencies (rad/s) to the respective $2p$-pole and $2q$-pole windings (Fig. 1) is [4]:

$$\omega_{rm} = \frac{\omega_p + \omega_s}{p_r} = \frac{(1-s)\cdot\omega_p}{p+q} = (1-s)\cdot\omega_{\text{syn}} \Leftrightarrow n_{rm} = 60\cdot\frac{f_p + f_s}{p_r} \quad (4)$$

where the generalized slip is s $= -\ \omega_s/\omega_p$, and $\omega_{\text{syn}} = \omega_p/p_r$ is the synchronous speed (for $\omega_s = 0$, i.e., a DC secondary) as with a $2p_r$-pole wound rotor synchronous turbo-machine. Notice that $\omega_s > 0$ for super-synchronous operation, and $\omega_s < 0$ at sub-synchronous speeds (i.e., an opposite phase sequence of the secondary to the primary winding). It is interesting that the two speed modes of the BDFRG are equivalent to a $2p_r$-pole induction generator ($s < 0$), and that the speed can be expressed in the same generic form in terms of the slip despite the quite distinct operating principles [4].

The machine instantaneous torque and the rotor movement (i.e., the acceleration torque) taking into account friction terms can be expressed as follows [4]:

$$T_e = \frac{3p_r L_{ps}}{2L_p}(\lambda_{pd} i_{sq} + \lambda_{pq} i_{sd}) = \frac{3p_r}{2}(\lambda_{ps_d} i_{sq} - \lambda_{ps_q} i_{sd}) = \frac{3p_r}{2}(\lambda_{pd} i_{pq} - \lambda_{pq} i_{pd}) \quad (5)$$

$$T_a = J \cdot \frac{d\omega_{rm}}{dt} = T_e - T_L(\omega_{rm}) - F \cdot \omega_{rm} \quad (6)$$

Some important observations should be made about (1–3). While all the ω_p rotating vectors in the primary voltage and flux equations are in ω_p frame, the corresponding secondary counterparts, including the λ_{ps} components in (5), are rotating at ω_s and are in $p_r\omega_{rm} - \omega_p = \omega_s$ frame according to (4) and the BDFRG theory in [4]. Note also that $\underline{i}_{sm} = \underline{i}_s$ and $\underline{i}_{pm} = \underline{i}_p$ in (1) are the magnetically coupled currents from one machine side to the other of the same magnitude but with different frequency to the originating current vectors [4]. Given that λ_p and λ_{ps} in (5) are approximately constant by the primary winding grid connection, torque control can be achieved through the secondary dq currents in the ω_s frame.

Using (4), one can easily derive the mechanical power equation showing individual contributions of each BDFRG winding:

$$P_m = T_e \cdot \omega_{rm} = \underbrace{\frac{T_e \cdot \omega_p}{p_r}}_{P_p} + \underbrace{\frac{T_e \cdot \omega_s}{p_r}}_{P_s} = P_p \cdot \left(1 + \frac{\omega_s}{\omega_p}\right) = P_p \cdot (1 - s) \quad (7)$$

The machine operating mode is therefore determined by the power flow in the primary winding, i.e., to the grid for generating ($T_e < 0$) regime under consideration, while the secondary winding can either take or deliver real power (P_s) subject to its phase sequence, i.e., the ω_s sign; the BDFRG would absorb (produce) positive secondary power at sub (super)-synchronous speeds. Furthermore, following on the comments made on (4), note that (7) is the same form expression used for classical induction machines with P_p and ω_s playing the role of electromagnetic (rotor) power and slip frequency, respectively.

3 Controller Design

A structural block-diagram of the primary voltage/flux angle and frequency estimation technique with appropriate dq frame alignment options for FOC/VC in discrete form for real-time implementation is shown in Fig. 2. The entire BDFRG drive system configuration with a generic controller design is shown Fig. 3. The necessary computations and sequential control actions being made are largely self-evident from both the schematics. The functionality of the frame angle calculation blocks (A and B) in Fig. 3 has been detailed in Fig. 2. An angular form of (4), which provides a crucial link between the reference frame d-axis positions ($\theta_{p,s}$) and shaft encoder measurements (θ_{rm}) for control is:

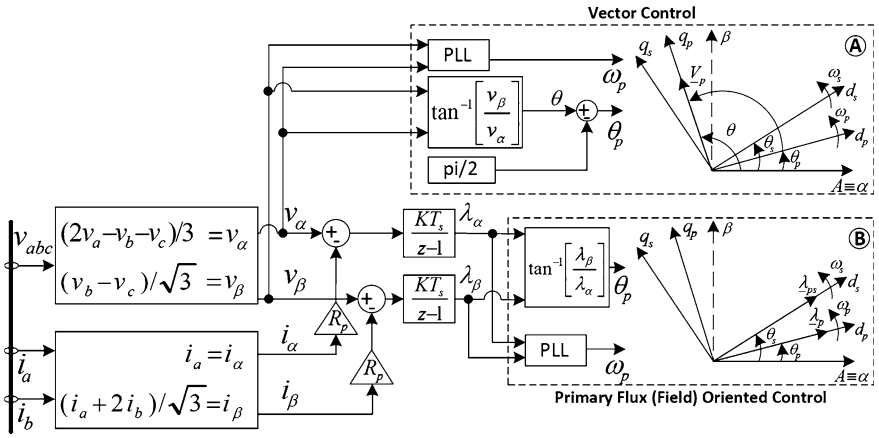

Fig. 2 Identification of primary voltage and flux vectors in a stationary α–β frame

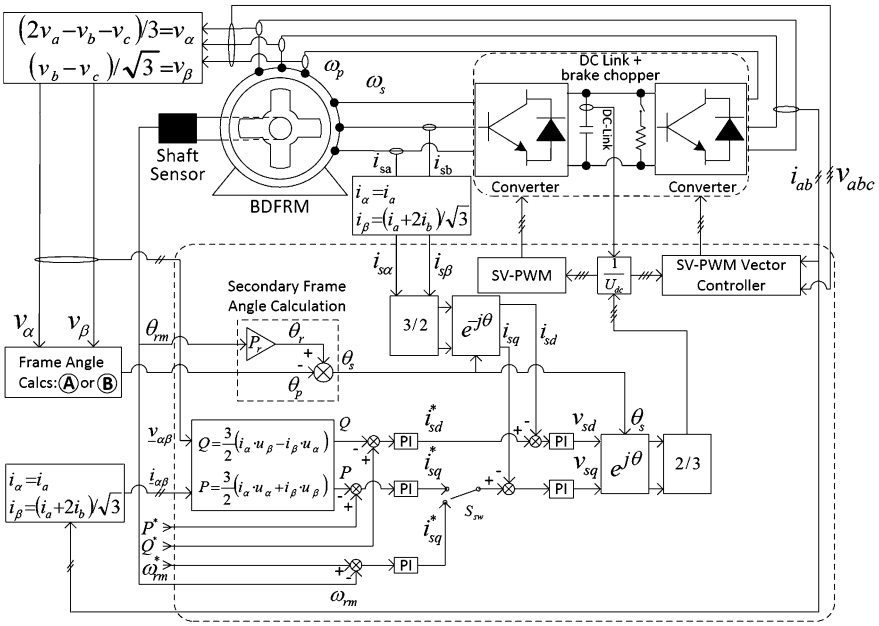

Fig. 3 Structure of the BDFRG drive setup

$$\omega_r = p_r \omega_{rm} = \omega_p + \omega_s \Leftrightarrow \theta_r = p_r \theta_{rm} = \theta_p + \theta_s \tag{8}$$

where $\omega_{rm} = d\theta_{rm}/dt$ is the rotor mechanical angular velocity.

For clarification, one should also be aware of the following important points in relation to Figs. 2 and 3:

- A standard phase-locked-loop (PLL) algorithm from the Simulink® library has been used to retrieve the primary voltage/flux angular velocities (ω_p), but not the respective stationary α–β frame angles (θ/θ_p), from the measured voltages and/or currents (Fig. 2). While a band-pass filter inside the PLL blocks undoubtedly helps deal with noise and DC offset in measurements introduced by the voltage and current transducers, it has a well-known down side of causing inevitable phase delays and inaccurate θ/θ_p estimates. Much better results can be achieved by estimating these directly from the voltage/flux $\alpha\beta$ components using an "atan" function. The ω_p estimation is immune to this problem as being affected by incremental and not absolute positions (i.e., $\omega_p = \Delta\theta_p/\Delta t$).
- The starting circuitry is not shown in Fig. 3. If a partially rated power converter is used then an auxiliary contactor is required to short the secondary terminals directly or through external resistors to avoid the inverter transient over-currents and allow the BDFRG to start as an unloaded induction machine. After reaching the no-load speed, the contactors are opened and the converter is connected. An alternative method may be to start the machine from the secondary side through the controllable inverter and then synchronize the primary winding to the grid applying the procedure for commercial DFIGs [28].
- A conventional vector controller with space-vector PWM of the active rectifier (e.g., the line-side IGBT converter) has been implemented (Fig. 3) for control of DC link voltage and unity line power factor. The relevant design details are beyond the scope of this chapter and can be found in [11, 29].
- The common PI regulators with anti-windup on the integrators and limiters (i.e., saturated outputs), readily available in Simulink®, have been employed throughout for power or speed control given the selector position (Fig. 3).
- The primary real (P) and reactive (Q) power have been worked out using the stationary frame voltage ($v_{\alpha\beta}$) and current ($i_{\alpha\beta}$) components (Fig. 3) despite the fact that the control has actually been done in the rotating secondary $d_s - q_s$ frame (Fig. 2). Considering that the power calculations are reference frame invariant, this is the least computationally intensive approach as unnecessary conversions of $v_{\alpha\beta}$ and $i_{\alpha\beta}$ into their $d_s - q_s$ equivalents and therefore the use of time-consuming trigonometric functions, can be avoided with obvious implications on the higher control rates and superior performance achievable in practice.
- The Y-connected primary and secondary windings have been derived with an isolated neutral point allowing the use of only two current sensors (e.g., in phases "a" and "b" so, $i_c = -i_a - i_b$) on each side (Fig. 3). However, as the primary supply voltages may not be balanced, having three rather than only two line voltage transducers is recommended for higher accuracy.
- The Q reference is often set to zero ($Q^* = 0$) for the unity primary power factor but can be any other value of interest for a given real power setting (P^*) in open-loop speed (i.e., power or torque) mode of the machine (Fig. 3). In variable speed drive or generator systems, ω^*_{rm} is the desired angular velocity. For example, either P^* or ω^*_{rm} may correspond to the Maximum Power Point

Tracking (MPPT) operating point of a wind turbine [2, 12] while Q^* may be chosen to optimize certain performance indicator of the machine like torque (power) per secondary ampere.

4 Control Principles

4.1 Vector Control

The control expressions can be derived from the BDFRG space-vector model (1) written in ω_p (e.g., $d_p - q_p$ for the primary winding) and ω_s (e.g., $d_s - q_s$ for the secondary winding) rotating frames (Fig. 2). This selection maps the variables into their natural reference frames where the respective vector components appear as DC quantities which are easier to control. Of particular interest is the secondary voltage equation in (1). Using (3), this can be simplified in steady state to:

$$\underline{v}_s = j\omega_s \underline{\lambda}_{ps} + (R_s + j\omega_s \sigma L_s)\underline{i}_s \tag{9}$$

The above expression shows a fairly proportional relationship (in vector sense) between the control voltage and the secondary current with the exception of nonlinearities introduced by the existing back-emf component. This gives an incentive for using a secondary current feedback loop PI controller (one in each $d_s q_s$ control axis) for determining the appropriate control voltage modulation index as illustrated in Fig. 3. A control law can be simply formulated as

$$\underline{v}_{s_{\text{ref}}} = PI(\underline{i}_{s_{\text{ref}}} - \underline{i}_s) \tag{10}$$

To avoid coupling effects between the controllable dq currents, the back-emf related disturbance should be compensated for improved performance.

Substituting for $\underline{i}_p$ from the $\underline{\lambda}_p$ equation of (1) into $\underline{S}_p = \frac{3}{2}\underline{v}_p \underline{i}_p^*$, with $\underline{i}_{sm} = \underline{i}_s$ in the respective frames, would lead to the following relationships for the primary mechanical (i.e., electrical power minus losses) and reactive power:

$$P_{p_{vc}} = P_{p_{el}} - \frac{3}{2} R_p i_p^2 = \frac{3}{2}(\lambda_{ps_d} i_{sq} - \lambda_{ps_q} i_{sd}) = P_{p_{\text{foc}}} - \frac{3}{2}\omega_p \lambda_{ps_q} i_{sd} \tag{11}$$

$$Q_{p_{vc}} = \frac{3}{2}\omega_p \left(\frac{\lambda_p^2}{L_p} - \lambda_{ps_d} i_{sd} - \lambda_{ps_q} i_{sq} \right) = Q_{p_{\text{foc}}} - \frac{3}{2}\omega_p \lambda_{ps_q} i_{sq} \tag{12}$$

Note that (11) could have also been derived using (5) and (7).

As can be seen from the above expressions, VC of P_p and Q_p is coupled as both the i_{sd} and i_{sq} secondary current components appear in (11) and (12). The level of coupling can be reduced by aligning the q_p-axis of the reference frame to the primary voltage vector as proposed in Fig. 2. In this case, $\underline{\lambda}_p$ would be phase shifted ahead of the corresponding d_p-axis depending on the winding resistance

values. This angular displacement is generally smaller with larger machines having lower resistances. Therefore, for the frame alignment choice as in Fig. 2, VC should be similar to FOC as $\lambda_{ps_d} > > \lambda_{ps_q}$ i.e., $\lambda_{ps_d} > > \lambda_{ps}$ so that (11) and (12) become

$$P_{p_{vc}} \approx P_{p_{foc}} = \frac{3}{2}\omega_p \lambda_{ps} i_{sq} = \frac{3}{2}\frac{L_{ps}}{L_p}\omega_p \lambda_p i_{sq} \tag{13}$$

$$Q_{p_{vc}} \approx Q_{p_{foc}} = \frac{3}{2}\frac{\omega_p \lambda_p^2}{L_p} - \frac{3}{2}\omega_p \lambda_{ps} i_{sd} = \frac{3}{2}\frac{\omega_p \lambda_p}{L_p}(\lambda_p - L_{ps} i_{sd}) = \frac{3}{2}\omega_p \lambda_p i_{pd} \tag{14}$$

With the λ_p, and thus λ_{ps}, magnitudes being fixed by the primary winding grid connection at line frequency (ω_p), the P_p versus i_{sq} and Q_p versus i_{sd} relationships are nearly linear according to (13) and (14), which justifies the use of PI power controllers (Fig. 3) as indicated below:

$$\begin{cases} i_{sq\text{ref}} = PI(P - P_{\text{ref}}) \\ i_{sd\text{ref}} = PI(Q - Q_{\text{ref}}) \end{cases} \tag{15}$$

By analogy to (10), feed-forward compensation for coupling terms in (11) and (12) may also be added to (15) to achieve decoupled control similar to FOC but at the expense of having to know the machine inductances.

4.2 Field-Oriented Control

The primary flux oriented (e.g., with the reference frame d_p-axis aligned to $\underline{\lambda}_p$ as in Fig. 2) forms of (2), (3) and (5) become [4, 19, 20]:

$$\underline{\lambda}_p = \underbrace{L_p i_{pd} + L_{ps} i_{sd}}_{\lambda_{pd}=\lambda_p} + j \cdot \underbrace{(L_p i_{pq} - L_{ps} i_{sq})}_{\lambda_{pd}=0} \tag{16}$$

$$\underline{\lambda}_s = \underbrace{\sigma L_s i_{sd} + \lambda_{ps_d}}_{\lambda_{sd}} + j \cdot \underbrace{\sigma L_s i_{sq}}_{\lambda_{sq}} = \sigma L_s \underline{i}_s + \underbrace{\frac{L_{ps}}{L_p}\lambda_p}_{\lambda_{ps}} \tag{17}$$

$$T_e = \frac{3 p_r L_{ps}}{2 L_p}\lambda_p i_{sq} = \frac{3 p_r}{2}\lambda_{ps} i_{sq} = \frac{3 p_r}{2}\lambda_p i_{pq} \tag{18}$$

The corresponding real and reactive powers are now given by (13) and (14).

The most important advantage of FOC over VC is the inherently decoupled control of P_p (or T_e) and Q_p through i_{sq} and i_{sd} variations, respectively, which is immediately obvious from (13), (14) and (18). This fact greatly facilitates the controller design as most AC machines, and especially if vector controlled, need

model-based decoupling schemes to eliminate cross-coupling between the *d*-*q* control axes for enhanced performance. In favor of VC, it is fair to say that these appealing FOC properties come at the cost of the $\underline{\lambda}_p$ angle estimation (θ_p in B block of Fig. 2) and difficulties with suppressing the detrimental DC offset effects on the voltage integration accuracy. In addition, the primary winding resistance (R_p) needs to be known in low to medium power applications this requirement being superficial with large-scale machines having virtually negligible resistance values. As entirely parameter independent, the VC approach clearly does not suffer from any of these FOC constraints.

Another interesting observation that can be made from (16) is that the i_{pq}, as being immediately related to i_{sq} since $\lambda_{pq} = 0$, is also indirectly torque producing, while the respective *d*-axis counterparts, i_{sd} and i_{pd}, jointly participate in the machine magnetization as $\lambda_p = L_p i_{pd} + L_{ps} i_{sd}$. Also, note from Fig. 2 that if the d_p-axis lies along the $\underline{\lambda}_p$, then this will automatically get the respective d_s-axis of the secondary frame (where the control is actually being executed), aligned to $\underline{\lambda}_{ps}$. In the BDFRG case, such an unusual frame-flux mapping is inherent with the decoupled FOC but surely does not take place under the VC conditions.

4.3 BDFRG Turbine Operating Conditions

The viability and performance comparisons of the FOC/VC a scheme in Fig. 3 has been demonstrated on a large-scale proof-of-concept machine for wind turbines. The machine ratings and remaining parameters, shown in Table 1, are used throughout this work if not otherwise stated.

In order to make the computer simulations as real as possible, which is a necessary initial step for their successful practical validation, the following actions have been taken: (i) The power electronic models from the SimPowerSystems® library have been implemented; (ii) High-frequency uncorrelated white noise and unknown slowly varying DC offset have been superimposed to the ideal signals to account for practical effects of the measurement noise and current/voltage transducers errors; (iii) Furthermore, a correct way of extracting the primary voltage/flux angles was put into place with the PLL only being used to get accurate estimates of the respective angular velocities as Fig. 2 implies; (iv) Finally, it has been assumed that both the rotor position and speed information has been provided by a shaft sensor (e.g., an incremental encoder in our case).

4.4 Optimal Control Strategy

The maximum torque per inverter ampere (MTPIA) strategy [1, 2] has been implemented in Fig. 3 by setting: (1) $i_{sd}^* = 0$, or (2) Q_p^* value for $i_{sd} = 0$ and $\lambda_p \approx u_p/\omega_p$ in (14), subject to the Q_p controller status i.e., is it (1) disabled or

Table 1 The BDFRG design specifications

Rotor inertia [J]	3.8 kgm^2	Power [P_r]	2 MW
Primary resistance [R_p]	0.0375 Ω	Rated speed [n_r]	1000 rev/min
Secondary resistance [R_s]	0.0575 Ω	Stator currents [$I_{p,s}$]	1.5 kA rms
Primary inductance [L_p]	1.17 mH	Stator voltages [$V_{p,s}$]	690 V rms
Secondary inductance [L_s]	2.89 mH	Stator frequencies [$f_{p,s}$]	50 Hz
Mutual inductance [L_{ps}]	0.98 mH	Winding connections	Y/Y
Rotor poles [p_r]	4	Stator poles [p/q]	6/2

(2) active. The advantage of the first option is one fewer PI regulator to tune, but has the limitations of model-based Q_p control. The second choice is machine parameter independent, and thus more robust from this point of view, allowing Q_p to be controlled directly but makes the overall tuning process more difficult by adding an extra PI regulator to the existing three (two for the secondary dq currents and one for the speed). Whatever the set-point selection, the primary winding would be almost entirely responsible for the machine magnetisation with most of the secondary current being torque producing. This implies the minimum current loading in the secondary winding and the machine-side converter for a given torque, reduction of resistive and switching losses, and an efficiency improvement.

4.5 Wind Turbine Characteristics

A common geared wind turbine driving the BDFRG has been operated in a variable speed range of 2:1 or so, which is usual in these applications. For a 6/2-pole example machine (Table 1), this is [$n_{\min} = 500$; $n_{\max} = 1000$] rev/min, i.e., 250 rev/min around the synchronous speed of $n_{\text{syn}} = 750$ rev/min for a $f_p = 50$ Hz supply, the boundary secondary frequencies of $f_s = \pm f_p/3$, and the respective "slip" limits of $s = -f_s/f_p = \mp 1/3$ according to (4). It can be easily shown using (7) that $P_s \approx 0.25 P_m$ meaning that the inverter would need to handle at most 25 % of the mechanical power (plus total losses on the secondary side).

In a typical wind energy conversion system, the turbine output torque on the generator side of the gear-box for the maximum energy extraction from the wind in the base speed region (i.e., between the minimum "cut-in," $u_{\min}$, and the rated wind speed, u_r), can be represented as [2, 12]:

$$T_{\text{opt}} = \frac{A \cdot \rho \cdot C_p(\lambda_{\text{opt}}, \gamma) \cdot R^3}{2 \cdot g^3 \cdot \lambda_{\text{opt}}^2} \cdot \omega_{rm}^2 = K_{\text{opt}} \cdot \omega_{rm}^2 \tag{19}$$

where ρ is the air density, $C_p(\lambda, \gamma)$is the power (performance) coefficient (i.e., the maximum turbine efficiency as $\lambda = \lambda_{\text{opt}}$ in this case), $\lambda_{\text{opt}} = R\omega_t/u$ is the optimum tip speed ratio for a given wind speed u, ω_t is the turbine rotor angular velocity, γ is the pitch angle (normally fixed to zero to maximize C_p), R is the blade length

(i.e., the radius of the circular swept area, $A = \pi R^2$), and $g = \omega_{rm}/\omega_t$ is the gear ratio. The main task of the gear box is to provide mapping of the actual wind and generator operating speed ranges, i.e., $[u_{\min}, u_r]$ and $[n_{\min}, n_{\max}]$ through an appropriate g value. In practice, the latter is normally chosen to allow matching of the respective midrange speeds, $(u_{\min} + u_r)/2$ and $(n_{\min} + n_{\max})/2$ ($=n_{\text{syn}}$ for the BDFRG or DFIG). At gusty wind speeds beyond u_r and up to the "cut-out" limit, C_p has to be sacrificed to avoid generator overloading. However, issues related to constant power control of the turbine are out of scope here.

The simulated BDFRG (Table 1) has been assumed to have a shaft torque-speed characteristic of the same form as (19).

$$T_L = -T_r \cdot \left(\frac{\omega_{rm}}{\omega_{\max}}\right)^2 = -\frac{P_r}{\omega_r} \cdot \left(\frac{n_{rm}}{n_{\max}}\right)^2 \approx -19 \cdot \left(\frac{n_{rm}}{1000}\right)^2 \text{ kNm} \tag{20}$$

5 Preliminary Results

The simulation results have been produced by running the FOC and VC algorithms in Fig. 3 in speed mode at 5 kHz corresponding to the switching rate for the IGBT converter. The DC link voltage has been maintained at $\approx$ 1200 V by the PWM rectifier (i.e., the line-side bridge) supplied at 690 V, 50 Hz.

Figure 4 shows the excellent speed tracking with no overshoot of the BDFRG controlled at synchronous (750 rev/min), super-synchronous (900 rev/min), and sub-synchronous (600 rev/min) speeds in the secondary frequency range of $f_s = \pm 10$ Hz following the start-up period. The reference speed trajectory is set as a ramp for dynamically not demanding target applications. Note that the machine speed response is virtually identical for either the FOC or VC.

The primary electrical power (P) and electromagnetic torque (T_e) curves in Fig. 4 reflect the BDFRG speed-torque profile represented by (20) for three typical speed set-points in the control region (from 4 s onward). Except for a difference in losses, and considering that $\omega_p \approx$ const by the primary winding grid connection, P and T_e are directly related as follows from (7) and (11) which explain a close resemblance in shape of the two waveforms. The Te deviations from the desired load profile during the speed transients refer to the acceleration or deceleration torque term in (6) depending on whether the machine is to speed-up ($T_a > 0$) or slowdown ($T_a < 0$). One can also hardly see any disparity between the FOC and VC results for either P or Te given (11) and (13) for $i_{sd}^* = 0$.

The reactive power (Q) is kept at 1.35 MVAr (Fig. 4) by adopting the control option 2 elaborated in Sect. 5.1. This approach allows to minimize the i_s magnitude for a given shaft torque and therefore to achieve the desired MTPIA performance. Note that the Q behavior of the BDFRG with the decoupled FOC is largely unaffected by the P variations. However, the VC waveform is rather

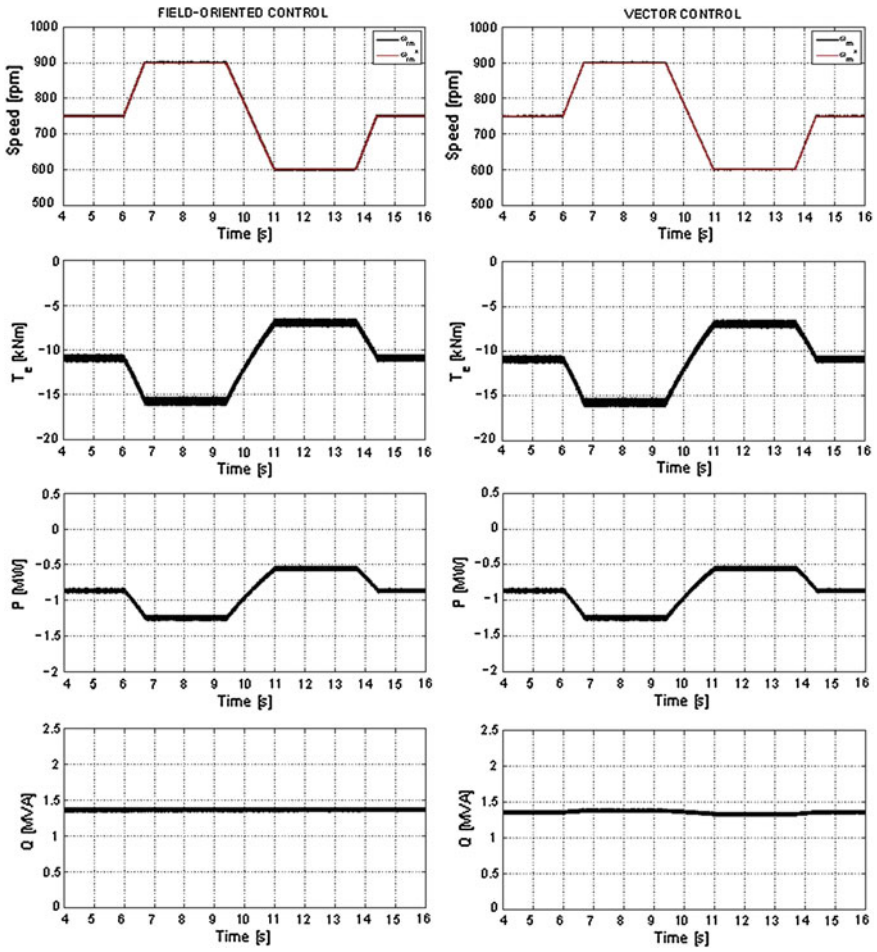

Fig. 4 MTPIA performance of the BDFRG in a narrow range around synchronous speed

distorted and looks like a scaled mirror image of the P counterpart due to the cross-coupling (i_{sq}) term in (12).

The secondary current components ($i_{sd,\,q}$) and their primary winding equivalents ($i_{pd,\,q}$) are presented in Fig. 5. The waveforms are notably smooth with no transient overcurrents as the PI regulators do not need to be saturated to allow accurate tracking of the desired trajectories for the moderate trapezoidal speed variations.

The i_{sd} is controlled at ≈ 0, while the i_{pd} is required to establish the machine flux and to satisfy the specific Q_p demand according to (14). A close analogy between the active q currents and the complementary real power (torque), as well as the magnetizing d currents and Q, is immediately visible from the relevant

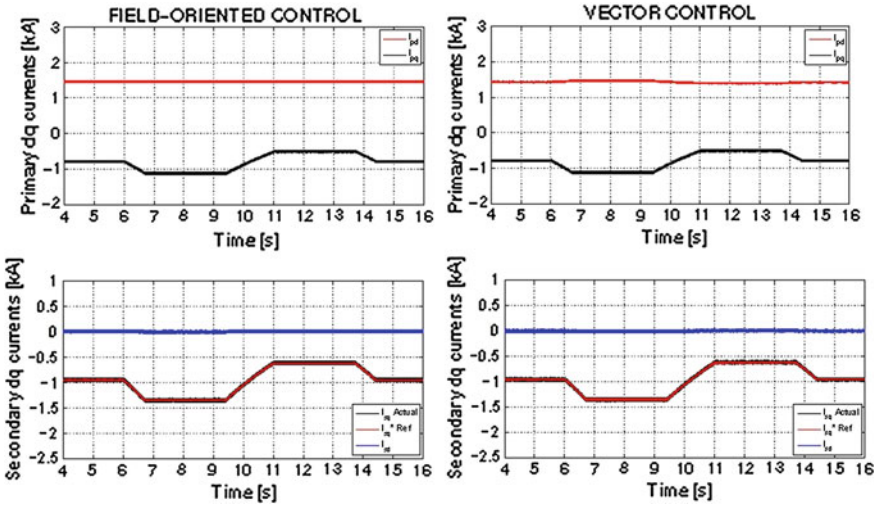

Fig. 5 BDFRG *dq* currents in the respective frames complementing the results in Fig. 4

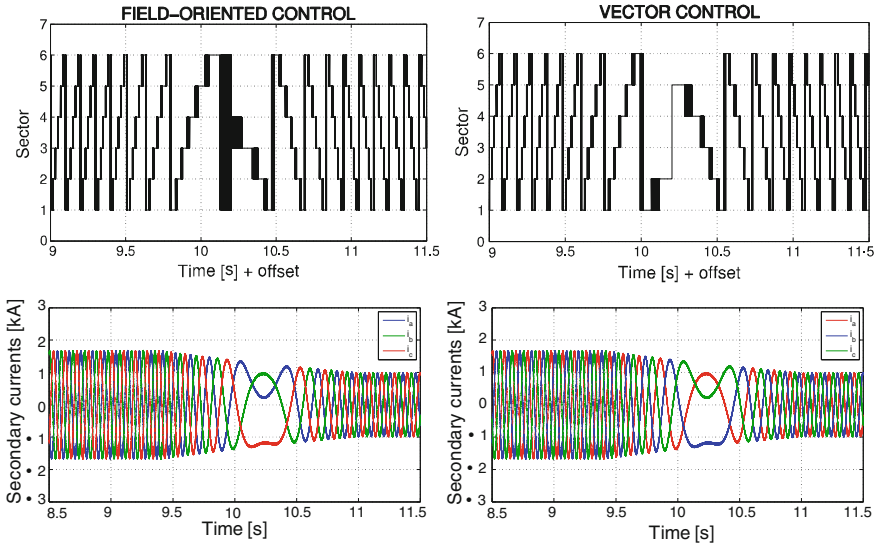

Fig. 6 BDFRG inferred secondary voltage positions and secondary current waveforms showing a phase sequence reversal during the transition from super- to sub-synchronous speed modes

waveforms in Figs. 4 and 5. The cross-coupling effects of the i_{sq} clearly manifest themselves as speed (torque)-dependent disturbance (e.g., offsets) in the respective noncontrollable i_{pd} profiles (Fig. 5) in the VC case (in a manner similar to the

P and Q scenario in Fig. 4). The corresponding FOC i_{pd} (and Q) levels are, however, constant in an average sense throughout the entire speed range.

An interesting observation from Fig. 6 is the step-wise PWM sector change of the modulated secondary voltage vector ($\underline{v}_s$) during a speed reduction from 900 to 600 rev/min. In the super-synchronous mode, $\underline{v}_s$ rotates anticlockwise as indicated by the ascending sector numbers for the same phase sequence of the windings when $\omega_s > 0$ in (4). At sub-synchronous speeds, on the other hand, $\underline{v}_s$ rotates clockwise with the sector numbers descending which comes from the opposite phase sequence of the secondary to the primary winding since $\omega_s < 0$ in (4). Notice that $\underline{v}_s$ becomes stationary at synchronous speed (750 rev/min) as the secondary currents are then DC i.e., $\omega_s = 0$ in (4).

6 Conclusions

The main contribution of the work is the comparative development and performance analysis of field (primary flux) oriented control (FOC) and vector (primary voltage oriented) control (VC) algorithms for optimum operation of the BDFRG—a viable, low cost, and reliable alternative to its widely used companion, the conventional slip-ring doubly fed induction generator (DFIG). Such a control framework can serve as a basis for further research on this emerging brushless machine topology for applications with limited variable speed ranges foremost wind turbines (but also large pump-alike drives) where the cost advantages of partially rated power electronics can be fully exploited. The results presented have illustrated the high potential and effectiveness of the control methods considered using the MTPIA strategy which offers the machine efficiency improvement.

The realistic simulation studies taking into account the usual practical effects as transducer DC offsets and noise in measurements, have clearly demonstrated that despite the necessity for primary flux estimation (which largely becomes obsolete with increasing machine sizes and negligible resistances), the FOC technique can still allow superior Q control quality in an inherently decoupled fashion from torque (power). The VC, on the other hand, is more robust from a parameter knowledge point of view but suffers from uncompensated cross-coupling issues and disturbed Q waveforms of speed (and hence load)-dependent steady-state levels as a trade-off. Although the implementation of decoupling mechanisms for enhanced performance may be possible, this approach has not been adopted primarily to avoid the consequent model-based limitations (e.g., sensitivity and accuracy problems associated with parameter identification uncertainties) and retain the complete parameter independence of the VC in order to make fair and valid comparisons with the FOC.

References

1. Betz RE, Jovanovic MG (2002) Theoretical analysis of control properties for the brushless doubly fed reluctance machine. IEEE Trans Energy Convers 17:332–339
2. Jovanovic MG, Betz RE, Yu J (2002) The use of doubly fed reluctance machines for large pumps and wind turbines. IEEE Trans Ind Appl 38:1508–1516
3. Wang F, Zhang F, Xu L (2002) Parameter and performance comparison of doubly-fed brushless machine with cage and reluctance rotors. IEEE Trans Ind Appl 38(5):1237–1243
4. Betz RE, Jovanovic MG (2003) Introduction to the space vector modelling of the brushless doubly-fed reluctance machine. Electr Power Comp Syst 31(8):729–755
5. Jovanovic MG, Yu J, Levi E (2006) Encoderless direct torque controller for limited speed range applications of brushless doubly fed reluctance motors. IEEE Trans Ind Appl 42(3):712–722
6. Dorrell DG, Jovanovic M (2008) On the possibilities of using a brushless doubly-fed reluctance generator in a 2 MW wind turbine. IEEE Ind Appl Soc Annu Meet (IAS) 1–8
7. McMahon RA, Roberts PC, Wang X, Tavner PJ (2006) Performance of BDFM as generator and motor. IEE Proc Electr Power Appl 153(2):289–299
8. Poza J, Oyarbide E, Sarasola I, Rodriguez M (2009) Vector control design and experimental evaluation for the brushless doubly fed machine. IET Electr Power Appl 3(4):247–256
9. Protsenko K, Xu D (2008) Modeling and control of brushless doubly-fed induction generators in wind energy applications. IEEE Trans Power Electron 23(3):1191–1197
10. Shao S, Abdi E, Barati F, McMahon R (2009) Stator-flux-oriented vector control for brushless doubly fed induction generator. IEEE Trans Industr Electron 56(10):4220–4228
11. Pena R, Clare JC, Asher GM (1996) Doubly fed induction generator using back-to-backPWMconverters and its application to variable-speed wind-energy generation. IEE Proc Electr Power Appl 143(3):231–241
12. Valenciaga F, Puleston PF (2007) Variable structure control of a wind energy conversion system based on a brushless doubly fed reluctance generator. IEEE Trans Energy Convers 22(2):499–506
13. Williamson S, Ferreira A, Wallace A (1997) Generalised theory of the brushless doubly-fed machine. Part 1: Analysis. IEE Proc Electr Power Appl 144(2):111–122
14. Betz RE, Jovanovic MG (2000) The brushless doubly fed reluctance machine and the synchronous reluctance machine-a comparison. IEEE Trans Ind Appl 36:1103–1110
15. Knight A, Betz R, Dorrell D (2013) Design and analysis of brushless doubly fed reluctance machines. IEEE Trans Ind Appl 49(1):50–58
16. Schulz EM, Betz RE (2005) Optimal torque per amp for brushless doubly fed reluctance machines. Proc IEEE IAS Annu Meet 3:1749–1753
17. Long T, Shao S, Malliband P, Abdi E, McMahon R (2013) Crowbarless fault ride-through of the brushless doubly fed induction generator in a wind turbine under symmetrical voltage dips. IEEE Trans Industr Electron 60(7):2833–2841
18. Shao S, Long T, Abdi E, McMahon RA (2013) Dynamic control of the brushless doubly fed induction generator under unbalanced operation. IEEE Trans Industr Electron 60(6):2465–2476
19. Jovanovic M (2009) Sensored and sensorless speed control methods for brushless doubly fed reluctance motors. IET Electr Power Appl 3(6):503–513
20. Xu L, Zhen L, Kim E (1998) Field-orientation control of a doubly excited brushless reluctance machine. IEEE Trans Ind Appl 34(1):148–155
21. Chaal H, Jovanovic M (2012) Practical implementation of sensorless torque and reactive power control of doubly fed machines. IEEE Trans Industr Electron 59(6):2645–2653
22. Chaal H, Jovanovic M (2012) Toward a generic torque and reactive power controller for doubly fed machines. IEEE Trans Power Electron 27(1):113–121
23. Chaal H, Jovanovic M (2012) Power control of brushless doubly-fed reluctance drive and generator systems. Renew Energy 37(1):419–425

24. Tremblay E, Atayde S, Chandra A (2011) Comparative study of control strategies for the doubly fed induction generator in wind energy conversion systems: a DSP-based implementation approach. IEEE Trans Sustain Energy 2(3):288–299
25. Muller S, Deicke M, De Doncker R (2002) Doubly fed induction generator systems for wind turbines. IEEE Ind Appl Mag 8:26–33
26. Zhou D, Spee R, Alexander GC (1997) Experimental evaluation of a rotor flux oriented control algorithm for brushless doubly-fed machines. IEEE Trans Power Electron 12:72–78
27. Tazil M, Kumar V, Bansal R, Kong S, Dong Z, Freitas W (2010) Three-phase doubly fed induction generators: an overview. IET Electr Power Appl 4(2):75–89
28. Morel L, Godfroid H, Mirzaian A, Kauffmann JM (1998) Double-fed induction machine: converter optimisation and field oriented control without position sensor. IEE Proc Electr Power Appl 145(4):360–368
29. Malinowski M, Kazmierkowski M, Trzynadlowski A (2003) A comparative study of control techniques for PWM rectifiers in ac adjustable speed drives. IEEE Trans Power Electron 18(6):1390–1396

Energy Hub Management with Intermittent Wind Power

Alireza Soroudi, Behnam Mohammadi-Ivatloo and Abbas Rabiee

Abstract The optimal energy management in energy hubs has recently attracted a great deal of attention around the world. The energy hub consists of several inputs (energy resources) and outputs (energy consumptions) and also some energy conversion/storage devices. The energy hub can be a home, large consumer, power plant, etc. The objective is to minimize the energy procurement costs (fuel/electricity/environmental aspects) subject to a set of technical constraints. One of the popular options to be served as the input resource is renewable energy like wind or solar power. Using the renewable energy has various benefits such as low marginal costs and zero environmental pollution. On the other hand, the uncertainties associated with them make the operation of the energy hub a difficult and risky task. Besides, there are other resources of uncertainties such as the hourly electricity prices and demand values. Hence, it is important to determine an economic schedule for energy hubs, with an acceptable level of energy procurement risk. Thus, in this chapter a comprehensive multiobjective model is proposed to minimize both the energy procurement cost and risk level in energy hub. For controlling the pernicious effects of the uncertainties, conditional value at risk (CVaR) is used as risk management tool. The proposed model is formulated as a mixed integer nonlinear programming (MINLP) problem and solved using GAMS.

A. Soroudi (✉)
Renewable Energies and Environment Department, Faculty of New Sciences and Technologies, University of Tehran, North Kargar Street, Tehran, Iran
e-mail: soroudi@ut.ac.ir; alireza.soroudi@ut.ac.ir

B. Mohammadi-Ivatloo
Faculty of Electrical and Computer Engineering, University of Tabriz, 5166614766 Tabriz, Iran
e-mail: mohammadi@ieee.org

A. Rabiee
Department of Electrical Engineering, Faculty of Engineering, University of Zanjan, 4537138791 Zanjan, Iran
e-mail: rabiee@znu.ac.ir

J. Hossain and A. Mahmud (eds.), *Large Scale Renewable Power Generation*, Green Energy and Technology, DOI: 10.1007/978-981-4585-30-9_16,

Simulation results on an illustrative test system are carried out to demonstrate the applicability of the proposed method.

Keywords Stochastic optimization · Scenario-based modeling · Wind energy · Price uncertainty modeling · Energy hub

1 Introduction

1.1 Problem Statement

The increasing price of fuel and energy, combined with environmental laws and regulations, have led many different energy producers to integrate renewable, clean energy sources with nonrenewable ones, forming the idea of energy hubs. A typical energy hub consists of energy transformation devices, some distributed energy generation potential, electrical load, heat load, and some energy storage capabilities. The energy hub can be a commercial building, large consumer, power plant, etc. Figure 1 shows an example energy hub, which provides interface between participants, i.e., the energy producers, consumers, and storage along with the transportation infrastructure.

In this chapter, a risk averse stochastic framework is proposed for optimal energy management of an energy hub. The problem is analyzed with the following constraints, decision variables, and objective function:

- Decision variables:
  - Electricity purchase from the electricity market.
  - Gas purchase from the gas network.
  - Operation schedule of energy storage/conversion devices.
- Constraints:
  - Uncertainty of electricity prices.
  - Uncertainty of electricity demand.
  - Uncertainty of energy production of renewable resources.
  - Technical constraints of energy conversion/storage devices.
  - Demand balance.
  - Risk of energy procurement from different resources.

1.2 Review of Related Works

A comprehensive framework for modeling of energy systems composed of multiple energy carriers has been presented in [1]. Different energy careers such as electricity, heat, gas, and biomass are considered. The modeling framework is

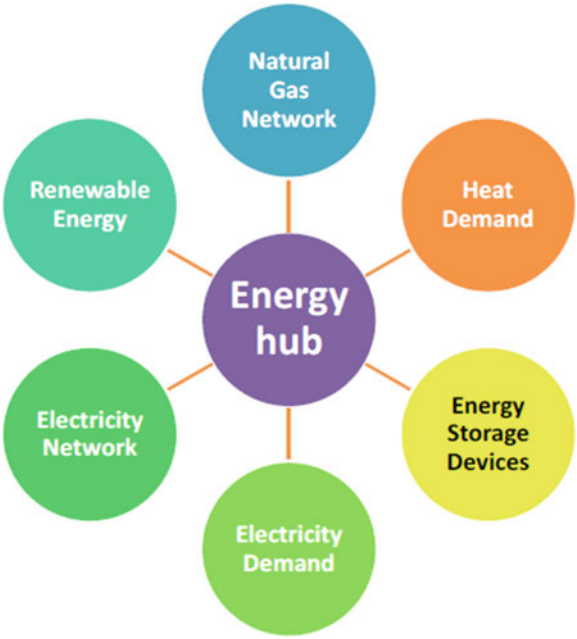

Fig. 1 The energy hub concept

based on the energy hub approach. They have used conversion matrix for modeling the interactions between different participants of the energy hub. The modeling is deterministic and the effects of the uncertainties are not considered. A model based on energy hub concept, for the analysis of reliability of supply in multicarrier energy systems has been presented in [2]. It is concluded that considering the mutual interconnections between multiple energy careers increases the supply redundancy and reliability. In [3] an optimization method is proposed for determination of optimal size of hybrid power systems, based on the energy hub concept.

In [4] and [5] an energy hub Monte Carlo valuation model is proposed. By means of this model, integrated systems of multienergy conversion and storage devices can be valued together with load management schemes. The energy hub's ability to flexibly adapt its output to uncertain and volatile market prices is explicitly considered. In [6] the energy hub framework is adopted to determine a modeling procedure for a generic building energy system. In [7] application of model predictive control (MPC) to multicarrier energy systems including storage devices, renewable infeeds, and forecast uncertainties is studied. Due to the forecast errors in price and load profiles, the MPC strategy is used for reduction of the consequences of forecast uncertainties. Reference [8] proposes a tool for analyzing large-scale interconnected energy hub networks. Electrical and natural gas networks, wind generating capacity, district heat loads, converters, and energy storage are considered as the main elements of energy. In [9] a generic framework is proposed that allows the analysis of energy efficiency in multicarrier energy

systems taking into account the physical properties of the energy networks. It is shown that a trade-off should be made between the cost minimization and maximization of energy efficiency in these systems.

Different methods have been used to model wind uncertainty. Scenario-based stochastic optimization modeling has been proposed in [10–12]. In this method some scenarios are generated as the representatives of the wind generation based on the a presumed probability distribution function. Although different risk measures can be used to model risk, CVaR is used widely as a risk measure in scenario-based methods. CVaR has been used in [10, 11] for risk modeling of wind power generation uncertainty. Fuzzy scenario-based has been used in [13] for modeling wind uncertainty. The Interval optimization is also used in [14] in for uncertainty handling of wind power. This method is compared with scenario-based methods in [15].

2 Risk Management

Suppose an objective function $C(\psi, Z)$, in which, Ψ is the decision variable vector and Z are the input uncertain parameters. If the probability density functions of the uncertain parameters are known then these parameters can be described using scenario-based approach and treated with two-stage optimization techniques. The scenario-based approach divides the uncertain continuous universe of discourse for parameter Z into $|\Omega_s|$ scenarios with specific probabilityπ_s. The next step is the proper treatment of optimization procedure. The two-stage optimization technique states that the decision variable vector Ψ consists of two types of variables. the first type are called "here and now" or "first stage" variables and are denoted by X. These variables remain the same for all possible scenarios. The second type of the variables are called "wait and see" or "second stage" variables and are denoted by Y_s. These variables are determined specifically for each scenario s.

$$\min_{\psi} \text{OF} = \Xi(C(\psi, Z_s)) \tag{1}$$

$$\Xi(C) = \sum_{s} \pi_s C(\psi, Z_s) \tag{2}$$

$$Z_s \in \Omega_s(z) \tag{3}$$

$$\psi = \{X, Y_s\} \tag{4}$$

where $\Xi(.)$ is expected value operator. π_s is the probability of scenario s. The main problem with this approach is ignorance of the risk. The term "risk" can be interpreted in many ways depending on the context it is being used. Formally, it is defined as a situation involving exposure to an undesired event which is mainly due to the existence of uncertainties involved in decision-making procedure. This

event may be an unpleasant technical, economical, or environmental situation. Each risk management strategy involves answering the following questions [16]:

- What can happen?
- How to quantify the impacts/risk measures?
- What are the consequences?
- What are the preventive/remedial actions?

The methods of risk modeling can be divided into different categories [17], namely; fuzzy methods [18], scenario-based methods [19–21], information gap decision theory (IGDT)-based methods [22, 23], and robust optimization [24]. In context of the scenario-based models, there are various methods for quantifying the risk impacts such as variance [25], shortfall probability [26], stochastic dominance [27], value at risk VaR [28], and CVaR [29]. In this chapter, the CVaR method is used as a risk measure. The CVaR is defined as the expected value of losses exceeding the VaR. While the VaR gives the frequency of extreme events, CVaR considers not only the frequency but also the severity of losses in case of undesired events [30]. For example, although the expected value of cost function $C(\psi, Z_s)$ is minimized but the decision-maker may still face with severe outcomes in some scenarios with low probability. Comparing with VaR, CVaR is a more conservative index, because it measures the average loss exceeding the VaR value for a given confidence level [31]. CVaR is defined as follows:

$$\mathrm{CVaR} = \mathrm{VaR} + \frac{\Xi(\nabla_s)}{1-\alpha} \tag{5}$$

$$\nabla_s \geq C_s - \mathrm{VaR} \tag{6}$$

$$\nabla_s \geq 0 \tag{7}$$

where CVaR is the mean of the worst $\alpha\%$ of C_s values. CVaR is conditional value at risk, VaRis value at risk.

Let's reformulate the (1) with a risk averse attitude:

$$\min_{\psi} \mathrm{OF} = \beta \ \Xi(C(\psi, Z_s)) + (1-\beta)\mathrm{CVaR} \tag{8}$$

$$\Xi(C) = \sum_{s} \pi_s C(\psi, Z_s) \tag{9}$$

$$Z_s \in \Omega_s(z) \tag{10}$$

$$\psi = \{X, Y_s\} \tag{11}$$

where β is weighting factor for risk averse decision making and specifies the attitude of decision-maker toward the risk.

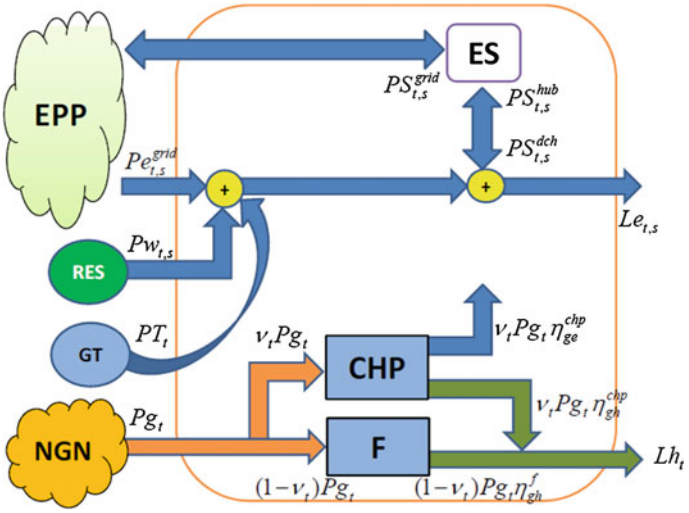

Fig. 2 Energy hub configuration

3 Problem Formulation

The relations between different variables and parameters of an energy hub basically depend on the energy hub's configuration. The configuration of a typical energy hub is depicted in Fig. 2

The calculation of objective function as well as the assumptions and technical constraints are described in this section as follows:

3.1 Energy Hub Modeling

This hub is fed by four sources of energy, namely: electric power pool (EPP), renewable energy sources (RES), gas turbines (GT), and natural gas network (NGN). It should supply two types of demand namely heat and electrical demand. It can also sell its excessive energy to the EPP. This energy hub is equipped with a CHP, electric energy storage (EES) unit. and a Furnace (F) unit.

The state of charge (SOC) in energy storage device in hour t depends on SOC in hour $t-1$, energy loss (EL) and the energy charge or discharge in hour t. It also depends on the scenario s. It can be described mathematically as follows:

$$\mathrm{SOC}_{t,s} = \mathrm{SOC}_{t-1,s} + E^{\mathrm{chg}}_{t,s} - E^{\mathrm{dch}}_{t,s} - \mathrm{EL} \tag{12}$$

$$\mathrm{SOC}_{t_1,s} = E_{\mathrm{ini}} \tag{13}$$

$$\mathrm{SOC}_{t_{24},s} = E_{\mathrm{fin}} \tag{14}$$

$$E_{\min} \leq \mathrm{SOC}_{t,s} \leq E_{\max} \tag{15}$$

$$E_{t,s}^{\mathrm{chg}} = \left(\mathrm{PS}_{t,s}^{\mathrm{grid}} + \mathrm{PS}_{t,s}^{\mathrm{hub}}\right) \times \eta \tag{16}$$

$$E_{t,s}^{\mathrm{dch}} = \left(\mathrm{PS}_{t,s}^{\mathrm{sold}} + \mathrm{PS}_{t,s}^{\mathrm{dch}}\right) \Big/ \eta \tag{17}$$

where η is the efficiency of charge and discharge of EES unit. $E_{t,s}^{\mathrm{chg}}$ is energy charge in EES in time t and scenario s in MWh, $E_{t,s}^{\mathrm{dch}}$ is energy discharge in EES in time t and scenario s in MWh, $\mathrm{SOC}_{t,s}$ is state of charge for EES in time t and scenario s in MWh, E_{ini} is the initial value of state of charge at the beginning of operating horizon, E_{fin} is the final value of state of charge at the end of operating horizon, $E_{\max}$ is the maximum value of state of charge, $E_{\min}$ is the minimum value of state of charge.

The energy storage device can be charged by using either energy hub ($\mathrm{PS}_{t,s}^{\mathrm{hub}}$) or by EPP ($\mathrm{PS}_{t,s}^{\mathrm{grid}}$). It also discharges to supply the hub ($\mathrm{PS}_{t,s}^{\mathrm{dch}}$) or to sell its energy to EPP ($\mathrm{PS}_{t,s}^{\mathrm{sold}}$).

The heat and electric demands should be satisfied in hour t and scenario s as follows:

$$\begin{aligned} Le_{t,s} = {} & \mathrm{PS}_{t,s}^{\mathrm{dch}} + (Pe_{t,s} + Pw_{t,s}) + \\ & P\mathrm{ge}_t^{\mathrm{chp}} - \mathrm{PS}_{t,s}^{\mathrm{hub}} + \sum_i (\mathrm{PS}_t^i) \end{aligned} \tag{18}$$

$$Lh_t = P\mathrm{gh}_t^{\mathrm{chp}} + P\mathrm{gh}_t^f \tag{19}$$

where $Le_{t,s}$ is the electrical demand in time t and scenario s in MW, $Pw_{t,s}$ is the wind power generation in time t and scenario s in MW, $Pe_{t,s}$ is the power purchased from EPP to supply energy hub in time t and scenario s in MW, $P\mathrm{ge}_t^{\mathrm{chp}}$ is the converted power from gas to electricity by CHP unit in time t in MW, $P\mathrm{gh}_t^{\mathrm{chp}}$ is the converted power from gas to heat by CHP unit in time t in MW, $P\mathrm{gh}_t^f$ is the converted power from gas to heat by Furnace unit in time t in MW, and $Lh_{t,s}$ is the heat demand in time t and scenario s in MW.

The internal variables of energy hub are described as follows:

$$P\mathrm{ge}_t^{\mathrm{chp}} = v_t \times Pg_t \times \eta_{\mathrm{ge}}^{\mathrm{chp}} \tag{20}$$

$$P\mathrm{gh}_t^{\mathrm{chp}} = v_t \times Pg_t \times \eta_{\mathrm{gh}}^{\mathrm{chp}} \tag{21}$$

$$P\mathrm{gh}_t^f = (1 - v_t) \times Pg_t \times \eta_{\mathrm{ge}}^f \tag{22}$$

where v_t is the dispatch factor which specifies the share of natural gas entering the CHP or Furnace. η_{ge}^{chp} is the gas to electricity conversion efficiency of CHP unit, η_{gh}^{chp} is the gas to heat conversion efficiency of CHP unit, and η_{gh}^{f} is the gas to heat conversion efficiency of Furnace unit.

3.2 Thermal Unit Constraints

- Ramp rate limits [32]

$$p_t^i \geq P_{\min}^i \times U_t^i \tag{23}$$

$$p_t^i \geq p_{t-1}^i \times U_t^i - \mathrm{RD}^i \times U_t^i \tag{24}$$

$$p_t^i \leq (P_{\max}^i [U_t^i - Z_{t+1}^i] \times Z_{t+1}^i \times \mathrm{SD}^i) \times U_t^i \tag{25}$$

$$p_t^i \leq (p_{t-1}^i + \mathrm{RU}^i \times U_{t-1}^i + Y_t^i \times \mathrm{SU}^i) \times U_t^i \tag{26}$$

where P_t^i is the generated power of thermal unit i in time t in MW, U_t^i is On/off state of unit i in time t, Y_t^i/Z_t^i, are binary variables that describe the startup/shutdown status of the thermal unit i in time t. SU_i is startup limit of unit i in MW, SD_i is shutdown limit of unit i in MW, $\mathrm{RU}_i/\mathrm{RD}_i$ are Up/Down ramp rate of ith thermal unit in MW/h and $P_{max/min}^i$ is maximum/minimum power output of ith thermal unit in MW.

- On/off states

$$Y_t^i - Z_t^i = U_t^i - U_{t-1}^i \tag{27}$$

$$Y_t^i + Z_t^i \leq 1 \tag{28}$$

- Minimum up/down time

$$\left[\tau_{t-1}^i + \mathrm{DT}_i\right]\left[U_t^i - U_{t-1}^i\right] \leq 0 \tag{29}$$

$$\left[\tau_{t-1}^i - \mathrm{UT}_i\right]\left[U_{t-1}^i - U_t^i\right] \geq 0 \tag{30}$$

where, τ_t^i is the number of hours unit i has been on/off at the end of hour t, UT_i is the minimum up time of ith thermal unit, and DT_i is the minimum down time of ith thermal unit.

- The generation cost of thermal units is defined as

$$\mathrm{OC}_t^i = a_i (p_t^i)^2 + b_i p_t^i + c_i \times U_t^i \tag{31}$$

where a_i, b_i, c_i are the quadratic cost coefficients of thermal unit i. OC_t^i is the operating cost of thermal unit i in time t in \$.

• Total thermal units costs in time t

$$\mathrm{TTUC}_t = \sum_i \left[\mathrm{OC}_i(t) + Y_t^i \mathrm{STC}_i + Z_t^i \mathrm{SDC}_i\right] \tag{32}$$

where, TTUC_t is the total operating cost of thermal units in time t in \$, STC_i is the startup cost of unit i in \$, and SDC_i is shutdown cost of unit i in \$.

3.3 Critical Uncertainty Modeling of Wind Power Generation, Electricity Prices, and Demands

The variation of wind turbine power generation is an uncertain parameter which can be probabilistically modeled using historical data records of wind speed [33, 34]. A suitable PDF for modeling the variation of wind speed, v, is found to be Rayleigh probability density function (PDF) [34], which is a special case of Weibull PDF. The mathematical expressions of Weibull PDF is as follows:

$$\mathrm{PDF}(v) = \left(\frac{B}{A}\right)\left(\frac{v}{A}\right)^{B-1} \exp\left(-\left(\frac{v}{A}\right)^{B}\right) \tag{33}$$

where v is wind speed. B is the shape factor and A is the scale factor of the Weibull PDF of wind speed. Rayleigh PDF is a special case of Weibull PDF for $B = 2$ and $A = \sqrt{2}b$ which can be expressed as follows:

$$\mathrm{PDF}(v) = \left(\frac{v}{b^2}\right)\exp\left(-\left(\frac{v}{\sqrt{2}b}\right)^{2}\right) \tag{34}$$

The scale factor of the Rayleigh PDF can be calculated using the mean of the wind speed in the studied area as follows:

$$v_m = \int_0^{+\infty} \left(\frac{v^2}{b^2}\right)\exp\left(-\left(\frac{v}{\sqrt{2}b}\right)^{2}\right)\mathrm{dv} = \frac{\sqrt{\pi}b}{\sqrt{2}} \tag{35}$$

Figure 3 shows the Rayleigh PDF for $b = 11.28$ which corresponds to $v_m = 17.72$ m/s.

For generation of wind power scenarios, a technique described in [34] is implemented in this chapter. In this techniques, the PDF of wind speed is divided into several intervals. The probability that wind speed in scenario s falls into the interval $[v_{1,s}\ \ v_{2,s}]$ i.e., $v \in [v_{1,s}\ \ v_{2,s}]$, is calculated using the following equations:

$$\pi_s^w = \int_{v_{1,s}}^{v_{2,s}} \left(\frac{v}{c^2}\right)\exp\left[-\left(\frac{v}{\sqrt{2}c}\right)^{2}\right] dv \tag{36}$$

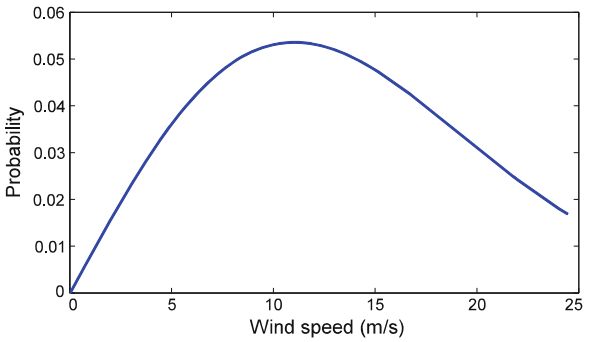

Fig. 3 Rayleigh PDF expression of wind speed

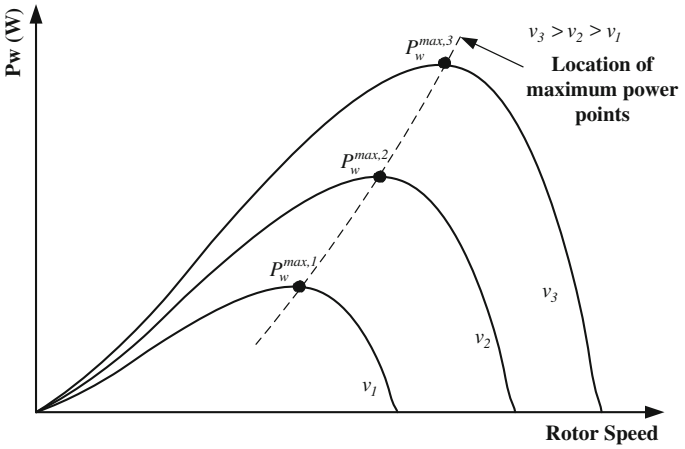

Fig. 4 Wind turbine power versus rotor speed characteristic [12]

$$v_s = \frac{v_{2,s} + v_{1,s}}{2} \tag{37}$$

where $v_{1,s}, v_{2,s}$ are the starting and ending points of the wind speed's interval defined in scenario s ($\in [v_{1,s}\ v_{2,s}]$), respectively. A typical wind turbine output power versus rotor angular speed is depicted in Fig. 4 [12]. The operating strategy of wind turbine is to adjust the rotor speed to generate power continuously close to the maximum power points which changes the power-speed characteristic. It can be accomplished by a variable speed system design and operation, which is utilized in the wind farms equipped by doubly fed induction generator (DFIG) [35].

In order to pick up maximum possible power from wind, the wind turbine should be operated at the peak power point at all wind speeds. By refering to Fig. 4, this happens at points $P_w^{max,1}, P_w^{max,2}, P_w^{max,3}$ in wind speeds v_1, v_2, v_3, respectively. These peak power production points have a common property which

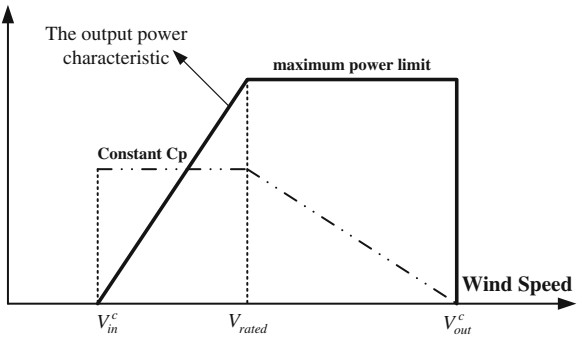

Fig. 5 The wind turbine rotor speed control regimes, and output power curve [12]

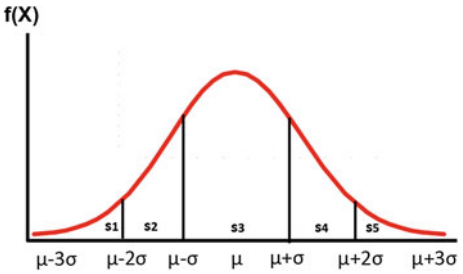

Fig. 6 The normal probability density function

is the constant high value of tip speed ratio (TSR). Consequently, the speed and power controls in the variable speed wind power systems consist of three distinct regimes as shown in Fig. 5, where the solid curve is the output power (i.e., $P_w(v)$) and the dotted curve is the rotor power coefficient (Cp) [36].

From Fig. 5, the generated power of the wind turbine is obtained using its output power characteristics and the obtained v_s through (37), as follows:

$$P_w(v) = \begin{cases} 0 & if \ \ \mathrm{v_s} \le \mathrm{v}_{in}^{c} \ \ or \ \ \mathrm{v} \ge \mathrm{v}_{out}^{c} \\ \frac{v - v_{in}^{c}}{v_{rated} - v_{in}^{c}} P_w^r & if \ \ \mathrm{v}_{in}^{c} \le \mathrm{v} \le \mathrm{v}_{rated} \\ P_w^r & else \end{cases} \tag{38}$$

where, v_{in}^{c}, v_{rated}^{c}, and v_{out}^{c} are the cut-in, rated and cut-out wind speed of wind turbine in m/s, respectively. Also, P_w^r is the rated power of the wind turbine. It is noteworthy that the practical values of v_{in}^{c}, v_{rated}^{c} and v_{out}^{c} for an industrial wind turbine (model E-70/E4 manufactured by ENERCON) are 2, 14, and 25, respectively [37].

Normal PDF is used for modeling the uncertainties associated with demand and electricity prices as shown in Fig. 6. As can be observed from this figure, mean (μ) and variance (σ) of the uncertain parameters are required for using normal PDF. According to this figure, the normal PDF is divided into 5 distinct areas. Table 1 gives the mean and the corresponding probabilities of these areas.

Table 1 Normal PDF states for electricity prices and demands

State	Mean value	Probability (%)
s_1	$\mu - 2.5\sigma$	2.5
s_2	$\mu - 1.5\sigma$	13.5
s_3	μ	68.0
s_4	$\mu + 1.5\sigma$	13.5
s_5	$\mu + 2.5\sigma$	2.5

It is assumed that the load, price, and wind power generation states are independent, thus these states are combined to construct the whole set of states (scenarios) as follows:

$$\pi_s = \pi_s^l \times \pi_s^\lambda \times \pi_s^w \tag{39}$$

The total number of states, i.e., N_s, would be $l_n \times \lambda_n \times w_n$. It is obvious that for large number of scenarios (i.e., states) the computational burden of the optimization procedure drastically increased. There are some techniques to reduce the number of scenarios to decrease the computational burdens while maintaining the accuracy (see Appendix-I).

3.4 Decision Variables

The decision variables (ϕ) are categorized into two groups as:

- First stage decision variables (X):

$$X \in \left\{ Y_t^i, Z_t^i, P_t^i, U_t^i, \mathrm{TTUC}_t, \mathrm{OC}_t^i, Pge_t^{chp}, Pgh_t^{chp}, Pgh_t^f, v_t \right\} \tag{40}$$

- Second stage decision variables (Y_s):

$$Y_s \in \left\{ \mathrm{SOC}_{t,s}, E_{t,s}^{\mathrm{chg}}, E_{t,s}^{\mathrm{dch}}, \mathrm{PS}_{t,s}^{\mathrm{grid}}, \mathrm{PS}_{t,s}^{\mathrm{hub}}, PS_{t,s}^{sold}, PS_{t,s}^{dch}, Pw_{t,s}, Pe_{t,s} \right\} \tag{41}$$

Finally $\phi = \{X, Y_s\}$

3.5 Objective Function

$$\min_{\phi} \mathrm{OF} \tag{42}$$

Table 2 Thermal unit characteristics

i	a_i	b_i	c_i	RD_i	RU_i	P^i_{min}	P^i_{max}	SU^i	SD^i
1	0.0080	2	25	20	20	10	75	20	60
2	0.0030	1.8	60	10	10	20	125	30	85
3	0.0012	2.1	100	20	20	30	175	40	100
4	0.0010	2	120	12	12	10	250	15	200
5	0.0015	1.8	40	15	15	10	300	20	250

$$\mathrm{OF} = \left\{ \mathrm{OF}_1 = \sum_s \pi_s \mathrm{Cost}_s, \mathrm{OF}_2 = \mathrm{CVaR} \right\} \tag{43}$$

$$\mathrm{CVaR} = \mathrm{VaR} + \frac{\left(\sum_s \pi_s \nabla_s \right)}{1 - \alpha} \tag{44}$$

$$\nabla_s \geq \mathrm{cost}_s - \mathrm{VaR} \tag{45}$$

$$\nabla_s \geq 0 \tag{46}$$

The total cost of each scenario Cost_s consists of different terms as follows:

$$\mathrm{Cost}_s = \sum_t \left(\left(\mathrm{PS}^{\mathrm{grid}}_{t,s} + Pe_{t,s} - \mathrm{PS}^{\mathrm{sold}}_{t,s} \right) \lambda^e_{t,s} + TTUC_t + Pg_t \times \lambda^g \right) \tag{47}$$

The first term indicates the power flowing toward/from EPP and its associated payments. The second term is related to the operating costs of thermal units. The last term is about the gas purchase from NGN.

4 Simulation Results

4.1 Data

The proposed approach is implemented in GAMS [38] environment solved by DICOPT solver running on an Intel Core 2 Duo Processor T5300 (1.73 GHz) PC with 1 GB RAM. It is applied to a 5-thermal units system as described in Table 2. The cost coefficients of the thermal units are adapted from [39]. The UT_i and DT_i for all units are considered to be 5 and 2 h, respectively. The available percent of wind capacity in each wind speed scenario is given in Table 3. The total wind capacity (i.e., P^r_w) is assumed to be 300 MW. The mean values of electricity prices, electricity demand, and heat demand for the upcoming day are given in Table 4. The corresponding standard deviations (σ) is assumed to be 1 % of the mean values given in Table 4. The energy hub characteristics and data are described in Table 5.

Table 3 Wind turbine available percent of power in different scenarios

States	wp_s (%)	π_s
1	0	0.2059
2	5	0.0661
3	15	0.1123
4	20	0.1037
5	35	0.1122
6	45	0.0912
7	55	0.0773
8	65	0.0501
9	75	0.0451
10	85	0.0326
11	95	0.0250
12	100	0.0784

Table 4 Average values of electricity price, electric demand, and heat demand

Hour	Price ($)	μ_{Le_t} (MWh)	Lh_t (MWh)
t_1	35.62	260.24	57.28
t_2	31.37	352.05	40.93
t_3	29.73	308.79	40.93
t_4	25.65	277.18	49.05
t_5	23.30	343.39	89.98
t_6	27.48	375.16	196.42
t_7	37.56	334.53	409.07
t_8	49.19	398.94	450.00
t_9	54.35	624.10	392.72
t_{10}	53.66	663.80	310.86
t_{11}	51.54	686.46	229.12
t_{12}	51.45	603.47	171.84
t_{13}	47.77	708.92	155.49
t_{14}	45.20	800.00	147.26
t_{15}	43.94	791.43	130.91
t_{16}	42.54	630.62	98.21
t_{17}	42.01	437.77	188.19
t_{18}	46.09	141.75	204.54
t_{19}	51.54	83.47	212.77
t_{20}	55.31	132.06	196.42
t_{21}	50.36	84.82	188.19
t_{22}	45.91	50.19	179.95
t_{23}	50.24	18.39	155.49
t_{24}	41.25	64.89	89.98

4.2 Pareto Optimal Front Determination

The proposed risk-based energy management strategy is solved using multiobjective optimization technique and the Pareto optimal front of the solutions is obtained as depicted in Fig. 7. The concept of Pareto optimality is explained in

Table 5 Energy hub characteristics and data

Parameter	Value	Dimension
η	90	%
η_{ge}^{chp}	35	%
η_{gh}^{chp}	45	%
η_{gh}^{f}	75	%
λ^{g}	30	\$/MWh
E_{ini}	500	MWh
E_{fin}	500	MWh
E_{max}	3000	MWh
E_{min}	50	MWh

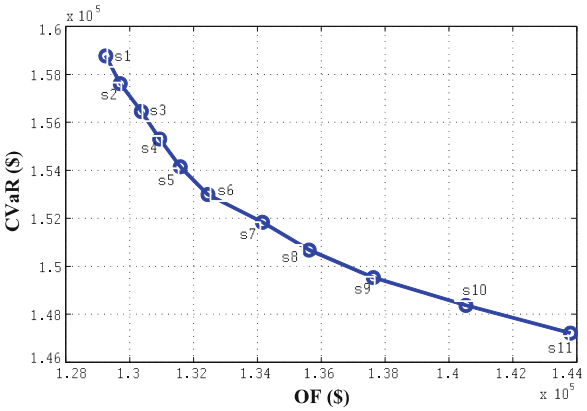

Fig. 7 The Pareto optimal front of risk versus expected value of cost

Table 6 Attributes of Pareto optimal front solutions

Solution	$\Xi(\text{Cost}_s)$	VAR	CVAR	$min_s(\text{Cost}_s)$	$max_s(\text{Cost}_s)$
S1	129235.72	138970.10	158788.49	116952.91	167001.34
S2	129687.69	139179.83	157633.21	117726.39	166632.98
S3	130350.68	139159.03	156477.92	119311.38	164917.40
S4	130927.30	139065.94	155322.63	120803.32	163233.71
S5	131569.88	139005.60	154167.34	122384.58	161536.05
S6	132436.47	139090.44	153012.05	124308.02	159765.03
S7	134144.13	139683.94	151856.77	127479.90	157741.69
S8	135603.97	140126.84	150701.48	128573.45	155791.96
S9	137614.67	140894.79	149546.19	130074.14	153680.98
S10	140513.33	142522.68	148390.90	132350.19	151297.27
S11	143786.49	145571.89	147235.62	135011.20	148146.53

Appendix-II. This front is obtained using ε-constraint method, which is an efficient technique to solve problems with non-convex Pareto front. This method sets an upper limit for one objective function and minimizes the other one. This limit is gradually decreased and the Pareto front is obtained. The next step after finding the

Table 7 Degree of optimization satisfaction for each solution

Solution	$\mu^1_{\Xi(\text{cost}_s)}$	μ^2_{CVaR}	$min(\mu^1, \mu^2)$	$\sum(\mu^1, \mu^2)/2$
S1	**1.00**	0.00	0.00	0.50
S2	0.97	0.10	0.10	0.53
S3	0.92	0.20	0.20	0.56
S4	0.88	0.30	0.30	0.59
S5	0.84	0.40	0.40	0.62
S6	0.78	0.50	0.50	**0.64**
S7	0.66	0.60	**0.60**	0.63
S8	0.56	0.70	0.56	0.63
S9	0.42	0.80	0.42	0.61
S10	0.22	0.90	0.22	0.56
S11	0.00	**1.00**	0.00	0.50

Table 8 Characteristics of solution no. 1

Hour	Pg_t	$\Xi\left(Pe^{\text{grid}}_{t,s}\right)$	$\Xi\left(\text{PS}^{\text{sold}}_{t,s}\right)$	$\Xi\left(\text{PS}^{\text{grid}}_{t,s}\right)$	$\Xi(\text{SOC}_{t,s})$	$\Xi\left(\text{PS}^{\text{hub}}_{t,s}\right)$	$\Xi\left(\text{PS}^{\text{dch}}_{t,s}\right)$
t_1	76.37	193.40		125.54	500.00	41.19	0.05
t_2	54.57	237.36	2.87	0.07	339.38		6.75
t_3	54.57	200.58	0.04	1.02	189.98	0.09	0.32
t_4	65.40	172.78		12.03	53.99	3.72	0.15
t_5	119.97	528.32		3099.72	2957.34	293.08	0.16
t_6	261.89	312.18		142.95	2976.46	45.18	0.17
t_7	545.43	246.93		145.35	2975.59	20.58	0.19
t_8	600.00	288.49	2.35	0.89	2821.00	0.18	2.64
t_9	523.63	61.08	1235.30	1.24	793.94	0.15	455.18
t_{10}	414.48	551.82	1.51	1.26	638.95	0.08	4.07
t_{11}	305.49	578.28		1.45	489.98	0.32	0.51
t_{12}	229.12	495.60		1.58	341.48	0.26	0.13
t_{13}	207.32	601.23		2.83	194.20	0.72	0.43
t_{14}	196.34	693.02		6.24	50.65	1.41	0.40
t_{15}	174.54	702.43		147.76	50.49	20.12	1.13
t_{16}	130.95	547.87		145.71	54.30	25.47	0.23
t_{17}	250.91	722.16		2957.57	2919.22	392.58	0.20
t_{18}	272.71	62.30		3.14	2797.65	28.47	0.01
t_{19}	283.69	28.57	0.07	1.05	2696.21	53.00	0.01
t_{20}	261.89	5.82	1973.07	0.99	327.86	31.15	49.47
t_{21}	250.91	29.38	0.17	1.41	226.13	52.46	0.02
t_{22}	239.94	13.72	0.04	2.51	142.49	71.28	0.01
t_{23}	207.32	4.14	0.13	1.40	77.76	93.51	0.00
t_{24}	119.97	148.35		444.50	500.00	191.33	0.01

Pareto optimal front is the selection of final solution which is done using fuzzy satisfying approach [20] (see Appendix-III). The attributes of Pareto optimal front solutions are described in Table 6.

Table 9 Characteristics of solution no. 11

Hour	Pg_t	$\sum_i P_t^i$	$\Xi\left(Pe_{t,s}^{\text{grid}}\right)$	$\Xi\left(\text{PS}_{t,s}^{\text{sold}}\right)$	$\Xi\left(\text{PS}_{t,s}^{\text{grid}}\right)$	$\Xi(\text{SOC}_{t,s})$	$\Xi\left(\text{PS}_{t,s}^{\text{hub}}\right)$	$\Xi\left(\text{PS}_{t,s}^{\text{dch}}\right)$
t_1	76.37		195.20		123.73	500.00	42.98	0.03
t_2	54.57		231.14	7.51	0.00	327.23	0.02	13.00
t_3	54.57	50.00	154.42	0.04	0.88	181.12	3.99	0.40
t_4	65.40	75.00	107.64		8.89	51.18	13.45	0.04
t_5	119.97	140.00	438.13		3054.54	2958.70	342.73	0.01
t_6	261.89	205.00	105.62		143.61	2977.01	43.43	0.03
t_7	545.43	270.00	42.05	5.79	87.30	2976.01	85.40	
t_8	600.00	335.00	19.05	9.97	0.55	2872.10	63.07	0.08
t_9	523.63	395.00	13.06	1709.09	1.11	702.38	7.89	115.95
t_{10}	414.48	440.00	123.61	4.72	0.68	554.56	8.78	0.98
t_{11}	305.49	485.00	106.32		1.06	417.05	12.91	0.07
t_{12}	229.12	525.00	26.16	0.00	0.66	317.71	55.66	0.02
t_{13}	207.32	545.00	77.58		2.02	188.98	21.67	0.04
t_{14}	196.34	560.00	138.92		5.98	50.56	6.98	0.08
t_{15}	174.54	575.00	135.37		139.54	50.35	27.02	0.10
t_{16}	130.95	583.50	28.08	0.17	87.78	59.13	88.85	0.00
t_{17}	250.91	598.50	413.88	1.03	1794.58	2137.07	682.19	
t_{18}	272.71	613.50		3.32	0.05	2504.02	578.42	
t_{19}	283.69	628.50		11.65	0.17	2927.12	651.00	
t_{20}	261.89	650.00		2959.93	0.16	50.34	624.31	
t_{21}	250.91	652.00		410.05	0.15	50.69	673.14	
t_{22}	239.94	662.00		5.23	0.12	540.70	717.48	0.01
t_{23}	207.32	662.00	0.01	896.26	0.20	70.13	750.09	
t_{24}	119.97	662.00	0.00	48.86	0.44	500.00	704.18	

4.3 Final Solution Selection

Using the technique described in Appendix-III, the degree of optimization satisfaction is calculated for each solution as shown in Table 7.

In order to clarify the final solution selection, four different decision-making options are considered. Each option represents a unique attitude of decision-maker toward the risk and cost of energy hub management. Next, each option is described and analyzed.

Using the technique described in Appendix-III, the degree of optimization satisfaction is calculated for each solution as shown in Table 7.

In order to clarify the final solution selection, four different decision-making options are considered. Each option represents a unique attitude of decision-maker toward the risk and cost of energy hub management. Next, each option is described and analyzed.

Table 10 Optimal schedule of thermal units in solution no. 11

Hour	$P_t^{i=1}$	$P_t^{i=2}$	$P_t^{i=3}$	$P_t^{i=5}$	TTUC_t(\$)
t_3		30		20	433.00
t_4		40		35	240.85
t_5		50	40	50	595.83
t_6	20	60	60	65	758.39
t_7	40	70	80	80	784.34
t_8	60	80	100	95	938.93
t_9	75	90	120	110	1086.04
t_{10}	75	100	140	125	1189.59
t_{11}	75	110	160	140	1295.38
t_{12}	75	120	175	155	1390.81
t_{13}	75	125	175	170	1437.40
t_{14}	75	125	175	185	1472.07
t_{15}	75	125	175	200	1507.42
t_{16}	68.5	125	175	215	1523.14
t_{17}	68.5	125	175	230	1559.83
t_{18}	68.5	125	175	245	1597.20
t_{19}	68.5	125	175	260	1635.25
t_{20}	75	125	175	275	1694.26
t_{21}	62	125	175	290	1693.74
t_{22}	62	125	175	300	1720.30
t_{23}	62	125	175	300	1720.30
t_{24}	62	125	175	300	1720.30

(1) Risk neutral attitude

In this option, the decision-maker neglects the risk and tries to minimize the expected costs. The best solution for this purpose is solution no. 1. This solution has the maximum value of $\mu_{\Xi(\text{cost}_s)}$ compared to other solutions. The characteristics of this solution are given in Table 8.

The simulation results show that the thermal units are off for this option since it only uses the gas and electricity power pool to meet the different demands. It also stores the energy bought from EPP ($\Xi\left(\text{PS}_{t,s}^{\text{grid}}\right)$) and produced by energy hub ($\Xi\left(\text{PS}_{t,s}^{\text{hub}}\right)$).

(2) Risk averse attitude

In some situations, the cost issue does not matter while risk issue constitutes the whole concerns. This option deals with such a situation where the most important issue for the decision maker is the risk and it tries to minimize CVaR. The best solution for this purpose is solution no. 11. This solution has the minimum value of μ_{CVaR} compared to other solutions. The characteristics of this solution are given in Table 9.

The optimal schedule of thermal units in solution no. 11 are given in Table 10.

Table 11 Characteristics of solution no. 7

Hour	Pg_t	$\sum_i P_t^i$	$\Xi\left(Pe_{t,s}^{\text{grid}}\right)$	$\Xi\left(\text{PS}_{t,s}^{\text{sold}}\right)$	$\Xi\left(\text{PS}_{t,s}^{\text{grid}}\right)$	$\Xi(\text{SOC}_{t,s})$	$\Xi\left(\text{PS}_{t,s}^{\text{hub}}\right)$	$\Xi\left(\text{PS}_{t,s}^{\text{dch}}\right)$
t_1	76.37		202.03		116.91	500	49.82	0.05
t_2	54.57		233.19	2.66	0.01	334.93		10.91
t_3	54.57	20	181.51		0.8	186.21	1.05	0.34
t_4	65.4	35	141.11		11.28	52.56	6.96	0.06
t_5	119.97	50	1157.23		2419.6	2954.82	971.96	0.14
t_6	261.89	65	243.28		150.78	2977.5	41.17	0.06
t_7	545.43	100	163.36		128.09	2975.89	36.9	0.1
t_8	600	135	158.38	0.4	1.05	2828.34	3.56	1.14
t_9	523.63	170	60.1	1411.09	1.14	793.65	0.16	286.18
t_{10}	414.48	200	352.38	1.59	0.88	638.84	0.13	3.56
t_{11}	305.49	215	363.37		1.46	490	0.26	0.36
t_{12}	229.12	230	265.69		1.76	341.76	0.3	0.08
t_{13}	207.32	235.25	365.59		3.13	194.44	0.16	0.26
t_{14}	196.34	240.5	452.32		6.28	50.74	1.19	0.38
t_{15}	174.54	200	498.92		151.05	50.51	15.92	0.45
t_{16}	130.95	215	336.3		142.65	54.68	28.8	0.12
t_{17}	250.91	230	645.07		2633.17	2765.28	545.31	0.03
t_{18}	272.71	245	0.02	0.62	0.2	2804.49	210.8	
t_{19}	283.69	260		2.51	0.17	2907.18	283.7	
t_{20}	261.89	275	0.01	2639.16	0.15	50.3	250.44	0
t_{21}	250.91	285.5		91.74	0.1	75.52	307.85	
t_{22}	239.94	276.01		1.64	0.22	223.24	332.6	
t_{23}	207.32	285.5		112.74	0.28	285.08	374.28	
t_{24}	119.97	285.5	6.84	0.01	70.45	500	335.04	

(3) Conservative trade-off between risk and cost attitude

In some situations, both risk and cost are important and none of them should be degraded. This option deals with such a situation where the most attractive solution is the one which has the maximum value of minimum satisfaction of objective functions. The best solution in this option is solution no. 7. This solution has the degree of satisfaction for $\mu_{\text{CVaR}} = 0.6$ and $\mu^1_{\Xi(\text{cost}_s)} = 0.66$. The characteristics of this solution are given in Table 11.

The optimal schedule of thermal units in solution no. 7 are given in Table 12.

(4) Compromised trade-off between risk and cost attitude

In some situations, both risk and cost are important but it is accepted that if one of them is degraded to significantly improve the other one. This option deals with such a situation where the most attractive solution is the one which has the maximum value of sum of satisfaction of objective functions. The best solution in this regard is solution no. 6. This solution has the degree of satisfaction for $\mu_{\text{CVaR}} = 0.5$ and $\mu^1_{\Xi(\text{cost}_s)} = 0.78$. The characteristics of this solution are given in Table 13.

The optimal schedule of thermal units in solution no. 6 are given in Table 14.

Table 12 Characteristics of solution no. 7

Hour	$P_t^{i=1}$	$P_t^{i=5}$	TTUC_t(\$)
t_3		20	196.45
t_4		35	104.36
t_5		50	132.94
t_6		65	162.19
t_7	20	80	380.07
t_8	40	95	339.76
t_9	60	110	426.52
t_{10}	75	125	504.27
t_{11}	75	140	536.89
t_{12}	75	155	570.19
t_{13}	65.25	170	574.00
t_{14}	55.5	185	580.01
t_{15}		200	575.90
t_{16}		215	491.92
t_{17}		230	528.61
t_{18}		245	565.98
t_{19}		260	604.02
t_{20}		275	642.74
t_{21}		285.5	670.17
t_{22}		276	645.37
t_{23}		285.5	670.17
t_{24}		285.5	670.17

5 Discussion

- The proposed methodology for energy hub management provides the ability for decision-maker to react to uncertain energy prices, demands, and renewable power generations. Numerical results show that in order to obtain lower values of expected energy procurement cost, more level of risk is inevitable. Hence, the decision-maker should take a compromise between economy and reliability of the energy hub.
- The proposed model can be easily adapted to any energy hub.
- Future work may address the issue of environmental impacts of energy hub. Furthermore, it could be assessed if trading emission allowance would be an interesting economic option for an energy hub.

Table 13 Characteristics of solution no. 6

Hour	Pg_t	$\sum_i P_t^i$	$\Xi(Pe_{t,s}^{\text{grid}})$	$\Xi\left(\text{PS}_{t,s}^{\text{sold}}\right)$	$\Xi\left(\text{PS}_{t,s}^{\text{grid}}\right)$	$\Xi(\text{SOC}_{t,s})$	$\Xi\left(\text{PS}_{t,s}^{\text{hub}}\right)$	$\Xi\left(\text{PS}_{t,s}^{\text{dch}}\right)$
t_1	76.37		189.26		129.69	500.00	37.08	0.08
t_2	54.57		234.29	2.72	0.06	336.17		9.79
t_3	54.57		200.59		0.71	186.55	0.09	0.31
t_4	65.40	20.00	154.48		11.58	51.70	5.39	0.10
t_5	119.97	35.00	754.69		2833.97	2951.04	554.74	0.45
t_6	261.89	50.00	257.96		153.86	2976.21	40.87	0.08
t_7	545.43	65.00	207.02		120.00	2975.11	45.57	0.10
t_8	600.00	80.00	209.64	3.29	1.03	2820.89	0.17	1.48
t_9	523.63	95.00	106.31	1374.11	1.08	795.28	0.11	314.91
t_{10}	414.48	110.00	442.02	2.18	1.27	639.74	0.19	3.98
t_{11}	305.49	125.00	453.09	0.35	1.51	490.22	0.37	0.75
t_{12}	229.12	140.00	355.60		1.65	341.77	0.33	0.21
t_{13}	207.32	155.00	446.36		2.49	194.34	0.67	0.24
t_{14}	196.34	170.00	522.42		6.85	50.81	0.72	0.31
t_{15}	174.54	185.00	525.06		140.03	50.72	27.00	0.38
t_{16}	130.95	198.50	380.70		113.00	53.27	56.87	0.30
t_{17}	250.91	198.50	533.86		2821.12	2804.58	402.61	0.05
t_{18}	272.71	213.50	0.07	0.49	0.36	2815.88	179.46	
t_{19}	283.69	227.50	0.00	1.83	0.18	2890.30	251.43	
t_{20}	261.89	240.92	0.00	2590.76	0.14	56.60	216.44	
t_{21}	250.91	225.92	0.01	48.05	0.15	76.88	248.38	
t_{22}	239.94	210.92	0.00	1.31	0.20	166.73	267.92	
t_{23}	207.32	195.92	0.04	41.32	0.23	227.40	284.85	
t_{24}	119.97	180.92	36.42		209.53	500.00	260.02	

Table 14 Optimal schedule of thermal units in solution no. 6

Hour	$P_t^{i=5}$	TTUC_t(\$)
t_4	20	196.45
t_5	35	104.36
t_6	50	132.94
t_7	65	162.19
t_8	80	192.12
t_9	95	222.73
t_{10}	110	254.00
t_{11}	125	285.96
t_{12}	140	318.58
t_{13}	155	351.88
t_{14}	170	385.88
t_{15}	185	420.55
t_{16}	198.5	452.30
t_{17}	198.5	452.30
t_{18}	213.5	488.26
t_{19}	227.5	522.40
t_{20}	240.9	555.72
t_{21}	225.9	518.56
t_{22}	210.9	482.06
t_{23}	195.9	446.24
t_{24}	180.9	411.09

6 Conclusion

A two-stage optimization technique is proposed as a powerful decision-making tool for energy management of an energy hub. The proposed model considers the impacts of price, demand, and wind power generation uncertainties and energy hub technical and economical constraints. It allows the decision-maker to decide about the amount of energy to be stored/released/consumed by energy hub. One of the main features of the proposed multiobjective optimization model is to consider both the cost of energy procurement and the associated risk. This chapter also demonstrates that employing a probabilistic approach for scheduling of energy hubs while considering the risk of energy procurement quantitatively, can make the decision-making process more reliable, economical, and resilient against various existing uncertainties.

Appendix-I

Scenario Reduction Technique

Suppose that the original set of the scenarios is denoted by Ω_J and we want to reduce the number of scenarios to N_{Ω_S}. Hence, scenario reduction proposes a method for selection of a set, i.e., Ω_S, with the cardinality of N_{Ω_S}, from Ω_J. The number of the reduced scenarios should be selected in a way that the computation burden reduced while not drastically reducing the accuracy [25]. The scenario reduction technique used in this chapter can be carried out using the following steps [40]: [step. 1]

1. Construct the matrix containing the distance between each pair of scenarios $c(w, w')$
2. Select the fist scenario w_1 as follows:

$$w_1 = \arg\left\{ \min_{w' \in \Omega_J} \sum_{w \in \Omega_J} \pi_w c(w, w') \right\}$$

$$\Omega_S = \{w_1\}, \Omega_J = \Omega_J - \Omega_S$$

3. Select the next scenario to be added to Ω_S as follows:

$$w_n = \arg\left\{ \min_{w' \in \Omega_J} \sum_{w \in \Omega_J - \{w'\}} \pi_w \min_{w'' \in \Omega_S \cup \{w\}} c(w, w'') \right\}$$

$$\Omega_S = \Omega_S \cup \{w_n\}, \Omega_J = \Omega_J - \Omega_S$$

4. If the number of selected set is sufficient then end and go to step 2; else continue.
5. The probabilities of each nonselected scenario will be added to its closest scenario in the selected set.
6. End.

Appendix-II

Pareto Optimality

Assume $F(X)$ is the vector of objective functions, and $H(X)$ and $G(X)$ represent equality and inequality constraints, respectively. A multiobjective minimization problem can be formulated as follows [41]:

$$\begin{gathered} \min F(X) = [f_1(X), \ldots, f_{N_O}(X)] \\ \text{Subject to:} \\ \{G(X) = \bar{0}, H(X) \leq \bar{0}\} \\ X = [x_1, \ldots, x_m] \end{gathered}$$

X_1 dominates X_2 if:

$$\forall k \in \{1 \ldots N_O\} f_k(X_1) \leq f_k(X_2)$$

$$\exists k' \in \{1 \ldots N_O\} f_{k'}(X_1) < f_{k'}(X_2)$$

Any solution which is not dominated by any other is called to belong to a Pareto optimal front which is referred to as the first Pareto front or optimal front or nondominated front.

Appendix-III

Fuzzy Satisfying Method

Fuzzy satisfying (or *max(min)*) method is a popular technique for selection of the best solution among the obtained N_p Pareto optimal solutions [20]. Suppose we have a problem with N objectives to be minimized. The linear membership function for the nth solution of the kth objective function is defined as [42]:

$$\mu_k^n = \begin{cases} 1 & f_k^n \le f_k^{\min} \\ \frac{f_k^{\max} - f_k^n}{f_k^{\max} - f_k^{\min}} & f_k^{\min} \le f_k^n \le f_k^{\max} \\ 0 & f_k^n \ge f_k^{\max} \end{cases}$$

$$k = 1, \ldots, N, n = 1, \ldots, N_p$$

where $f_k^{\max}$ and $f_k^{\min}$ are maximum and minimum values of the objective function k in solutions of Pareto optimal set. μ_k^n represents the optimality degree of the nth solution of the kth objective function. The membership function of nth solution can be calculated using the following equation:

$$\begin{aligned} \mu^n &= min\left(\mu_1^n, \ldots, \mu_N^n\right) \\ n &= 1, \ldots, N_p \end{aligned} \tag{48}$$

The solution with the maximum weakest membership function is the best solution. The corresponding membership function of this solution ($\mu^{\max}$), is calculated as follows:

$$\mu^{\max} = max\left(\mu^1, \ldots, \mu^{N_p}\right)$$

.

References

1. Krause T, Andersson G, Frohlich K, Vaccaro A (2011) Multiple-energy carriers: modeling of production, delivery, and consumption. Proc IEEE 99(1):15–27
2. Koeppel G, Andersson G (2009) Reliability modeling of multi-carrier energy systems. Energy 34(3):235–244
3. del Real AJ, Arce A, Bordons C (2009) Optimization strategy for element sizing in hybrid power systems. J Power Sources 193(1):315–321
4. Kienzle F, Ahcin P, Andersson G (2011) Valuing investments in multi-energy conversion, storage, and demand-side management systems under uncertainty. IEEE Trans Sustain Energy 2(2):194–202
5. Kienzle F, Andersson G (2010) Location-dependent valuation of energy hubs with storage in multi-carrier energy systems. In: IEEE 7th International Conference on the European Energy Market (EEM). pp 1–6
6. Fabrizio E, Corrado V, Filippi M (2010) A model to design and optimize multi-energy systems in buildings at the design concept stage. Renew Energy 35(3):644–655
7. Arnold M, Andersson G (2011) Model predictive control of energy storage including uncertain forecasts. In: Power Systems Computation Conference (PSCC). Stockholm, Sweden
8. Almassalkhi M, Hiskens I (2011) Optimization framework for the analysis of large-scale networks of energy hubs. In: Power Systems Computation Conference (PSCC). Stockholm, Sweden
9. Krause T, Kienzle F, Art S, Andersson G (2010) Maximizing exergy efficiency in multi-carrier energy systems. In: IEEE Power and Energy Society General Meeting. pp 1–8

10. Morales J, Conejo A, Perez-Ruiz J (2010) Short-term trading for a wind power producer. IEEE Trans Power Syst 25(1):554–564
11. Catalao JP, Pousinho HM, Mendes VM (2012) Optimal offering strategies for wind power producers considering uncertainty and risk. IEEE Syst J 6(2):270–277
12. Rabiee A, Soroudi A (2013) Stochastic multiperiod OPF model of power systems with HVDC-connected intermittent wind power generation. IEEE Trans Power Delivery 99:1–1 (Early access)
13. Soroudi A, Ehsan M (2011) A possibilistic-probabilistic tool for evaluating the impact of stochastic renewable and controllable power generation on energy losses in distribution networks–a case study. Renew Sustain Energy Rev 15(1):794–800
14. Wang Y, Xia Q, Kang C (2011) Unit commitment with volatile node injections by using interval optimization. IEEE Trans Power Syst 26(3):1705–1713
15. Wu L, Shahidehpour M, Li Z (2012) Comparison of scenario-based and interval optimization approaches to stochastic SCUC. IEEE Trans Power Syst 27(2):913–921
16. Koonce A, Apostolakis G, Cook B (2008) Bulk power risk analysis: ranking infrastructure elements according to their risk significance. Int J Electr Power Energy Syst 30(3):169–183
17. Soroudi A, Amraee T (2013) Decision making under uncertainty in energy systems: state of the art. Renew Sustain Energy Rev 28:376–384
18. Soroudi A (2012) Possibilistic-scenario model for DG impact assessment on distribution networks in an uncertain environment. IEEE Trans Power Syst 27(3):1283–1293
19. Soroudi A, Afrasiab M (2012) Binary PSO-based dynamic multi-objective model for distributed generation planning under uncertainty. IET Renew Power Gener 6(2):67–78
20. Soroudi A, Caire R, Hadjsaid N, Ehsan M (2011) Probabilistic dynamic multi-objective model for renewable and non-renewable distributed generation planning. IET Gener Transm Distrib 5(11):1173–1182
21. Soroudi A, Aien M, Ehsan M (2012) A probabilistic modelling of photo voltaic modules and wind power generation impact on distribution networks. IEEE Syst J 6(2):254–259
22. Mohammadi-Ivatloo B, Zareipour H, Amjady N, Ehsan M (2013) Application of information-gap decision theory to risk-constrained self-scheduling of GenCos. IEEE Trans Power Syst 28(2):1093–1102
23. Soroudi A, Ehsan M (2012) IGDT based robust decision making tool for DNOs in load procurement under severe uncertainty. IEEE Trans Smart Grid 4(2):886–895
24. Soroudi A (2013) Smart self-scheduling of GenCos with thermal and energy storage units under price uncertainty. Int Trans Electr Energy Syst 1–11. http://dx.doi.org/10.1002/etep.1780
25. Conejo AJ, Carrion M, Morales JM (2010) Decision making under uncertainty in electricity markets. Springer, New York
26. Albrecht P (1993) Shortfall returns and shortfall risk. Institut für Versicherungswissenschaft
27. Whitmore GA, Findlay MC (1978) Stochastic dominance: an approach to decision-making under risk. Lexington Books, Lexington
28. Linsmeier TJ, Pearson ND (2000) Value at risk. Financ Anal J 56:47–67
29. Rockafellar RT, Uryasev S (2000) Optimization of conditional value-at-risk. J Risk 2:21–42
30. Agarwal V, Naik NY (2004) Risks and portfolio decisions involving hedge funds. Rev Financ Stud 17(1):63–98
31. Mohammadi-Ivatloo B, Zareipour H, Ehsan M, Amjady N (2011) Economic impact of price forecasting inaccuracies on self-scheduling of generation companies. Electr Power Syst Res 81(2):617–624
32. Mohammadi-Ivatloo B, Rabiee A, Soroudi A (2013) Nonconvex dynamic economic power dispatch problems solution using hybrid immune genetic algorithm. IEEE Syst J 7(4):777–785
33. Ding Y, Wang P, Goel L, Loh PC, Wu Q (2011) Long-term reserve expansion of power systems with high wind power penetration using universal generating function methods. IEEE Trans Power Syst 26(2):766–774

34. Atwa Y, El-Saadany E (2011) Probabilistic approach for optimal allocation of wind-based distributed generation in distribution systems. IET Renew Power Gener 5(1):79–88
35. Patel MR (2005) Wind and solar power systems: design, analysis, and operation. CRC, Boca Raton
36. Stiebler M (2008) Wind energy systems for electric power generation. Springer, Heidelberg
37. Windpro http://www.enercon.de/p/downloads/ENProduktuebersicht0710.pdf. Accessed Feb 2013
38. Brooke AMA, Kendrick D, Roman R (1998) GAMS: a user's guide. GAMS development corporation. Washington
39. Mohammadi-ivatloo B, Rabiee A, Soroudi A, Ehsan M (2012) Imperialist competitive algorithm for solving non-convex dynamic economic power dispatch. Energy 44(1):228–240
40. Pineda S, Conejo A (2010) Scenario reduction for risk-averse electricity trading. IET Gener Transm Distrib 4(6):694–705
41. Soroudi A, Ehsan M, Caire R, Hadjsaid N (2011) Hybrid immune-genetic algorithm method for benefit maximisation of distribution network operators and distributed generation owners in a deregulated environment. IET Gener Transm Distrib 5(9):961–972
42. Rabiee A, Soroudi A (2013) Optimal multi-area generation schedule considering renewable resources mix: a real-time approach. IET Gener Transm Distrib 7(9):1011–1026

Adopting the IEC Common Information Model to Enable Smart Grid Interoperability and Knowledge Representation Processes

N. B. Hargreaves, S. M. Pantea and G. A. Taylor

Abstract Information interoperability is a key process underpinning the development of flexible and efficient electrical networks capable of integrating large-scale renewable and conventional energy technologies into smart grids to supply consumers with sustainable energy. The smart grid concept requires technologies ranging from smart meters to utility-level energy management systems to share information on an unprecedented scale. The availability of data and information about grid systems will also increase dramatically as the smart grid develops but its value and usefulness will depend on the degree to which it can be formed into representative knowledge of the real smart grid. At the heart of power utility and smart grid information interoperability is the IEC Common Information Model (CIM), a suite of open international standards addressing energy management, asset management, and market systems. This chapter discusses the philosophy and processes underpinning smart grid information interoperability to enable power utilities to build and control the emerging smart grid and it elaborates upon how the CIM fits within a standardized power system interoperability framework. It will explain how model-driven information integration using the IEC CIM can be implemented by utilities to leverage the value and validity of data into realistic knowledge representations of smart grid reality and address the need for situational awareness, business intelligence, and process efficiency.

N. B. Hargreaves (✉) · G. A. Taylor
Brunel Institute of Power Systems, School of Engineering and Design, Brunel University, Uxbridge UB8 3PH, UK
e-mail: nigel.hargreaves@brunel.ac.uk

G. A. Taylor
e-mail: gareth.taylor@brunel.ac.uk

S. M. Pantea
Future Control Systems, National Grid Electricity Transmission Plc. St. Catherine's Lodge, Wokingham RG41 5BN Berkshire, UK
e-mail: stefan.pantea@nationalgrid.com

J. Hossain and A. Mahmud (eds.), *Large Scale Renewable Power Generation*, Green Energy and Technology, DOI: 10.1007/978-981-4585-30-9_17,

Keywords Common information model · CIM · Interoperability · Model-driven architecture · Smart grid standards

1 Introduction

The grand vision for sustainability can be accredited to The Club of Rome's report, "Limits to Growth" [1] for setting the stage upon which environmental sustainability was raised as a crucial issue alongside the economic development of society. Its theme was later championed by the UN-sponsored Earth Summit in Rio de Janeiro in 1992. Since then, in various legislative guises, sustainability has been receiving mixed acceptance into the *triple bottom line* of economics, society, and the environment. In recognition of the centrality of energy to all of these considerations however, there is a general acceptance of the need to link energy conversion and transfer with sustainability. The chapters of this book testify to the current pursuit for sustainable energy being an essential pillar supporting our continued presence on Earth, alongside others such as biodiversity and the availability of environmental services perhaps. The smart grid, as a principal means of integrating the conversion processes and transport of sustainable energy, addresses many of the parameters we associate with this new paradigm, including decarbonization, security of supply, energy security and infrastructure lifecycle refresh. It is thus an essential element in our pursuit of sustainability. What makes the smart grid *smart* is its ability to flexibly respond to changes in both supply and demand while maintaining an optimum economy and reliable service. This would not be possible without a high degree of intelligible interaction, known as *interoperability* between its many systems and their components. The "integral component" of interoperability is effective information exchange, which like a shared language in linguistics enables parties speaking different native languages to understand each other. *Understanding* in this case depends on a common semantic model, syntactic agreements for message composition and knowledge of the context to which the information exchange is associated. Development of the International Electrotechnical Commission (IEC) CIM aims to satisfy these essential requirements for enabling interoperability in support of a functional smart grid. However opportunities arise from wide deployment of common semantic model-driven applications, to leverage the value of data and measurements made for situational awareness into a closer representation of smart grid reality. Such knowledge representation reinforces the possibility that the smart grid could herald our evolution in energy management from the "age of information" into the "age of 'intelligence," a vision shared by the "Internet of Things" concept which is just as dependent on a semantic backbone [2]. This chapter will discuss these issues and present the theory behind interoperability in the context of the smart grid as well as the IEC CIM as an evolving core semantic model standard supporting smart grid interoperability and knowledge representation.

2 The Smart Grid Concept

The smart grid has been described as a *cyber-physical* entity, which reflects the emergence of an increasing interdependence between the "hard" and "soft" infrastructure it is made up of [3, 4]. A striking contrast between electricity networks of the past and present is the rapid rise of data availability from a wider range of sensing technologies. Notwithstanding the advancements in network and generation processes, these are driving the rapid reformation of the modern electricity industry. Tighter integration with market, service, and consumer domains is being enabled but extension of the scope of the smart grid to other energy prime movers such as gas and possibly water is conceivable in future. Management of the smart grid is challenged by the increase in data volume and the requirement for interoperability. For example, some 50 million electricity and gas smart meters are to be installed in the UK alone in the next 7 years. The smart grid requires a guiding intelligence that extends from domestic to transmission voltages across generation to service provider domains. Its reflexive nature, supported by Information and Communications Technology (ICT) systems, is undisputed [5].

Electricity transmission networks are already smart but with the addition of renewable and Variable Energy Resources (VERs), Distributed Energy Resources (DERs), and Advanced Metering Infrastructures (AMIs) a holistic approach to conceptualization of the smart grid is necessary, covering not only the domain of transmission but also distribution, storage, generation, markets, service providers, and customers [6]. To establish the role and importance of the CIM and associated standards in the information networks that support operation of the physical electricity networks, it is necessary to frame them within the smart grid concept. In practical terms, this understanding is also essential to making the business cases necessary to justify investment in the changes to power utility information architecture and infrastructure. In responding to the greater flexibility and responsiveness called for in smart grid capabilities these business cases acknowledge the need to manage and leverage the value of the increasing amounts of available data that will not be possible without an established standards framework relating to generally agreed conceptual models of what the emerging smart grid actually is [7].

The origins of the smart grid concept have been described in [8] and the US Department of Energy (DoE) initiating research and development [9], with outcomes such as the Electric Power Research Institute (EPRI) *Intelligrid* programme. The strategic prerogatives for sustainable energy and security, functionality, and management of electricity networks have formed the basis of smart grid development initiatives around the world [10–13]. In [14] the European Commission (EC) views the smart grid as having an essential role in achieving the "20/20/20 Targets" set for the European Union (EU) countries. EC mandate M/490 is the umbrella directive for smart grid development coordination and has driven the formation of the Joint Working Group (JWG), also known as the "Smart Grids Coordination Group" (SC-CG), comprising CEN, CENELEC, and ETSI standards

development organizations. Previous EU mandates already existed for the development of open smart metering standards (M/441) and electric vehicle charging standards (M/468). These initiatives lead us to a broad functional definition of a smart grid having at least the following characteristics:

- Maintains and enhances security of supply (self-healing).
- Facilitates connection to low carbon generating plant.
- Enables innovative demand-side technologies and strategies.
- Facilitates further consumer choice over energy management by providing tariff-based choices.
- Features a holistic communications system providing greater clarity of the grid state and allows it to operate in a way coherent with its decarbonization priorities (reflexive).
- Allows optimization of cost and carbon impacts upon networks.

Given its broad scope, which effects millions of stakeholders and draws upon massive investment to realise, it is imperative that the conceptual models drawn from different viewpoints of the smart grid are widely accepted and established as reference architectural standards. Reed et al. highlight this point by indicating, while different players define the smart grid according to their particular perspectives, it will be difficult to arrive at consensus on gaps in standards and technologies without a standard definition [15]. Two models are continuing to converge and form the dominant standard for high-level smart grid conceptual reference architectures however. These are the National Institute of Standards and Technology (NIST) "Conceptual Architectural Framework" [16] and the EU SG-CG "Smart Grid Reference Architecture" [17]. The NIST framework is based upon seven interoperating domains comprising, "Bulk Generation, Transmission, Distribution, Customer, Operations, Markets and Service Provider." The SG-CG architecture, or Smart Grid Architecture Model (SGAM), generally corresponds to the NIST reference architecture but has extended it with the addition of an eighth domain for "Distributed Energy Resources." Its three-dimensional presentation reflects the flexibility of the smart grid in a range of manifestations from centralized to noncentralized, as well as accommodating forward-looking local area energy systems such as micro-grids.

3 The Theory of Interoperability

Rather like the Internet, the smart grid is a coupled "system of systems" requiring strong coordination across the participating domains and their subsystems. The NIST and SG-CG reference architectural models reflect the need for a disparate number of technologies and functional domains to interoperate effectively. Different definitions of *interoperability* exist but in the context of the smart grid it should incorporate the following characteristics:

- A capability between two or more systems, networks, organizations, applications, components, processes, or devices to exchange meaningful information that is readily usable.
- A shared understanding of the exchanged information.
- An expectation of the response to such information that is agreed upon.
- A requisite quality of service in terms of security, reliability, and fidelity even though the information may be exchanged over different systems, infrastructures, or regions.

The GridWise® Architecture Council (GWAC) was formed by the US DoE to lead on promotion of interoperability between the entities in the USA that make up the smart grid in recognition of interoperability as a key enabler of the smart grid as a whole. The GWAC "Stack" methodology [18] has now been adopted by NIST and the SG-CG as an interoperability reference framework between the different domains and actors in their models. By being integrated into the dominant conceptual reference architectures this interoperability framework has become fundamental to our conceptualization of smart grid interoperability. Although not standardized in itself and modifiable to suit the context, it remains an important reference to what we mean by interoperability. The GridWise® vision acknowledges the premise that ICT will revolutionalise the planning and operation of the power grid, just as it has in other business domains (such as healthcare, telecoms, and finance), and that ICT will form the *nervous system* that integrates smart grid technologies.

The GWAC Stack comprises eight levels in its conceptualization of *end-to-end* interoperability, ranging from "Basic Connectivity" at the physical level of component interoperability to "Economic/Regulatory Policy" at the organizational level where it incorporates Business Objectives and Procedures. "End-to-end" interoperability is a term used to describe effective interoperability across all levels between its extremities. It is within the *Informational* layers of "Business Context" and "Semantic Understanding" in the middle of the Stack, that the IEC CIM can be deployed. These layers form the bridge that transfers meaning in the form of *syntactic conformity, semantic understanding*, and *context* from the signals arising from the lower technical layers (mainly concerned with physical interoperability), upwards to the Business Objectives and Policy layers at the top of the Stack. This is of critical importance as it is necessary for the business components involved at each level to share information between themselves and others (as in an enterprise-to-enterprise scope) in order to achieve their tactical and strategic objectives (Fig. 1.) This can only happen if they are working in a sympathetic and federated manner across their boundaries of jurisdiction with full understanding of message content and close conceptual conformance with actual reality.

Any "standard approach" to interoperability must be scalable and be able to recognize agreements established at component interfaces as well as boundaries of jurisdiction. Scaling-up will inevitably encounter hierarchical, organizational, and structural challenges, such as when different business domains interoperate or integrate with an Enterprise Data Model (EDM) because of the use of different

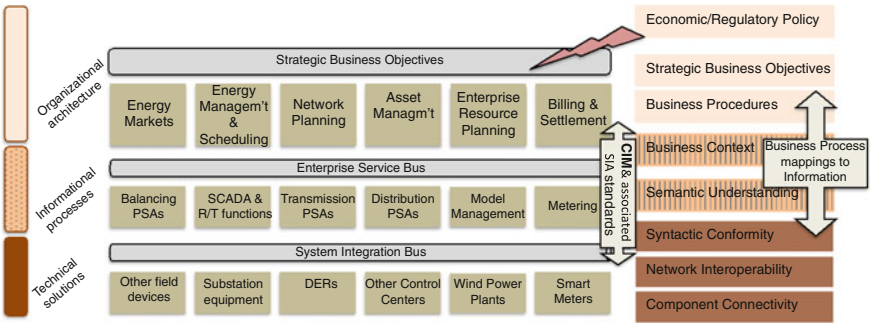

Fig. 1 A Typical smart grid organizational architecture identifying the role of the IEC CIM in supporting end-to-end interoperability

models. In the case of wider manifestation of the smart grid such as with system operation and intersystem operation [19], it will also be necessary to interoperate across enterprise boundaries. A Transmission System Operator (TSO) will have to interoperate with Distribution Network Operators (DNOs), requiring novel infrastructure protecting security, privacy, and service level agreements [20]. Nevertheless, from a resilience point of view, the smart grid is also composed of small and in some cases autonomous operations, such as with DER and protection systems management, which could reduce the scope and scaling challenges. Despite the scalability of the smart grid, therefore, many of the processes to establish interoperability will be cross-cutting issues, effective at all levels of scale. Ambrosio and Widergren in [21] discuss many examples of cross-cutting issues including resource identification, time synchronization, security, and privacy that are important to establish interoperability at any level of the smart grid.

Data model exchange within the context of utility information integration is a key part of the interoperable *glue* between corporate objectives in terms of business positioning and Power System Application (PSA) solutions that facilitate the enterprise orientating as intended. It is likely therefore that the *form* of the information architecture will *inform* the function of the enterprise and raise the question of whether it is fit for purpose [22]. Such an appraisal informs the need for enterprise architecture to be coherent with corporate objectives and regulatory constraints. Connecting this concept to the "solutions level" (levels 1–4 in the GWAC Stack) of the enterprise, especially in times of rapid market change, places greater emphasis upon *information integration* and the removal of legacy system obstacles such as data silos and manual trans-literation interfaces between bespoke systems.

Tolk has addressed these concerns in his *Levels of Conceptual Interoperability Model* (LCIM), and observed that the "conceptual ideas of the enterprise and the implementation details of the systems" often do not connect [23]. This may be due to inappropriate architectural design but also that the interoperability of legacy systems within a complex multisystem architecture cannot always be *decidable* in

advance. Examples of undecidable problems (there is no algorithmic solution but a result relies upon a good heuristic) include questions such as, "Is the specification complete or minimal?" "Is the order of two modeled actions independent or requiring orchestration?" In [23] Tolk proposes that the utility of enterprise architecture to fully support interoperability develops through three broad stages.

- Integratability—concerns physical and technical connectivity of systems, including hardware, networks, firmware, and protocols.
- Interoperability—concerns software and firmware to support information exchange through the use of common semantic models.
- Composabililty—concerns the alignment of the use of models as conceptual abstractions of reality for given business intentions.

The LCIM was created to present these related issues in a consistent framework that exposed six levels of interoperability, ranging from "Technical" to "Conceptual" Interoperability. These levels rise from the physical concern of infrastructure communications to the more abstract concern of the interoperability composition in meeting the objectives it was conceived for. At the center of this hierarchy we find "Semantic Interoperability" linking the "Syntactic" level to the "Pragmatic" interoperability level. The Syntactic level deals with protocol challenges while the Pragmatic level deals challenges of interpreting message patterns. The LCIM was adopted and informed the creation of the GWAC Stack framework, underpinning the centrality of the IEC CIM and the importance of ICT interoperability to smart grid control and integrity as it infuses all levels of the energy domain.

System architectures are developed to fill the gaps in enterprise capabilities. The architecture should map to the detail of the functional requirements but in a rapidly developing environment like the smart grid where there is added pressure to evolve the enterprise alongside multiple independent stakeholder interventions, the risk of Conceptual Interoperability intentions misaligning with actual interoperability outcomes are high. Tolk identifies some major practical challenges to maintaining interoperability in alignment with the overall conceptual design:

- Interoperability satisfies the needs of a limited number of stakeholders due to independent interventions and becomes unaligned with enterprise interoperability concepts.
- The implementation suffers from not being maintained in step with the latest developments.
- The diversity of smart grid developers, regulators, implementers, and other actors are not as aligned as desirable.
- Interventions of one kind have negative secondary impacts on other systems.

These are familiar concerns to system integrators within electricity utilities involved in developing greater interoperability at PSA and enterprise levels. They are especially likely to develop in situations without hierarchical supervision and coordination of stakeholder interventions and where insufficient attention is paid to

cross-cutting challenges. The fourth issue is particularly relevant to the topic of resource identification. Where multiple independent actors who share a common domain exist, the opportunity for the same network entity or resource (such as a power transformer, substation, circuit breaker, or process) to be identified differently is very real. Within a single actors' model of the network, this may not give rise to ambiguity but when models are exchanged and shared with other actors the issue of resource identity can cause conflicts in semantic understanding and disrupt interoperability. It is a vexing challenge to the application of a common information model across multiple PSAs and business domains where there are multiple uncoordinated points of data entry.

3.1 Systems Engineering Interoperability

Rather like the Internet, the smart grid is a coupled "system of systems" requiring strong coordination across the participating domains and their sub-systems. Taking a systems engineering approach at the PSA-to-PSA level, the use of metadata is important in assessing the possibility for, and then supporting interoperability. Between two PSAs with a common operational intention there would be the need for three sets of metadata, one set describing each PSA and the third describing the design for the desired functionality. It is then possible for an assessment of composable interoperation between heterogeneous PSAs to be made, subject to the decidability of the interoperability outcome as previously discussed. Ralyté et al. say that due to the complexity of the interoperability challenge across multiple domains, including business and technology, it is not possible to find a solution to the decidability problem captured by a single method. They discuss a Situational Method Engineering (SME) approach to interoperability problems that involves modularized reusable *method chunks* to compose situation-specific interoperability solutions as they arise [24]. Hug et al. [25] support this view from an information systems engineering perspective and say even the use of standardized metamodels may reveal the limitations of a "one-size fits all approach" in future. This could mean, as the use and understanding of metamodels becomes more widely appreciated, we see the need for more situational metamodel engineering (SMME) to underpin process interoperability in the power industry. Such a Model Driven Engineering (MDE) approach would employ the key principles of a standardized method to building the metamodel appropriate to the situation, and a general trend toward the use of higher levels of abstraction.

Similarly, this has already started to happen within the power industry through developments involving the IEC CIM as a *domain ontology* [26]. For example, in [27], Britton and deVos recognize, "The trouble with a global information model is precisely that *global* is a pretty big area to manage." They see the value in the CIM moving from an "explicit interface specification role to a design methodology role" and the possibility for it to underpin a service-oriented architecture (SOA). SOA is a software model in which the concept of a *service* is an abstraction

of a function used by an application [28]. Services either provide information, or change data from one state to another. A service is a function that may be *reusable* within a business process [29]. Once these functional components of the business process have been identified and related to a semantic model, it becomes possible to model them into an efficient structure, such as to emphasize the value of service reusability, interoperability, and open-availability of data. In this way modeling can be used to drive better understanding of business processes and further their integration within the enterprise.

3.2 Interoperability and Service-Oriented Architecture

SOA can therefore further the scope of interoperability through closer integration of Business Process Management (BPM) to reusable information message exchanges that call for different service operations. Such an approach is summarized by Soley in [30], where he sees BPM design being linked to SOA infrastructure by the "vital bridge" of Model Driven Architecture (MDA). MDA is underpinned by the use of metadata standards to adapt business process models to service requirements in a changing environment such as the smart grid. MDA, itself based on the principles of Model Driven Design (MDD) [31] can also aid in the recovery of design knowledge from existing applications through its use of standards. This approach has been adopted by McMorran et al. to develop transformation applications for CIM-structured metadata files to the Siemens Power System Simulation (PSS/E) standard for model exchanges supporting PSA–PSA interoperability [32, 33].

Another important aspect of SOA is that it opens the way for data to be shared across an enterprise by way of a web service. Web Services Description Language (WSDL) is a commonly supported means of describing the necessary interactions between a service requester and a service provider. It rests as a separate layer upon the data architecture of the enterprise, independent of the code required to implement the service but offering the potential to develop common interfaces for various types of interactions, which leverage the value of software assets as well as data resources. As this web-based approach also opens the number of data access points, security becomes a greater consideration to protect the integrity of proprietary data and system functionality.

In this way, SOA enables a looser connection to the service provider technology and enhances the scope to offer vendor-neutral solutions. In [34] Cao et al. also propose the use of the CIM within an SOA to address information-islanding problems encountered within Enterprise Application Integration (EAI) challenges. Khare et al. [35] develop this theme, describing the use of an Enterprise Service Bus (ESB) within the SOA to "simplify and manage interconnectedness." They also describe the use of metadata within "design patterns" to support interoperability problem description and contribute to process design for common modeling practices such as CIM extension, profiling, and model validation.

Announcement and discovery of metadata underpins the ability to access and leverage the available data and services in an interoperable infrastructure. Rohjans et al. [36] propose a SOA based on the Open Platform for Communications (OPC) Unified Architecture (UA), a standardized server-client architecture specification (see IEC 62451) that embraces security, platform independence, and information models to support interoperability. Their approach brings together a general automation industry SOA solution (OPC UA) for access to real time and historical data and events, to run semantic web services that interact with the Platform Independent Model (PIM) provided by the CIM. Service descriptions are provided by metadata annotations derived from Web Service Modeling Language (WSML) ontology.

3.3 Interoperability and CIM

Neumann and Nielsen in [37] refer to *profiles*, or context-constrained sets of CIM classes that make up the Common Power System Model (CPSM) and the Common Distribution Power System Model (CDPSM) [38, 39]. These "sub-models" of the CIM are accredited standards in themselves and like other available profiles address "common integration patterns" within interoperability challenges and therefore resemble the approach to situational interoperability advocated above. The earliest releases of the IEC CIM were designed to only support interoperability of control center applications [40, 41]. As packages of classes are now added to it that refer to the operation of more diverse aspects of the smart grid, it is conceivable that "method chunks" of the reference metamodel could be applied to interoperability challenges yet to come. Effort is also being made on the harmonization of adjacent standards, such as IEC 61970 with IEC 61850 [42, 43] and IEC 60870 [44] in the interest of extending interoperability across different conceptual metamodels. The power of standards-based metadata at all levels of interoperability described in the LCIM then becomes evident, subject to the limitations of one-size-fits-all, in supporting composable solutions appropriate to the capability-requirement gaps within the enterprise architecture.

Metadata plays a key role in the absence of a fully self-organizing system of systems, in which operational systems have built-in evidence of their components' functionality, necessary for their level of interoperability to be evident to the other interoperating parties. We may currently approach this level of *self-evidence* by exploiting the built-in rules in Resource Description Framework (RDF) and Extensible Markup Language (XML) notation in "knowledge representation" [45, 46] but these form only the surface of interactions between our enterprise component systems at present. Deeper evidence of the capacity for interoperability in future could be evinced from meaning encoded into the structure of the metadata, thus raising the attraction of standard forms of metadata as in the cases of the IEC Common Information Model standards. The intention of building this kind of "structural intelligence" into our metadata models would be to make it possible to

see some degree of self-organization (perhaps similar to biological systems) at the interface between interoperating entities. This degree of interoperability could then extend the current aim of "self-description" and "self-discovery" for advanced distribution automation systems for example.

4 Use Cases

Smart grid interoperability depends on standards used by the diverse range of equipment and processes it is composed of. Standards also ensure against premature obsolescence and support security implementation within the technologies they apply to. Utility PSA and equipment interface requirements have driven the need for a reference ICT standards architecture that can be mapped to the conceptual smart grid reference architectures to satisfy actor interaction requirements. The linkages between the standards architecture and smart grid conceptual architecture are *use cases.* These describe the series of events involving an actor and a technology or process, necessary to execute the intended smart grid capabilities and functions. In this sense, by forming the essential connection between a subject and its objective, the use case reflects the notion of the "subject-predicate-object" *triple* familiar within RDF notation. The scope for standards extension, modification or for new standards to be included in the reference architecture widens as the use cases for smart grid information and communications integration increase.

Use cases vary in the detail of their specification according to NIST by being either "prescriptive" or "descriptive" [16]. The latter omits the specification for the implementation of the use case but describes the actor and functional requirements of the intended goal. Rigorous definition of use cases is therefore advisable to avoid confusion not only over the objective of an intended functionality but also to limit duplication of standards development effort. The reference for defining smart grid use cases according to the EPRI IntelliGrid methodology is given in IEC Publicly Available Specification (PAS) 62559 [47]. Its application process under M/490 is given in [48]. Smart Grid use case repositories are being developed in the EU and the USA with one of the most mature managed by EPRI [49] (see also the NIST Interoperability Knowledge Base [50]).

5 Smart Grid Standards Architecture

In [16] NIST identify 75 existing standards and 15 high-priority gaps in support of smart grid interoperability, in addition to cyber-security issues, as a starting point for standards development and harmonization by standards setting and development organizations. Sixteen Priority Action Programs (PAPs) have been initiated by NIST to address areas in which standards need revision or development to

complete the standards framework according to their smart grid vision. The IEC Standardization Management Board of Technical Committee (TC) 57 identified over 100 standards and standard parts in a strategic review of power system information exchange [51]. Both of these studies concluded however, that only a small number of standards lie at the core of smart grid interoperability and they can be organized into a corresponding layered reference architecture described in IEC/TR 62357 [52]. This reference SOA shows how these standards relate to each other, require harmonization and presents the gaps where further standards development work is required. In general all standards setting and development organizations advocate a collaborative approach to the development of open standards for the smart grid, with the reuse of existing standards as far as possible.

Rohjans et al. in [53, 54] conduct global surveys of smart grid standardization studies and confirm that the IEC/TR 62357 standard, also known as the "Seamless Integration Architecture" (SIA), represents a general consensus of what are the core smart grid standards, subject to two additional standards. These are IEC 61400-25 series: Communications and Monitoring for Wind Power Plants and IEC 62056: Companion Specifications for Energy Metering (COSEM). In Fig. 2, the standards groups included in the IEC SIA and the additions recommended above are shown in simplified form to support the smart grid organizational architecture of Fig. 1. The cross-cutting issue relating to cyber-security is addressed by the standards group on the left hand side of Fig. 2. The evolution of IEC/TR 62357 reflects the broadening scope of TC 57 in step with smart grid use cases from its original charter of "Power System Control and Associated Telecommunications" to "Power System Management and Associated Information Exchange." Generally this change reflects the shift in emphasis from lower level interconnection protocols to abstract information models in the higher levels of the architecture as the number of business functions needing to interoperate with PSAs has increased with smart grid evolution. The TC57 architecture generally follows the form of the GWAC Stack layers 1–7, as it ascends from standards concerned with communications relating to the connectivity of field devices through to information exchanges to support business processes and enterprise objectives. Due to the wide range of perspectives upon what is a smart grid from the countries surveyed, maintenance of the SIA as a central reference is a priority to keep abreast of smart grid evolution. Recommended initial work to extend the SIA would include CIM standards for DER and the increasing number of CIM profiles, electric mobility, and charging, as well as relevant standards referring to the OPC UA.

The middle layers of the GWAC Stack are in transition from a technical to an organizational focus requiring information interoperability. These "Informational" layers correspond to "Business Context" and "Semantic Understanding." They align with the CIM standards IEC 61970, IEC 61968 in IEC/TR 62357. In IEC/TR 62357-1 [55], a further standard, IEC 62352, is added to the CIM. These standards make up the current specification for the IEC Common Information Model (CIM) and broadly apply to the functions of EMS application integration, distribution system application integration and energy market system communications integration respectively. Their importance has been described by NIST as central to

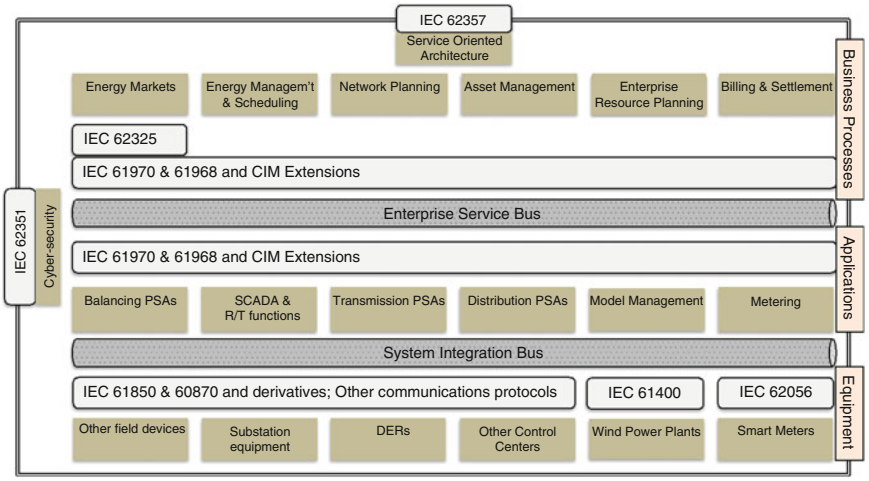

Fig. 2 A simplified representation of IEC TR 62357-1, Seamless Integration Architecture. Standard series are shown with additions representing monitoring and control of wind power plants and smart metering

the foundations of smart grid interoperability [56]. The specific designations for the CIM standards are IEC 61970-301, IEC 61968-11, and IEC 62325-301. Recent development of IEC 62325 to suit a European energy market context is ongoing and a finished extension to this standard is expected to be published by the IEC in 2014.

The EU Task Force for Smart Grids, Expert Group 1, have analyzed smart grid interoperation from the three perspectives of Transmission, Distribution, and Home, and have also summarized international standards harmonization initiatives in [57]. Their standardization methodology recommends a top-down approach with three levels, taking into account Mandate M/441 to ensure that smart metering is included in wider smart grid application standards. The three levels are as follows:

- Harmonize smart grid use cases in member states.
- Harmonize smart grid data modeling and description language.
- Harmonize communication protocols.

A further significant standards framework in support of a SIA is the Institute for Electrical and Electronic Engineers (IEEE) Smart Grid Interoperability Reference Model (SGIRM) [58], which addresses interaction between the actors within the 7 domains identified in the NIST Conceptual Architecture Framework. Its focus is upon interface architectures and data flow characteristics from three architectural perspectives: communications, power systems, and information technology platforms. It provides a scalable model of functional interoperability that can be extended as the scope of the smart grid evolves.

6 The IEC Common Information Model (CIM)

The significance of the CIM standards relates to their function as a scalable and extensible semantic model for power systems. An authoritative description of its design and class composition is given in the associated IEC Standards (IEC 61970-301, IEC 61968, and IEC 62325) and it is further described in [59–61]. Misconceptions about the CIM in terms of its use in database design and the "CIM compliancy" of technology interfaces are addressed in [62]. The structure of the CIM is designed to be flexible. It is object-oriented and presented as a Unified Modelling Language (UML) class model. Flexibility of the model derives from its properties of *extensibility* and *scalability*. Extensibility applies when new objects not available within the standard set are needed, they can be added, underlining the *open* nature of standard model. If these additions are considered of general use and subject to subsequent interoperability testing, they can become inducted into the internationally standardized version [63].

Examples of IEC CIM extension to suit utility use cases are numerous and reflect business case evolution in managing the smart grid through use of Model Driven Architecture (MDA). Extensions to the CIM can be categorized for different purposes, such as widening its domain scope into substation equipment representation [64] or High-Voltage Direct Current (HVDC) modeling [65], to extending its ability to represent dynamic models for contingency analysis [66]. As it is canonical in its design, it is possible to integrate new "packages" of UML classes with dependency to the Core package as the scope of use cases for information exchanges widens. Nielsen and Neumann give a good overview of the processes associated with CIM extension management in [67]. An important recommendation from consensually accepted definitions of smart grid standards identified in [53] featured extension of the SIA to accommodate DERs. With respect to future smart grid operational requirements, this recommendation was responded to in [68] with a proposed design for an energy storage extension comprising a package of classes addressing control of grid-scale energy storage technologies. The CIM is also being used as the design basis for a variety of new model-driven applications including state estimation [69], wide area measurement [70], and secondary equipment management [71].

The CIM is designed to be *scalable*, such that if a subset (or profile) of the standard reference classes are sufficient to model a given use case in a particular context then the rest of the reference metamodel can be ignored. Well-established profiles such as the CPSM and CDPSM have already been mentioned but the tendency to profiling for reusable functionality within the exchange of network models has become more common. The second edition of the European Network of Transmission System Operators for Electricity (ENTSOE) profile version 2.0, which was based upon CIM release 15, is an example of a combination of a bundle of standardized CIM profiles, each referring to specific functionality, including:

- Geographical profile, IEC 61968-13;
- Equipment profile, IEC 61970-452;

- Diagram layout profile, IEC 61970-453;
- State variables profile, IEC 61970-456;
- Topology profile, IEC 61970-456;
- Dynamics profile, IEC 61970-457.

The relationships between CIM UML classes are structured to provide a standardized object-oriented modeling architecture. It is a canonical taxonomy in the form of packages of UML class diagrams *referring to* the components of power utility networks with functional definitions and measurement types to a high degree of granularity. Wang and Van Ausdall give an overview of how business data semantics are represented in the CIM and propose some rules to clarify the UML modeling concepts used [72]. They describe how an XML *namespace* defines the scope of a class name and observe how a CIM class name (and therefore the concept represented by that CIM class) must be unique within the CIM XML namespace to maintain the integrity of the CIM logical model. This raises the distinction between the CIM as a static logical model, a standard conceptual representation of smart grid components, and the *instantiation* of CIM objects in models created by PSA CIM adaptors to represent their functional data models.

Power system applications use the CIM as a reference logic when processing CIM models for export and import. CIM metadata files communicated between PSAs vary in size depending on the scope of the modeled network (for example, a transmission system with complex topology) as well as the detail of the CIM representation of network parameters being communicated. With the most detailed representations of complex networks made up of millions of CIM objects forming multi-Gigabyte sized files, concerns over the amount of data, and the capacity to handle it within the smart grid environment may arise. This topic has been acknowledged and addressed by McMorran in [73] in which a number of strategies are discussed for reducing the size of, and handling, communicated CIM files. The principal strategies for handling large CIM representations of power system networks include communication of layered representations of a network constrained to CIM profiles (see profiles above); the use of difference models (see IEC 61970-552) that only update the status of larger parent models as changes to them occur; the use of compression technologies such as the ZIP file format that can perform better than 20:1 compression on CIM RDF XML. It is unlikely therefore with RDF forming the backbone of communicated CIM files that any great stress will be placed on the data communications and storage capabilities within the smart grid environment.

The semantic definitions and logical integrity of the exchanged model depends on the CIM standards but its “physical” integrity or connectivity depends upon a system of object identification provided by RDF. RDF links objects together by means of a triple, defining a subject in relation to an object using a *predicate*. The predicate as a system of address is used to form the identity description of the object and is generated within the CIM adaptor of the PSA when processing a CIM model. An instantiated model of CIM objects must conform to the logic and

semantic definitions of the standard CIM static model but will only use a portion, or profile, of its set of CIM classes to represent the real network. If each interoperating PSA places its instantiated CIM objects within the same namespace, such as "xmlns:CIM," then the opportunity for object identity *collisions* will arise when these models are shared [74]. This is because the namespace defines the scope of validity for an object identity just as it does for the semantic descriptions of the object. Identity collisions therefore are a vexing problem currently challenging smart grid PSA interoperability.

6.1 The CIM as Ontology for the Electrical Power Domain

If we consider a model as "an abstraction of reality according to a certain conceptualisation" [75], then these standardized models, as meta-conceptualizations *representing* PSA data models, support the view of the CIM as a metamodel in accordance with [76, 77]. The canonical nature of the CIM in giving rise to a range of submodels (profiles) that describe specific context-constrained applications enable it to also be described, in terms of a "model of models" which concurs with the Object Management Group (OMG) definition of a metamodel [78].

Harmonization with other existing information models, such as the IEC 61850 substation automation standard, to widen the integrated semantic standards framework supporting smart grid interoperability is seen as a priority. Gruber defines ontology as a "specification of a representational vocabulary for a shared domain of discourse—definitions of classes, relations, functions and other objects" [79]. As the scope of the CIM extends, placed at the heart of a harmonized federation of standards, it conforms to Gruber's definition of ontology for the smart grid domain. In this sense ontology supports the description of our knowledge about a domain, linking the IEC CIM to knowledge representation of the smart grid. This proposal is fundamental to the capacity of the CIM within the smart grid domain for knowledge representation and sharing. Chandrasekaran et al. argue it is not the representational vocabulary of the domain that defines the ontology as much as the conceptualizations that the vocabulary is intended to capture [80]. Careful analysis of the objects and their relationships within the domain is required to create the vocabulary and conceptualizations necessary for true representation of the domain reality and explains why CIM development is marked by much debate amongst domain experts as well as the importance of interoperability testing. For, as Uslar et al. indicate in [81], the strength of the CIM as a domain ontology not only depends on the expertise of the domain experts building it, but also extending its application to link control center ICT with field-automated devices while further developing the SIA.

6.2 Harmonization of the CIM with Other Standards

Regarding the link between the CIM and field devices, Santodomingo et al. [43] discuss the harmonization of the CIM with IEC 61850 (substation control language) using an ontology matching approach that required the use of Web Ontology Language (OWL) to represent semantic correspondences between the two standards. Their methodology was based on a top-down application of service descriptions that were used to annotate CIM metadata mentioned in [36]. The CIM and IEC 61850 ontologies supported a layered framework created to bridge the semantic definitions of their classes and attributes and the relationships of these entities. In this way the harmonization of these two standards, designed from different origins and for different purposes but now increasingly required to interoperate to develop smart grid functionality, is being established.

In another initiative, linking the CIM to IEC 60870 for high-voltage meter control and management is described [82]. The semantic alignment of these two standards is seen as part of the development of the Spanish smart grid. Mapping of the classes from the IEC 60870 protocol to the CIM was reported as straightforward and described in the sense of aligning one "service" to another. The sense of model classes representing services is another indication of the way the CIM lends itself to SOA. What is more, with the application of 'Simple Protocol and RDF Query Language' (SPARQL) the opportunity to interrogate RDF databases annotated with metadata makes possible the benefits of the Semantic Web paradigm. SPARQL is designed to seek out query matches with RDF triples for data stored in an RDF format such as CIM RDF XML. In this case the use of multiple namespaces, as metadata annotation of the meter data captured in CIM RDF XML, enabled the machine-to-machine (M2M) access required by the query. This methodology presents another example of how a layered architecture builds interoperability between the source of data and an end use. Whereas the use of Web Ontology Language (OWL) as a layer will focus on the resource description logic, SPARQL will focus on the knowledge representation of the RDF triple.

7 Information Integration and Knowledge Representation

Knowledge representation (KR) reinforces the possibility that the smart grid could herald our evolution in energy management from the "Age of Information" into the "Age of 'Intelligence." This vision, shared by the State Grid Corporation of China in their "Framework and Roadmap for Strong and Smart Grids" [83] would bring energy management within the realm of "Internet of Things" [2].

The pivotal importance of a semantic model to support understanding within KR is underlined by its central position in the GWAC Stack and therefore interoperability. Whether it is to provide a standard means for message exchange between PSAs operating with heterogeneous perspectives of the smart grid, or a

standardized interface specification, the CIM's platform independence and ability to support information integration is strengthened as a domain ontology. Neumann et al. recognize that the rapid growth of the CIM gives rise to questions about its scope and how best to apply it to a variety of roles ranging from information management and systems integration to information exchanges and application modeling [84]. It could eventually be viewed as a combination of ontologies made from the packages of UML classes of which it is composed, or as part of a federation of ontologies when considered amongst other smart grid standards as well as OPC and MultiSpeak. Either way, it has a range of applications that depend to a greater or lesser extent on the *richness* of the semantic language to convey the meaning of vocabulary and conceptualizations.

Quirolgico et al. in [85] assert self-managing systems in a domain comprising disparate applications, devices, components, and subsystems depend on a formal ontology to support knowledge interoperability and reasoning. While they were referring in this case to a computing and networks environment, these are some useful pointers to the evolving role of ICT within the smart grid. Not least the importance of full and formal semantic definitions within the vocabulary of the CIM as well as the capability of the languages used for construction and messaging to convey the intended meaning and knowledge representations within the ontology. This is in the interest of reducing the burden of a priori knowledge and reasoning on the part of the participating PSAs. In [86] Tang et al. make the point that the presence of ontology not only serves to promote knowledge sharing across different departments but also makes knowledge reuse available when there are changes to domain technologies through innovation. In [87] Sourouni et al. say ontologies can be employed at different levels of understanding. Examples of these range from contributing to the specification, reliability, and reusability of systems, through making data exchange easier, up to full functional interoperability of data and function.

Referring to the role of the IEC CIM within the "Semantic Understanding" layer of the GWAC Stack, we may then consider the need for richer information transport not simply supporting information interoperability but *knowledge interoperability* in future smart grid systems. The latter will depend on the ability of the encoding language to support the knowledge and reasoning constructs intended by the semantics and metadata of the ontology. Semantics are supported by the formality of the CIM descriptions and are combined with metadata using the schema definitions carried by the schema language for machine interpretation. The XML schema definition (XSD) is used to specify the structure and contents of an XML file, and therefore also serves to validate its contents. OWL is designed to explicitly represent the meanings of terms and their relationships in the vocabularies of ontologies. Thus for purposes requiring a higher degree of knowledge representation it may be necessary to consider as schema language, the use of the more powerful Web Ontology Language (OWL) over CIM RDFS expressions in future.

The value of framing the CIM as a metamodel in recognized terms is that we can utilize established methods from related domains such as Artificial Intelligence and Computer Science. For example we can envisage the CIM occupying "Level M2" of OMG's "Four Layer Hierarchy" [88]. Thus metadata models derived from

the CIM become instances of the data models belonging to PSAs at "Level M1", which in turn are composed of instances of data at "Level M0". Each level higher is an abstraction of the level below it and supports opportunities for integration of a wider range of conceptualizations of smart grid reality. Hargreaves et al. report on a methodology using this convention to create a CIM-based metamodel repository as a means of smart grid knowledge representation and development [89]. Alignment of different PSA conceptualizations of the same electrical network helps to optimize power utility processes and understanding of smart grid reality. As the repository integrates CIM-based metadata models aligned over boundaries marked by semantically common power system resources, a fuller knowledge representation of the smart grid reality comes into focus. While semantic commonality is a requisite for boundary alignment, identification of the same power system resource, derived from different PSA meta-conceptualizations, usually differs due to the different processes for data manipulation employed in each PSA. The issue of multiple identities attributed to the same object is a common feature in human nature where understanding the distinction between one object identity and another often depends on *context*. As the PSA metadata models are encoded in CIM RDF XML, the use of an XML namespace to "contextualise" each PSA representation provides the means to maintain resource identities in their original form while at the same time rendering them receptive to alignment within the repository. In this way an integrated metamodel repository can offer a rich environment for information integration and knowledge extraction across utility business domains as well as forming the basis of a central network model management system [59]. Such a resource will become of increasing importance with the integration of large-scale renewable power generation and storage facilities as the smart grid develops.

8 Conclusion

This chapter began by explaining the importance of the smart grid for integrating novel energy processes and technologies to deliver sustainable energy. Depending on interoperability to be reflexive to the changes in supply and demand as well as deliver energy with optimum reliability and economy we examined the centrality of the IEC CIM within model-driven interoperability processes. The value of semantic modeling in building ontology was then discussed leading to the proposal that combined with syntactic agreement provided by schema definitions and management of context provided by namespace, a metadata model repository can leverage the value of PSA data models into KR for better business understanding of smart grid reality. Using this design pattern, we can advance in accordance with interoperability at all levels, including data to data (D2D), model to model (M2M), application to application (A2A), and enterprise-to-enterprise (E2E) in building the vision for the smart grid to move from the age of information toward the age of intelligence.

References

1. Meadows DH, Meadows DI, Randers J, Behrens WW (1972) The limits of growth: a report to the club of Rome. Available via www.clubofrome.org/docs/limits.rtf
2. Barnaghi P, Wang W, Henson C, Taylor K (2012) Semantics for the internet of things: early progress and back to the future. Int J Semant Web Inf Syst 8:1–21
3. Banerjee A, Venkatasubramanian KK, Mukherjee T, Gupta SKS (2012) Ensuring Safety, Security, and Sustainability of Mission-Critical Cyber–Physical Systems. Proc IEEE 100:283–299
4. Hiskens IA (2010) What's smart about the smart grid? In: Design automation conference (DAC), 2010 47th ACM/IEEE, 2010, pp 937–939
5. Gao J, Xiao Y, Liu J, Liang W, Chen CLP (2012) A survey of communication/networking in Smart Grids. Future Gener Comput Syst 28(2):391–404
6. Brown HE, Suryanarayanan S, Heydt GT (2010) Some characteristics of emerging distribution systems considering the smart grid initiative. Electr J 23(6):64–75
7. Hargreaves N, Taylor G, Carter A (2012) Information standards to support application and enterprise interoperability for the smart grid. In: Power and energy society general meeting, 2012. IEEE, pp. 1–6
8. Amin SM, Wollenberg BF (2005) Toward a smart grid: power delivery for the 21st century. Power Energy Mag IEEE 3:34–41
9. US Department of Energy (2003) Grid 2030: a national vision for electricity's second 100 years. Department of Energy Office of Electric Transmission and Distribution
10. German Commission for Electrical, Electronic and Information Technologies of DIN (DKE) (2010) The German roadmap: e-energy/smart grid, VDE, 2010
11. Electricity Networks Strategy Group (2010) A smart grid routemap. ENSG, 2010
12. European Network of Transmission System Operators for Electricity (2010) European grid towards 2020 challenges and beyond, 1st edn. Research and Development Plan
13. Hashmi M, Hanninen S, Maki K (2011) Survey of smart grid concepts, architectures, and technological demonstrations worldwide. In: IEEE PES Conference on innovative smart grid technologies (ISGT Latin America), 2011, pp 1–7
14. European Commission (2011) Standardization mandate to European Standardisation Organisations (ESOs) to support European smart grid deployment. Directorate-General for Energy, M/490
15. Reed GF, Philip PA, Barchowsky A, Lippert CJ, Sparacino AR (2010) Sample survey of smart grid approaches and technology gap analysis. In: Innovative smart grid technologies conference Europe (ISGT Europe), 2010 IEEE PES, pp 1–10
16. National Institute of Standards and Technology (2012) NIST framework and roadmap for smart grid interoperability standards. Office of the National Coordinator for Smart Grid Interoperability, 2012. Release 2.0
17. Smart Grid-Coordination Group (2013) Smart grid reference architecture. CEN-CENELEC-ETSI, 2012, v3
18. GridWise Architecture Council (2008) GridWise® interoperability context setting framework, 2008
19. Ivanov C, Chury D (2009) European electric power system on the way towards implementation of CIM based data exchange format. In: Power and energy Society general meeting, 2009. PES'09. IEEE, pp 1–5
20. Wallom D, Turilli M, Taylor G, Hargreaves N, Martin A, Raun A, McMoran A (2011) myTrustedCloud: trusted cloud infrastructure for security-critical computation and data managment. In: IEEE third international conference on cloud computing technology and science (CloudCom), 2011, pp 247–254
21. Ambrosio R, Widergren S (2007) A framework for addressing interoperability issues. In: Power engineering society general meeting, 2007. IEEE, pp 1–5

22. Hargreaves N, Taylor G, Carter A, McMorran A (2011) Developing emerging standards for power system data exchange to enable interoperable and scalable operational modelling and analysis. In: Proceedings of 2011 46th international universities' power engineering conference (UPEC), pp 1–5
23. Tolk A (2010) Architecture constraints for interoperability and composability in a smart grid. In: Power and energy society general meeting, 2010. IEEE, pp 1–5
24. Ralyté J, Jeusfeld MA, Backlund P, Kühn H, Arni-Bloch N (2008) A knowledge-based approach to manage information systems interoperability. Inf Syst 33:754–784
25. Hug C, Front A, Rieu D, Henderson-Sellers B (2009) A method to build information systems engineering process metamodels. J Syst Softw 82(10):1730–1742
26. Joint Working Group on Standards for Smart Grids (2011) Final report of the JWG on standards for smart grids. CEN-CENELEC-ETSI
27. Britton JP, deVos AN (2005) CIM-based standards and CIM evolution. IEEE Trans Power Syst 20:758–764
28. Freund T, Niblett P (2008) ESB interoperability standards. IBM Corporation
29. Colan M (2004) Service oriented architecture expands the vision of web services. IBM, Part 1. http://www.ibm.com/developerworks/library/ws-soaintro.html
30. Soley R (2008) Service oriented architecture: Making the leap, leveraging model driven architecture and achieving software agility with BPM, SOA and MDA®. In: 19th Australian conference on software engineering, ASWEC 2008, pp 32–34
31. Balasubramanian K, Gokhale A, Karsai G, Sztipanovits J, Neema S (2006) Developing applications using model-driven design environments. Computer 39:33–40
32. McMorran AW, Ault GW, Elders IM, Foote CET, Burt GM, McDonald JR (2004) Translating CIM XML power system data to a proprietary format for system simulation. IEEE Trans Power Syst 19:229–235
33. McMorran AW, Ault GW, Morgan C, Elders IM, McDonald JR (2006) A common information model (CIM) toolkit framework implemented in Java. IEEE Trans Power Syst 21:194–201
34. Cao JZ, Zhou HJ, Tang YZ, Guo CX (2010) Realization of electric power enterprise application integration based on service oriented architecture. In: Power and energy society general meeting, 2010, IEEE, pp 1–5
35. Khare R, Khadem M, Moorty S, Methaprayoon K, Jun Z (2011) Patterns and practices for CIM applications. In: Power and energy society general meeting, 2011. IEEE, pp 1–8
36. Rohjans S, Uslar M, Juergen Appelrath H (2010) OPC UA and CIM: semantics for the smart grid. In: Transmission and distribution conference and exposition, 2010. IEEE PES, pp 1–8
37. S. A. Neumann and T. D. Nielsen, "CIM interoperability challenges. In: Power and energy society general meeting, 2010. IEEE, pp 1–5
38. Becker D, Saxton TL (2008) CIM standard for model exchange between planning and operations. In: Power and energy society general meeting—conversion and delivery of electrical energy in the 21st century, 2008. IEEE, pp 1–5
39. Lambert E (2011) CDPSM: common distribution power system model: when, why, what, how, who? In: Power systems conference and exposition (PSCE), 2011. IEEE/PES, pp 1–10
40. Electric Power Research Institute (1996) Guidelines for control center application program interfaces, technical report. EPRI, 1996. Available via http://my.epri.com/portal/server.pt?Abstract_id=TR-106324
41. Lee ST (1999) The EPRI common information model for operation and planning, vol 2. In: Power engineering society summer meeting, 1999. IEEE, pp 866–871
42. Pradeep Y, Seshuraju P, Khaparde SA, Warrier VS, Cherian S (2009) CIM and IEC 61850 integration issues: application to power systems. In: Power and energy society general meeting, PES '09. IEEE, pp 1–6
43. Santodomingo R, Rodríguez-Mondéjar JA, Sanz-Bobi MA (2010) Ontology matching approach to the harmonization of CIM and IEC 61850 standards. In: First IEEE international conference on smart grid communications (SmartGridComm), 2010, pp 55–60

44. Penya YK, Pena A, Esteban OK (2011) Semantic integration of IEC 60870 into CIM. In: IEEE International conference on smart grid communications (SmartGridComm), 2011, pp 428–433
45. de Vos A, Rowbotham CT (2001) Knowledge representation for power system modelling. In: 22nd IEEE power engineering society international conference on power industry computer applications, PICA 2001. Innovative computing for power—electric energy meets the market, 2001, pp 50–56
46. De Vos A, Widergren SE, Zhu J (2001) XML for CIM model exchange. In: 22nd IEEE power engineering society international conference on power industry computer applications, PICA 2001. Innovative computing for power—electric energy meets the market, pp 31–37
47. Electric Power Research Institute (2008) IntelliGrid methodology for developing requirements for energy systems, 1st edn. IEC PAS 62559
48. Smart Grid-Coordination Group (2011) Use case description. CEN CENELEC ETSI. Draft, version 0.55
49. Electric Power Research Institute (2013) Use case repository. Smart grid resource center. Available via http://smartgrid.epri.com/Repository/Repository.aspx
50. National Institute of Standards and Technology (2012) IKB use cases. NIST. Available via http://collaborate.nist.gov/twiki-sggrid/bin/view/SmartGrid/IKBUseCases
51. International Electrotechnical Commission (2010) IEC Smart grid standardisation roadmap, 1st edn. SMB Smart Grid Strategic Group (SG3)
52. International Electrotechnical Commission (2011) IEC 62357: TC 57 Architecture; reference architecture for power system information exchange, Part 1, 2nd edn. Draft, Revision 6
53. Rohjans S, Uslar M, Bleiker R, González J, Specht M, Suding T, Weidelt T (2010) Survey of smart grid standardization studies and recommendations. In: Smart grid communications (SmartGridComm), 2010 first IEEE international conference on, pp 583–588
54. Uslar M, Rohjans S, Bleiker R, González J, Specht M, Suding T, Weidelt T (2010) Survey of smart grid standardization studies and recommendations—part 2. In: Innovative smart grid technologies conference europe (Isgt Europe), 2010 IEEE PES, pp 1–6
55. International Electrotechnical Commission (2012) IEC 62357-1: TC 57 Architecture; reference architecture for power system information exchange, Part 1, Edition 1.0
56. National Institute of Standards and Technology (NIST), NIST identifies five 'foundational' smart grid standards. Available via http://www.nist.gov/public_affairs/releases/smartgrid_100710.cfm
57. European Union Commission Task Force for Smart Grids (2010) Functionalities of smart grids and smart meters, Expert group 1, Final deliverable
58. Institute of Electrical and Electronic Engineers (2011) 2030-2011—IEEE guide for smart grid interoperability of energy technology and information technology operation with the electric power system (EPS), End-use applications and loads, IEEE-SA standards board
59. Hargreaves NB (2013) Novel processes for smart grid information exchange and knowledge representation using the IEC common information model. Ph D Thesis, Brunel University, Uxbridge, UK
60. Electric Power Research Institute (2011) Common information model primer, EPRI, Edition 1.0
61. Uslar M, Specht M, Rohjans S, Trefke J, Vasquez González JM (2012) The common information model CIM, IEC 61968/61970 and 62325—a practical introduction to the CIM, Springer, Heidelberg
62. McMorran AW, Lincoln RW, Taylor GA, Stewart EM (2011) Addressing misconceptions about the common information model (CIM). In: Power and energy society general meeting, IEEE, pp 1–4
63. Goodrich ME (2009) Role of interoperability tests in standardizing CIM. In: Power & energy society general meeting, 2009. PES '09. IEEE, pp 1–4
64. Popovic DS, Varga E, Perlic Z (2007) Extension of the common information model with a catalog of topologies. IEEE Trans Power Syst 22:770–777

65. Hongbin S, Boming Z, Wenchuan W (2009) Applications and extension of CIM standard in chinese electrical power control centers. In: Power & energy society general meeting, 2009. PES '09. IEEE, pp 1–4
66. Becker D, Saxton TL, Goodrich M (2010) CIM standard for dynamic model exchange. In: Power and energy society general meeting, 2010 IEEE, pp 1–3
67. Nielsen TD, Neumann SA, King TL (2009) A methodology for managing model extensions when using the common information model for systems integration. In: Power & energy society general meeting, 2009. PES '09. IEEE, pp 1–5
68. Hargreaves N, Taylor G, Carter A (2012) Smart grid interoperability use cases for extending electricity storage modeling within the IEC common information model. In: Universities power engineering conference (UPEC), 2012 47th international, pp 1–6
69. Xu K-N, Cheng X-G, Xu X-J, Chong Y-S (2009) Model design of electric system state estimation based on CIM. In: Power and energy engineering conference, APPEEC 2009. Asia-Pacific, pp 1–4
70. Qin L, Guo Q, Hao C, Jin H (2011) A new wide area measurement system model based on common information model. In: Electric utility deregulation and restructuring and power technologies (DRPT), 2011 4th International Conference on, pp 1061–1066
71. Xu K, Zhou H (2012) Design of secondary equipment management system based on CIM. In: Power and energy engineering conference (APPEEC), 2012 Asia-Pacific, pp 1–4
72. Wang X, Van Ausdall S(2006) Representing business data semantics in CIM using UML. In: Power systems conference and exposition, 2006. PSCE '06. IEEE PES, pp 480–486
73. McMorran AW, deVos AN, Britton JP, Ault GW (2010) ZCIM: a compressed, modular CIM data exchange format. In: Power and energy society general meeting, IEEE
74. Hargreaves N, Pantea S, Taylor G, Irving M (2012) A critical comparison of approaches to resource name management within the IEC common information model. In: Innovative smart grid technologies (ISGT Europe), 2012 3rd IEEE PES international conference and exhibition on, 2012
75. Guizzardi G (2005) Ontological foundations for structural conceptual models. CTIT Ph D Thesis, Series No. 05-74, Enschede, The Netherlands
76. Seidewitz E (2003) What models mean. IEEE Softw 20:26–32
77. Gonzalez-Perez C, Sellers BH (2007) Modelling software development methodologies: a conceptual foundation. J Syst Softw 80:1778–1796
78. Object Management Group (2003) MDA Guide, OMG, document omg/03-06-01, Version 1.0.1
79. Gruber TR (1993) A translation approach to portable ontology specifications. Knowl Acquis 5:199–220
80. Chandrasekaran B, Josephson JR, Benjamins VR (1999) What are ontologies, and why do we need them? IEEE Intell Syst Appl 14:20–26
81. Uslar M, Rohjans S, Specht M, Vázquez JMG (2010) What is the CIM lacking? In: Innovative smart grid technologies conference europe (ISGT Europe), 2010 IEEE PES, pp 1–8
82. Penya YK, Pena A, Esteban OK (2011) Semantic integration of IEC 60870 into CIM. In: Smart grid communications (SmartGridComm), 2011 IEEE international conference on, pp 428–433
83. State Grid Corporation of China (2010) SGCC Framework and roadmap for strong and smart grid standards, Whitepaper
84. Neumann S, Britton J, DeVos A, Widergren S (2006) Use of the CIM Ontology. DistribuTech, 2006. Available via http://uisol.com/uisol/papers/Use_of_the_CIM_Ontology_DistribuTech_2006_Paper.pdf
85. Quirolgico S, Assis P, Westerinen A, Baskey M, Stokes E (2004) Toward a formal common information model ontology. In: Web information systems—wise 2004 workshops, proceedings, vol 3307. pp 11–21

86. Tang H, Song L (2011) Ontologies in financial services: Design and applications. In: Business management and electronic information (BMEI), 2011 international conference on, pp 364–367
87. Sourouni AM, Mouzakitis S, Kourlimpinis G, Askounis D, Velegrakis G (2009) E-business transactions modelling; an ontology-based repository. In: Interoperability for enterprise software and applications China, 2009. IESA '09. International conference on, 2009, pp 63–69
88. Henderson-Sellers B, Unhelkar B (2000) OPEN modeling with UML, 2000. Harlow, UK: Addison-Wesley, p 245
89. Hargreaves NB, Pantea SM, Taylor GA (2013) Foundations of a Metamodel Repository for use with the IEC Common Information Model. IEEE Trans Power Syst (Accepted, June 2013)